Dynamics of Gyroelastic Continua

by

Soroosh Hassanpour

A thesis
presented to the University of Waterloo
in fulfillment of the
thesis requirement for the degree of
Doctor of Philosophy
in
Mechanical and Mechatronics Engineering

Waterloo, Ontario, Canada, 2014

Declaration

I hereby declare that I am the sole author of this thesis. This is a true copy of the thesis, including any required final revisions, as accepted by my examiners.

I understand that my thesis may be made electronically available to the public.

Abstract

This work is concerned with the theoretical development of dynamic equations for gyroelastic systems which are dynamic systems with four basic types of continuous mechanical influences, *i.e.* inertia, elasticity, damping, and gyricity or stored angular momentum. Assuming unrestricted or large attitude changes for the axes of the gyros and utilizing two different theories of elasticity, *i.e.* the classical and micropolar theories of elasticity, the energy expressions and equations of motion for the undamped classical and micropolar gyroelastic continua are derived. Whereas the micropolar gyroelastic continuum model with extra coefficients and degrees of freedom is primarily developed to account for the asymmetric elasticity, it also proves itself to be more comprehensive in describing the actual gyroscopic system or structure.

The dynamic equations of the general three-dimensional gyroelastic continua are reduced to the case of a one-dimensional gyroelastic continua in the three-dimensional space, *i.e.* three-dimensional gyrobeams. Two different gyrobeam models are developed, one based on the classical beam torsion and bending theories and one based on the simplified micropolar beam torsion and bending theories. Finite element models corresponding to the classical and micropolar gyrobeams are built in MATLAB® and used for numerical analysis.

The classical and micropolar gyrobeam models are analyzed and compared, against the earlier gyrobeam models developed by other authors and also against each other, through numerical examples. It is shown that there are significant differences between the developed unrestricted classical gyrobeam model and the previously derived zero-order restricted classical gyrobeam models. These differences are more pronounced in the shorter beams and for the transverse gyricity case. The results also indicate that the unrestricted classical and micropolar gyrobeam models behave very diversely in a wide range of micropolar elastic constants even where the classical and micropolar elasticity models coincide.

As a foundation for development of the above-mentioned theories, the correct approach for simplification of the micropolar elasticity to the classical elasticity, the simple torsion and bending theories for micropolar beams, and the correct approximation of infinitesimal rotations or microrotations are derived and presented.

Acknowledgements

First, I would like to thank my supervisor Professor Glenn R. Heppler for his invaluable and never-ending guidance, support, and encouragement throughout the course of this research. Without his trust I would never have been in a position to pursue my doctorate degree. It has always been a great honour for me to work under his supervision.

Furthermore, I like to thank the members of my advisory committee, Professors Gregory Glinka, Hamid Jahed, Wei-Chau Xie, and Christopher J. Damaren for reading my thesis and their valuable comments. Special thank goes to Professor Christopher J. Damaren as the leader in the field of my research for accepting to be on my advisory committee. I also would like to acknowledge the financial assistance of the University of Waterloo and the Natural Science and Engineering Research Council of Canada (NSERC) for which I am grateful.

There are also many friends to thank for making my life in Waterloo, far away from my family and country, an enjoyable experience. They are too numerous to name, but I would particularly like to mention Saman Mohammadi, Omid Aminfar, Amir Fazeli, Mahsa Moshrefi, Saman Hosseini, Roozbeh Borjian, Babak Ebrahimi, Masoud Ansari, Mehrdad Iravani, Mohammad Pournazeri, Neda Darivandi, Vahid Fallah, and Ali Hosseini.

Last of all, but foremost, I wish to thank my wonderful parents, Fakhrossadat Mirenayat and Gholamhossein Hassanpour, and my darling wife, Sara Aghakazemjourabbaf, for their loving support and supporting love. Words cannot be brought to express my deepest gratitude for their untiring kindness, support, understanding, and encouragement.

To the most beautiful persons in my life

my parents, FAKHROSSADAT and GHOLAMHOSSEIN

and

my wife, SARA

Contents

List of Tables

List of Figures

Appendix

Chapter 1

Introduction

1.1 A historical overview of gyroelastic systems

With the general trend towards larger and lighter (and hence, more flexible) spacecraft, of which some have been proposed that may extend up to a kilometer in length and breadth, spacecraft shape and pose control problems have become increasingly important. An example of such spacecraft (usually very large truss structures with regular repetitive lattices) is shown in Figure 1.1. Generally, for such flexible spacecraft, three classes of control problems can be characterized; motion control (path tracking), attitude control, and shape control.

For stabilization (passive control) and attitude/shape control (active control) purposes, using "angular momentum devices" or "stored angular momentum", *i.e.* "momentum wheels" (having an angular momentum vector with fixed direction and time-varying magnitude) and "control-moment gyros" or "gyroscopes" (having an angular momentum vector with fixed magnitude and time-varying direction), mounted on rigid or flexible parts of spacecraft has been an attractive strategy due to abundantly available solar energy for actuator operation. Indeed, there are many advantages to using angular momentum devices (momentum wheels or control moment gyros) instead of force devices (thrusters) for controlling the spacecraft; they are efficient, light-weight, linear, and clean actuators which

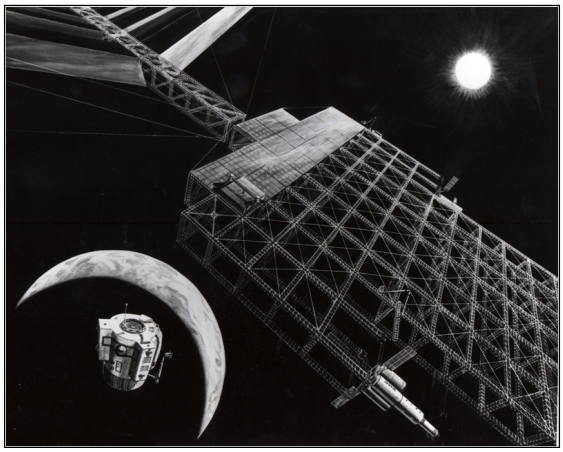

Figure 1.1: Conceptual schematic of a Solar Power Satellite (SPS) [1].

can be operated with accessible solar energy, do not need to be refueled, need very low power to apply considerable moment, and need relatively little maintenance. However, it is worthwhile to note that moment actuators are not applicable for path tracking control of spacecraft and force actuators are essential for this purpose. Generally, angular momentum devices can provide moment actuation to complement the force actuation of thrusters.

In this document, angular momentum devices will be referred to by the more general term "gyro" (an actively controlled device which has an angular momentum vector with time-varying magnitude and direction) and this work will be concerned with the dynamics of flexible space structures which use the gyros for stabilization and attitude/shape control.

Attempts to use spin-stabilizing of orbiting satellites began in 1958 with Explorer I (the first satellite of the United States) [2, 3]. Later, gyroscopic stabilization was extended further by the appearance of dual-spin spacecraft (gyrostat) and three-axis stabilized satellites [2]. Dynamics, control, and stability analysis of flexible spacecraft with spinning parts, often called gyroscopes, using discrete-coordinate representations, can be found in the works of Meirovitch *et al.* [4–7]. Likins, Gale, Cherchas, Hughes, and Sharpe [8–12] have also made considerable advances in this field. The space structures containing a/some gyro(s) as discrete stored angular momentum are referred to as "gyroscopic systems".

Aubrun and Margulies [13] addressed the use of actively controlled distributed gyros,

referred to as gyrodampers, for active vibration control of large structures. Considering the achievable damping factors, they showed the superiority of using many small gyrodampers to the use of one large gyrodamper. Hablani and Skelton [14, 15] investigated the effect of stored angular momentum, labeled as "gyroscopicity", on the characteristics of a flexible vehicle. D'Eleuterio and Hughes [2, 16] proposed the term "gyricity" for stored angular momentum in a flexible spacecraft and introduced the idea of flexible spacecraft with four basic types of mechanical influences, *i.e.* inertia (mass), elasticity (stiffness), damping (dissipation), and gyricity (gyroscope) influences. These factors can be modeled as both lumped parameters and distributed parameters. The space structures ideally modeled as systems with continuous distributions of inertia, elasticity, damping, and gyricity are referred to as "gyroelastic systems".

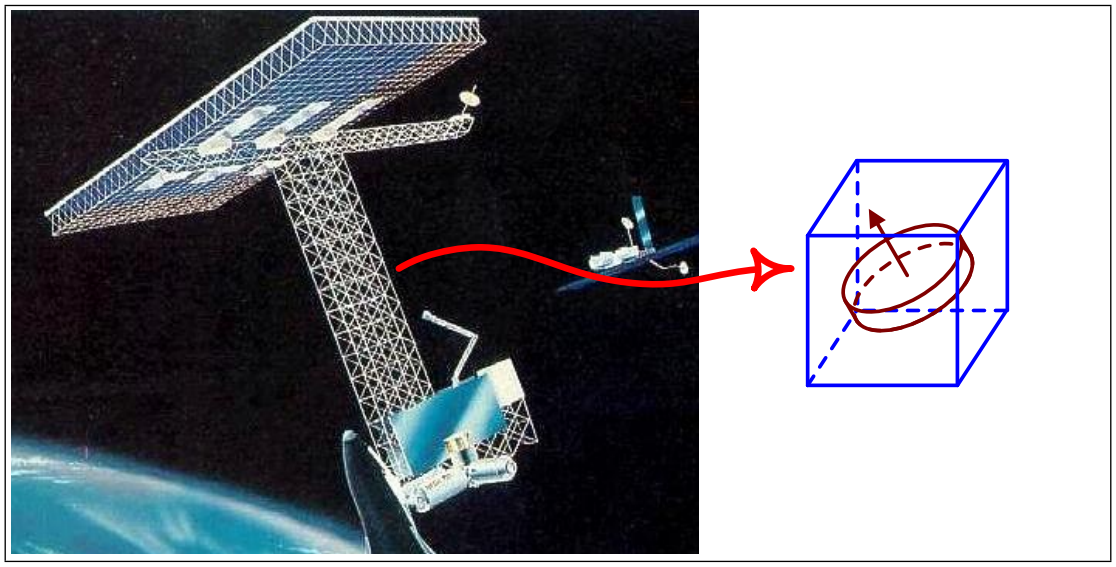

Figure 1.2: Schematic of a very large lattice structure [17] with the potential of housing a gyro in each lattice.

For clarity of the (continuous) gyroelastic systems idea, consider a very large truss structure with repetitive regular lattices. To avoid the complexity of working with a huge number of (thousands of) ordinary differential equations such a structure is usually idealized as an equivalent continuum with distributed parameters (continuous distributions

of inertia, elasticity, and damping) which will result in a few partial differential equations of motion [18]. Now assume that every lattice of this truss structure houses a small gyro at its center, and therefore, the structure possesses many (thousands of) gyros or angular momentum devices (see Figure 1.2). In the same way, to facilitate the dynamic analysis, these many gyros can be ideally treated as a distributed parameter, *i.e.* a continuous gyricity (stored angular momentum) distribution, and the real system can be modeled as an ideal (continuous) gyroelastic body (gyroelastic continuum or more briefly gyrocontinuum). In this way, it is assumed that every infinitesimal element of the equivalent continuum houses its own gyro and the gyricity is treated as a time-varying field quantity (similar to the commonly-time-invariant inertia, elasticity, and damping field quantities).

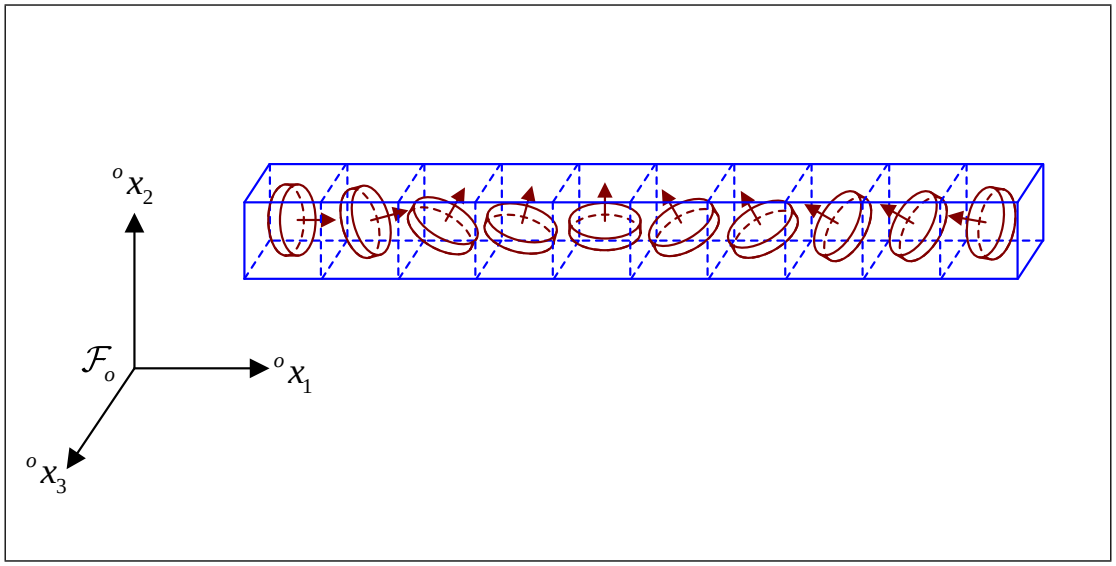

Figure 1.3: A gyroelastic beam.

An example of ideal gyroelastic systems, *i.e.* a gyroelastic beam or more briefly a gyrobeam, is shown in Figure 1.3 where the depicted discrete gyros are symbolic and represent the continuous gyricity distribution over the beam. It is noteworthy that the continuous gyroelastic continua (which is indeed an idealization of the real discrete gyroscopic structure) can be analyzed using either a continuous technique (such as the Fourier method) or a discrete technique (such as the finite element method). In addition, keep in mind

that (like every new idea) whereas the gyroelastic systems seems not to be realistic at the moment, there is the possibility that such systems become common as communication and solar power satellites in future. Indeed, the idea of gyroelastic systems is one of those cases when theory precedes the experiment.

The previous work on gyroelastic systems can be reviewed better by categorizing these systems based on the approaches utilized for modeling them. Recalling that the two essential parts of every gyroelastic system are elastic body and gyros (gyricity) distribution, the key parameter for categorizing the models of gyroelastic systems will be the methods and assumptions used for modeling the elasticity and gyricity.

The most popular theory for treating an elastic body (a continuum) is the linear "classical" (conventional) theory of elasticity, suitable for symmetric stress-strain analysis. However, a more complete theory is the linear "micropolar" (Cosserat) theory of elasticity, useful for asymmetric stress-strain analysis. This asymmetric theory of elasticity is specially desirable for modeling the gyroelastic systems where an asymmetric stress tensor is expected due to the presence of gyricity which results in a volume moment distribution over the elastic body. Whereas there are other elasticity theories, the linear classical and micropolar theories of elasticity will be used in this thesis for modeling the elastic body of gyroelastic systems. These two theories will be explained in more detail in Chapter 2.

On the other hand, the gyros can be treated in two different ways. One way is to assume that the axis of the gyros' spinning wheel rotates (with respect to the elastic body) just through very small angles; this results in the linear or "restricted" equations of motion after neglecting the higher order terms (note that there is no limit on the spin rotation of gyros' wheels around their axes of rotation). The other way is to consider no restriction on the rotation angles (*i.e.* rotation angles of the wheel axis and spin rotation of the wheel around this axis); this gives rise to the general or "unrestricted" equations of motion.

Consequently, four categories can be characterized for gyroelastic systems; "restricted classical gyroelastic systems", "restricted micropolar gyroelastic systems", "unrestricted classical gyroelastic systems", and "unrestricted micropolar gyroelastic systems". As an example, unrestricted micropolar gyroelastic systems or unrestricted micropolar gyrocontinua are those in which linear micropolar theory of elasticity is utilized for modeling the

elasticity and the gyros' rotation angles are considered to be unrestricted (large).

The work on "restricted classical gyroelastic systems" has been mostly done by Hughes, D'Eleuterio, and Damaren. D'Eleuterio and Hughes [2, 16, 19] examined the dynamics of gyroelastic systems (bodies with continuous distributions of inertia, elasticity, and gyricity) with a time-invariant distribution of gyricity and no dissipation. Their analysis contained two main classes; constrained dynamics and unconstrained dynamics. For each class, the equations of motion were derived, modal analysis was carried out, and the gyricity effect on vibrational frequencies and mode shapes was investigated. The modal parameters (modal coefficients), *i.e.*integrals of the mode shapes, were attained and a series of modal identities, which these modal parameters should satisfy, were proved.

D'Eleuterio and Hughes found that for a nonspinning unconstrained gyroelastic system (gyroelastic vehicle) the unconstrained motion can be described in terms of constrained modal parameters and such a vehicle can exhibit a scleromorphic mode (pseudorigid mode) with zero frequency and nonzero strain energy. In this mode, the gyroelastic vehicle rotates uniformly while having a deformed state [20, 21]. It is worthwhile to note that for unconstrained gyroelastic systems it was assumed that the orbital reference frame can be taken as inertial.

A series of numerical examples (elastic structures containing a/some flexible rod(s) with distributed gyricity) were presented by D'Eleuterio and Hughes to demonstrate the theoretical results [2, 16, 19–21]. Usually in these examples, the Rayleigh-Ritz method was utilized to obtain an approximate solution for the equations of motion (a set of partial differential equations). Moreover, D'Eleuterio derived the equations of motion of a gyroelastic vehicle from the force equilibrium (balance) equations of continuum mechanics and verified the equations previously obtained from the Newtonian mechanics and Hamilton's principle [22].

Damaren and D'Eleuterio [23, 24] extended the work to the case of lightly damped (linear viscous damping) gyroelastic continua and obtained the governing equations of motion. They used a first-order perturbation approach to find the eigenvalues and eigenfunctions of this system. In addition, using the results of the modal analysis and a modal expansion of the Riccati operator, they found the controllability conditions of gyroelastic systems

and solved the optimal control problem of these systems. The theoretical results were illustrated using a numerical example, *i.e.* a gyroelastic plate. They considered a gyricity distribution with time-varying direction and constant magnitude, for the control problem. The variation in direction of gyricity distribution was assumed to be small enough, that the governing equations of motion were linearizable. In other words, a distribution of control moment gyros was considered in which angular displacements of the gyros' axis were small. Results showed the effectiveness of the gyricity distribution for active shape control of flexible spacecraft in addition to passive shape control or shape stabilization.

Controllability and observability of the gyroelastic continua were studied further by Damaren and D'Eleuterio [25] and the concept of gyroelastic nodes and its relation to sensor locating were investigated. The modal parameters were used for expressing the controllability and observability conditions and it was mentioned that the results can be used for determination of the minimum number of required sensors and the optimal distribution of actuators. The bending of a uniform free-free rod was presented as a numerical example. Also, using a modal approximation method and considering a quadratic performance index, optimal control of gyroelastic systems was examined by Damaren and D'Eleuterio [26]. The optimization of actuators placement was addressed and simple examples, *i.e.* the classical gyroelastic beam and plate, were used for illustration of the results.

The dynamics and stability of a special case of the gyroelastic systems, *i.e.* an Euler-Bernoulli beam containing a single tip-rotor, was studied by Yamanaka *et al.* [27, 28]. Using the Rayleigh-Ritz approximate solution for the equations of motion, stability, static instability (divergence) and dynamic instability (flutter) regions were obtained and the possibility of gyroscopic stabilization was examined. Analogous analyses for cantilevered thin-walled beams with a tip-rotor were carried out by Song, Kwon, and Librescu [29–32].

Zee and Heppler [33] and Yamanaka *et al.* [34] examined the dynamics of a gyroelastic beam in which both the magnitude and direction of the gyricity distribution may vary in time and throughout the body. Again, the variation in direction of distributed gyricity was assumed to be small. Numerical examples were focused on the vibrational response of a gyroelastic beam to a gyricity distribution with ramped-up magnitude and fixed direction.

Peck and Cavender [35, 36] proposed that embedded angular momentum could be used

for structural adaptation, *e.g.* frequency shifting, modal coupling/decoupling, damping redistribution, steady-state deflection, and phase adjustment. They performed experiments on a testbed (2003 MSC/LOS) for validation of their results.

Whereas there are numerous papers on restricted classical gyroelastic systems, there is only one preliminary paper on "restricted micropolar gyroelastic systems". The idea of a micropolar gyroelastic system, *i.e.* a micropolar (Cosserat) continuum with lots of very small gyros, called a gyrocontinuum, was proposed by Brocato and Capriz [37]. Considering some simplifying assumptions and using an unusual notation (for solid mechanics), they derived the kinetic energy and inertia expressions and balance laws (*i.e.* conservation of mass and balance of momentum) for such a continuum. However, the examples provided by them illustrated the simple case of the linear elastic classical material containing a time-invariant gyricity distribution (*i.e.* gyros with fixed axis and constant spin rate), which was previously addressed by D'Eleuterio and Hughes [2, 16].

Finally, it is noteworthy that to the best of the author's knowledge there is no work on "unrestricted classical and micropolar gyroelastic systems".

1.2 Thesis objectives and scope

As can be concluded, in almost all of the previous works, despite the existence of a volume (body) moment distribution over the elastic body (due to the gyricity distribution) which results in an asymmetric stress tensor, the linear theory of classical (conventional, symmetric) elasticity has been used for modeling the elasticity in the gyroelastic systems. In these works, the volume moment distribution has been substituted by an equivalent volume force distribution producing the same displacement field. Therefore, there has not been any source for generating the asymmetry in the stress tensor. There is one paper by D'Eleuterio [22] which has briefly mentioned the asymmetry of the stress tensor, and there is one paper by Brocato and Capriz [37] which has suggested the idea of the micropolar gyrocontinua. However, in the former, due to considering a very simple theory of asymmetric elasticity with the classical constitutive relation (relating the symmetric portion of the stress tensor to the symmetric strain tensor), the effect of this asymmetry has been in-

cluded as an effective volume force and the results obtained previously (using the theory of symmetric classical elasticity and the concept of equivalent volume force distribution) have been repeated. The latter paper is unclear due to not using the usual notation of solid mechanics and not providing any example illustrating the attained results for the micropolar gyrocontinua. Hence, the first goal of this thesis is to utilize the more advanced theory of asymmetric elasticity, *i.e.* linear theory of micropolar (Cosserat) elasticity, for the derivation of the dynamic equations of gyroelastic continua, and to compare this formulation to that obtained from the classical theory of elasticity.

In addition, the previous works in the field of gyroelasticity have been based on assumptions of small deformations for the elastic body and small attitude changes for the gyros' axis which lead to restricted linearized equations of motion. In this thesis, while keeping the assumption of small elastic deformations, formulating the general (unrestricted) equations of motion for gyroelastic systems, when the rotation angles of gyros' axis are not small, is taken as the second goal.

The final goal is to study and compare the behaviors of the so-obtained unrestricted classical and micropolar gyroelastic continua which will be done via the numerical analysis of gyroelastic beams as a case study.

To sum up, it can be said that the focus of this thesis is on the development and analysis of ideal continuous gyroelastic models (or gyrocontinuum models) without studying the relationship between the practical or realistic discrete gyroscopic systems (structures) and these idealized continuous models, which is the concern in an "equivalent continuum modeling" or "equivalent continuous modeling".

1.3 Thesis overview

The work is arranged into seven chapters. After this chapter (Chapter 1), containing the introduction and the literature review, the background theories needed for the derivation of the gyroelastic continua equations of motion, *i.e.* the general classical and micropolar elasticity theories, dynamics of a gyro, and Hamilton's principle are reviewed in Chapter 2. The energy expressions and dynamic equations of general three-dimensional classical and

micropolar gyroelastic continua are derived in Chapter 3. As a simple case of gyroelastic continua, the three-dimensional classical and micropolar gyroelastic beams are addressed in Chapter 4 where, in addition to the energy expressions and dynamic equations, the nondimensionalization and finite element discretization of the dynamic equations are presented. By implementing the finite element discretized models in MATLAB®, the classical and micropolar gyroelastic beams are numerically analyzed and compared during Chapters 5 and 6. Finally, the summary of the work, conclusions, and future work recommendations are given in Chapter 7.

Affixed to these chapters, there are six appendices which provide the extra information to support the main chapters' theories. A detailed review of the micropolar elasticity theory, its associated apparent inconsistencies, and the correct approach for its simplification to the classical elasticity theory are given in Appendix A. As one of the key subjects of this work, the kinematics of rotating frames and bodies is reviewed in Appendix B where the main focus is on the kinematics of infinitesimal rotations and the correct approximation of them. A better understanding of the herein-developed micropolar beam torsion and bending theories is provided in Appendix C where the statics and dynamics of micropolar elastic beams (without any gyricity distribution) are numerically analyzed. The Euler-Bernoulli gyroelastic beam model, as a reference for investigation of current author's classical and micropolar gyroelastic beam models, is constructed and verified in Appendix D. As a groundwork for future work on the effects of the gyricity distribution shape, a few gyroelastic beams with non-uniform gyricity distributions are quickly presented in Appendix E. Finally, Appendix F provides the conventions and definitions for the notations and symbols used in this text.

Chapter 2

Background Theories

2.1 Introduction

As mentioned before, the essential parts of a gyrocontinuum are the elastic body and the gyricity distribution. Therefore, studying them is a preliminary step for derivation of the gyrocontinuum dynamic equations. This chapter is devoted to the preparation of this background study. More precisely, the theories of elasticity utilized in this thesis to represent the elasticity of a gyrocontinuum are reviewed and useful equations are derived. Then, dynamics of a gyro mounted in a body element as a representation for the gyricity distribution is taken into account and the corresponding equations are developed. Finally, application of Hamilton's principle and the calculus of variations for dynamic formulation of a general continuous mechanical system is studied.

2.2 Theories of elasticity

When dealing with an elastic system, one of the most important steps in the derivation of the equations of motion is selection of the proper theory of elasticity. The theory of elasticity is utilized to relate the stress field, external force/moment distributions, deformation (strain) field, and displacement field to each other. It makes it possible to obtain

dynamic partial differential equations (PDEs) in terms of just the displacement field variables and external force/moment distributions. Selection of the proper theory of elasticity must be made based on the nature of deformation (small or large deformation, dependent or independent rotation field), the material properties (linear or nonlinear, isotropic or anisotropic), and the nature of the stress (symmetric or asymmetric, force stress or force/couple stress).

The most popular elasticity theory is the classical theory of linear elasticity [38–41] in which strain terms are small compared to unity, and the microrotation field vector is dependent on the displacement field vector. In addition, it is assumed that internal interactions between neighboring elements of an elastic body occur only by means of the force stress (or simply stress) vector (elements of the stress tensor related to an interface form the stress vector at any point). These assumptions lead to symmetric stress and strain tensors and hence, this theory is also known as the symmetric theory of elasticity.

Actually, in the classical theory of elasticity, the presence of a volume moment distribution over the elastic body will result in an asymmetric stress tensor. For such a case, the conventional (or classical) constitutive law, relating the symmetric part of the stress tensor to the symmetric strain tensor, can be utilized to determine the symmetric part of the stress tensor. However, there will be no constitutive relation for determining the antisymmetric (or skew-symmetric) part of the stress tensor. Instead, this antisymmetric part can be determined from the angular momentum balance equation, relating the antisymmetric part of the stress tensor to the volume moment distribution. Taking into account the linear momentum balance equation, decomposing the stress tensor into its symmetric and antisymmetric parts, and using the angular momentum balance equation to substitute the antisymmetric part, the effect of the volume moment distribution will appear as an effective (equivalent) force in the linear momentum balance equation. Hence, the antisymmetric part of the stress tensor will not appear directly in the equations of motion. This extended form of the classical theory of elasticity, in which a volume moment distribution is used to determine the antisymmetric part of the stress tensor and is simply included as an equivalent volume force distribution in the linear momentum balance equation, can be regarded as the simplest theory of asymmetric elasticity and can be referred to as the classical theory of asymmetric elasticity. However, for simplicity and to avoid

misunderstanding, in this text it is referred to as just classical theory of elasticity and in fact this classical theory of asymmetric elasticity is meant whenever the phrase "classical theory of elasticity" is used.

The classical theory of elasticity produces acceptable results in numerous engineering problems with various structural materials. However, for the cases with large stress gradients (*e.g.* in the vicinity of holes and cracks) or materials with significant microstructure contribution (*e.g.* composites, polymers, soil, and bone), the classical theory of elasticity fails to produce acceptable results [42]. In addition, it is not an appropriate theory for asymmetric stress-strain analysis (which is the case when dealing with an elastic body under the action of a volume moment distribution).

To improve the results of the classical theory of elasticity, Voigt added an independent couple stress vector to the previous force stress vector to describe the interactions between neighboring elements of an elastic body [42,43]. Voigt's theory (couple-stress elasticity) was developed further by the brothers E. and F. Cosserat who made another step and suggested independent displacement and microrotation field vectors for describing the deformations of an elastic body [42]. These assumptions (existence of the couple stress tensor and independency of the displacement and microrotation fields) lead to six degrees of freedom (DOFs) for every element of the body and a description of stress and strain in terms of asymmetric tensors. The (geometrically nonlinear) Cosserat theory of elasticity, formulated in an unclear manner, was further developed in a restricted linearized setting by other scholars later. Notably, Eringen extended the theory to include microinertia effects and renamed that into the micropolar theory of elasticty [42,44]. Nowadays, the linear theory is known as linear theory of micropolar, Cosserat, or asymmetric elasticity. A complementary discussion on characteristics of the "micropolar theory of elasticity" is given in Appendix A.

To provide a brief overview of the three-dimensional (3D) linear theory of micropolar elasticity, consider a general homogeneous, isotropic, and centrally symmetric elastic body (which means the elastic properties of the body are independent of the position, direction, and inversion of the coordinate system) occupying a volume domain V in $\mathbb{R}^3$, bounded by surface S. A body frame $\mathcal{F}_b$ and a position vector $\underset{\rightarrow}{p}$ (described with respect to the inertial frame $\mathcal{F}_o$) correspond to each representative infinitesimal element of the body. Frames $\mathcal{F}_b$ are body fixed frames which move and rotate with (are attached to) the elements of the

body (see Figure 2.1).

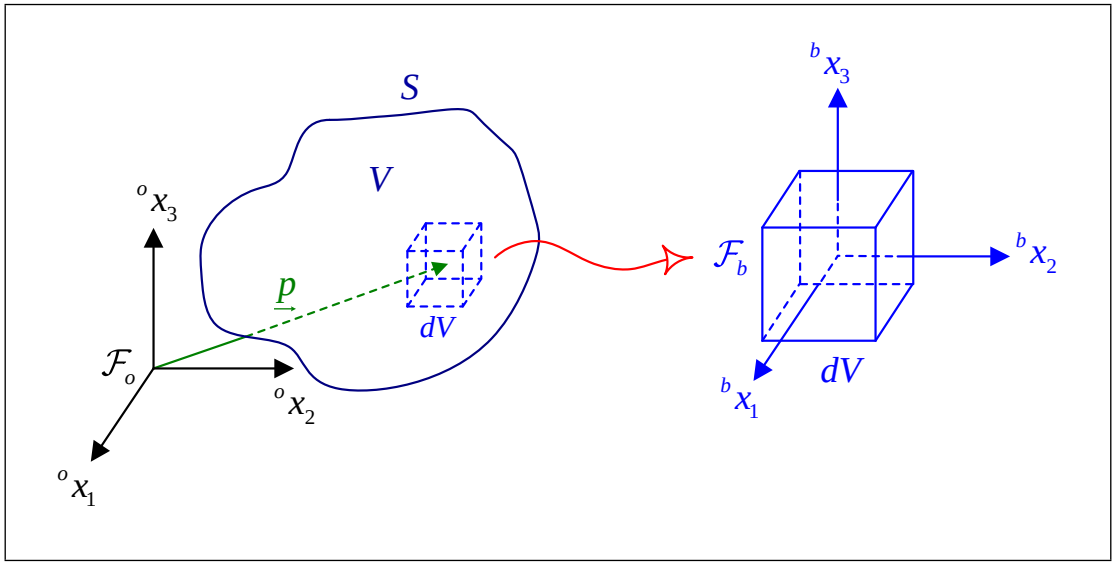

Figure 2.1: A general elastic body and its representative infinitesimal element.

Assume that the body undergoes a motion and deformation due to the action of external volume, surface, line, and point forces/moments ($\underset{\rightarrow}{f}^V$, $\underset{\rightarrow}{f}^S$, $\underset{\rightarrow}{f}^L$, $\underset{\rightarrow}{f}^P$, $\underset{\rightarrow}{m}^V$, $\underset{\rightarrow}{m}^S$, $\underset{\rightarrow}{m}^L$, and $\underset{\rightarrow}{m}^P$, respectively). As mentioned previously, the internal loading at each point of the body can be represented by means of an asymmetric force stress tensor $\underset{\leftrightarrow}{\sigma}$ and an asymmetric couple stress tensor $\underset{\leftrightarrow}{\chi}$ of the forms (see Figure 2.2):

$$\underline{\underline{\boldsymbol{\sigma}}} = \begin{bmatrix} \sigma_{11} & \sigma_{12} & \sigma_{13} \\ \sigma_{21} & \sigma_{22} & \sigma_{23} \\ \sigma_{31} & \sigma_{32} & \sigma_{33} \end{bmatrix} = [\sigma_{ij}]\,, \qquad \underline{\underline{\boldsymbol{\chi}}} = \begin{bmatrix} \chi_{11} & \chi_{12} & \chi_{13} \\ \chi_{21} & \chi_{22} & \chi_{23} \\ \chi_{31} & \chi_{32} & \chi_{33} \end{bmatrix} = [\chi_{ij}] \tag{2.1}$$

The motion and deformation of the body can be expressed by a displacement field vector $\underset{\rightarrow}{u}(\underset{\rightarrow}{p}, t)$ and an independent microrotation field vector $\underset{\rightarrow}{\vartheta}(\underset{\rightarrow}{p}, t)$ (see Appendix B regarding the characteristics of this microrotation vector), assuming that the elastic body has no (large)

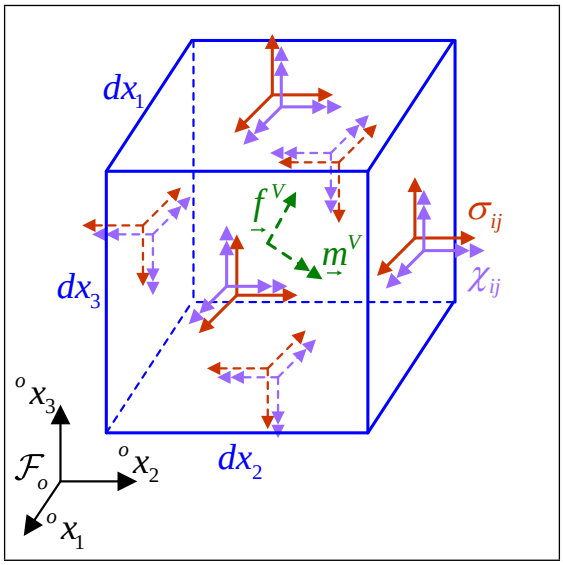

Figure 2.2: Free body diagram of a representative element in a micropolar elastic body.

rigid body rotation. This leads to the description of the asymmetric strain tensor $\underset{\leftrightarrow}{\varepsilon}$:

$$\underset{\equiv}{\boldsymbol{\varepsilon}} = \begin{bmatrix} \varepsilon_{11} & \varepsilon_{12} & \varepsilon_{13} \\ \varepsilon_{21} & \varepsilon_{22} & \varepsilon_{23} \\ \varepsilon_{31} & \varepsilon_{32} & \varepsilon_{33} \end{bmatrix} = [\varepsilon_{ij}] = \underset{\_}{\boldsymbol{\nabla}}\, \underset{\_}{\boldsymbol{u}}^{\mathrm{T}} + \underset{\equiv}{\boldsymbol{\vartheta}}^{\times}, \qquad \varepsilon_{ij} = u_{j,i} - \epsilon_{ijk}\, \vartheta_k \tag{2.2}$$

and the asymmetric twist (wryness or torsion) tensor $\underset{\leftrightarrow}{\tau}$:

$$\underset{\equiv}{\boldsymbol{\tau}} = \begin{bmatrix} \tau_{11} & \tau_{12} & \tau_{13} \\ \tau_{21} & \tau_{22} & \tau_{23} \\ \tau_{31} & \tau_{32} & \tau_{33} \end{bmatrix} = [\tau_{ij}] = \underset{\_}{\boldsymbol{\nabla}}\, \underset{\_}{\boldsymbol{\vartheta}}^{\mathrm{T}}, \qquad \tau_{ij} = \vartheta_{j,i} \tag{2.3}$$

In the linear theory of micropolar elasticity, the constitutive relations have the forms:

$$\begin{aligned} \sigma_{ij} &= \Big(\mu + \kappa\Big)\, \varepsilon_{ij} + \Big(\mu - \kappa\Big)\, \varepsilon_{ji} + \lambda\, \varepsilon_{kk}\, \mathbb{1}_{ij} \\ \chi_{ij} &= \Big(\gamma + \beta\Big)\, \tau_{ij} + \Big(\gamma - \beta\Big)\, \tau_{ji} + \alpha\, \tau_{kk}\, \mathbb{1}_{ij} \end{aligned} \tag{2.4}$$

where μ and λ are the Lamé coefficients (μ is also known as the shear modulus) as in the classical theory of elasticity, and κ, γ, β, and α are referred to as the micropolar (Cosserat)

elastic constants. A more detailed explanation of the micropolar elastic constants can be found in Appendix A.

Considering the free-body diagram shown in Figure 2.2 the (first-order) differential form of the micropolar equations of motion in terms of force stresses and couple stresses are:

$$\begin{aligned} \sigma_{ji,j} + f_i^V &= \rho_{ij}^V \, \ddot{u}_j \\ \epsilon_{ijk} \, \sigma_{jk} + \chi_{ji,j} + m_i^V &= \imath_{ij}^V \, \ddot{\vartheta}_j \end{aligned} \tag{2.5}$$

where $\underset{\leftrightarrow}{\rho}^V$ ($\underset{\leftrightarrow}{\rho}^V = \rho^V \, \underset{\leftrightarrow}{\mathbb{1}}$, and ρ^V is the volume mass density of the body) is the tensor of translational inertia per unit volume for the elastic body, $\underset{\leftrightarrow}{\imath}^V$ (usually $\underset{\leftrightarrow}{\imath}^V = \imath^V \, \underset{\leftrightarrow}{\mathbb{1}}$, and $\imath^V$ is the volume microinertia density [42]) is the tensor of body microrotational inertia per unit volume, and $\underset{\rightarrow}{\ddot{\vartheta}}$ is the angular acceleration field vector defined as:

$$\underset{\rightarrow}{\ddot{\vartheta}} = \frac{d^2}{dt^2}\left(\underset{\rightarrow}{\vartheta}\right), \qquad \underset{\sim}{\ddot{\boldsymbol{\vartheta}}} = \frac{d^2}{dt^2}\left(\underset{\sim}{\boldsymbol{\vartheta}}\right) \tag{2.6}$$

It is worthwhile to mention that the body angular velocity vector is:

$$\underset{\rightarrow}{\dot{\vartheta}} = \frac{d}{dt}\left(\underset{\rightarrow}{\vartheta}\right), \qquad \underset{\sim}{\dot{\boldsymbol{\vartheta}}} = \frac{d}{dt}\left(\underset{\sim}{\boldsymbol{\vartheta}}\right) \tag{2.7}$$

Also, the second relation in Eq. (2.5) can be rewritten into the following form:

$$\sigma_{ij} - \sigma_{ji} + \epsilon_{ijk}\left(\chi_{lk,l} + m_k^V\right) = \epsilon_{ijk} \, \imath_{kl}^V \, \ddot{\vartheta}_l \tag{2.8}$$

Using the constitutive relations of Eq. (2.4) and the definition of the strain and twist tensors (given by Eqs. (2.2) and (2.3)), the dynamic equations given by Eq. (2.5) can be formulated in terms of the displacement and microrotation vectors as:

$$\begin{aligned} \left(\mu + \kappa\right)\left(\underset{\rightarrow}{\nabla} \cdot \underset{\rightarrow}{\nabla}\right)\underset{\rightarrow}{u} + \left(\mu - \kappa + \lambda\right)\underset{\rightarrow}{\nabla}\left(\underset{\rightarrow}{\nabla} \cdot \underset{\rightarrow}{u}\right) + 2\,\kappa\,\underset{\leftrightarrow}{\nabla}^{\times} \cdot \underset{\rightarrow}{\vartheta} + \underset{\rightarrow}{f}^V &= \underset{\leftrightarrow}{\rho}^V \cdot \underset{\rightarrow}{\ddot{u}} \\ \left(\left(\gamma + \beta\right)\underset{\rightarrow}{\nabla} \cdot \underset{\rightarrow}{\nabla} - 4\,\kappa\right)\underset{\rightarrow}{\vartheta} + \left(\gamma - \beta + \alpha\right)\underset{\rightarrow}{\nabla}\left(\underset{\rightarrow}{\nabla} \cdot \underset{\rightarrow}{\vartheta}\right) + 2\,\kappa\,\underset{\leftrightarrow}{\nabla}^{\times} \cdot \underset{\rightarrow}{u} + \underset{\rightarrow}{m}^V &= \underset{\leftrightarrow}{\imath}^V \cdot \underset{\rightarrow}{\ddot{\vartheta}} \end{aligned} \tag{2.9}$$

The system of governing dynamic equations of a micropolar elastic body in Eq. (2.9) is a system of coupled linear PDEs with six unknowns; three displacements and three independent microrotations. These linear governing equations can be written in tensor form as:

$$\begin{aligned} \mathcal{M}_{ij}^{\text{lin}} \, \ddot{u}_j + \mathcal{K}_{ij}^{\text{lin}} \, u_j + \mathcal{C}_{ij}^{\text{lin}} \, \vartheta_j &= f_i^V \\ \mathcal{M}_{ij}^{\text{ang}} \, \ddot{\vartheta}_j + \mathcal{K}_{ij}^{\text{ang}} \, \vartheta_j + \mathcal{C}_{ij}^{\text{ang}} \, u_j &= m_i^V \end{aligned} \tag{2.10}$$

where the inertia operators are:

$$\begin{aligned} \mathcal{M}_{ij}^{\text{lin}} &= \rho_{ij}^{V} = \rho^{V}\, \mathbb{1}_{ij} \\ \mathcal{M}_{ij}^{\text{ang}} &= \imath_{ij}^{V} \end{aligned} \tag{2.11}$$

and the stiffness operators have the form:

$$\begin{aligned} \mathcal{K}_{ij}^{\text{lin}} &= -\left(\mu+\kappa\right)\frac{d^2}{dx_k\,dx_k}\,\mathbb{1}_{ij} - \left(\mu-\kappa+\lambda\right)\frac{d^2}{dx_i\,dx_j} \\ \mathcal{K}_{ij}^{\text{ang}} &= -\left(\left(\gamma+\beta\right)\frac{d^2}{dx_k\,dx_k} - 4\,\kappa\right)\mathbb{1}_{ij} - \left(\gamma-\beta+\alpha\right)\frac{d^2}{dx_i\,dx_j} \end{aligned} \tag{2.12}$$

and the circulatory operators are:

$$\mathcal{C}_{ij}^{\text{lin}} = \mathcal{C}_{ij}^{\text{ang}} = 2\,\kappa\,\epsilon_{ijk}\,\frac{d}{dx_k} \tag{2.13}$$

The above are actually the elements of the linear mass, stiffness, and circulatory tensor operators [45] respectively.

Finally, based on the linear theory of micropolar elasticity, the elastic energy (*i.e.* the total strain energy) $\mathcal{U}_{\text{e}}$ takes the form:

$$\mathcal{U}_{\text{e}} = \int_{V} \mathcal{U}_{\text{e}}^{V}\, dV, \qquad \mathcal{U}_{\text{e}}^{V} = \frac{1}{2}\,\sigma_{ij}\,\varepsilon_{ij} + \frac{1}{2}\,\chi_{ij}\,\tau_{ij} \tag{2.14}$$

where $\mathcal{U}_{\text{e}}^{V}$ is the elastic (or strain) energy density.

Considering the assumptions of the classical theory of elasticity [38–41] the general equations derived from the micropolar theory of elasticity, *i.e.* Eqs. (2.1)–(2.14), can be reduced to the well-known equations of the classical elasticity. Based on the classical theory of elasticity, the internal loading at each point of the body is represented by means of the force stress tensor, there is no couple stress and no microrotational inertia, and the microrotation and displacement field vectors are dependent (indeed, as shown in Appendix A, the microrotation vector is identical with the macrorotation vector which is dependent on the displacement vector). The dependency between the microrotation and displacement

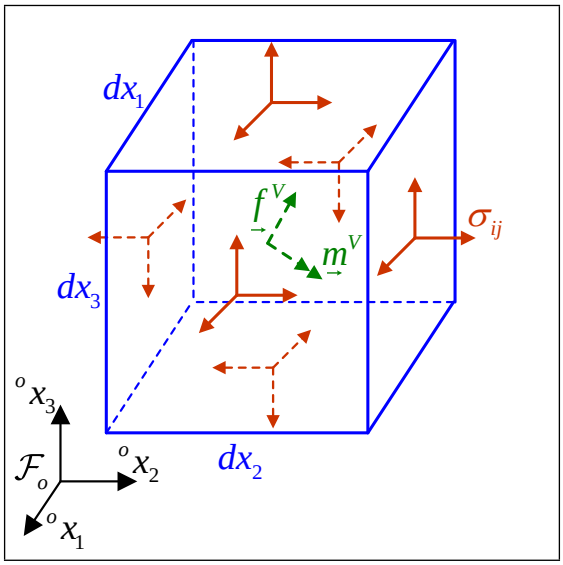

Figure 2.3: Free body diagram of a representative element in a classical elastic body.

field vectors and their time derivatives can be described by the following relations:

$$\begin{aligned} \underset{\rightarrow}{\vartheta} &= \frac{1}{2} \underset{\leftrightarrow}{\nabla}^{\times} \cdot \underset{\rightarrow}{u} \\ \dot{\underset{\rightarrow}{\vartheta}} &= \frac{1}{2} \underset{\leftrightarrow}{\nabla}^{\times} \cdot \dot{\underset{\rightarrow}{u}} \\ \ddot{\underset{\rightarrow}{\vartheta}} &= \frac{1}{2} \underset{\leftrightarrow}{\nabla}^{\times} \cdot \ddot{\underset{\rightarrow}{u}} \end{aligned} \tag{2.15}$$

Note that the tensor $\underset{\leftrightarrow}{\vartheta}^{\times}$ is the rotation tensor mentioned in the books on the classical theory of elasticity. These assumptions lead to a description of the asymmetric force stress (see Figure 2.3) and the symmetric strain tensors as follows:

$$\underset{\equiv}{\boldsymbol{\sigma}} = \begin{bmatrix} \sigma_{11} & \sigma_{12} & \sigma_{13} \\ \sigma_{21} & \sigma_{22} & \sigma_{23} \\ \sigma_{31} & \sigma_{32} & \sigma_{33} \end{bmatrix} = [\sigma_{ij}] \tag{2.16}$$

$$\underset{\equiv}{\boldsymbol{\varepsilon}} = \begin{bmatrix} \varepsilon_{11} & \varepsilon_{12} & \varepsilon_{13} \\ \varepsilon_{21} & \varepsilon_{22} & \varepsilon_{23} \\ \varepsilon_{31} & \varepsilon_{32} & \varepsilon_{33} \end{bmatrix} = [\varepsilon_{ij}] = \frac{1}{2} \left(\underline{\boldsymbol{\nabla}}\, \underline{\boldsymbol{u}}^{\mathrm{T}} + \left(\underline{\boldsymbol{\nabla}}\, \underline{\boldsymbol{u}}^{\mathrm{T}} \right)^{\mathrm{T}} \right), \qquad \varepsilon_{ij} = \frac{1}{2} \left(u_{i,j} + u_{j,i} \right) \tag{2.17}$$

Recall that in the classical elasticity theory the couple stress tensor $\underset{\leftrightarrow}{\chi}$ is zero. Moreover, though the twist tensor $\underset{\leftrightarrow}{\tau}$ is not zero (indeed $\underset{\leftrightarrow}{\tau}$ can be still given by Eq. (2.3) where $\underset{\rightarrow}{\vartheta}$ is obtained from Eq. (2.15)), there is no need to define that as it will not appear in the formulation of the classical elasticity.

In the linear theory of classical elasticity the only constitutive relation is of the form (compare this to Eq. (2.4)):

$$\sigma^{s}_{ij} = \frac{1}{2}\left(\sigma_{ij} + \sigma_{ji}\right) = 2\,\mu\,\varepsilon_{ij} + \lambda\,\varepsilon_{kk}\,\mathbb{1}_{ij} \tag{2.18}$$

where μ and λ are the Lamé coefficients. In comparison to Eq. (2.5), from the free-body diagram shown in Figure 2.2 the differential form of the dynamic equations in terms of force stresses will be derived as:

$$\begin{aligned} \sigma_{ji,j} + f^{V}_{i} &= \rho^{V}_{ij}\,\ddot{u}_{j} \\ \epsilon_{ijk}\,\sigma_{jk} + m^{V}_{i} &= 0 \end{aligned} \tag{2.19}$$

Again, the second relation in Eq. (2.19) can be rearranged into the following form:

$$\sigma_{ij} - \sigma_{ji} + \epsilon_{ijk}\,m^{V}_{k} = 0 \tag{2.20}$$

Using the constitutive relation in Eq. (2.18), the dynamic equations given by Eqs. (2.19) and (2.20) can be combined and formulated in terms of the displacement vector as:

$$\mu\left(\underset{\rightarrow}{\nabla}\cdot\underset{\rightarrow}{\nabla}\right)\underset{\rightarrow}{u} + \left(\mu+\lambda\right)\underset{\rightarrow}{\nabla}\left(\underset{\rightarrow}{\nabla}\cdot\underset{\rightarrow}{u}\right) + \underset{\rightarrow}{f}^{V} + \frac{1}{2}\,\underset{\leftrightarrow}{\nabla}^{\times}\cdot\underset{\rightarrow}{m}^{V} = \underset{\leftrightarrow}{\rho}^{V}\cdot\underset{\rightarrow}{\ddot{u}} \tag{2.21}$$

Here, the system of governing dynamic equations is a relatively simpler system of linear PDEs (compared to Eq. (2.9)) with the three elements of the displacement vector as independent unknowns.

Once more, the tensor form of the linear equations of motion for a classical elastic body can be written as:

$$\mathcal{M}^{\text{lin}}_{ij}\,\ddot{u}_{j} + \mathcal{K}^{\text{lin}}_{ij}\,u_{j} = f^{V}_{i} + \frac{1}{2}\,\epsilon_{ijk}\,m^{V}_{k\,,j} \tag{2.22}$$

where:

$$\mathcal{M}^{\text{lin}}_{ij} = \rho^{V}_{ij} = \rho^{V}\,\mathbb{1}_{ij} \tag{2.23}$$

and:

$$\mathcal{K}_{ij}^{\text{lin}} = -\mu \frac{d^2}{dx_k\, dx_k}\, \mathbb{1}_{ij} - \Big(\mu + \lambda\Big) \frac{d^2}{dx_i\, dx_j} \tag{2.24}$$

are elements of the linear mass and stiffness tensor operators. Finally, in the linear theory of classical elasticity, the elastic (strain) energy $\mathcal{U}_{\text{e}}$ takes the following form:

$$\mathcal{U}_{\text{e}} = \int_V \mathcal{U}_{\text{e}}^V \, dV, \qquad \mathcal{U}_{\text{e}}^V = \frac{1}{2}\, \sigma_{ij}\, \varepsilon_{ij} = \frac{1}{2}\, \sigma_{ij}^{\text{s}}\, \varepsilon_{ij} \tag{2.25}$$

Notice that based on Eq. (2.21), in the classical theory of elasticity, the continuous volume moment $\underset{\rightarrow}{m}^V$ can be substituted by an effective volume force $\underset{\rightarrow}{f}^V$ defined as:

$$\underset{\rightarrow}{f}^V = \frac{1}{2}\, \underset{\leftrightarrow}{\nabla}^{\times} \cdot \underset{\rightarrow}{m}^V \tag{2.26}$$

This is the effective or equivalent volume force distribution mentioned before. Note that for Eq. (2.26) to be true, the volume moment $\underset{\rightarrow}{m}^V$ should be differentiable over all the domain V. In addition, it should vanish on the boundary surface S, or the volume moments on the boundary surface S should be substituted with proper boundary surface forces.

A summary of the equations mentioned in this section can be found in Table 2.1. It is noteworthy that the similarities between the subjects related to the force stresses and displacements (in the classical or micropolar theory of elasticity) and those related to the couple stresses and microrotations (in the micropolar theory of elasticity), *i.e.* parallel or analogous forms of the definitions and equations mentioned so far, suggests a parallel terminology to be used for denotation of these subjects. The dual terminologies used in this text are listed in Table 2.2. Note that in Table 2.2 there are new terms which will be discussed and used later in the following (see for example Chapter 4 or Appendix A).

Table 2.1: A summary comparison of the classical and micropolar theories of elasticity.

Subject	**Classical Theory of Elasticity**	**Micropolar Theory of Elasticity**
Assumptions	$\vartheta_i = -\frac{1}{2}\,\epsilon_{ijk} u_{j,k}$	independent u_i and ϑ_i
	existence of just σ_{ij}, and $\chi_{ij} = 0$	existence of both σ_{ij} and χ_{ij}
Deformation Tensor(s)	$\varepsilon_{ij} = \frac{1}{2}\,(u_{i,j} + u_{j,i})$	$\varepsilon_{ij} = u_{j,i} - \epsilon_{ijk}\,\vartheta_k$ $\tau_{ij} = \vartheta_{j,i}$
Constitutive Relation(s)	$\frac{1}{2}\,(\sigma_{ij} + \sigma_{ji}) = 2\,\mu\,\varepsilon_{ij} + \lambda\,\varepsilon_{kk}\,\mathbb{1}_{ij}$	$\sigma_{ij} = (\mu + \kappa)\,\varepsilon_{ij} + (\mu - \kappa)\,\varepsilon_{ji} + \lambda\,\varepsilon_{kk}\,\mathbb{1}_{ij}$ $\chi_{ij} = (\gamma + \beta)\,\tau_{ij} + (\gamma - \beta)\,\tau_{ji} + \alpha\,\tau_{kk}\,\mathbb{1}_{ij}$
Equations of Motion	$\sigma_{ji,j} + f_i^V = \rho_{ij}^V\,\ddot{u}_j$ $\epsilon_{ijk}\,\sigma_{jk} + m_i^V = 0$	$\sigma_{ji,j} + f_i^V = \rho_{ij}^V\,\ddot{u}_j$ $\epsilon_{ijk}\,\sigma_{jk} + \chi_{ji,j} + m_i^V = \imath_{ij}^V\,\ddot{\vartheta}_j$
	$\mu\,u_{i,jj} + (\mu+\lambda)\,u_{j,ji} + f_i^V - \frac{1}{2}\,\epsilon_{ijk}\,m_j^V{}_{,k} = \rho_{ij}^V\,\ddot{u}_j$	$(\mu + \kappa)\,u_{i,jj} + (\mu - \kappa + \lambda)\,u_{j,ji} - 2\,\kappa\,\epsilon_{ijk}\,\vartheta_{j,k} + f_i^V = \rho_{ij}^V\,\ddot{u}_j$ $(\gamma + \beta)\,\vartheta_{i,jj} - 4\,\kappa\,\vartheta_i + (\gamma - \beta + \alpha)\,\vartheta_{j,ji} - 2\,\kappa\,\epsilon_{ijk}\,u_{j,k} + m_i^V = \imath_{ij}^V\,\ddot{\vartheta}_j$
Force System	combined (or effective) $f_i^V - \frac{1}{2}\,\epsilon_{ijk}\,m_j^V{}_{,k}$	separate f_i^V and m_i^V
Elastic Energy	$\mathcal{U}_{\mathrm{e}}^V = \frac{1}{2}\,\sigma_{ij}\,\varepsilon_{ij}$	$\mathcal{U}_{\mathrm{e}}^V = \frac{1}{2}\,\sigma_{ij}\,\varepsilon_{ij} + \frac{1}{2}\,\chi_{ij}\,\tau_{ij}$

Table 2.2: Duality between terminologies in classical and micropolar theories of elasticity.

Term in Classical Elasticity	**Dual Term in Micropolar Elasticity**
displacement u	microrotation ϑ
(mass) density ρ^V	microinertia density $\imath^V$
(force) stress σ	couple stress χ
classical or Lamé constants μ and λ	micropolar or Cosserat constants κ, γ, β, and α
strain ε	twist or wryness τ
normal strain	normal twist or torsion
tension	torsion
tensile	tortile or torsional
tensile or Young's modulus E	tortile or torsional modulus $\mathcal{E}$
(tensile) bulk modulus B	tortile or torsional bulk modulus $\mathcal{B}$
(strain) Poisson's ratio ν	twist Poisson's ratio ξ

2.3 Dynamics of a gyro

A gyro or gyroscope is a device composed of a high-speed spinning wheel with a direction-varying axis of rotation which is mounted on a body. There also may be a/some actuator(s) (or motors) for controlling the direction of the wheel's axis, controlling the spinning speed of the wheel, and compensating for energy dissipated by friction. Currently, gyros are an important component in the aerospace industry. They have been used extensively as sensors (in modern guidance systems) and as actuators (in stabilizing and controlling devices). This section is devoted to the dynamic modeling of a gyro mounted in a representative infinitesimal element of a moving body with no (large) rigid body rotation (see Figure 2.4). Readers are referred to Appendix B for a review on rotational kinematics used in this section for dynamic formulation of a gyro.

For the body element, there is a body frame $\mathcal{F}_b$ attached to it and the element motion in

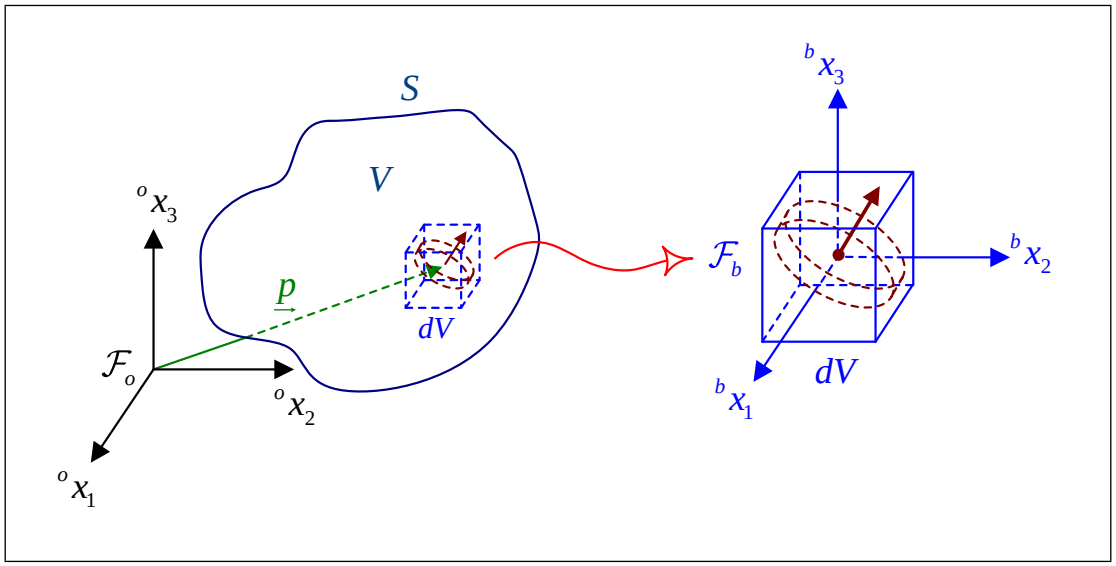

Figure 2.4: A gyro mounted in a representative element of a moving body.

$\mathbb{R}^3$ is expressed by the displacement vector $\underset{\rightarrow}{u}$ and microrotation vector $\underset{\rightarrow}{\vartheta}$ of this frame with respect to the inertial reference frame $\mathcal{F}_o$. Based on this, the translational and rotational (angular) velocities and accelerations of the body element (or frame $\mathcal{F}_b$) will be $\dot{\underset{\rightarrow}{u}}$, $\dot{\underset{\rightarrow}{\vartheta}}$, $\ddot{\underset{\rightarrow}{u}}$, and $\ddot{\underset{\rightarrow}{\vartheta}}$. The gyro is mounted in this element using the gimbals which enable the spinning wheel's axis to take any orientation in the body frame $\mathcal{F}_b$, but prevent the gyro from being translated with respect to the body element. Therefore, the translational motion of the gyro is the same as the translational motion of the body element and can be defined by the vectors $\underset{\rightarrow}{u}$, $\dot{\underset{\rightarrow}{u}}$, and $\ddot{\underset{\rightarrow}{u}}$, too.

To define the rotational motion of the gyro, consider a new frame, called the axis frame $\mathcal{F}_a$, attached to the axis of the spinning wheel and not to the wheel itself (see Figure 2.5). This means that the wheel has an angular velocity with respect to the axis frame $\mathcal{F}_a$ which is its spinning velocity $\dot{\varphi}_3$ in the $^a x_3$ (the third coordinate axis of $\mathcal{F}_a$) direction. In this way, the orientation of the axis frame $\mathcal{F}_a$ with respect to the body frame $\mathcal{F}_b$ can be described using two Euler angles; starting with the axis frame $\mathcal{F}_a$ coinciding with the body frame $\mathcal{F}_b$, frame $\mathcal{F}_a$ rotates about $^a x_1$ (or $^b x_1$) by an angle φ_1, followed by a second rotation of φ_2 about $^a x_2$ (see Figure 2.5). The angles φ_1 and φ_2 can correspond to the gyro's gimbals

angles which form a natural set of Euler angles.

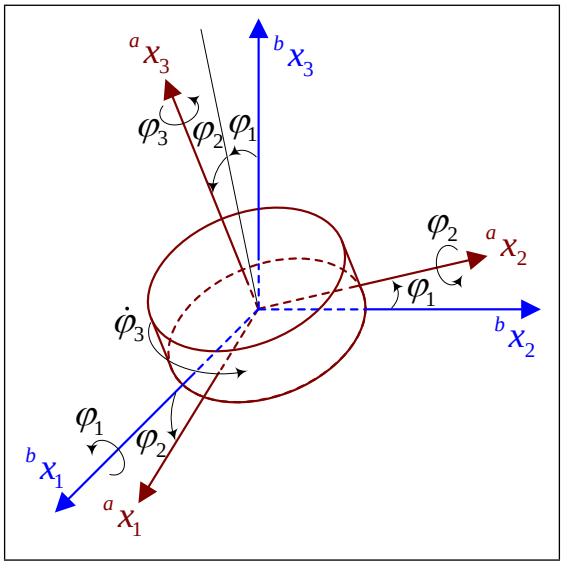

Figure 2.5: Orientation of the axis frame with respect to the body frame.

Based on Figure 2.5, the rotation matrix from axis frame $\mathcal{F}_a$ to frame $\mathcal{F}_b$ will be:

$$ {}^{ba}\underset{\sim}{C} = \begin{bmatrix} \mathrm{c}_{\varphi_2} & 0 & \mathrm{s}_{\varphi_2} \\ \mathrm{s}_{\varphi_1}\,\mathrm{s}_{\varphi_2} & \mathrm{c}_{\varphi_1} & -\,\mathrm{s}_{\varphi_1}\,\mathrm{c}_{\varphi_2} \\ -\,\mathrm{c}_{\varphi_1}\,\mathrm{s}_{\varphi_2} & \mathrm{s}_{\varphi_1} & \mathrm{c}_{\varphi_1}\,\mathrm{c}_{\varphi_2} \end{bmatrix} \tag{2.27} $$

where s and c are the shortened forms of sine and cosine. The other useful rotation matrices are:

$$ \begin{aligned} {}^{ob}\underset{\sim}{C} &= \underset{\equiv}{\mathbb{1}} + \underset{\equiv}{\vartheta}^{\times} \\ {}^{oa}\underset{\sim}{C} &= {}^{ob}\underset{\sim}{C}\,{}^{ba}\underset{\sim}{C} \end{aligned} \tag{2.28} $$

Besides, the angular velocity of the axis frame $\mathcal{F}_a$ with respect to the body frame $\mathcal{F}_b$ and the angular velocity of the rotor (gyro spinning wheel) relative to the axis frame $\mathcal{F}_a$, represented by $\underset{\rightarrow}{\dot{\phi}}$ and $\underset{\rightarrow}{\dot{\psi}}$ respectively, can be described in the axis frame as:

$$ {}^{a}\underset{\sim}{\dot{\phi}} = \begin{bmatrix} \mathrm{c}_{\varphi_2} \\ 0 \\ \mathrm{s}_{\varphi_2} \end{bmatrix} \dot{\varphi}_1 + \begin{bmatrix} 0 \\ 1 \\ 0 \end{bmatrix} \dot{\varphi}_2 \tag{2.29} $$

$$ {}^{a}\dot{\underset{\sim}{\boldsymbol{\psi}}} = \begin{bmatrix} 0 \\ 0 \\ 1 \end{bmatrix} \dot{\varphi}_3 \tag{2.30} $$

Note that the time integrals of angular velocity vectors $\dot{\underset{\rightarrow}{\phi}}$ and $\dot{\underset{\rightarrow}{\psi}}$, *i.e.* vectors $\underset{\rightarrow}{\phi}$ and $\underset{\rightarrow}{\psi}$, generally, have no physical meaning.

Based on the aforementioned descriptions the angular velocities of the axis frame $\mathcal{F}_a$ and the gyro's spinning wheel with respect to the inertial frame will be $\left(\dot{\underset{\rightarrow}{\vartheta}}+\dot{\underset{\rightarrow}{\phi}}\right)$ and $\left(\dot{\underset{\rightarrow}{\vartheta}}+\dot{\underset{\rightarrow}{\phi}}+\dot{\underset{\rightarrow}{\psi}}\right)$ respectively. Now, by using the Newton-Euler formulation, the gyro's equations of motion will be obtained as:

$$ \begin{aligned} -\underset{\rightarrow}{f}^{V} &= \underset{\leftrightarrow}{\varrho}^{V} \cdot \ddot{\underset{\rightarrow}{u}} \\ -\underset{\rightarrow}{m}^{V} &= \underset{\leftrightarrow}{\jmath}^{V} \cdot {}^{a}\frac{d}{dt}\left(\dot{\underset{\rightarrow}{\vartheta}} + \dot{\underset{\rightarrow}{\phi}} + \dot{\underset{\rightarrow}{\psi}}\right) + \left(\dot{\underset{\leftrightarrow}{\vartheta}}^{\times} + \dot{\underset{\leftrightarrow}{\phi}}^{\times}\right) \cdot \underset{\leftrightarrow}{\jmath}^{V} \cdot \left(\dot{\underset{\rightarrow}{\vartheta}} + \dot{\underset{\rightarrow}{\phi}} + \dot{\underset{\rightarrow}{\psi}}\right) \end{aligned} \tag{2.31} $$

where $\underset{\rightarrow}{f}^{V}$ and $\underset{\rightarrow}{m}^{V}$ are vectors of volume forces and moments applied by the gyro on the body element. In addition, $\underset{\leftrightarrow}{\varrho}^{V}$ ($\underset{\leftrightarrow}{\varrho}^{V} = \varrho^{V}\,\underset{\leftrightarrow}{\mathbb{1}}$, where ϱ^{V} is the mass of the gyro per unit volume of the body) and $\underset{\leftrightarrow}{\jmath}^{V}$ are tensors of the gyro translational and rotational inertia per unit volume of body (not per unit volume of gyro). Note that ${}^{a}\underset{\equiv}{\boldsymbol{\jmath}}^{V}$, *i.e.* the component matrix of gyro rotational inertia in axis frame $\mathcal{F}_a$, is usually a known constant and therefore the time derivative of $\underset{\leftrightarrow}{\jmath}^{V}$ with respect to the axis frame vanishes.

Then, by expressing:

$$ {}^{a}\frac{d}{dt}\left(\dot{\underset{\rightarrow}{\phi}}\right) = \ddot{\underset{\rightarrow}{\phi}}, \qquad {}^{a}\ddot{\underset{\sim}{\boldsymbol{\phi}}} = \frac{d}{dt}\left({}^{a}\dot{\underset{\sim}{\boldsymbol{\phi}}}\right) = \begin{bmatrix} \mathrm{c}_{\varphi_2} \\ 0 \\ \mathrm{s}_{\varphi_2} \end{bmatrix} \ddot{\varphi}_1 + \begin{bmatrix} 0 \\ 1 \\ 0 \end{bmatrix} \ddot{\varphi}_2 + \begin{bmatrix} -\mathrm{s}_{\varphi_2} \\ 0 \\ \mathrm{c}_{\varphi_2} \end{bmatrix} \dot{\varphi}_1\,\dot{\varphi}_2 \tag{2.32} $$

$$ {}^{a}\frac{d}{dt}\left(\dot{\underset{\rightarrow}{\psi}}\right) = \ddot{\underset{\rightarrow}{\psi}}, \qquad {}^{a}\ddot{\underset{\sim}{\boldsymbol{\psi}}} = \frac{d}{dt}\left({}^{a}\dot{\underset{\sim}{\boldsymbol{\psi}}}\right) = \begin{bmatrix} 0 \\ 0 \\ 1 \end{bmatrix} \ddot{\varphi}_3 \tag{2.33} $$

and:

$$ {}^{a}\frac{d}{dt}\left(\dot{\underset{\rightarrow}{\vartheta}}\right) = \frac{d}{dt}\left(\dot{\underset{\rightarrow}{\vartheta}}\right) - \left(\dot{\underset{\rightarrow}{\vartheta}} + \dot{\underset{\rightarrow}{\phi}}\right) \times \dot{\underset{\rightarrow}{\vartheta}} = \ddot{\underset{\rightarrow}{\vartheta}} - \dot{\underset{\leftrightarrow}{\phi}}^{\times} \cdot \dot{\underset{\rightarrow}{\vartheta}} \tag{2.34} $$

the gyro equations of motion can be rewritten as:

$$\begin{aligned} -\underset{\rightarrow}{f}^{V} &= \underset{\leftrightarrow}{\varrho}^{V} \cdot \underset{\rightarrow}{\ddot{u}} \\ -\underset{\rightarrow}{m}^{V} &= \underset{\leftrightarrow}{\jmath}^{V} \cdot \left(\underset{\rightarrow}{\ddot{\vartheta}} - \underset{\leftrightarrow}{\dot{\phi}}^{\times} \cdot \underset{\rightarrow}{\dot{\vartheta}} + \underset{\rightarrow}{\ddot{\phi}} + \underset{\rightarrow}{\ddot{\psi}}\right) + \left(\underset{\leftrightarrow}{\dot{\vartheta}}^{\times} + \underset{\leftrightarrow}{\dot{\phi}}^{\times}\right) \cdot \underset{\leftrightarrow}{\jmath}^{V} \cdot \left(\underset{\rightarrow}{\dot{\vartheta}} + \underset{\rightarrow}{\dot{\phi}} + \underset{\rightarrow}{\dot{\psi}}\right) \end{aligned} \tag{2.35}$$

By using the matrix definitions given in Eqs. (2.27)–(2.30) and Eqs. (2.32) and (2.33) and considering the following matrix relations:

$$\begin{aligned} \underset{\equiv}{\boldsymbol{\jmath}}^{V} &= \left(\underset{\equiv}{\mathbb{1}} + \underset{\equiv}{\boldsymbol{\vartheta}}^{\times}\right) {}^{b}\underset{\equiv}{\boldsymbol{\jmath}}^{V} \left(\underset{\equiv}{\mathbb{1}} - \underset{\equiv}{\boldsymbol{\vartheta}}^{\times}\right), & {}^{b}\underset{\equiv}{\boldsymbol{\jmath}}^{V} &= {}^{ba}\underset{\sim}{\boldsymbol{C}}\, {}^{a}\underset{\equiv}{\boldsymbol{\jmath}}^{V}\, {}^{ba}\underset{\sim}{\boldsymbol{C}}^{\mathrm{T}} = {}^{b}\underset{\equiv}{\boldsymbol{\jmath}}^{V}(\varphi_1, \varphi_2) \\ \underset{\equiv}{\dot{\boldsymbol{\phi}}} &= \left(\underset{\equiv}{\mathbb{1}} + \underset{\equiv}{\boldsymbol{\vartheta}}^{\times}\right) {}^{b}\underset{\equiv}{\dot{\boldsymbol{\phi}}}, & {}^{b}\underset{\equiv}{\dot{\boldsymbol{\phi}}} &= {}^{ba}\underset{\sim}{\boldsymbol{C}}\, {}^{a}\underset{\equiv}{\dot{\boldsymbol{\phi}}} = {}^{b}\underset{\equiv}{\dot{\boldsymbol{\phi}}}(\varphi_1, \varphi_2, \dot{\varphi}_1, \dot{\varphi}_2) \\ \underset{\equiv}{\dot{\boldsymbol{\psi}}} &= \left(\underset{\equiv}{\mathbb{1}} + \underset{\equiv}{\boldsymbol{\vartheta}}^{\times}\right) {}^{b}\underset{\equiv}{\dot{\boldsymbol{\psi}}}, & {}^{b}\underset{\equiv}{\dot{\boldsymbol{\psi}}} &= {}^{ba}\underset{\sim}{\boldsymbol{C}}\, {}^{a}\underset{\equiv}{\dot{\boldsymbol{\psi}}} = {}^{b}\underset{\equiv}{\dot{\boldsymbol{\psi}}}(\varphi_1, \varphi_2, \dot{\varphi}_3) \\ \underset{\equiv}{\ddot{\boldsymbol{\phi}}} &= \left(\underset{\equiv}{\mathbb{1}} + \underset{\equiv}{\boldsymbol{\vartheta}}^{\times}\right) {}^{b}\underset{\equiv}{\ddot{\boldsymbol{\phi}}}, & {}^{b}\underset{\equiv}{\ddot{\boldsymbol{\phi}}} &= {}^{ba}\underset{\sim}{\boldsymbol{C}}\, {}^{a}\underset{\equiv}{\ddot{\boldsymbol{\phi}}} = {}^{b}\underset{\equiv}{\ddot{\boldsymbol{\phi}}}(\varphi_1, \varphi_2, \dot{\varphi}_1, \dot{\varphi}_2, \ddot{\varphi}_1, \ddot{\varphi}_2) \\ \underset{\equiv}{\ddot{\boldsymbol{\psi}}} &= \left(\underset{\equiv}{\mathbb{1}} + \underset{\equiv}{\boldsymbol{\vartheta}}^{\times}\right) {}^{b}\underset{\equiv}{\ddot{\boldsymbol{\psi}}}, & {}^{b}\underset{\equiv}{\ddot{\boldsymbol{\psi}}} &= {}^{ba}\underset{\sim}{\boldsymbol{C}}\, {}^{a}\underset{\equiv}{\ddot{\boldsymbol{\psi}}} = {}^{b}\underset{\equiv}{\ddot{\boldsymbol{\psi}}}(\varphi_1, \varphi_2, \ddot{\varphi}_3) \end{aligned} \tag{2.36}$$

one can derive the inertial frame description of these gyro dynamic equations.

It is also useful to determine the kinetic energy density $\mathcal{T}^{V}$ of the system including the body element and gyro. Recalling that $\underset{\leftrightarrow}{\varrho}^{V}$ and $\underset{\leftrightarrow}{\jmath}^{V}$ are tensors of the body element translational and microrotational inertia per unit volume, this expression will be:

$$\begin{aligned} \mathcal{T}^{V} = \frac{1}{2}\, \underset{\rightarrow}{\dot{u}} \cdot \underset{\leftrightarrow}{\varrho}^{V} \cdot \underset{\rightarrow}{\dot{u}} + \frac{1}{2}\, \underset{\rightarrow}{\dot{\vartheta}} \cdot \underset{\leftrightarrow}{\jmath}^{V} \cdot \underset{\rightarrow}{\dot{\vartheta}} + \frac{1}{2}\, \underset{\rightarrow}{\dot{u}} \cdot \underset{\leftrightarrow}{\varrho}^{V} \cdot \underset{\rightarrow}{\dot{u}} \\ + \frac{1}{2} \left(\underset{\rightarrow}{\dot{\vartheta}} + \underset{\rightarrow}{\dot{\phi}} + \underset{\rightarrow}{\dot{\psi}}\right) \cdot \underset{\leftrightarrow}{\jmath}^{V} \cdot \left(\underset{\rightarrow}{\dot{\vartheta}} + \underset{\rightarrow}{\dot{\phi}} + \underset{\rightarrow}{\dot{\psi}}\right) \end{aligned} \tag{2.37}$$

for a micropolar body element, and:

$$\mathcal{T}^{V} = \frac{1}{2}\, \underset{\rightarrow}{\dot{u}} \cdot \underset{\leftrightarrow}{\rho}^{V} \cdot \underset{\rightarrow}{\dot{u}} + \frac{1}{2}\, \underset{\rightarrow}{\dot{u}} \cdot \underset{\leftrightarrow}{\varrho}^{V} \cdot \underset{\rightarrow}{\dot{u}} + \frac{1}{2} \left(\underset{\rightarrow}{\dot{\vartheta}} + \underset{\rightarrow}{\dot{\phi}} + \underset{\rightarrow}{\dot{\psi}}\right) \cdot \underset{\leftrightarrow}{\jmath}^{V} \cdot \left(\underset{\rightarrow}{\dot{\vartheta}} + \underset{\rightarrow}{\dot{\phi}} + \underset{\rightarrow}{\dot{\psi}}\right) \tag{2.38}$$

for a classical body element.

2.4 Hamilton's principle

After selection of the theory of elasticity, the next step for dynamic analysis of an elastic system is making the decision about the method of formulating the equations of motion.

There are different methods (*e.g.* Newton-Euler, D'Alembert, Lagrange, and Hamilton) for formulating the motion equations of a dynamic system. However, these methods can be classified into two major groups.

The methods in the first group are based on differential principles, *e.g.* Newton's second law or D'Alembert's principle, and consider the instantaneous state of the system to apply their differential principle and derive the dynamic equations. On the other hand, methods of the second group are founded on the more general integral principles, *e.g.* Hamilton's principle, and consider the entire motion of the system between two specific times to apply their integral principle.

Hamilton's principle is the most familiar integral principle for dynamic modeling of mechanical systems. It originates from the more general principle of least action (or more accurately the principle of stationary action) [46]. Hamilton's principle states that out of all possible paths between two specific states of a dynamic system at times t_1 and t_2, the system will actually travel along the path which is an extremal or a stationary curve (a minimum, maximum, or saddle curve) of a functional (real-valued function of functions). For a holonomic conservative system, described by N independent generalized coordinates $q_1(t)$, $q_2(t)$, ..., and $q_N(t)$, the functional is called the action integral and takes the following form:

$$\mathcal{A} = \int_t \mathcal{L}(q_1, q_2, \ldots, q_N, \dot{q}_1, \dot{q}_2, \ldots, \dot{q}_N, t)\, dt = \int_t \mathcal{L}(\underset{\sim}{\boldsymbol{q}}, \underset{\sim}{\dot{\boldsymbol{q}}}, t)\, dt \tag{2.39}$$

where $\underset{\sim}{\boldsymbol{q}}$ and $\underset{\sim}{\dot{\boldsymbol{q}}}$ are the $N \times 1$ matrices of independent generalized coordinates and their time derivative (generalized velocities) defined as:

$$\begin{aligned} \underset{\sim}{\boldsymbol{q}} &= \begin{bmatrix} q_1 & q_2 & \cdots & q_N \end{bmatrix}^{\mathrm{T}} \\ \underset{\sim}{\dot{\boldsymbol{q}}} &= \frac{d}{dt}\left(\underset{\sim}{\boldsymbol{q}}\right) = \begin{bmatrix} \dot{q}_1 & \dot{q}_2 & \cdots & \dot{q}_N \end{bmatrix}^{\mathrm{T}} \end{aligned} \tag{2.40}$$

and $\mathcal{L}(\underset{\sim}{\boldsymbol{q}}, \underset{\sim}{\dot{\boldsymbol{q}}}, t)$ is the Lagrangian function of the system defined as the difference between the kinetic energy $\mathcal{T}(\underset{\sim}{\boldsymbol{q}}, \underset{\sim}{\dot{\boldsymbol{q}}}, t)$ of the system and its potential energy $\mathcal{U}(\underset{\sim}{\boldsymbol{q}}, t)$:

$$\mathcal{L}(\underset{\sim}{\boldsymbol{q}}, \underset{\sim}{\dot{\boldsymbol{q}}}, t) = \mathcal{T}(\underset{\sim}{\boldsymbol{q}}, \underset{\sim}{\dot{\boldsymbol{q}}}, t) - \mathcal{U}(\underset{\sim}{\boldsymbol{q}}, t) \tag{2.41}$$

Based on the calculus of variations, the extremum value for the functional given in Eq. (2.39) is obtained when its first variation is zero, that is when:

$$\Delta\mathcal{A} = \Delta\Big(\int_t \mathcal{L}(\underset{\sim}{\boldsymbol{q}}, \underset{\sim}{\dot{\boldsymbol{q}}}, t)\, dt\Big) = \int_t \Big(\delta\underset{\sim}{\boldsymbol{q}}^{\mathrm{T}} \frac{\partial\mathcal{L}}{\partial\underset{\sim}{\boldsymbol{q}}} + \delta\underset{\sim}{\dot{\boldsymbol{q}}}^{\mathrm{T}} \frac{\partial\mathcal{L}}{\partial\underset{\sim}{\dot{\boldsymbol{q}}}}\Big)\, dt = 0 \tag{2.42}$$

where $\delta\underset{\sim}{\boldsymbol{q}}$ and $\delta\underset{\sim}{\dot{\boldsymbol{q}}}$ are $N \times 1$ matrices of the virtual generalized displacements and velocities [47], and $\frac{\partial\mathcal{L}}{\partial\underset{\sim}{\boldsymbol{q}}}$ and $\frac{\partial\mathcal{L}}{\partial\underset{\sim}{\dot{\boldsymbol{q}}}}$ are $N \times 1$ matrices of the form:

$$\begin{aligned} \frac{\partial\mathcal{L}}{\partial\underset{\sim}{\boldsymbol{q}}} &= \begin{bmatrix} \frac{\partial\mathcal{L}}{\partial q_1} & \frac{\partial\mathcal{L}}{\partial q_2} & \cdots & \frac{\partial\mathcal{L}}{\partial q_N} \end{bmatrix}^{\mathrm{T}} \\ \frac{\partial\mathcal{L}}{\partial\underset{\sim}{\dot{\boldsymbol{q}}}} &= \begin{bmatrix} \frac{\partial\mathcal{L}}{\partial \dot{q}_1} & \frac{\partial\mathcal{L}}{\partial \dot{q}_2} & \cdots & \frac{\partial\mathcal{L}}{\partial \dot{q}_N} \end{bmatrix}^{\mathrm{T}} \end{aligned} \tag{2.43}$$

Using the integration by parts, Eq. (2.42) takes the form:

$$\Delta\mathcal{A} = \int_t \delta\underset{\sim}{\boldsymbol{q}}^{\mathrm{T}} \frac{\partial\mathcal{L}}{\partial\underset{\sim}{\boldsymbol{q}}}\, dt + \Big[\delta\underset{\sim}{\boldsymbol{q}}^{\mathrm{T}} \frac{\partial\mathcal{L}}{\partial\underset{\sim}{\dot{\boldsymbol{q}}}}\Big]_{t_1}^{t_2} - \int_t \delta\underset{\sim}{\boldsymbol{q}}^{\mathrm{T}} \frac{d}{dt}\Big(\frac{\partial\mathcal{L}}{\partial\underset{\sim}{\dot{\boldsymbol{q}}}}\Big)\, dt = 0 \tag{2.44}$$

and finally:

$$\Delta\mathcal{A} = \Big[\delta\underset{\sim}{\boldsymbol{q}}^{\mathrm{T}} \frac{\partial\mathcal{L}}{\partial\underset{\sim}{\dot{\boldsymbol{q}}}}\Big]_{t_1}^{t_2} + \int_t \delta\underset{\sim}{\boldsymbol{q}}^{\mathrm{T}} \Big(\frac{\partial\mathcal{L}}{\partial\underset{\sim}{\boldsymbol{q}}} - \frac{d}{dt}\Big(\frac{\partial\mathcal{L}}{\partial\underset{\sim}{\dot{\boldsymbol{q}}}}\Big)\Big)\, dt = 0 \tag{2.45}$$

Since the elements of the generalized coordinate matrix $\underset{\sim}{\boldsymbol{q}}$ are independent, and virtual displacement matrix $\delta\underset{\sim}{\boldsymbol{q}}$ is arbitrary, the necessary condition for $\Delta\mathcal{A}$ to be zero is that the coefficient matrix of the $\delta\underset{\sim}{\boldsymbol{q}}$, inside the integral given in Eq. (2.45), vanishes:

$$\frac{\partial\mathcal{L}}{\partial\underset{\sim}{\boldsymbol{q}}} - \frac{d}{dt}\Big(\frac{\partial\mathcal{L}}{\partial\underset{\sim}{\dot{\boldsymbol{q}}}}\Big) = \underset{\sim}{\mathbf{0}} \tag{2.46}$$

or:

$$\frac{\partial\mathcal{L}}{\partial q_i} - \frac{d}{dt}\Big(\frac{\partial\mathcal{L}}{\partial \dot{q}_i}\Big) = 0, \qquad i = 1, 2, \ldots, N \tag{2.47}$$

and for endpoints (*i.e.* $t = t_1$ and $t = t_2$) the following initial conditions (ICs) should be satisfied:

$$\text{at } t = t_1, t_2: \quad \delta\underset{\sim}{\boldsymbol{q}} = \underset{\sim}{\mathbf{0}} \quad \text{or} \quad \frac{\partial\mathcal{L}}{\partial\underset{\sim}{\dot{\boldsymbol{q}}}} = \underset{\sim}{\mathbf{0}} \tag{2.48}$$

The set of differential equations given by Eq. (2.47) is known as the set of Euler-Lagrange differential equations. These equations along with the ICs given by Eq. (2.48) (or the value of $\underset{\sim}{\boldsymbol{q}}(t_1)$ and $\underset{\sim}{\dot{\boldsymbol{q}}}(t_1)$) will be solved to produce a unique dynamic solution of the system.

Now, again consider a general continuous elastic body occupying a domain V in $\mathbb{R}^3$, bounded by surface S, which is under the action of both conservative and nonconservative forces/moments. For such a system, which can be described by N continuous generalized coordinates $q_1(\underset{\rightarrow}{p}, t)$, $q_2(\underset{\rightarrow}{p}, t)$, ..., and $q_N(\underset{\rightarrow}{p}, t)$, the extended or unrestricted form of Hamilton's principle states that the time integral of the sum of the variation of the Lagrangian function $\Delta\mathcal{L}$ and the virtual work done by nonconservative forces/moments $\delta\mathcal{W}_{\text{nc}}$ vanishes:

$$\int_t \Big(\Delta\mathcal{L} + \delta\mathcal{W}_{\text{nc}}\Big)\, dt = 0 \tag{2.49}$$

Recall that $\delta\mathcal{W}_{\text{nc}}$ is the virtual work, not the variation of $\mathcal{W}_{\text{nc}}$.

Here, a more general form of Hamilton's principle can be written as:

$$\int_t \Big(\Delta\mathcal{L} + \delta\mathcal{W}_{\text{nc}} + \delta\mathcal{W}_{\text{cn}}\Big)\, dt = \int_t \Big(\Delta\mathcal{L} + \delta\mathcal{W}\Big)\, dt = 0 \tag{2.50}$$

where $\delta\mathcal{W}_{\text{cn}}$ is the work done by conservative forces/moments which are not included in the Lagrangian function. Using this form of Hamilton's principle, there are two ways to consider the effect of every conservative force/moment; either by including its corresponding potential energy in the potential energy part of $\mathcal{L}$ or by including its virtual work in $\delta\mathcal{W}_{\text{cn}}$. Even the terms included in the kinetic energy part of $\mathcal{L}$ can be considered as inertial forces/moments, and instead of considering them in the kinetic energy part, their virtual work can be included in $\delta\mathcal{W}_{\text{cn}}$. To sum up, the term $\delta\mathcal{W}$ is the virtual work done by all the forces and moments whose effects are not included in the Lagrangian function as potential or kinetic energy.

For the aforesaid continuous system, the Lagrangian appears as an integral over the volume V and will have the form:

$$\mathcal{L} = \int_V \mathcal{L}^V(\underset{\sim}{\boldsymbol{q}}, \underset{\sim}{\dot{\boldsymbol{q}}}, \underset{\sim}{\boldsymbol{q}}_{,1}, \underset{\sim}{\boldsymbol{q}}_{,2}, \underset{\sim}{\boldsymbol{q}}_{,3}, \underset{\sim}{\dot{\boldsymbol{q}}}_{,1}, \underset{\sim}{\dot{\boldsymbol{q}}}_{,2}, \underset{\sim}{\dot{\boldsymbol{q}}}_{,3}, \underset{\sim}{\boldsymbol{q}}_{,11}, \underset{\sim}{\boldsymbol{q}}_{,12}, \ldots, \underset{\rightarrow}{p}, t)\, dV \tag{2.51}$$

where $\mathcal{L}^V$ is known as the Lagrangian density and $\underset{\sim}{\boldsymbol{q}}$ is the matrix of continuous generalized coordinates. Here, depending on the theory used for modeling the elasticity of the system, and the generalized coordinates chosen, the Lagrangian density will be a function, not only of $\underset{\sim}{\boldsymbol{q}}$ and $\underset{\sim}{\dot{\boldsymbol{q}}}$, but also of their spatial derivatives, *e.g.* $\underset{\sim}{\boldsymbol{q}}_{,1}$, $\underset{\sim}{\boldsymbol{q}}_{,12}$, and $\underset{\sim}{\dot{\boldsymbol{q}}}_{,2}$. Assuming that in $\mathcal{L}^V$, third- and higher-order spatial derivatives of $\underset{\sim}{\boldsymbol{q}}$, and second- and higher-order spatial derivatives of $\underset{\sim}{\dot{\boldsymbol{q}}}$ do not appear, the variation of $\mathcal{L}^V$ will be:

$$\Delta\mathcal{L}^V = \delta\underset{\sim}{\boldsymbol{q}}^{\mathrm{T}} \frac{\partial\mathcal{L}^V}{\partial\underset{\sim}{\boldsymbol{q}}} + \delta\underset{\sim}{\dot{\boldsymbol{q}}}^{\mathrm{T}} \frac{\partial\mathcal{L}^V}{\partial\underset{\sim}{\dot{\boldsymbol{q}}}} + \delta\underset{\sim}{\boldsymbol{q}}_{,i}^{\mathrm{T}} \frac{\partial\mathcal{L}^V}{\partial\underset{\sim}{\boldsymbol{q}}_{,i}} + \delta\underset{\sim}{\dot{\boldsymbol{q}}}_{,i}^{\mathrm{T}} \frac{\partial\mathcal{L}^V}{\partial\underset{\sim}{\dot{\boldsymbol{q}}}_{,i}} + \delta\underset{\sim}{\boldsymbol{q}}_{,ij}^{\mathrm{T}} \frac{\partial\mathcal{L}^V}{\partial\underset{\sim}{\boldsymbol{q}}_{,ij}} \tag{2.52}$$

where for the terms with repeated subscripts the Einstein summation convention over those subscripts, from 1 to 3, is understood.

In addition, the virtual work $\delta\mathcal{W}$ can be described in terms of the generalized force matrix $\underset{\sim}{\boldsymbol{\mathcal{Q}}}$ and the virtual displacement matrix $\delta\underset{\sim}{\boldsymbol{q}}$ as:

$$\delta\mathcal{W} = \int_V \delta\underset{\sim}{\boldsymbol{q}}^{\mathrm{T}}\, \underset{\sim}{\boldsymbol{\mathcal{Q}}}^V\, dV + \oint_S \delta\underset{\sim}{\boldsymbol{q}}^{\mathrm{T}}\, \underset{\sim}{\boldsymbol{\mathcal{Q}}}^S\, dS + \oint_L \delta\underset{\sim}{\boldsymbol{q}}^{\mathrm{T}}\, \underset{\sim}{\boldsymbol{\mathcal{Q}}}^L\, dL + \sum_P \delta\underset{\sim}{\boldsymbol{q}}^{\mathrm{T}}\, \underset{\sim}{\boldsymbol{\mathcal{Q}}}^P \tag{2.53}$$

Here the superscripts V, S, L, and P are used to distinguish between volume, surface, line, and point generalized forces/moments, respectively, and the generalized force matrix has the following form:

$$\underset{\sim}{\boldsymbol{\mathcal{Q}}} = \begin{bmatrix} \mathcal{Q}_1 & \mathcal{Q}_2 & \cdots & \mathcal{Q}_N \end{bmatrix}^{\mathrm{T}} \tag{2.54}$$

The elements of the generalized force matrix $\underset{\sim}{\boldsymbol{\mathcal{Q}}}$ are the generalized forces corresponding to the elements of the generalized coordinate matrix $\underset{\sim}{\boldsymbol{q}}$.

Consequently, Eq. (2.50) can be rewritten as:

$$\begin{aligned} \int_t \int_V \Big(\delta\underset{\sim}{\boldsymbol{q}}^{\mathrm{T}} \frac{\partial\mathcal{L}^V}{\partial\underset{\sim}{\boldsymbol{q}}} + \delta\underset{\sim}{\dot{\boldsymbol{q}}}^{\mathrm{T}} \frac{\partial\mathcal{L}^V}{\partial\underset{\sim}{\dot{\boldsymbol{q}}}} + \delta\underset{\sim}{\boldsymbol{q}}_{,i}^{\mathrm{T}} \frac{\partial\mathcal{L}^V}{\partial\underset{\sim}{\boldsymbol{q}}_{,i}} + \delta\underset{\sim}{\dot{\boldsymbol{q}}}_{,i}^{\mathrm{T}} \frac{\partial\mathcal{L}^V}{\partial\underset{\sim}{\dot{\boldsymbol{q}}}_{,i}} + \delta\underset{\sim}{\boldsymbol{q}}_{,ij}^{\mathrm{T}} \frac{\partial\mathcal{L}^V}{\partial\underset{\sim}{\boldsymbol{q}}_{,ij}} \Big)\, dV\, dt \\ + \int_t \int_V \delta\underset{\sim}{\boldsymbol{q}}^{\mathrm{T}}\, \underset{\sim}{\boldsymbol{\mathcal{Q}}}^V\, dV\, dt + \int_t \oint_S \delta\underset{\sim}{\boldsymbol{q}}^{\mathrm{T}}\, \underset{\sim}{\boldsymbol{\mathcal{Q}}}^S\, dS\, dt + \int_t \oint_L \delta\underset{\sim}{\boldsymbol{q}}^{\mathrm{T}}\, \underset{\sim}{\boldsymbol{\mathcal{Q}}}^L\, dL\, dt \\ + \int_t \sum_P \delta\underset{\sim}{\boldsymbol{q}}^{\mathrm{T}}\, \underset{\sim}{\boldsymbol{\mathcal{Q}}}^P\, dt = 0 \end{aligned} \tag{2.55}$$

In Eq. (2.55), the terms involving the $\dot{\underset{\sim}{\boldsymbol{q}}}$, $\underset{\sim}{\boldsymbol{q}}_{,i}$, and $\dot{\underset{\sim}{\boldsymbol{q}}}_{,i}$ can be manipulated employing the integration by parts and Gauss' theorem. In this way, the following relations will be obtained:

$$\int_t \int_V \delta\dot{\underset{\sim}{\boldsymbol{q}}}^{\mathrm{T}} \frac{\partial \mathcal{L}^V}{\partial \dot{\underset{\sim}{\boldsymbol{q}}}}\, dV\, dt = \left[\int_V \delta\underset{\sim}{\boldsymbol{q}}^{\mathrm{T}} \frac{\partial \mathcal{L}^V}{\partial \dot{\underset{\sim}{\boldsymbol{q}}}}\, dV\right]_{t_1}^{t_2} - \int_t \int_V \delta\underset{\sim}{\boldsymbol{q}}^{\mathrm{T}} \left(\frac{\partial \mathcal{L}^V}{\partial \dot{\underset{\sim}{\boldsymbol{q}}}}\right)_{,t} dV\, dt \tag{2.56}$$

$$\int_t \int_V \delta\underset{\sim}{\boldsymbol{q}}_{,i}^{\mathrm{T}} \frac{\partial \mathcal{L}^V}{\partial \underset{\sim}{\boldsymbol{q}}_{,i}}\, dV\, dt = \int_t \oint_S \delta\underset{\sim}{\boldsymbol{q}}^{\mathrm{T}} \frac{\partial \mathcal{L}^V}{\partial \underset{\sim}{\boldsymbol{q}}_{,i}}\, n_i\, dS\, dt - \int_t \int_V \delta\underset{\sim}{\boldsymbol{q}}^{\mathrm{T}} \left(\frac{\partial \mathcal{L}^V}{\partial \underset{\sim}{\boldsymbol{q}}_{,i}}\right)_{,i} dV\, dt \tag{2.57}$$

$$\begin{aligned}\int_t \int_V \delta\dot{\underset{\sim}{\boldsymbol{q}}}_{,i}^{\mathrm{T}} \frac{\partial \mathcal{L}^V}{\partial \dot{\underset{\sim}{\boldsymbol{q}}}_{,i}}\, dV\, dt = &\left[\oint_S \delta\underset{\sim}{\boldsymbol{q}}^{\mathrm{T}} \frac{\partial \mathcal{L}^V}{\partial \dot{\underset{\sim}{\boldsymbol{q}}}_{,i}}\, n_i\, dS\right]_{t_1}^{t_2} - \left[\int_V \delta\underset{\sim}{\boldsymbol{q}}^{\mathrm{T}} \left(\frac{\partial \mathcal{L}^V}{\partial \dot{\underset{\sim}{\boldsymbol{q}}}_{,i}}\right)_{,i} dV\right]_{t_1}^{t_2} \\ &- \int_t \oint_S \delta\underset{\sim}{\boldsymbol{q}}^{\mathrm{T}} \left(\frac{\partial \mathcal{L}^V}{\partial \dot{\underset{\sim}{\boldsymbol{q}}}_{,i}}\right)_{,t} n_i\, dS\, dt + \int_t \int_V \delta\underset{\sim}{\boldsymbol{q}}^{\mathrm{T}} \left(\frac{\partial \mathcal{L}^V}{\partial \dot{\underset{\sim}{\boldsymbol{q}}}_{,i}}\right)_{,t\,i} dV\, dt\end{aligned} \tag{2.58}$$

Additionally, by utilizing the Gauss' theorem, the term including $\underset{\sim}{\boldsymbol{q}}_{,ij}$ can be manipulated in two different ways. The suitable form when $i = j$ is as follows:

$$\begin{aligned}\int_t \int_V \delta\underset{\sim}{\boldsymbol{q}}_{,ij}^{\mathrm{T}} \frac{\partial \mathcal{L}^V}{\partial \underset{\sim}{\boldsymbol{q}}_{,ij}}\, dV\, dt = &\int_t \oint_S \delta\underset{\sim}{\boldsymbol{q}}_{,i}^{\mathrm{T}} \frac{\partial \mathcal{L}^V}{\partial \underset{\sim}{\boldsymbol{q}}_{,ij}}\, n_j\, dS\, dt - \int_t \oint_S \delta\underset{\sim}{\boldsymbol{q}}^{\mathrm{T}} \left(\frac{\partial \mathcal{L}^V}{\partial \underset{\sim}{\boldsymbol{q}}_{,ij}}\right)_{,j} n_i\, dS\, dt \\ &+ \int_t \int_V \delta\underset{\sim}{\boldsymbol{q}}^{\mathrm{T}} \left(\frac{\partial \mathcal{L}^V}{\partial \underset{\sim}{\boldsymbol{q}}_{,ij}}\right)_{,ij} dV\, dt \\ = &\int_t \oint_S \delta\underset{\sim}{\boldsymbol{q}}_{,j}^{\mathrm{T}} \frac{\partial \mathcal{L}^V}{\partial \underset{\sim}{\boldsymbol{q}}_{,ij}}\, n_i\, dS\, dt - \int_t \oint_S \delta\underset{\sim}{\boldsymbol{q}}^{\mathrm{T}} \left(\frac{\partial \mathcal{L}^V}{\partial \underset{\sim}{\boldsymbol{q}}_{,ij}}\right)_{,j} n_i\, dS\, dt \\ &+ \int_t \int_V \delta\underset{\sim}{\boldsymbol{q}}^{\mathrm{T}} \left(\frac{\partial \mathcal{L}^V}{\partial \underset{\sim}{\boldsymbol{q}}_{,ij}}\right)_{,ij} dV\, dt\end{aligned} \tag{2.59}$$

and when $i \neq j$, the suitable form will be:

$$\begin{aligned}
\int_t \int_V \delta \underset{\sim}{\boldsymbol{q}}^{\mathrm{T}}_{,ij} \frac{\partial \mathcal{L}^V}{\partial \underset{\sim}{\boldsymbol{q}}_{,ij}} \, dV \, dt &= \int_t \oint_S \Big(\delta \underset{\sim}{\boldsymbol{q}}^{\mathrm{T}} \frac{\partial \mathcal{L}^V}{\partial \underset{\sim}{\boldsymbol{q}}_{,ij}} \Big)_{,i} n_j \, dS \, dt - \int_t \oint_S \delta \underset{\sim}{\boldsymbol{q}}^{\mathrm{T}} \Big(\frac{\partial \mathcal{L}^V}{\partial \underset{\sim}{\boldsymbol{q}}_{,ij}} \Big)_{,i} n_j \, dS \, dt \\
&\quad - \int_t \oint_S \delta \underset{\sim}{\boldsymbol{q}}^{\mathrm{T}} \Big(\frac{\partial \mathcal{L}^V}{\partial \underset{\sim}{\boldsymbol{q}}_{,ij}} \Big)_{,j} n_i \, dS \, dt + \int_t \int_V \delta \underset{\sim}{\boldsymbol{q}}^{\mathrm{T}} \Big(\frac{\partial \mathcal{L}^V}{\partial \underset{\sim}{\boldsymbol{q}}_{,ij}} \Big)_{,ij} dV \, dt \\
&= \int_t \oint_S \Big(\delta \underset{\sim}{\boldsymbol{q}}^{\mathrm{T}} \frac{\partial \mathcal{L}^V}{\partial \underset{\sim}{\boldsymbol{q}}_{,ji}} \Big)_{,j} n_i \, dS \, dt - \int_t \oint_S \delta \underset{\sim}{\boldsymbol{q}}^{\mathrm{T}} \Big(\frac{\partial \mathcal{L}^V}{\partial \underset{\sim}{\boldsymbol{q}}_{,ji}} \Big)_{,j} n_i \, dS \, dt \\
&\quad - \int_t \oint_S \delta \underset{\sim}{\boldsymbol{q}}^{\mathrm{T}} \Big(\frac{\partial \mathcal{L}^V}{\partial \underset{\sim}{\boldsymbol{q}}_{,ij}} \Big)_{,j} n_i \, dS \, dt + \int_t \int_V \delta \underset{\sim}{\boldsymbol{q}}^{\mathrm{T}} \Big(\frac{\partial \mathcal{L}^V}{\partial \underset{\sim}{\boldsymbol{q}}_{,ij}} \Big)_{,ij} dV \, dt
\end{aligned} \tag{2.60}$$

Considering the independence of the generalized coordinates and arbitrariness of the virtual displacement matrix, and substituting from the Eqs. (2.56)–(2.60) into Eq. (2.55), the following set of PDEs (in matrix form) will be obtained:

$$\frac{\partial \mathcal{L}^V}{\partial \underset{\sim}{\boldsymbol{q}}} - \Big(\frac{\partial \mathcal{L}^V}{\partial \dot{\underset{\sim}{\boldsymbol{q}}}} \Big)_{,t} - \Big(\frac{\partial \mathcal{L}^V}{\partial \underset{\sim}{\boldsymbol{q}}_{,i}} \Big)_{,i} + \Big(\frac{\partial \mathcal{L}^V}{\partial \dot{\underset{\sim}{\boldsymbol{q}}}_{,i}} \Big)_{,t\,i} + \Big(\frac{\partial \mathcal{L}^V}{\partial \underset{\sim}{\boldsymbol{q}}_{,ij}} \Big)_{,ij} + \underset{\sim}{\boldsymbol{\mathcal{Q}}}^V = 0 \tag{2.61}$$

Here for endpoints (*i.e.* $t = t_1$ and $t = t_2$) the following ICs should be satisfied:

$$\begin{aligned}
&\text{at } t = t_1, t_2; \text{ and over } V: \quad \delta \underset{\sim}{\boldsymbol{q}} = \underset{\sim}{\boldsymbol{0}} \quad \text{or} \quad \frac{\partial \mathcal{L}^V}{\partial \dot{\underset{\sim}{\boldsymbol{q}}}} - \Big(\frac{\partial \mathcal{L}^V}{\partial \dot{\underset{\sim}{\boldsymbol{q}}}_{,i}} \Big)_{,i} = \underset{\sim}{\boldsymbol{0}} \\
&\text{at } t = t_1, t_2; \text{ and over } S: \quad \delta \underset{\sim}{\boldsymbol{q}} = \underset{\sim}{\boldsymbol{0}} \quad \text{or} \quad \frac{\partial \mathcal{L}^V}{\partial \dot{\underset{\sim}{\boldsymbol{q}}}_{,i}} n_i = \underset{\sim}{\boldsymbol{0}}
\end{aligned} \tag{2.62}$$

Besides, the procedure will result in the following valuable essential and natural boundary

conditions (EBCs and NBCs):

$$\begin{aligned}
&\text{over } S: \quad \underbrace{\delta \underset{\sim}{\boldsymbol{q}} = \underset{\sim}{\mathbf{0}}}_{\text{EBCs}} \quad \text{or} \quad \underbrace{\begin{aligned} &\frac{\partial \mathcal{L}^V}{\partial \underset{\sim}{\boldsymbol{q}}_{,i}} n_i - \left(\frac{\partial \mathcal{L}^V}{\partial \underset{\sim}{\dot{\boldsymbol{q}}}_{,i}}\right)_{,t} n_i - \left(\frac{\partial \mathcal{L}^V}{\partial \underset{\sim}{\boldsymbol{q}}_{,ij}} + \frac{\partial \mathcal{L}^V}{\partial \underset{\sim}{\boldsymbol{q}}_{,ji}}\right)_{,j} n_i \\ &+ \left(\frac{\partial \mathcal{L}^V}{\partial \underset{\sim}{\boldsymbol{q}}_{,11}}\right)_{,1} n_1 + \left(\frac{\partial \mathcal{L}^V}{\partial \underset{\sim}{\boldsymbol{q}}_{,22}}\right)_{,2} n_2 + \left(\frac{\partial \mathcal{L}^V}{\partial \underset{\sim}{\boldsymbol{q}}_{,33}}\right)_{,3} n_3 \\ &+ \underset{\sim}{\boldsymbol{\mathcal{Q}}}^S = \underset{\sim}{\mathbf{0}} \end{aligned}}_{\text{NBCs}} \\
&\text{over } S: \quad \delta \underset{\sim}{\boldsymbol{q}}_{,1} = \underset{\sim}{\mathbf{0}} \quad \text{or} \quad \frac{\partial \mathcal{L}^V}{\partial \underset{\sim}{\boldsymbol{q}}_{,11}} n_1 = \underset{\sim}{\mathbf{0}} \\
&\text{over } S: \quad \delta \underset{\sim}{\boldsymbol{q}}_{,2} = \underset{\sim}{\mathbf{0}} \quad \text{or} \quad \frac{\partial \mathcal{L}^V}{\partial \underset{\sim}{\boldsymbol{q}}_{,22}} n_2 = \underset{\sim}{\mathbf{0}} \\
&\text{over } S: \quad \delta \underset{\sim}{\boldsymbol{q}}_{,3} = \underset{\sim}{\mathbf{0}} \quad \text{or} \quad \frac{\partial \mathcal{L}^V}{\partial \underset{\sim}{\boldsymbol{q}}_{,33}} n_3 = \underset{\sim}{\mathbf{0}}
\end{aligned} \tag{2.63}$$

In addition to the set of PDEs given by Eq. (2.61), the ICs in Eq. (2.62), and the boundary conditions (BCs) in Eq. (2.63), the following equation should be satisfied:

$$\begin{aligned}
&- \oint_S \left(\left(\delta q^{\mathrm{T}} \frac{\partial \mathcal{L}^V}{\partial \underset{\sim}{\boldsymbol{q}}_{,11}} \right)_{,1} n_1 + \left(\delta q^{\mathrm{T}} \frac{\partial \mathcal{L}^V}{\partial \underset{\sim}{\boldsymbol{q}}_{,22}} \right)_{,2} n_2 + \left(\delta q^{\mathrm{T}} \frac{\partial \mathcal{L}^V}{\partial \underset{\sim}{\boldsymbol{q}}_{,33}} \right)_{,3} n_3 \right) dS \\
&\quad + \oint_S \left(\delta q^{\mathrm{T}} \frac{\partial \mathcal{L}^V}{\partial \underset{\sim}{\boldsymbol{q}}_{,ij}} \right)_{,j} n_i \, dS + \oint_L \delta \underset{\sim}{\boldsymbol{q}}^{\mathrm{T}} \underset{\sim}{\boldsymbol{\mathcal{Q}}}^L \, dL + \sum_P \delta \underset{\sim}{\boldsymbol{q}}^{\mathrm{T}} \underset{\sim}{\boldsymbol{\mathcal{Q}}}^P = 0
\end{aligned} \tag{2.64}$$

which itself can be divided into more subequations (*i.e.* other BCs over some boundary curves or at some boundary points) depending on the problem to be solved.

The set of PDEs given in Eq. (2.61) are the corresponding Euler-Lagrange differential equations for a continuous system. These equations along with the ICs in Eq. (2.62) (or the value of $\underset{\sim}{\boldsymbol{q}}(\underset{\rightarrow}{p}, t_1)$ and $\underset{\sim}{\dot{\boldsymbol{q}}}(\underset{\rightarrow}{p}, t_1)$) and the BCs in Eqs. (2.63) and (2.64) should be solved to produce the unique dynamic solution of the system. Note that NBCs are not

easily established without the use of Hamilton's principle and the calculus of variations, and it can be concluded that the NBCs are valuable products of this approach. Another important benefit of using Hamilton's principle for dynamic modeling of the continuous systems is that some very powerful approximation procedures will be made available with the integral form of the equations of motion (*i.e.* the equation given by Eq. (2.55)).

At last, it is noteworthy that the virtual work expression for a continuous elastic system may also contain the terms including the spatial derivatives of the virtual displacement matrix, *i.e.* the virtual work expression may be obtained as:

$$\begin{aligned}\delta\mathcal{W} = &\int_V \left(\delta\underset{\sim}{\boldsymbol{q}}^{\mathrm{T}}\,\underset{\sim}{\boldsymbol{\mathcal{Q}}}^{V} + \delta\underset{\sim}{\boldsymbol{q}}_{,i}^{\mathrm{T}}\,\underset{\sim}{\boldsymbol{\mathcal{R}}_{\boldsymbol{i}}}^{V}\right) dV + \oint_S \left(\delta\underset{\sim}{\boldsymbol{q}}^{\mathrm{T}}\,\underset{\sim}{\boldsymbol{\mathcal{Q}}}^{S} + \delta\underset{\sim}{\boldsymbol{q}}_{,i}^{\mathrm{T}}\,\underset{\sim}{\boldsymbol{\mathcal{R}}_{\boldsymbol{i}}}^{S}\right) dS \\ &+ \oint_L \left(\delta\underset{\sim}{\boldsymbol{q}}^{\mathrm{T}}\,\underset{\sim}{\boldsymbol{\mathcal{Q}}}^{L} + \delta\underset{\sim}{\boldsymbol{q}}_{,i}^{\mathrm{T}}\,\underset{\sim}{\boldsymbol{\mathcal{R}}_{\boldsymbol{i}}}^{L}\right) dL + \sum_P \left(\delta\underset{\sim}{\boldsymbol{q}}^{\mathrm{T}}\,\underset{\sim}{\boldsymbol{\mathcal{Q}}}^{P} + \delta\underset{\sim}{\boldsymbol{q}}_{,i}^{\mathrm{T}}\,\underset{\sim}{\boldsymbol{\mathcal{R}}_{\boldsymbol{i}}}^{P}\right)\end{aligned} \tag{2.65}$$

where the matrix $\underset{\sim}{\boldsymbol{\mathcal{R}}_{\boldsymbol{i}}}$ (which can be named the generalized moment matrix) has the following form:

$$\underset{\sim}{\boldsymbol{\mathcal{R}}_{\boldsymbol{i}}} = \begin{bmatrix} \mathcal{R}_{i1} & \mathcal{R}_{i2} & \cdots & \mathcal{R}_{iN} \end{bmatrix}^{\mathrm{T}} \tag{2.66}$$

whose elements correspond to the elements of matrix $\delta\underset{\sim}{\boldsymbol{q}}_{,i}$. To manipulate such terms in the virtual work expression the following relation will be useful:

$$\int_t \int_V \delta\underset{\sim}{\boldsymbol{q}}_{,i}^{\mathrm{T}}\,\underset{\sim}{\boldsymbol{\mathcal{R}}_{\boldsymbol{i}}}^{V}\, dV\, dt = \int_t \oint_S \delta\underset{\sim}{\boldsymbol{q}}^{\mathrm{T}}\,\underset{\sim}{\boldsymbol{\mathcal{R}}_{\boldsymbol{i}}}^{V}\, n_i\, dS\, dt - \int_t \int_V \delta\underset{\sim}{\boldsymbol{q}}^{\mathrm{T}}\,\underset{\sim}{\boldsymbol{\mathcal{R}}_{\boldsymbol{i}}}_{,i}^{V}\, dV\, dt \tag{2.67}$$

2.5 Theories for other dimensional bodies

At the end, it is noteworthy that this chapter's results and equations, obtained for a general 3D body in the 3D space, can be simplified to obtain the corresponding results and equations for a two-dimensional (2D) or a one-dimensional (1D) body in the 3D, 2D, or 1D space. These simplified equations will be of interest when dealing with bodies which can be modeled as plates (2D bodies) or beams (1D bodies). They will be provided in the following chapters where they are being used.

Chapter 3

Gyroelastic Continua

3.1 Introduction

As mentioned previously a general 3D gyrocontinuum is a dynamic system with four basic types of continuous mechanical influences; inertia, elasticity, damping, and gyricity. In a gyrocontinuum it is assumed that every infinitesimal element of the continuum houses an infinitesimal gyro with an infinitesimal stored angular momentum, known as gyricity, and the parameters related to this gyricity are treated as field quantities.

This chapter is devoted to the derivation of the equations of motion for a general 3D gyrocontinuum, without any damping, occupying a volume domain V in $\mathbb{R}^3$, bounded by surface S, and under the action of some forces/moments, where it is assumed that the continuum does not undergo any (large) rigid body rotation.

One of the best approaches for dynamic modeling of such a system is through Hamilton's principle which will result in the BCs as well as the equations of motion and in addition will make some approximation methods available. To apply Hamilton's principle however, the expressions for the potential and kinetic energy of the system and the virtual work done by external forces/moments are needed. Most of these have been reviewed to some extent in Chapter 2 and therefore, in the following sections they will be presented briefly.

3.2 Potential energy expression

The potential energy expression of a gyrocontinuum usually contains two terms; the potential energy due to the elasticity and the potential energy due to the gravity. However, in this thesis the gravity effect (whenever needed) will be taken into account as an external volume force applied on the body:

$$\underset{\rightarrow}{f}^{V} = \left(\rho^{V} + \varrho^{V}\right) \underset{\rightarrow}{g} \tag{3.1}$$

where $\underset{\rightarrow}{g}$ is the gravity vector. This body force produces a virtual work term and will appear in the system virtual work expression.

Therefore, the only source of potential energy in the system will be the elasticity of the body which when based on the micropolar theory of elasticity takes the following form:

$$\mathcal{U} = \mathcal{U}_{\text{e}} = \frac{1}{2} \int_{V} \left(\sigma_{ij}\, \varepsilon_{ij} + \chi_{ij}\, \tau_{ij}\right) dV \tag{3.2}$$

Substitution from the micropolar constitutive relations given by Eq. (2.4) into Eq. (3.2) will result in:

$$\begin{aligned}
\mathcal{U} = {} & \frac{1}{2} \int_{V} \Big(\Big(\mu + \kappa\Big)\, \varepsilon_{ij}\, \varepsilon_{ij} + \Big(\mu - \kappa\Big)\, \varepsilon_{ji}\, \varepsilon_{ij} + \lambda\, \varepsilon_{kk}\, \varepsilon_{jj} \Big)\, dV \\
& + \frac{1}{2} \int_{V} \Big(\Big(\gamma + \beta\Big)\, \tau_{ij}\, \tau_{ij} + \Big(\gamma - \beta\Big)\, \tau_{ji}\, \tau_{ij} + \alpha\, \tau_{kk}\, \tau_{jj} \Big)\, dV \\
= {} & \frac{1}{2} \int_{V} \Big(2\,\mu \left(\varepsilon_{11}\, \varepsilon_{11} + \varepsilon_{22}\, \varepsilon_{22} + \varepsilon_{33}\, \varepsilon_{33}\right) + \lambda \left(\varepsilon_{11} + \varepsilon_{22} + \varepsilon_{33}\right)^{2} \Big)\, dV \\
& + \frac{1}{2} \int_{V} \mu \left(\left(\varepsilon_{12} + \varepsilon_{21}\right)^{2} + \left(\varepsilon_{13} + \varepsilon_{31}\right)^{2} + \left(\varepsilon_{23} + \varepsilon_{32}\right)^{2} \right) dV \\
& + \frac{1}{2} \int_{V} \kappa \left(\left(\varepsilon_{12} - \varepsilon_{21}\right)^{2} + \left(\varepsilon_{13} - \varepsilon_{31}\right)^{2} + \left(\varepsilon_{23} - \varepsilon_{32}\right)^{2} \right) dV \\
& + \frac{1}{2} \int_{V} \Big(\Big(\gamma + \beta\Big)\, \tau_{ij}\, \tau_{ij} + \Big(\gamma - \beta\Big)\, \tau_{ji}\, \tau_{ij} + \alpha\, \tau_{kk}\, \tau_{jj} \Big)\, dV
\end{aligned} \tag{3.3}$$

Now based on the definition of the strain tensor $\underset{\leftrightarrows}{\varepsilon}$ given by Eq. (2.2) and the definition of the twist tensor $\underset{\leftrightarrows}{\tau}$ given by Eq. (2.3) one can obtain the following relations:

$$\begin{aligned}
\varepsilon_{ij}\,\varepsilon_{ij} &= \Big(u_{j,i} - \epsilon_{ijk}\,\vartheta_k\Big)\,\Big(u_{j,i} - \epsilon_{ijl}\,\vartheta_l\Big) \\
&= u_{j,i}\,u_{j,i} - \epsilon_{ijl}\,\vartheta_l\,u_{j,i} - \epsilon_{ijk}\,\vartheta_k\,u_{j,i} + \epsilon_{ijk}\,\epsilon_{ijl}\,\vartheta_k\,\vartheta_l \\
&= u_{i,j}\,u_{i,j} + 2\,\epsilon_{ijk}\,\vartheta_k\,u_{i,j} + 2\,\vartheta_k\,\vartheta_k \\
\varepsilon_{ji}\,\varepsilon_{ij} &= \Big(u_{i,j} + \epsilon_{ijk}\,\vartheta_k\Big)\,\Big(u_{j,i} - \epsilon_{ijl}\,\vartheta_l\Big) \\
&= u_{i,j}\,u_{j,i} - \epsilon_{ijl}\,\vartheta_l\,u_{i,j} + \epsilon_{ijk}\,\vartheta_k\,u_{j,i} - \epsilon_{ijk}\,\epsilon_{ijl}\,\vartheta_k\,\vartheta_l \\
&= u_{i,j}\,u_{j,i} - 2\,\epsilon_{ijk}\,\vartheta_k\,u_{i,j} - 2\,\vartheta_k\,\vartheta_k \\
\varepsilon_{kk}\,\varepsilon_{jj} &= u_{k,k}\,u_{j,j} = u_{i,i}\,u_{j,j}
\end{aligned} \tag{3.4}$$

and:

$$\begin{aligned}
\tau_{ij}\,\tau_{ij} &= \vartheta_{j,i}\,\vartheta_{j,i} = \vartheta_{i,j}\,\vartheta_{i,j} \\
\tau_{ji}\,\tau_{ij} &= \vartheta_{i,j}\,\vartheta_{j,i} \\
\tau_{kk}\,\tau_{jj} &= \vartheta_{k,k}\,\vartheta_{j,j} = \vartheta_{i,i}\,\vartheta_{j,j}
\end{aligned} \tag{3.5}$$

Utilizing these relations, the potential energy expressions in Eq. (3.3) can be rewritten as:

$$\begin{aligned}
\mathcal{U} &= \frac{1}{2}\int_V \Big(\Big(\mu+\kappa\Big)\,u_{i,j}\,u_{i,j} + \Big(\mu-\kappa\Big)\,u_{i,j}\,u_{j,i} + \lambda\,u_{i,i}\,u_{j,j}\Big)\,dV \\
&\quad + \frac{1}{2}\int_V \Big(4\,\kappa\,\epsilon_{ijk}\,\vartheta_k\,u_{i,j} + 4\,\kappa\,\vartheta_k\,\vartheta_k\Big)\,dV \\
&\quad + \frac{1}{2}\int_V \Big(\Big(\gamma+\beta\Big)\,\vartheta_{i,j}\,\vartheta_{i,j} + \Big(\gamma-\beta\Big)\,\vartheta_{i,j}\,\vartheta_{j,i} + \alpha\,\vartheta_{i,i}\,\vartheta_{j,j}\Big)\,dV \\
&= \frac{1}{2}\int_V \Big(\mu\,u_{i,j}\,u_{i,j} + \mu\,u_{i,j}\,u_{j,i} + \lambda\,u_{i,i}\,u_{j,j}\Big)\,dV \\
&\quad + \frac{1}{2}\int_V \Big(\kappa\,u_{i,j}\Big(u_{i,j} - u_{j,i}\Big) + 4\,\kappa\,\epsilon_{ijk}\,\vartheta_k\,u_{i,j} + 4\,\kappa\,\vartheta_k\,\vartheta_k\Big)\,dV \\
&\quad + \frac{1}{2}\int_V \Big(\Big(\gamma+\beta\Big)\,\vartheta_{i,j}\,\vartheta_{i,j} + \Big(\gamma-\beta\Big)\,\vartheta_{i,j}\,\vartheta_{j,i} + \alpha\,\vartheta_{i,i}\,\vartheta_{j,j}\Big)\,dV
\end{aligned} \tag{3.6}$$

The potential energy expression given by Eq. (3.6) can be simplified when the classical theory of elasticity is used to model the elasticity of the system (*i.e.* when the couple stress tensor $\underset{\leftrightarrow}{\chi}$ is zero and the microrotation field vector $\underset{\rightarrow}{\vartheta}$ is dependent to the displacement field vector $\underset{\rightarrow}{u}$ through Eq. (2.15)). In this way, the following expression will be obtained:

$$\mathcal{U} = \frac{1}{2} \int_V \Big(\mu \, u_{i,j} \, u_{i,j} + \mu \, u_{i,j} \, u_{j,i} + \lambda \, u_{i,i} \, u_{j,j} \Big) \, dV \tag{3.7}$$

Hence, based on the theory chosen for modeling the elasticity of the gyrocontinuum, its potential energy will be obtained from Eq. (3.6) or (3.7); the expression given by Eq. (3.6) contains six independent unknowns (*i.e.* u_1, u_2, u_3, ϑ_1, ϑ_2, and ϑ_3) but the expression given by Eq. (3.7) has just three independent unknowns (*i.e.* u_1, u_2, and u_3).

3.3 Kinetic energy expression

The kinetic energy of a gyrocontinuum is the summation of the elastic body kinetic energy and the gyricity kinetic energy. The kinetic energy of the elastic body is a result of its linear velocity field vector $\dot{\underset{\rightarrow}{u}}(\underset{\rightarrow}{p}, t)$ and also its angular velocity field vector $\dot{\underset{\rightarrow}{\vartheta}}(\underset{\rightarrow}{p}, t)$, but only if it is micropolar. The kinetic energy of the gyricity is caused by its linear velocity field vector, which is the same as the elastic body linear velocity vector $\dot{\underset{\rightarrow}{u}}(\underset{\rightarrow}{p}, t)$, and its rotation rate field scalars $\dot{\varphi}_1(\underset{\rightarrow}{p}, t)$, $\dot{\varphi}_2(\underset{\rightarrow}{p}, t)$, and $\dot{\varphi}_3(\underset{\rightarrow}{p}, t)$ along with the elastic body angular velocity field vector $\dot{\underset{\rightarrow}{\vartheta}}(\underset{\rightarrow}{p}, t)$ (which can be independent or dependent on the linear velocity field vector $\dot{\underset{\rightarrow}{u}}(\underset{\rightarrow}{p}, t)$). The rotation rate field scalars and the elastic body angular velocity field vector describe the gyricity angular velocity field vector.

Based on Eq. (2.37) which gives the kinetic energy density ($\mathcal{T}^V$) of an infinitesimal micropolar body element containing a gyro, the kinetic energy of a micropolar gyrocontinuum

takes the following form:

$$
\begin{aligned}
\mathcal{T} &= \int_V \mathcal{T}^V \, dV \\
&= \frac{1}{2} \int_V \left(\left(\rho^V + \varrho^V \right) \underset{\rightarrow}{\dot{u}} \cdot \underset{\rightarrow}{\dot{u}} + \underset{\rightarrow}{\dot{\vartheta}} \cdot \left(\underset{\leftrightarrow}{\imath}^V + \underset{\leftrightarrow}{\jmath}^V \right) \cdot \underset{\rightarrow}{\dot{\vartheta}} + 2 \left(\underset{\rightarrow}{\dot{\phi}} + \underset{\rightarrow}{\dot{\psi}} \right) \cdot \underset{\leftrightarrow}{\jmath}^V \cdot \underset{\rightarrow}{\dot{\vartheta}} \right) dV \\
&\quad + \frac{1}{2} \int_V \left(\left(\underset{\rightarrow}{\dot{\phi}} + \underset{\rightarrow}{\dot{\psi}} \right) \cdot \underset{\leftrightarrow}{\jmath}^V \cdot \left(\underset{\rightarrow}{\dot{\phi}} + \underset{\rightarrow}{\dot{\psi}} \right) \right) dV \\
&= \frac{1}{2} \int_V \left(\left(\rho^V + \varrho^V \right) \dot{u}_i \, \dot{u}_i + \left(\imath_{ij}^V + \jmath_{ij}^V \right) \dot{\vartheta}_j \, \dot{\vartheta}_i + 2 \, \jmath_{ij}^V \left(\dot{\phi}_j + \dot{\psi}_j \right) \dot{\vartheta}_i \right) dV \\
&\quad + \frac{1}{2} \int_V \jmath_{ij}^V \left(\dot{\phi}_j \, \dot{\phi}_i + \dot{\psi}_j \, \dot{\psi}_i + 2 \, \dot{\phi}_j \, \dot{\psi}_i \right) dV
\end{aligned}
\tag{3.8}
$$

and from Eq. (2.38) the kinetic energy of a classical gyrocontinuum will be:

$$
\begin{aligned}
\mathcal{T} &= \int_V \mathcal{T}^V \, dV \\
&= \frac{1}{2} \int_V \left(\left(\rho^V + \varrho^V \right) \underset{\rightarrow}{\dot{u}} \cdot \underset{\rightarrow}{\dot{u}} + \underset{\rightarrow}{\dot{\vartheta}} \cdot \underset{\leftrightarrow}{\jmath}^V \cdot \underset{\rightarrow}{\dot{\vartheta}} + 2 \left(\underset{\rightarrow}{\dot{\phi}} + \underset{\rightarrow}{\dot{\psi}} \right) \cdot \underset{\leftrightarrow}{\jmath}^V \cdot \underset{\rightarrow}{\dot{\vartheta}} \right) dV \\
&\quad + \frac{1}{2} \int_V \left(\left(\underset{\rightarrow}{\dot{\phi}} + \underset{\rightarrow}{\dot{\psi}} \right) \cdot \underset{\leftrightarrow}{\jmath}^V \cdot \left(\underset{\rightarrow}{\dot{\phi}} + \underset{\rightarrow}{\dot{\psi}} \right) \right) dV \\
&= \frac{1}{2} \int_V \left(\left(\rho^V + \varrho^V \right) \dot{u}_i \, \dot{u}_i + \jmath_{ij}^V \, \dot{\vartheta}_j \, \dot{\vartheta}_i + 2 \, \jmath_{ij}^V \left(\dot{\phi}_j + \dot{\psi}_j \right) \dot{\vartheta}_i \right) dV \\
&\quad + \frac{1}{2} \int_V \jmath_{ij}^V \left(\dot{\phi}_j \, \dot{\phi}_i + \dot{\psi}_j \, \dot{\psi}_i + 2 \, \dot{\phi}_j \, \dot{\psi}_i \right) dV
\end{aligned}
\tag{3.9}
$$

Recall that for a classical gyrocontinuum the angular velocity vector $\underset{\rightarrow}{\dot{\vartheta}}(\underset{\rightarrow}{p}, t)$ is dependent on the translational velocity field vector $\underset{\rightarrow}{\dot{u}}(\underset{\rightarrow}{p}, t)$, as in Eq. (2.15).

3.4 Virtual work expression

Assume that the gyrocontinuum is under the action of some volume, surface, line, and point forces/moments which can be conservative, *e.g.* a gravity force, or nonconservative, *e.g.* a damping force/moment. The resultants of these forces/moments are denoted by $\underset{\rightarrow}{f}^{V}$, $\underset{\rightarrow}{f}^{S}$, $\underset{\rightarrow}{f}^{L}$, $\underset{\rightarrow}{f}^{P}$, $\underset{\rightarrow}{m}^{V}$, $\underset{\rightarrow}{m}^{S}$, $\underset{\rightarrow}{m}^{L}$, and $\underset{\rightarrow}{m}^{P}$, respectively. For such a system, the virtual work expression in terms of the body virtual translational and rotational motions will be:

$$\begin{aligned}\delta\mathcal{W} &= \int_{V}\left(\underset{\rightarrow}{f}^{V}\cdot\delta\underset{\rightarrow}{u}+\underset{\rightarrow}{m}^{V}\cdot\delta\underset{\rightarrow}{\vartheta}\right)dV+\oint_{S}\left(\underset{\rightarrow}{f}^{S}\cdot\delta\underset{\rightarrow}{u}+\underset{\rightarrow}{m}^{S}\cdot\delta\underset{\rightarrow}{\vartheta}\right)dS\\ &\quad+\oint_{L}\left(\underset{\rightarrow}{f}^{L}\cdot\delta\underset{\rightarrow}{u}+\underset{\rightarrow}{m}^{L}\cdot\delta\underset{\rightarrow}{\vartheta}\right)dL+\sum_{P}\left(\underset{\rightarrow}{f}^{P}\cdot\delta\underset{\rightarrow}{u}+\underset{\rightarrow}{m}^{P}\cdot\delta\underset{\rightarrow}{\vartheta}\right)\\ &= \int_{V}\left(f_i^{V}\,\delta u_i+m_i^{V}\,\delta\vartheta_i\right)dV+\oint_{S}\left(f_i^{S}\,\delta u_i+m_i^{S}\,\delta\vartheta_i\right)dS\\ &\quad+\oint_{L}\left(f_i^{L}\,\delta u_i+m_i^{L}\,\delta\vartheta_i\right)dL+\sum_{P}\left(f_i^{P}\,\delta u_i+m_i^{P}\,\delta\vartheta_i\right)\end{aligned}\tag{3.10}$$

Again, note that for a classical gyrocontinua (*i.e.* when the classical theory of elasticity is being utilized) the microrotation and displacement field vectors will be dependent.

3.5 Equations of motion

As mentioned before the best approach to obtain a gyrocontinuum's equations of motion along with its ICs and BCs is through Hamilton's principle. However, in this section, just the equations of motion are of interest and the corresponding ICs and BCs will not be considered. As a consequence, the motion equations can be simply derived as a combination of the equations of motion of a general 3D elastic body (under the action of force and moment distributions) and the equations of motion of the gyricity distribution (*i.e.* the dynamic equations of a gyro mounted in a body element). These equations are given by Eqs. (2.9), (2.21), and (2.35) and in fact, it is enough to substitute a portion of (*i.e.* the

gyricity-effects portion of) the volume force and moment in Eq. (2.9) or (2.21) by the volume force and moment terms in Eq. (2.35).

In this way, the equations of motion for a micropolar gyrocontinuum (a gyrocontinuum where the micropolar theory is used for modeling the elasticity) take the form:

$$\begin{aligned}
\underset{\rightarrow}{f}^{V} = & -\Big(\mu+\kappa\Big)\Big(\underset{\rightarrow}{\nabla}\cdot\underset{\rightarrow}{\nabla}\Big)\,\underset{\rightarrow}{u}-\Big(\mu-\kappa+\lambda\Big)\,\underset{\rightarrow}{\nabla}\Big(\underset{\rightarrow}{\nabla}\cdot\underset{\rightarrow}{u}\Big)-2\,\kappa\,\underset{\leftrightarrow}{\nabla}^{\times}\cdot\underset{\rightarrow}{\vartheta}\\
& +\rho^{V}\,\underset{\rightarrow}{\ddot{u}}+\varrho^{V}\,\underset{\rightarrow}{\ddot{u}}\\
\underset{\rightarrow}{m}^{V} = & -\Big(\Big(\gamma+\beta\Big)\,\underset{\rightarrow}{\nabla}\cdot\underset{\rightarrow}{\nabla}-4\,\kappa\Big)\,\underset{\rightarrow}{\vartheta}-\Big(\gamma-\beta+\alpha\Big)\,\underset{\rightarrow}{\nabla}\Big(\underset{\rightarrow}{\nabla}\cdot\underset{\rightarrow}{\vartheta}\Big)-2\,\kappa\,\underset{\leftrightarrow}{\nabla}^{\times}\cdot\underset{\rightarrow}{u}\\
& +\underset{\leftrightarrow}{\imath}^{V}\cdot\underset{\rightarrow}{\ddot{\vartheta}}+\underset{\leftrightarrow}{\jmath}^{V}\cdot\underset{\rightarrow}{\ddot{\vartheta}}+\underset{\leftrightarrow}{\dot{\vartheta}}^{\times}\cdot\underset{\leftrightarrow}{\jmath}^{V}\cdot\underset{\rightarrow}{\dot{\vartheta}}\\
& +\underset{\leftrightarrow}{\dot{\vartheta}}^{\times}\cdot\underset{\leftrightarrow}{\jmath}^{V}\cdot\Big(\underset{\rightarrow}{\dot{\phi}}+\underset{\rightarrow}{\dot{\psi}}\Big)+\Big(\underset{\leftrightarrow}{\dot{\phi}}^{\times}\cdot\underset{\leftrightarrow}{\jmath}^{V}-\underset{\leftrightarrow}{\jmath}^{V}\cdot\underset{\leftrightarrow}{\dot{\phi}}^{\times}\Big)\cdot\underset{\rightarrow}{\dot{\vartheta}}\\
& +\underset{\leftrightarrow}{\jmath}^{V}\cdot\underset{\rightarrow}{\ddot{\phi}}+\underset{\leftrightarrow}{\jmath}^{V}\cdot\underset{\rightarrow}{\ddot{\psi}}+\underset{\leftrightarrow}{\dot{\phi}}^{\times}\cdot\underset{\leftrightarrow}{\jmath}^{V}\cdot\Big(\underset{\rightarrow}{\dot{\phi}}+\underset{\rightarrow}{\dot{\psi}}\Big)
\end{aligned}\tag{3.11}$$

and the corresponding equations for a classical gyrocontinuum (a gyrocontinuum where the classical theory is utilized for modeling the elasticity) will be:

$$\begin{aligned}
\underset{\rightarrow}{f}^{V}+\frac{1}{2}\,\underset{\leftrightarrow}{\nabla}^{\times}\cdot\underset{\rightarrow}{m}^{V} = & -\mu\Big(\underset{\rightarrow}{\nabla}\cdot\underset{\rightarrow}{\nabla}\Big)\,\underset{\rightarrow}{u}-\Big(\mu+\lambda\Big)\,\underset{\rightarrow}{\nabla}\Big(\underset{\rightarrow}{\nabla}\cdot\underset{\rightarrow}{u}\Big)\\
& +\rho^{V}\,\underset{\rightarrow}{\ddot{u}}+\varrho^{V}\,\underset{\rightarrow}{\ddot{u}}+\frac{1}{2}\,\underset{\leftrightarrow}{\nabla}^{\times}\cdot\Big(\underset{\leftrightarrow}{\jmath}^{V}\cdot\underset{\rightarrow}{\ddot{\vartheta}}+\underset{\leftrightarrow}{\dot{\vartheta}}^{\times}\cdot\underset{\leftrightarrow}{\jmath}^{V}\cdot\underset{\rightarrow}{\dot{\vartheta}}\Big)\\
& +\frac{1}{2}\,\underset{\leftrightarrow}{\nabla}^{\times}\cdot\Big(\underset{\leftrightarrow}{\dot{\vartheta}}^{\times}\cdot\underset{\leftrightarrow}{\jmath}^{V}\cdot\Big(\underset{\rightarrow}{\dot{\phi}}+\underset{\rightarrow}{\dot{\psi}}\Big)+\Big(\underset{\leftrightarrow}{\dot{\phi}}^{\times}\cdot\underset{\leftrightarrow}{\jmath}^{V}-\underset{\leftrightarrow}{\jmath}^{V}\cdot\underset{\leftrightarrow}{\dot{\phi}}^{\times}\Big)\cdot\underset{\rightarrow}{\dot{\vartheta}}\Big)\\
& +\frac{1}{2}\,\underset{\leftrightarrow}{\nabla}^{\times}\cdot\Big(\underset{\leftrightarrow}{\jmath}^{V}\cdot\underset{\rightarrow}{\ddot{\phi}}+\underset{\leftrightarrow}{\jmath}^{V}\cdot\underset{\rightarrow}{\ddot{\psi}}+\underset{\leftrightarrow}{\dot{\phi}}^{\times}\cdot\underset{\leftrightarrow}{\jmath}^{V}\cdot\Big(\underset{\rightarrow}{\dot{\phi}}+\underset{\rightarrow}{\dot{\psi}}\Big)\Big)
\end{aligned}\tag{3.12}$$

Recall that the volume force and moment vectors $\underset{\rightarrow}{f}^{V}$ and $\underset{\rightarrow}{m}^{V}$ in Eqs. (3.11) and (3.12) may include the damping and gravity forces and moments as well as the external force and moment distributions. In addition, vectors $\underset{\rightarrow}{\dot{\vartheta}}$ and $\underset{\rightarrow}{\ddot{\vartheta}}$ in Eq. (3.12) are dependent to the vectors $\underset{\rightarrow}{\dot{u}}$ and $\underset{\rightarrow}{\ddot{u}}$ as in Eq. (2.15).

In the first relation of Eq. (3.11), the first three terms of the right-hand side represent the contribution of the body elasticity due to the force stress tensor variation inside the body and the next two terms are translational inertia terms due to elastic body and gyricity mass densities. In the second relation of Eq. (3.11), again the first three terms of the right-hand side are the body elasticity contribution due to the antisymmetric portion of the

force stress tensor and the variation of the couple stress tensor inside the body. The rest of terms in the right-hand side of the second relation in Eq. (3.11) represent the contribution of elastic body and gyricity (micro)rotational inertia due to the microrotation of the elastic body, the axis and spin rotations of the gyricity, and the interactions of these rotations.

An analogous explanation can be given for the right-hand side terms in Eq. (3.12). In the right-hand side of this equation, the first two terms correspond to the contribution of the body elasticity due to the variation of the symmetric portion of force stress tensor, the next two terms indicate the role of the body and gyricity translational inertias, and the rest of terms reflect the effect of gyricity rotational inertia. As mentioned previously in Eq. (2.26), note that for a classical gyrocontinuum one half of the curl of the terms acting as a volume moment will contribute in the equations of translational motion as an equivalent volume force. Indeed, the effect of the volume moment-like terms on the variation of the antisymmetric portion of the force stress tensor is reflected (with some limitations) by the equivalent force-like terms.

The useful matrix form of the equations of motion, in Eqs. (3.11) and (3.12), can be written as:

$$
\begin{aligned}
\underline{\boldsymbol{f}}^{V} = & -\Big(\mu+\kappa\Big)\,\underline{\boldsymbol{\nabla}}^{\mathrm{T}}\,\underline{\boldsymbol{\nabla}}\,\underline{\underline{\mathbb{1}}}\,\underline{\boldsymbol{u}} - \Big(\mu-\kappa+\lambda\Big)\,\underline{\boldsymbol{\nabla}}\,\underline{\boldsymbol{\nabla}}^{\mathrm{T}}\,\underline{\boldsymbol{u}} - 2\,\kappa\,\underline{\underline{\boldsymbol{\nabla}}}^{\times}\,\underline{\boldsymbol{\vartheta}} \\
& + \rho^{V}\,\underline{\ddot{\boldsymbol{u}}} + \varrho^{V}\,\underline{\ddot{\boldsymbol{u}}} \\
\underline{\boldsymbol{m}}^{V} = & -\Big(\Big(\gamma+\beta\Big)\,\underline{\boldsymbol{\nabla}}^{\mathrm{T}}\,\underline{\boldsymbol{\nabla}} - 4\,\kappa\Big)\underline{\underline{\mathbb{1}}}\,\underline{\boldsymbol{\vartheta}} - \Big(\gamma-\beta+\alpha\Big)\,\underline{\boldsymbol{\nabla}}\,\underline{\boldsymbol{\nabla}}^{\mathrm{T}}\,\underline{\boldsymbol{\vartheta}} - 2\,\kappa\,\underline{\underline{\boldsymbol{\nabla}}}^{\times}\,\underline{\boldsymbol{u}} \\
& + \underline{\underline{\boldsymbol{\imath}}}^{V}\,\underline{\ddot{\boldsymbol{\vartheta}}} + \underline{\underline{\boldsymbol{\jmath}}}^{V}\,\underline{\ddot{\boldsymbol{\vartheta}}} + \underline{\dot{\underline{\boldsymbol{\vartheta}}}}^{\times}\,\underline{\underline{\boldsymbol{\jmath}}}^{V}\,\underline{\dot{\boldsymbol{\vartheta}}} \\
& + \underline{\dot{\underline{\boldsymbol{\vartheta}}}}^{\times}\,\underline{\underline{\boldsymbol{\jmath}}}^{V}\Big(\underline{\dot{\boldsymbol{\phi}}}+\underline{\dot{\boldsymbol{\psi}}}\Big) + \Big(\underline{\dot{\underline{\boldsymbol{\phi}}}}^{\times}\,\underline{\underline{\boldsymbol{\jmath}}}^{V} - \underline{\underline{\boldsymbol{\jmath}}}^{V}\,\underline{\dot{\underline{\boldsymbol{\phi}}}}^{\times}\Big)\,\underline{\dot{\boldsymbol{\vartheta}}} \\
& + \underline{\underline{\boldsymbol{\jmath}}}^{V}\,\underline{\ddot{\boldsymbol{\phi}}} + \underline{\underline{\boldsymbol{\jmath}}}^{V}\,\underline{\ddot{\boldsymbol{\psi}}} + \underline{\dot{\underline{\boldsymbol{\phi}}}}^{\times}\,\underline{\underline{\boldsymbol{\jmath}}}^{V}\Big(\underline{\dot{\boldsymbol{\phi}}}+\underline{\dot{\boldsymbol{\psi}}}\Big)
\end{aligned}
\tag{3.13}
$$

and:

$$\begin{aligned}\underline{\boldsymbol{f}}^{V}+\frac{1}{2}\,\underline{\underline{\boldsymbol{\nabla}}}^{\times}\,\underline{\boldsymbol{m}}^{V}=&-\mu\,\underline{\boldsymbol{\nabla}}^{\mathrm{T}}\,\underline{\boldsymbol{\nabla}}\,\underline{\underline{\mathbb{1}}}\,\underline{\boldsymbol{u}}-\Big(\mu+\lambda\Big)\,\underline{\boldsymbol{\nabla}}\,\underline{\boldsymbol{\nabla}}^{\mathrm{T}}\,\underline{\boldsymbol{u}}\\&+\rho^{V}\,\underline{\ddot{\boldsymbol{u}}}+\varrho^{V}\,\underline{\ddot{\boldsymbol{u}}}+\frac{1}{2}\,\underline{\underline{\boldsymbol{\nabla}}}^{\times}\Big(\underline{\underline{\boldsymbol{\jmath}}}^{V}\,\underline{\ddot{\boldsymbol{\vartheta}}}+\underline{\dot{\boldsymbol{\vartheta}}}^{\times}\,\underline{\underline{\boldsymbol{\jmath}}}^{V}\,\underline{\dot{\boldsymbol{\vartheta}}}\Big)\\&+\frac{1}{2}\,\underline{\underline{\boldsymbol{\nabla}}}^{\times}\Big(\underline{\dot{\boldsymbol{\vartheta}}}^{\times}\,\underline{\underline{\boldsymbol{\jmath}}}^{V}\Big(\underline{\dot{\boldsymbol{\phi}}}+\underline{\dot{\boldsymbol{\psi}}}\Big)+\Big(\underline{\dot{\boldsymbol{\phi}}}^{\times}\,\underline{\underline{\boldsymbol{\jmath}}}^{V}-\underline{\underline{\boldsymbol{\jmath}}}^{V}\,\underline{\dot{\boldsymbol{\phi}}}^{\times}\Big)\,\underline{\dot{\boldsymbol{\vartheta}}}\Big)\\&+\frac{1}{2}\,\underline{\underline{\boldsymbol{\nabla}}}^{\times}\Big(\underline{\underline{\boldsymbol{\jmath}}}^{V}\,\underline{\ddot{\boldsymbol{\phi}}}+\underline{\underline{\boldsymbol{\jmath}}}^{V}\,\underline{\ddot{\boldsymbol{\psi}}}+\underline{\dot{\boldsymbol{\phi}}}^{\times}\,\underline{\underline{\boldsymbol{\jmath}}}^{V}\Big(\underline{\dot{\boldsymbol{\phi}}}+\underline{\dot{\boldsymbol{\psi}}}\Big)\Big)\end{aligned}\tag{3.14}$$

Now, by recalling the matrix relations given in Section 2.3, especially those defined by Eq. (2.36), and by imposing the necessary first-order approximation with respect to the microrotation vector $\underline{\vartheta}$ (as explained and justified in Appendix B) the matrix form of the equations of motion given by Eqs. (3.13) and (3.14) can be rewritten (approximately) as:

$$\begin{aligned}\underline{\boldsymbol{f}}^{V}=&-\Big(\mu+\kappa\Big)\,\underline{\boldsymbol{\nabla}}^{\mathrm{T}}\,\underline{\boldsymbol{\nabla}}\,\underline{\underline{\mathbb{1}}}\,\underline{\boldsymbol{u}}-\Big(\mu-\kappa+\lambda\Big)\,\underline{\boldsymbol{\nabla}}\,\underline{\boldsymbol{\nabla}}^{\mathrm{T}}\,\underline{\boldsymbol{u}}-2\,\kappa\,\underline{\underline{\boldsymbol{\nabla}}}^{\times}\,\underline{\boldsymbol{\vartheta}}\\&+\rho^{V}\,\underline{\ddot{\boldsymbol{u}}}+\varrho^{V}\,\underline{\ddot{\boldsymbol{u}}}\\\underline{\boldsymbol{m}}^{V}=&-\Big(\Big(\gamma+\beta\Big)\,\underline{\boldsymbol{\nabla}}^{\mathrm{T}}\,\underline{\boldsymbol{\nabla}}-4\,\kappa\Big)\,\underline{\underline{\mathbb{1}}}\,\underline{\boldsymbol{\vartheta}}-\Big(\gamma-\beta+\alpha\Big)\,\underline{\boldsymbol{\nabla}}\,\underline{\boldsymbol{\nabla}}^{\mathrm{T}}\,\underline{\boldsymbol{\vartheta}}-2\,\kappa\,\underline{\underline{\boldsymbol{\nabla}}}^{\times}\,\underline{\boldsymbol{u}}\\&+{}^{b}\underline{\underline{\boldsymbol{\imath}}}^{V}\,\underline{\ddot{\boldsymbol{\vartheta}}}+{}^{b}\underline{\underline{\boldsymbol{\jmath}}}^{V}\,\underline{\ddot{\boldsymbol{\vartheta}}}\\&+\underline{\dot{\boldsymbol{\vartheta}}}^{\times}\,{}^{b}\underline{\underline{\boldsymbol{\jmath}}}^{V}\Big({}^{b}\underline{\dot{\boldsymbol{\phi}}}+{}^{b}\underline{\dot{\boldsymbol{\psi}}}\Big)+\Big({}^{b}\underline{\dot{\boldsymbol{\phi}}}^{\times}\,{}^{b}\underline{\underline{\boldsymbol{\jmath}}}^{V}-{}^{b}\underline{\underline{\boldsymbol{\jmath}}}^{V}\,{}^{b}\underline{\dot{\boldsymbol{\phi}}}^{\times}\Big)\,\underline{\dot{\boldsymbol{\vartheta}}}\\&+\Big(\underline{\underline{\mathbb{1}}}+\underline{\boldsymbol{\vartheta}}^{\times}\Big)\Big({}^{b}\underline{\underline{\boldsymbol{\jmath}}}^{V}\,{}^{b}\underline{\ddot{\boldsymbol{\phi}}}+{}^{b}\underline{\underline{\boldsymbol{\jmath}}}^{V}\,{}^{b}\underline{\ddot{\boldsymbol{\psi}}}+{}^{b}\underline{\dot{\boldsymbol{\phi}}}^{\times}\,{}^{b}\underline{\underline{\boldsymbol{\jmath}}}^{V}\Big({}^{b}\underline{\dot{\boldsymbol{\phi}}}+{}^{b}\underline{\dot{\boldsymbol{\psi}}}\Big)\Big)\end{aligned}\tag{3.15}$$

and:

$$\begin{aligned}\underline{\boldsymbol{f}}^{V}+\frac{1}{2}\,\underline{\underline{\boldsymbol{\nabla}}}^{\times}\,\underline{\boldsymbol{m}}^{V}=&-\mu\,\underline{\boldsymbol{\nabla}}^{\mathrm{T}}\,\underline{\boldsymbol{\nabla}}\,\underline{\underline{\mathbb{1}}}\,\underline{\boldsymbol{u}}-\Big(\mu+\lambda\Big)\,\underline{\boldsymbol{\nabla}}\,\underline{\boldsymbol{\nabla}}^{\mathrm{T}}\,\underline{\boldsymbol{u}}\\&+\rho^{V}\,\underline{\ddot{\boldsymbol{u}}}+\varrho^{V}\,\underline{\ddot{\boldsymbol{u}}}+\frac{1}{2}\,\underline{\underline{\boldsymbol{\nabla}}}^{\times}\,{}^{b}\underline{\underline{\boldsymbol{\jmath}}}^{V}\,\underline{\ddot{\boldsymbol{\vartheta}}}\\&+\frac{1}{2}\,\underline{\underline{\boldsymbol{\nabla}}}^{\times}\Big(\underline{\dot{\boldsymbol{\vartheta}}}^{\times}\,{}^{b}\underline{\underline{\boldsymbol{\jmath}}}^{V}\Big({}^{b}\underline{\dot{\boldsymbol{\phi}}}+{}^{b}\underline{\dot{\boldsymbol{\psi}}}\Big)+\Big({}^{b}\underline{\dot{\boldsymbol{\phi}}}^{\times}\,{}^{b}\underline{\underline{\boldsymbol{\jmath}}}^{V}-{}^{b}\underline{\underline{\boldsymbol{\jmath}}}^{V}\,{}^{b}\underline{\dot{\boldsymbol{\phi}}}^{\times}\Big)\,\underline{\dot{\boldsymbol{\vartheta}}}\Big)\\&+\frac{1}{2}\,\underline{\underline{\boldsymbol{\nabla}}}^{\times}\Big(\underline{\underline{\mathbb{1}}}+\underline{\boldsymbol{\vartheta}}^{\times}\Big)\Big({}^{b}\underline{\underline{\boldsymbol{\jmath}}}^{V}\,{}^{b}\underline{\ddot{\boldsymbol{\phi}}}+{}^{b}\underline{\underline{\boldsymbol{\jmath}}}^{V}\,{}^{b}\underline{\ddot{\boldsymbol{\psi}}}+{}^{b}\underline{\dot{\boldsymbol{\phi}}}^{\times}\,{}^{b}\underline{\underline{\boldsymbol{\jmath}}}^{V}\Big({}^{b}\underline{\dot{\boldsymbol{\phi}}}+{}^{b}\underline{\dot{\boldsymbol{\psi}}}\Big)\Big)\end{aligned}\tag{3.16}$$

It is noteworthy that the approximation included in relations given by Eqs. (3.15) and (3.16) is enforced by the microrotation kinematics in the continuum elasticity model and

not by the gyros' kinematics. Therefore, in these equations no restriction or approximation is imposed on the gyricity and gyricity-related parameters. The restrictions on gyricity and gyricity-related parameters, if any, should be considered and imposed separately.

Finally, by applying the assumptions (restrictions) suggested by Damaren [23], *i.e.*:

$$\begin{aligned} \| \underset{\rightarrow}{\vartheta} \| &\ll 1 \\ \| \dot{\underset{\rightarrow}{\vartheta}} \|, \| \dot{\underset{\rightarrow}{\phi}} \| &\ll 1 \ (1/\mathrm{s}) \\ \| \ddot{\underset{\rightarrow}{\vartheta}} \|, \| \ddot{\underset{\rightarrow}{\phi}} \| &\ll 1 \ (1/\mathrm{s}^2) \\ \| \dot{\underset{\rightarrow}{\psi}} \| &\gg 1 \ (1/\mathrm{s}) \\ \| \ddot{\underset{\rightarrow}{\psi}} \| &= 0 \ (1/\mathrm{s}^2) \end{aligned} \tag{3.17}$$

and considering a zero-order approximation, *i.e.* neglecting the terms of order one and higher, the equation given in Eq. (3.16) takes the following form:

$$\begin{aligned} \underline{\boldsymbol{f}}^{V} + \frac{1}{2} \underline{\underline{\boldsymbol{\nabla}}}^{\times} \underline{\boldsymbol{m}}^{V} = & -\mu \underline{\boldsymbol{\nabla}}^{\mathrm{T}} \underline{\boldsymbol{\nabla}} \underline{\underline{\mathbb{1}}} \underline{\boldsymbol{u}} - \left(\mu + \lambda\right) \underline{\boldsymbol{\nabla}} \underline{\boldsymbol{\nabla}}^{\mathrm{T}} \underline{\boldsymbol{u}} \\ & + \rho^{V} \underline{\ddot{\boldsymbol{u}}} + \varrho^{V} \underline{\ddot{\boldsymbol{u}}} \\ & + \frac{1}{2} \underline{\underline{\boldsymbol{\nabla}}}^{\times} \left(\underline{\dot{\boldsymbol{\vartheta}}}^{\times} \, {}^{b}\underline{\underline{\boldsymbol{\jmath}}}^{V} \, {}^{b}\underline{\dot{\boldsymbol{\psi}}} \right) + \frac{1}{2} \underline{\underline{\boldsymbol{\nabla}}}^{\times} \left({}^{b}\underline{\dot{\boldsymbol{\phi}}}^{\times} \, {}^{b}\underline{\underline{\boldsymbol{\jmath}}}^{V} \, {}^{b}\underline{\dot{\boldsymbol{\psi}}} \right) \end{aligned} \tag{3.18}$$

or equivalently:

$$\begin{aligned} \left(\rho^{V} + \varrho^{V}\right) \underline{\ddot{\boldsymbol{u}}} - \frac{1}{4} \underline{\underline{\boldsymbol{\nabla}}}^{\times} \, {}^{b}\underline{\underline{\boldsymbol{h}}}^{\times} \underline{\underline{\boldsymbol{\nabla}}}^{\times} \underline{\dot{\boldsymbol{u}}} - \left(\mu \underline{\boldsymbol{\nabla}}^{\mathrm{T}} \underline{\boldsymbol{\nabla}} \underline{\underline{\mathbb{1}}} + \left(\mu + \lambda\right) \underline{\boldsymbol{\nabla}} \underline{\boldsymbol{\nabla}}^{\mathrm{T}}\right) \underline{\boldsymbol{u}} = \\ \underline{\boldsymbol{f}}^{V} + \frac{1}{2} \underline{\underline{\boldsymbol{\nabla}}}^{\times} \underline{\boldsymbol{m}}^{V} + \frac{1}{2} \underline{\underline{\boldsymbol{\nabla}}}^{\times} \, {}^{b}\underline{\underline{\boldsymbol{h}}}^{\times} \, {}^{b}\underline{\dot{\boldsymbol{\phi}}} \end{aligned} \tag{3.19}$$

where [23]:

$$\underset{\rightarrow}{h} = \underset{\leftrightarrow}{J}^{V} \cdot \dot{\underset{\rightarrow}{\psi}}, \qquad {}^{b}\underline{\boldsymbol{h}} = {}^{b}\underline{\underline{\boldsymbol{\jmath}}}^{V} \, {}^{b}\underline{\dot{\boldsymbol{\psi}}} \tag{3.20}$$

The equation given by Eq. (3.19) is the same as the equation derived by Damaren [23]. Compared to the zero-order restricted dynamic equations given in Eq. (3.18) or (3.19), the here-in derived unrestricted dynamic equations given by Eq. (3.16) contain extra terms due to considering a nonzero acceleration for the spin rotation of the gyros and assuming nonsmall velocity and acceleration for their axes rotations.

3.6 Justification of gyrocontinuum models

As noted in Section 1.2, the focus of this thesis is on gyrocontinuum modeling without concern for the relationship between the realistic discrete gyroscopic system (structure) and the idealized gyrocontinuum model which is the question of an "equivalent continuum modeling". However, a quick investigation of the actual gyroscopic structure can be very useful, first for justifying the developed gyrocontinuum models and, second for clarifying the capabilities and advantages of each gyrocontinuum model.

Recall that the gyroscopic structures suitable to be modeled as gyroelastic systems are usually thought of as very large structures with repetitive regular lattices where every lattice houses a small gyro at its center, similar to the one shown in Figure 1.2. In such structures, each gyro or gyroscope is indeed more complex than just a spinning wheel and also includes a casing or housing with all the required mechanisms (*i.e.* gimbals and driving motors) for controlling the speed and direction of the gyro's spinning wheel. The exterior housing of the gyro is itself mounted in the structural lattice via a separate fixing mechanism (which can be as simple as a piece of welding or a few bolts and nuts). Finally, there might also exist (though very weak) interactions or elastic couplings (*e.g.* due to a sort of reinforcement or connection) between the gyros mounted in neighboring lattices. Compared to the simple spinning wheel model (shown in Figure 1.2), a more advanced model (but not the most complex model that can be imagined) for a gyro mounted in a structural lattice is schematically depicted in Figure 3.1. Note that the illustration in Figure 3.1 is a 2D view of a 3D segment of the very large 3D gyroscopic lattice structure extending in all three directions of the $\mathbb{R}^3$ space.

In Figure 3.1 the blue square and the dark red disk illustrate a structural lattice and its mounted-in gyro's spinning wheel. The black circle denotes the gyro's housing including the gimbals and the driving motors. The spring symbols are used to illustrate the possible flexibilities, or the elastic couplings, between different parts or mechanisms in the model; the green spring symbols represent the possible flexibility of the fixing mechanism between the lattice and the gyro's housing, the purple spring symbols show the flexibility of the gyro's gimbals and driving motors between the gyro's housing and spinning wheel, and the orange spring symbols denote the possible elastic coupling between the neighboring gyros.

It is also worth mentioning that each depicted spring symbol may represent all types of tension, compression, and torsion flexibilities or elastic couplings.

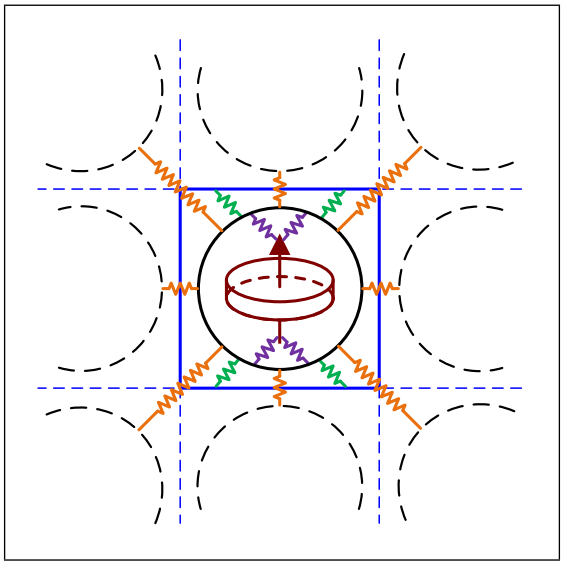

Figure 3.1: An advanced schematic model for a gyro mounted in a representative lattice of a gyroscopic structure with regular repetitive lattices.

By matching the equations derived in the previous sections (especially the dynamic equations given in Eqs. (3.11) and (3.12)) with the schematic shown in Figure 3.1, one can conclude that a classical or micropolar gyrocontinuum model is an idealized continuous model of a gyroscopic lattice structure where the mass and elasticity of the structure are respectively characterized by the volume body mass density ρ^V and the Lamé coefficients μ and λ, and the translational mass and rotational inertia of the gyros' spinning wheel are accounted for by the volume gyro mass density ϱ^V and the volume gyro rotational inertia density $\underset{\leftrightarrow}{\jmath}^V$. The deformations of the structure are ideally characterized by a continuous displacement field vector $\underset{\rightarrow}{u}$ and the rotations of the gyros' housing are identified as a (dependent or independent) continuous microrotation field vector $\underset{\rightarrow}{\vartheta}$ (in classical or micropolar gyrocontinuum models). The rotations of a gyro's spinning wheel with respect to the gyro's housing are given as continuous field variables φ_1, φ_2, and φ_3.

In addition to the aforementioned parameters which are common between the classical

and micropolar gyrocontinuum models, there are extra parameters in a micropolar gyrocontinuum model (*i.e.* the microinertia density $\underset{\leftrightarrow}{\imath}^V$, the micropolar coupling elastic constant κ, and the micropolar twist elastic constants γ, β, and α) which can help in representing the actual gyroscopic lattice structure more accurately.

To be more precise, in a micropolar gyrocontinuum model the microinertia density $\underset{\leftrightarrow}{\imath}^V$ can represent the rotational inertia of the gyro's gimbals and driving motors (depicted as a black circle in Figure 3.1), the micropolar coupling constant κ may quantify the flexibility of the fixing mechanism (illustrated by green spring symbols in Figure 3.1), and the micropolar constants γ, β, and α can measure the elastic coupling between the housings of the neighboring gyros (shown by purple spring symbols in Figure 3.1).

Note that in both classical and micropolar gyrocontinuum models the mass of the gyros' housing can be integrated into ϱ^V as the relative translational displacement between the housing and the spinning wheel, if any is insignificant. However, one should be careful not to integrate the rotational inertia of the gyros' housing into $\underset{\leftrightarrow}{\jmath}^V$ as there is a significant difference between the rotational displacements of the gyro's housing and spinning wheel (*i.e.* wheel's spin rotation). Unlike the micropolar model, in the classical gyrocontinuum model there is no parameter for quantifying the rotational inertia of the gyros' housing and it should be assumed negligible. Also, whereas the micropolar gyrocontinuum model is not capable of explicitly modeling the flexibility of the gyro's gimbals and driving motors (denoted by purple spring symbols in Figure 3.1), for the cases where the rotational inertia of the gyro's gimbals and driving motors (represented as the microinertia density $\underset{\leftrightarrow}{\imath}^V$ in a micropolar gyrocontinuum model) is significantly smaller than the rotational inertia of the gyro's spinning wheel (denoted as the gyro rotational inertia density $\underset{\leftrightarrow}{\jmath}^V$), one can assume that the micropolar coupling elastic constant κ is also representing the flexibility of the gyro's gimbals and driving motors in addition to the flexibility of the fixing mechanism. Indeed, in such a case one can assume that the flexibility of the gyro's gimbals and driving motors is in series with the flexibility of the fixing mechanism.

To sum up, as expected a micropolar gyrocontinuum has the advantage of being a more comprehensive model of the actual gyroscopic system (lattice structure) at the price of being a more complicated model; as mentioned earlier by employing the extra parameters $\underset{\leftrightarrow}{\imath}^V$, κ, γ, β, and α it can conveniently account for the effects of rotational inertia of the gyros'

housing, flexibility of the gyros' gimbals and driving motors, and elastic coupling between the neighboring gyros. A classical gyrocontinuum is, however, a more straightforward and simpler model of the actual gyroscopic system which is especially advantageous where the rotational inertia of the gyros' housing can be assumed negligible, the gyros' gimbals and driving motors can be presumed rigid, and the effects of elastic coupling or interaction between the neighboring gyros may be ignored. It is worth mentioning that in a micropolar gyrocontinuum model these three conditions can be reflected by letting $\underset{\leftrightarrow}{\imath}^V \to 0$, $\kappa \to \infty$, and $\gamma, \beta, \alpha \to 0$ which, as one may anticipate, reduces the micropolar gyrocontinuum model to the classical gyrocontinuum model (as shown in Appendix A for this set of parameters the micropolar elastic model simplifies to the classical elastic model).

Chapter 4

Gyroelastic Beams

4.1 Introduction

This chapter is concerned with the dynamic modeling of classical and micropolar gyroelastic beams. A gyroelastic beam, or more briefly a gyrobeam, is a linear elastic beam of classical or micropolar material carrying a 1D distribution of gyros or gyricity where this 1D gyricity distribution can be time-invarient or time-varying. Note that the term "classical gyrobeams" refers to the gyrobeams which are characterized based on the classical theory of elasticity simplified for beams, *e.g.* Timoshenko beam theory [48], and the term "micropolar gyrobeams" refers to those illustrated based on the simplified micropolar theory of elasticity, *e.g.* the theory developed by Ramezani [49]. Despite the fact that the elastic beam is linear, the system as a whole (*i.e.* the gyrobeam) can be linear or nonlinear.

For such a system, shown in Figure 4.1, the dynamic equations can be derived by reducing the equations of motion of a general 3D gyrocontinuum (derived in Chapter 3) to the special case of a 1D gyrobeam. The other way of writing the gyrobeam dynamic equations is to start with derivation of the system Lagrangian (including the potential and kinetic energy expressions) and virtual work expressions which are indeed the simplified versions of the corresponding expressions for a general 3D gyrocontinuum (also derived in Chapter 3). Then applying Hamilton's principle to these expressions will result in the

equations of motion along with the initial and boundary conditions (I/BCs). Recall that in addition to generation of the BCs, some very useful approximation methods will be made available through the Hamilton's principle approach.

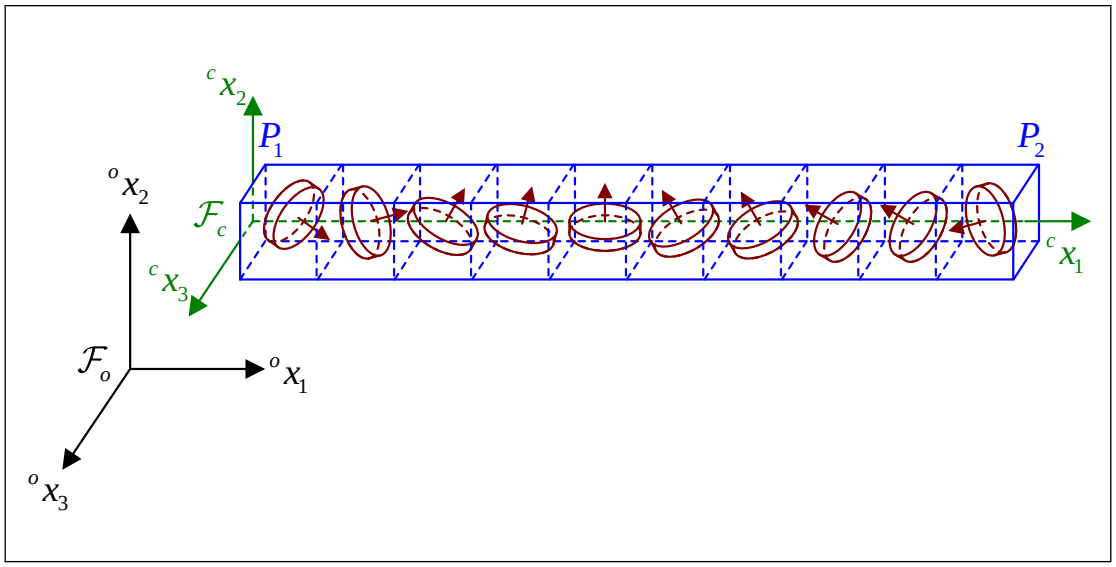

Figure 4.1: A gyrobeam parallel to the first coordinate axis of the inertial frame.

Accordingly, in this thesis, the second approach will be utilized for dynamic modeling of a gyrobeam where for simplicity, it is assumed that the system has no source of damping. In this way, to obtain the gyrobeam equations of motion, it will be enough to obtain the system potential and kinetic energy expressions, combine them into the system Lagrangian, derive the system virtual work expression, and apply Hamilton's principle to these Lagrangian and virtual work expressions. However, a preliminary step before developing the potential and kinetic energy and virtual work expressions is to choose the appropriate beam theories and formulate the corresponding assumptions about the form of deformation (*i.e.* displacement and microrotation) fields in the beam. Therefore, in the following sections, the chosen beam theories and kinematics of the beam will be reported firstly, and then the results will be used in derivation of the gyrobeam potential and kinetic energy expressions, virtual work expression, and equations of motion. To help with understanding of the derived equations and reporting of the developed models results,

nondimensionalization of the gyrobeams equations is presented. Numerical solutions of the nondimensionalized gyrobeams equations are initiated via a finite element formulation and a numerical time integration.

4.2 Deformation theories

As mentioned before this chapter deals with both classical and micropolar gyrobeams which require their own proper beam theories for modeling. The selection of these proper beam theories is the subject of this section.

By assuming that the beam plane sections remain plane after torsion and a diameter remains a straight line, the French engineer Alphonse Duleau derived an analytical solution for the torsion problem of a classical circular beam in 1820 [50]. The Duleau torsion theory is the most celebrated theory for torsion of classical beams with circular cross sections. It is also widely applied to the torsion problem of classical beams with non-circular cross section when an integrated torsion correction factor is introduced. On the other hand, the most recognized and complete classical beam bending theory is the theory developed by Stephen Timoshenko in the beginning of the 20^{th} century [48]. Consequently, the combination of simple longitudinal (tension-compression or axial tensile) deformation theory (generalized Hooke's law), Duleau torsion theory, and Timoshenko bending theory (with required correction factors) is used in this thesis for modeling the classical gyrobeams (regardless of the beam cross section shape).

About modeling the micropolar gyrobeams, however, the selection of the proper beam theories is not that straightforward. This is due to the fact that whereas the kinematics of classical beams and different theories for modeling them have been addressed extensively in the literature [38, 40, 51, 52], there are only a limited number of papers on the theory of micropolar beam deformations, the complexity of most of them being far beyond what is needed in the present work (note that simple enough beam theories are essential for modal analysis of gyrobeams and equivalent continuum modeling of beam-like truss structures).

The torsion problem of micropolar elastic beams of various cross sectional shapes was solved by Iesan [53], Gauthier [54], Park [55], and Potapenko [56]. In these works, for beams

with noncircular cross sections, a warping function was considered in the deformation fields which gives rise to extremely complicated solutions [53, 55, 56]. Even for circular cross section beams, the obtained solution is very complex, containing Bessel functions [54].

There are also some papers on bending of the micropolar elastic beams [57–59]. However, the solutions provided in these papers are complicated as well, and therefore are not suitable to be used in the present work. A simple solution of the micropolar beams bending problem was developed by Haung [60] where it was assumed that shear deformation is negligible and microrotation over the beam cross section is constant and is equal to the rotation of the beam plane section due to bending. Haung's micropolar beam theory can be considered as an extension of the classical Euler-Bernoulli beam bending theory. Another simple but more general solution of the micropolar beams bending problem was addressed by Ramezani [49]. In his paper, Ramezani followed Eringen's method [61] of constructing the micropolar plate theory and used a power series expansion technique to obtain the dynamic equations of micropolar elastic beams. He assumed that the microrotation (which is constant through the beam cross section) is different from the bending rotation of the beam plane section and developed a bending theory which is indeed an extension of the classical Timoshenko beam theory to the case of micropolar beams. However, it is noteworthy that due to a mistake made in the first step of the derivation of the equations (*i.e.* using an incorrect definition for the strain tensor in terms of displacement and microrotation fields), there are some errors in the equations of motion obtained by Ramezani.

Based on the aforementioned facts, the simple longitudinal deformation theory (generalized Hooke's law) combined with an extended form of the Duleau torsion theory and a revised and extended form of the Ramezani's micropolar beam bending theory, including the complementary correction factors, will be utilized in the present work to model the micropolar gyrobeams of arbitrary cross-sectional shapes.

4.3 Kinematics

Taking into account the chosen beam theories (mentioned in the previous section), it is generally assumed for a linear elastic beam deformed in 3D space that the deformations

are very small and plane sections of the beam remain plane after these deformations. Accordingly, the beam total deformation is calculated as a summation of longitudinal (axial), axial torsional, and lateral bending deformations (containing the effects of lateral shear and microrotations if necessary).

Now consider the beam, shown in Figure 4.1 or more simply in Figure 4.2, whose neutral (reference) axis is parallel to the first coordinate axis of the inertial reference frame, *i.e.* ${}^{o}x_1$. The principal axes of the beam's cross section (which is assumed uniform along the beam length) are parallel to the other coordinate axes of the inertial reference frame, *i.e.* ${}^{o}x_2$ and ${}^{o}x_3$. The most left and right points on the beam neutral axis are the beam's boundary points denoted by P_1 and P_2. As shown in Figure 4.2, a body fixed frame, called beam frame $\mathcal{F}_c$, is located at the left end of the beam (with its origin at boundary point P_1) such that (neglecting the beam deformations) its first coordinate axis, *i.e.* ${}^{c}x_1$, is coincident with the beam neutral axis and its second and third coordinate axes, *i.e.* ${}^{c}x_2$ and ${}^{c}x_3$, are coincident with the principal axes of the beam cross section. It is noteworthy that the beam frame $\mathcal{F}_c$ is different from the body frames $\mathcal{F}_b$ corresponding to infinitesimal elements of the beam and by assuming that the beam does not undergo any (large) rigid body rotation, this beam frame $\mathcal{F}_c$ is always parallel to the inertial reference frame $\mathcal{F}_o$.

The beam is of length L and its cross section is of area A, polar moment of area (polar moment of inertia) I_1 (about axis ${}^{c}x_1$), and second moments of area (area moments of inertia) I_2 and I_3 (about axes ${}^{c}x_2$ and ${}^{c}x_3$ respectively). Note that:

$$\int_A {}^{c}x_2 \, dA = 0, \qquad \int_A {}^{c}x_3 \, dA = 0 \tag{4.1}$$

and:

$$I_2 = \int_A {}^{c}x_3 \, {}^{c}x_3 \, dA, \qquad I_3 = \int_A {}^{c}x_2 \, {}^{c}x_2 \, dA, \qquad I_1 = I_2 + I_3 \tag{4.2}$$

where $\int_A \square \, dA$ represents the integral over the beam cross section.

Assuming that the deformations are very small, plane sections of the beam remain plane after these deformations, and the torsional warping effects on the cross section are

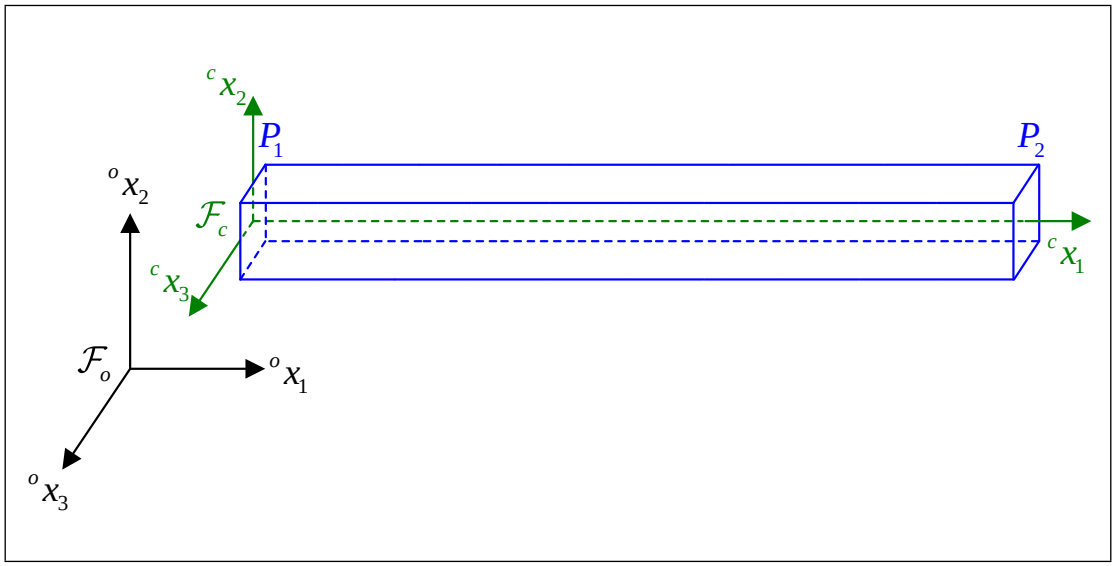

Figure 4.2: An elastic beam parallel to the first coordinate axis of the inertial frame.

negligible (*i.e.* any straight line on the beam cross section remains a straight line), the total deformation of a micropolar elastic beam can be characterized by a displacement field of the form:

$$\begin{aligned} u_1 &= \bar{u}_1(t, {}^c x_1) + {}^c x_2\, \bar{y}_{12}(t, {}^c x_1) + {}^c x_3\, \bar{y}_{13}(t, {}^c x_1) \\ u_2 &= \bar{u}_2(t, {}^c x_1) + {}^c x_2\, \bar{y}_{22}(t, {}^c x_1) + {}^c x_3\, \bar{y}_{23}(t, {}^c x_1) \\ u_3 &= \bar{u}_3(t, {}^c x_1) + {}^c x_2\, \bar{y}_{32}(t, {}^c x_1) + {}^c x_3\, \bar{y}_{33}(t, {}^c x_1) \end{aligned} \tag{4.3}$$

and a microrotation field of the form:

$$\begin{aligned} \vartheta_1 &= \bar{\vartheta}_1(t, {}^c x_1) + {}^c x_2\, \bar{z}_{12}(t, {}^c x_1) + {}^c x_3\, \bar{z}_{13}(t, {}^c x_1) \\ \vartheta_2 &= \bar{\vartheta}_2(t, {}^c x_1) + {}^c x_2\, \bar{z}_{22}(t, {}^c x_1) + {}^c x_3\, \bar{z}_{23}(t, {}^c x_1) \\ \vartheta_3 &= \bar{\vartheta}_3(t, {}^c x_1) + {}^c x_2\, \bar{z}_{32}(t, {}^c x_1) + {}^c x_3\, \bar{z}_{33}(t, {}^c x_1) \end{aligned} \tag{4.4}$$

which are actually the first-order (or linear Taylor) expansions of the displacement and microrotation fields on the beam's cross section and around the beam's neutral axis, *i.e.* at ${}^c x_2 = 0$ and ${}^c x_3 = 0$. The variables $\bar{u}_i$ and $\bar{\vartheta}_i$ $(i = 1, 2, 3)$ are deformations (*i.e.* displacements and microrotations) on the beam's neutral axis, and the variables $\bar{y}_{ij}$ and $\bar{z}_{ij}$ $(i = 1, 2, 3$ and $j = 2, 3)$ are unknown coefficients to be determined later. Notice that, as

given in Eqs. (4.3) and (4.4), these first-order expansions necessitate the unknown variables $\bar{y}_{ij}$ and $\bar{z}_{ij}$ to be constant over the beam cross section (*i.e.* do not vary with ${}^{c}x_2$ and ${}^{c}x_3$).

Based on the assumed displacement and microrotation fields, given by Eqs. (4.3) and (4.4), and considering the fact that:

$$\frac{d}{dx_i} = {}^{c}\frac{d}{dx_i} \tag{4.5}$$

the elements of the strain and twist tensors will be obtained as:

$$\begin{aligned}
\varepsilon_{11} &= \bar{u}_{1,1} + {}^{c}x_2\,\bar{y}_{12,1} + {}^{c}x_3\,\bar{y}_{13,1} \\
\varepsilon_{22} &= \bar{y}_{22} \\
\varepsilon_{33} &= \bar{y}_{33} \\
\varepsilon_{12} &= \bar{u}_{2,1} + {}^{c}x_2\,\bar{y}_{22,1} + {}^{c}x_3\,\bar{y}_{23,1} - \bar{\vartheta}_3 - {}^{c}x_2\,\bar{z}_{32} - {}^{c}x_3\,\bar{z}_{33} \\
\varepsilon_{21} &= \bar{y}_{12} + \bar{\vartheta}_3 + {}^{c}x_2\,\bar{z}_{32} + {}^{c}x_3\,\bar{z}_{33} \\
\varepsilon_{13} &= \bar{u}_{3,1} + {}^{c}x_2\,\bar{y}_{32,1} + {}^{c}x_3\,\bar{y}_{33,1} + \bar{\vartheta}_2 + {}^{c}x_2\,\bar{z}_{22} + {}^{c}x_3\,\bar{z}_{23} \\
\varepsilon_{31} &= \bar{y}_{13} - \bar{\vartheta}_2 - {}^{c}x_2\,\bar{z}_{22} - {}^{c}x_3\,\bar{z}_{23} \\
\varepsilon_{23} &= \bar{y}_{32} - \vartheta_1 - {}^{c}x_2\,\bar{z}_{12} - {}^{c}x_3\,\bar{z}_{13} \\
\varepsilon_{32} &= \bar{y}_{23} + \vartheta_1 + {}^{c}x_2\,\bar{z}_{12} + {}^{c}x_3\,\bar{z}_{13}
\end{aligned} \tag{4.6}$$

and:

$$\begin{aligned}
\tau_{11} &= \bar{\vartheta}_{1,1} + {}^{c}x_2\,\bar{z}_{12,1} + {}^{c}x_3\,\bar{z}_{13,1} \\
\tau_{22} &= \bar{z}_{22} \\
\tau_{33} &= \bar{z}_{33} \\
\tau_{12} &= \bar{\vartheta}_{2,1} + {}^{c}x_2\,\bar{z}_{22,1} + {}^{c}x_3\,\bar{z}_{23,1} \\
\tau_{21} &= \bar{z}_{12} \\
\tau_{13} &= \bar{\vartheta}_{3,1} + {}^{c}x_2\,\bar{z}_{32,1} + {}^{c}x_3\,\bar{z}_{33,1} \\
\tau_{31} &= \bar{z}_{13} \\
\tau_{23} &= \bar{z}_{32} \\
\tau_{32} &= \bar{z}_{23}
\end{aligned} \tag{4.7}$$

However, when solving a 3D beam problem it is common to assume the problem as a superposition of two plane force/couple stress problems (and not two plane strain/twist

problems) in the ${}^{c}x_1{}^{c}x_2$ and ${}^{c}x_1{}^{c}x_3$ planes (or the ${}^{o}x_1{}^{o}x_2$ and ${}^{o}x_1{}^{o}x_3$ planes) where:

$$\sigma_{22} = \sigma_{33} = 0, \qquad \chi_{22} = \chi_{33} = 0 \tag{4.8}$$

Whereas assuming a zero value for shear stresses σ_{23} and σ_{32} is natural in a classical elastic beam (in fact, this results in some difficulties which are resolved by introducing a shear correction factor), here for a micropolar elastic beam (where the existence of asymmetric stress and strain tensors is not unusual) there is no need to add such an assumption. Instead, it is helpful or natural to additionally assume:

$$\chi_{23} = \chi_{32} = 0 \tag{4.9}$$

Finally, to assure that a straight line on the beam cross section remains a straight line when the beam undergoes a deformation of the form given by Eqs. (4.3) and (4.4), it is necessary to have:

$$u_{2,3} = -u_{3,2} \tag{4.10}$$

By using the force and couple stresses given in Eqs. (4.8) and (4.9) to substitute into the constitutive relations of the micropolar elasticity, given by Eq. (2.4), one can obtain the following relations for the corresponding strain and twist elements:

$$\begin{aligned} \varepsilon_{22} = \varepsilon_{33} &= -\nu\,\varepsilon_{11} \\ \tau_{22} = \tau_{33} &= -\xi\,\tau_{11} \\ \tau_{23} = \tau_{32} &= 0 \end{aligned} \tag{4.11}$$

In Eq. (4.11), ν is the strain Poisson's ratio, relating normal strains to each other in a plane force stress problem, and ξ is the twist Poisson's ratio, relating normal twists (torsions) to each other in a plane couple stress problem. These Poisson's ratios are related to the other material elastic constants as:

$$\nu = \frac{\lambda}{2\left(\mu + \lambda\right)}, \qquad \xi = \frac{\alpha}{2\left(\gamma + \alpha\right)} \tag{4.12}$$

Substitutions from Eq. (4.3) into Eq. (4.10) and from Eqs. (4.6) and (4.7) into Eq. (4.11),

while noting that $\bar{y}_{ij}$ and $\bar{z}_{ij}$ should be constant over the beam cross section, result in:

$$\begin{aligned}
\bar{y}_{23} &= -\bar{y}_{32} \\
\bar{y}_{22} = \bar{y}_{33} &= -\nu\,\bar{u}_{1,1} \\
\bar{z}_{22} = \bar{z}_{33} &= -\xi\,\bar{\vartheta}_{1,1} \\
\bar{z}_{23} = \bar{z}_{32} &= 0
\end{aligned} \tag{4.13}$$

Additionally, one can define the torsional and bending rotations of the beam plane sections, denoted by $\bar{\theta}_i$, such that:

$$\begin{aligned}
-\bar{\theta}_1 &= \frac{1}{A}\int_A u_{2,3}\,dA = \frac{1}{A}\int_A -u_{3,2}\,dA \\
\bar{\theta}_2 &= \frac{1}{A}\int_A u_{1,3}\,dA \\
-\bar{\theta}_3 &= \frac{1}{A}\int_A u_{1,2}\,dA
\end{aligned} \tag{4.14}$$

where Eq. (4.10) is recalled and the negative signs before $\bar{\theta}_1$ and $\bar{\theta}_3$, in the first and third relations, are introduced to insure the positiveness of a plane rotation $\bar{\theta}_i$ if it has the same sense as the positive direction of the beam frame coordinate axis ${}^{c}x_i$ (or in other words if, based on the right-hand rule, it is pointing toward the positive direction of the beam frame coordinate axis ${}^{c}x_i$). Substitution from Eq. (4.3) into Eq. (4.14) results in:

$$\begin{aligned}
\bar{y}_{23} &= -\bar{y}_{32} = -\bar{\theta}_1 \\
\bar{y}_{12} &= -\bar{\theta}_3 \\
\bar{y}_{13} &= \bar{\theta}_2
\end{aligned} \tag{4.15}$$

At the end, regarding the determination of $\bar{z}_{12}$ and $\bar{z}_{13}$, as in this text the simple micropolar beam torsion and bending theories are desired and as there is no more necessary constraint to add or reasonable assumption to make, one can simply assign:

$$\bar{z}_{12} = \bar{z}_{13} = 0 \tag{4.16}$$

By substituting the unknown coefficients $\bar{y}_{ij}$ and $\bar{z}_{ij}$ $(i = 1, 2, 3$ and $j = 2, 3)$ from Eqs. (4.13), (4.15), and (4.16) into Eqs. (4.3) and (4.4), the displacement and microrotation fields in a micropolar elastic beam can be rewritten as:

$$\begin{aligned} u_1 &= \bar{u}_1(t, {}^c x_1) - {}^c x_2\, \bar{\theta}_3(t, {}^c x_1) + {}^c x_3\, \bar{\theta}_2(t, {}^c x_1) \\ u_2 &= \bar{u}_2(t, {}^c x_1) - {}^c x_2\, \nu\, \bar{u}_{1,1}(t, {}^c x_1) - {}^c x_3\, \bar{\theta}_1(t, {}^c x_1) \\ u_3 &= \bar{u}_3(t, {}^c x_1) + {}^c x_2\, \bar{\theta}_1(t, {}^c x_1) - {}^c x_3\, \nu\, \bar{u}_{1,1}(t, {}^c x_1) \end{aligned} \tag{4.17}$$

$$\begin{aligned} \vartheta_1 &= \bar{\vartheta}_1(t, {}^c x_1) \\ \vartheta_2 &= \bar{\vartheta}_2(t, {}^c x_1) - {}^c x_2\, \xi\, \bar{\vartheta}_{1,1}(t, {}^c x_1) \\ \vartheta_3 &= \bar{\vartheta}_3(t, {}^c x_1) - {}^c x_3\, \xi\, \bar{\vartheta}_{1,1}(t, {}^c x_1) \end{aligned} \tag{4.18}$$

which give rise to the following strain and twist fields:

$$\begin{aligned} \varepsilon_{11} &= \bar{u}_{1,1} - {}^c x_2\, \bar{\theta}_{3,1} + {}^c x_3\, \bar{\theta}_{2,1} \\ \varepsilon_{22} &= \varepsilon_{33} = -\nu\, \varepsilon_{11} \\ \varepsilon_{12} &= \bar{u}_{2,1} - {}^c x_3\, \bar{\theta}_{1,1} - \bar{\vartheta}_3 + {}^c x_3\, \xi\, \bar{\vartheta}_{1,1} \\ \varepsilon_{21} &= -\bar{\theta}_3 + \bar{\vartheta}_3 - {}^c x_3\, \xi\, \bar{\vartheta}_{1,1} \\ \varepsilon_{13} &= \bar{u}_{3,1} + {}^c x_2\, \bar{\theta}_{1,1} + \bar{\vartheta}_2 - {}^c x_2\, \xi\, \bar{\vartheta}_{1,1} \\ \varepsilon_{31} &= \bar{\theta}_2 - \bar{\vartheta}_2 + {}^c x_2\, \xi\, \bar{\vartheta}_{1,1} \\ \varepsilon_{23} &= -\varepsilon_{32} = \bar{\theta}_1 - \vartheta_1 \end{aligned} \tag{4.19}$$

$$\begin{aligned} \tau_{11} &= \bar{\vartheta}_{1,1} \\ \tau_{22} &= \tau_{33} = -\xi\, \tau_{11} \\ \tau_{12} &= \bar{\vartheta}_{2,1} \\ \tau_{13} &= \bar{\vartheta}_{3,1} \\ \tau_{21} &= \tau_{31} = 0 \\ \tau_{23} &= \tau_{32} = 0 \end{aligned} \tag{4.20}$$

where Eq. (4.11) is recalled and the terms containing the second-order spatial derivatives (with respect to coordinate axis ${}^c x_1$ or ${}^o x_1$) as higher order terms are neglected. Remember the difference between the symbol $\bar{\vartheta}$ denoting the beam's neutral axis microrotations and

the symbol $\bar{\theta}$ denoting the beam plane section rotations. Also note that the beam microrotations are absolute rotations measured with respect to the inertial reference frame $\mathcal{F}_o$ (not relative rotations with respect to the beam cross sectional plane).

Based on Eqs. (4.17) and (4.18), one can conclude that a micropolar beam has nine independent continuous generalized coordinates, *i.e.* three beam neutral axis displacements $\bar{u}_i$, three rotations (one torsional and two bending rotations) of the beam's plane section $\bar{\theta}_i$, and three beam neutral axis microrotations $\bar{\vartheta}_i$ $(i = 1, 2, 3)$.

In the same way, by utilizing the simple longitudinal deformation theory, Duleau torsion theory, and Timoshenko bending theory, the kinematics of a classical elastic beam can be formulated as:

$$\begin{aligned} u_1 &= \bar{u}_1(t, {}^c x_1) - {}^c x_2\, \bar{\theta}_3(t, {}^c x_1) + {}^c x_3\, \bar{\theta}_2(t, {}^c x_1) \\ u_2 &= \bar{u}_2(t, {}^c x_1) - {}^c x_2\, \nu\, \bar{u}_{1,1}(t, {}^c x_1) - {}^c x_3\, \bar{\theta}_1(t, {}^c x_1) \\ u_3 &= \bar{u}_3(t, {}^c x_1) + {}^c x_2\, \bar{\theta}_1(t, {}^c x_1) - {}^c x_3\, \nu\, \bar{u}_{1,1}(t, {}^c x_1) \end{aligned} \tag{4.21}$$

and:

$$\begin{aligned} \varepsilon_{11} &= \bar{u}_{1,1} - {}^c x_2\, \bar{\theta}_{3,1} + {}^c x_3\, \bar{\theta}_{2,1} \\ \varepsilon_{22} &= \varepsilon_{33} = -\nu\, \varepsilon_{11} \\ \varepsilon_{12} &= \varepsilon_{21} = \frac{1}{2}\left(\bar{u}_{2,1} - {}^c x_3\, \bar{\theta}_{1,1} - \bar{\theta}_3\right) \\ \varepsilon_{13} &= \varepsilon_{31} = \frac{1}{2}\left(\bar{u}_{3,1} + {}^c x_2\, \bar{\theta}_{1,1} + \bar{\theta}_2\right) \\ \varepsilon_{23} &= \varepsilon_{32} = 0 \end{aligned} \tag{4.22}$$

where:

$$\nu = \frac{\lambda}{2\left(\mu + \lambda\right)} \tag{4.23}$$

Here, the microrotations (being identical with the macrorotations) are dependent on the displacements as given by the first relation of Eq. (2.15), *i.e.* (compare this to Eq. (4.18)):

$$\begin{aligned} \vartheta_1 &= \frac{1}{2}\left(u_{3,2} - u_{2,3}\right) = \frac{1}{2}\left(\bar{\theta}_1 + \bar{\theta}_1\right) = \bar{\theta}_1(t, {}^c x_1) \\ \vartheta_2 &= \frac{1}{2}\left(u_{1,3} - u_{3,1}\right) = \frac{1}{2}\left(\bar{\theta}_2 - \bar{u}_{3,1} - {}^c x_2\, \bar{\theta}_{1,1}\right) \approx \bar{\theta}_2(t, {}^c x_1) - {}^c x_2\, \frac{1}{2}\, \bar{\theta}_{1,1}(t, {}^c x_1) \\ \vartheta_3 &= \frac{1}{2}\left(u_{2,1} - u_{1,2}\right) = \frac{1}{2}\left(\bar{u}_{2,1} - {}^c x_3\, \bar{\theta}_{1,1} + \bar{\theta}_3\right) \approx \bar{\theta}_3(t, {}^c x_1) - {}^c x_3\, \frac{1}{2}\, \bar{\theta}_{1,1}(t, {}^c x_1) \end{aligned} \tag{4.24}$$

Consequently, a classical beam has six independent continuous generalized coordinates, *i.e.* three beam's neutral axis displacements $\bar{u}_i$ and three rotations (one torsional and two bending rotations) of the beam's plane section $\bar{\theta}_i$ $(i = 1, 2, 3)$.

It is worth noting that the displacement fields given by Eqs. (4.17) and (4.21) are useful for derivation of the strains (except ε_{22} and ε_{33} which are obtained using Eq. (4.11)) and the potential energy expression. However, when deriving the kinetic energy and virtual work expressions it is more helpful to approximately express the displacements as:

$$\begin{aligned} u_1 &= \bar{u}_1(t, {}^c x_1) - {}^c x_2\, \bar{\theta}_3(t, {}^c x_1) + {}^c x_3\, \bar{\theta}_2(t, {}^c x_1) \\ u_2 &\approx \bar{u}_2(t, {}^c x_1) - {}^c x_3\, \bar{\theta}_1(t, {}^c x_1) \\ u_3 &\approx \bar{u}_3(t, {}^c x_1) + {}^c x_2\, \bar{\theta}_1(t, {}^c x_1) \end{aligned} \tag{4.25}$$

in both classical and micropolar elastic beams. Accordingly, the linear velocity and acceleration fields and the virtual displacement field will be obtained as:

$$\begin{aligned} \dot{u}_1 &= \dot{\bar{u}}_1(t, {}^c x_1) - {}^c x_2\, \dot{\bar{\theta}}_3(t, {}^c x_1) + {}^c x_3\, \dot{\bar{\theta}}_2(t, {}^c x_1) \\ \dot{u}_2 &\approx \dot{\bar{u}}_2(t, {}^c x_1) - {}^c x_3\, \dot{\bar{\theta}}_1(t, {}^c x_1) \\ \dot{u}_3 &\approx \dot{\bar{u}}_3(t, {}^c x_1) + {}^c x_2\, \dot{\bar{\theta}}_1(t, {}^c x_1) \end{aligned} \tag{4.26}$$

$$\begin{aligned} \ddot{u}_1 &= \ddot{\bar{u}}_1(t, {}^c x_1) - {}^c x_2\, \ddot{\bar{\theta}}_3(t, {}^c x_1) + {}^c x_3\, \ddot{\bar{\theta}}_2(t, {}^c x_1) \\ \ddot{u}_2 &\approx \ddot{\bar{u}}_2(t, {}^c x_1) - {}^c x_3\, \ddot{\bar{\theta}}_1(t, {}^c x_1) \\ \ddot{u}_3 &\approx \ddot{\bar{u}}_3(t, {}^c x_1) + {}^c x_2\, \ddot{\bar{\theta}}_1(t, {}^c x_1) \end{aligned} \tag{4.27}$$

$$\begin{aligned} \delta u_1 &= \delta\bar{u}_1(t, {}^c x_1) - {}^c x_2\, \delta\bar{\theta}_3(t, {}^c x_1) + {}^c x_3\, \delta\bar{\theta}_2(t, {}^c x_1) \\ \delta u_2 &\approx \delta\bar{u}_2(t, {}^c x_1) - {}^c x_3\, \delta\bar{\theta}_1(t, {}^c x_1) \\ \delta u_3 &\approx \delta\bar{u}_3(t, {}^c x_1) + {}^c x_2\, \delta\bar{\theta}_1(t, {}^c x_1) \end{aligned} \tag{4.28}$$

Analogously, whereas the microrotation fields given by Eqs. (4.18) and (4.24) are useful for derivation of the strain and twist tensors and the potential energy expression, when deriving the kinetic energy and virtual work expressions it is more helpful to approximate the microrotation field vector as:

$$\underset{\rightarrow}{\vartheta} \approx \underset{\rightarrow}{\bar{\vartheta}}(t, {}^c x_1), \qquad \underline{\boldsymbol{\vartheta}} \approx \underline{\bar{\boldsymbol{\vartheta}}}(t, {}^c x_1), \qquad \vartheta_i \approx \bar{\vartheta}_i(t, {}^c x_1) \tag{4.29}$$

in a micropolar beam, and as:

$$\underset{\rightarrow}{\vartheta} \approx \underset{\rightarrow}{\bar{\theta}}(t, {}^{c}x_1), \qquad \underline{\boldsymbol{\vartheta}} \approx \underline{\bar{\boldsymbol{\theta}}}(t, {}^{c}x_1), \qquad \vartheta_i \approx \bar{\theta}_i(t, {}^{c}x_1) \tag{4.30}$$

in a classical beam. Based on this definition the microrotational velocity and acceleration field vectors (*i.e.* the time derivatives of $\underset{\rightarrow}{\vartheta}$) will approximately be:

$$\begin{aligned} &\dot{\underset{\rightarrow}{\vartheta}} \approx \dot{\underset{\rightarrow}{\bar{\vartheta}}}(t, {}^{c}x_1), \qquad \underline{\dot{\boldsymbol{\vartheta}}} \approx \underline{\dot{\bar{\boldsymbol{\vartheta}}}}(t, {}^{c}x_1), \qquad \dot{\vartheta}_i \approx \dot{\bar{\vartheta}}_i(t, {}^{c}x_1) \\ &\ddot{\underset{\rightarrow}{\vartheta}} \approx \ddot{\underset{\rightarrow}{\bar{\vartheta}}}(t, {}^{c}x_1), \qquad \underline{\ddot{\boldsymbol{\vartheta}}} \approx \underline{\ddot{\bar{\boldsymbol{\vartheta}}}}(t, {}^{c}x_1), \qquad \ddot{\vartheta}_i \approx \ddot{\bar{\vartheta}}_i(t, {}^{c}x_1) \end{aligned} \tag{4.31}$$

for a micropolar beam, and:

$$\begin{aligned} &\dot{\underset{\rightarrow}{\vartheta}} \approx \dot{\underset{\rightarrow}{\bar{\theta}}}(t, {}^{c}x_1), \qquad \underline{\dot{\boldsymbol{\vartheta}}} \approx \underline{\dot{\bar{\boldsymbol{\theta}}}}(t, {}^{c}x_1), \qquad \dot{\vartheta}_i \approx \dot{\bar{\theta}}_i(t, {}^{c}x_1) \\ &\ddot{\underset{\rightarrow}{\vartheta}} \approx \ddot{\underset{\rightarrow}{\bar{\theta}}}(t, {}^{c}x_1), \qquad \underline{\ddot{\boldsymbol{\vartheta}}} \approx \underline{\ddot{\bar{\boldsymbol{\theta}}}}(t, {}^{c}x_1), \qquad \ddot{\vartheta}_i \approx \ddot{\bar{\theta}}_i(t, {}^{c}x_1) \end{aligned} \tag{4.32}$$

for a classical beam. Finally, one can approximately represent the virtual microrotation field vector, correspondingly in micropolar and classical beams, as:

$$\delta\underset{\rightarrow}{\vartheta} \approx \delta\underset{\rightarrow}{\bar{\vartheta}}(t, {}^{c}x_1), \qquad \delta\underline{\boldsymbol{\vartheta}} \approx \delta\underline{\bar{\boldsymbol{\vartheta}}}(t, {}^{c}x_1), \qquad \delta\vartheta_i \approx \delta\bar{\vartheta}_i(t, {}^{c}x_1) \tag{4.33}$$

and:

$$\delta\underset{\rightarrow}{\vartheta} \approx \delta\underset{\rightarrow}{\bar{\theta}}(t, {}^{c}x_1), \qquad \delta\underline{\boldsymbol{\vartheta}} \approx \delta\underline{\bar{\boldsymbol{\theta}}}(t, {}^{c}x_1), \qquad \delta\vartheta_i \approx \delta\bar{\theta}_i(t, {}^{c}x_1) \tag{4.34}$$

4.4 Potential energy expression

As mentioned in Chapter 3, the only source of the potential energy in a gyrocontinuum is the elasticity of the system and the system potential energy is equal to its total strain energy. On the other hand, to derive the total strain energy expression of a gyrocontinuum, the force and couple stress tensors are needed in addition to the strain and twist tensors. Based on the results obtained in the previous section and by utilizing the constitutive relations given by Eq. (2.4) the elements of the force and couple stress tensors for a micropolar

elastic beam will be derived as:

$$\begin{aligned}
\sigma_{11} &= E\,\varepsilon_{11} \\
\sigma_{22} &= \sigma_{33} = 0 \\
\sigma_{12} &= \Big(\mu + \kappa\Big)\,\varepsilon_{12} + \Big(\mu - \kappa\Big)\,\varepsilon_{21} \\
\sigma_{21} &= \Big(\mu + \kappa\Big)\,\varepsilon_{21} + \Big(\mu - \kappa\Big)\,\varepsilon_{12} \\
\sigma_{13} &= \Big(\mu + \kappa\Big)\,\varepsilon_{13} + \Big(\mu - \kappa\Big)\,\varepsilon_{31} \\
\sigma_{31} &= \Big(\mu + \kappa\Big)\,\varepsilon_{31} + \Big(\mu - \kappa\Big)\,\varepsilon_{13} \\
\sigma_{23} &= -\,\sigma_{32} = 2\,\kappa\,\varepsilon_{23}
\end{aligned} \tag{4.35}$$

and:

$$\begin{aligned}
\chi_{11} &= \mathcal{E}\,\tau_{11} \\
\chi_{22} &= \chi_{33} = 0 \\
\chi_{12} &= \Big(\gamma + \beta\Big)\,\tau_{12} \\
\chi_{21} &= \Big(\gamma - \beta\Big)\,\tau_{12} \\
\chi_{13} &= \Big(\gamma + \beta\Big)\,\tau_{13} \\
\chi_{31} &= \Big(\gamma - \beta\Big)\,\tau_{13} \\
\chi_{23} &= \chi_{32} = 0
\end{aligned} \tag{4.36}$$

where E is the tensile (Young's) modulus, relating the normal force stresses to the normal strains in a plane force stress problem, and $\mathcal{E}$ is the tortile (torsional) modulus, relating the normal couple stresses to the normal twists (torsions) in a plane couple stress problem. These moduli are defined as:

$$\begin{aligned}
E &= \frac{\mu\,\Big(2\,\mu + 3\,\lambda\Big)}{\mu + \lambda} = 2\,\mu\,\Big(1 + \nu\Big) \\
\mathcal{E} &= \frac{\gamma\,\Big(2\,\gamma + 3\,\alpha\Big)}{\gamma + \alpha} = 2\,\gamma\,\Big(1 + \xi\Big)
\end{aligned} \tag{4.37}$$

By substitution from Eqs. (4.35) and (4.36) into Eq. (3.2) (which gives the potential energy expression of a general gyrocontinuum), the following expression will be obtained

for the potential energy of a micropolar gyrobeam:

$$\begin{aligned}\mathcal{U} = \frac{1}{2}\,E \int\limits_V \varepsilon_{11}\,\varepsilon_{11}\,dV + \frac{1}{2}\left(\mu+\kappa\right) \int\limits_V \Big(\varepsilon_{12}\,\varepsilon_{12} + \varepsilon_{21}\,\varepsilon_{21} + \varepsilon_{13}\,\varepsilon_{13} + \varepsilon_{31}\,\varepsilon_{31}\Big)\,dV \\ + \left(\mu-\kappa\right) \int\limits_V \Big(\varepsilon_{12}\,\varepsilon_{21} + \varepsilon_{13}\,\varepsilon_{31}\Big)\,dV + 2\,\kappa \int\limits_V \varepsilon_{23}\,\varepsilon_{23}\,dV \\ + \frac{1}{2}\,\mathcal{E} \int\limits_V \tau_{11}\,\tau_{11}\,dV + \frac{1}{2}\left(\gamma+\beta\right) \int\limits_V \Big(\tau_{12}\,\tau_{12} + \tau_{13}\,\tau_{13}\Big)\,dV\end{aligned} \tag{4.38}$$

which (analogous to the rearrangement in Eq. (3.3)) can be rearranged into:

$$\begin{aligned}\mathcal{U} = \frac{1}{2}\,E \int\limits_V \varepsilon_{11}\,\varepsilon_{11}\,dV + \frac{1}{2}\,\mu \int\limits_V \Big(\varepsilon_{12}+\varepsilon_{21}\Big)^2\,dV + \frac{1}{2}\,\mu \int\limits_V \Big(\varepsilon_{13}+\varepsilon_{31}\Big)^2\,dV \\ + \frac{1}{2}\,\kappa \int\limits_V \Big(\varepsilon_{12}-\varepsilon_{21}\Big)^2\,dV + \frac{1}{2}\,\kappa \int\limits_V \Big(\varepsilon_{13}-\varepsilon_{31}\Big)^2\,dV + \frac{1}{2}\,\kappa \int\limits_V \Big(\varepsilon_{23}-\varepsilon_{32}\Big)^2\,dV \\ + \frac{1}{2}\,\mathcal{E} \int\limits_V \tau_{11}\,\tau_{11}\,dV + \frac{1}{2}\left(\gamma+\beta\right) \int\limits_V \Big(\tau_{12}\,\tau_{12} + \tau_{13}\,\tau_{13}\Big)\,dV\end{aligned} \tag{4.39}$$

where V is the volume of the beam.

Now by splitting the volume integration into the integration over the cross section A and the integration over the length L, substituting from Eqs. (4.19) and (4.20), and taking the integration over the cross section, the potential energy expression, given by Eq. (4.39),

takes the following form:

$$\begin{aligned}
\mathcal{U} = \frac{1}{2}\,E\,A\int_L \bar{u}_{1,1}\,\bar{u}_{1,1}\,dL + \frac{1}{2}\,E\,I_2\int_L \bar{\theta}_{2,1}\,\bar{\theta}_{2,1}\,dL + \frac{1}{2}\,E\,I_3\int_L \bar{\theta}_{3,1}\,\bar{\theta}_{3,1}\,dL \\
+ \frac{1}{2}\,\mu\,A\int_L \Big(\bar{u}_{2,1} - \bar{\theta}_3\Big)^2\,dL + \frac{1}{2}\,\mu\,A\int_L \Big(\bar{u}_{3,1} + \bar{\theta}_2\Big)^2\,dL + \frac{1}{2}\,\mu\,I_1\int_L \bar{\theta}_{1,1}\,\bar{\theta}_{1,1}\,dL \\
+ \frac{1}{2}\,\kappa\,A\int_L \Big(\bar{u}_{2,1} + \bar{\theta}_3 - 2\,\bar{\vartheta}_3\Big)^2\,dL + \frac{1}{2}\,\kappa\,A\int_L \Big(\bar{u}_{3,1} - \bar{\theta}_2 + 2\,\bar{\vartheta}_2\Big)^2\,dL \\
+ \frac{1}{2}\,\kappa\,I_1\int_L \Big(\bar{\theta}_{1,1} - 2\,\xi\,\bar{\vartheta}_{1,1}\Big)^2\,dL + 2\,\kappa\,A\int_L \Big(\bar{\theta}_1 - \bar{\vartheta}_1\Big)^2\,dL \\
+ \frac{1}{2}\,\mathcal{E}\,A\int_L \bar{\vartheta}_{1,1}\,\bar{\vartheta}_{1,1}\,dL + \frac{1}{2}\,\Big(\gamma + \beta\Big)\,A\int_L \Big(\bar{\vartheta}_{2,1}\,\bar{\vartheta}_{2,1} + \bar{\vartheta}_{3,1}\,\bar{\vartheta}_{3,1}\Big)\,dL \\
= \int_L \mathcal{U}^L\,dL
\end{aligned} \tag{4.40}$$

where $\mathcal{U}^L$ is the linear density of the potential energy or the potential energy per unit length and recall that μ is the shear modulus.

The potential energy expression of a micropolar beam given by Eq. (4.40) will reduce to the potential energy expression of a classical Timoshenko beam (including the contribution from axial and torsional deformations) if the assumptions of the classical theory of elasticity are applied. In this way, the following expression will be obtained for the potential energy of a classical beam:

$$\begin{aligned}
\mathcal{U} = \frac{1}{2}\,E\,A\int_L \bar{u}_{1,1}\,\bar{u}_{1,1}\,dL + \frac{1}{2}\,E\,I_2\int_L \bar{\theta}_{2,1}\,\bar{\theta}_{2,1}\,dL + \frac{1}{2}\,E\,I_3\int_L \bar{\theta}_{3,1}\,\bar{\theta}_{3,1}\,dL \\
+ \frac{1}{2}\,\mu\,A\int_L \Big(\bar{u}_{2,1} - \bar{\theta}_3\Big)^2\,dL + \frac{1}{2}\,\mu\,A\int_L \Big(\bar{u}_{3,1} + \bar{\theta}_2\Big)^2\,dL + \frac{1}{2}\,\mu\,I_1\int_L \bar{\theta}_{1,1}\,\bar{\theta}_{1,1}\,dL \\
= \int_L \mathcal{U}^L\,dL
\end{aligned} \tag{4.41}$$

4.5 Kinetic energy expression

The kinetic energy expression of a gyrobeam contains the terms due to translational and rotational motions of the elastic beam and the mounted-in gyros. This expression can be derived by simplifying the general expressions given by Eqs. (3.8) and (3.9) characterizing the kinetic energy of 3D micropolar and classical gyrocontinua. The simplification is done by splitting the volume integration into the integration over the beam length L and the integration over the beam cross section A, substituting from Eqs. (4.25), (4.29), and (4.30), and taking the integration over A while assuming that the gyricity parameters (*i.e.* $\underset{\leftrightarrow}{\jmath}^{V}$, $\dot{\underset{\rightarrow}{\phi}}$, and $\dot{\underset{\rightarrow}{\psi}}$) are constant over A. Note that the microrotation approximations mentioned in Eqs. (4.29) and (4.30) especially make sense as the gyricity parameters are assumed constant over A (they just vary with time t and along coordinate axis ${}^{c}x_1$).

Accordingly, for a micropolar gyrobeam one can derive the following kinetic energy expression:

$$\begin{aligned}
\mathcal{T} &= \frac{1}{2}\left(\rho^{V}+\varrho^{V}\right) A \int_{L}\left(\dot{\bar{u}}_1\,\dot{\bar{u}}_1+\dot{\bar{u}}_2\,\dot{\bar{u}}_2+\dot{\bar{u}}_3\,\dot{\bar{u}}_3\right) dL \\
&+\frac{1}{2}\left(\rho^{V}+\varrho^{V}\right) \int_{L}\left(I_1\,\dot{\bar{\theta}}_1\,\dot{\bar{\theta}}_1+I_2\,\dot{\bar{\theta}}_2\,\dot{\bar{\theta}}_2+I_3\,\dot{\bar{\theta}}_3\,\dot{\bar{\theta}}_3\right) dL \\
&+\frac{1}{2} A \int_{L}\left(\imath_{ij}^{V}+\jmath_{ij}^{V}\right)\dot{\bar{\vartheta}}_j\,\dot{\bar{\vartheta}}_i\,dL + A\int_{L}\jmath_{ij}^{V}\left(\dot{\phi}_j+\dot{\psi}_j\right)\dot{\bar{\vartheta}}_i\,dL \\
&+\frac{1}{2} A \int_{L}\jmath_{ij}^{V}\left(\dot{\phi}_j\,\dot{\phi}_i+\dot{\psi}_j\,\dot{\psi}_i+2\,\dot{\phi}_j\,\dot{\psi}_i\right) dL \\
&= \int_{L}\mathcal{T}^{L}\,dL
\end{aligned} \tag{4.42}$$

and for a classical gyrobeam the following kinetic energy expression will be obtained:

$$\begin{aligned}\mathcal{T} &= \frac{1}{2}\left(\rho^{V}+\varrho^{V}\right) A \int_{L}\left(\dot{\bar{u}}_1\,\dot{\bar{u}}_1+\dot{\bar{u}}_2\,\dot{\bar{u}}_2+\dot{\bar{u}}_3\,\dot{\bar{u}}_3\right) dL \\ &+ \frac{1}{2}\left(\rho^{V}+\varrho^{V}\right) \int_{L}\left(I_1\,\dot{\bar{\theta}}_1\,\dot{\bar{\theta}}_1+I_2\,\dot{\bar{\theta}}_2\,\dot{\bar{\theta}}_2+I_3\,\dot{\bar{\theta}}_3\,\dot{\bar{\theta}}_3\right) dL \\ &+ \frac{1}{2} A \int_{L} \jmath_{ij}^{V}\dot{\bar{\theta}}_j\,\dot{\bar{\theta}}_i\,dL + A\int_{L}\jmath_{ij}^{V}\left(\dot{\phi}_j+\dot{\psi}_j\right)\dot{\bar{\theta}}_i\,dL \\ &+ \frac{1}{2} A \int_{L}\jmath_{ij}^{V}\left(\dot{\phi}_j\,\dot{\phi}_i+\dot{\psi}_j\,\dot{\psi}_i+2\,\dot{\phi}_j\,\dot{\psi}_i\right) dL \\ &= \int_{L}\mathcal{T}^{L}\,dL\end{aligned} \tag{4.43}$$

where $\mathcal{T}^{L}$ is the linear density of the kinetic energy or the kinetic energy per unit length and the tensor summation convention is used to summarize the expressions.

4.6 Virtual work expression

Assuming that the gyrobeam is subjected to the action of external (nonconservative) volume and boundary surface forces and moments $\underset{\rightarrow}{f}^{V}$, $\underset{\rightarrow}{m}^{V}$, $\underset{\rightarrow}{f}^{S}$, and $\underset{\rightarrow}{m}^{S}$ (where boundary surface forces and moments are applied only on the most left and right beam cross sections), the general virtual work expression for a (micropolar or classical) gyrobeam can be written as:

$$\delta\mathcal{W} = \int_{V}\left(\underset{\rightarrow}{f}^{V}\cdot\delta\underset{\rightarrow}{u}+\underset{\rightarrow}{m}^{V}\cdot\delta\underset{\rightarrow}{\vartheta}\right) dV + \oint_{S}\left(\underset{\rightarrow}{f}^{S}\cdot\delta\underset{\rightarrow}{u}+\underset{\rightarrow}{m}^{S}\cdot\delta\underset{\rightarrow}{\vartheta}\right) dS \tag{4.44}$$

This general expression can be written in terms of the beam generalized coordinates by splitting the volume integration into the integration over the length L and the integration over the cross section A, substituting from Eqs. (4.25), (4.29), and (4.30), and taking the integration over the beam cross section.

Utilizing the general virtual work expression in Eq. (4.44) and the approximations in Eqs. (4.28) and (4.33) the virtual work expression for a micropolar gyrobeam takes the following form:

$$\begin{aligned}\delta\mathcal{W} &= \int_L \Big(A\,\bar{f}_i^{\,V}\,\delta\bar{u}_i + \bar{m}_i^{\,L}\,\delta\bar{\theta}_i + A\,\bar{m}_i^{\,V}\,\delta\bar{\vartheta}_i \Big)\, dL \\ &\quad + A\,\bar{f}_i^{\,S}(P_1)\,\delta\bar{u}_i(P_1) + \bar{m}_i^{\,P}(P_1)\,\delta\bar{\theta}_i(P_1) + A\,\bar{m}_i^{\,S}(P_1)\,\delta\bar{\vartheta}_i(P_1) \\ &\quad + A\,\bar{f}_i^{\,S}(P_2)\,\delta\bar{u}_i(P_2) + \bar{m}_i^{\,P}(P_2)\,\delta\bar{\theta}_i(P_2) + A\,\bar{m}_i^{\,S}(P_2)\,\delta\bar{\vartheta}_i(P_2) \\ &= \int_L \delta\mathcal{W}^L\, dL + \delta\mathcal{W}^P\end{aligned} \tag{4.45}$$

where:

$$\begin{aligned} A\,\bar{f}_i^{\,V} &= \int_A f_i^V\, dA, \qquad A\,\bar{m}_i^{\,V} = \int_A m_i^V\, dA \\ A\,\bar{f}_i^{\,S} &= \int_A f_i^S\, dA, \qquad A\,\bar{m}_i^{\,S} = \int_A m_i^S\, dA \end{aligned} \tag{4.46}$$

and:

$$\begin{aligned} \bar{m}_1^{\,L} &= \int_A \Big({}^c x_2\, f_3^V - {}^c x_3\, f_2^V \Big)\, dA \\ \bar{m}_2^{\,L} &= \int_A {}^c x_3\, f_1^V\, dA \\ -\bar{m}_3^{\,L} &= \int_A {}^c x_2\, f_1^V\, dA \\ \bar{m}_1^{\,P} &= \int_A \Big({}^c x_2\, f_3^S - {}^c x_3\, f_2^S \Big)\, dA \\ \bar{m}_2^{\,P} &= \int_A {}^c x_3\, f_1^S\, dA \\ -\bar{m}_3^{\,P} &= \int_A {}^c x_2\, f_1^S\, dA \end{aligned} \tag{4.47}$$

On the other hand, based on Eqs. (4.44), (4.28), and (4.34), the virtual work expression for a classical gyrobeam will be:

$$\begin{aligned}\delta\mathcal{W} = &\int_L \left(A\,\bar{f}_i^{\,V}\,\delta\bar{u}_i + \bar{m}_i^{\,L}\,\delta\bar{\theta}_i + A\,\bar{m}_i^{\,V}\,\delta\bar{\theta}_i \right) dL \\ &\quad + A\,\bar{f}_i^{\,S}(P_1)\,\delta\bar{u}_i(P_1) + \bar{m}_i^{\,P}(P_1)\,\delta\bar{\theta}_i(P_1) + A\,\bar{m}_i^{\,S}(P_1)\,\delta\bar{\theta}_i(P_1) \\ &\quad + A\,\bar{f}_i^{\,S}(P_2)\,\delta\bar{u}_i(P_2) + \bar{m}_i^{\,P}(P_2)\,\delta\bar{\theta}_i(P_2) + A\,\bar{m}_i^{\,S}(P_2)\,\delta\bar{\theta}_i(P_2) \\ = &\int_L \delta\mathcal{W}^{\,L}\,dL + \delta\mathcal{W}^{\,P}\end{aligned} \tag{4.48}$$

where again $\bar{f}_i^{\,V}$, $\bar{f}_i^{\,S}$, $\bar{m}_i^{\,V}$, $\bar{m}_i^{\,S}$, $\bar{m}_i^{\,L}$, and $\bar{m}_i^{\,P}$ are as defined by Eqs. (4.46) and (4.47).

For both micropolar and classical gyrobeams $\delta\mathcal{W}^{\,L}$ is the linear density of the virtual work or the virtual work per unit length and $\delta\mathcal{W}^{\,P}$ is the point virtual work.

4.7 Equations of motion

Having the potential and kinetic energy expressions along with the virtual work expression, Hamilton's principle can be used to derive the gyrobeam equations of motion and the corresponding I/BCs. Here, it should be noted that the matrix of generalized coordinates for a micropolar gyrobeam is:

$$\underset{\sim}{\boldsymbol{q}} = \begin{bmatrix} \bar{u}_1 & \bar{u}_2 & \bar{u}_3 & \bar{\theta}_1 & \bar{\theta}_2 & \bar{\theta}_3 & \bar{\vartheta}_1 & \bar{\vartheta}_2 & \bar{\vartheta}_3 \end{bmatrix}^{\mathrm{T}} \tag{4.49}$$

and for a classical gyrobeam is:

$$\underset{\sim}{\boldsymbol{q}} = \begin{bmatrix} \bar{u}_1 & \bar{u}_2 & \bar{u}_3 & \bar{\theta}_1 & \bar{\theta}_2 & \bar{\theta}_3 \end{bmatrix}^{\mathrm{T}} \tag{4.50}$$

Consequently, considering the discussions in Appendix B, special care is needed when taking the variation of the terms including the time derivative of beam microrotations $\bar{\vartheta}_i$ and beam plane section rotations $\bar{\theta}_i$ as generalized coordinates.

To be more specific, noting that:

$$
\begin{aligned}
&{}^{b}\Delta\Big(I_1\Big) = {}^{b}\Delta\Big(I_2\Big) = {}^{b}\Delta\Big(I_3\Big) = 0 \\
&{}^{b}\Delta\Big(\underset{\leftrightarrow}{\imath}^{V}\Big) = {}^{b}\Delta\Big(\underset{\leftrightarrow}{\jmath}^{V}\Big) = {}^{b}\Delta\Big(\underset{\rightarrow}{\dot{\phi}}\Big) = {}^{b}\Delta\Big(\underset{\rightarrow}{\dot{\psi}}\Big) = 0
\end{aligned}
\tag{4.51}
$$

and:

$$
\begin{aligned}
&\frac{d}{dt}\Big(I_1\Big) = \frac{d}{dt}\Big(I_2\Big) = \frac{d}{dt}\Big(I_3\Big) = 0 \\
&\frac{d}{dt}\Big(\underset{\leftrightarrow}{\imath}^{V}\Big) = \underset{\leftrightarrow}{\dot{\vartheta}}^{\times} \cdot \underset{\leftrightarrow}{\imath}^{V} - \underset{\leftrightarrow}{\imath}^{V} \cdot \underset{\leftrightarrow}{\dot{\vartheta}}^{\times} \\
&\frac{d}{dt}\Big(\underset{\leftrightarrow}{\jmath}^{V}\Big) = \Big(\underset{\leftrightarrow}{\dot{\vartheta}}^{\times} + \underset{\leftrightarrow}{\dot{\phi}}^{\times}\Big) \cdot \underset{\leftrightarrow}{\jmath}^{V} - \underset{\leftrightarrow}{\jmath}^{V} \cdot \Big(\underset{\leftrightarrow}{\dot{\vartheta}}^{\times} + \underset{\leftrightarrow}{\dot{\phi}}^{\times}\Big) \\
&\frac{d}{dt}\Big(\underset{\rightarrow}{\dot{\vartheta}}\Big) = \underset{\rightarrow}{\ddot{\vartheta}} \\
&\frac{d}{dt}\Big(\underset{\rightarrow}{\dot{\phi}}\Big) = \underset{\rightarrow}{\ddot{\phi}} + \underset{\leftrightarrow}{\dot{\vartheta}}^{\times} \cdot \underset{\rightarrow}{\dot{\phi}} \\
&\frac{d}{dt}\Big(\underset{\rightarrow}{\dot{\psi}}\Big) = \underset{\rightarrow}{\ddot{\psi}} + \Big(\underset{\leftrightarrow}{\dot{\vartheta}}^{\times} + \underset{\leftrightarrow}{\dot{\phi}}^{\times}\Big) \cdot \underset{\rightarrow}{\dot{\psi}}
\end{aligned}
\tag{4.52}
$$

the relation given by Eq. (B.52) and the second relation in Eq. (B.69) will be desirably used for taking the variation of the kinetic energy expression. In other words, for the kinetic energy expression, the variations are taken with respect to body frame $\mathcal{F}_b$ while the time derivatives are with respect to the inertial frame $\mathcal{F}_o$. For the potential energy expression however, the required variations and space derivatives are taken with respect to $\mathcal{F}_o$.

Afterwards, based on the results obtained in Chapter 2, the motion equations and I/BCs will take the following matrix forms:

$$
\underset{\sim}{\mathcal{Q}}^{L} = \Big(\frac{\partial \mathcal{T}^{L}}{\partial \underset{\sim}{\dot{\boldsymbol{q}}}}\Big)_{,t} - \Big(\frac{\partial \mathcal{U}^{L}}{\partial \underset{\sim}{\boldsymbol{q}}_{,1}}\Big)_{,1} + \frac{\partial \mathcal{U}^{L}}{\partial \underset{\sim}{\boldsymbol{q}}}
\tag{4.53}
$$

and:

$$\begin{aligned}
&\text{at } t=t_1,t_2\ ; \qquad \text{and over } L: \qquad \delta\underset{\sim}{\boldsymbol{q}}=\underset{\sim}{\mathbf{0}} \quad \text{or} \qquad \frac{\partial\mathcal{T}^{L}}{\partial\dot{\underset{\sim}{\boldsymbol{q}}}}=\underset{\sim}{\mathbf{0}}\\
&\text{at } P_1\ ; \qquad \text{and during } t: \qquad \delta\underset{\sim}{\boldsymbol{q}}=\underset{\sim}{\mathbf{0}} \quad \text{or} \quad \underset{\sim}{\boldsymbol{\mathcal{Q}}}^{P}+\frac{\partial\mathcal{U}^{L}}{\partial\underset{\sim}{\boldsymbol{q}}_{,1}}=\underset{\sim}{\mathbf{0}}\\
&\text{at } P_2\ ; \qquad \text{and during } t: \qquad \delta\underset{\sim}{\boldsymbol{q}}=\underset{\sim}{\mathbf{0}} \quad \text{or} \quad \underset{\sim}{\boldsymbol{\mathcal{Q}}}^{P}-\frac{\partial\mathcal{U}^{L}}{\partial\underset{\sim}{\boldsymbol{q}}_{,1}}=\underset{\sim}{\mathbf{0}}
\end{aligned} \tag{4.54}$$

where:

$$\underset{\sim}{\boldsymbol{\mathcal{Q}}}^{L}=\frac{\delta\mathcal{W}^{L}}{\delta\underset{\sim}{\boldsymbol{q}}}, \qquad \underset{\sim}{\boldsymbol{\mathcal{Q}}}^{P}=\frac{\delta\mathcal{W}^{P}}{\delta\underset{\sim}{\boldsymbol{q}}} \tag{4.55}$$

Before writing the final dynamic equations and I/BCs for a micropolar gyrobeam through utilizing Eqs. (4.53) and (4.54), it is useful to define the vectors of body and gyros angular momenta per unit volume, *i.e.* $\underset{\rightarrow}{\mathcal{I}}^{V}$ and $\underset{\rightarrow}{\mathcal{J}}^{V}$, and their first time derivatives with respect to the inertial frame, *i.e.* $\dot{\underset{\rightarrow}{\mathcal{I}}}^{V}$ and $\dot{\underset{\rightarrow}{\mathcal{J}}}^{V}$, as:

$$\begin{aligned}
\underset{\rightarrow}{\mathcal{I}}^{V}&=\underset{\leftrightarrow}{\jmath}^{V}\cdot\dot{\underset{\rightarrow}{\vartheta}}\\
\dot{\underset{\rightarrow}{\mathcal{I}}}^{V}&=\frac{d}{dt}\left(\underset{\rightarrow}{\mathcal{I}}^{V}\right)=\underset{\leftrightarrow}{\jmath}^{V}\cdot\ddot{\underset{\rightarrow}{\vartheta}}+\dot{\underset{\leftrightarrow}{\vartheta}}^{\times}\cdot\underset{\leftrightarrow}{\jmath}^{V}\cdot\dot{\underset{\rightarrow}{\vartheta}}
\end{aligned} \tag{4.56}$$

and:

$$\begin{aligned}
\underset{\rightarrow}{\mathcal{J}}^{V}&=\underset{\leftrightarrow}{\jmath}^{V}\cdot\left(\dot{\underset{\rightarrow}{\vartheta}}+\dot{\underset{\rightarrow}{\phi}}+\dot{\underset{\rightarrow}{\psi}}\right)\\
\dot{\underset{\rightarrow}{\mathcal{J}}}^{V}&=\frac{d}{dt}\left(\underset{\rightarrow}{\mathcal{J}}^{V}\right)=\underset{\leftrightarrow}{\jmath}^{V}\cdot\ddot{\underset{\rightarrow}{\vartheta}}+\dot{\underset{\leftrightarrow}{\vartheta}}^{\times}\cdot\underset{\leftrightarrow}{\jmath}^{V}\cdot\dot{\underset{\rightarrow}{\vartheta}}+\dot{\underset{\leftrightarrow}{\vartheta}}^{\times}\cdot\underset{\leftrightarrow}{\jmath}^{V}\cdot\left(\dot{\underset{\rightarrow}{\phi}}+\dot{\underset{\rightarrow}{\psi}}\right)\\
&\quad+\left(\dot{\underset{\leftrightarrow}{\phi}}^{\times}\cdot\underset{\leftrightarrow}{\jmath}^{V}-\underset{\leftrightarrow}{\jmath}^{V}\cdot\dot{\underset{\leftrightarrow}{\phi}}^{\times}\right)\cdot\dot{\underset{\rightarrow}{\vartheta}}+\underset{\leftrightarrow}{\jmath}^{V}\cdot\ddot{\underset{\rightarrow}{\phi}}+\underset{\leftrightarrow}{\jmath}^{V}\cdot\ddot{\underset{\rightarrow}{\psi}}+\dot{\underset{\leftrightarrow}{\phi}}^{\times}\cdot\underset{\leftrightarrow}{\jmath}^{V}\cdot\left(\dot{\underset{\rightarrow}{\phi}}+\dot{\underset{\rightarrow}{\psi}}\right)
\end{aligned} \tag{4.57}$$

whose component matrices in the inertial frame (after imposing the required first-order approximation on the microrotations as mentioned in Appendix B) are:

$$\begin{aligned}
\underline{\boldsymbol{\mathcal{I}}}^{V}&={}^{b}\underline{\underline{\boldsymbol{\jmath}}}^{V}\,\dot{\underline{\boldsymbol{\vartheta}}}\\
\dot{\underline{\boldsymbol{\mathcal{I}}}}^{V}&={}^{b}\underline{\underline{\boldsymbol{\jmath}}}^{V}\,\ddot{\underline{\boldsymbol{\vartheta}}}
\end{aligned} \tag{4.58}$$

and:

$$
\begin{aligned}
\underline{\mathcal{J}}^{V} &= {}^{b}\underline{\underline{\mathcal{J}}}^{V}\left(\underline{\dot{\vartheta}} + {}^{b}\underline{\dot{\phi}} + {}^{b}\underline{\dot{\psi}}\right)\\
\underline{\dot{\mathcal{J}}}^{V} &= {}^{b}\underline{\underline{\mathcal{J}}}^{V}\,\underline{\ddot{\vartheta}} + \underline{\dot{\vartheta}}^{\times}\,{}^{b}\underline{\underline{\mathcal{J}}}^{V}\left({}^{b}\underline{\dot{\phi}} + {}^{b}\underline{\dot{\psi}}\right) + \left({}^{b}\underline{\dot{\phi}}^{\times}\,{}^{b}\underline{\underline{\mathcal{J}}}^{V} - {}^{b}\underline{\underline{\mathcal{J}}}^{V}\,{}^{b}\underline{\dot{\phi}}^{\times}\right)\underline{\dot{\vartheta}}\\
&\quad + \left(\underline{\underline{\mathbb{1}}} + \underline{\vartheta}^{\times}\right)\left({}^{b}\underline{\underline{\mathcal{J}}}^{V}\,{}^{b}\underline{\ddot{\phi}} + {}^{b}\underline{\underline{\mathcal{J}}}^{V}\,{}^{b}\underline{\ddot{\psi}} + {}^{b}\underline{\dot{\phi}}^{\times}\,{}^{b}\underline{\underline{\mathcal{J}}}^{V}\left({}^{b}\underline{\dot{\phi}} + {}^{b}\underline{\dot{\psi}}\right)\right)
\end{aligned}
\tag{4.59}
$$

Now, by utilizing Eq. (4.53) and after adding the required correction factors (*i.e.* including k_{s_2} and k_{s_3} as the shear correction factors and k_t as the torsion correction factor), the final equations of motion for a micropolar gyrobeam can be written as the following nine equations:

$$
\begin{aligned}
A\,\bar{f}_1^{V} &= \left(\rho^{V} + \varrho^{V}\right) A\,\ddot{\bar{u}}_1 - E\,A\,\bar{u}_{1,11}\\
A\,\bar{f}_2^{V} &= \left(\rho^{V} + \varrho^{V}\right) A\,\ddot{\bar{u}}_2 - k_{s_2}\,\mu\,A\left(\bar{u}_{2,11} - \bar{\theta}_{3,1}\right) - \kappa\,A\left(\bar{u}_{2,11} + \bar{\theta}_{3,1} - 2\,\bar{\vartheta}_{3,1}\right)\\
A\,\bar{f}_3^{V} &= \left(\rho^{V} + \varrho^{V}\right) A\,\ddot{\bar{u}}_3 - k_{s_3}\,\mu\,A\left(\bar{u}_{3,11} + \bar{\theta}_{2,1}\right) - \kappa\,A\left(\bar{u}_{3,11} - \bar{\theta}_{2,1} + 2\,\bar{\vartheta}_{2,1}\right)\\
\bar{m}_1^{L} &= \left(\rho^{V} + \varrho^{V}\right) I_1\,\ddot{\bar{\theta}}_1 - k_t\,\mu\,I_1\,\bar{\theta}_{1,11} - \kappa\,I_1\left(\bar{\theta}_{1,11} - 2\,\xi\,\bar{\vartheta}_{1,11}\right) + 4\,\kappa\,A\left(\bar{\theta}_1 - \bar{\vartheta}_1\right)\\
\bar{m}_2^{L} &= \left(\rho^{V} + \varrho^{V}\right) I_2\,\ddot{\bar{\theta}}_2 - E\,I_2\,\bar{\theta}_{2,11} + k_{s_3}\,\mu\,A\left(\bar{u}_{3,1} + \bar{\theta}_2\right) - \kappa\,A\left(\bar{u}_{3,1} - \bar{\theta}_2 + 2\,\bar{\vartheta}_2\right)\\
\bar{m}_3^{L} &= \left(\rho^{V} + \varrho^{V}\right) I_3\,\ddot{\bar{\theta}}_3 - E\,I_3\,\bar{\theta}_{3,11} - k_{s_2}\,\mu\,A\left(\bar{u}_{2,1} - \bar{\theta}_3\right) + \kappa\,A\left(\bar{u}_{2,1} + \bar{\theta}_3 - 2\,\bar{\vartheta}_3\right)\\
A\,\bar{m}_1^{V} &= A\,\dot{\mathcal{I}}_1^{V} + A\,\dot{\mathcal{J}}_1^{V} - \mathcal{E}\,A\,\bar{\vartheta}_{1,11} + 2\,\xi\,\kappa\,I_1\left(\bar{\theta}_{1,11} - 2\,\xi\,\bar{\vartheta}_{1,11}\right) - 4\,\kappa\,A\left(\bar{\theta}_1 - \bar{\vartheta}_1\right)\\
A\,\bar{m}_2^{V} &= A\,\dot{\mathcal{I}}_2^{V} + A\,\dot{\mathcal{J}}_2^{V} - \left(\gamma + \beta\right) A\,\bar{\vartheta}_{2,11} + 2\,\kappa\,A\left(\bar{u}_{3,1} - \bar{\theta}_2 + 2\,\bar{\vartheta}_2\right)\\
A\,\bar{m}_3^{V} &= A\,\dot{\mathcal{I}}_3^{V} + A\,\dot{\mathcal{J}}_3^{V} - \left(\gamma + \beta\right) A\,\bar{\vartheta}_{3,11} - 2\,\kappa\,A\left(\bar{u}_{2,1} + \bar{\theta}_3 - 2\,\bar{\vartheta}_3\right)
\end{aligned}
\tag{4.60}
$$

It is noteworthy that four modes of deformation are characterized by the relations in Eq. (4.60); longitudinal displacement along the ${}^{c}x_1$ axis by the first relation, torsional rotation around the ${}^{c}x_1$ axis by the fourth and seventh relations, bending deformation in the ${}^{c}x_1{}^{c}x_2$ plane by the second, sixth, and ninth relations, and bending deformation in the ${}^{c}x_1{}^{c}x_3$ plane by the third, fifth, and eighth relations. Also as can be expected, the relations describing the two bending modes in the ${}^{c}x_1{}^{c}x_2$ and ${}^{c}x_1{}^{c}x_3$ planes are very similar. In fact, the differences between the relations of these two modes are due to the fact that in the ${}^{c}x_1{}^{c}x_2$ plane, $\bar{\theta}_3$, $\bar{\vartheta}_3$, and $\bar{u}_{2,1}$ are of the same positive direction, however, in the ${}^{c}x_1{}^{c}x_3$ plane, the positive direction of $\bar{\theta}_2$ and $\bar{\vartheta}_2$ is opposite of the positive direction for $\bar{u}_{3,1}$.

One can show that the dynamic equations in Eq. (4.61) correspond to the following equilibrium equations:

$$
\begin{aligned}
&\sigma_{11,1}+\sigma_{21,2}+\sigma_{31,3}+f_1^V-\rho^V\,\ddot{u}_1=0\\
&\sigma_{12,1}+f_2^V-\rho^V\,\ddot{u}_2=0\\
&\sigma_{13,1}+f_3^V-\rho^V\,\ddot{u}_3=0\\
&{}^cx_2\left(\sigma_{13,1}+f_3^V-\rho^V\,\ddot{u}_3\right)-{}^cx_3\left(\sigma_{12,1}+f_2^V-\rho^V\,\ddot{u}_2\right)=0\\
&{}^cx_3\left(\sigma_{11,1}+\sigma_{21,2}+\sigma_{31,3}+f_1^V-\rho^V\,\ddot{u}_1\right)=0\\
&{}^cx_2\left(\sigma_{11,1}+\sigma_{21,2}+\sigma_{31,3}+f_1^V-\rho^V\,\ddot{u}_1\right)=0\\
&\sigma_{23}-\sigma_{32}+\chi_{11,1}+m_1^V-\imath_{1j}^V\,\ddot{\vartheta}_j=0\\
&\sigma_{31}-\sigma_{13}+\chi_{12,1}+m_2^V-\imath_{2j}^V\,\ddot{\vartheta}_j=0\\
&\sigma_{12}-\sigma_{21}+\chi_{13,1}+m_3^V-\imath_{3j}^V\,\ddot{\vartheta}_j=0
\end{aligned}
\tag{4.61}
$$

The dynamic equations given in Eq. (4.60) should be solved along with the following I/BCs which are obtained by using Eq. (4.54):

$$
\begin{aligned}
&\text{at } t=t_1,t_2\ ;\ \text{ and over } L:\\
&\quad\delta\bar{u}_1=0\quad\text{or}\quad\left(\rho^V+\varrho^V\right)A\,\dot{\bar{u}}_1=0\\
&\quad\delta\bar{u}_2=0\quad\text{or}\quad\left(\rho^V+\varrho^V\right)A\,\dot{\bar{u}}_2=0\\
&\quad\delta\bar{u}_3=0\quad\text{or}\quad\left(\rho^V+\varrho^V\right)A\,\dot{\bar{u}}_3=0\\
&\quad\delta\bar{\theta}_1=0\quad\text{or}\quad\left(\rho^V+\varrho^V\right)I_1\,\dot{\bar{\theta}}_1=0\\
&\quad\delta\bar{\theta}_2=0\quad\text{or}\quad\left(\rho^V+\varrho^V\right)I_2\,\dot{\bar{\theta}}_2=0\\
&\quad\delta\bar{\theta}_3=0\quad\text{or}\quad\left(\rho^V+\varrho^V\right)I_3\,\dot{\bar{\theta}}_3=0\\
&\quad\delta\bar{\vartheta}_1=0\quad\text{or}\quad A\,\mathcal{I}_1^V+A\,\mathcal{J}_1^V=0\\
&\quad\delta\bar{\vartheta}_2=0\quad\text{or}\quad A\,\mathcal{I}_2^V+A\,\mathcal{J}_2^V=0\\
&\quad\delta\bar{\vartheta}_3=0\quad\text{or}\quad A\,\mathcal{I}_3^V+A\,\mathcal{J}_3^V=0
\end{aligned}
\tag{4.62}
$$

at P_1 ; and during t :

$$
\begin{aligned}
&\delta\bar{u}_1 = 0 \quad \text{or} \quad && A\,\bar{f}_1^S + E\,A\,\bar{u}_{1,1} = 0 \\
&\delta\bar{u}_2 = 0 \quad \text{or} \quad && A\,\bar{f}_2^S + k_{s_2}\,\mu\,A\left(\bar{u}_{2,1} - \bar{\theta}_3\right) + \kappa\,A\left(\bar{u}_{2,1} + \bar{\theta}_3 - 2\,\bar{\vartheta}_3\right) = 0 \\
&\delta\bar{u}_3 = 0 \quad \text{or} \quad && A\,\bar{f}_3^S + k_{s_3}\,\mu\,A\left(\bar{u}_{3,1} + \bar{\theta}_2\right) + \kappa\,A\left(\bar{u}_{3,1} - \bar{\theta}_2 + 2\,\bar{\vartheta}_2\right) = 0 \\
&\delta\bar{\theta}_1 = 0 \quad \text{or} \quad && \bar{m}_1^P + k_t\,\mu\,I_1\,\bar{\theta}_{1,1} + \kappa\,I_1\left(\bar{\theta}_{1,1} - 2\,\xi\,\bar{\vartheta}_{1,1}\right) = 0 \\
&\delta\bar{\theta}_2 = 0 \quad \text{or} \quad && \bar{m}_2^P + E\,I_2\,\bar{\theta}_{2,1} = 0 \\
&\delta\bar{\theta}_3 = 0 \quad \text{or} \quad && \bar{m}_3^P + E\,I_3\,\bar{\theta}_{3,1} = 0 \\
&\delta\bar{\vartheta}_1 = 0 \quad \text{or} \quad && A\,\bar{m}_1^S + \mathcal{E}\,A\,\bar{\vartheta}_{1,1} - 2\,\xi\,\kappa\,I_1\left(\bar{\theta}_{1,1} - 2\,\xi\,\bar{\vartheta}_{1,1}\right) = 0 \\
&\delta\bar{\vartheta}_2 = 0 \quad \text{or} \quad && A\,\bar{m}_2^S + \left(\gamma + \beta\right) A\,\bar{\vartheta}_{2,1} = 0 \\
&\delta\bar{\vartheta}_3 = 0 \quad \text{or} \quad && A\,\bar{m}_3^S + \left(\gamma + \beta\right) A\,\bar{\vartheta}_{3,1} = 0
\end{aligned}
\tag{4.63}
$$

at P_2 ; and during t :

$$
\begin{aligned}
&\delta\bar{u}_1 = 0 \quad \text{or} \quad && A\,\bar{f}_1^S - E\,A\,\bar{u}_{1,1} = 0 \\
&\delta\bar{u}_2 = 0 \quad \text{or} \quad && A\,\bar{f}_2^S - k_{s_2}\,\mu\,A\left(\bar{u}_{2,1} - \bar{\theta}_3\right) - \kappa\,A\left(\bar{u}_{2,1} + \bar{\theta}_3 - 2\,\bar{\vartheta}_3\right) = 0 \\
&\delta\bar{u}_3 = 0 \quad \text{or} \quad && A\,\bar{f}_3^S - k_{s_3}\,\mu\,A\left(\bar{u}_{3,1} + \bar{\theta}_2\right) - \kappa\,A\left(\bar{u}_{3,1} - \bar{\theta}_2 + 2\,\bar{\vartheta}_2\right) = 0 \\
&\delta\bar{\theta}_1 = 0 \quad \text{or} \quad && \bar{m}_1^P - k_t\,\mu\,I_1\,\bar{\theta}_{1,1} - \kappa\,I_1\left(\bar{\theta}_{1,1} - 2\,\xi\,\bar{\vartheta}_{1,1}\right) = 0 \\
&\delta\bar{\theta}_2 = 0 \quad \text{or} \quad && \bar{m}_2^P - E\,I_2\,\bar{\theta}_{2,1} = 0 \\
&\delta\bar{\theta}_3 = 0 \quad \text{or} \quad && \bar{m}_3^P - E\,I_3\,\bar{\theta}_{3,1} = 0 \\
&\delta\bar{\vartheta}_1 = 0 \quad \text{or} \quad && A\,\bar{m}_1^S - \mathcal{E}\,A\,\bar{\vartheta}_{1,1} + 2\,\xi\,\kappa\,I_1\left(\bar{\theta}_{1,1} - 2\,\xi\,\bar{\vartheta}_{1,1}\right) = 0 \\
&\delta\bar{\vartheta}_2 = 0 \quad \text{or} \quad && A\,\bar{m}_2^S - \left(\gamma + \beta\right) A\,\bar{\vartheta}_{2,1} = 0 \\
&\delta\bar{\vartheta}_3 = 0 \quad \text{or} \quad && A\,\bar{m}_3^S - \left(\gamma + \beta\right) A\,\bar{\vartheta}_{3,1} = 0
\end{aligned}
\tag{4.64}
$$

The sets of dynamic PDEs and I/BCs for a micropolar gyrobeam, given by Eqs. (4.60)–(4.64), can be revised provided that in each set the relations corresponding to each $\bar{\theta}_i$ are replaced with the sum of relations corresponding to $\bar{\theta}_i$ and $\bar{\vartheta}_i$ in that set ($i = 1, 2, 3$). Accordingly, the following sets of dynamic equations and I/BCs will be obtained for a

micropolar gyrobeam:

$$
\begin{aligned}
\bar{f}_1^{\,V} &= \left(\rho^{V}+\varrho^{V}\right)\ddot{\bar{u}}_1 - E\,\bar{u}_{1,11}\\
\bar{f}_2^{\,V} &= \left(\rho^{V}+\varrho^{V}\right)\ddot{\bar{u}}_2 - k_{s_2}\,\mu\left(\bar{u}_{2,11}-\bar{\theta}_{3,1}\right) - \kappa\left(\bar{u}_{2,11}+\bar{\theta}_{3,1}-2\,\bar{\vartheta}_{3,1}\right)\\
\bar{f}_3^{\,V} &= \left(\rho^{V}+\varrho^{V}\right)\ddot{\bar{u}}_3 - k_{s_3}\,\mu\left(\bar{u}_{3,11}+\bar{\theta}_{2,1}\right) - \kappa\left(\bar{u}_{3,11}-\bar{\theta}_{2,1}+2\,\bar{\vartheta}_{2,1}\right)\\
\bar{m}_1^{L}+A\,\bar{m}_1^{V} &= \left(\rho^{V}+\varrho^{V}\right)I_1\,\ddot{\bar{\theta}}_1 + A\,\dot{\mathcal{I}}_1^{\,V} + A\,\dot{\mathcal{J}}_1^{\,V} - k_{t}\,\mu\,I_1\,\bar{\theta}_{1,11} - \mathcal{E}\,A\,\bar{\vartheta}_{1,11}\\
&\quad - \left(1-2\,\xi\right)\kappa\,I_1\left(\bar{\theta}_{1,11}-2\,\xi\,\bar{\vartheta}_{1,11}\right)\\
\bar{m}_2^{L}+A\,\bar{m}_2^{V} &= \left(\rho^{V}+\varrho^{V}\right)I_2\,\ddot{\bar{\theta}}_2 + A\,\dot{\mathcal{I}}_2^{\,V} + A\,\dot{\mathcal{J}}_2^{\,V} - E\,I_2\,\bar{\theta}_{2,11} - \left(\gamma+\beta\right)A\,\bar{\vartheta}_{2,11}\\
&\quad + k_{s_3}\,\mu\,A\left(\bar{u}_{3,1}+\bar{\theta}_2\right) + \kappa\,A\left(\bar{u}_{3,1}-\bar{\theta}_2+2\,\bar{\vartheta}_2\right)\\
\bar{m}_3^{L}+A\,\bar{m}_3^{V} &= \left(\rho^{V}+\varrho^{V}\right)I_3\,\ddot{\bar{\theta}}_3 + A\,\dot{\mathcal{I}}_3^{\,V} + A\,\dot{\mathcal{J}}_3^{\,V} - E\,I_3\,\bar{\theta}_{3,11} - \left(\gamma+\beta\right)A\,\bar{\vartheta}_{3,11}\\
&\quad - k_{s_2}\,\mu\,A\left(\bar{u}_{2,1}-\bar{\theta}_3\right) - \kappa\,A\left(\bar{u}_{2,1}+\bar{\theta}_3-2\,\bar{\vartheta}_3\right)\\
\bar{m}_1^{V} &= \dot{\mathcal{I}}_1^{\,V} + \dot{\mathcal{J}}_1^{\,V} - \mathcal{E}\,\bar{\vartheta}_{1,11} + 2\,\xi\,\kappa\,\frac{I_1}{A}\left(\bar{\theta}_{1,11}-2\,\xi\,\bar{\vartheta}_{1,11}\right) - 4\,\kappa\left(\bar{\theta}_1-\bar{\vartheta}_1\right)\\
\bar{m}_2^{V} &= \dot{\mathcal{I}}_2^{\,V} + \dot{\mathcal{J}}_2^{\,V} - \left(\gamma+\beta\right)\bar{\vartheta}_{2,11} + 2\,\kappa\left(\bar{u}_{3,1}-\bar{\theta}_2+2\,\bar{\vartheta}_2\right)\\
\bar{m}_3^{V} &= \dot{\mathcal{I}}_3^{\,V} + \dot{\mathcal{J}}_3^{\,V} - \left(\gamma+\beta\right)\bar{\vartheta}_{3,11} - 2\,\kappa\left(\bar{u}_{2,1}+\bar{\theta}_3-2\,\bar{\vartheta}_3\right)
\end{aligned}
\tag{4.65}
$$

at $t = t_1, t_2$; and over L :

$$
\begin{aligned}
&\delta\bar{u}_1 = 0 && \text{or} && \left(\rho^{V}+\varrho^{V}\right)A\,\dot{\bar{u}}_1 = 0\\
&\delta\bar{u}_2 = 0 && \text{or} && \left(\rho^{V}+\varrho^{V}\right)A\,\dot{\bar{u}}_2 = 0\\
&\delta\bar{u}_3 = 0 && \text{or} && \left(\rho^{V}+\varrho^{V}\right)A\,\dot{\bar{u}}_3 = 0\\
&\delta\bar{\theta}_1+\delta\bar{\vartheta}_1 = 0 && \text{or} && \left(\rho^{V}+\varrho^{V}\right)I_1\,\dot{\bar{\theta}}_1 + A\,\mathcal{I}_1^{\,V} + A\,\mathcal{J}_1^{\,V} = 0\\
&\delta\bar{\theta}_2+\delta\bar{\vartheta}_2 = 0 && \text{or} && \left(\rho^{V}+\varrho^{V}\right)I_2\,\dot{\bar{\theta}}_2 + A\,\mathcal{I}_2^{\,V} + A\,\mathcal{J}_2^{\,V} = 0\\
&\delta\bar{\theta}_3+\delta\bar{\vartheta}_3 = 0 && \text{or} && \left(\rho^{V}+\varrho^{V}\right)I_3\,\dot{\bar{\theta}}_3 + A\,\mathcal{I}_3^{\,V} + A\,\mathcal{J}_3^{\,V} = 0\\
&\delta\bar{\vartheta}_1 = 0 && \text{or} && A\,\mathcal{I}_1^{\,V} + A\,\mathcal{J}_1^{\,V} = 0\\
&\delta\bar{\vartheta}_2 = 0 && \text{or} && A\,\mathcal{I}_2^{\,V} + A\,\mathcal{J}_2^{\,V} = 0\\
&\delta\bar{\vartheta}_3 = 0 && \text{or} && A\,\mathcal{I}_3^{\,V} + A\,\mathcal{J}_3^{\,V} = 0
\end{aligned}
\tag{4.66}
$$

at P_1 ; and during t :

$$
\begin{aligned}
&\delta\bar{u}_1 = 0 \quad \text{or} \quad && A\,\bar{f}_1^S + E\,A\,\bar{u}_{1,1} = 0 \\
&\delta\bar{u}_2 = 0 \quad \text{or} \quad && A\,\bar{f}_2^S + k_{s_2}\,\mu\,A\left(\bar{u}_{2,1} - \bar{\theta}_3\right) + \kappa\,A\left(\bar{u}_{2,1} + \bar{\theta}_3 - 2\,\bar{\vartheta}_3\right) = 0 \\
&\delta\bar{u}_3 = 0 \quad \text{or} \quad && A\,\bar{f}_3^S + k_{s_3}\,\mu\,A\left(\bar{u}_{3,1} + \bar{\theta}_2\right) + \kappa\,A\left(\bar{u}_{3,1} - \bar{\theta}_2 + 2\,\bar{\vartheta}_2\right) = 0 \\
&\delta\bar{\theta}_1 + \delta\bar{\vartheta}_1 = 0 \quad \text{or} \quad && \bar{m}_1^P + A\,\bar{m}_1^S + k_t\,\mu\,I_1\,\bar{\vartheta}_{1,1} + \mathcal{E}\,A\,\bar{\vartheta}_{1,1} \\
&\qquad\qquad && \quad + \left(1 - 2\,\xi\right)\kappa\,I_1\left(\bar{\theta}_{1,1} - 2\,\xi\,\bar{\vartheta}_{1,1}\right) = 0 \\
&\delta\bar{\theta}_2 + \delta\bar{\vartheta}_2 = 0 \quad \text{or} \quad && \bar{m}_2^P + A\,\bar{m}_2^S + E\,I_2\,\bar{\theta}_{2,1} + \left(\gamma + \beta\right)A\,\bar{\vartheta}_{2,1} = 0 \\
&\delta\bar{\theta}_3 + \delta\bar{\vartheta}_3 = 0 \quad \text{or} \quad && \bar{m}_3^P + A\,\bar{m}_3^S + E\,I_3\,\bar{\theta}_{3,1} + \left(\gamma + \beta\right)A\,\bar{\vartheta}_{3,1} = 0 \\
&\delta\bar{\vartheta}_1 = 0 \quad \text{or} \quad && A\,\bar{m}_1^S + \mathcal{E}\,A\,\bar{\vartheta}_{1,1} - 2\,\xi\,\kappa\,I_1\left(\bar{\theta}_{1,1} - 2\,\xi\,\bar{\vartheta}_{1,1}\right) = 0 \\
&\delta\bar{\vartheta}_2 = 0 \quad \text{or} \quad && A\,\bar{m}_2^S + \left(\gamma + \beta\right)A\,\bar{\vartheta}_{2,1} = 0 \\
&\delta\bar{\vartheta}_3 = 0 \quad \text{or} \quad && A\,\bar{m}_3^S + \left(\gamma + \beta\right)A\,\bar{\vartheta}_{3,1} = 0
\end{aligned}
\tag{4.67}
$$

at P_2 ; and during t :

$$
\begin{aligned}
&\delta\bar{u}_1 = 0 \quad \text{or} \quad && A\,\bar{f}_1^S - E\,A\,\bar{u}_{1,1} = 0 \\
&\delta\bar{u}_2 = 0 \quad \text{or} \quad && A\,\bar{f}_2^S - k_{s_2}\,\mu\,A\left(\bar{u}_{2,1} - \bar{\theta}_3\right) - \kappa\,A\left(\bar{u}_{2,1} + \bar{\theta}_3 - 2\,\bar{\vartheta}_3\right) = 0 \\
&\delta\bar{u}_3 = 0 \quad \text{or} \quad && A\,\bar{f}_3^S - k_{s_3}\,\mu\,A\left(\bar{u}_{3,1} + \bar{\theta}_2\right) - \kappa\,A\left(\bar{u}_{3,1} - \bar{\theta}_2 + 2\,\bar{\vartheta}_2\right) = 0 \\
&\delta\bar{\theta}_1 + \delta\bar{\vartheta}_1 = 0 \quad \text{or} \quad && \bar{m}_1^P + A\,\bar{m}_1^S - k_t\,\mu\,I_1\,\bar{\vartheta}_{1,1} - \mathcal{E}\,A\,\bar{\vartheta}_{1,1} \\
&\qquad\qquad && \quad - \left(1 - 2\,\xi\right)\kappa\,I_1\left(\bar{\theta}_{1,1} - 2\,\xi\,\bar{\vartheta}_{1,1}\right) = 0 \\
&\delta\bar{\theta}_2 + \delta\bar{\vartheta}_2 = 0 \quad \text{or} \quad && \bar{m}_2^P + A\,\bar{m}_2^S - E\,I_2\,\bar{\theta}_{2,1} - \left(\gamma + \beta\right)A\,\bar{\vartheta}_{2,1} = 0 \\
&\delta\bar{\theta}_3 + \delta\bar{\vartheta}_3 = 0 \quad \text{or} \quad && \bar{m}_3^P + A\,\bar{m}_3^S - E\,I_3\,\bar{\theta}_{3,1} - \left(\gamma + \beta\right)A\,\bar{\vartheta}_{3,1} = 0 \\
&\delta\bar{\vartheta}_1 = 0 \quad \text{or} \quad && A\,\bar{m}_1^S - \mathcal{E}\,A\,\bar{\vartheta}_{1,1} + 2\,\xi\,\kappa\,I_1\left(\bar{\theta}_{1,1} - 2\,\xi\,\bar{\vartheta}_{1,1}\right) = 0 \\
&\delta\bar{\vartheta}_2 = 0 \quad \text{or} \quad && A\,\bar{m}_2^S - \left(\gamma + \beta\right)A\,\bar{\vartheta}_{2,1} = 0 \\
&\delta\bar{\vartheta}_3 = 0 \quad \text{or} \quad && A\,\bar{m}_3^S - \left(\gamma + \beta\right)A\,\bar{\vartheta}_{3,1} = 0
\end{aligned}
\tag{4.68}
$$

These new sets of dynamic equations and I/BCs are more desirable as now they can be more easily simplified to and compared with the corresponding sets for a classical gyrobeam.

For a classical gyrobeam there is no need to define the vectors $\underset{\rightarrow}{\mathcal{I}}^{V}$ and $\dot{\underset{\rightarrow}{\mathcal{I}}}^{V}$ as in the classical elasticity the microinertia effects are ignored. However, it is useful to define the vectors $\underset{\rightarrow}{\mathcal{J}}^{V}$ and $\dot{\underset{\rightarrow}{\mathcal{J}}}^{V}$ as:

$$\begin{aligned}
\underset{\rightarrow}{\mathcal{J}}^{V} &= \underset{\leftrightarrow}{\jmath}^{V} \cdot \left(\underset{\rightarrow}{\dot{\theta}} + \underset{\rightarrow}{\dot{\phi}} + \underset{\rightarrow}{\dot{\psi}}\right) \\
\dot{\underset{\rightarrow}{\mathcal{J}}}^{V} &= \frac{d}{dt}\left(\underset{\rightarrow}{\mathcal{J}}^{V}\right) = \underset{\leftrightarrow}{\jmath}^{V} \cdot \underset{\rightarrow}{\ddot{\theta}} + \underset{\leftrightarrow}{\dot{\theta}}^{\times} \cdot \underset{\leftrightarrow}{\jmath}^{V} \cdot \underset{\rightarrow}{\dot{\theta}} + \underset{\leftrightarrow}{\dot{\theta}}^{\times} \cdot \underset{\leftrightarrow}{\jmath}^{V} \cdot \left(\underset{\rightarrow}{\dot{\phi}} + \underset{\rightarrow}{\dot{\psi}}\right) \\
&\quad + \left(\underset{\leftrightarrow}{\dot{\phi}}^{\times} \cdot \underset{\leftrightarrow}{\jmath}^{V} - \underset{\leftrightarrow}{\jmath}^{V} \cdot \underset{\leftrightarrow}{\dot{\phi}}^{\times}\right) \cdot \underset{\rightarrow}{\dot{\theta}} + \underset{\leftrightarrow}{\jmath}^{V} \cdot \underset{\rightarrow}{\ddot{\phi}} + \underset{\leftrightarrow}{\jmath}^{V} \cdot \underset{\rightarrow}{\ddot{\psi}} + \underset{\leftrightarrow}{\dot{\phi}}^{\times} \cdot \underset{\leftrightarrow}{\jmath}^{V} \cdot \left(\underset{\rightarrow}{\dot{\phi}} + \underset{\rightarrow}{\dot{\psi}}\right)
\end{aligned} \tag{4.69}$$

which imply:

$$\begin{aligned}
\underline{\boldsymbol{\mathcal{J}}}^{V} &= {}^{b}\underline{\underline{\boldsymbol{\jmath}}}^{V}\left(\underline{\dot{\boldsymbol{\theta}}} + {}^{b}\underline{\dot{\boldsymbol{\phi}}} + {}^{b}\underline{\dot{\boldsymbol{\psi}}}\right) \\
\dot{\underline{\boldsymbol{\mathcal{J}}}}^{V} &= {}^{b}\underline{\underline{\boldsymbol{\jmath}}}^{V}\,\underline{\ddot{\boldsymbol{\theta}}} + \underline{\dot{\boldsymbol{\theta}}}^{\times}\,{}^{b}\underline{\underline{\boldsymbol{\jmath}}}^{V}\left({}^{b}\underline{\dot{\boldsymbol{\phi}}} + {}^{b}\underline{\dot{\boldsymbol{\psi}}}\right) + \left({}^{b}\underline{\dot{\boldsymbol{\phi}}}^{\times}\,{}^{b}\underline{\underline{\boldsymbol{\jmath}}}^{V} - {}^{b}\underline{\underline{\boldsymbol{\jmath}}}^{V}\,{}^{b}\underline{\dot{\boldsymbol{\phi}}}^{\times}\right)\underline{\dot{\boldsymbol{\theta}}} \\
&\quad + \left(\underline{\underline{\mathbb{1}}} + \underline{\underline{\boldsymbol{\theta}}}^{\times}\right)\left({}^{b}\underline{\underline{\boldsymbol{\jmath}}}^{V}\,{}^{b}\underline{\ddot{\boldsymbol{\phi}}} + {}^{b}\underline{\underline{\boldsymbol{\jmath}}}^{V}\,{}^{b}\underline{\ddot{\boldsymbol{\psi}}} + {}^{b}\underline{\dot{\boldsymbol{\phi}}}^{\times}\,{}^{b}\underline{\underline{\boldsymbol{\jmath}}}^{V}\left({}^{b}\underline{\dot{\boldsymbol{\phi}}} + {}^{b}\underline{\dot{\boldsymbol{\psi}}}\right)\right)
\end{aligned} \tag{4.70}$$

Consequently, by either using Eqs. (4.53) and (4.54) or simplifying Eqs. (4.65)–(4.68), the corresponding motion equations and I/BCs for a classical gyrobeam will be derived as:

$$\begin{aligned}
\bar{f}_1^{V} &= \left(\rho^{V} + \varrho^{V}\right)\ddot{\bar{u}}_1 - E\,\bar{u}_{1,11} \\
\bar{f}_2^{V} &= \left(\rho^{V} + \varrho^{V}\right)\ddot{\bar{u}}_2 - k_{s_2}\,\mu\left(\bar{u}_{2,11} - \bar{\theta}_{3,1}\right) \\
\bar{f}_3^{V} &= \left(\rho^{V} + \varrho^{V}\right)\ddot{\bar{u}}_3 - k_{s_3}\,\mu\left(\bar{u}_{3,11} + \bar{\theta}_{2,1}\right) \\
\bar{m}_1^{L} + A\,\bar{m}_1^{V} &= \left(\rho^{V} + \varrho^{V}\right) I_1\,\ddot{\bar{\theta}}_1 + A\,\dot{\mathcal{J}}_1^{V} - k_t\,\mu\,I_1\,\bar{\theta}_{1,11} \\
\bar{m}_2^{L} + A\,\bar{m}_2^{V} &= \left(\rho^{V} + \varrho^{V}\right) I_2\,\ddot{\bar{\theta}}_2 + A\,\dot{\mathcal{J}}_2^{V} - E\,I_2\,\bar{\theta}_{2,11} + k_{s_3}\,\mu\,A\left(\bar{u}_{3,1} + \bar{\theta}_2\right) \\
\bar{m}_3^{L} + A\,\bar{m}_3^{V} &= \left(\rho^{V} + \varrho^{V}\right) I_3\,\ddot{\bar{\theta}}_3 + A\,\dot{\mathcal{J}}_3^{V} - E\,I_3\,\bar{\theta}_{3,11} - k_{s_2}\,\mu\,A\left(\bar{u}_{2,1} - \bar{\theta}_3\right)
\end{aligned} \tag{4.71}$$

and:

$$
\begin{aligned}
&\text{at } t = t_1, t_2 \ ; \ \text{ and over } L : \\
&\delta\bar{u}_1 = 0 \quad \text{or} \quad \left(\rho^V + \varrho^V\right) A\, \ddot{\bar{u}}_1 = 0 \\
&\delta\bar{u}_2 = 0 \quad \text{or} \quad \left(\rho^V + \varrho^V\right) A\, \ddot{\bar{u}}_2 = 0 \\
&\delta\bar{u}_3 = 0 \quad \text{or} \quad \left(\rho^V + \varrho^V\right) A\, \ddot{\bar{u}}_3 = 0 \\
&\delta\bar{\theta}_1 = 0 \quad \text{or} \quad \left(\rho^V + \varrho^V\right) I_1\, \ddot{\bar{\theta}}_1 + A\, \mathcal{J}_1^V = 0 \\
&\delta\bar{\theta}_2 = 0 \quad \text{or} \quad \left(\rho^V + \varrho^V\right) I_2\, \ddot{\bar{\theta}}_2 + A\, \mathcal{J}_2^V = 0 \\
&\delta\bar{\theta}_3 = 0 \quad \text{or} \quad \left(\rho^V + \varrho^V\right) I_3\, \ddot{\bar{\theta}}_3 + A\, \mathcal{J}_3^V = 0
\end{aligned}
\tag{4.72}
$$

$$
\begin{aligned}
&\text{at } P_1 \ ; \ \text{ and during } t : \\
&\delta\bar{u}_1 = 0 \quad \text{or} \quad A\, \bar{f}_1^S + E\, A\, \bar{u}_{1,1} = 0 \\
&\delta\bar{u}_2 = 0 \quad \text{or} \quad A\, \bar{f}_2^S + k_{s_2}\, \mu\, A \left(\bar{u}_{2,1} - \bar{\theta}_3\right) = 0 \\
&\delta\bar{u}_3 = 0 \quad \text{or} \quad A\, \bar{f}_3^S + k_{s_3}\, \mu\, A \left(\bar{u}_{3,1} + \bar{\theta}_2\right) = 0 \\
&\delta\bar{\theta}_1 = 0 \quad \text{or} \quad \bar{m}_1^P + A\, \bar{m}_1^S + k_t\, \mu\, I_1\, \bar{\theta}_{1,1} = 0 \\
&\delta\bar{\theta}_2 = 0 \quad \text{or} \quad \bar{m}_2^P + A\, \bar{m}_2^S + E\, I_2\, \bar{\theta}_{2,1} = 0 \\
&\delta\bar{\theta}_3 = 0 \quad \text{or} \quad \bar{m}_3^P + A\, \bar{m}_3^S + E\, I_3\, \bar{\theta}_{3,1} = 0
\end{aligned}
\tag{4.73}
$$

$$
\begin{aligned}
&\text{at } P_2 \ ; \ \text{ and during } t : \\
&\delta\bar{u}_1 = 0 \quad \text{or} \quad A\, \bar{f}_1^S - E\, A\, \bar{u}_{1,1} = 0 \\
&\delta\bar{u}_2 = 0 \quad \text{or} \quad A\, \bar{f}_2^S - k_{s_2}\, \mu\, A \left(\bar{u}_{2,1} - \bar{\theta}_3\right) = 0 \\
&\delta\bar{u}_3 = 0 \quad \text{or} \quad A\, \bar{f}_3^S - k_{s_3}\, \mu\, A \left(\bar{u}_{3,1} + \bar{\theta}_2\right) = 0 \\
&\delta\bar{\theta}_1 = 0 \quad \text{or} \quad \bar{m}_1^P + A\, \bar{m}_1^S - k_t\, \mu\, I_1\, \bar{\theta}_{1,1} = 0 \\
&\delta\bar{\theta}_2 = 0 \quad \text{or} \quad \bar{m}_2^P + A\, \bar{m}_2^S - E\, I_2\, \bar{\theta}_{2,1} = 0 \\
&\delta\bar{\theta}_3 = 0 \quad \text{or} \quad \bar{m}_3^P + A\, \bar{m}_3^S - E\, I_3\, \bar{\theta}_{3,1} = 0
\end{aligned}
\tag{4.74}
$$

Analogous to the micropolar gyrobeam dynamic equations, there are four modes of deformation characterized by the classical gyrobeam dynamic equations given in Eq. (4.71); longitudinal displacement along the ${}^c x_1$ axis by the first relation, torsional rotation around the ${}^c x_1$ axis by the fourth relation, bending deformation in the ${}^c x_1 {}^c x_2$ plane by the second and sixth relations, and bending deformation in the ${}^c x_1 {}^c x_3$ plane by the third and fifth

relations. Again, there are minor sign differences between the relations expressing the two bending modes as the positive directions for $\bar{\theta}_3$ and $\bar{u}_{2,1}$ are the same while $\bar{\theta}_2$ and $\bar{u}_{3,1}$ have opposite positive directions.

It is worthwhile to note that (unlike the classical beam theories which do commonly need shear correction factors) the micropolar beam theory presented here is expected to need no shear correction factor (*i.e.* no correction factor needs to be introduced for reduction of the potential energy associated with transverse shears). Moreover, the torsion correction factor corresponding to a micropolar beam is likely to be different from the classical torsion correction factor. However, all shear and torsion correction factors have been added to the micropolar beam dynamic equations and I/BCs given in Eqs. (4.65)–(4.68), in the same way as in the classical Duleau torsion and Timoshenko bending theories. This has been done to allow for the recovery of the classical beam equations in the limit when the required conditions are met. There is no loss of generality as the inserted correction factors can be set to unity if it is determined this is the most appropriate choice for the micropolar beam theory. However, derivations of the suitable shear and torsion correction factors, corresponding to the presented micropolar beam torsion and bending theories, are beyond the scope of this thesis and will not be pursued in this text.

4.8 Nondimensionalized equations of motion

Nondimensionalization is a technique for the partial or full removal of dimensions from the equations describing a problem by a suitable grouping of involved dimensional parameters. The method results in insight into the underlying problem and provides useful dimensionless (or dimension-reduced) groups of parameters for reporting the results [62]. Here, the dimensional gyrobeam equations of motion can have the dimensions reduced or eliminated through nondimensionalization, which begins with dimensional analysis of the descriptive equations, and involves scaling some parameters by the characteristic units of the system while collecting the others into the dimensionless (or dimension-reduced) groups.

A dimensional analysis of the previously-derived dynamic equations indicates that the fundamental dimensions involved in the gyrobeam dynamic problem are mass, length,

and time denoted by M, L, and T in dimensional analyses. As it is common in the similar problems, the next step for deriving the nondimensional equations is to scale the lengths, coordinates, and displacements by the characteristic length of the system which is chosen here to be the beam's length (note that the microrotations and beam plane section rotations do not need to be scaled as they are dimensionless). This scaling will result into the following dimensionless parameters (dimensionless or dimension-reduced parameters are denoted with a $\hat{\square}$ symbol):

$$\begin{aligned} \hat{L} &= \frac{L}{L} = 1 \\ {}^{c}\hat{x}_i &= \frac{{}^{c}x_i}{L} \\ {}^{o}\hat{x}_i &= \frac{{}^{o}x_i}{L} \\ \hat{\bar{u}}_i &= \frac{\bar{u}_i}{L} \end{aligned} \tag{4.75}$$

It is also useful to define the nondimensional space derivative along the ${}^{o}\hat{x}_1$ direction and nondimensional line integral over the beam length as:

$$\begin{aligned} z_{,\hat{1}} &= L\, z_{,1} \\ \int_{\hat{L}} z\, d\hat{L} &= \frac{1}{L} \int_{L} z\, dL \end{aligned} \tag{4.76}$$

where z is an arbitrary field variable.

Substituting from Eqs. (4.75) and (4.76) into the expressions for potential energy, kinetic energy, and virtual work of a gyrobeam (given by Eqs. (4.40), (4.42), and (4.45) for a micropolar gyrobeam and by Eqs. (4.41), (4.43), and (4.48) for a classical gyrobeam), one can conclude that it is also useful to scale (or nondimesionalize) the time as:

$$\hat{t} = \frac{t}{\hat{T}} \tag{4.77}$$

where

$$\hat{T} = \sqrt{\frac{\rho^{V} L^2}{E}}, \qquad [\hat{T}] = \mathsf{T} \tag{4.78}$$

is a dimension-reduced group parameter directly proportional to the longitudinal natural periods of the beam (or inversely proportional to the longitudinal natural frequencies of the beam). Note that dimension of a parameter is represented by $[\square]$.

Analogous to usage of dimensionless coordinate ${}^{o}\hat{x}_1$ in Eq. (4.76), the dimensionless time $\hat{t}$ can be used to define the nondimensional time derivative and nondimensional time integral as:

$$\begin{aligned} \mathring{z} &= z_{,\hat{t}} = \hat{T}\, z_{,t} = \hat{T}\, \dot{z} \\ \int_{\hat{t}} z\, d\hat{t} &= \frac{1}{\hat{T}} \int_{t} z\, dt \end{aligned} \tag{4.79}$$

In addition to the group parameter $\hat{T}$ there are other dimensionless parameter groups which one may deduce to be useful for writing the nondimensional gyrobeam equations. They are; dimensionless elastic moduli:

$$\begin{aligned} \hat{\mu} &= \frac{\mu}{E}, & \hat{\kappa} &= \frac{\kappa}{E} \\ \hat{\gamma} &= \frac{\gamma}{E\,L^2}, & \hat{\beta} &= \frac{\beta}{E\,L^2}, & \hat{\mathcal{E}} &= \frac{\mathcal{E}}{E\,L^2} \end{aligned} \tag{4.80}$$

dimensionless polar/second moments of area:

$$\hat{I}_1 = \frac{I_1}{A\,L^2}, \qquad \hat{I}_2 = \frac{I_2}{A\,L^2}, \qquad \hat{I}_3 = \frac{I_3}{A\,L^2} \tag{4.81}$$

dimensionless slenderness ratios:

$$\hat{R}_i = \sqrt{\frac{1}{\hat{I}_i}} = \frac{L}{\sqrt{\frac{I_i}{A}}} \tag{4.82}$$

dimensionless inertias:

$$\begin{aligned} \hat{\varrho}^{V} &= \frac{\varrho^{V}}{\rho^{V}} \\ {}^{b}\hat{\imath}^{V}_{ij} &= \frac{{}^{b}\imath^{V}_{ij}}{\rho^{V}\,L^2} \\ {}^{a}\hat{\jmath}^{V}_{ij} &= \frac{{}^{a}\jmath^{V}_{ij}}{\rho^{V}\,L^2} \end{aligned} \tag{4.83}$$

dimensionless forces:

$$\begin{aligned} \hat{\bar{f}}^{V}_{i} &= \frac{\bar{f}^{V}_{i}\,L}{E} \\ \hat{\bar{f}}^{S}_{i} &= \frac{\bar{f}^{S}_{i}}{E} \end{aligned} \tag{4.84}$$

dimensionless moments:

$$\begin{aligned}
\hat{\bar{m}}_i^{\,V} &= \frac{\bar{m}_i^V}{E} \\
\hat{\bar{m}}_i^{\,S} &= \frac{\bar{m}_i^S}{E\,L} \\
\hat{\bar{m}}_i^{\,L} &= \frac{\bar{m}_i^L}{E\,A} \\
\hat{\bar{m}}_i^{\,P} &= \frac{\bar{m}_i^P}{E\,A\,L}
\end{aligned} \tag{4.85}$$

dimensionless potential and kinetic energy and virtual work:

$$\begin{aligned}
\hat{\mathcal{U}} &= \frac{\mathcal{U}}{E\,A\,L}, & \hat{\mathcal{T}} &= \frac{\mathcal{T}}{E\,A\,L}, & \delta\hat{\mathcal{W}} &= \frac{\delta\mathcal{W}}{E\,A\,L} \\
\hat{\mathcal{U}}^{\,L} &= \frac{\mathcal{U}^{\,L}}{E\,A}, & \hat{\mathcal{T}}^{\,L} &= \frac{\mathcal{T}^{\,L}}{E\,A}, & \delta\hat{\mathcal{W}}^{\,L} &= \frac{\delta\mathcal{W}^{\,L}}{E\,A} \\
& & & & \delta\hat{\mathcal{W}}^{\,P} &= \frac{\delta\mathcal{W}^{\,P}}{E\,A\,L}
\end{aligned} \tag{4.86}$$

and dimensionless body and gyros angular momenta:

$$\begin{aligned}
\hat{\mathcal{I}}_i^{\,V} &= \frac{\mathcal{I}_i^{\,V}\,\hat{T}}{\rho^V\,L^2} \\
\mathring{\hat{\mathcal{I}}}_i^{\,V} &= \hat{T}\,\frac{d\hat{\mathcal{I}}_i^{\,V}}{dt} = \frac{\dot{\mathcal{I}}_i^{\,V}\,\hat{T}^2}{\rho^V\,L^2} = \frac{\dot{\mathcal{I}}_i^{\,V}}{E} \\
\hat{\mathcal{J}}_i^{\,V} &= \frac{\mathcal{J}_i^{\,V}\,\hat{T}}{\rho^V\,L^2} \\
\mathring{\hat{\mathcal{J}}}_i^{\,V} &= \hat{T}\,\frac{d\hat{\mathcal{J}}_i^{\,V}}{dt} = \frac{\dot{\mathcal{J}}_i^{\,V}\,\hat{T}^2}{\rho^V\,L^2} = \frac{\dot{\mathcal{J}}_i^{\,V}}{E}
\end{aligned} \tag{4.87}$$

Finally, when dealing with a theoretical modal analysis on the gyrobeams, the gyrobeam natural frequencies $\omega^{(i)}$ can be nondimesionalized as:

$$\hat{\omega}^{(i)} = \sqrt{\frac{\rho^V\,L^2}{E}}\,\omega^{(i)} = \hat{T}\,\omega^{(i)} \tag{4.88}$$

Indeed, one can show that a theoretical modal analysis of the nondimensionalized gyrobeam equations naturally results in dimensionless natural frequencies in the form given by Eq. (4.88).

By utilizing the definitions given by Eqs. (4.75)–(4.87) the following dimensionless expressions will be obtained for a micropolar gyrobeam:

$$\begin{aligned}
\hat{\mathcal{U}} = \int_{\hat{L}} \hat{\mathcal{U}}^{L}\, d\hat{L} = {} & \frac{1}{2} \int_{\hat{L}} \hat{\bar{u}}_{1,\hat{1}}\, \hat{\bar{u}}_{1,\hat{1}}\, d\hat{L} + \frac{1}{2}\, \hat{I}_2 \int_{\hat{L}} \bar{\theta}_{2,\hat{1}}\, \bar{\theta}_{2,\hat{1}}\, d\hat{L} + \frac{1}{2}\, \hat{I}_3 \int_{\hat{L}} \bar{\theta}_{3,\hat{1}}\, \bar{\theta}_{3,\hat{1}}\, d\hat{L} \\
& + \frac{1}{2}\, k_{s_2}\, \hat{\mu} \int_{\hat{L}} \left(\hat{\bar{u}}_{2,\hat{1}} - \bar{\theta}_3 \right)^2 d\hat{L} + \frac{1}{2}\, k_{s_3}\, \hat{\mu} \int_{\hat{L}} \left(\hat{\bar{u}}_{3,\hat{1}} + \bar{\theta}_2 \right)^2 d\hat{L} \\
& + \frac{1}{2}\, k_{t}\, \hat{\mu}\, \hat{I}_1 \int_{\hat{L}} \bar{\theta}_{1,\hat{1}}\, \bar{\theta}_{1,\hat{1}}\, d\hat{L} \\
& + \frac{1}{2}\, \hat{\kappa} \int_{\hat{L}} \left(\hat{\bar{u}}_{2,\hat{1}} + \bar{\theta}_3 - 2\, \bar{\vartheta}_3 \right)^2 d\hat{L} + \frac{1}{2}\, \hat{\kappa} \int_{\hat{L}} \left(\hat{\bar{u}}_{3,\hat{1}} - \bar{\theta}_2 + 2\, \bar{\vartheta}_2 \right)^2 d\hat{L} \\
& + \frac{1}{2}\, \hat{\kappa}\, \hat{I}_1 \int_{\hat{L}} \left(\bar{\theta}_{1,\hat{1}} - 2\, \xi\, \bar{\vartheta}_{1,\hat{1}} \right)^2 d\hat{L} + 2\, \hat{\kappa} \int_{\hat{L}} \left(\bar{\theta}_1 - \bar{\vartheta}_1 \right)^2 d\hat{L} \\
& + \frac{1}{2}\, \hat{\mathcal{E}} \int_{\hat{L}} \bar{\vartheta}_{1,\hat{1}}\, \bar{\vartheta}_{1,\hat{1}}\, d\hat{L} + \frac{1}{2} \left(\hat{\gamma} + \hat{\beta} \right) \int_{\hat{L}} \left(\bar{\vartheta}_{2,\hat{1}}\, \bar{\vartheta}_{2,\hat{1}} + \bar{\vartheta}_{3,\hat{1}}\, \bar{\vartheta}_{3,\hat{1}} \right) d\hat{L}
\end{aligned} \tag{4.89}$$

$$\begin{aligned}
\hat{\mathcal{T}} = \int_{\hat{L}} \hat{\mathcal{T}}^{L}\, d\hat{L} = {} & \frac{1}{2} \left(1 + \hat{\varrho}^{V} \right) \int_{\hat{L}} \left(\mathring{\hat{\bar{u}}}_1\, \mathring{\hat{\bar{u}}}_1 + \mathring{\hat{\bar{u}}}_2\, \mathring{\hat{\bar{u}}}_2 + \mathring{\hat{\bar{u}}}_3\, \mathring{\hat{\bar{u}}}_3 \right) d\hat{L} \\
& + \frac{1}{2} \left(1 + \hat{\varrho}^{V} \right) \int_{\hat{L}} \left(\hat{I}_1\, \mathring{\bar{\theta}}_1\, \mathring{\bar{\theta}}_1 + \hat{I}_2\, \mathring{\bar{\theta}}_2\, \mathring{\bar{\theta}}_2 + \hat{I}_3\, \mathring{\bar{\theta}}_3\, \mathring{\bar{\theta}}_3 \right) d\hat{L} \\
& + \frac{1}{2} \int_{\hat{L}} \left(\hat{\imath}^{V}_{ij} + \hat{\jmath}^{V}_{ij} \right) \mathring{\bar{\vartheta}}_j\, \mathring{\bar{\vartheta}}_i\, d\hat{L} + \int_{\hat{L}} \hat{\jmath}^{V}_{ij} \left(\mathring{\phi}_j + \mathring{\psi}_j \right) \mathring{\bar{\vartheta}}_i\, d\hat{L} \\
& + \frac{1}{2} \int_{\hat{L}} \hat{\jmath}^{V}_{ij} \left(\mathring{\phi}_j\, \mathring{\phi}_i + \mathring{\psi}_j\, \mathring{\psi}_i + 2\, \mathring{\phi}_j\, \mathring{\psi}_i \right) d\hat{L}
\end{aligned} \tag{4.90}$$

$$\begin{aligned}\delta\hat{\mathcal{W}} &= \int_{\hat{L}} \delta\hat{\mathcal{W}}^{L}\, d\hat{L} + \sum_{P} \delta\hat{\mathcal{W}}^{P} \\ &= \int_{\hat{L}} \left(\hat{\bar{f}}_i^{V}\, \delta\hat{\bar{u}}_i + \hat{\bar{m}}_i^{L}\, \delta\bar{\theta}_i + \hat{\bar{m}}_i^{V}\, \delta\bar{\vartheta}_i \right) d\hat{L} + \sum_{P} \left(\hat{\bar{f}}_i^{S}\, \delta\hat{\bar{u}}_i + \hat{\bar{m}}_i^{P}\, \delta\bar{\theta}_i + \hat{\bar{m}}_i^{S}\, \delta\bar{\vartheta}_i \right)\end{aligned} \tag{4.91}$$

$$\underset{\sim}{\hat{\boldsymbol{q}}} = \left[\begin{array}{ccccccccc} \hat{\bar{u}}_1 & \hat{\bar{u}}_2 & \hat{\bar{u}}_3 & \bar{\theta}_1 & \bar{\theta}_2 & \bar{\theta}_3 & \bar{\vartheta}_1 & \bar{\vartheta}_2 & \bar{\vartheta}_3 \end{array} \right]^{\mathrm{T}} \tag{4.92}$$

The corresponding dimensionless expressions for a classical gyrobeam will be:

$$\begin{aligned}\hat{\mathcal{U}} = \int_{\hat{L}} \hat{\mathcal{U}}^{L}\, d\hat{L} = \frac{1}{2} \int_{\hat{L}} \hat{\bar{u}}_{1,\hat{1}}\, \hat{\bar{u}}_{1,\hat{1}}\, d\hat{L} + \frac{1}{2}\, \hat{I}_2 \int_{\hat{L}} \bar{\theta}_{2,\hat{1}}\, \bar{\theta}_{2,\hat{1}}\, d\hat{L} + \frac{1}{2}\, \hat{I}_3 \int_{\hat{L}} \bar{\theta}_{3,\hat{1}}\, \bar{\theta}_{3,\hat{1}}\, d\hat{L} \\ + \frac{1}{2}\, k_{\mathrm{s}_2}\, \hat{\mu} \int_{\hat{L}} \left(\hat{\bar{u}}_{2,\hat{1}} - \bar{\theta}_3 \right)^2 d\hat{L} + \frac{1}{2}\, k_{\mathrm{s}_3}\, \hat{\mu} \int_{\hat{L}} \left(\hat{\bar{u}}_{3,\hat{1}} + \bar{\theta}_2 \right)^2 d\hat{L} \\ + \frac{1}{2}\, k_{\mathrm{t}}\, \hat{\mu}\, \hat{I}_1 \int_{\hat{L}} \bar{\theta}_{1,\hat{1}}\, \bar{\theta}_{1,\hat{1}}\, d\hat{L}\end{aligned} \tag{4.93}$$

$$\begin{aligned}\hat{\mathcal{T}} = \int_{\hat{L}} \hat{\mathcal{T}}^{L}\, d\hat{L} = \frac{1}{2} \left(1 + \hat{\varrho}^{V} \right) \int_{\hat{L}} \left(\mathring{\hat{\bar{u}}}_1\, \mathring{\hat{\bar{u}}}_1 + \mathring{\hat{\bar{u}}}_2\, \mathring{\hat{\bar{u}}}_2 + \mathring{\hat{\bar{u}}}_3\, \mathring{\hat{\bar{u}}}_3 \right) d\hat{L} \\ + \frac{1}{2} \left(1 + \hat{\varrho}^{V} \right) \int_{\hat{L}} \left(\hat{I}_1\, \mathring{\bar{\theta}}_1\, \mathring{\bar{\theta}}_1 + \hat{I}_2\, \mathring{\bar{\theta}}_2\, \mathring{\bar{\theta}}_2 + \hat{I}_3\, \mathring{\bar{\theta}}_3\, \mathring{\bar{\theta}}_3 \right) d\hat{L} \\ + \frac{1}{2} \int_{\hat{L}} \hat{\jmath}_{ij}^{V}\, \mathring{\bar{\theta}}_j\, \mathring{\bar{\theta}}_i\, d\hat{L} + \int_{\hat{L}} \hat{\jmath}_{ij}^{V} \left(\mathring{\phi}_j + \mathring{\psi}_j \right) \mathring{\bar{\theta}}_i\, d\hat{L} \\ + \frac{1}{2} \int_{\hat{L}} \hat{\jmath}_{ij}^{V} \left(\mathring{\phi}_j\, \mathring{\phi}_i + \mathring{\psi}_j\, \mathring{\psi}_i + 2\, \mathring{\phi}_j\, \mathring{\psi}_i \right) d\hat{L}\end{aligned} \tag{4.94}$$

$$\begin{aligned}\delta\hat{\mathcal{W}} &= \int_{\hat{L}} \delta\hat{\mathcal{W}}^{L}\, d\hat{L} + \sum_{P} \delta\hat{\mathcal{W}}^{P} \\ &= \int_{\hat{L}} \left(\hat{\bar{f}}_i^{V}\, \delta\hat{\bar{u}}_i + \hat{\bar{m}}_i^{V}\, \delta\bar{\theta}_i + \hat{\bar{m}}_i^{L}\, \delta\bar{\theta}_i \right) d\hat{L} + \sum_{P} \left(\hat{\bar{f}}_i^{S}\, \delta\hat{\bar{u}}_i + \hat{\bar{m}}_i^{S}\, \delta\bar{\theta}_i + \hat{\bar{m}}_i^{P}\, \delta\bar{\theta}_i \right)\end{aligned} \tag{4.95}$$

$$\underset{\sim}{\hat{\boldsymbol{q}}} = \begin{bmatrix} \hat{\bar{u}}_1 & \hat{\bar{u}}_2 & \hat{\bar{u}}_3 & \bar{\theta}_1 & \bar{\theta}_2 & \bar{\theta}_3 \end{bmatrix}^{\mathrm{T}} \tag{4.96}$$

Now by using the obtained dimensionless expressions, the dimensionless equations of motion and dimensionless I/BCs take the following general matrix forms:

$$\underset{\sim}{\hat{\boldsymbol{\mathcal{Q}}}}^{L} = \left(\frac{\partial \hat{\mathcal{T}}^{L}}{\partial \underset{\sim}{\hat{\dot{\boldsymbol{q}}}}} \right)_{,\hat{t}} - \left(\frac{\partial \hat{\mathcal{U}}^{L}}{\partial \underset{\sim}{\hat{\boldsymbol{q}}}_{,\hat{1}}} \right)_{,\hat{1}} + \frac{\partial \hat{\mathcal{U}}^{L}}{\partial \underset{\sim}{\hat{\boldsymbol{q}}}} \tag{4.97}$$

and:

$$\begin{aligned}&\text{at } \hat{t} = \hat{t}_1, \hat{t}_2 \,; \quad \text{and over } \hat{L}: \quad \delta\underset{\sim}{\hat{\boldsymbol{q}}} = \underset{\sim}{\boldsymbol{0}} \quad \text{or} \quad \frac{\partial \hat{\mathcal{T}}^{L}}{\partial \underset{\sim}{\hat{\dot{\boldsymbol{q}}}}} = \underset{\sim}{\boldsymbol{0}} \\ &\text{at } P_1 \,; \quad \text{and during } \hat{t}: \quad \delta\underset{\sim}{\hat{\boldsymbol{q}}} = \underset{\sim}{\boldsymbol{0}} \quad \text{or} \quad \underset{\sim}{\hat{\boldsymbol{\mathcal{Q}}}}^{P} + \frac{\partial \hat{\mathcal{U}}^{L}}{\partial \underset{\sim}{\hat{\boldsymbol{q}}}_{,\hat{1}}} = \underset{\sim}{\boldsymbol{0}} \\ &\text{at } P_2 \,; \quad \text{and during } \hat{t}: \quad \delta\underset{\sim}{\hat{\boldsymbol{q}}} = \underset{\sim}{\boldsymbol{0}} \quad \text{or} \quad \underset{\sim}{\hat{\boldsymbol{\mathcal{Q}}}}^{P} - \frac{\partial \hat{\mathcal{U}}^{L}}{\partial \underset{\sim}{\hat{\boldsymbol{q}}}_{,\hat{1}}} = \underset{\sim}{\boldsymbol{0}}\end{aligned} \tag{4.98}$$

where:

$$\underset{\sim}{\hat{\boldsymbol{\mathcal{Q}}}}^{L} = \frac{\delta\hat{\mathcal{W}}^{L}}{\delta\underset{\sim}{\hat{\boldsymbol{q}}}}, \qquad \underset{\sim}{\hat{\boldsymbol{\mathcal{Q}}}}^{P} = \frac{\delta\hat{\mathcal{W}}^{P}}{\delta\underset{\sim}{\hat{\boldsymbol{q}}}} \tag{4.99}$$

Specially, the dimensionless equations of motion for micropolar and classical gyrobeams

are:

$$
\begin{aligned}
\hat{\bar{f}}_1^{\,V} &= \left(1+\hat{\varrho}^{\,V}\right)\overset{\circ\circ}{\hat{\bar{u}}}_1 - \hat{\bar{u}}_{1,\hat{1}\hat{1}} \\
\hat{\bar{f}}_2^{\,V} &= \left(1+\hat{\varrho}^{\,V}\right)\overset{\circ\circ}{\hat{\bar{u}}}_2 - k_{s_2}\,\hat{\mu}\left(\hat{\bar{u}}_{2,\hat{1}\hat{1}} - \bar{\theta}_{3,\hat{1}}\right) - \hat{\kappa}\left(\hat{\bar{u}}_{2,\hat{1}\hat{1}} + \bar{\theta}_{3,\hat{1}} - 2\,\bar{\vartheta}_{3,\hat{1}}\right) \\
\hat{\bar{f}}_3^{\,V} &= \left(1+\hat{\varrho}^{\,V}\right)\overset{\circ\circ}{\hat{\bar{u}}}_3 - k_{s_3}\,\hat{\mu}\left(\hat{\bar{u}}_{3,\hat{1}\hat{1}} + \bar{\theta}_{2,\hat{1}}\right) - \hat{\kappa}\left(\hat{\bar{u}}_{3,\hat{1}\hat{1}} - \bar{\theta}_{2,\hat{1}} + 2\,\bar{\vartheta}_{2,\hat{1}}\right) \\
\hat{\bar{m}}_1^{\,L} &= \left(1+\hat{\varrho}^{\,V}\right)\hat{I}_1\,\overset{\circ\circ}{\bar{\theta}}_1 - k_{t}\,\hat{\mu}\,\hat{I}_1\,\bar{\theta}_{1,\hat{1}\hat{1}} - \hat{\kappa}\,\hat{I}_1\left(\bar{\theta}_{1,\hat{1}\hat{1}} - 2\,\xi\,\bar{\vartheta}_{1,\hat{1}\hat{1}}\right) + 4\,\hat{\kappa}\left(\bar{\theta}_1 - \bar{\vartheta}_1\right) \\
\hat{\bar{m}}_2^{\,L} &= \left(1+\hat{\varrho}^{\,V}\right)\hat{I}_2\,\overset{\circ\circ}{\bar{\theta}}_2 - \hat{I}_2\,\bar{\theta}_{2,\hat{1}\hat{1}} + k_{s_3}\,\hat{\mu}\left(\hat{\bar{u}}_{3,\hat{1}} + \bar{\theta}_2\right) - \hat{\kappa}\left(\hat{\bar{u}}_{3,\hat{1}} - \bar{\theta}_2 + 2\,\bar{\vartheta}_2\right) \\
\hat{\bar{m}}_3^{\,L} &= \left(1+\hat{\varrho}^{\,V}\right)\hat{I}_3\,\overset{\circ\circ}{\bar{\theta}}_3 - \hat{I}_3\,\bar{\theta}_{3,\hat{1}\hat{1}} - k_{s_2}\,\hat{\mu}\left(\hat{\bar{u}}_{2,\hat{1}} - \bar{\theta}_3\right) + \hat{\kappa}\left(\hat{\bar{u}}_{2,\hat{1}} + \bar{\theta}_3 - 2\,\bar{\vartheta}_3\right) \\
\hat{\bar{m}}_1^{\,V} &= \overset{\circ}{\hat{\mathcal{I}}}_1^{\,V} + \overset{\circ}{\hat{\mathcal{J}}}_1^{\,V} - \hat{\mathcal{E}}\,\bar{\vartheta}_{1,\hat{1}\hat{1}} + 2\,\xi\,\hat{\kappa}\,\hat{I}_1\left(\bar{\theta}_{1,\hat{1}\hat{1}} - 2\,\xi\,\bar{\vartheta}_{1,\hat{1}\hat{1}}\right) - 4\,\hat{\kappa}\left(\bar{\theta}_1 - \bar{\vartheta}_1\right) \\
\hat{\bar{m}}_2^{\,V} &= \overset{\circ}{\hat{\mathcal{I}}}_2^{\,V} + \overset{\circ}{\hat{\mathcal{J}}}_2^{\,V} - \left(\hat{\gamma}+\hat{\beta}\right)\bar{\vartheta}_{2,\hat{1}\hat{1}} + 2\,\hat{\kappa}\left(\hat{\bar{u}}_{3,\hat{1}} - \bar{\theta}_2 + 2\,\bar{\vartheta}_2\right) \\
\hat{\bar{m}}_3^{\,V} &= \overset{\circ}{\hat{\mathcal{I}}}_3^{\,V} + \overset{\circ}{\hat{\mathcal{J}}}_3^{\,V} - \left(\hat{\gamma}+\hat{\beta}\right)\bar{\vartheta}_{3,\hat{1}\hat{1}} - 2\,\hat{\kappa}\left(\hat{\bar{u}}_{2,\hat{1}} + \bar{\theta}_3 - 2\,\bar{\vartheta}_3\right)
\end{aligned}
\tag{4.100}
$$

and:

$$
\begin{aligned}
\hat{\bar{f}}_1^{\,V} &= \left(1+\hat{\varrho}^{\,V}\right)\overset{\circ\circ}{\hat{\bar{u}}}_1 - \hat{\bar{u}}_{1,\hat{1}\hat{1}} \\
\hat{\bar{f}}_2^{\,V} &= \left(1+\hat{\varrho}^{\,V}\right)\overset{\circ\circ}{\hat{\bar{u}}}_2 - k_{s_2}\,\hat{\mu}\left(\hat{\bar{u}}_{2,\hat{1}\hat{1}} - \bar{\theta}_{3,\hat{1}}\right) \\
\hat{\bar{f}}_3^{\,V} &= \left(1+\hat{\varrho}^{\,V}\right)\overset{\circ\circ}{\hat{\bar{u}}}_3 - k_{s_3}\,\hat{\mu}\left(\hat{\bar{u}}_{3,\hat{1}\hat{1}} + \bar{\theta}_{2,\hat{1}}\right) \\
\hat{\bar{m}}_1^{\,L} + \hat{\bar{m}}_1^{\,V} &= \left(1+\hat{\varrho}^{\,V}\right)\hat{I}_1\,\overset{\circ\circ}{\bar{\theta}}_1 + \overset{\circ}{\hat{\mathcal{J}}}_1^{\,V} - k_{t}\,\hat{\mu}\,\hat{I}_1\,\bar{\theta}_{1,\hat{1}\hat{1}} \\
\hat{\bar{m}}_2^{\,L} + \hat{\bar{m}}_2^{\,V} &= \left(1+\hat{\varrho}^{\,V}\right)\hat{I}_2\,\overset{\circ\circ}{\bar{\theta}}_2 + \overset{\circ}{\hat{\mathcal{J}}}_2^{\,V} - \hat{I}_2\,\bar{\theta}_{2,\hat{1}\hat{1}} + k_{s_3}\,\hat{\mu}\left(\hat{\bar{u}}_{3,\hat{1}} + \bar{\theta}_2\right) \\
\hat{\bar{m}}_3^{\,L} + \hat{\bar{m}}_3^{\,V} &= \left(1+\hat{\varrho}^{\,V}\right)\hat{I}_3\,\overset{\circ\circ}{\bar{\theta}}_3 + \overset{\circ}{\hat{\mathcal{J}}}_3^{\,V} - \hat{I}_3\,\bar{\theta}_{3,\hat{1}\hat{1}} - k_{s_2}\,\hat{\mu}\left(\hat{\bar{u}}_{2,\hat{1}} - \bar{\theta}_3\right)
\end{aligned}
\tag{4.101}
$$

4.9 Finite element formulation

As derived in the previous sections, the essential first-order approximation with respect to the microrotation vector $\underset{\rightarrow}{\vartheta}$ (which in micropolar and classical gyrobeams is approximately

equivalent to $\underset{\rightarrow}{\bar{\vartheta}}$ and $\underset{\rightarrow}{\bar{\theta}}$ respectively), imposed when deriving the component matrices of vectors $\underset{\rightarrow}{\mathcal{I}}^{V}$, $\underset{\rightarrow}{\dot{\mathcal{I}}}^{V}$, $\underset{\rightarrow}{\mathcal{J}}^{V}$, and $\underset{\rightarrow}{\dot{\mathcal{J}}}^{V}$, linearizes the potentially nonlinear gyrobeam dynamic equations. Consequently, the dynamic problem of a gyrobeam, either micropolar or classical, can be characterized by a set of linear PDEs which seem quite effortless to solve in comparison with nonlinear ones.

Indeed, the linear (dimensionless) equations of motion for micropolar and classical gyrobeams, given by Eqs. (4.100) and (4.101), are two sets of linear hyperbolic PDEs which are of second order in both space and time. These equations are known to be well-posed (*i.e.* their solutions exist, are unique, and depend continuously on the auxiliary data such as BCs) provided the corresponding linear dimensionless I/BCs are added to them. Yet, no analytical solution is known for these linear PDEs and in practice they should be solved approximately using a numerical technique.

In a numerical approach, usually the main stage (known as discretization) is converting the continuous PDEs into a discrete system of algebraic equations which will be solved to obtain an approximate solution. Considering the dynamics of a gyrobeam, the unknown state variables (or functions) of the derived PDEs evolve in both space and time where their variations in space are related to their variations in time. A common numerical approach for solving such equations is to take different discretization methods (which are applied in sequence) for handling the space and time derivatives separately (against discretization of space and time derivatives in an integrated way). To be more precise, firstly, the displacement-based finite element method (FEM) is used to only discretize the space while the time derivatives are left untouched. This semi-discretization transforms the continuous PDEs into a set of coupled ordinary differential equations (ODEs) with a finite number of DOFs which can then be integrated using any standard ODE integration technique. The so obtained set of ODEs can also be used for modal vibration analysis (*i.e.* determination of natural frequencies and the corresponding mode shapes).

It is worthwhile to mention that the FEM is a well-developed and well-accepted numerical method. It is also versatile and easy to use for our problem as it uses the (well-established) shape functions instead of trivial functions (which are usually tricky to find). In this approach, the FEM matrices and formulation should be developed based on the problem (or PDEs) being analyzed, and in the present work the displacement-based FEM

discretization is founded on the dimensionless forms of the potential and kinetic energy and virtual work expressions (*i.e.* the dimensionless variational formulation or weak form is used). In such a form, unlike the essential (or kinematic or geometric) BCs which should be stated separately, the natural (or kinetic) BCs are implicitly contained in the functional expression and are naturally satisfied in the limit when the number of elements increases. Here, recall that the dimensionless gyrobeam dynamic PDEs are derived from a C^0 variational problem [63] whose functional, created based on the dimensionless potential and kinetic energy and virtual work expressions, contains at most first-order spatial derivatives of the state variables. In such a problem, the orders of spatial derivatives in EBCs and NBCs are zero and one, respectively, and the governing PDEs contain the spatial derivatives of the state variables up to the second order.

In light of the above-mentioned problem characteristics, a dimensionless isoparametric four-node element with (linear independent) cubic Lagrange polynomial basis functions and C^0 continuity is selected to generate the consistent displacement-based finite element matrices. The idea of expanding the element coordinates and element (generalized) displacements using the same shape functions is the basis of an isoparametric element, and the C^0 continuity means that the element displacement fields have continuous spatial derivatives inside the element and are continuous across element boundaries (between adjacent elements). The consistency of the finite element matrices is equivalent to employing the same basis (or interpolation) functions, which are integrated exactly, for evaluation of all the element matrices, *e.g.* mass, stiffness, and generalized force. These conditions fulfill the completeness and compatibility requirements of the FEM (monotonic) convergence [63,64].

The conceptual (and not literal) and schematic pictures of the selected element as a part of a gyrobeam (shown in Figure 4.1) are depicted in Figure 4.3. Note that in this figure the three discrete gyros are symbolic (as are the discrete gyros in Figure 4.1) and represent the continuous gyricity distribution over the element. In this text, the gyricity distribution (and therefore the gyricity-related parameters) is (are) assumed to be constant over the length of every element.

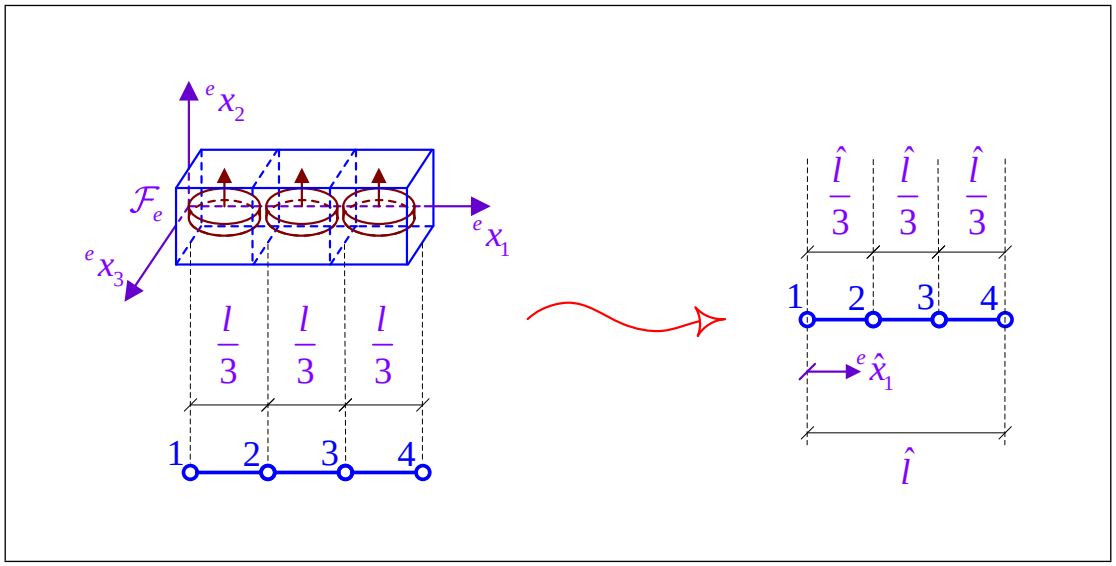

Figure 4.3: Dimensional and dimensionless forms of the gyrobeam four-node element.

The selected dimensionless four-node element has four basis shape functions as:

$$\begin{aligned}
\hat{H}^{\langle 1 \rangle}({}^e\hat{x}_1) &= -\frac{9}{2\hat{l}^3}\left({}^e\hat{x}_1 - \frac{\hat{l}}{3}\right)\left({}^e\hat{x}_1 - \frac{2\hat{l}}{3}\right)\left({}^e\hat{x}_1 - \hat{l}\right) \\
\hat{H}^{\langle 2 \rangle}({}^e\hat{x}_1) &= +\frac{27}{2\hat{l}^3}\,{}^e\hat{x}_1\left({}^e\hat{x}_1 - \frac{2\hat{l}}{3}\right)\left({}^e\hat{x}_1 - \hat{l}\right) \\
\hat{H}^{\langle 3 \rangle}({}^e\hat{x}_1) &= -\frac{27}{2\hat{l}^3}\,{}^e\hat{x}_1\left({}^e\hat{x}_1 - \frac{\hat{l}}{3}\right)\left({}^e\hat{x}_1 - \hat{l}\right) \\
\hat{H}^{\langle 4 \rangle}({}^e\hat{x}_1) &= +\frac{9}{2\hat{l}^3}\,{}^e\hat{x}_1\left({}^e\hat{x}_1 - \frac{\hat{l}}{3}\right)\left({}^e\hat{x}_1 - \frac{2\hat{l}}{3}\right)
\end{aligned} \tag{4.102}$$

where $\hat{l}$ and ${}^e\hat{x}_1$ are the dimensionless forms of the element's length l and local frame coordinate ${}^e x_1$ defined as:

$$\begin{aligned}
\hat{l} &= \frac{l}{L} \\
{}^e\hat{x}_1 &= \frac{{}^e x_1}{L}, \qquad 0 \le {}^e\hat{x}_1 \le \hat{l}
\end{aligned} \tag{4.103}$$

It is noteworthy that whereas the summation of the dimensional element lengths is L,

the summation of the dimensionless element lengths equals $\hat{L}$ or simply 1. Additionally, from now on the adjectives "dimensionless" and "dimension-reduced" will be dropped for brevity and the circumflex (*i.e.* the over-hat) denotes if a parameter is dimensionless or dimension-reduced.

As the element is isoparametric, the element basis shape functions given by Eq. (4.102) are used to interpolate the coordinates as well as the generalized coordinates (*i.e.* translational and rotational displacements) within the element. Denoting the nodal coordinates by ${}^{o}\hat{x}_i^{\langle \mathrm{j} \rangle}$ and ${}^{c}\hat{x}_i^{\langle \mathrm{j} \rangle}$ and the nodal generalized coordinates by $\hat{q}_i^{\langle \mathrm{j} \rangle}$, one can expand the within-element coordinates ${}^{o}\hat{x}_i$ and ${}^{c}\hat{x}_i$ and generalized coordinates $\hat{q}_i$ as:

$$\begin{aligned} {}^{o}\hat{x}_i &= \hat{H}^{\langle 1 \rangle}\, {}^{o}\hat{x}_i^{\langle 1 \rangle} + \hat{H}^{\langle 2 \rangle}\, {}^{o}\hat{x}_i^{\langle 2 \rangle} + \hat{H}^{\langle 3 \rangle}\, {}^{o}\hat{x}_i^{\langle 3 \rangle} + \hat{H}^{\langle 4 \rangle}\, {}^{o}\hat{x}_i^{\langle 4 \rangle} \\ {}^{c}\hat{x}_i &= \hat{H}^{\langle 1 \rangle}\, {}^{c}\hat{x}_i^{\langle 1 \rangle} + \hat{H}^{\langle 2 \rangle}\, {}^{c}\hat{x}_i^{\langle 2 \rangle} + \hat{H}^{\langle 3 \rangle}\, {}^{c}\hat{x}_i^{\langle 3 \rangle} + \hat{H}^{\langle 4 \rangle}\, {}^{c}\hat{x}_i^{\langle 4 \rangle} \\ \hat{q}_i &= \hat{H}^{\langle 1 \rangle}\, \hat{q}_i^{\langle 1 \rangle} + \hat{H}^{\langle 2 \rangle}\, \hat{q}_i^{\langle 2 \rangle} + \hat{H}^{\langle 3 \rangle}\, \hat{q}_i^{\langle 3 \rangle} + \hat{H}^{\langle 4 \rangle}\, \hat{q}_i^{\langle 4 \rangle} \end{aligned} \tag{4.104}$$

Also noting that:

$$\frac{d}{d\hat{x}_i} = \frac{{}^{c}d}{d\hat{x}_i} = \frac{{}^{e}d}{d\hat{x}_i} \tag{4.105}$$

the first spatial derivative of $\hat{q}_i$ along ${}^{o}\hat{x}_1$ can be expanded as:

$$\hat{q}_{i,\hat{1}} = \hat{H}'^{\langle 1 \rangle}\, {}^{o}\hat{x}_i^{\langle 1 \rangle} + \hat{H}'^{\langle 2 \rangle}\, {}^{o}\hat{x}_i^{\langle 2 \rangle} + \hat{H}'^{\langle 3 \rangle}\, {}^{o}\hat{x}_i^{\langle 3 \rangle} + \hat{H}'^{\langle 4 \rangle}\, {}^{o}\hat{x}_i^{\langle 4 \rangle} \tag{4.106}$$

where:

$$\hat{H}'^{\langle \mathrm{j} \rangle} = \hat{H}'^{\langle \mathrm{j} \rangle}({}^{e}\hat{x}_1) = \frac{{}^{e}d}{d\hat{x}_i}\left(\hat{H}^{\langle \mathrm{j} \rangle}({}^{e}\hat{x}_1)\right) = \frac{{}^{e}d\hat{H}^{\langle \mathrm{j} \rangle}}{d\hat{x}_i} \tag{4.107}$$

Regarding the nodal generalized coordinates, recall that every point of a micropolar gyrobeam has nine DOFs and there are six DOFs corresponding to every point of a classical gyrobeam. These DOFs are summarized in the matrix of generalized coordinates $\underset{\sim}{\hat{\boldsymbol{q}}}$ which for micropolar and classical gyrobeams is respectively given by Eqs. (4.92) and (4.96). Accordingly, the nodal generalized coordinates, being the generalized coordinates corresponding to a specific node j (*i.e.* a point), are also combined in a matrix denoted by $\underset{\sim}{\hat{\boldsymbol{q}}}^{\langle \mathrm{j} \rangle}$. This matrix has respectively nine and six elements for micropolar and classical

gyrobeams:

$$\begin{aligned}
\underset{\sim}{\hat{\boldsymbol{q}}}^{\langle \mathrm{j} \rangle} &= \left[\hat{q}_i^{\langle \mathrm{j} \rangle}\right] = \left[\begin{array}{cccccccccc} \hat{\bar{u}}_1^{\langle \mathrm{j} \rangle} & \hat{\bar{u}}_2^{\langle \mathrm{j} \rangle} & \hat{\bar{u}}_3^{\langle \mathrm{j} \rangle} & \bar{\theta}_1^{\langle \mathrm{j} \rangle} & \bar{\theta}_2^{\langle \mathrm{j} \rangle} & \bar{\theta}_3^{\langle \mathrm{j} \rangle} & \bar{\vartheta}_1^{\langle \mathrm{j} \rangle} & \bar{\vartheta}_2^{\langle \mathrm{j} \rangle} & \bar{\vartheta}_3^{\langle \mathrm{j} \rangle} \end{array}\right]^{\mathrm{T}} \\
\underset{\sim}{\hat{\boldsymbol{q}}}^{\langle \mathrm{j} \rangle} &= \left[\hat{q}_i^{\langle \mathrm{j} \rangle}\right] = \left[\begin{array}{cccccccccc} \hat{\bar{u}}_1^{\langle \mathrm{j} \rangle} & \hat{\bar{u}}_2^{\langle \mathrm{j} \rangle} & \hat{\bar{u}}_3^{\langle \mathrm{j} \rangle} & \bar{\theta}_1^{\langle \mathrm{j} \rangle} & \bar{\theta}_2^{\langle \mathrm{j} \rangle} & \bar{\theta}_3^{\langle \mathrm{j} \rangle} \end{array}\right]^{\mathrm{T}}
\end{aligned} \tag{4.108}$$

Now, one can define the matrix of the element(al) generalized displacements or the matrix of the element(al) generalized coordinates as:

$$\underset{\sim}{\hat{\boldsymbol{q}}}^{\langle \mathrm{e} \rangle} = \left[\underset{\sim}{\hat{\boldsymbol{q}}}^{\langle \mathrm{j} \rangle}\right] = \left[\begin{array}{cccc} \underset{\sim}{\hat{\boldsymbol{q}}}^{\langle 1 \rangle\,\mathrm{T}} & \underset{\sim}{\hat{\boldsymbol{q}}}^{\langle 2 \rangle\,\mathrm{T}} & \underset{\sim}{\hat{\boldsymbol{q}}}^{\langle 3 \rangle\,\mathrm{T}} & \underset{\sim}{\hat{\boldsymbol{q}}}^{\langle 4 \rangle\,\mathrm{T}} \end{array}\right]^{\mathrm{T}} \tag{4.109}$$

with 36 and 24 entries for micropolar and classical gyrobeams, respectively.

The element generalized coordinate matrix $\underset{\sim}{\hat{\boldsymbol{q}}}^{\langle \mathrm{e} \rangle}$ can be used to rewrite the expansion of a generalized coordinate $\hat{q}_i$ in Eq. (4.104) as:

$$\hat{q}_i = \underset{\sim}{\hat{\boldsymbol{H}}}_{\hat{q}_i}\, \underset{\sim}{\hat{\boldsymbol{q}}}^{\langle \mathrm{e} \rangle} \tag{4.110}$$

where $\underset{\sim}{\hat{\boldsymbol{H}}}_{\hat{q}_i}$ is the shape function matrix corresponding to the generalized coordinate $\hat{q}_i$. Denoting the $N_1 \times N_2$ zero matrix as $\underset{\sim}{\mathbf{0}}_{N_1 \times N_2}$, the shape function matrices of the micropolar gyrobeam DOFs, being of dimensions 1×36 and 3×36, can be given as:

$$\begin{aligned}
\underset{\sim}{\hat{\boldsymbol{H}}}_{\hat{\bar{u}}_1} &= \left[\begin{array}{cccccccc} \hat{H}^{\langle 1 \rangle} & \underset{\sim}{\mathbf{0}}_{1\times 8} & \hat{H}^{\langle 2 \rangle} & \underset{\sim}{\mathbf{0}}_{1\times 8} & \hat{H}^{\langle 3 \rangle} & \underset{\sim}{\mathbf{0}}_{1\times 8} & \hat{H}^{\langle 4 \rangle} & \underset{\sim}{\mathbf{0}}_{1\times 8} \end{array}\right] \\
\underset{\sim}{\hat{\boldsymbol{H}}}_{\hat{\bar{u}}_2} &= \left[\begin{array}{cccccccc} \underset{\sim}{\mathbf{0}}_{1\times 1} & \hat{H}^{\langle 1 \rangle} & \underset{\sim}{\mathbf{0}}_{1\times 8} & \hat{H}^{\langle 2 \rangle} & \underset{\sim}{\mathbf{0}}_{1\times 8} & \hat{H}^{\langle 3 \rangle} & \underset{\sim}{\mathbf{0}}_{1\times 8} & \hat{H}^{\langle 4 \rangle} \quad \underset{\sim}{\mathbf{0}}_{1\times 7} \end{array}\right] \\
\underset{\sim}{\hat{\boldsymbol{H}}}_{\hat{\bar{u}}_3} &= \left[\begin{array}{cccccccc} \underset{\sim}{\mathbf{0}}_{1\times 2} & \hat{H}^{\langle 1 \rangle} & \underset{\sim}{\mathbf{0}}_{1\times 8} & \hat{H}^{\langle 2 \rangle} & \underset{\sim}{\mathbf{0}}_{1\times 8} & \hat{H}^{\langle 3 \rangle} & \underset{\sim}{\mathbf{0}}_{1\times 8} & \hat{H}^{\langle 4 \rangle} \quad \underset{\sim}{\mathbf{0}}_{1\times 6} \end{array}\right] \\
\underset{\sim}{\hat{\boldsymbol{H}}}_{\bar{\theta}_1} &= \left[\begin{array}{cccccccc} \underset{\sim}{\mathbf{0}}_{1\times 3} & \hat{H}^{\langle 1 \rangle} & \underset{\sim}{\mathbf{0}}_{1\times 8} & \hat{H}^{\langle 2 \rangle} & \underset{\sim}{\mathbf{0}}_{1\times 8} & \hat{H}^{\langle 3 \rangle} & \underset{\sim}{\mathbf{0}}_{1\times 8} & \hat{H}^{\langle 4 \rangle} \quad \underset{\sim}{\mathbf{0}}_{1\times 5} \end{array}\right] \\
\underset{\sim}{\hat{\boldsymbol{H}}}_{\bar{\theta}_2} &= \left[\begin{array}{cccccccc} \underset{\sim}{\mathbf{0}}_{1\times 4} & \hat{H}^{\langle 1 \rangle} & \underset{\sim}{\mathbf{0}}_{1\times 8} & \hat{H}^{\langle 2 \rangle} & \underset{\sim}{\mathbf{0}}_{1\times 8} & \hat{H}^{\langle 3 \rangle} & \underset{\sim}{\mathbf{0}}_{1\times 8} & \hat{H}^{\langle 4 \rangle} \quad \underset{\sim}{\mathbf{0}}_{1\times 4} \end{array}\right] \\
\underset{\sim}{\hat{\boldsymbol{H}}}_{\bar{\theta}_3} &= \left[\begin{array}{cccccccc} \underset{\sim}{\mathbf{0}}_{1\times 5} & \hat{H}^{\langle 1 \rangle} & \underset{\sim}{\mathbf{0}}_{1\times 8} & \hat{H}^{\langle 2 \rangle} & \underset{\sim}{\mathbf{0}}_{1\times 8} & \hat{H}^{\langle 3 \rangle} & \underset{\sim}{\mathbf{0}}_{1\times 8} & \hat{H}^{\langle 4 \rangle} \quad \underset{\sim}{\mathbf{0}}_{1\times 3} \end{array}\right] \\
\underset{\sim}{\hat{\boldsymbol{H}}}_{\bar{\vartheta}_1} &= \left[\begin{array}{cccccccc} \underset{\sim}{\mathbf{0}}_{1\times 6} & \hat{H}^{\langle 1 \rangle} & \underset{\sim}{\mathbf{0}}_{1\times 8} & \hat{H}^{\langle 2 \rangle} & \underset{\sim}{\mathbf{0}}_{1\times 8} & \hat{H}^{\langle 3 \rangle} & \underset{\sim}{\mathbf{0}}_{1\times 8} & \hat{H}^{\langle 4 \rangle} \quad \underset{\sim}{\mathbf{0}}_{1\times 2} \end{array}\right] \\
\underset{\sim}{\hat{\boldsymbol{H}}}_{\bar{\vartheta}_2} &= \left[\begin{array}{cccccccc} \underset{\sim}{\mathbf{0}}_{1\times 7} & \hat{H}^{\langle 1 \rangle} & \underset{\sim}{\mathbf{0}}_{1\times 8} & \hat{H}^{\langle 2 \rangle} & \underset{\sim}{\mathbf{0}}_{1\times 8} & \hat{H}^{\langle 3 \rangle} & \underset{\sim}{\mathbf{0}}_{1\times 8} & \hat{H}^{\langle 4 \rangle} \quad \underset{\sim}{\mathbf{0}}_{1\times 1} \end{array}\right] \\
\underset{\sim}{\hat{\boldsymbol{H}}}_{\bar{\vartheta}_3} &= \left[\begin{array}{cccccccc} \underset{\sim}{\mathbf{0}}_{1\times 8} & \hat{H}^{\langle 1 \rangle} & \underset{\sim}{\mathbf{0}}_{1\times 8} & \hat{H}^{\langle 2 \rangle} & \underset{\sim}{\mathbf{0}}_{1\times 8} & \hat{H}^{\langle 3 \rangle} & \underset{\sim}{\mathbf{0}}_{1\times 8} & \hat{H}^{\langle 4 \rangle} \end{array}\right] \\
\underset{\sim}{\hat{\boldsymbol{H}}}_{\bar{\boldsymbol{\vartheta}}} &= \left[\begin{array}{cccccccc} \underset{\sim}{\mathbf{0}}_{3\times 6} & \left(\hat{H}^{\langle 1 \rangle}\, \underset{\equiv}{\mathbb{1}}\right) & \underset{\sim}{\mathbf{0}}_{3\times 6} & \left(\hat{H}^{\langle 2 \rangle}\, \underset{\equiv}{\mathbb{1}}\right) & \underset{\sim}{\mathbf{0}}_{3\times 6} & \left(\hat{H}^{\langle 3 \rangle}\, \underset{\equiv}{\mathbb{1}}\right) & \underset{\sim}{\mathbf{0}}_{3\times 6} & \left(\hat{H}^{\langle 4 \rangle}\, \underset{\equiv}{\mathbb{1}}\right) \end{array}\right]
\end{aligned} \tag{4.111}$$

and for the classical gyrobeam DOFs, the 1×24 and 3×24 shape function matrices are:

$$
\begin{aligned}
\hat{\underset{\sim}{\boldsymbol{H}}}_{\hat{\bar{u}}_1} &= \begin{bmatrix} \hat{H}^{\langle 1 \rangle} & \underset{\sim}{\mathbf{0}}_{1\times 5} & \hat{H}^{\langle 2 \rangle} & \underset{\sim}{\mathbf{0}}_{1\times 5} & \hat{H}^{\langle 3 \rangle} & \underset{\sim}{\mathbf{0}}_{1\times 5} & \hat{H}^{\langle 4 \rangle} & \underset{\sim}{\mathbf{0}}_{1\times 5} \end{bmatrix} \\
\hat{\underset{\sim}{\boldsymbol{H}}}_{\hat{\bar{u}}_2} &= \begin{bmatrix} \underset{\sim}{\mathbf{0}}_{1\times 1} & \hat{H}^{\langle 1 \rangle} & \underset{\sim}{\mathbf{0}}_{1\times 5} & \hat{H}^{\langle 2 \rangle} & \underset{\sim}{\mathbf{0}}_{1\times 5} & \hat{H}^{\langle 3 \rangle} & \underset{\sim}{\mathbf{0}}_{1\times 5} & \hat{H}^{\langle 4 \rangle} & \underset{\sim}{\mathbf{0}}_{1\times 4} \end{bmatrix} \\
\hat{\underset{\sim}{\boldsymbol{H}}}_{\hat{\bar{u}}_3} &= \begin{bmatrix} \underset{\sim}{\mathbf{0}}_{1\times 2} & \hat{H}^{\langle 1 \rangle} & \underset{\sim}{\mathbf{0}}_{1\times 5} & \hat{H}^{\langle 2 \rangle} & \underset{\sim}{\mathbf{0}}_{1\times 5} & \hat{H}^{\langle 3 \rangle} & \underset{\sim}{\mathbf{0}}_{1\times 5} & \hat{H}^{\langle 4 \rangle} & \underset{\sim}{\mathbf{0}}_{1\times 3} \end{bmatrix} \\
\hat{\underset{\sim}{\boldsymbol{H}}}_{\bar{\theta}_1} &= \begin{bmatrix} \underset{\sim}{\mathbf{0}}_{1\times 3} & \hat{H}^{\langle 1 \rangle} & \underset{\sim}{\mathbf{0}}_{1\times 5} & \hat{H}^{\langle 2 \rangle} & \underset{\sim}{\mathbf{0}}_{1\times 5} & \hat{H}^{\langle 3 \rangle} & \underset{\sim}{\mathbf{0}}_{1\times 5} & \hat{H}^{\langle 4 \rangle} & \underset{\sim}{\mathbf{0}}_{1\times 2} \end{bmatrix} \\
\hat{\underset{\sim}{\boldsymbol{H}}}_{\bar{\theta}_2} &= \begin{bmatrix} \underset{\sim}{\mathbf{0}}_{1\times 4} & \hat{H}^{\langle 1 \rangle} & \underset{\sim}{\mathbf{0}}_{1\times 5} & \hat{H}^{\langle 2 \rangle} & \underset{\sim}{\mathbf{0}}_{1\times 5} & \hat{H}^{\langle 3 \rangle} & \underset{\sim}{\mathbf{0}}_{1\times 5} & \hat{H}^{\langle 4 \rangle} & \underset{\sim}{\mathbf{0}}_{1\times 1} \end{bmatrix} \\
\hat{\underset{\sim}{\boldsymbol{H}}}_{\bar{\theta}_3} &= \begin{bmatrix} \underset{\sim}{\mathbf{0}}_{1\times 5} & \hat{H}^{\langle 1 \rangle} & \underset{\sim}{\mathbf{0}}_{1\times 5} & \hat{H}^{\langle 2 \rangle} & \underset{\sim}{\mathbf{0}}_{1\times 5} & \hat{H}^{\langle 3 \rangle} & \underset{\sim}{\mathbf{0}}_{1\times 5} & \hat{H}^{\langle 4 \rangle} \end{bmatrix} \\
\hat{\underset{\sim}{\boldsymbol{H}}}_{\bar{\boldsymbol{\theta}}} &= \begin{bmatrix} \underset{\sim}{\mathbf{0}}_{3\times 3} & \left(\hat{H}^{\langle 1 \rangle}\, \underset{\equiv}{\mathbb{1}}\right) & \underset{\sim}{\mathbf{0}}_{3\times 3} & \left(\hat{H}^{\langle 2 \rangle}\, \underset{\equiv}{\mathbb{1}}\right) & \underset{\sim}{\mathbf{0}}_{3\times 3} & \left(\hat{H}^{\langle 3 \rangle}\, \underset{\equiv}{\mathbb{1}}\right) & \underset{\sim}{\mathbf{0}}_{3\times 3} & \left(\hat{H}^{\langle 4 \rangle}\, \underset{\equiv}{\mathbb{1}}\right) \end{bmatrix}
\end{aligned}
\tag{4.112}
$$

These matrices are employed to derive the finite element matrices of the selected four-node element from the potential and kinetic energy and virtual work expressions.

By using the expansions of the form given by Eq. (4.110) and the shape function matrices given by Eq. (4.111), and taking into account the essential first-order approximation with respect to $\underset{\rightarrow}{\bar{\vartheta}}$, the expressions for the potential and kinetic energy variations and the virtual work of a micropolar gyrobeam element can be obtained as:

$$
\Delta\hat{\mathcal{U}}^{\langle \mathrm{e} \rangle} = \delta\hat{\underset{\sim}{\boldsymbol{q}}}^{\langle \mathrm{e} \rangle\,\mathrm{T}}\, \hat{\underset{\sim}{\boldsymbol{\mathcal{K}}}}^{\langle \mathrm{e} \rangle}\, \hat{\underset{\sim}{\boldsymbol{q}}}^{\langle \mathrm{e} \rangle}
\tag{4.113}
$$

$$
\begin{aligned}
\Delta\hat{\mathcal{T}}^{\langle \mathrm{e} \rangle} &= \delta\mathring{\hat{\underset{\sim}{\boldsymbol{q}}}}^{\langle \mathrm{e} \rangle\,\mathrm{T}}\, \hat{\underset{\sim}{\boldsymbol{\mathcal{M}}}}^{\langle \mathrm{e} \rangle}\, \mathring{\hat{\underset{\sim}{\boldsymbol{q}}}}^{\langle \mathrm{e} \rangle} + \delta\mathring{\hat{\underset{\sim}{\boldsymbol{q}}}}^{\langle \mathrm{e} \rangle\,\mathrm{T}} \int_{\hat{l}} \hat{\underset{\sim}{\boldsymbol{H}}}_{\underset{\rightarrow}{\bar{\vartheta}}}^{\mathrm{T}}\, \hat{\underset{\equiv}{\boldsymbol{j}}}^{V} \left(\mathring{\underset{\rightarrow}{\phi}} + \mathring{\underset{\rightarrow}{\psi}}\right) d\hat{l} \\
&= -\delta\hat{\underset{\sim}{\boldsymbol{q}}}^{\langle \mathrm{e} \rangle\,\mathrm{T}} \frac{d}{d\hat{t}}\left(\hat{\underset{\sim}{\boldsymbol{\mathcal{M}}}}^{\langle \mathrm{e} \rangle}\, \mathring{\hat{\underset{\sim}{\boldsymbol{q}}}}^{\langle \mathrm{e} \rangle}\right) - \delta\hat{\underset{\sim}{\boldsymbol{q}}}^{\langle \mathrm{e} \rangle\,\mathrm{T}} \frac{d}{d\hat{t}}\left(\int_{\hat{l}} \hat{\underset{\sim}{\boldsymbol{H}}}_{\underset{\rightarrow}{\bar{\vartheta}}}^{\mathrm{T}}\, \hat{\underset{\equiv}{\boldsymbol{j}}}^{V} \left(\mathring{\underset{\rightarrow}{\phi}} + \mathring{\underset{\rightarrow}{\psi}}\right) d\hat{l}\right) \\
&= -\delta\hat{\underset{\sim}{\boldsymbol{q}}}^{\langle \mathrm{e} \rangle\,\mathrm{T}}\, \hat{\underset{\sim}{\boldsymbol{\mathcal{M}}}}^{\langle \mathrm{e} \rangle}\, \mathring{\mathring{\hat{\underset{\sim}{\boldsymbol{q}}}}}^{\langle \mathrm{e} \rangle} - \delta\hat{\underset{\sim}{\boldsymbol{q}}}^{\langle \mathrm{e} \rangle\,\mathrm{T}}\, \hat{\underset{\sim}{\boldsymbol{\mathcal{G}}}}^{\langle \mathrm{e} \rangle}\, \mathring{\hat{\underset{\sim}{\boldsymbol{q}}}}^{\langle \mathrm{e} \rangle} - \delta\hat{\underset{\sim}{\boldsymbol{q}}}^{\langle \mathrm{e} \rangle\,\mathrm{T}}\, \hat{\underset{\sim}{\boldsymbol{\mathcal{C}}}}^{\langle \mathrm{e} \rangle}\, \hat{\underset{\sim}{\boldsymbol{q}}}^{\langle \mathrm{e} \rangle} - \delta\hat{\underset{\sim}{\boldsymbol{q}}}^{\langle \mathrm{e} \rangle\,\mathrm{T}}\, \hat{\underset{\sim}{\boldsymbol{\mathcal{R}}}}^{\langle \mathrm{e} \rangle}
\end{aligned}
\tag{4.114}
$$

$$
\delta\hat{\mathcal{W}}^{\langle \mathrm{e} \rangle} = \delta\hat{\underset{\sim}{\boldsymbol{q}}}^{\langle \mathrm{e} \rangle\,\mathrm{T}}\, \hat{\underset{\sim}{\boldsymbol{\mathcal{Q}}}}^{\langle \mathrm{e} \rangle}
\tag{4.115}
$$

where:

$$
\begin{aligned}
\hat{\underset{\sim}{\boldsymbol{\mathcal{K}}}}^{\langle \mathrm{e} \rangle} = & \int_{\hat{l}} \hat{\underset{\sim}{\boldsymbol{H}}}'_{\hat{\bar{u}}_1}{}^{\mathrm{T}} \hat{\underset{\sim}{\boldsymbol{H}}}'_{\hat{\bar{u}}_1} \, d\hat{l} + \hat{I}_2 \int_{\hat{l}} \hat{\underset{\sim}{\boldsymbol{H}}}'_{\bar{\theta}_2}{}^{\mathrm{T}} \hat{\underset{\sim}{\boldsymbol{H}}}'_{\bar{\theta}_2} \, d\hat{l} + \hat{I}_3 \int_{\hat{l}} \hat{\underset{\sim}{\boldsymbol{H}}}'_{\bar{\theta}_3}{}^{\mathrm{T}} \hat{\underset{\sim}{\boldsymbol{H}}}'_{\bar{\theta}_3} \, d\hat{l} \\
& + k_{\mathrm{s}_2} \, \hat{\mu} \int_{\hat{l}} \left(\hat{\underset{\sim}{\boldsymbol{H}}}'_{\hat{\bar{u}}_2} - \hat{\underset{\sim}{\boldsymbol{H}}}_{\bar{\theta}_3} \right)^{\mathrm{T}} \left(\hat{\underset{\sim}{\boldsymbol{H}}}'_{\hat{\bar{u}}_2} - \hat{\underset{\sim}{\boldsymbol{H}}}_{\bar{\theta}_3} \right) d\hat{l} \\
& + k_{\mathrm{s}_3} \, \hat{\mu} \int_{\hat{l}} \left(\hat{\underset{\sim}{\boldsymbol{H}}}'_{\hat{\bar{u}}_3} + \hat{\underset{\sim}{\boldsymbol{H}}}_{\bar{\theta}_2} \right)^{\mathrm{T}} \left(\hat{\underset{\sim}{\boldsymbol{H}}}'_{\hat{\bar{u}}_3} + \hat{\underset{\sim}{\boldsymbol{H}}}_{\bar{\theta}_2} \right) d\hat{l} + k_{\mathrm{t}} \, \hat{\mu} \, \hat{I}_1 \int_{\hat{l}} \hat{\underset{\sim}{\boldsymbol{H}}}'_{\bar{\theta}_1}{}^{\mathrm{T}} \hat{\underset{\sim}{\boldsymbol{H}}}'_{\bar{\theta}_1} \, d\hat{l} \\
& + \hat{\kappa} \int_{\hat{l}} \left(\hat{\underset{\sim}{\boldsymbol{H}}}'_{\hat{\bar{u}}_2} + \hat{\underset{\sim}{\boldsymbol{H}}}_{\bar{\theta}_3} - 2 \, \hat{\underset{\sim}{\boldsymbol{H}}}_{\bar{\vartheta}_3} \right)^{\mathrm{T}} \left(\hat{\underset{\sim}{\boldsymbol{H}}}'_{\hat{\bar{u}}_2} + \hat{\underset{\sim}{\boldsymbol{H}}}_{\bar{\theta}_3} - 2 \, \hat{\underset{\sim}{\boldsymbol{H}}}_{\bar{\vartheta}_3} \right) d\hat{l} \\
& + \hat{\kappa} \int_{\hat{l}} \left(\hat{\underset{\sim}{\boldsymbol{H}}}'_{\hat{\bar{u}}_3} - \hat{\underset{\sim}{\boldsymbol{H}}}_{\bar{\theta}_2} + 2 \, \hat{\underset{\sim}{\boldsymbol{H}}}_{\bar{\vartheta}_2} \right)^{\mathrm{T}} \left(\hat{\underset{\sim}{\boldsymbol{H}}}'_{\hat{\bar{u}}_3} - \hat{\underset{\sim}{\boldsymbol{H}}}_{\bar{\theta}_2} + 2 \, \hat{\underset{\sim}{\boldsymbol{H}}}_{\bar{\vartheta}_2} \right) d\hat{l} \\
& + \hat{\kappa} \, \hat{I}_1 \int_{\hat{l}} \left(\hat{\underset{\sim}{\boldsymbol{H}}}'_{\bar{\theta}_1} - 2 \, \xi \, \hat{\underset{\sim}{\boldsymbol{H}}}'_{\bar{\vartheta}_1} \right)^{\mathrm{T}} \left(\hat{\underset{\sim}{\boldsymbol{H}}}'_{\bar{\theta}_1} - 2 \, \xi \, \hat{\underset{\sim}{\boldsymbol{H}}}'_{\bar{\vartheta}_1} \right) d\hat{l} \\
& + 4 \, \hat{\kappa} \int_{\hat{l}} \left(\hat{\underset{\sim}{\boldsymbol{H}}}_{\bar{\theta}_1} - \hat{\underset{\sim}{\boldsymbol{H}}}_{\bar{\vartheta}_1} \right)^{\mathrm{T}} \left(\hat{\underset{\sim}{\boldsymbol{H}}}_{\bar{\theta}_1} - \hat{\underset{\sim}{\boldsymbol{H}}}_{\bar{\vartheta}_1} \right) d\hat{l} \\
& + \hat{\mathcal{E}} \int_{\hat{l}} \hat{\underset{\sim}{\boldsymbol{H}}}'_{\bar{\vartheta}_1}{}^{\mathrm{T}} \hat{\underset{\sim}{\boldsymbol{H}}}'_{\bar{\vartheta}_1} \, d\hat{l} + \left(\hat{\gamma} + \hat{\beta} \right) \int_{\hat{l}} \left(\hat{\underset{\sim}{\boldsymbol{H}}}'_{\bar{\vartheta}_2}{}^{\mathrm{T}} \hat{\underset{\sim}{\boldsymbol{H}}}'_{\bar{\vartheta}_2} + \hat{\underset{\sim}{\boldsymbol{H}}}'_{\bar{\vartheta}_3}{}^{\mathrm{T}} \hat{\underset{\sim}{\boldsymbol{H}}}'_{\bar{\vartheta}_3} \right) d\hat{l}
\end{aligned}
\tag{4.116}
$$

$$
\begin{aligned}
\hat{\underset{\sim}{\boldsymbol{\mathcal{M}}}}^{\langle \mathrm{e} \rangle} = & \left(1 + \hat{\varrho}^{V} \right) \int_{\hat{l}} \left(\hat{\underset{\sim}{\boldsymbol{H}}}^{\mathrm{T}}_{\hat{\bar{u}}_1} \hat{\underset{\sim}{\boldsymbol{H}}}_{\hat{\bar{u}}_1} + \hat{\underset{\sim}{\boldsymbol{H}}}^{\mathrm{T}}_{\hat{\bar{u}}_2} \hat{\underset{\sim}{\boldsymbol{H}}}_{\hat{\bar{u}}_2} + \hat{\underset{\sim}{\boldsymbol{H}}}^{\mathrm{T}}_{\hat{\bar{u}}_3} \hat{\underset{\sim}{\boldsymbol{H}}}_{\hat{\bar{u}}_3} \right) d\hat{l} \\
& + \left(1 + \hat{\varrho}^{V} \right) \int_{\hat{l}} \left(\hat{I}_1 \, \hat{\underset{\sim}{\boldsymbol{H}}}^{\mathrm{T}}_{\bar{\theta}_1} \hat{\underset{\sim}{\boldsymbol{H}}}_{\bar{\theta}_1} + \hat{I}_2 \, \hat{\underset{\sim}{\boldsymbol{H}}}^{\mathrm{T}}_{\bar{\theta}_2} \hat{\underset{\sim}{\boldsymbol{H}}}_{\bar{\theta}_2} + \hat{I}_3 \, \hat{\underset{\sim}{\boldsymbol{H}}}^{\mathrm{T}}_{\bar{\theta}_3} \hat{\underset{\sim}{\boldsymbol{H}}}_{\bar{\theta}_3} \right) d\hat{l} \\
& + \int_{\hat{l}} \hat{\underset{\sim}{\boldsymbol{H}}}^{\mathrm{T}}_{\bar{\vartheta}} \left({}^{b}\hat{\underline{\underline{\boldsymbol{i}}}}^{V} + {}^{b}\hat{\underline{\underline{\boldsymbol{j}}}}^{V} \right) \hat{\underset{\sim}{\boldsymbol{H}}}_{\bar{\vartheta}} \, d\hat{l}
\end{aligned}
\tag{4.117}
$$

$$\hat{\underset{\sim}{\mathcal{G}}}^{\langle \mathrm{e} \rangle} = \int_{\hat{l}} \hat{\underset{\sim}{\boldsymbol{H}}}_{\underline{\bar{\vartheta}}}^{\mathrm{T}} \left({}^{b}\underset{=}{\mathring{\phi}}^{\times} \, {}^{b}\underset{=}{\hat{\jmath}}^{V} - {}^{b}\underset{=}{\hat{\jmath}}^{V} \, {}^{b}\underset{=}{\mathring{\phi}}^{\times} - \left({}^{b}\underset{=}{\hat{\jmath}}^{V} \left({}^{b}\underset{-}{\mathring{\phi}} + {}^{b}\underset{-}{\mathring{\psi}} \right) \right)^{\times} \right) \hat{\underset{\sim}{\boldsymbol{H}}}_{\underline{\bar{\vartheta}}} \, d\hat{l} \tag{4.118}$$

$$\hat{\underset{\sim}{\mathcal{C}}}^{\langle \mathrm{e} \rangle} = - \int_{\hat{l}} \hat{\underset{\sim}{\boldsymbol{H}}}_{\underline{\bar{\vartheta}}}^{\mathrm{T}} \left({}^{b}\underset{=}{\hat{\jmath}}^{V} \, {}^{b}\underset{-}{\mathring{\mathring{\phi}}} + {}^{b}\underset{=}{\hat{\jmath}}^{V} \, {}^{b}\underset{-}{\mathring{\mathring{\psi}}} + {}^{b}\underset{=}{\mathring{\phi}}^{\times} \, {}^{b}\underset{=}{\hat{\jmath}}^{V} \left({}^{b}\underset{-}{\mathring{\phi}} + {}^{b}\underset{-}{\mathring{\psi}} \right) \right)^{\times} \hat{\underset{\sim}{\boldsymbol{H}}}_{\underline{\bar{\vartheta}}} \, d\hat{l} \tag{4.119}$$

$$\hat{\underset{\sim}{\mathcal{R}}}^{\langle \mathrm{e} \rangle} = \int_{\hat{l}} \hat{\underset{\sim}{\boldsymbol{H}}}_{\underline{\bar{\vartheta}}}^{\mathrm{T}} \left({}^{b}\underset{=}{\hat{\jmath}}^{V} \, {}^{b}\underset{-}{\mathring{\mathring{\phi}}} + {}^{b}\underset{=}{\hat{\jmath}}^{V} \, {}^{b}\underset{-}{\mathring{\mathring{\psi}}} + {}^{b}\underset{=}{\mathring{\phi}}^{\times} \, {}^{b}\underset{=}{\hat{\jmath}}^{V} \left({}^{b}\underset{-}{\mathring{\phi}} + {}^{b}\underset{-}{\mathring{\psi}} \right) \right) d\hat{l} \tag{4.120}$$

$$\hat{\underset{\sim}{\mathcal{Q}}}^{\langle \mathrm{e} \rangle} = \int_{\hat{l}} \left(\hat{\underset{\sim}{\boldsymbol{H}}}_{\bar{u}_i}^{\mathrm{T}} \, \hat{\bar{f}}_i^{V} + \hat{\underset{\sim}{\boldsymbol{H}}}_{\bar{\theta}_i}^{\mathrm{T}} \, \hat{\bar{m}}_i^{L} + \hat{\underset{\sim}{\boldsymbol{H}}}_{\bar{\vartheta}_i}^{\mathrm{T}} \, \hat{\bar{m}}_i^{V} \right) d\hat{l} + \sum_{P} \left(\hat{\underset{\sim}{\boldsymbol{H}}}_{\bar{u}_i}^{\mathrm{T}} \, \hat{\bar{f}}_i^{S} + \hat{\underset{\sim}{\boldsymbol{H}}}_{\bar{\theta}_i}^{\mathrm{T}} \, \hat{\bar{m}}_i^{P} + \hat{\underset{\sim}{\boldsymbol{H}}}_{\bar{\vartheta}_i}^{\mathrm{T}} \, \hat{\bar{m}}_i^{S} \right) \tag{4.121}$$

Analogously, by using the expansions of the form given by Eq. (4.110) and the shape function matrices given by Eq. (4.112), and taking into account the essential first-order approximation with respect to $\underset{\rightarrow}{\bar{\theta}}$, the expressions for the potential and kinetic energy variations and the virtual work of a classical gyrobeam element will be derived as:

$$\Delta \hat{\mathcal{U}}^{\langle \mathrm{e} \rangle} = \delta \hat{\underset{\sim}{\boldsymbol{q}}}^{\langle \mathrm{e} \rangle \, \mathrm{T}} \, \hat{\underset{\sim}{\mathcal{K}}}^{\langle \mathrm{e} \rangle} \, \hat{\underset{\sim}{\boldsymbol{q}}}^{\langle \mathrm{e} \rangle} \tag{4.122}$$

$$\Delta \hat{\mathcal{T}}^{\langle \mathrm{e} \rangle} = - \delta \hat{\underset{\sim}{\boldsymbol{q}}}^{\langle \mathrm{e} \rangle \, \mathrm{T}} \, \hat{\underset{\sim}{\mathcal{M}}}^{\langle \mathrm{e} \rangle} \, \hat{\underset{\sim}{\boldsymbol{q}}}^{\mathring{\mathring{\langle \mathrm{e} \rangle}}} - \delta \hat{\underset{\sim}{\boldsymbol{q}}}^{\langle \mathrm{e} \rangle \, \mathrm{T}} \, \hat{\underset{\sim}{\mathcal{G}}}^{\langle \mathrm{e} \rangle} \, \hat{\underset{\sim}{\boldsymbol{q}}}^{\mathring{\langle \mathrm{e} \rangle}} - \delta \hat{\underset{\sim}{\boldsymbol{q}}}^{\langle \mathrm{e} \rangle \, \mathrm{T}} \, \hat{\underset{\sim}{\mathcal{C}}}^{\langle \mathrm{e} \rangle} \, \hat{\underset{\sim}{\boldsymbol{q}}}^{\langle \mathrm{e} \rangle} - \delta \hat{\underset{\sim}{\boldsymbol{q}}}^{\langle \mathrm{e} \rangle \, \mathrm{T}} \, \hat{\underset{\sim}{\mathcal{R}}}^{\langle \mathrm{e} \rangle} \tag{4.123}$$

$$\delta \hat{\mathcal{W}}^{\langle \mathrm{e} \rangle} = \delta \hat{\underset{\sim}{\boldsymbol{q}}}^{\langle \mathrm{e} \rangle \, \mathrm{T}} \, \hat{\underset{\sim}{\mathcal{Q}}}^{\langle \mathrm{e} \rangle} \tag{4.124}$$

where:

$$\begin{aligned} \hat{\underset{\sim}{\mathcal{K}}}^{\langle \mathrm{e} \rangle} = & \int_{\hat{l}} \hat{\underset{\sim}{\boldsymbol{H}}}'_{\hat{\bar{u}}_1}{}^{\mathrm{T}} \, \hat{\underset{\sim}{\boldsymbol{H}}}'_{\hat{\bar{u}}_1} \, d\hat{l} + \hat{I}_2 \int_{\hat{l}} \hat{\underset{\sim}{\boldsymbol{H}}}'_{\bar{\theta}_2}{}^{\mathrm{T}} \, \hat{\underset{\sim}{\boldsymbol{H}}}'_{\bar{\theta}_2} \, d\hat{l} + \hat{I}_3 \int_{\hat{l}} \hat{\underset{\sim}{\boldsymbol{H}}}'_{\bar{\theta}_3}{}^{\mathrm{T}} \, \hat{\underset{\sim}{\boldsymbol{H}}}'_{\bar{\theta}_3} \, d\hat{l} \\ & + k_{\mathrm{s}_2} \, \hat{\mu} \int_{\hat{l}} \left(\hat{\underset{\sim}{\boldsymbol{H}}}'_{\hat{\bar{u}}_2} - \hat{\underset{\sim}{\boldsymbol{H}}}_{\bar{\theta}_3} \right)^{\mathrm{T}} \left(\hat{\underset{\sim}{\boldsymbol{H}}}'_{\hat{\bar{u}}_2} - \hat{\underset{\sim}{\boldsymbol{H}}}_{\bar{\theta}_3} \right) d\hat{l} \\ & + k_{\mathrm{s}_3} \, \hat{\mu} \int_{\hat{l}} \left(\hat{\underset{\sim}{\boldsymbol{H}}}'_{\hat{\bar{u}}_3} + \hat{\underset{\sim}{\boldsymbol{H}}}_{\bar{\theta}_2} \right)^{\mathrm{T}} \left(\hat{\underset{\sim}{\boldsymbol{H}}}'_{\hat{\bar{u}}_3} + \hat{\underset{\sim}{\boldsymbol{H}}}_{\bar{\theta}_2} \right) d\hat{l} + k_{\mathrm{t}} \, \hat{\mu} \, \hat{I}_1 \int_{\hat{l}} \hat{\underset{\sim}{\boldsymbol{H}}}'_{\bar{\theta}_1}{}^{\mathrm{T}} \, \hat{\underset{\sim}{\boldsymbol{H}}}'_{\bar{\theta}_1} \, d\hat{l} \end{aligned} \tag{4.125}$$

$$\hat{\underset{\sim}{\mathcal{M}}}^{\langle \mathrm{e} \rangle} = \left(1+\hat{\varrho}^{V}\right) \int_{\hat{l}} \left(\hat{\underset{\sim}{H}}^{\mathrm{T}}_{\hat{\bar{u}}_1} \hat{\underset{\sim}{H}}_{\hat{\bar{u}}_1} + \hat{\underset{\sim}{H}}^{\mathrm{T}}_{\hat{\bar{u}}_2} \hat{\underset{\sim}{H}}_{\hat{\bar{u}}_2} + \hat{\underset{\sim}{H}}^{\mathrm{T}}_{\hat{\bar{u}}_3} \hat{\underset{\sim}{H}}_{\hat{\bar{u}}_3} \right) d\hat{l}$$
$$+ \left(1+\hat{\varrho}^{V}\right) \int_{\hat{l}} \left(\hat{I}_1 \hat{\underset{\sim}{H}}^{\mathrm{T}}_{\bar{\theta}_1} \hat{\underset{\sim}{H}}_{\bar{\theta}_1} + \hat{I}_2 \hat{\underset{\sim}{H}}^{\mathrm{T}}_{\bar{\theta}_2} \hat{\underset{\sim}{H}}_{\bar{\theta}_2} + \hat{I}_3 \hat{\underset{\sim}{H}}^{\mathrm{T}}_{\bar{\theta}_3} \hat{\underset{\sim}{H}}_{\bar{\theta}_3} \right) d\hat{l} \tag{4.126}$$
$$+ \int_{\hat{l}} \hat{\underset{\sim}{H}}^{\mathrm{T}}_{\bar{\boldsymbol{\theta}}} {}^{b}\hat{\underline{\underline{\boldsymbol{\jmath}}}}^{V} \hat{\underset{\sim}{H}}_{\bar{\boldsymbol{\theta}}} \, d\hat{l}$$

$$\hat{\underset{\sim}{\mathcal{G}}}^{\langle \mathrm{e} \rangle} = \int_{\hat{l}} \hat{\underset{\sim}{H}}^{\mathrm{T}}_{\bar{\boldsymbol{\theta}}} \left({}^{b}\mathring{\underline{\underline{\boldsymbol{\phi}}}}^{\times} {}^{b}\hat{\underline{\underline{\boldsymbol{\jmath}}}}^{V} - {}^{b}\hat{\underline{\underline{\boldsymbol{\jmath}}}}^{V} {}^{b}\mathring{\underline{\underline{\boldsymbol{\phi}}}}^{\times} - \left({}^{b}\hat{\underline{\underline{\boldsymbol{\jmath}}}}^{V} \left({}^{b}\mathring{\underline{\boldsymbol{\phi}}} + {}^{b}\mathring{\underline{\boldsymbol{\psi}}} \right) \right)^{\times} \right) \hat{\underset{\sim}{H}}_{\bar{\boldsymbol{\theta}}} \, d\hat{l} \tag{4.127}$$

$$\hat{\underset{\sim}{\mathcal{C}}}^{\langle \mathrm{e} \rangle} = -\int_{\hat{l}} \hat{\underset{\sim}{H}}^{\mathrm{T}}_{\bar{\boldsymbol{\theta}}} \left({}^{b}\hat{\underline{\underline{\boldsymbol{\jmath}}}}^{V} {}^{b}\mathring{\underline{\underline{\boldsymbol{\phi}}}}^{\circ} + {}^{b}\hat{\underline{\underline{\boldsymbol{\jmath}}}}^{V} {}^{b}\mathring{\underline{\underline{\boldsymbol{\psi}}}}^{\circ} + {}^{b}\mathring{\underline{\underline{\boldsymbol{\phi}}}}^{\times} {}^{b}\hat{\underline{\underline{\boldsymbol{\jmath}}}}^{V} \left({}^{b}\mathring{\underline{\boldsymbol{\phi}}} + {}^{b}\mathring{\underline{\boldsymbol{\psi}}} \right) \right)^{\times} \hat{\underset{\sim}{H}}_{\bar{\boldsymbol{\theta}}} \, d\hat{l} \tag{4.128}$$

$$\hat{\underset{\sim}{\mathcal{R}}}^{\langle \mathrm{e} \rangle} = \int_{\hat{l}} \hat{\underset{\sim}{H}}^{\mathrm{T}}_{\bar{\boldsymbol{\theta}}} \left({}^{b}\hat{\underline{\underline{\boldsymbol{\jmath}}}}^{V} {}^{b}\mathring{\underline{\underline{\boldsymbol{\phi}}}}^{\circ} + {}^{b}\hat{\underline{\underline{\boldsymbol{\jmath}}}}^{V} {}^{b}\mathring{\underline{\underline{\boldsymbol{\psi}}}}^{\circ} + {}^{b}\mathring{\underline{\underline{\boldsymbol{\phi}}}}^{\times} {}^{b}\hat{\underline{\underline{\boldsymbol{\jmath}}}}^{V} \left({}^{b}\mathring{\underline{\boldsymbol{\phi}}} + {}^{b}\mathring{\underline{\boldsymbol{\psi}}} \right) \right) d\hat{l} \tag{4.129}$$

$$\hat{\underset{\sim}{\mathcal{Q}}}^{\langle \mathrm{e} \rangle} = \int_{\hat{L}} \left(\hat{\underset{\sim}{H}}^{\mathrm{T}}_{\bar{u}_i} \hat{\bar{f}}_i^{V} + \hat{\underset{\sim}{H}}^{\mathrm{T}}_{\bar{\theta}_i} \hat{\bar{m}}_i^{L} + \hat{\underset{\sim}{H}}^{\mathrm{T}}_{\bar{\theta}_i} \hat{\bar{m}}_i^{V} \right) d\hat{L} + \sum_{P} \left(\hat{\underset{\sim}{H}}^{\mathrm{T}}_{\bar{u}_i} \hat{\bar{f}}_i^{S} + \hat{\underset{\sim}{H}}^{\mathrm{T}}_{\bar{\theta}_i} \hat{\bar{m}}_i^{P} + \hat{\underset{\sim}{H}}^{\mathrm{T}}_{\bar{\theta}_i} \hat{\bar{m}}_i^{S} \right) \tag{4.130}$$

For both cases of micropolar and classical gyrobeams, the stiffness matrix $\hat{\underset{\sim}{\mathcal{K}}}^{\langle \mathrm{e} \rangle}$, mass matrix $\hat{\underset{\sim}{\mathcal{M}}}^{\langle \mathrm{e} \rangle}$, gyricity matrix $\hat{\underset{\sim}{\mathcal{G}}}^{\langle \mathrm{e} \rangle}$, circulatory matrix $\hat{\underset{\sim}{\mathcal{C}}}^{\langle \mathrm{e} \rangle}$, generalized moment matrix $\hat{\underset{\sim}{\mathcal{R}}}^{\langle \mathrm{e} \rangle}$, and generalized force matrix $\hat{\underset{\sim}{\mathcal{Q}}}^{\langle \mathrm{e} \rangle}$ are the desired finite element matrices. Recall that, in this thesis, the exact (not reduced or numerical) integration is used for computation of these element matrices. In addition, the element mass, gyricity, circulatory, generalized moment, and generalized force matrices are consistent, as the same interpolation functions are employed in the derivation of them as in the derivation of the element stiffness matrix.

The aforementioned element matrices will be assembled, taking into consideration the correspondence between the local element DOFs summarized as $\hat{\underset{\sim}{\boldsymbol{q}}}^{\langle \mathrm{e} \rangle}$ and the global assemblage DOFs summarized as $\hat{\underset{\sim}{\boldsymbol{q}}}^{\langle \mathrm{g} \rangle}$ [63], to form the system global matrices $\hat{\underset{\sim}{\mathcal{K}}}^{\langle \mathrm{g} \rangle}$, $\hat{\underset{\sim}{\mathcal{M}}}^{\langle \mathrm{g} \rangle}$,

$\hat{\underset{\sim}{\mathcal{G}}}^{\langle g\rangle}$, $\hat{\underset{\sim}{\mathcal{C}}}^{\langle g\rangle}$, $\hat{\underset{\sim}{\mathcal{R}}}^{\langle g\rangle}$, and $\hat{\underset{\sim}{\mathcal{Q}}}^{\langle g\rangle}$. Note that the global generalized coordinate matrix $\hat{\underset{\sim}{q}}^{\langle g\rangle}$ is constructed by pulling together the nodal generalized coordinate matrices $\hat{\underset{\sim}{q}}^{\langle j\rangle}$ of the whole assemblage's nodes. Accordingly, the gyrobeam's potential and kinetic energy variations and virtual work can be expressed in terms of the global matrices as:

$$\begin{aligned}
\Delta\hat{\mathcal{U}} &= \delta\hat{\underset{\sim}{q}}^{\langle g\rangle\,\mathrm{T}}\,\hat{\underset{\sim}{\mathcal{K}}}^{\langle g\rangle}\,\hat{\underset{\sim}{q}}^{\langle g\rangle} \\
\Delta\hat{\mathcal{T}} &= -\delta\hat{\underset{\sim}{q}}^{\langle g\rangle\,\mathrm{T}}\,\hat{\underset{\sim}{\mathcal{M}}}^{\langle g\rangle}\,\hat{\underset{\sim}{q}}^{\circ\circ\langle g\rangle} - \delta\hat{\underset{\sim}{q}}^{\langle g\rangle\,\mathrm{T}}\,\hat{\underset{\sim}{\mathcal{G}}}^{\langle g\rangle}\,\hat{\underset{\sim}{q}}^{\circ\langle g\rangle} - \delta\hat{\underset{\sim}{q}}^{\langle g\rangle\,\mathrm{T}}\,\hat{\underset{\sim}{\mathcal{C}}}^{\langle g\rangle}\,\hat{\underset{\sim}{q}}^{\langle g\rangle} - \delta\hat{\underset{\sim}{q}}^{\langle g\rangle\,\mathrm{T}}\,\hat{\underset{\sim}{\mathcal{R}}}^{\langle g\rangle} \\
\delta\hat{\mathcal{W}} &= \delta\hat{\underset{\sim}{q}}^{\langle g\rangle\,\mathrm{T}}\,\hat{\underset{\sim}{\mathcal{Q}}}^{\langle g\rangle}
\end{aligned} \tag{4.131}$$

and (based on Hamilton's principle) the semi-discretized gyrobeam dynamic ODEs will be derived as:

$$\hat{\underset{\sim}{\mathcal{Q}}}^{\langle g\rangle} - \hat{\underset{\sim}{\mathcal{R}}}^{\langle g\rangle} = \hat{\underset{\sim}{\mathcal{M}}}^{\langle g\rangle}\,\hat{\underset{\sim}{q}}^{\circ\circ\langle g\rangle} + \hat{\underset{\sim}{\mathcal{G}}}^{\langle g\rangle}\,\hat{\underset{\sim}{q}}^{\circ\langle g\rangle} + \hat{\underset{\sim}{\mathcal{C}}}^{\langle g\rangle}\,\hat{\underset{\sim}{q}}^{\langle g\rangle} + \hat{\underset{\sim}{\mathcal{K}}}^{\langle g\rangle}\,\hat{\underset{\sim}{q}}^{\langle g\rangle} \tag{4.132}$$

Recall that in the set of dynamic ODEs given by Eq. (4.132) the NBCs are taken into account directly (in the evaluation of the generalized force matrix) and it is enough to just impose the EBCs via one of the methods explained in [63]. Imposition of EBCs will result in the final semi-discretized gyrobeam dynamic ODEs:

$$\hat{\underset{\sim}{\mathcal{Q}}} - \hat{\underset{\sim}{\mathcal{R}}} = \hat{\underset{\sim}{\mathcal{M}}}\,\hat{\underset{\sim}{q}}^{\circ\circ} + \hat{\underset{\sim}{\mathcal{G}}}\,\hat{\underset{\sim}{q}}^{\circ} + \hat{\underset{\sim}{\mathcal{C}}}\,\hat{\underset{\sim}{q}} + \hat{\underset{\sim}{\mathcal{K}}}\,\hat{\underset{\sim}{q}} \tag{4.133}$$

which can be integrated with an ODE integration technique provided the ICs are given, or can be used for modal vibration analysis even if the ICs are unknown.

4.10 Boundary conditions

As mentioned before in the weak formulation or variational form of the displacement-based FEM, the NBCs are naturally taken into account in the evaluation of the (nodal) generalized force and moment matrices and there are only EBCs which should be imposed separately using the procedure explained in [63].

Some simple (but very common) BCs which can be considered for nodal points of classical and micropolar gyrobeams and the essential generalized coordinates constraints

corresponding to them are presented in Table 4.1 where the BCs related to longitudinal, torsional, and bending deformations are taken into account separately.

A complete set of BCs for a 3D gyrobeam may be represented as a combination of three pairs of BCs corresponding to the tension-compression, torsion, and bending modes at the gyrobeam's left and right boundary points P_1 and P_2. For example, a classically cantilevered 3D gyrobeam can be addressed as having fixed-free BCs on tension-compression, (classical) fixed-free BCs on torsion, and (classical) clamped-free BCs on bending at the left and right boundary points P_1 and P_2, or more clearly having fixed tension-compression, (classical) fixed torsion, and (classical) clamped bending BCs at P_1 and free tension-compression, free torsion, and free bending BCs at P_2.

4.11 Time integration

Among different time integration techniques, a few are known to take advantage of the special characteristics of the finite element matrices and to be very effective in the context of FEM. These effective techniques can be categorized as direct integration methods and mode superposition methods. Direct integration methods are those in which a numerical step-by-step procedure is used on the original form of the differential equations to integrate them. In the mode superposition methods, on the other hand, a transformation of the differential equations is firstly carried out and then the transformed equations are integrated exactly or numerically (using a step-by-step procedure).

The central difference method, Houbolt method, Wilson-θ method, and the Newmark method are a few commonly used direct integration techniques. The central difference method is an explicit conditionally stable integration method [63]. The Houbolt is an implicit unconditionally stable method which needs a special starting procedure and provides relatively high artificial damping [63, 65]. The Wilson-θ method with an optional coefficient θ is indeed a family of implicit integration methods which are unconditionally stable provided $\theta \geq 1.37$ [63]. The Wilson-θ method with $\theta = 1.4$ is a very common second-order accurate and unconditionally stable method with algorithmic damping (which is sometimes desirable). The Newmark method with two optional coefficients β and γ represents a family

of implicit integration methods which are unconditionally stable provided $2\beta \geq \gamma \geq \frac{1}{2}$ [65]. The Newmark method with $\gamma = \frac{1}{2}$ is second-order accurate and unconditionally stable but introduce no algorithmic damping. The Newmark method with $\gamma > \frac{1}{2}$ is unconditionally stable and bring in some artificial damping but is only first-order accurate (taking $\gamma > \frac{1}{2}$ and $\beta = \frac{1}{4}(\gamma + \frac{1}{2})^2$ maximizes the artificial damping).

The fact that in the Newmark method the algorithmic damping is only achievable by sacrificing the accuracy is a disadvantage of this method. This shortcoming can be overcome by using a variation of the Newmatk method, called α-method [65], which has three coefficients α, β, and γ. Provided $-\frac{1}{3} \leq \alpha \leq 0$, $\beta = \frac{1}{4}(1-\alpha)^2$, and $\gamma = \frac{1}{2}(1-2\,\alpha)$, the α-method represents a family of implicit, unconditionally stable, and second-order accurate direct integration methods which also provide effective artificial damping.

The α-method can be used to find the approximate solution of the linear second-order dynamic ODEs of Eq. (4.133) when the ICs are given. This results in the dynamic solution in terms of the approximate time history of the state variables evaluated at assemblage nodes. As the method is unconditionally stable the time step should be selected to meet just the accuracy requirements.

Table 4.1: Simple boundary conditions applicable to the nodal points of gyrobeams.

BCs Group/Name	**Resultant Constraints in a Classical Gyrobeam**	**Resultant Constraints in a Micropolar Gyrobeam**
Longitudinal BCs/		
Free	no constraint	no constraint
Fixed	$\hat{\bar{u}}_1^{\langle \mathrm{j} \rangle} = 0$	$\hat{\bar{u}}_1^{\langle \mathrm{j} \rangle} = 0$
Torsional BCs/		
Free	no constraint	no constraint
(Classical) Fixed	$\bar{\theta}_1^{\langle \mathrm{j} \rangle} = 0$	$\bar{\theta}_1^{\langle \mathrm{j} \rangle} = 0$
Micropolar Fixed	not applicable	$\bar{\theta}_1^{\langle \mathrm{j} \rangle} = \bar{\vartheta}_1^{\langle \mathrm{j} \rangle} = 0$
Bending BCs/		
Free	no constraint	no constraint
Pinned	$\hat{\bar{u}}_2^{\langle \mathrm{j} \rangle} = \hat{\bar{u}}_3^{\langle \mathrm{j} \rangle} = 0$	$\hat{\bar{u}}_2^{\langle \mathrm{j} \rangle} = \hat{\bar{u}}_3^{\langle \mathrm{j} \rangle} = 0$
(Classical) Sliding	$\bar{\theta}_2^{\langle \mathrm{j} \rangle} = \bar{\theta}_3^{\langle \mathrm{j} \rangle} = 0$	$\bar{\theta}_2^{\langle \mathrm{j} \rangle} = \bar{\theta}_3^{\langle \mathrm{j} \rangle} = 0$
(Classical) Clamped	$\hat{\bar{u}}_2^{\langle \mathrm{j} \rangle} = \hat{\bar{u}}_3^{\langle \mathrm{j} \rangle} = 0$ $\bar{\theta}_2^{\langle \mathrm{j} \rangle} = \bar{\theta}_3^{\langle \mathrm{j} \rangle} = 0$	$\hat{\bar{u}}_2^{\langle \mathrm{j} \rangle} = \hat{\bar{u}}_3^{\langle \mathrm{j} \rangle} = 0$ $\bar{\theta}_2^{\langle \mathrm{j} \rangle} = \bar{\theta}_3^{\langle \mathrm{j} \rangle} = 0$
Micropolar Sliding	not applicable	$\bar{\theta}_2^{\langle \mathrm{j} \rangle} = \bar{\theta}_3^{\langle \mathrm{j} \rangle} = 0$ $\bar{\vartheta}_2^{\langle \mathrm{j} \rangle} = \bar{\vartheta}_3^{\langle \mathrm{j} \rangle} = 0$
Micropolar Clamped	not applicable	$\hat{\bar{u}}_2^{\langle \mathrm{j} \rangle} = \hat{\bar{u}}_3^{\langle \mathrm{j} \rangle} = 0$ $\bar{\theta}_2^{\langle \mathrm{j} \rangle} = \bar{\theta}_3^{\langle \mathrm{j} \rangle} = 0$ $\bar{\vartheta}_2^{\langle \mathrm{j} \rangle} = \bar{\vartheta}_3^{\langle \mathrm{j} \rangle} = 0$

Chapter 5

Numerical Analysis of Classical Gyroelastic Beams

5.1 Introduction

To illustrate the classical gyrobeam model developed in Chapter 4 a few numerical examples are presented in this chapter where the main focus is on the study of the modal behavior of the classical gyrobeams with uniform gyricity distribution (a few examples of classical gyrobeams with different non-uniform gyricity distributions are given in Appendix E).

The classical gyrobeam model developed in Chapter 4 employs the simple longitudinal deformation theory, Duleau torsion theory, and Timoshenko bending theory to model the beam elasticity and in this chapter will be simply referred to as the "3D Timoshenko gyrobeam model". On the other hand, the classical gyrobeam model suggested by D'Eleuterio [2, 16] and Zee [33], and reviewed in Appendix D, utilizes the simple longitudinal deformation theory, Duleau torsion theory, and Euler-Bernoulli bending theory and therefore in this chapter is simply called the "3D Euler-Bernoulli gyrobeam model". The more general term "classical gyrobeam model" will be used in this chapter whenever both Timoshenko and Euler-Bernoulli gyrobeam models are meant. The modal comparison of the 3D Timoshenko gyrobeam model against the 3D Euler-Bernoulli gyrobeam model will

be pursued in this chapter through the provided numerical examples. Note that, to have an even comparison, the unrestricted 3D Timoshenko gyrobeam model developed in Chapter 4 will be compared against the unrestricted 3D Euler-Bernoulli gyrobeam model presented in Appendix D and not against the zero-order restricted Euler-Bernoulli gyrobeam models developed by D'Eleuterio [2, 16] and Zee [33].

The 3D Euler-Bernoulli (EB) and Timoshenko (TM) gyrobeams selected for numerical analyses are (classically) cantilevered uniform beams along the first axis of the inertial reference frame (the principal axes of the beams' cross section are assumed to be parallel to the second and third coordinate axes of the inertial frame). The gyrobeams have constant geometries, inertia densities, and elastic constants over the length and carry a constant (time-invariant) uniform axial or transverse gyricity distribution as shown in Figure 5.1 or 5.16. The FEM-based numerical models of these gyrobeams are implemented in MATLAB® [66] using the parameters summarized in Tables 5.1, 5.2, and 5.3.

Table 5.1: Summary of the main dimensionless parameters used in the numerical classical gyrobeam models.

Parameter	**Value(s)**
$\hat{R}_3 = \hat{R}_2 = \sqrt{2}\,\hat{R}_1$	10, 50, and 250
$\hat{\mu}$	$\frac{3}{8}$
k_{t}	1
$k_{\mathrm{s}_2} = k_{\mathrm{s}_3}$	1
$\hat{\varrho}^V$	$\frac{1}{4}$
${}^a\hat{\underline{\underline{\boldsymbol{\jmath}}}}^V$	$\frac{\hat{\varrho}^V}{\hat{R}_3^2} \times \underline{\underline{\mathbb{1}}} = \hat{\varrho}^V\, \hat{I}_3 \times \underline{\underline{\mathbb{1}}}$
(φ_1, φ_2)	$(0, \frac{\pi}{2})$ (for axial gyricity)
	$(0, 0)$ (for transverse gyricity)
$(\mathring{\varphi}_1, \mathring{\varphi}_2)$	$(0, 0)$
$\mathring{\varphi}_{3\mathrm{T}}^{\frac{1}{2}}$	$[0, 60]$

In Table 5.1 the given value for the gyros' rotational inertia density $\hat{\underset{\leftrightarrow}{\jmath}}^V$ is based on

Table 5.2: Summary of the main FEM parameters used in the numerical Euler-Bernoulli gyrobeam model.

Parameter	**Value**
Element Type	C^0 two-node (for tension and torsion)
	C^1 two-node (for bending)
Basis Functions	linear Lagrange polynomials (for tension and torsion)
	cubic Hermitian polynomials (for bending)
Number of Elements	48
Number of Nodes	49 (distributed evenly)
DOFs per Node	6
Longitudinal BCs	fixed-free
Torsional BCs	classical fixed-free
Bending BCs	classical clamped-free
Gyricity Distribution	uniform axial/transverse

assuming a constant proportional relationship between the dimensions of the gyros and the beam thickness. Also, the total gyricity spin rate $\mathring{\varphi}_{3\mathrm{T}}$ is defined, analogous to the D'Eleuterio's total gyricity symbol $\hat{h}_T$ [2, 16], in terms of the gyricity spin rate function $\mathring{\varphi}_3({}^c\hat{x}_1)$ as:

$$\mathring{\varphi}_{3\mathrm{T}} = \int_{\hat{L}} |\mathring{\varphi}_3({}^c\hat{x}_1)| \, d\hat{L} \tag{5.1}$$

where $|\square|$ represents the absolute value of a parameter. Based on this definition the function of $\mathring{\varphi}_3({}^c\hat{x}_1)$ associated with a given $\mathring{\varphi}_{3\mathrm{T}}$, for example, in a uniform or half sinusoidal distribution, will respectively be:

$$\mathring{\varphi}_3({}^c\hat{x}_1) = \mathring{\varphi}_{3\mathrm{T}} \tag{5.2}$$

or:

$$\mathring{\varphi}_3({}^c\hat{x}_1) = \mathring{\varphi}_{3\mathrm{T}} \frac{\pi}{2} \sin(\pi \, {}^c\hat{x}_1) \tag{5.3}$$

Table 5.3: Summary of the main FEM parameters used in the numerical Timoshenko gyrobeam model.

Parameter	**Value**
Element Type	C^0 four-node
Basis Functions	cubic Lagrange polynomials
Number of Elements	16
Number of Nodes	49 (distributed evenly)
DOFs per Node	6
Longitudinal BCs	fixed-free
Torsional BCs	classical fixed-free
Bending BCs	classical clamped-free
Gyricity Distribution	uniform axial/transverse

Recall that both 3D Euler-Bernoulli and 3D Timoshenko gyrobeams have four modes of deformation, *i.e.* longitudinal displacement along the ${}^c\hat{x}_1$ axis, torsional rotation about the ${}^c\hat{x}_1$ axis, bending deformation in the ${}^c\hat{x}_1{}^c\hat{x}_2$ plane, and bending deformation in the ${}^c\hat{x}_1{}^c\hat{x}_3$ plane; in the presence of gyricity terms the torsional and bending deformation modes may be coupled together. In the following numerical examples only those deformation modes affected by the gyricity will be taken into account when comparing the natural frequencies and mode shapes of Euler-Bernoulli and Timoshenko gyrobeams.

5.2 Uniform axial gyricity distribution

A uniform axial gyricity distribution (over the beam length), *i.e.* a constant gyricity parallel to the beam's neutral axis, couples the two bending deformation modes of the gyrobeam in the ${}^c\hat{x}_1{}^c\hat{x}_2$ and ${}^c\hat{x}_1{}^c\hat{x}_3$ planes. These bending deformations, however, remain uncoupled from the gyrobeam longitudinal deformations along the ${}^c\hat{x}_1$ axis and torsional deformations about the ${}^c\hat{x}_1$ axis. Indeed, an axial gyricity distribution affects the bending modes while

the longitudinal and torsional modes are left untouched. The schematic of a gyrobeam with such a gyricity distribution, *i.e.* a uniform axial gyricity in the $c_{\vec{1}}$ direction, is shown in Figure 5.1.

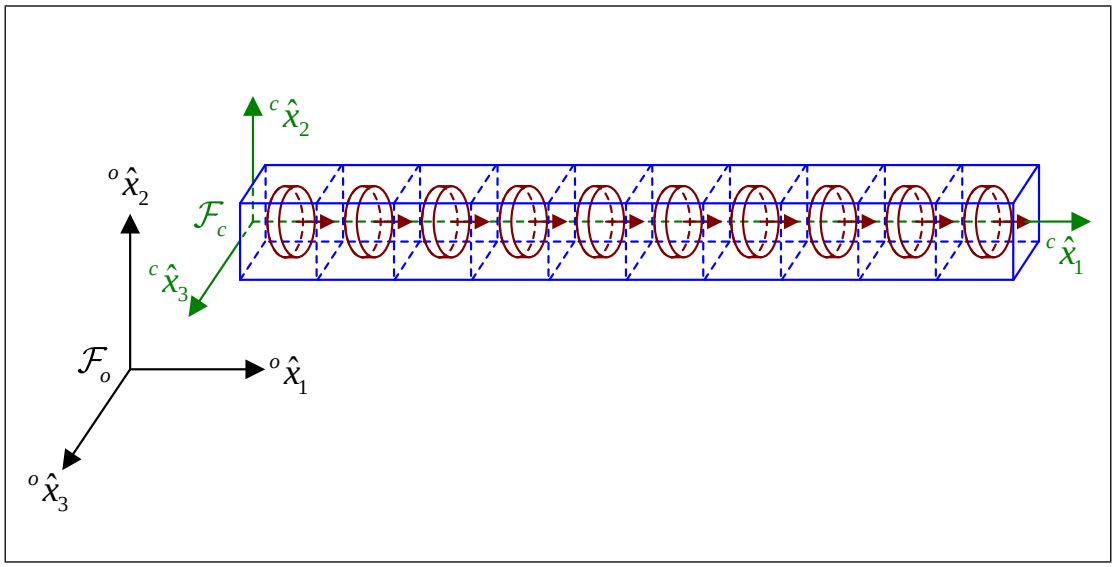

Figure 5.1: A gyrobeam carrying a uniform axial gyricity distribution.

The variations of the first 25 (gyricity-affected) bending natural frequencies for three different (thick, medium, and thin) Euler-Bernoulli and Timoshenko gyrobeams carrying a uniform axial gyricity with the variation of the total gyricity (or more exactly the gyros total spin rate $\mathring{\varphi}_{3\mathrm{T}}$) are shown in Figures 5.2–5.7. The depicted natural frequencies correspond to the coupled bending-bending deformation modes (and therefore their mode shapes consist of bending deformations in both the $^c\hat{x}_1{}^c\hat{x}_2$ and $^c\hat{x}_1{}^c\hat{x}_3$ planes).

Note that for a zero gyricity (zero spin rate) there is no coupling between the deformation modes and one can easily distinguish between the longitudinal, torsional, and two bending natural frequencies (all the natural frequencies correspond to single deformation modes). To facilitate tracking of the gyricity effects on different natural frequencies, different natural frequencies of the considered beams for the zero-gyricity case (*i.e.* the longitudinal, torsional, and bending natural frequencies) are shown in the left side of the plots in Figures 5.2–5.7. As noted in the legends (see the upper right corner of the plots)

the zero-gyricity longitudinal, torsional, and bending natural frequencies, *i.e.* $\hat{\omega}_{\mathrm{l}}$, $\hat{\omega}_{\mathrm{t}}$, and $\hat{\omega}_{\mathrm{b}}$, are respectively tagged by □, ○, and △ symbols. The natural frequency curves are, however, plotted only for gyricity-affected bending natural frequencies.

Whereas the natural frequency curves (or loci), given in Figures 5.2–5.7, seem to cross over each other in different points, one should note that this may not happen everywhere it seems to [2]. Indeed, at (some) points where they appear to cross smoothly, the curves instead approach one another quite closely and then veer away suddenly, each taking the path that the other would take was it permitted to cross. The curves may even tangentially coincide (specially here for a beam with symmetry in the two bending planes) without crossing. This phenomenon, referred to as "curve veering", has been thoroughly studied by different authors [67–70]. A detailed examination of the curve veering seen here between the natural frequency loci of gyrobeams is, however, beyond the scope of this work and is recommended as possible future work. Note that had the gyricity-unaffected natural frequency curves been plotted in Figures 5.2–5.7 (they would have appeared as horizontal lines) in addition to the gyricity-affected natural frequency curves, crossing over (instead of veering away) was likely between a gyricity-affected natural frequency curve and a gyricity-unaffected natural frequency curve.

In the natural frequency plots of this section, due to the beam symmetry in the two bending planes, the bending natural frequencies for zero-gyricity case always appear as pairs. By starting at zero and continuously increasing the gyricity one of the natural frequencies in each pair rises while the other one drops. This continues smoothly until the rising bending natural frequency of a lower mode comes close to the dropping bending natural frequency of a higher mode, where the natural frequencies are likely to veer away. For each natural frequency curve this veering away may occur multiple times and makes the curve seem to weave through the others. However, all the considered bending natural frequencies finally tend to zero for large enough gyricity (or large enough $\mathring{\varphi}_{3\mathrm{T}}$).

Now consider the Euler-Bernoulli gyrobeam model and its natural frequency loci depicted in Figures 5.2–5.4. As can be seen in these figures, in an Euler-Bernoulli gyrobeam the veering of the natural frequency curves (if any) occurs more abruptly (compare them to the natural frequency curves of an analogous Timoshenko gyrobeam in Figures 5.5–5.7).

For an Euler-Bernoulli gyrobeam the apparent smooth curves of the rising bending natural frequencies, *i.e.* the path they would take were they allowed to cross, tend to infinity as the gyricity increases (a steep line asymptotic to each apparent curve can be imagined).

Despite the natural frequency plots given in Section D.9 (*i.e.* Figures D.2 and D.6) which are the same for any slenderness ratio, the natural frequency curves of Euler-Bernoulli gyrobeams given in this section (*i.e.* in Figures 5.2–5.4) are different at different beam slenderness ratios. This is partially due to scaling a different parameter on the horizontal axis in the plots of Section D.9, *i.e.* $\hat{h}_T$, from that in the plots of this section, *i.e.* $\mathring{\varphi}_{3\mathrm{T}}$, and partially due to the fact that whereas the plots of Section D.9 are obtained using a zero-order restricted Euler-Bernoulli gyrobeam model, an unrestricted Euler-Bernoulli gyrobeam model, where the translational and rotational inertias of the gyricity (or gyros distribution) are taken into account, is used to produce the plots of this section (refer to Eq. (D.23) which can be compared against the equations derived by D'Eleuterio [2,16] and Zee [33]). Note that, based on Eq. (D.44) the vertical axis of this section plots represents the same quantity as the vertical axis of Section D.9 plots, *i.e.* the square root of product of the natural frequency and the slenderness ratio or $\sqrt{\hat{R}_3\,\hat{\omega}}$.

Note in Figures 5.2–5.4 that for the Euler-Bernoulli gyrobeam model the effect of lengthening (relative to the thickness) or thinning (relative to the length) the beam is to spread out the range of the first 25 natural frequencies and to require larger values of gyricity to get past the region where veering may occur. In other words, for Euler-Bernoulli gyrobeams (with different slenderness ratios) in which there is a proportional relationship between the gyros size (and equivalently the gyros rotational inertia $\hat{\jmath}^V$) and the beam thickness (or equivalently the beam cross sectional moment of inertia $\hat{I}_3$), the gyricity effects on thinner beams are slighter. This includes the slighter difference between the natural frequencies of an elastic beam without gyricity and the natural frequencies of a gyrobeam with a zero gyricity where $\mathring{\varphi}_{3\mathrm{T}} = 0$.

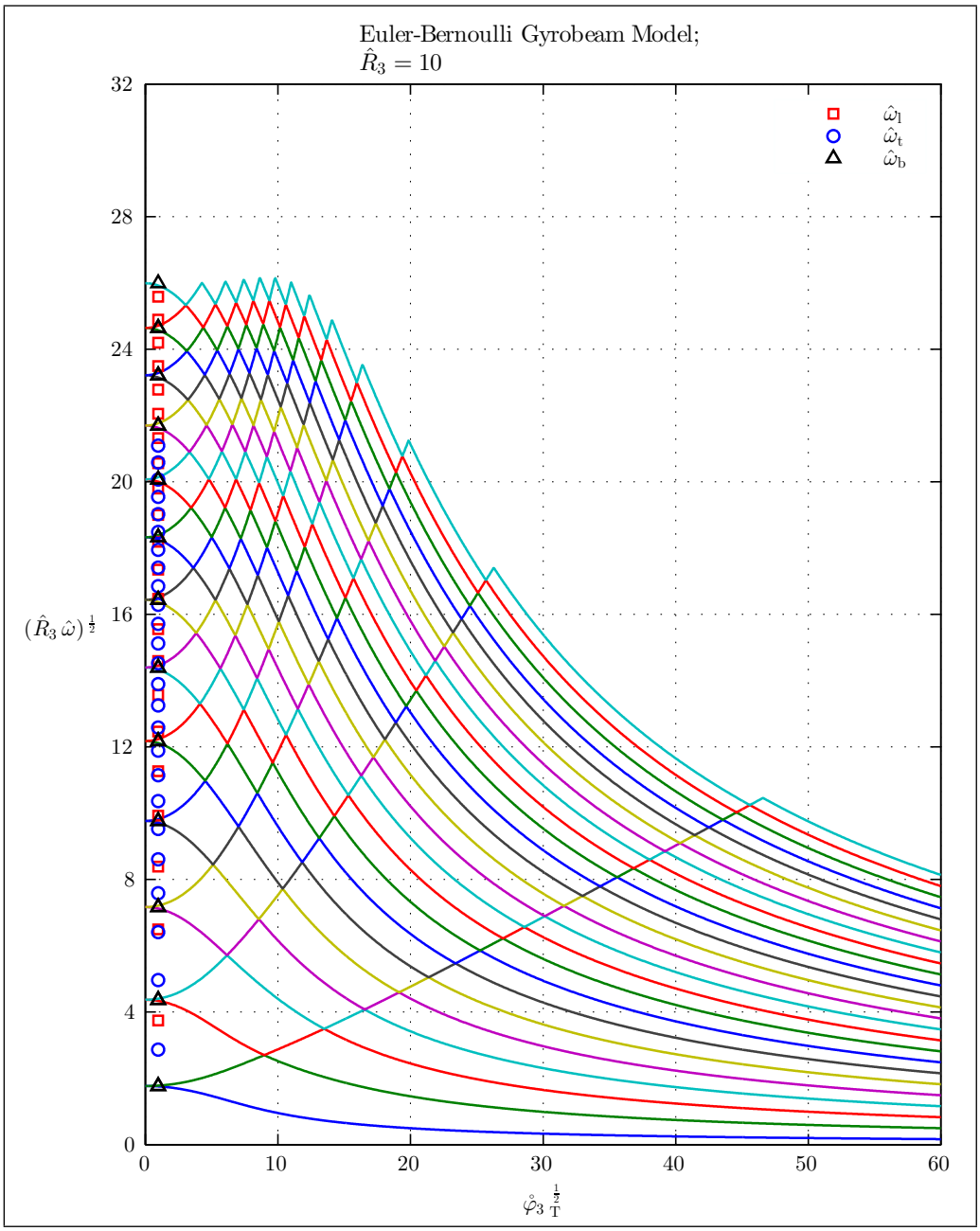

Figure 5.2: Natural frequencies of a thick Euler-Bernoulli gyrobeam with a uniform axial gyricity.

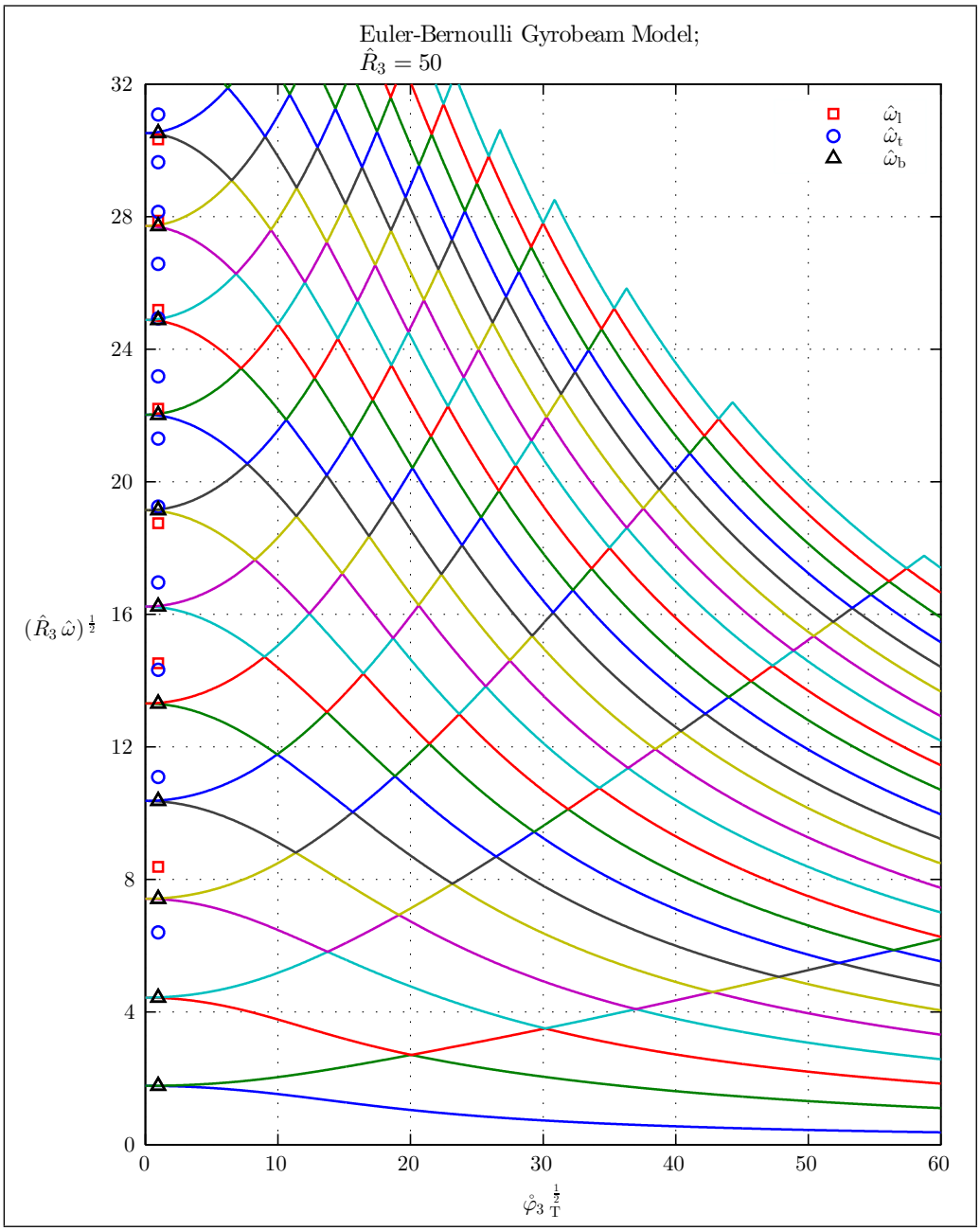

Figure 5.3: Natural frequencies of a medium Euler-Bernoulli gyrobeam with a uniform axial gyricity.

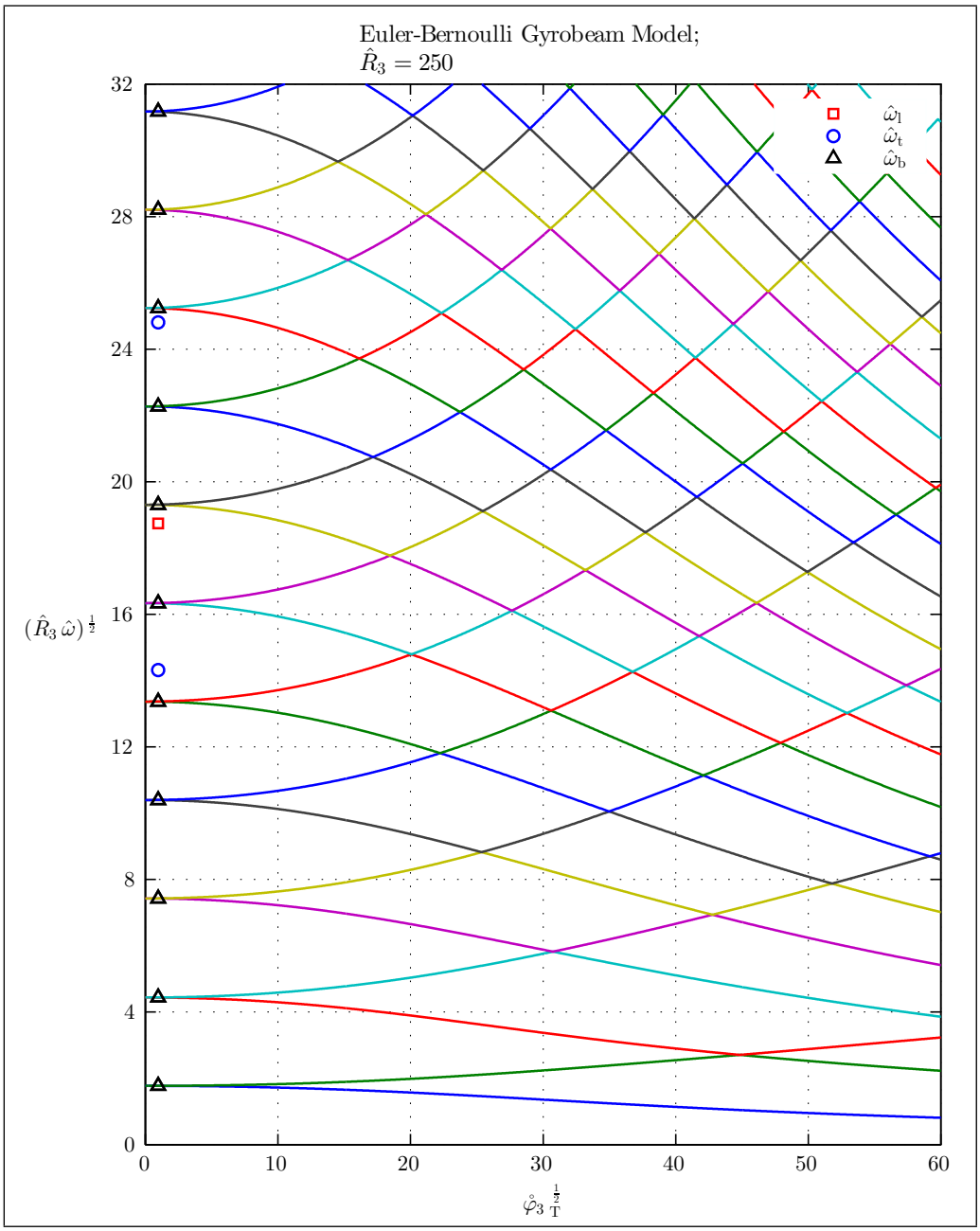

Figure 5.4: Natural frequencies of a thin Euler-Bernoulli gyrobeam with a uniform axial gyricity.

The natural frequency loci of the Timoshenko gyrobeams are plotted in Figures 5.5–5.7. In Figures 5.5–5.7 one can see, in comparison to Figures 5.2–5.4, that the addition of transverse shear effects via the Timoshenko beam model has a very visible effect on the frequency curves especially for the higher frequency modes. As expected, the differences between Figures 5.4 and 5.7 (the thin gyrobeam case) are slight but those for the short gyrobeam case (Figures 5.2 and 5.5) are very pronounced. In general, the natural frequencies of a Timoshenko gyrobeam are lower than the corresponding natural frequencies of an analogous Euler-Bernoulli gyrobeam.

In addition to the rapid curve veering observed earlier for an Euler-Benoulli gyrobeam, one can see gradual curve veering in the natural frequency loci of a Timoshenko gyrobeam which is due to the inclusion of shear deformations (note that the moment-like gyricity effects can activate the shear deformation mode of a Timoshenko beam, as can a volume body moment). The contribution of shear deformations is different in different vibration modes and this may disturb the symmetry between the coupled bending deformation modes to result in a slower curve veering. Accordingly, the gradual curve veering is more clear between the higher natural frequency curves where the contribution of the shear deformation mode is more significant (this is more noticeable in Figure 5.6).

The veering in the Timoshenko gyrobeam results continues to be present (in the lower frequency modes) at much higher values of gyricity than in the Euler-Bernoulli gyrobeam case. This is most evident for the short gyrobeams (Figures 5.2 and 5.5). Clearly the shear contribution to the model is very significant for anything but long slender gyrobeams.

Compared to the Euler-Bernoulli gyrobeams, the apparent smooth curves of the rising bending natural frequencies in a Timoshenko gyrobeam, *i.e.* the path that rising natural frequencies would take were they allowed to cross, tend to a constant value as the gyricity increases (a horizontal line asymptotic to each apparent curve can be imagined).

Finally, analogous to the Euler-Bernoulli gyrobeams, one can see that the gyricity effects become slighter in thinner Timoshenko gyrobeams (of course as the gyros rotational inertia density is proportional to the beam thickness).

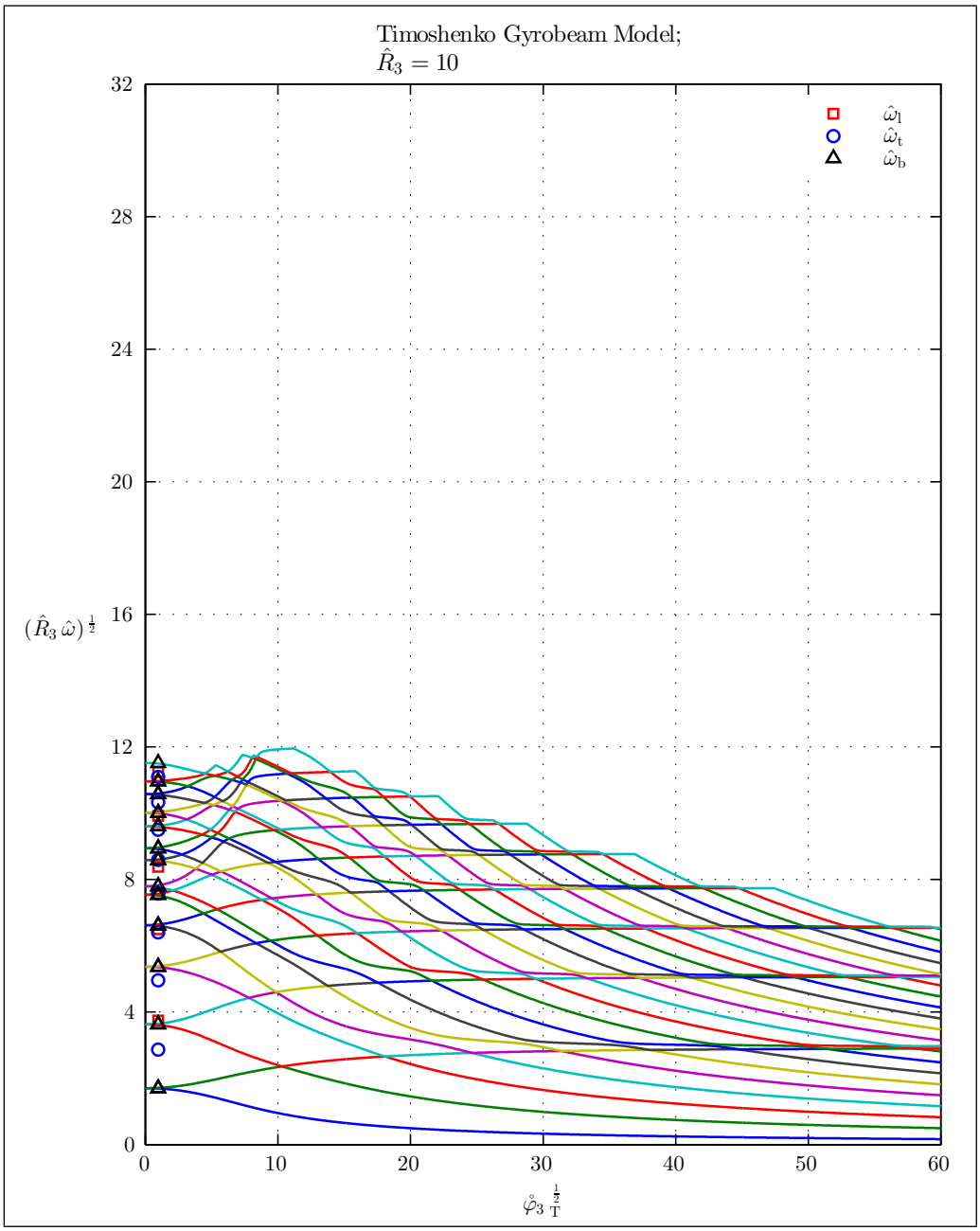

Figure 5.5: Natural frequencies of a thick Timoshenko gyrobeam with a uniform axial gyricity.

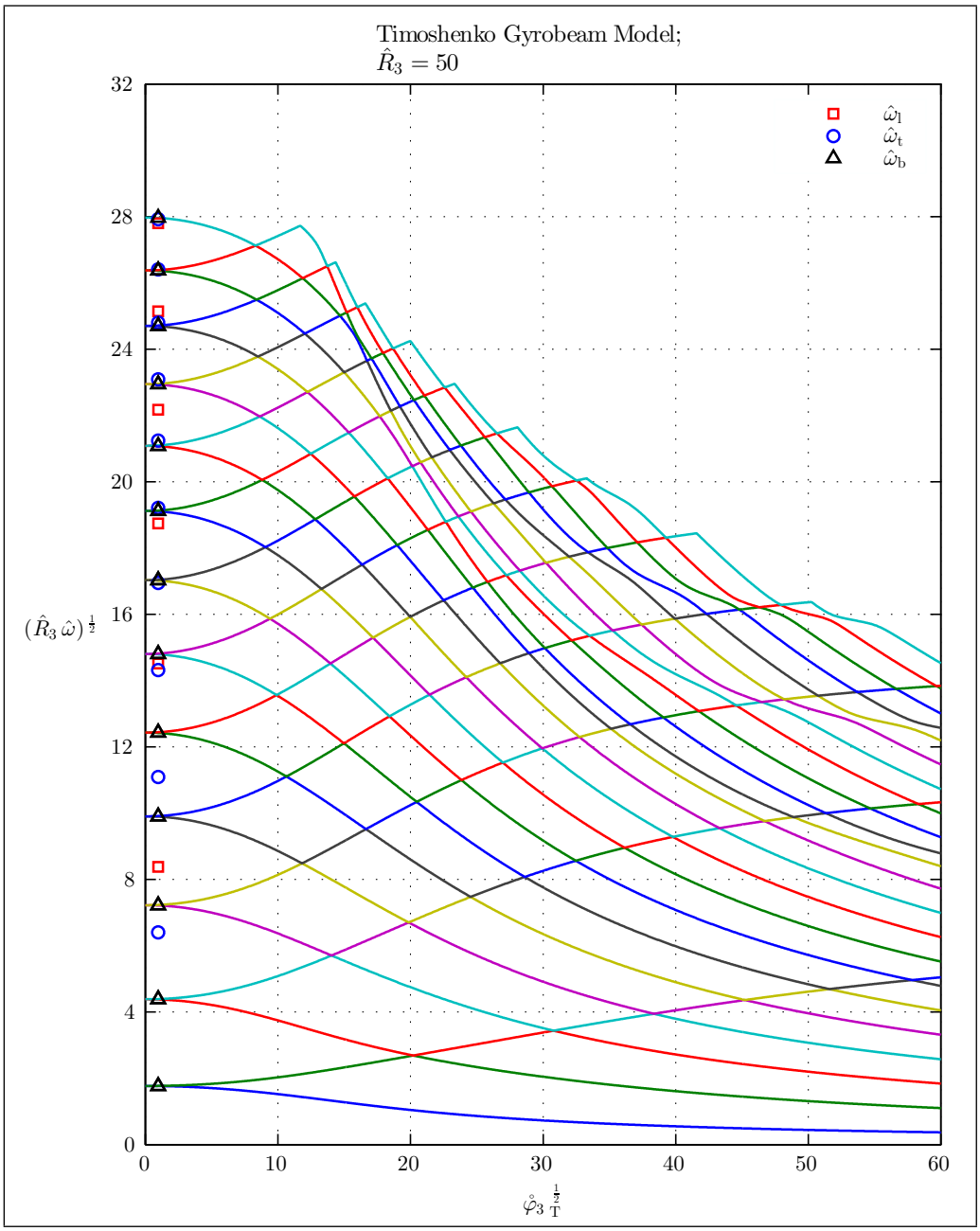

Figure 5.6: Natural frequencies of a medium Timoshenko gyrobeam with a uniform axial gyricity.

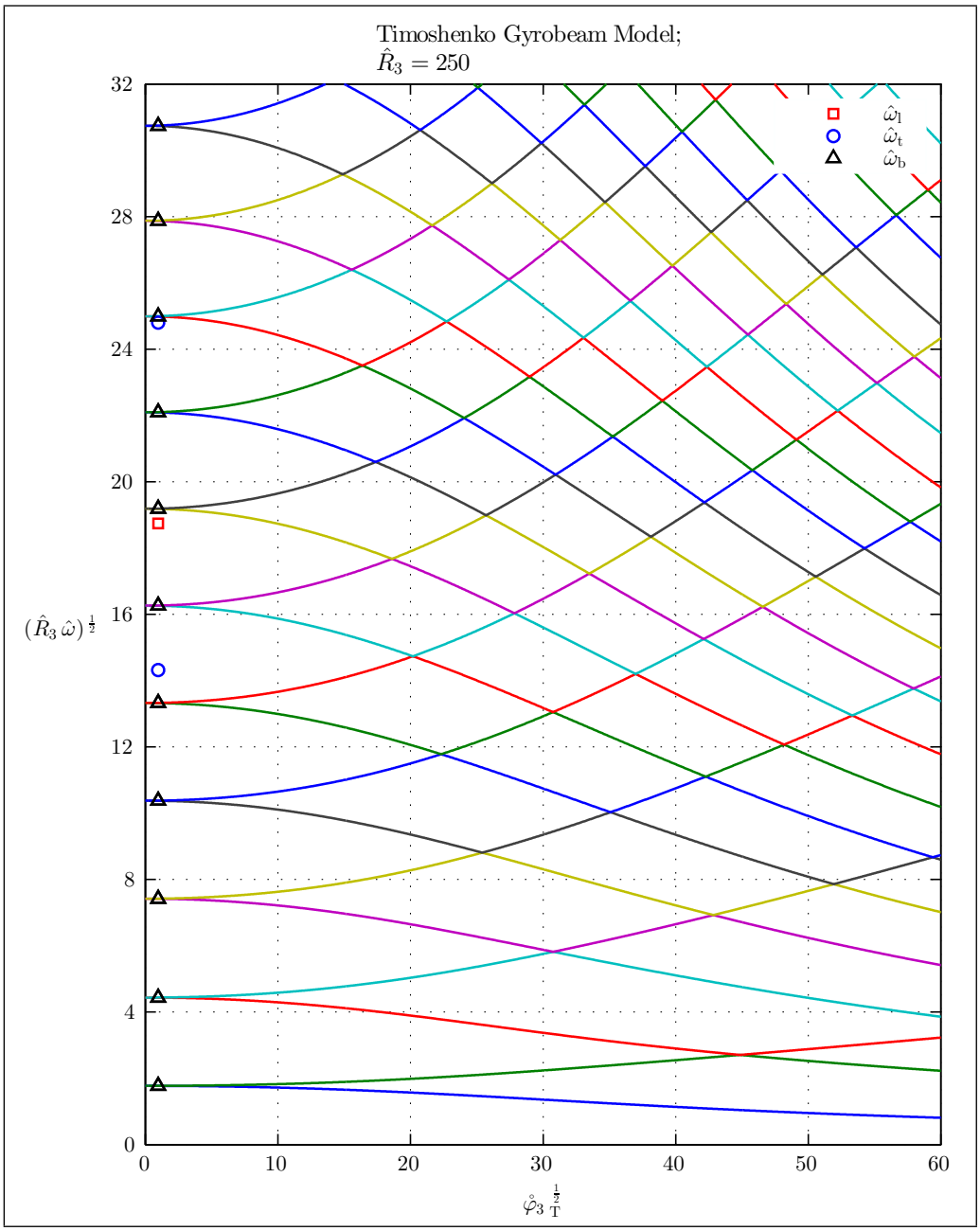

Figure 5.7: Natural frequencies of a thin Timoshenko gyrobeam with a uniform axial gyricity.

To accomplish the modal analysis of the classical gyrobeams with uniform axial gyricity, the first six gyricity-affected mode shapes of medium-thickness Euler-Bernoulli and Timoshenko gyrobeams, considering three values for the gyricity distribution magnitude, are plotted in Figures 5.8–5.13 where note that the mode shapes are numbered based on their actual rank among all the gyrobeam mode shapes.

As shown in the figures, each mode shapes of a gyrobeam with an axial gyricity is a combination of the two bending deformation modes in the ${}^c\hat{x}_1{}^c\hat{x}_2$ and ${}^c\hat{x}_1{}^c\hat{x}_3$ planes. When vibrating in one of its mode shapes the gyrobeam undergoes "precessional movement", which is a result of the time-varying contribution of the two bending deformation modes into the gyrobeam total deformation. Indeed, each mode shape illustrates the precessional rotation of the gyrobeam around the beam rest position (on the ${}^c\hat{x}_1$ axis) with an angular velocity which is the same as the mode shape natural frequency.

The "modal precession" of gyrobeams with axial gyricity is either in the same direction as the gyricity, called the "prograde precession" or in the opposite direction of the gyricity, called the "retrograde precession" [2]. There might be also complex mode shapes in which a portion of the mode has a prograde precession while the rest has a retrograde precession. In Figures 5.8–5.13 each mode shape's sense of precession is shown by two rotation arrows, one describing the sense of precession in the middle of the mode shape and one indicating the sense of precession at the end of the mode shape.

Comparing the mode shapes of the medium-thickness Euler-Bernoulli and Timoshenko gyrobeams one may notice no significant differences between them. However, for both gyrobeam models, it is worthy to note how the "single central nodes" (where the mode shape passes zero while changing sign) of the mode shapes at small gyricity transform into "double central nodes" (*i.e.* two very close central nodes) at medium gyricity and finally become "tangential nodes" (where the mode shape approaches zero but does not cross or change sign) at large gyricity. The tangential nodes are better shown in Figures 5.14 and 5.15 which correspond to a very large axial gyricity distribution. One may also observe in Figures 5.10 and 5.13 how for the large gyricity value all the mode shapes exhibit retrograde precession and the ends of the even gyricity-affected modes, shown in the right column plots, move toward the ${}^c\hat{x}_1$ axis for the large axial gyricity, *i.e.* appear to become nodes.

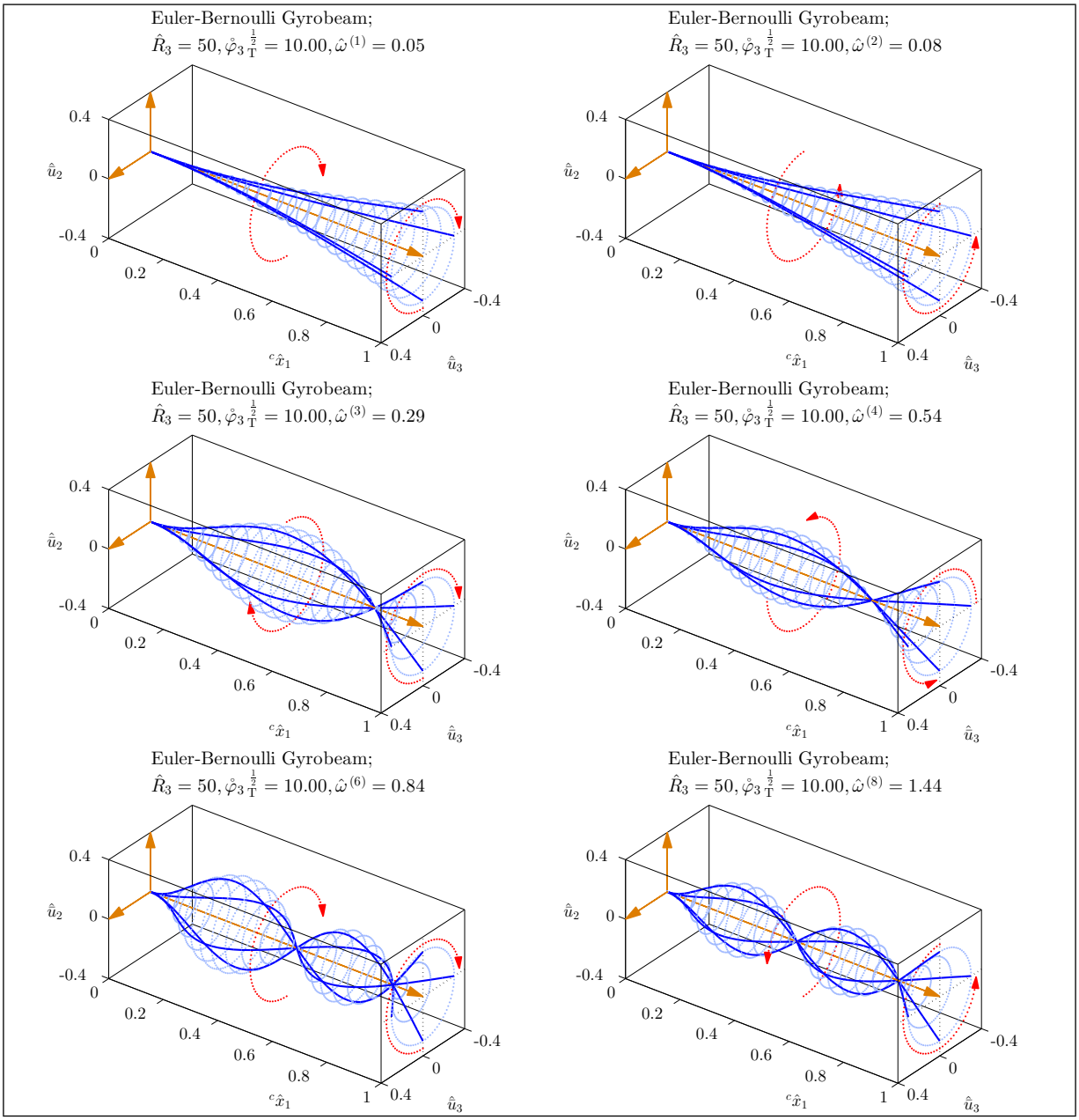

Figure 5.8: Mode shapes of a medium Euler-Bernoulli gyrobeam with a small uniform axial gyricity.

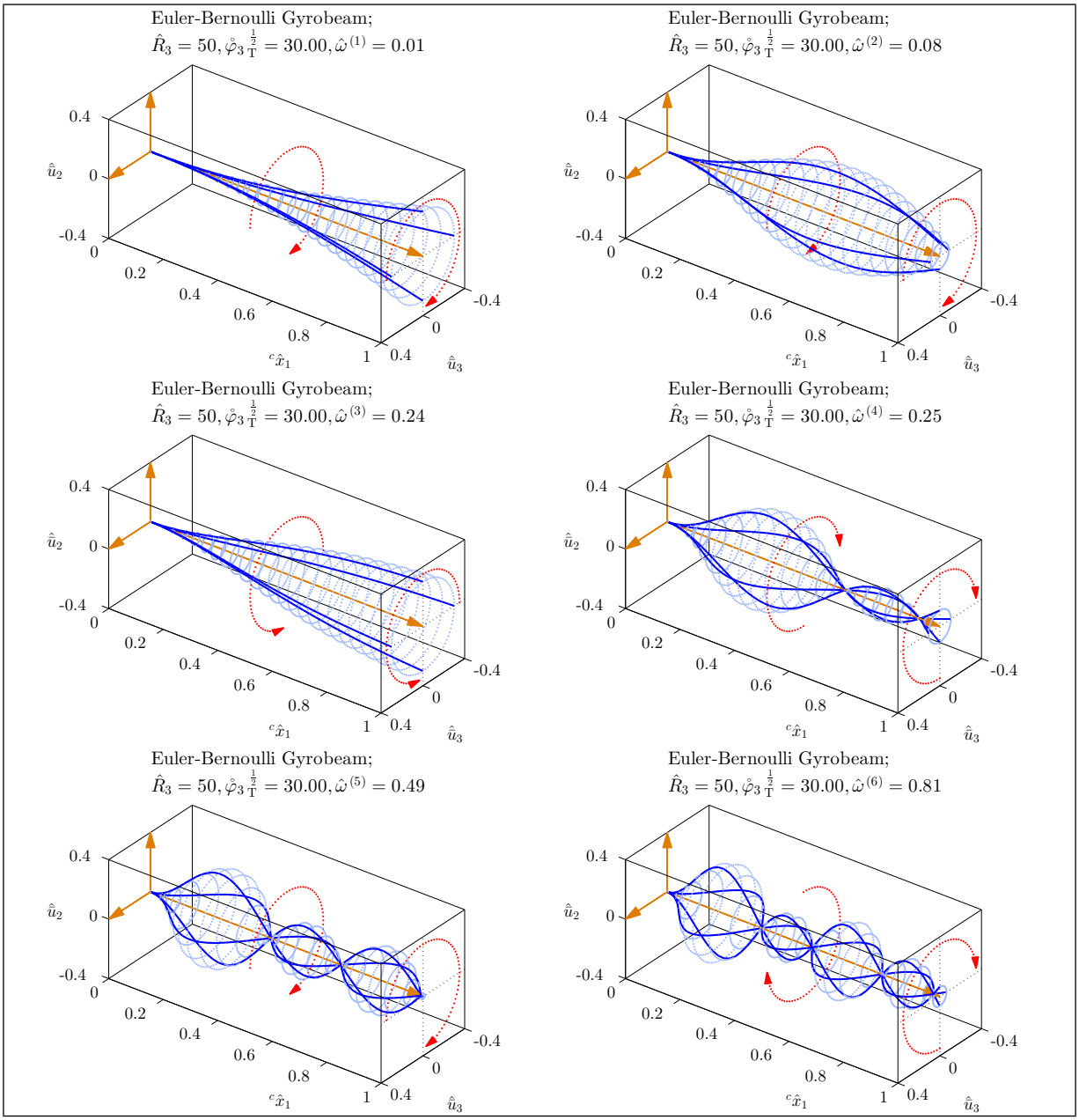

Figure 5.9: Mode shapes of a medium Euler-Bernoulli gyrobeam with a medium uniform axial gyricity.

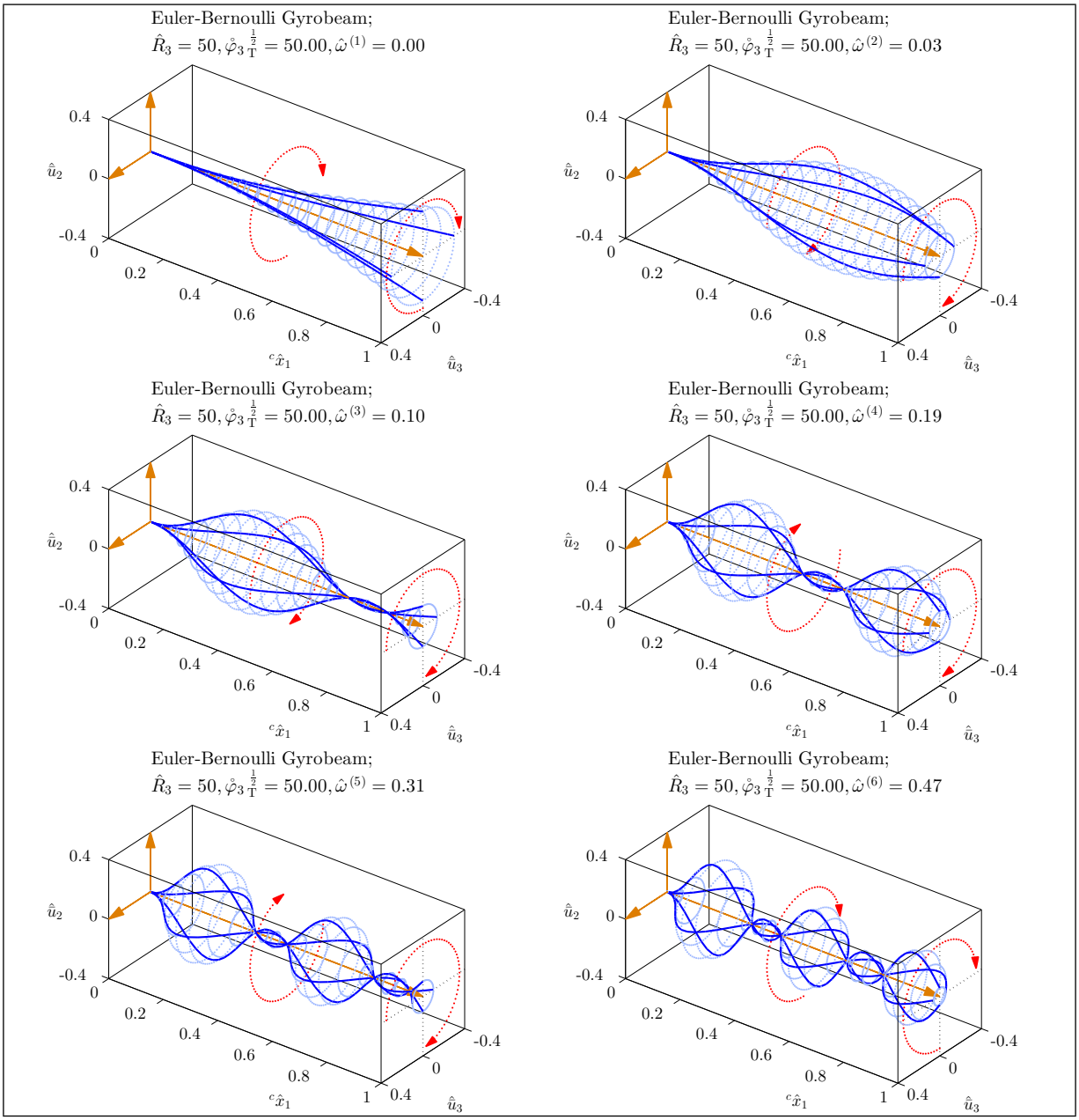

Figure 5.10: Mode shapes of a medium Euler-Bernoulli gyrobeam with a large uniform axial gyricity.

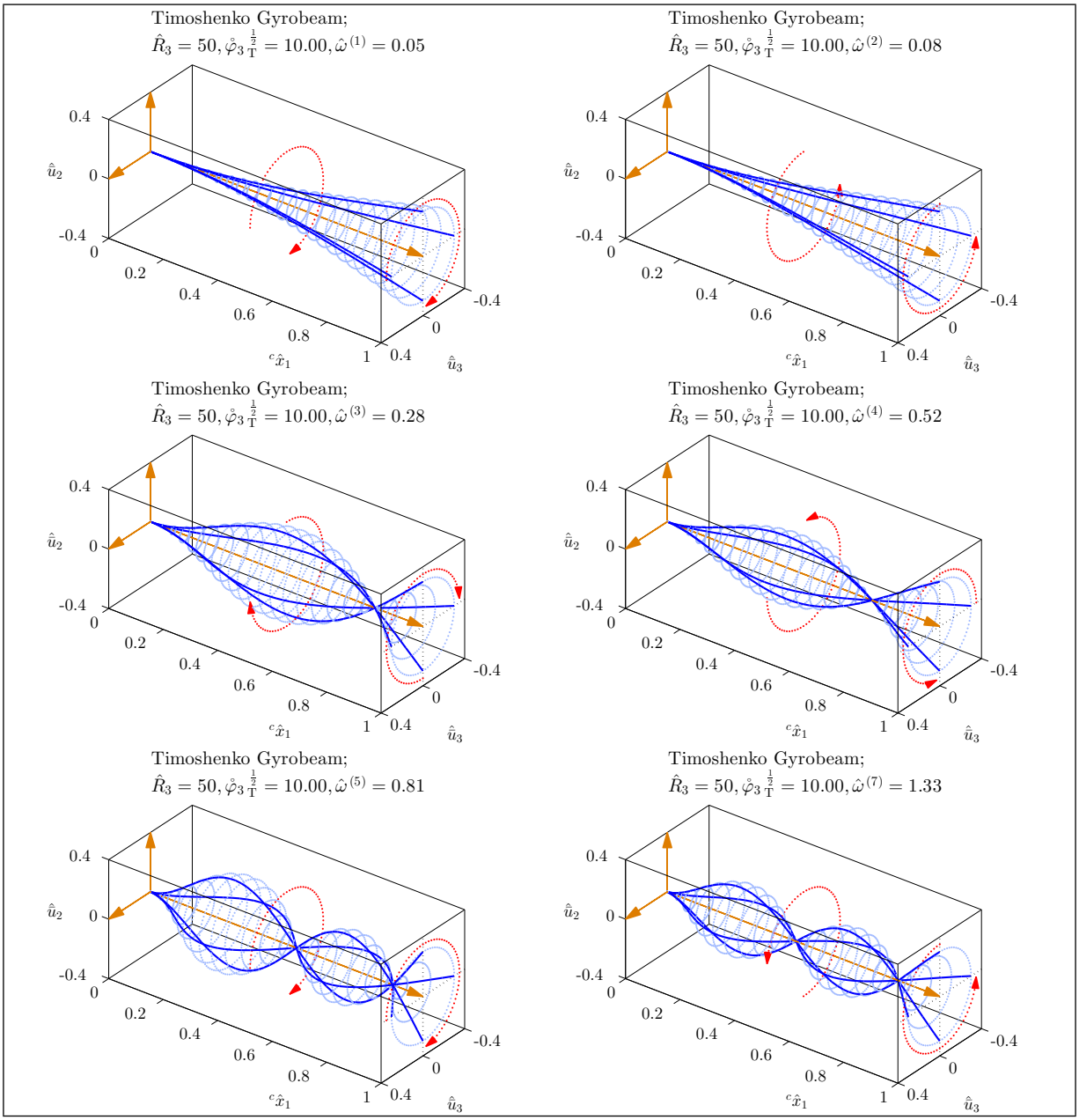

Figure 5.11: Mode shapes of a medium Timoshenko gyrobeam with a small uniform axial gyricity.

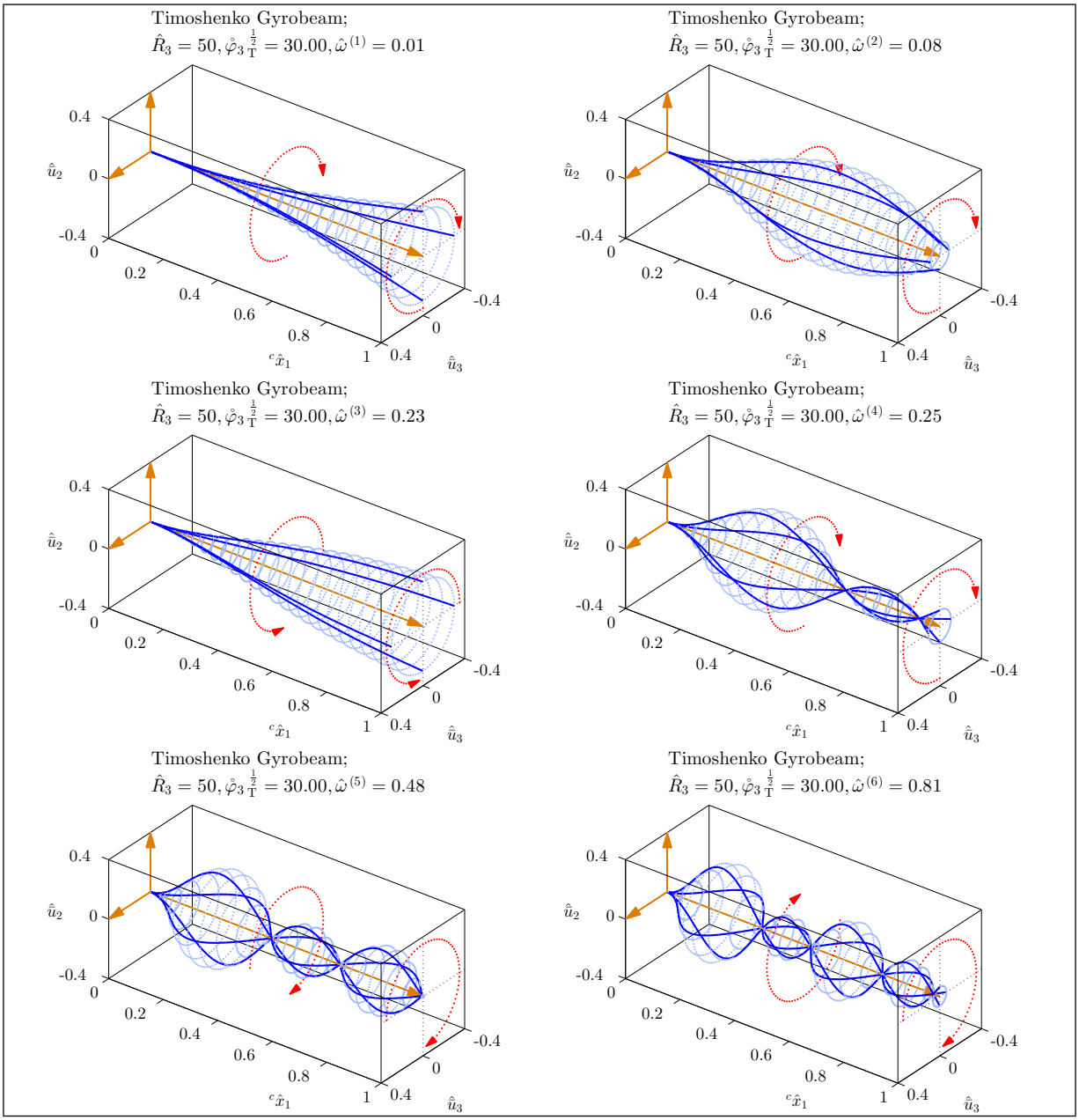

Figure 5.12: Mode shapes of a medium Timoshenko gyrobeam with a medium uniform axial gyricity.

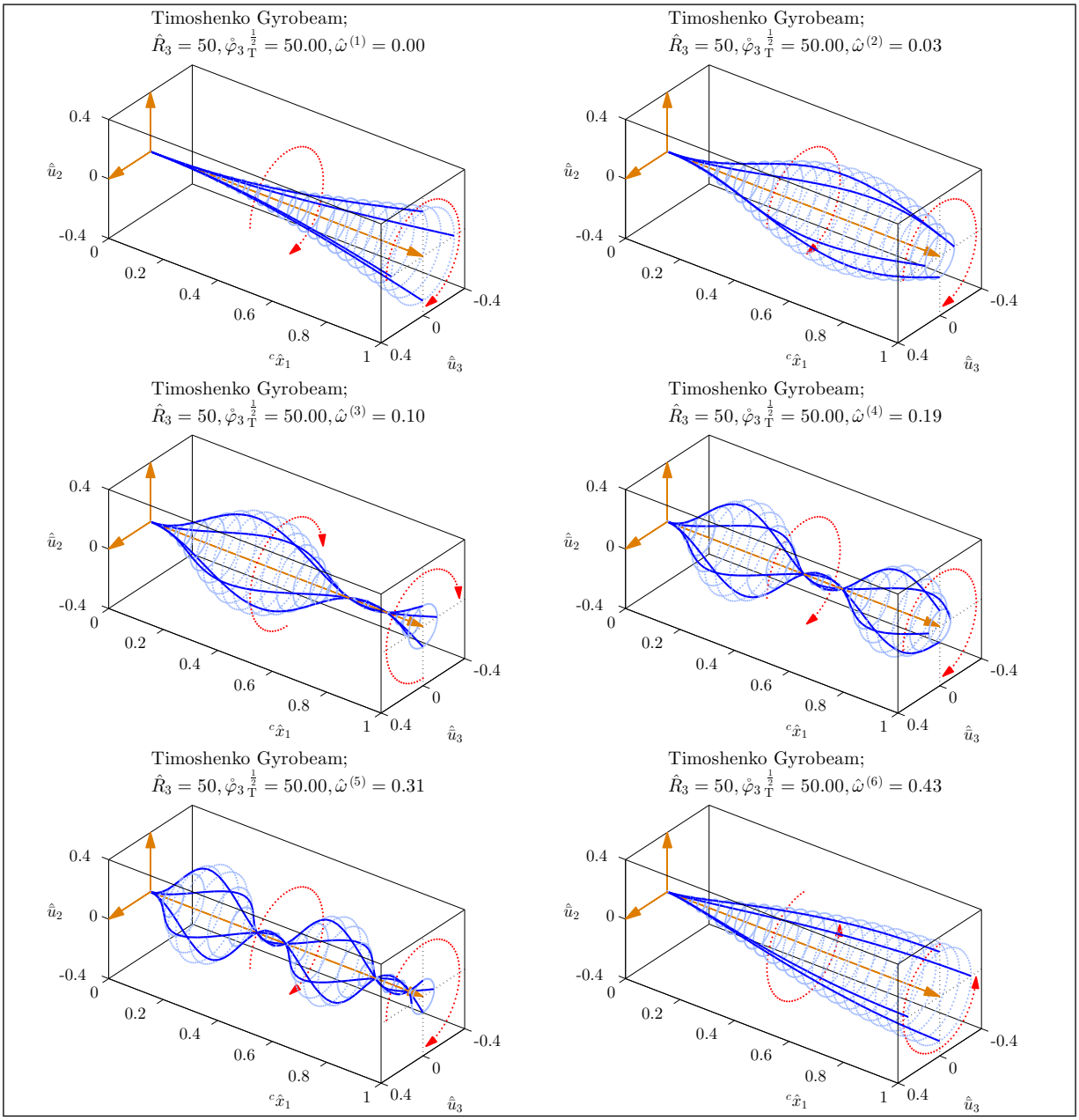

Figure 5.13: Mode shapes of a medium Timoshenko gyrobeam with a large uniform axial gyricity.

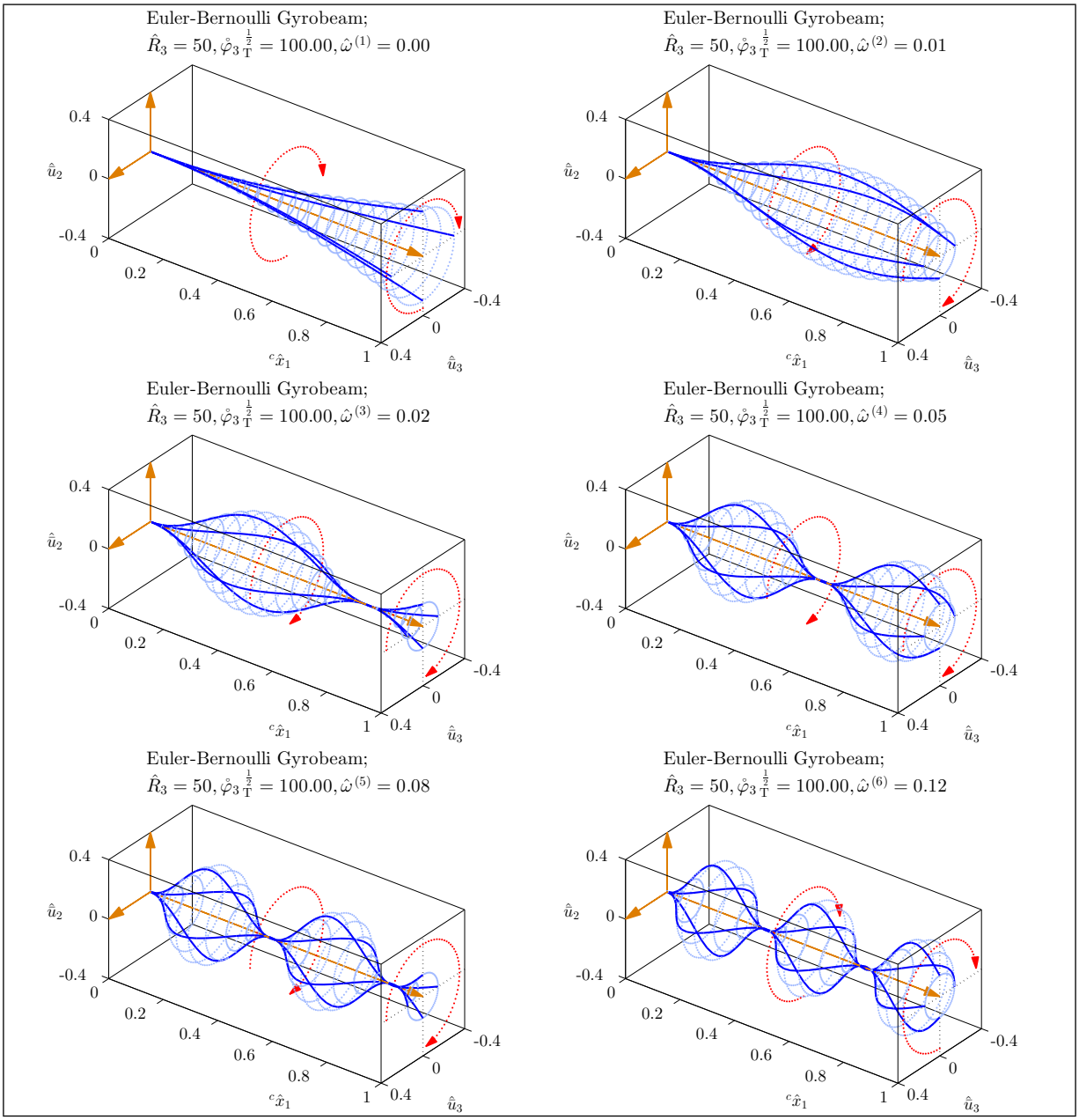

Figure 5.14: Mode shapes of a medium Euler-Bernoulli gyrobeam with a very large uniform axial gyricity.

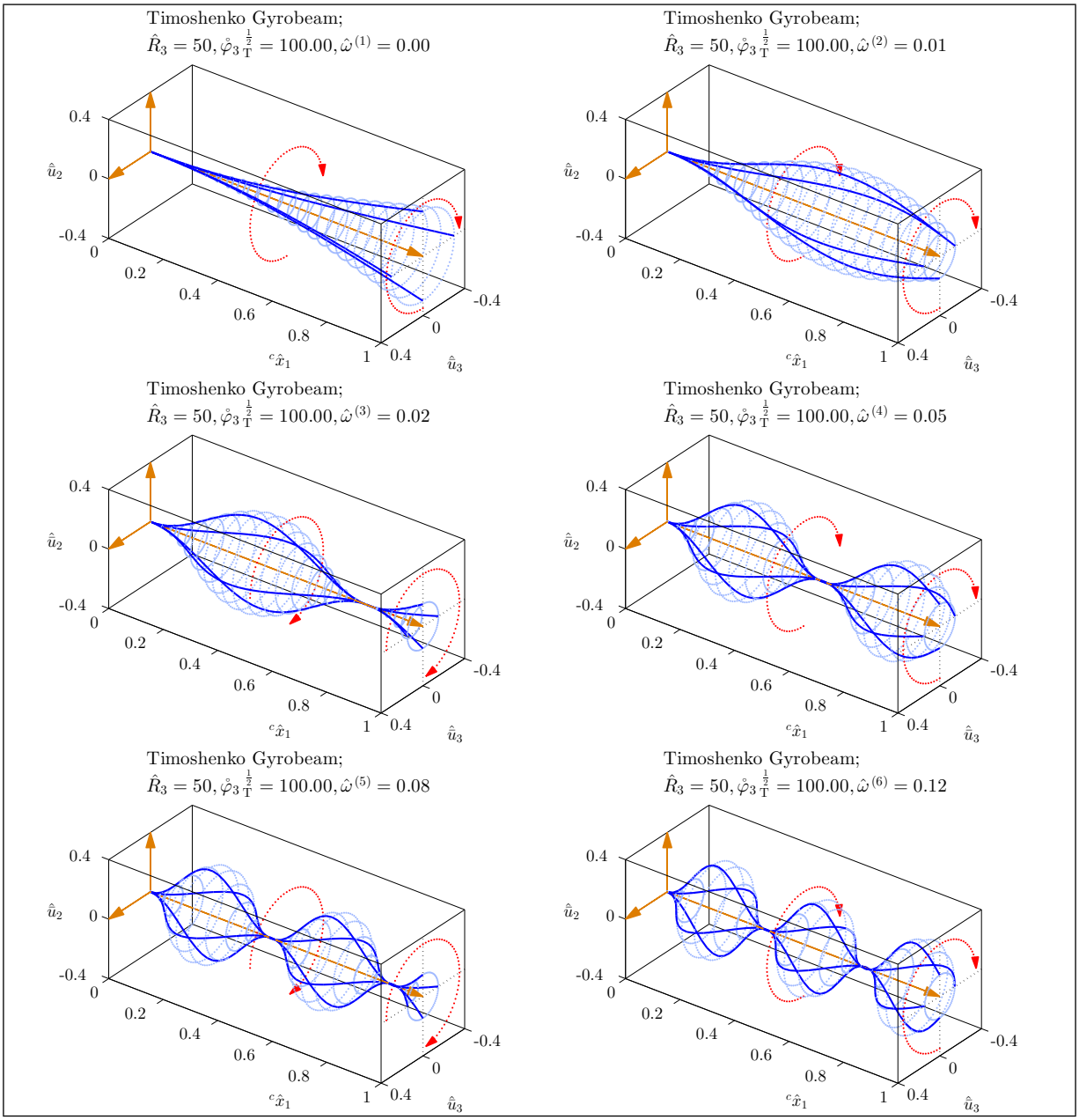

Figure 5.15: Mode shapes of a medium Timoshenko gyrobeam with a very large uniform axial gyricity.

5.3 Uniform transverse gyricity distribution

In a gyrobeam with a transverse gyricity distribution (over the beam length), *i.e.* a constant gyricity perpendicular to the beam's neutral axis, the torsional deformations about the ${}^c\hat{x}_1$ axis are coupled to the bending deformations in the plane spanned by the beam's neutral axis and the gyricity direction (gyros' spin axis). Here, the gyricity distribution is assumed to be in the $\underset{\rightarrow}{c_3}$ direction and, therefore, the torsional deformation mode about the ${}^c\hat{x}_1$ axis is coupled to the bending deformation mode in the ${}^c\hat{x}_1{}^c\hat{x}_3$ plane. These deformation modes, however, remain uncoupled from the gyrobeam longitudinal deformation mode, along the ${}^c\hat{x}_1$ axis, and the other bending deformation mode, in the ${}^c\hat{x}_1{}^c\hat{x}_2$ plane. Indeed, a transverse gyricity with the $\underset{\rightarrow}{c_3}$ direction affects the torsional deformation mode around the ${}^c\hat{x}_1$ axis and the bending deformation mode in the ${}^c\hat{x}_1{}^c\hat{x}_3$ plane while leaving the longitudinal deformation mode, along the ${}^c\hat{x}_1$ axis, and the second bending deformation mode, in the ${}^c\hat{x}_1{}^c\hat{x}_2$ plane, untouched. The schematic of a gyrobeam with such a gyricity distribution, *i.e.* a uniform transverse gyricity in the $\underset{\rightarrow}{c_3}$ direction, is shown in Figure 5.16.

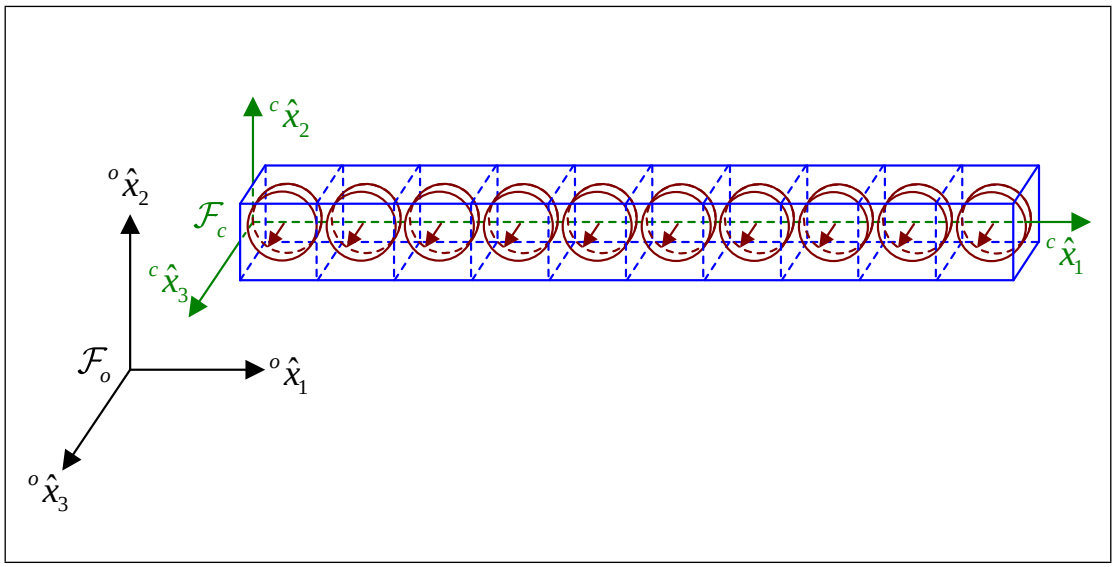

Figure 5.16: A gyrobeam carrying a uniform transverse gyricity distribution.

The variations of the first 25 (gyricity-affected) natural frequencies of three different

Timoshenko and Euler-Bernoulli gyrobeams carrying a uniform transverse gyricity (in the ${}^{c}\hat{x}_3$ direction) with the variation of the gyricity magnitude are shown in Figures 5.17–5.22. The presented natural frequencies correspond to the coupled torsional-bending deformation modes and, therefore, their mode shapes consist of torsional deformations about the ${}^{c}\hat{x}_1$ axis and bending deformations in the ${}^{c}\hat{x}_1{}^{c}\hat{x}_3$ plane.

The natural frequencies of the considered gyrobeams for the zero-gyricity case, when there is no coupling between the deformation modes and the natural frequencies correspond to the separate deformation modes, are shown in the left side of the plots in Figures 5.17–5.22 by single markers. To facilitate tracking of the gyricity effects on longitudinal, torsional, and bending natural frequencies, *i.e.* $\hat{\omega}_{\text{l}}$, $\hat{\omega}_{\text{t}}$, and $\hat{\omega}_{\text{b}}$, they are respectively distinguished by □, ○, and △ symbols (see the legend of each plot in its upper right corner). The gyricity-affected torsional-bending natural frequency curves are then plotted to illustrate the variations of the natural frequencies with the transverse gyricity.

The curve veering phenomenon, though with a lower intensity (or slighter abruption), can be observed again in the plots of Figures 5.17–5.22. Here, a less intense veering means that the transition zones where the veering is happening are generally larger and the changes in the natural frequency loci are mostly smoother and slower. A slower curve veering can be due to a different coupling in gyrobeams with transverse gyricity than that in gyrobeams with axial gyricity. In a gyrobeam with axial gyricity the coupling is between the similar bending deformation modes and this similarity makes the transition, if any, easier and faster. On the contrary, in a gyrobeam with transverse gyricity the coupling is between the unalike torsional and bending deformation modes and this results in a more difficult and slower transition and curve veering. This slower curve veering is much more noticeable in the most slender Timoshenko gyrobeam (see Figure 5.22).

Overall, the veering phenomenon observed in the natural frequencies of a gyrobeam with transverse gyricity (shown in Figures 5.17–5.22) is more unpredictable or irregular compared to that, if any, in the natural frequencies of a gyrobeam with axial gyricity (shown in Figures 5.2–5.7). Again, all the considered torsional-bending natural frequencies finally tend to zero for large enough gyricity.

The slower and more irregular curve veering in Figures 5.17–5.22 make it more difficult

to distinguish any apparent trends for the natural frequencies of the gyrobeams with a transverse gyricity, in comparison to those observed earlier for the gyrobeams with an axial gyricity. For example, although one can notice apparent smooth curves in Figures 5.17, 5.20, and 5.21, they are not as clear as those in Figures 5.2, 5.5, and 5.6, respectively. Also, there is no apparent smooth curves or trends observable in Figures 5.18, 5.19, and 5.22.

Based on Figures 5.17–5.22, the gyricity effects decrease as the beam gets thinner, evidently as the practical proportional relationship between the size of gyros and the beam thickness is presumed.

Again, one can see that the addition of transverse shear effects via the Timoshenko beam model has a very visible effect on the frequency curves especially for the higher frequency modes. However, as expected the differences between the Timoshenko and Euler-Bernoulli gyrobeam models is less apparent in the thinner beams.

The natural frequency loci of Euler-Bernoulli gyrobeams carrying a transverse gyricity in the $\vec{c_3}$ direction are shown in Figures 5.17–5.19. Compared to the natural frequencies of Timoshenko gyrobeams illustrated in Figures 5.20–5.22, the natural frequency loci of Euler-Bernoulli gyrobeams veer more rapidly (this is more clear when comparing the gyrobeams with medium thickness). Also, like in the axial gyricity case, the veering in the Timoshenko gyrobeam natural frequency loci continues to be present (in the lower frequency modes) at much higher values of gyricity than in the Euler-Bernoulli gyrobeam case which is most evident for the short gyrobeams (Figures 5.17 and 5.20).

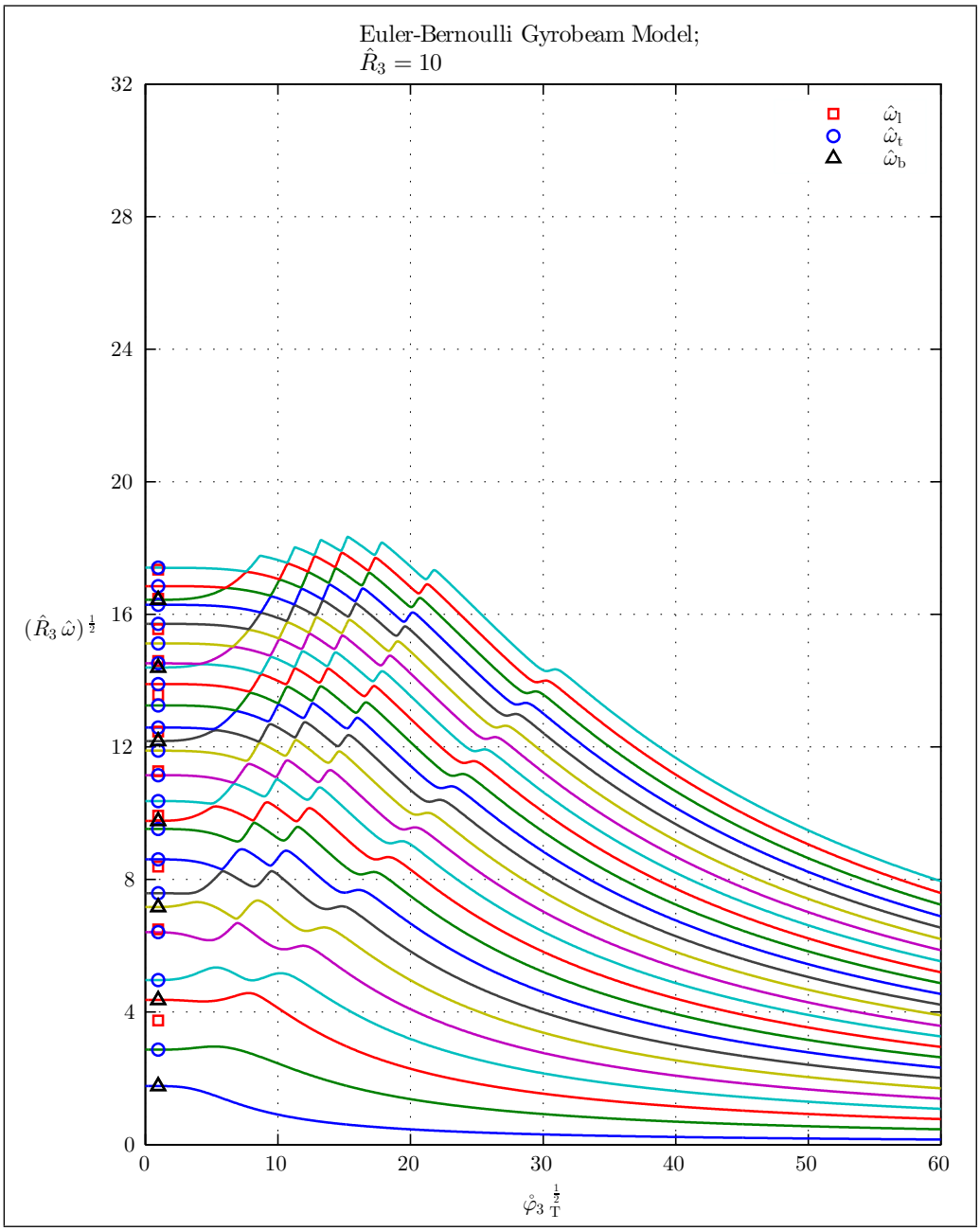

Figure 5.17: Natural frequencies of a thick Euler-Bernoulli gyrobeam with a uniform transverse gyricity.

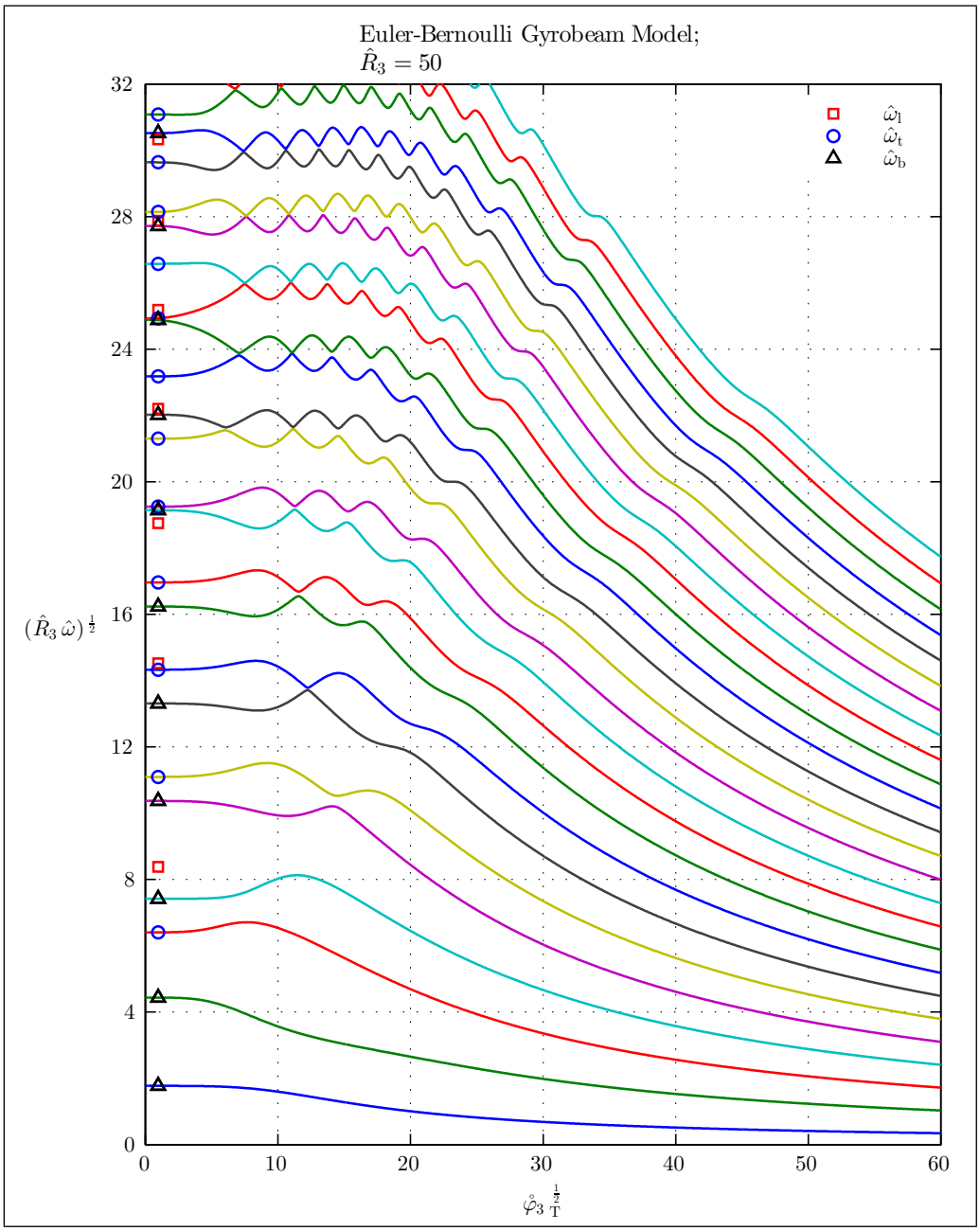

Figure 5.18: Natural frequencies of a medium Euler-Bernoulli gyrobeam with a uniform transverse gyricity.

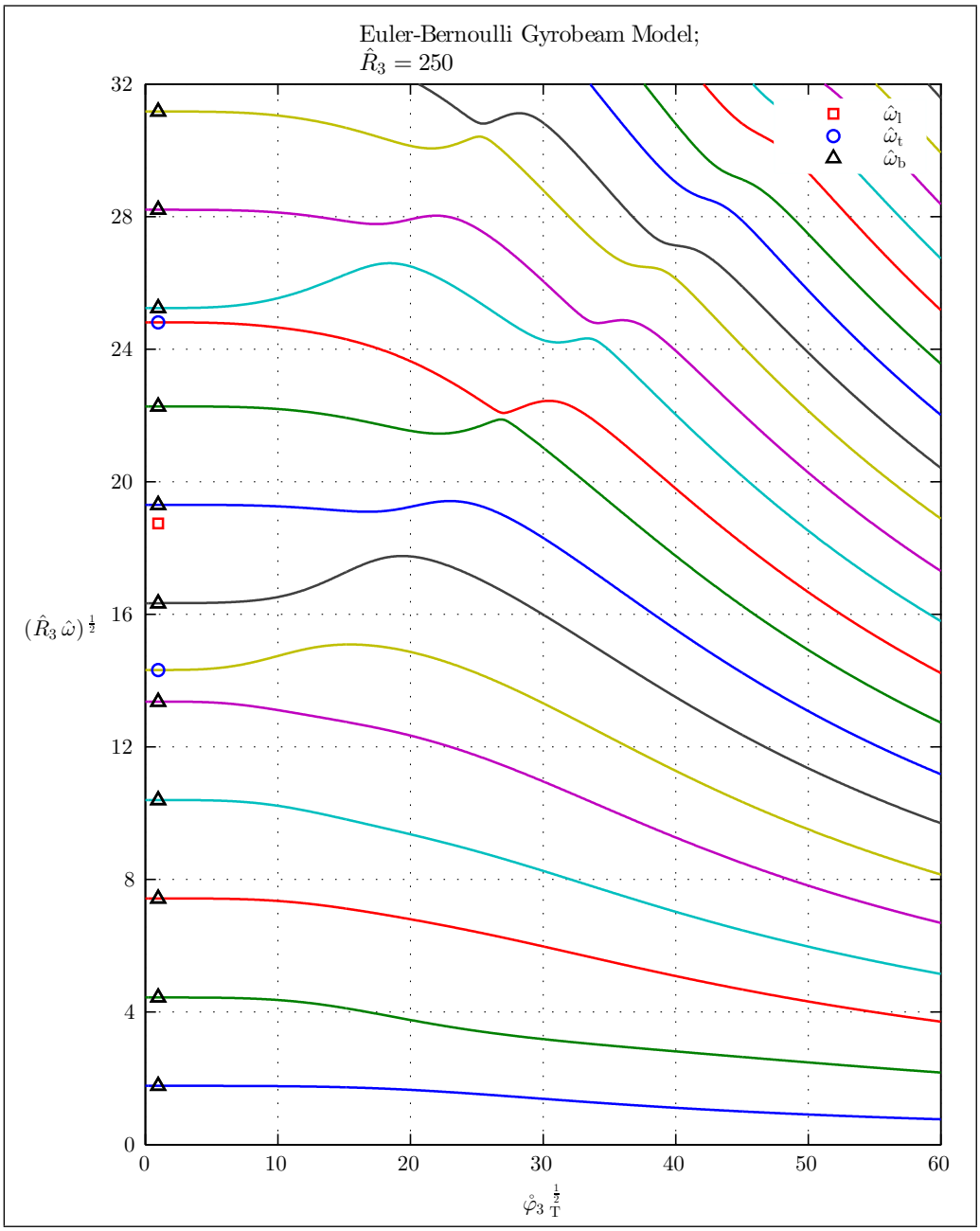

Figure 5.19: Natural frequencies of a thin Euler-Bernoulli gyrobeam with a uniform transverse gyricity.

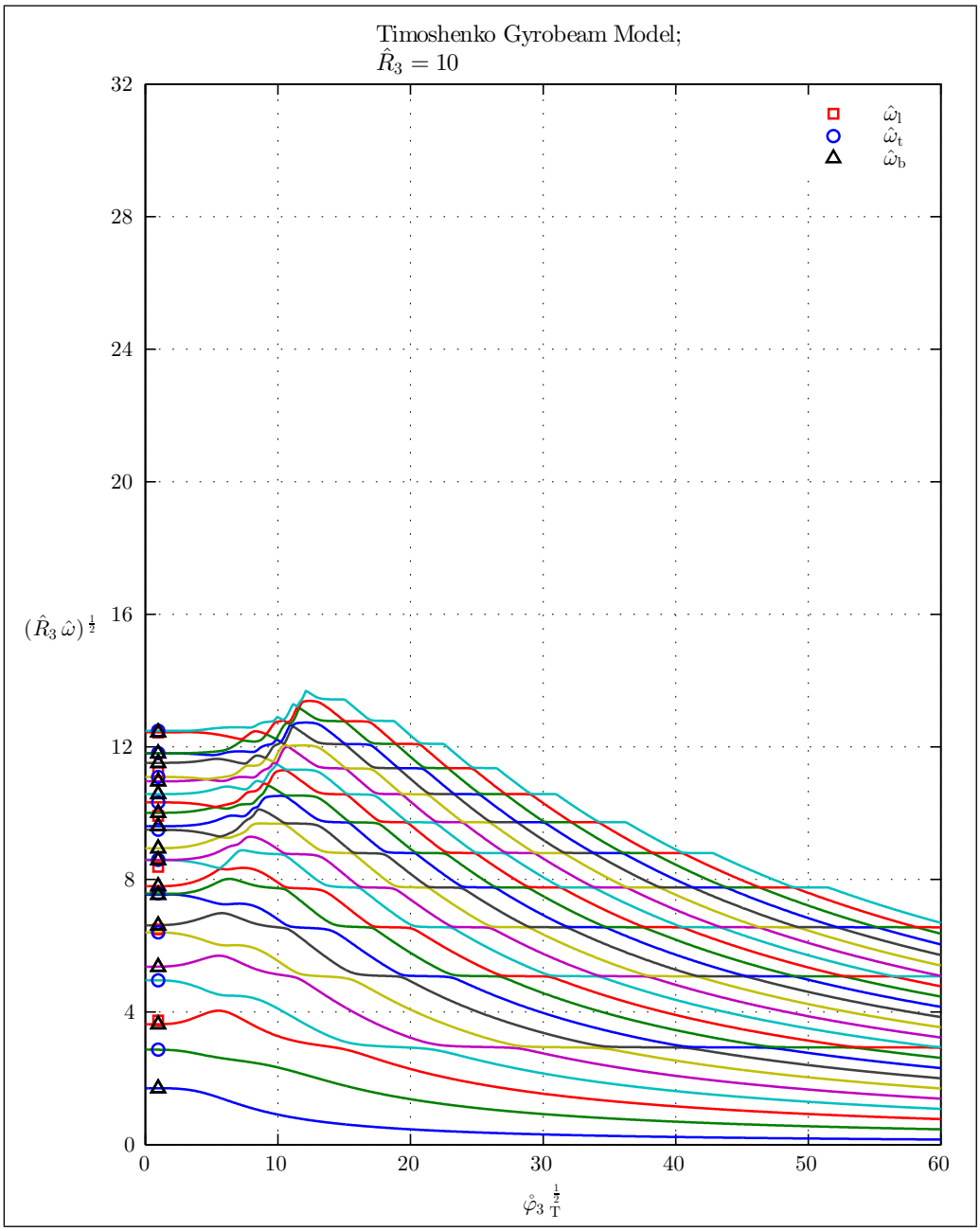

Figure 5.20: Natural frequencies of a thick Timoshenko gyrobeam with a uniform transverse gyricity.

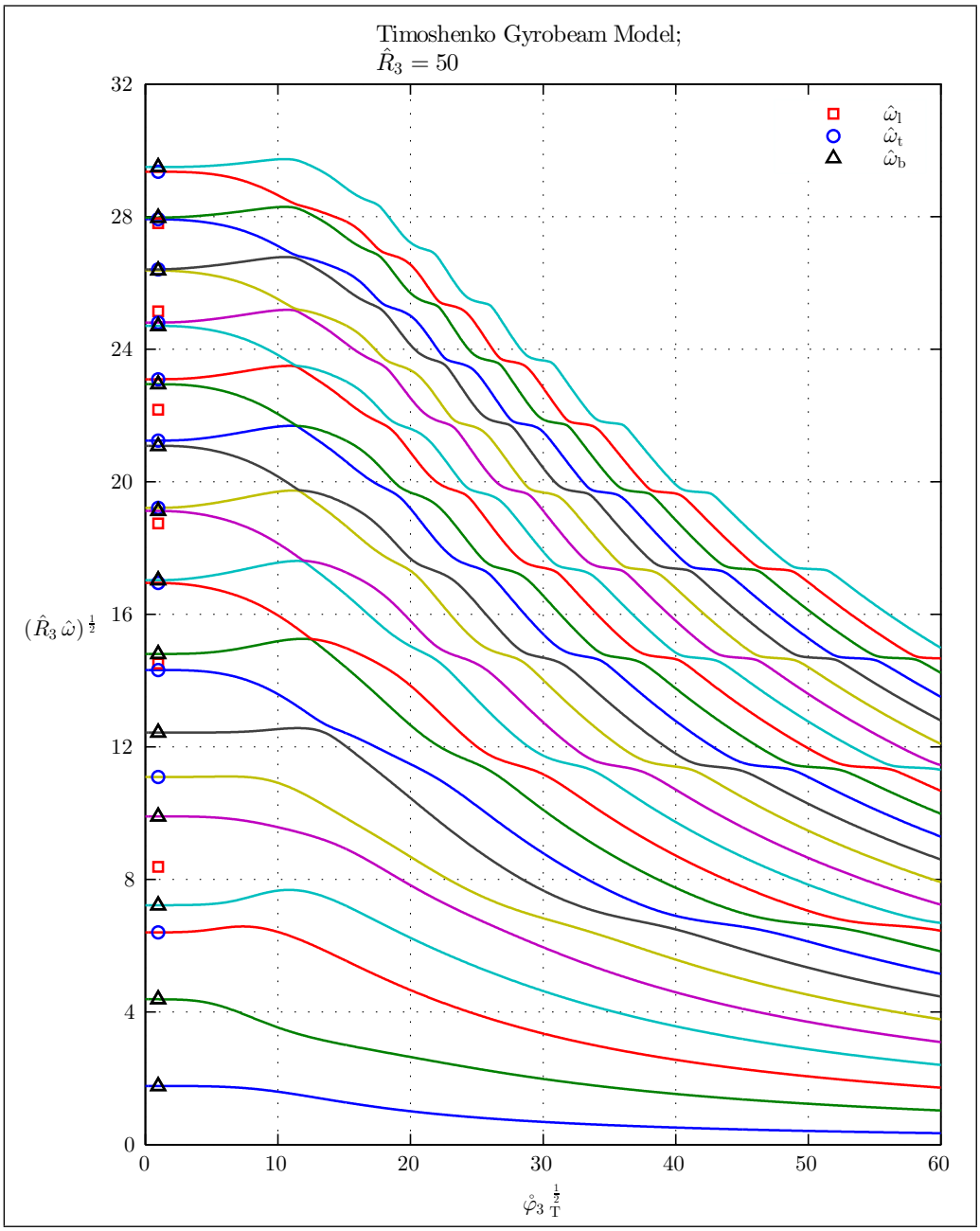

Figure 5.21: Natural frequencies of a medium Timoshenko gyrobeam with a uniform transverse gyricity.

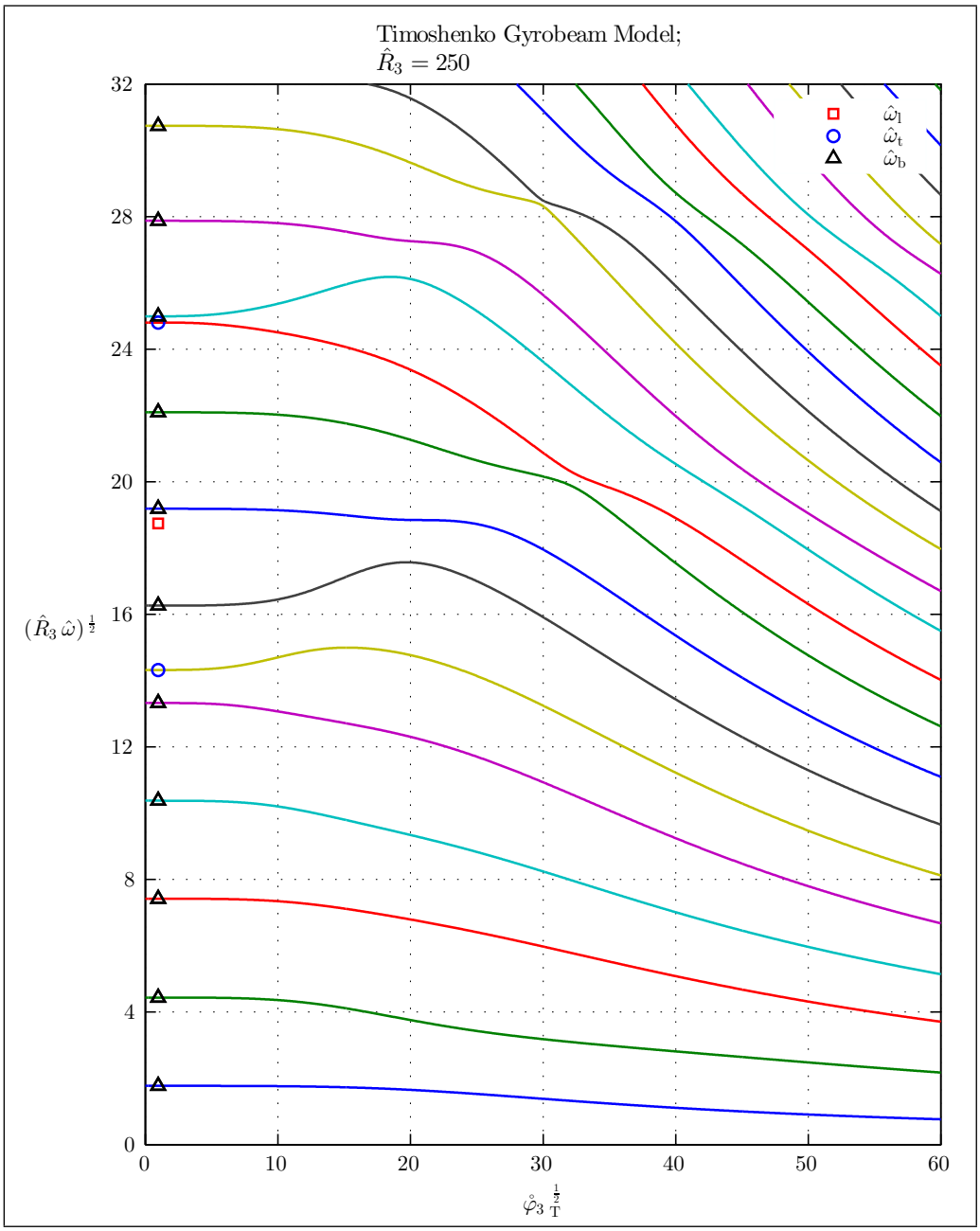

Figure 5.22: Natural frequencies of a thin Timoshenko gyrobeam with a uniform transverse gyricity.

The first six gyricity-affected mode shapes of medium-thickness Euler-Bernoulli and Timoshenko gyrobeams with small, medium, and large transverse gyricity distribution magnitudes in the $\underset{\rightarrow}{c_3}$ direction are plotted in Figures 5.23–5.28. Again, in these figures the mode shapes are numbered based on their actual rank when considering all of the gyricity-affected and gyricity-unaffected vibration modes.

In Figures 5.23–5.28, for gyrobeams with transverse gyricity in the $\underset{\rightarrow}{c_3}$ direction, the mode shapes consist of the torsional deformation mode about the ${}^{c}\hat{x}_1$ axis and the bending deformation mode in the ${}^{c}\hat{x}_1{}^{c}\hat{x}_3$ plane. Note that in these figures the bending portion of each mode shape is plotted in the horizontal plane and colored blue and the torsional portion of each mode shape is plotted in the vertical plane and shown in green.

The vibration in each mode is, indeed, based on the time-variation of the contributions of these torsional and bending deformation modes into the gyrobeam total deformation. Though there is no modal precession (as those seen for axial-gyricity gyrobeams) associated with the mode shapes of transverse-gyricity gyrobeams, there is a "modal transformation" between different states of each mode shape, *i.e.* from a fully torsional mode into a fully bending mode and *vice versa*, which is again done at a velocity which is the same as the natural frequency of the mode shape.

In Figures 5.23–5.28, the direction of the modal transformation for each mode is shown by two pairs of straight arrows; one pair in the middle of the mode shape and one pair at the end of the mode shape. The arrows of each pair show the direction of the evolution (or transformation) for the torsional and bending portions of the mode shape at that point. In other words two pairs of straight arrows illustrate the relative phase of torsional and bending portions in each mode shape.

For example, consider the pair of straight arrows at the end of the mode shape shown in the first (top left) plot of Figure 5.23. The arrow parallel to the $\bar{\theta}_1$ axis (vertical axis) represents the direction of transformation for the torsional portion of the mode shape at its end (from a positive $\bar{\theta}_1$ toward zero in this case). The arrow parallel to the $\hat{\bar{u}}_3$ axis (horizontal axis) corresponds to the direction of transformation for the bending portion of the mode shape at its end (from zero toward a positive $\hat{\bar{u}}_1$ in this case). In other words, the pair of arrows at the end of the mode shape illustrate that the transformation at the

end of the mode shape, during a full cycle, is from a positive $\bar{\theta}_1$ to a positive $\hat{\bar{u}}_3$, then from a positive $\hat{\bar{u}}_3$ to a negative $\bar{\theta}_1$, then from a negative $\bar{\theta}_1$ to a negative $\hat{\bar{u}}_3$, and finally from a negative $\hat{\bar{u}}_3$ to a positive $\bar{\theta}_1$. The modal transformation in the middle of the mode shape represented by the other pair of straight arrows is the same. Considering both pairs of arrows in the first plot of Figure 5.23, they illustrate that starting from a positive fully torsional mode (where the bending mode contribution is zero), the contribution of the torsional mode to the total mode shape decreases while the contribution of the bending mode increases, and finally, the mode shape transforms into a positive fully bending mode (where the torsional mode contribution is zero).

Analogous to the sense of precession associated with the mode shapes of the axial-gyricity gyrobeams, one can define a sense of transformation for the mode shapes of the transverse-gyricity gyrobeams; *e.g.* a positive sense if the transformation is from a positive torsional rotation to a positive bending displacement (or equivalently from a positive bending to a negative torsion, a negative torsion to a negative bending, and a negative bending to a positive torsion) and a negative sense provided the transformation is from a positive bending displacement to a positive torsional rotation (or equivalently from a positive torsion to a negative bending, a negative bending to a negative torsion, and a negative torsion to a positive bending). Again there might be complex mode shapes for which such a definition does not work well because of different modal transformation directions at different portions of the mode shape (see for example the mode shapes shown in the right column plots of Figure 5.23). Based on this convention the first mode shapes shown in Figure 5.23 (*i.e.* in the top left plot), for example, has a positive modal transformation.

Again, except for the sixth gyricity-affected mode shapes (eighth mode shapes if counting all the gyricity-affected and gyricity-unaffected modes) corresponding to a medium transverse gyricity (shown in the bottom right plots of Figures 5.24 and 5.27), there is no significant difference between the mode shapes of medium-thickness Euler-Bernoulli and Timoshenko gyrobeams with the small, medium, and large transverse gyricity distributions as shown in Figures 5.23–5.28. Even the difference between the natural frequency values is negligible for the large transverse gyricity. Regarding the aforementioned sixth gyricity-affected mode, shown in the bottom right plots of Figures 5.24 and 5.27, their variation is likely due to the more severe curve veering which the Euler-Bernoullli mode

shape experience during its path (see the sixth natural frequency locus, counting from the bottom, in Figure 5.18 and compare it against the corresponding locus in Figure 5.21).

Comparing the plots corresponding to the small, medium, and large transverse gyricity distributions for both Euler-Bernoulli and Timoshenko gyrobeams, it is interesting how the increase of transverse gyricity regulates the location of the nodes in the torsional and bending portions of the mode shapes; the nodes are rearranged such that the torsional portion nodes are placed where the bending portion has a node or a local maximum (see Figures 5.23–5.28). One may also notice how the nature of nodes changes during this relocation; whereas at small transverse gyricity the torsional and bending portions of mode shapes may possess both tangential nodes and central nodes, at large transverse gyricity the torsional portions own only central nodes and the bending portions have only tangential nodes. The transition from central nodes to tangential nodes and *vice verse* is through double central nodes.

Finally, it is worthy to note that, for both Euler-Bernoulli and Timoshenko gyrobeams, the ends of the bending portion of even gyricity-affected modes (*i.e.* the second, fifth, and seventh modes when considering all the modes), shown in the right column of Figures 5.25 and 5.28, move toward the ${}^{c}\hat{x}_1$ axis for large transverse gyricity.

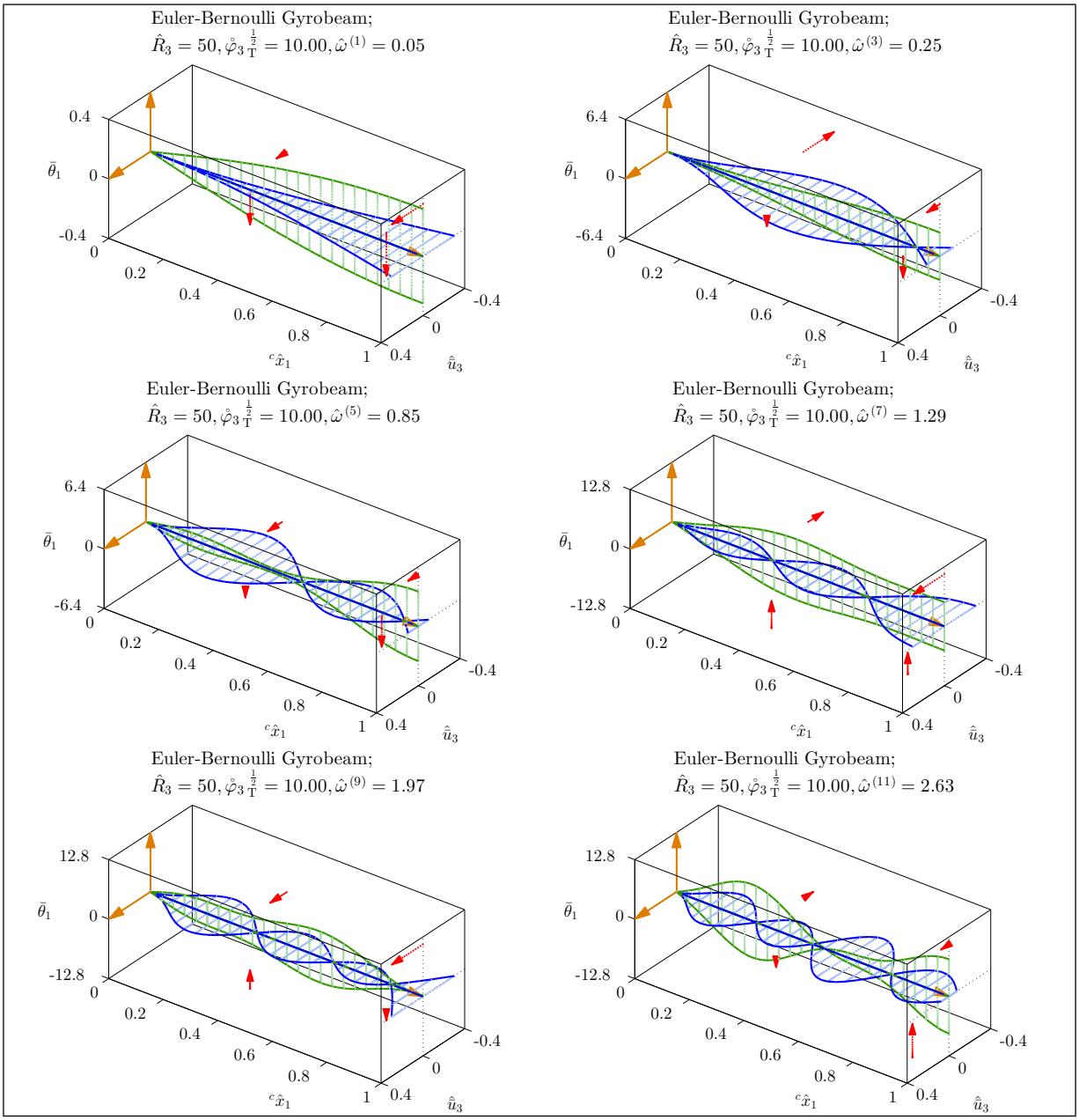

Figure 5.23: Mode shapes of a medium Euler-Bernoulli gyrobeam with a small uniform transverse gyricity.

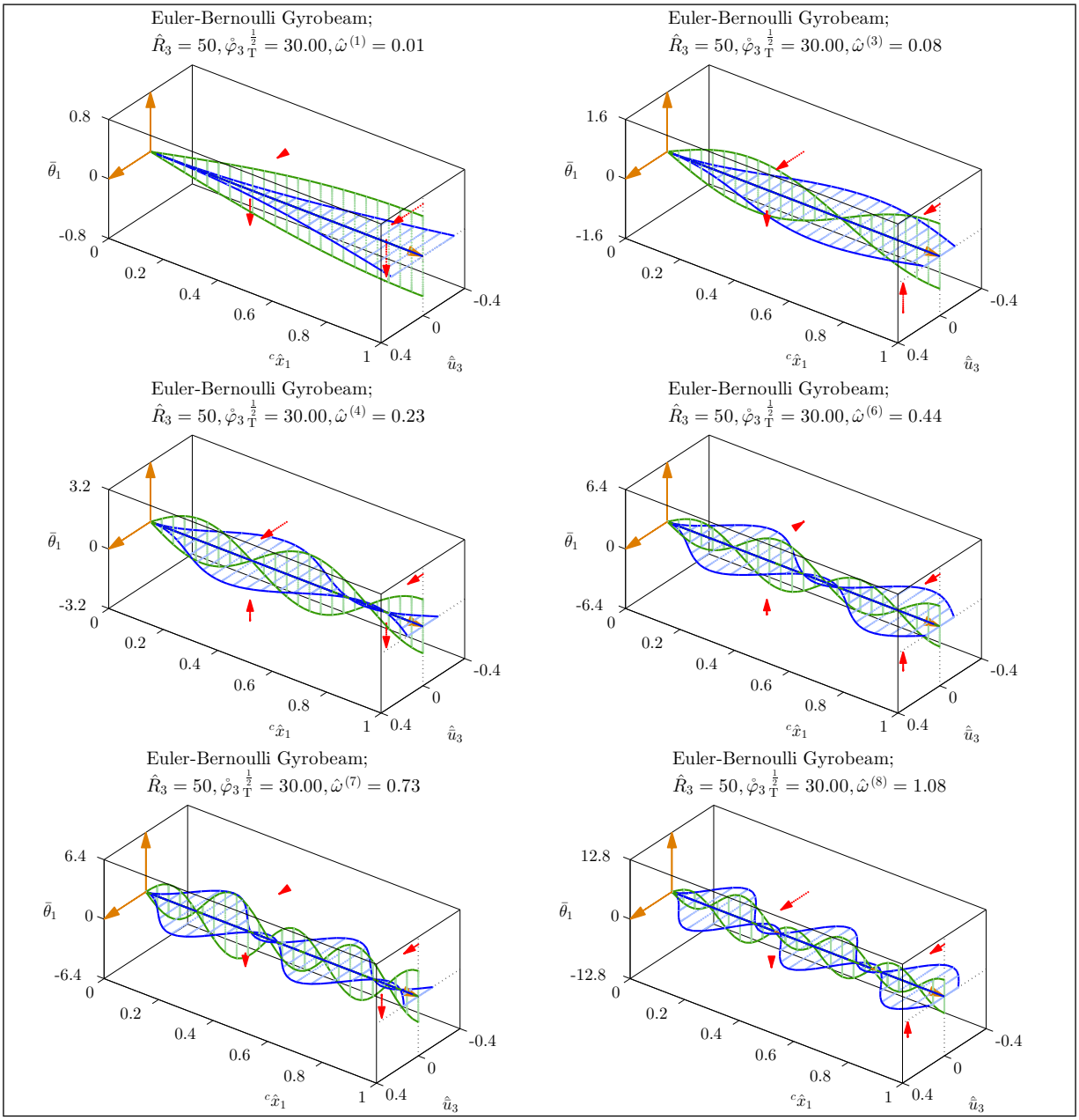

Figure 5.24: Mode shapes of a medium Euler-Bernoulli gyrobeam with a medium uniform transverse gyricity.

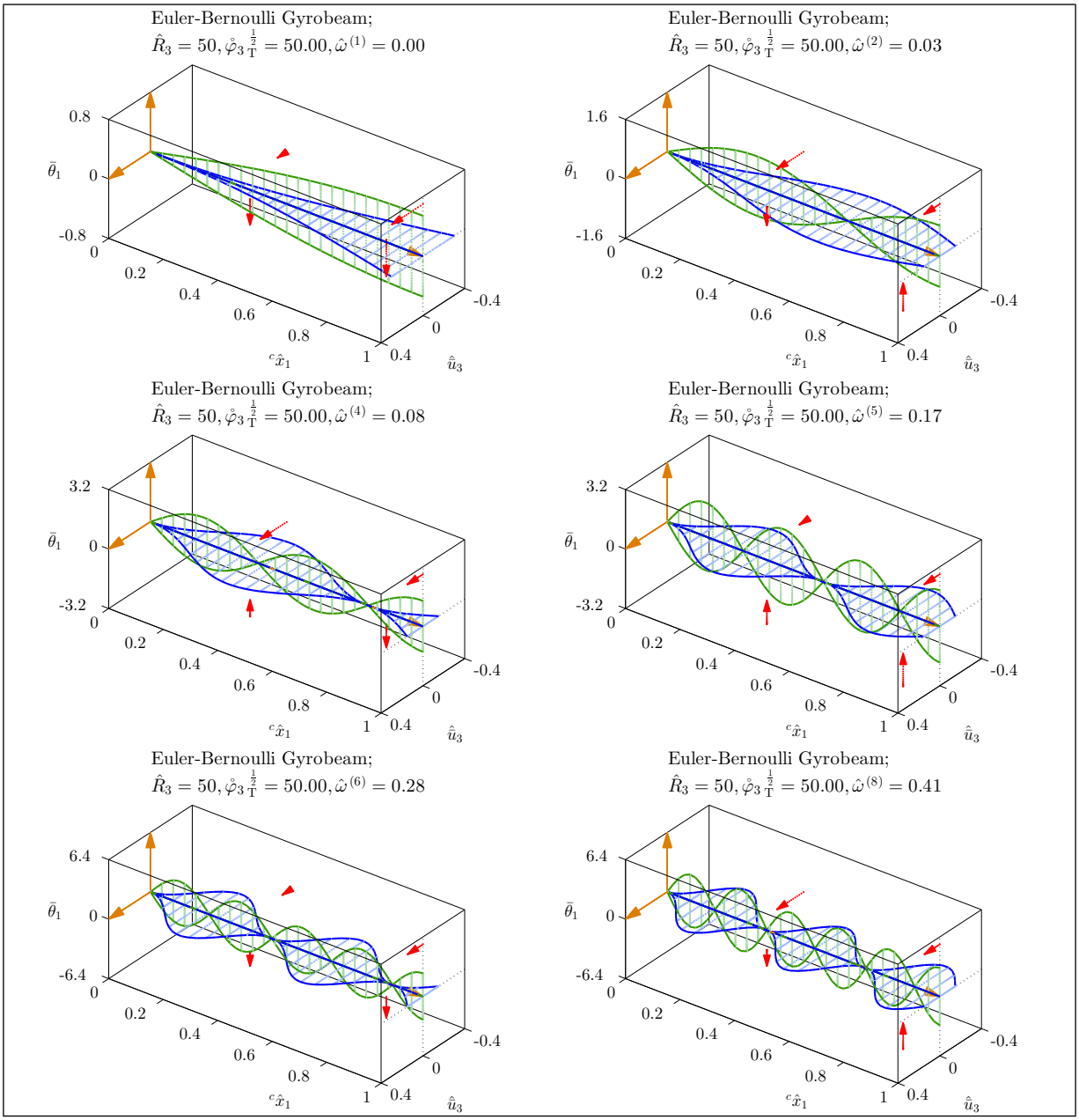

Figure 5.25: Mode shapes of a medium Euler-Bernoulli gyrobeam with a large uniform transverse gyricity.

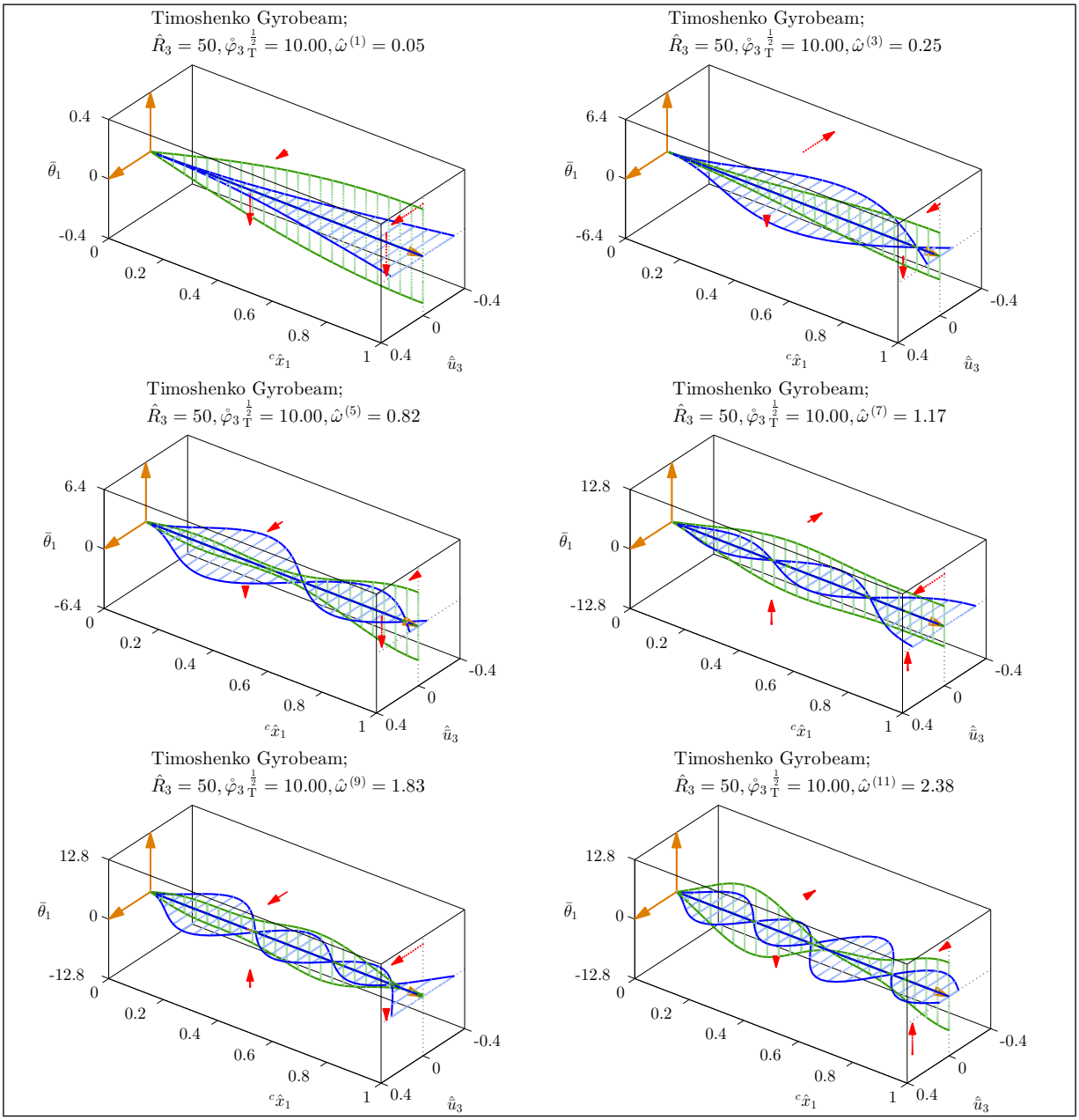

Figure 5.26: Mode shapes of a medium Timoshenko gyrobeam with a small uniform transverse gyricity.

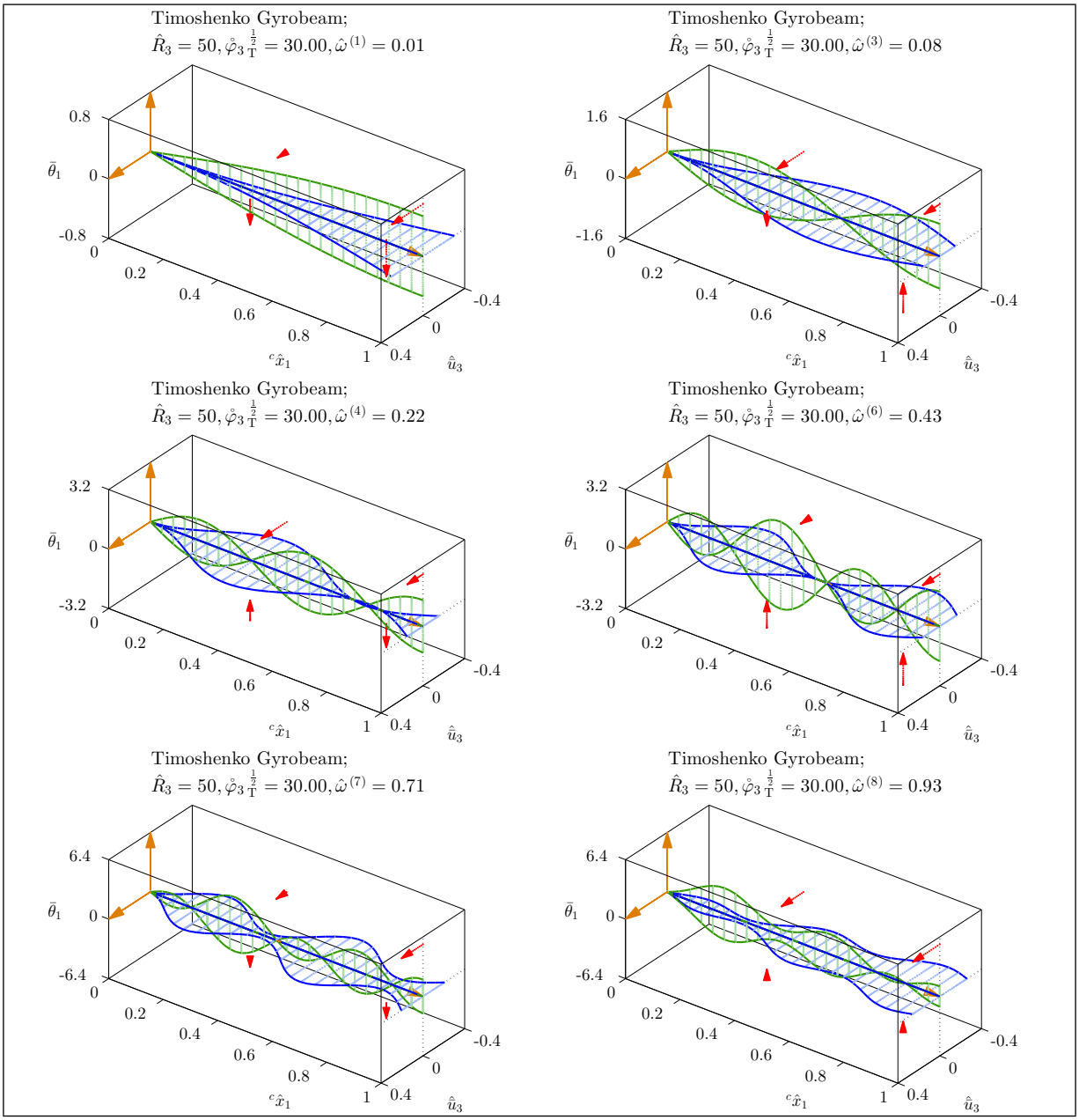

Figure 5.27: Mode shapes of a medium Timoshenko gyrobeam with a medium uniform transverse gyricity.

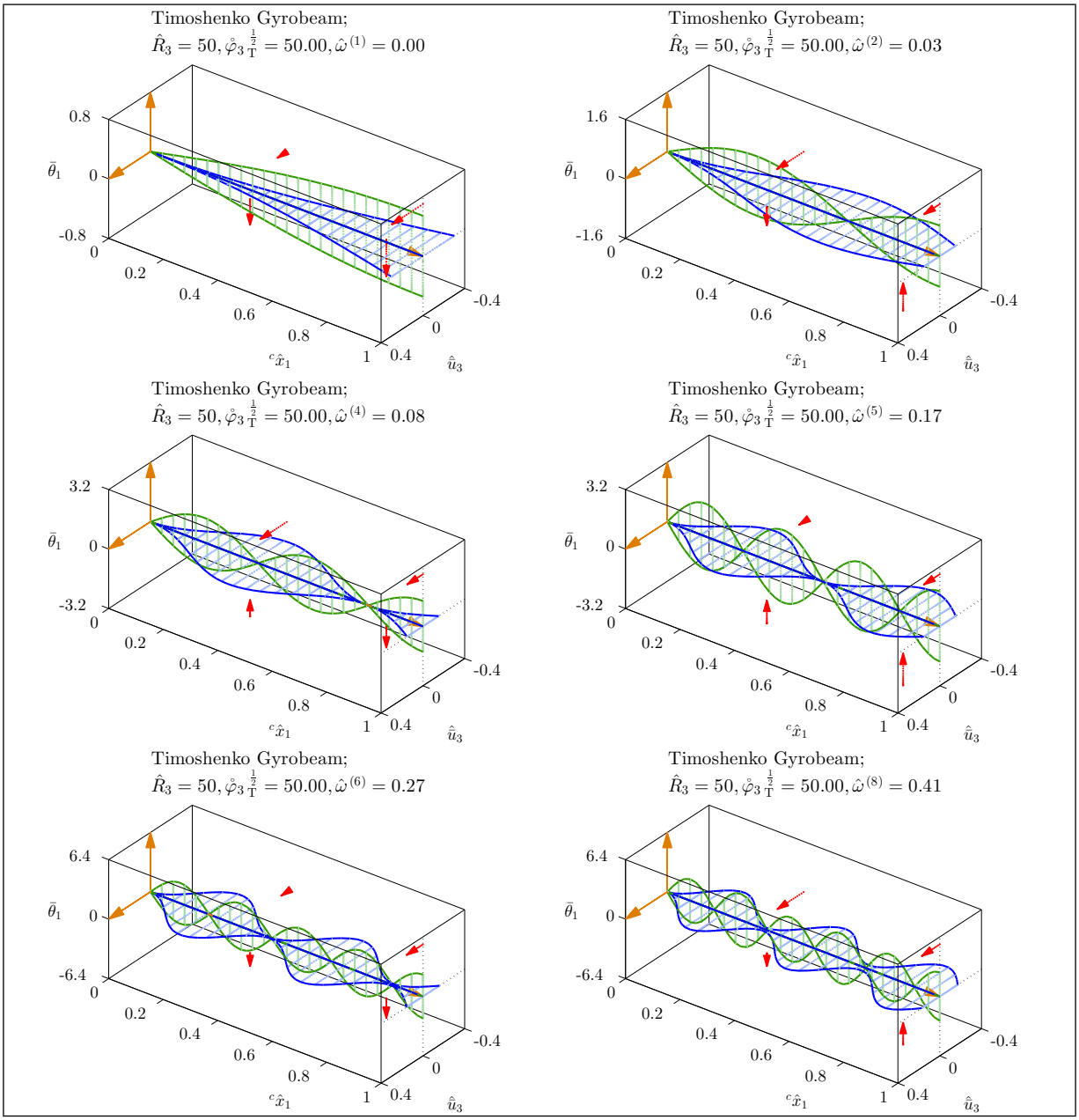

Figure 5.28: Mode shapes of a medium Timoshenko gyrobeam with a large uniform transverse gyricity.

5.4 Curve veering

As mentioned in the previous sections, the natural frequency loci of gyrobeams seem to cross over each other. However, a closer look, at the points where the natural frequency curves appear to simply cross, indicates that, indeed, a veering occurs between the natural frequency loci in (some of) these points [2, 16]. This very strange and interesting curve veering phenomenon is in conjunction with a strange drastic change of the mode shapes corresponding to the veering natural frequencies. Indeed, in the regions where curve veering occurs the mode shapes undergo dramatic, albeit continuous, changes during which the mode shapes (*i.e.* eigenvectors) associated with the veering natural frequencies (*i.e.* eigenvalues) are interchanged by exchanging their characteristics. This is the reason why the regions where the curve veering takes place are called "transition zones" [67–70]. The continuous change of mode shapes in the transition zones where the mode shapes are interchanged suggests that strange mode shapes can be seen near these zones. Whereas a thorough examination of curve veering and its associated abrupt changes of mode shapes is left for future work, this section provides a few examples for dramatic changes of mode shapes in the vicinity of curve veering points (or zones).

Consider the natural frequency loci of the medium-thickness Timoshenko gyrobeam with the uniform axial and transverse gyricity distributions which were previously plotted in Figures 5.6 and 5.21 and are repeated in Figures 5.29 and 5.30. In the latter figures two (arbitrarily selected) curve veering zones are also shown in which the drastic change of the mode shapes will be investigated.

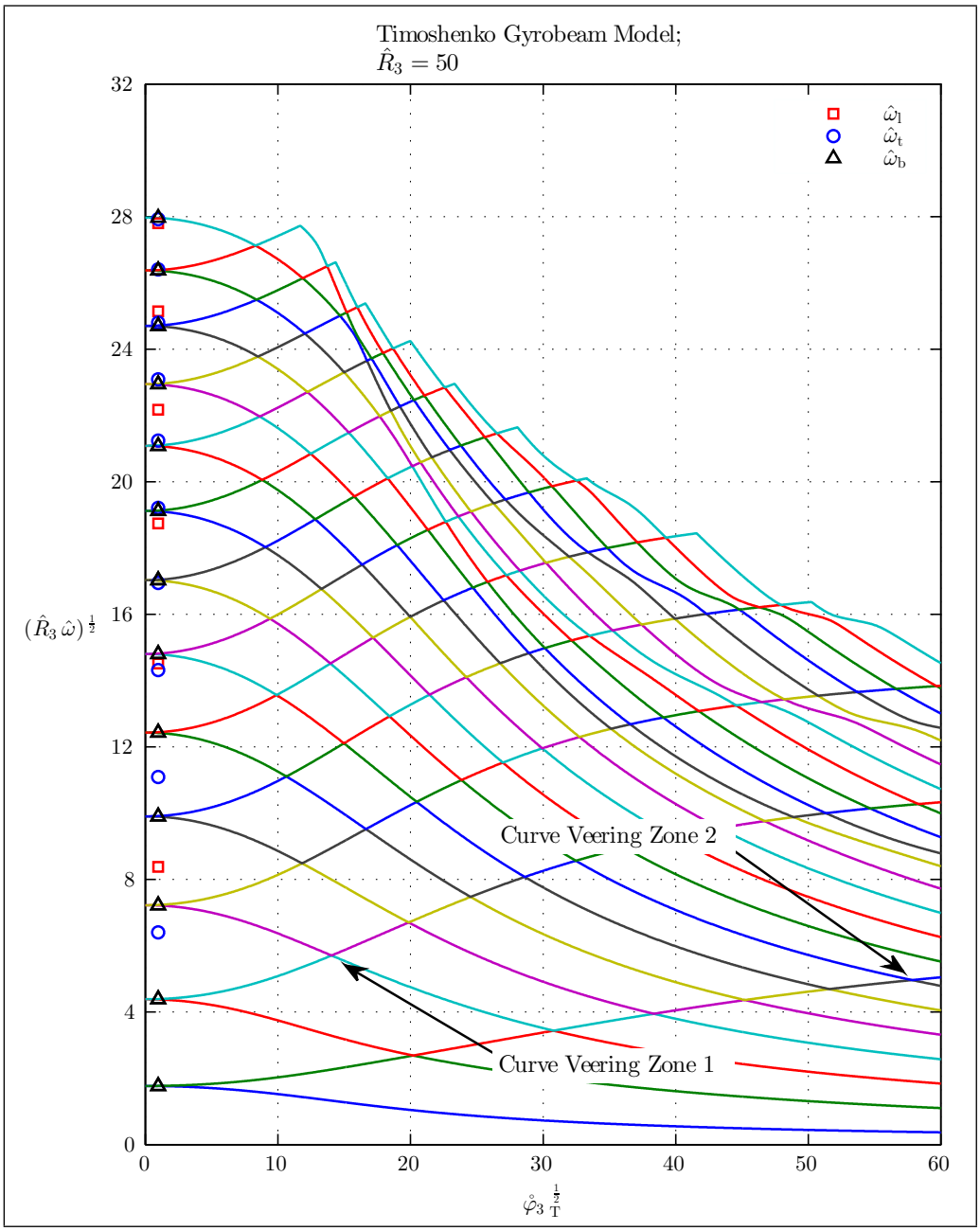

Figure 5.29: Selected curve veering zones in natural frequency loci of a medium Timoshenko gyrobeam with a uniform axial gyricity.

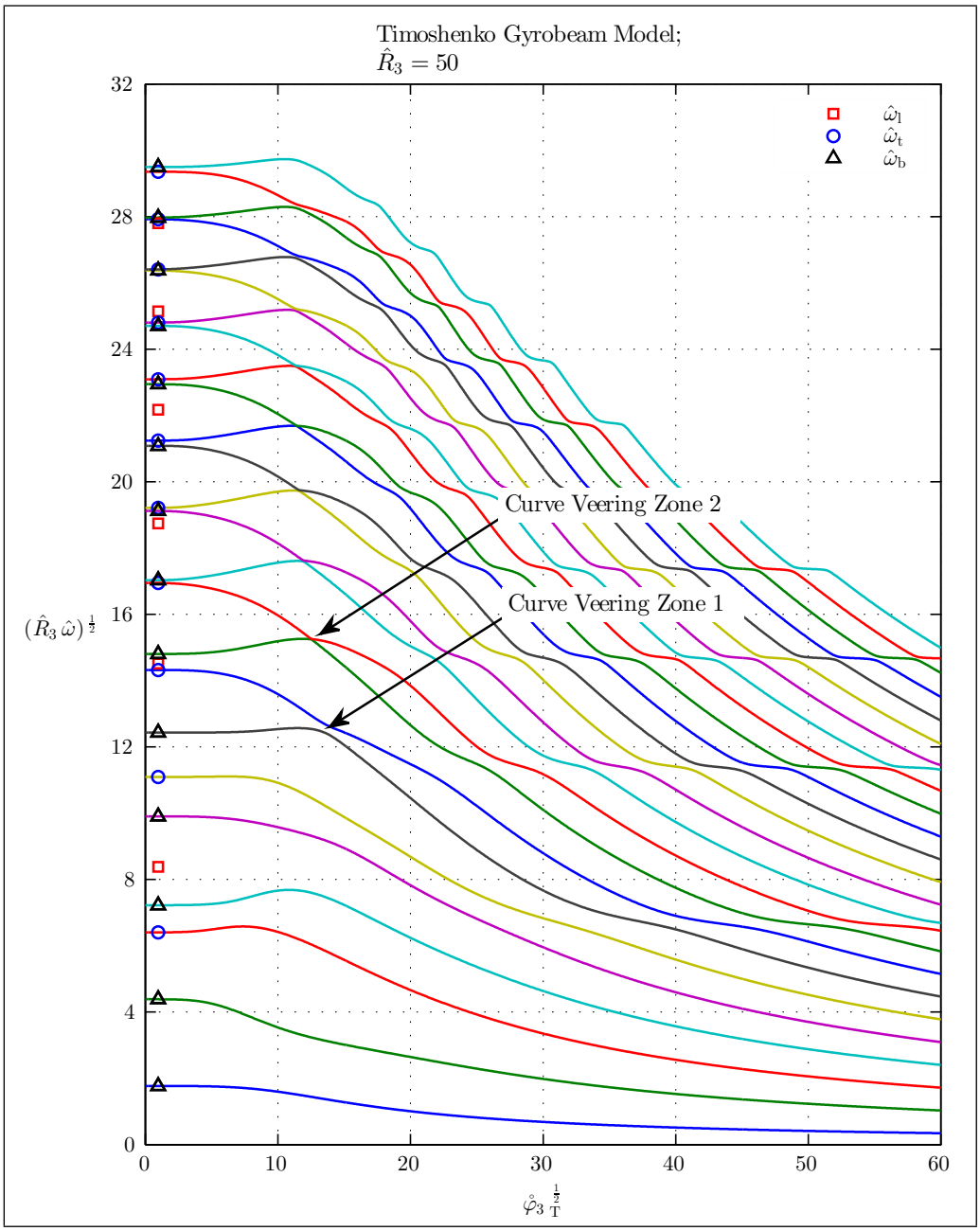

Figure 5.30: Selected curve veering zones in natural frequency loci of a medium Timoshenko gyrobeam with a uniform transverse gyricity.

In the first zone in Figure 5.29 the veering occurs between the fourth and fifth natural frequencies. The mode shapes associated with these frequencies for six different gyricity values inside the veering zone are plotted in Figures 5.31 and 5.32. It can be seen in these figures that the fourth and fifth mode shapes exchange their characteristic; the fourth mode shape "acquires a node" and rotates with a retrograde precession while the fifth mode shape "sheds a node" and rotates with a prograde precession.

The veering in the second zone is between the seventh and eighth natural frequencies. The mode shape transition in this zone is shown in Figures 5.33 and 5.34. Whereas the mode number changes just by one between these two, there are major differences between these mode shapes right before the curve veering zone (this can be seen by comparing the top left plots of Figures 5.33 and 5.34). Therefore, as one may guess, they undergo very violent changes in the trnasition zone to interchange their characteristics (*i.e.* their nodes and precession sense). As shown in Figures 5.33 and 5.34, in the transition zone the seventh mode shape "acquires multiple nodes" while the eighth mode shape "sheds multiple nodes".

One may observe in Figures 5.31–5.34 how a very small change in the gyricity value causes drastic changes in the mode shapes. Indeed, the very high sensitivity of the mode shapes to the gyricity value in the transition zones raises questions about the nature of abrupt mode shape changes in the transition zones; "Can they be a result of approximation or numerical precision errors?" and "Can they happen in the actual system or they just show up in the numerical simulations?", one may ask. These questions necessitate a through investigation of curve veering phenomenon in the gyroelastic systems as future work.

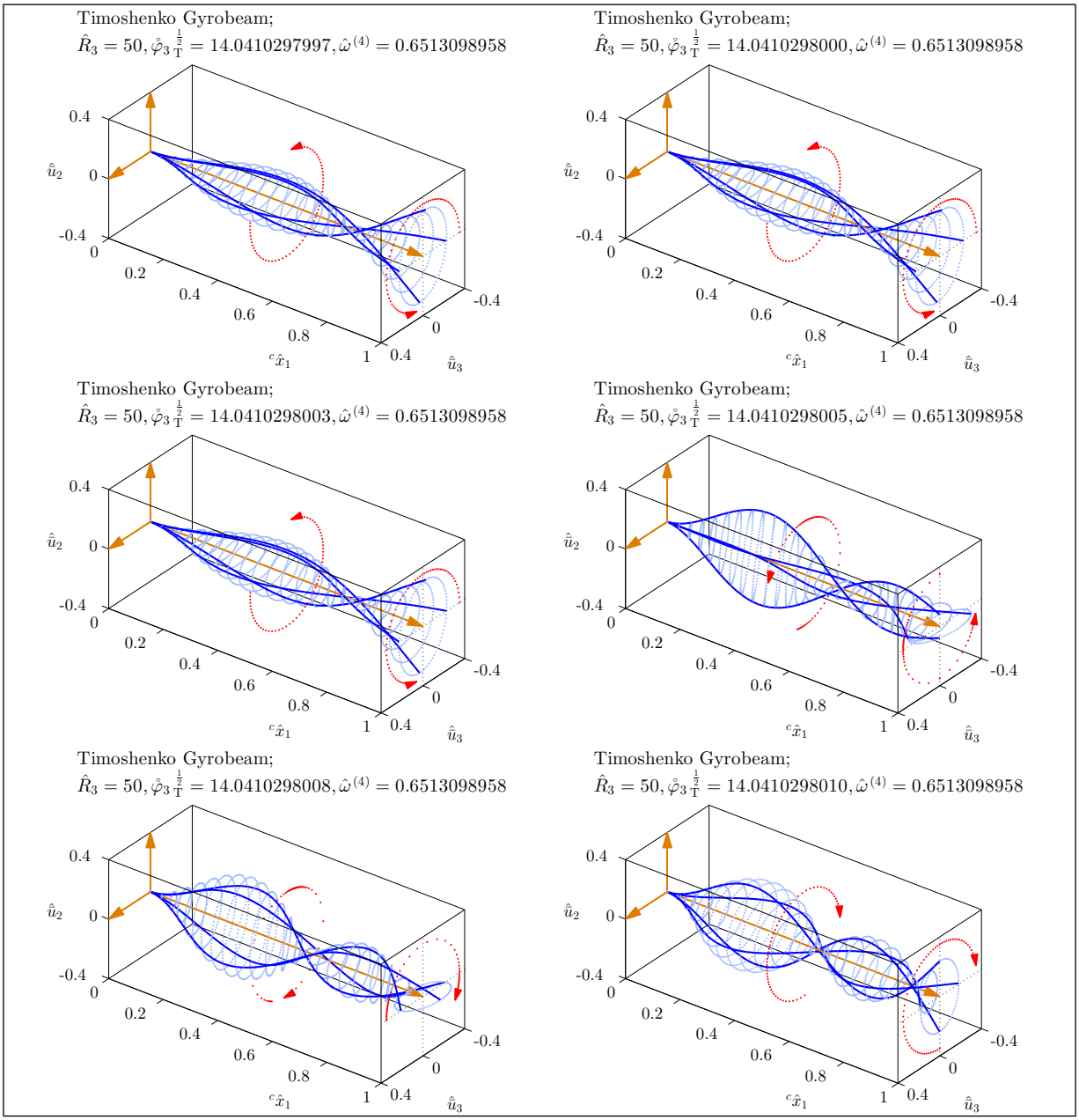

Figure 5.31: Abrupt transition of 4$^{\text{th}}$ mode shape in the 1$^{\text{st}}$ curve veering zone of Figure 5.29.

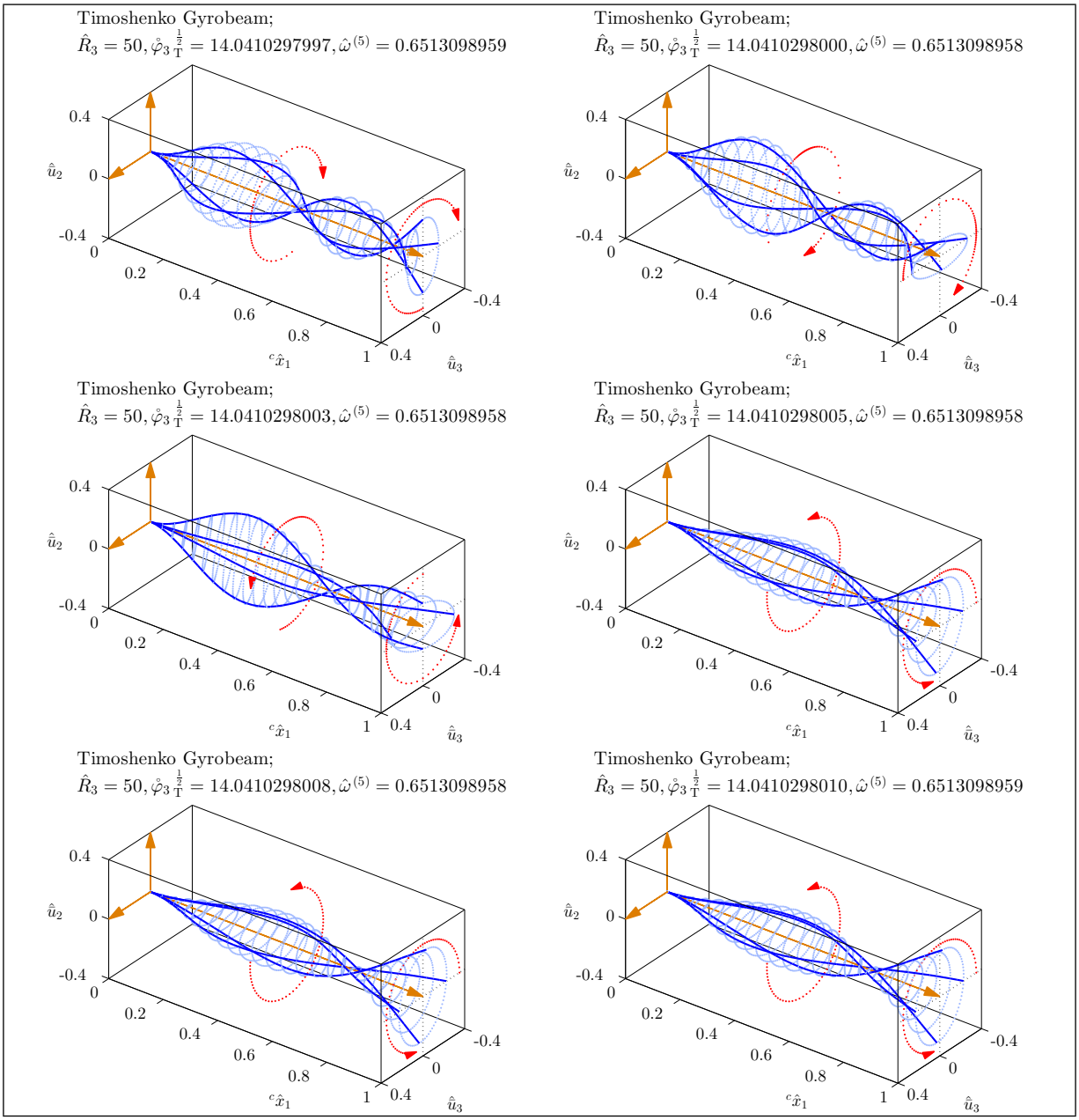

Figure 5.32: Abrupt transition of 5$^{\text{th}}$ mode shape in the 1$^{\text{st}}$ curve veering zone of Figure 5.29.

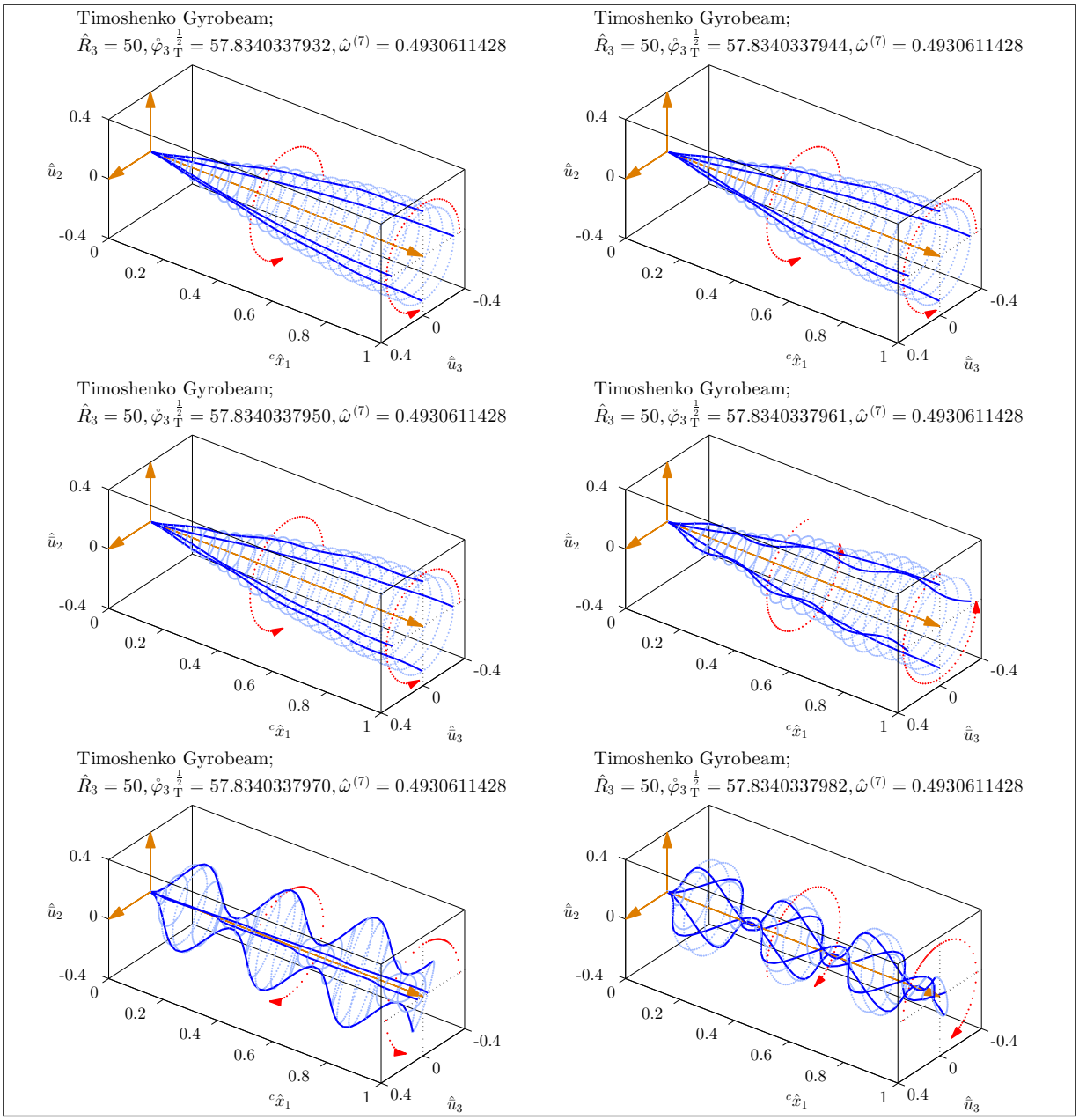

Figure 5.33: Abrupt transition of 7$^{\text{th}}$ mode shape in the 2$^{\text{nd}}$ curve veering zone of Figure 5.29.

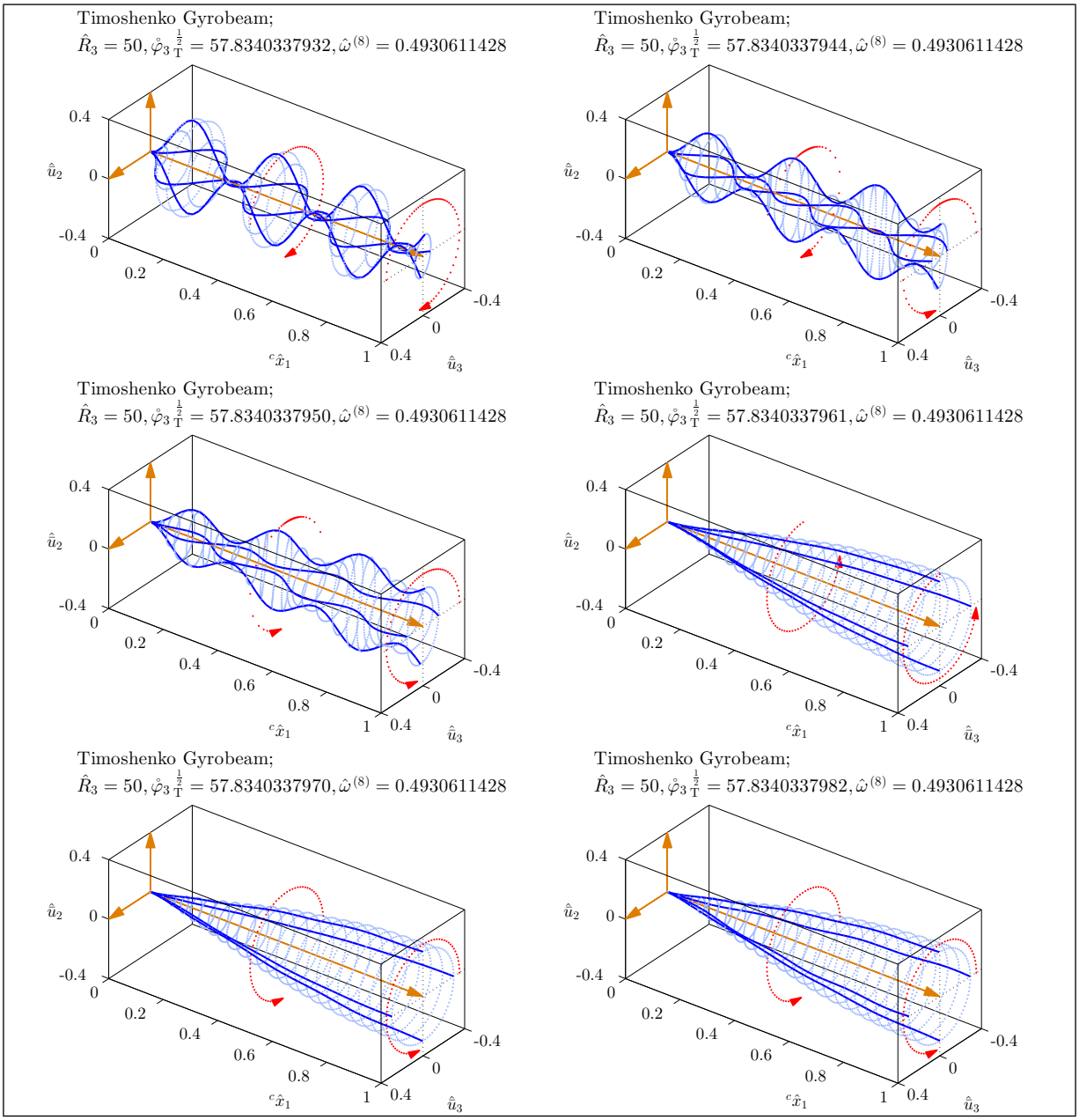

Figure 5.34: Abrupt transition of 8$^{\text{th}}$ mode shape in the 2$^{\text{nd}}$ curve veering zone of Figure 5.29.

The first selected zone in Figure 5.30 addresses the curve veering between the 13^{th} and 14^{th} natural frequencies. The mode shape transition in this zone is shown in Figures 5.35 and 5.36. It is interesting that the less abrupt or smoother curve veering in the first selected zone correspond to less abrupt or gradual changes of the mode shapes. The attribute interchange between the veering modes, if any, is not clear in Figures 5.35 and 5.36. However, it is certain that both torsional and bending potions of the mode shape vary themselves in the transition zone by acquiring or shedding nodes.

In the second zone the focus is on the 17^{th} and 18^{th} natural frequencies and their corresponding mode shapes. The variation of the mode shapes in this zone is shown in Figures 5.37 and 5.38. Compared to the first transition zone, in the second transition zone the curve veering takes place more abruptly (see Figure 5.30 again). As a result compared to the plots of Figures 5.35 and 5.36, there are more abrupt changes observable in the mode shape plots given in Figures 5.37 and 5.38. The exchange of characteristics (*i.e.* exchange of nodes and transformation sense) is much more clear in the plots of these latter figures corresponding to the second transition zone.

Overall, one may conclude that, as mentioned previously, the curve veering and mode shape transition in a gyrobeam with a transverse gyricity are more gradual compared to those in a gyrobeam with axial gyricity.

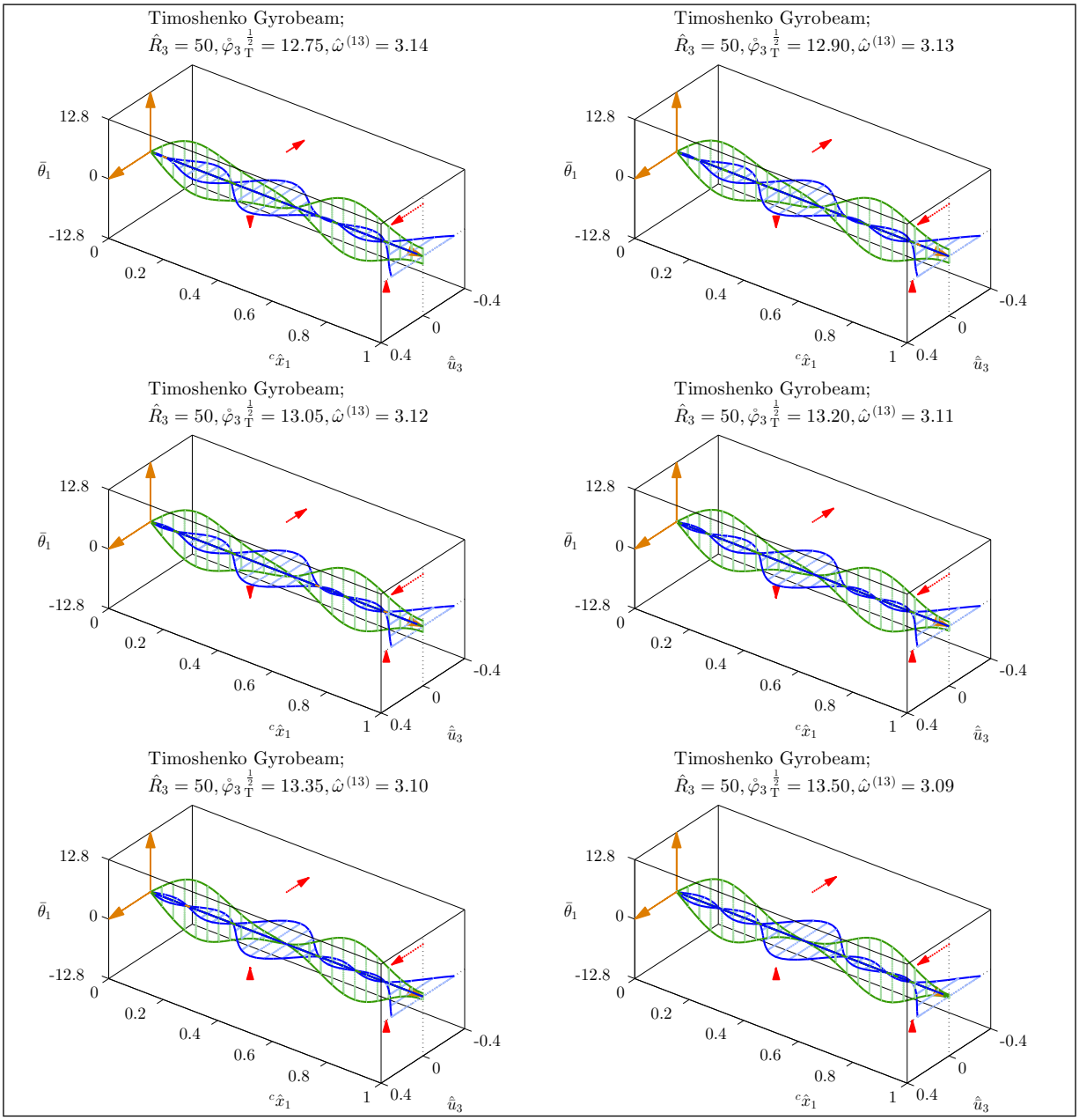

Figure 5.35: Abrupt transition of 13$^{\text{th}}$ mode shape in the 1$^{\text{st}}$ curve veering zone of Figure 5.30.

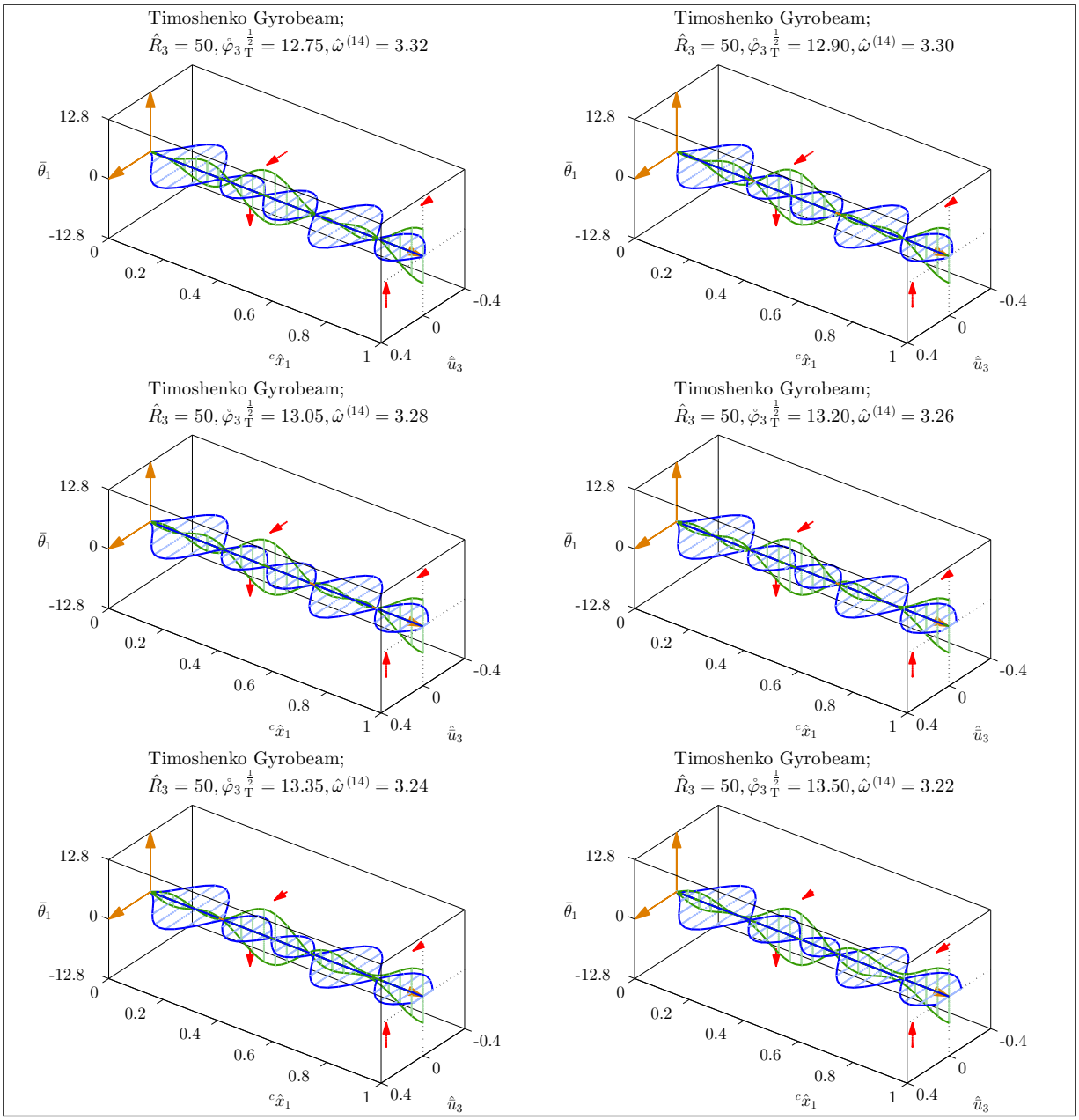

Figure 5.36: Abrupt transition of 14$^{\text{th}}$ mode shape in the 1$^{\text{st}}$ curve veering zone of Figure 5.30.

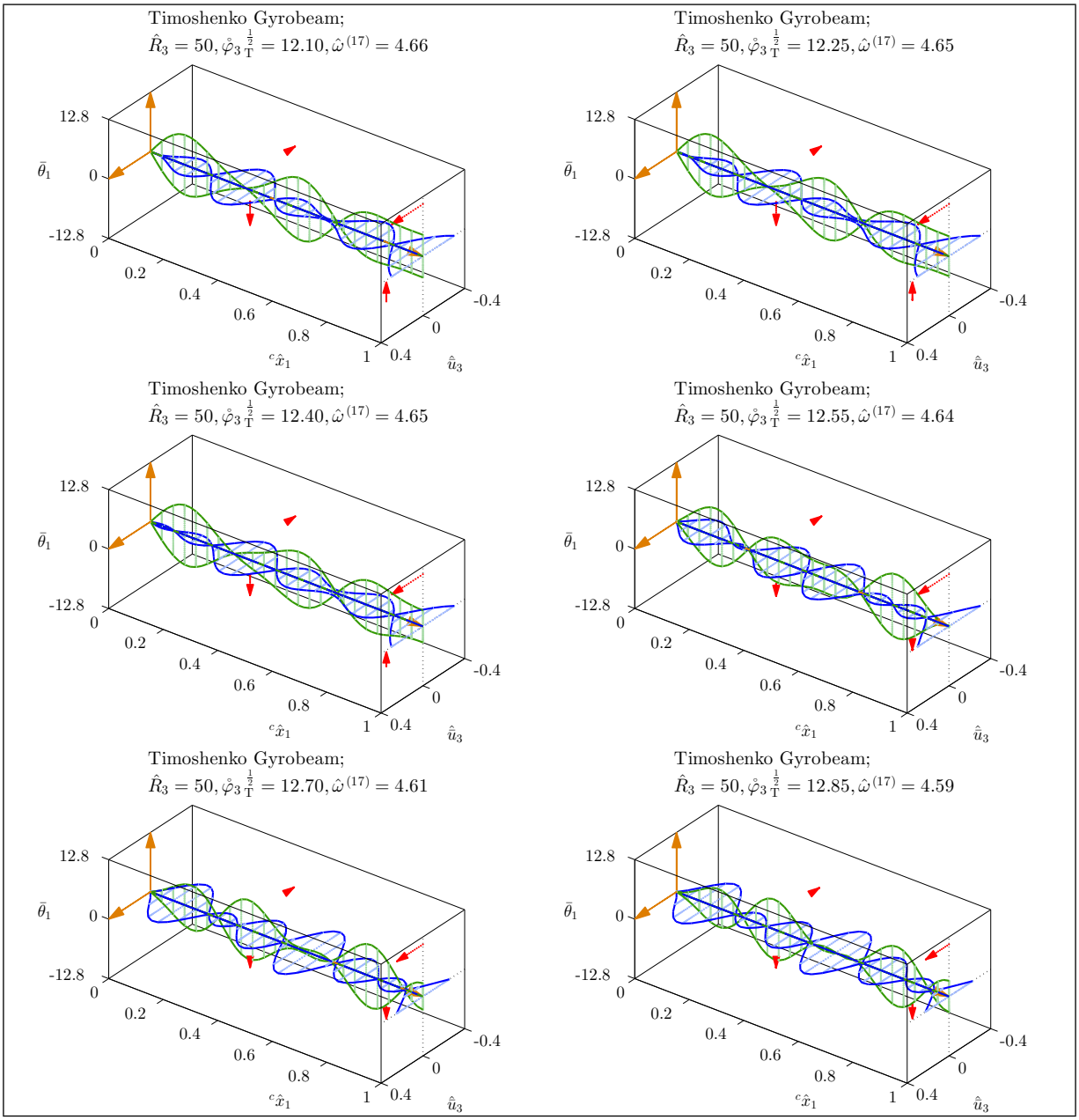

Figure 5.37: Abrupt transition of 17$^{\text{th}}$ mode shape in the 2$^{\text{nd}}$ curve veering zone of Figure 5.30.

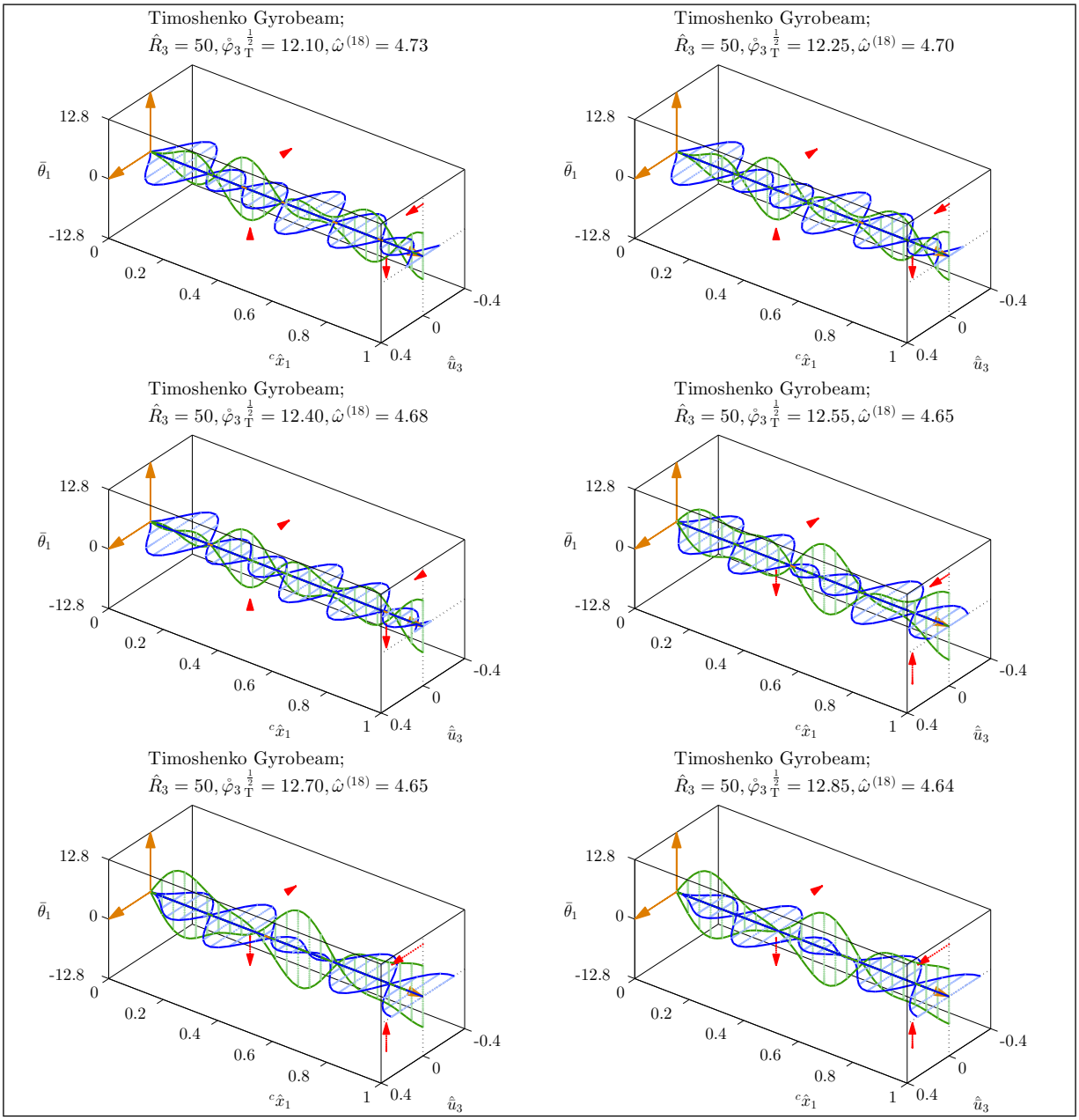

Figure 5.38: Abrupt transition of 18$^{\text{th}}$ mode shape in the 2$^{\text{nd}}$ curve veering zone of Figure 5.30.

Chapter 6

Numerical Analysis of Micropolar Gyroelastic Beams

6.1 Introduction

This chapter provides the numerical analysis of the micropolar gyrobeam model developed in Chapter 4 by investigating the natural frequencies and mode shapes of micropolar gyrobeams carrying a uniform axial or transverse gyricity distribution (a few examples of micropolar gyrobeams with non-uniform gyricity distributions can be found in Appendix E).

In this chapter the "3D classical gyrobeam model" refers to the gyrobeam model that employs the simple longitudinal deformation theory, Duleau torsion theory, and Timoshenko bending theory to model the beam elasticity (recall that in Chapter 5 this model is referred to as the 3D Timoshenko gyrobeam model). The "3D micropolar gyrobeam model" on the other hand represents the gyrobeam model in which the simple longitudinal deformation theory along with the herein-developed micropolar torsion and bending theories are used to model the beam elasticity. The numerical examples of this chapter address the modal comparison of the 3D micropolar gyrobeam model against the 3D classical (*i.e.* Timoshenko) gyrobeam model. Those readers interested in numerical analysis of micropolar elastic beams without gyricity (or equivalently numerical analysis of the newly

developed micropolar torsion and bending theories) and their comparison with classical elastic beams carrying no gyricity (or equivalently the well-known classical Duleau torsion and Timoshenko bending theories) are directed to Appendix C.

Table 6.1: Summary of the main dimensionless parameters used in the numerical micropolar gyrobeam model.

Parameter	**Value(s)**
$\hat{R}_3 = \hat{R}_2 = \sqrt{2}\,\hat{R}_1$	10, 50, and 250
$\hat{\mu}$	$\frac{3}{8}$
k_{t}	1
$k_{\mathrm{s}_2} = k_{\mathrm{s}_3}$	1
$\log(\hat{\kappa})$	$[-10, 2]$
$\log(\hat{\gamma}) = \log(\hat{\beta})$	$[-10, 2]$
ξ	$\frac{1}{2}$
$\hat{\imath}^V$ $({}^b\hat{\underline{\underline{\boldsymbol{\imath}}}}^V = \hat{\imath}^V\,\underline{\underline{\mathbb{1}}})$	1×10^{-6}
$\hat{\varrho}^V$	$\frac{1}{4}$
${}^a\hat{\underline{\underline{\boldsymbol{\jmath}}}}^V$	$\frac{\hat{\varrho}^V}{\hat{R}_3^2} \times \underline{\underline{\mathbb{1}}} = \hat{\varrho}^V\,\hat{I}_3 \times \underline{\underline{\mathbb{1}}}$
(φ_1, φ_2)	$(0, \frac{\pi}{2})$ (for axial gyricity)
	$(0, 0)$ (for transverse gyricity)
$(\mathring{\varphi}_1, \mathring{\varphi}_2)$	$(0, 0)$
$\mathring{\varphi}_{3\mathrm{T}}^{\frac{1}{2}}$	$[0, 60]$

Analogous to Chapter 5, the 3D classical (CL) and micropolar (MP) gyrobeams considered for the numerical analyses of this chapter are classically cantilevered uniform gyrobeams along the first axis of the inertial reference frame where the the principal axes of the beams' cross sections are assumed to be parallel to the second and third axes of the inertial frame. The gyrobeams have constant geometries, inertia densities, and elastic constants over the length and carry a constant (time-invariant) uniform axial or transverse gyricity distribution as shown in Figure 5.1 or 5.16. The FEM-based numerical model of

the micropolar gyrobeams is implemented in MATLAB® [66] using the parameters summarized in Tables 6.1 and 6.2. The parameters utilized in the FEM-based numerical model of the classical gyrobeams are those previously given in Tables 5.1 and 5.3.

Table 6.2: Summary of the main FEM parameters used in the numerical micropolar gyrobeam model.

Parameter	**Value**
Element Type	C^0 four-node
Basis Functions	cubic Lagrange polynomials
Number of Elements	16
Number of Nodes	49 (distributed evenly)
DOFs per Node	9
Longitudinal BCs	fixed-free
Torsional BCs	classical fixed-free
Bending BCs	classical clamped-free
Gyricity Distribution Function	uniform axial/transverse

Again, the dimensions of gyros are assumed to be proportional to the beam thickness and the value given in Table 6.1 as the rotational inertia density of gyros $\hat{\underset{\leftrightarrow}{j}}^V$ is reflecting this assumption. Also, the total gyricity spin rate $\mathring{\hat{\varphi}}_{3\mathrm{T}}$ is as previously defined by Eq. (5.1).

In the following a preliminary investigation of the micropolar gyrobeam model (with a uniform axial or transverse gyricity distribution) is first presented by plotting its first three gyricity-affected natural frequencies vs. the (nondimensional) micropolar elastic constants $\hat{\kappa}$ and $\hat{\gamma}$ which vary in the range $[10^{-10}, 10^{2}]$ (as given in Table 6.1). Then, out of the many (or indeed infinite) possible micropolar gyrobeam models which can be obtained by varying the micropolar elastic constants, four specific micropolar gyrobeam models are selected and considered for a more thorough examination of natural frequencies and mode shapes. The four models are chosen to differ by the values assigned to $\hat{\kappa}$ and $\hat{\gamma}$ while, as suggested in Table 6.1, in all of them it is assumed that $\hat{\beta} = \hat{\gamma}$ and $\xi = \frac{1}{2}$. The pair of

Table 6.3: The pair of micropolar elastic constants $(\hat{\kappa}, \hat{\gamma})$ in the four selected micropolar gyrobeam models.

Gyrobeam Model	**Pair of Micropolar Constants $(\hat{\boldsymbol{\kappa}}, \hat{\boldsymbol{\gamma}})$**
Micropolar Gyrobeam Model 1 (MGM1)	$(10^{2}, 10^{-10})$
Micropolar Gyrobeam Model 2 (MGM2)	$(10^{2}, 10^{-4})$
Micropolar Gyrobeam Model 3 (MGM3)	$(10^{-4}, 10^{-10})$
Micropolar Gyrobeam Model 4 (MGM4)	$(10^{-1}, 10^{-7})$

micropolar elastic constants $(\hat{\kappa}, \hat{\gamma})$ for these specific micropolar beam models are given in Table 6.3. The rest of the parameters in these models are as those given in Table 6.1 and the FEM parameters of the models are as those given in Table 6.2.

Recall that 3D classical and micropolar gyrobeams have four modes of deformation, *i.e.* longitudinal displacement along the ${}^{c}\hat{x}_1$ axis, torsional rotation about the ${}^{c}\hat{x}_1$ axis, bending deformation in the ${}^{c}\hat{x}_1{}^{c}\hat{x}_2$ plane, and bending deformation in the ${}^{c}\hat{x}_1{}^{c}\hat{x}_3$ plane; in the presence of gyricity terms the torsional and bending deformation modes may be coupled together. Out of these four deformation modes only those affected by the gyricity will be taken into account for analysis and comparison of the classical and micropolar gyrobeams.

The examples presented in this chapter are similar to those given in Chapter 5 and to avoid unnecessary lengthening of this document the figures of Chapter 5, unless indispensable, will not be repeated here. Thus, to compare the results of the micropolar gyrobeam model with those obtained from the classical (*i.e.* Timoshenko) gyrobeam model, the readers may have to frequently return to Chapter 5 and revisit the figures provided in there.

6.2 Uniform axial gyricity

As the first attempt to compare the classical and micropolar gyrobeam models carrying a uniform axial gyricity distribution, their first three gyricity-affected relative natural frequencies are plotted in Figures 6.1–6.9. In these figures which are analogous to the natural

frequency plots provided in Appendix C, three slenderness ratios or thicknesses (*i.e.* thick, medium, and thin) and three axial gyricity values (*i.e.* small, medium, and large) are considered to illustrate the gyrobeams' relative gyricity-affected natural frequencies (*i.e.* the classical gyrobeam's gyricity-affected natural frequency divided by the same-rank micropolar gyrobeam's gyricity-affected natural frequency) vs. the micropolar elastic constants $\hat{\kappa}$ and $\hat{\gamma}$. The figures have log-log-percentage scales and for each slenderness ratio a 2D contour plot and a 3D surface plot are provided; the 3D plot is obtained by looking at the 2D plot from a point over the 2D plot's upper right corner.

In Figures 6.1–6.9, first of all note that the strange noisy behavior of the natural frequency surface, observable in some plots in the region with very small $\hat{\kappa}$ and very large $\hat{\gamma}$ (*i.e.* in the lower right corner of the 2D plots), is due to the ill-conditionedness of the micropolar gyrobeam's FEM stiffness matrix (see Figure C.21 and its related explanation in Appendix C). Then, one may notice the singular behavior of the micropolar gyrobeam model with small values of $\hat{\kappa}$, appearing as abrupt jumps in the depicted natural frequency surfaces, which compared to the singular behavior of the micropolar elastic beam model (without gyricity) shown in Appendix C are more pronounced. Note that whereas for the first natural frequency the singular behavior appears as a surface jump to a very large value, for higher natural frequencies it shows up as a step to a (not very) larger or even smaller value. As explained in Appendix C, the inclusion of the decoupled micropolar vibration modes (with small natural frequencies) in the considered lower vibration modes and subsequently comparing the (same-rank but) non-corresponding natural frequencies of classical and micropolar gyrobeams is the source of these observed steps.

A comparison between the plots given in each of Figures 6.1–6.9 (*i.e.* a comparison between the plots corresponding to different slenderness ratios) reveals that the flat plateau of the natural frequency surfaces, corresponding to the upper right corner of 2D plots where classical and micropolar gyrobeam models are expected to coincide, changes its shape (or orientation) as the gyrobeam's thickness varies. Indeed, as the micropolar gyrobeam gets thinner the increasing size effects cause the plateau's width in the 2D plots to become smaller while the strengthening coupling effects and decreasing gyricity effects cause its height to become larger. As a result the shape of the flat plateau, in the 2D plots, changes from a horizontal rectangle for a thick gyrobeam to a vertical rectangle for a thin gyrobeam.

This is more clear in the plots corresponding to a small gyricity value, *i.e.* Figures 6.1–6.3, since the interfering singular behavior of the micropolar gyrobeam model with small $\hat{\kappa}$ is less significant at smaller gyricity values.

Comparing the corresponding plots of different natural frequencies (different vibration modes) one can in general conclude that the gyricity effects are more significant on higher natural frequencies. Consequently, the singular behavior of the micropolar gyrobeam models with small $\hat{\kappa}$ is more apparent (as it occurs in a larger region) at higher vibration modes. At the same time, the region where the classical and micropolar gyrobeam models are in agreement, *i.e.* the flat plateau in the 3D plots or the rectangle in the upper right corner of the 2D plots, reduces in size. As it is explained in Appendix C, whereas the size effects (represented by γ) are almost the same on different vibration modes, the coupling effects (illustrated by $\hat{\kappa}$) are slightly more evident at lower vibration modes. These behaviors are, however, slightly influenced by the gyricity terms in a micropolar gyrobeam.

The effect of increasing the gyricity value in Figures 6.1–6.9 is to shrink or even completely remove the flat plateau of agreement between the classical and micropolar gyrobeam models (in the upper left corner of the 2D plots). Overall, the addition of gyricity effects results in more apparent differences between the classical and micropolar beam models.

At the end, for micropolar gyrobeams with a zero microinertia, one can obtain the same results and behaviors as those shown in Figures 6.1–6.9. This holds true even when comparing the results of very slender micropolar gyrobeams (with $\hat{R}_3 = 250$) in which the ratio of body microinertia to gyros rotational inertia differs from $\frac{1}{4}$ (corresponding to $\hat{\imath}^V = 10^{-6}$) to zero (corresponding to $\hat{\imath}^V = 0$). It is interesting that for small $\hat{\kappa}$ the same singularity behavior, as that observed in the nonzero-microinertia case, can be seen in the zero-microinertia case; this is a result of the inclusion of gyricity terms. Note that for micropolar elastic beams carrying no gyricity, due to the sorting of the natural frequencies, the singularity of the model with small $\hat{\kappa}$ is concealed in the zero-microinertia case (refer to Appendix C for a detailed explanation).

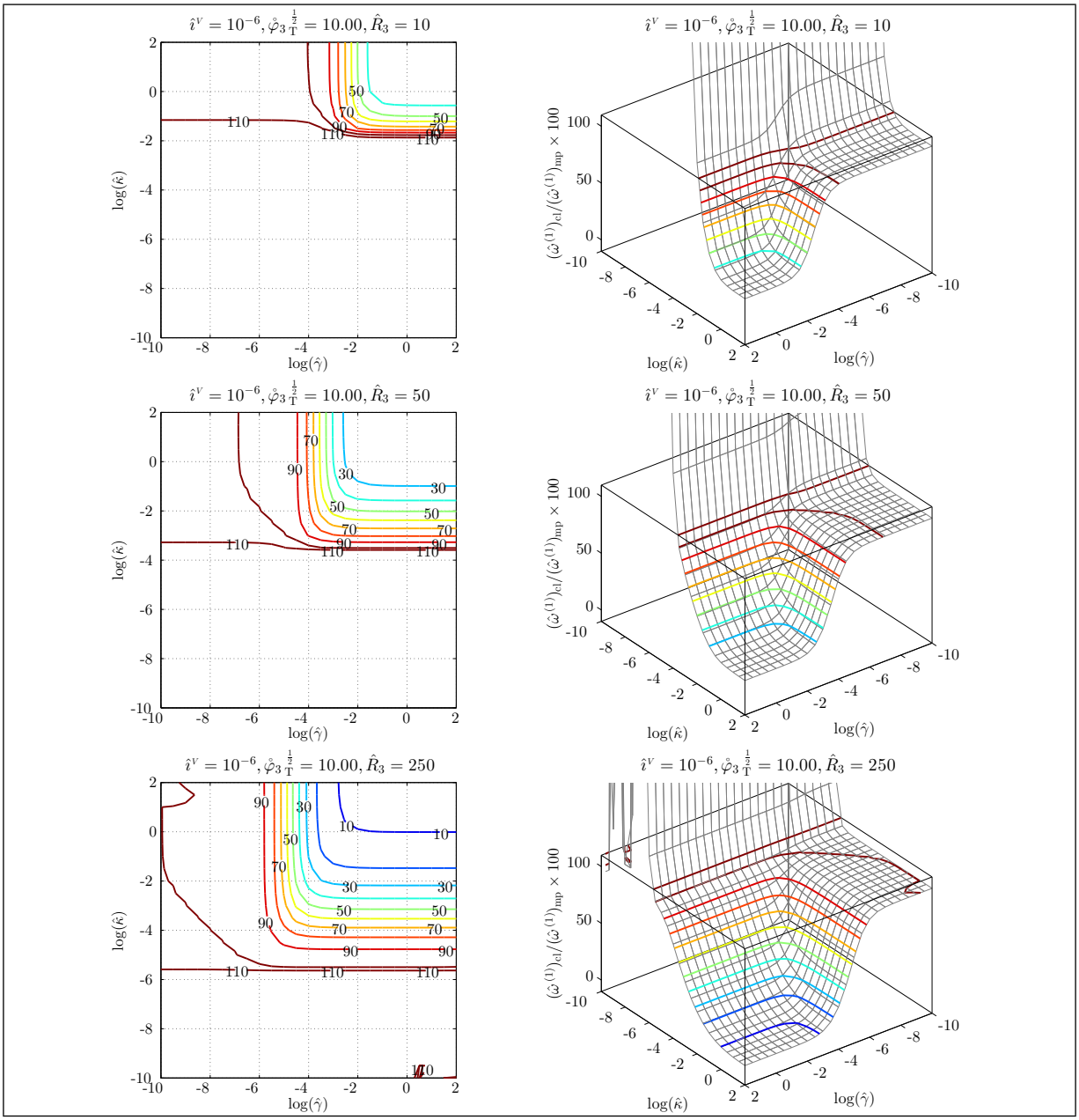

Figure 6.1: Relative 1st natural frequency $(\hat{\omega}^{(1)})_{\mathrm{cl}}/(\hat{\omega}^{(1)})_{\mathrm{mp}}$ of micropolar gyrobeams with a small uniform axial gyricity vs. micropolar elastic constants.

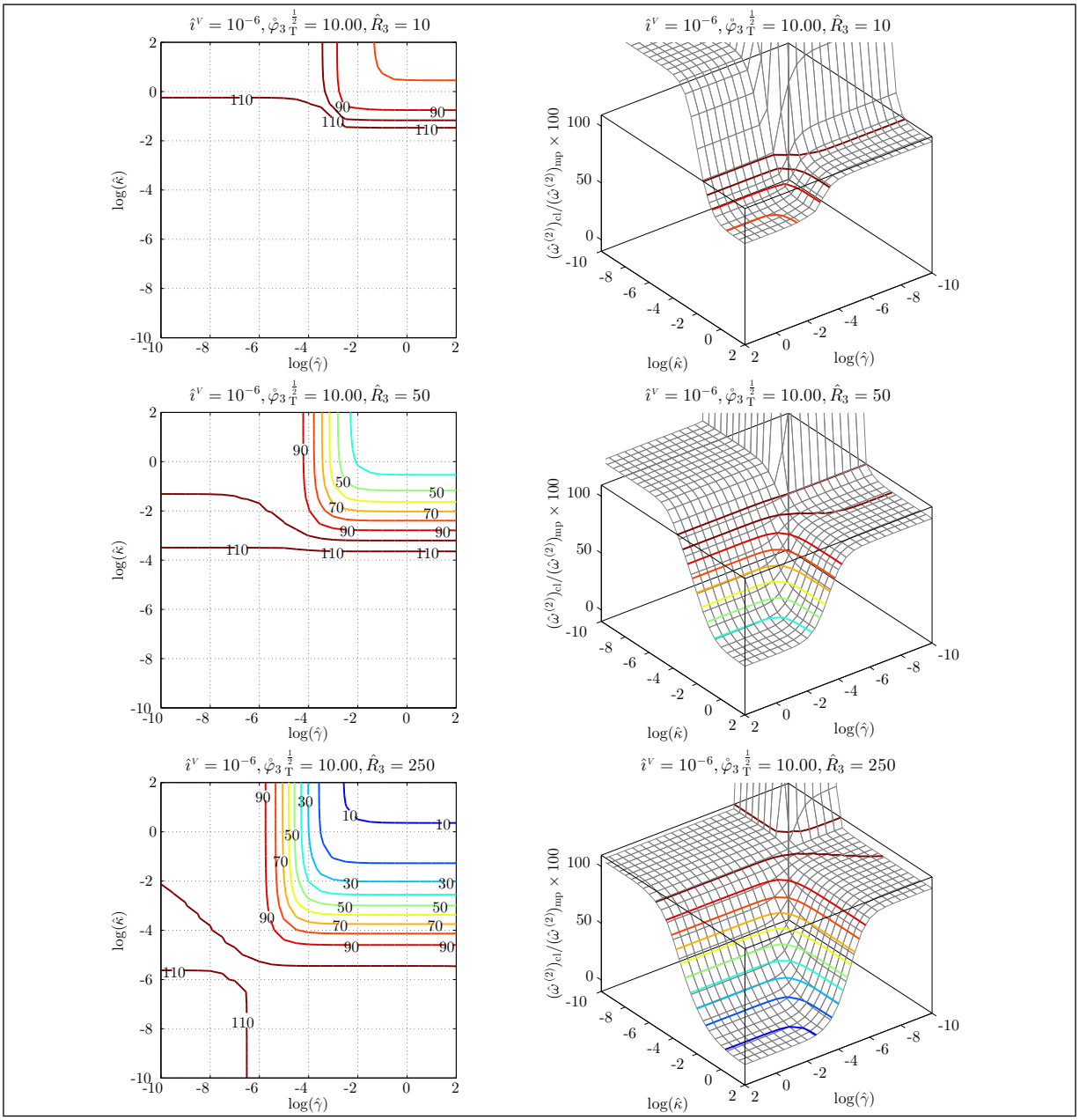

Figure 6.2: Relative 2nd natural frequency $(\hat{\omega}^{(2)})_{\mathrm{cl}}/(\hat{\omega}^{(2)})_{\mathrm{mp}}$ of micropolar gyrobeams with a small uniform axial gyricity vs. micropolar elastic constants.

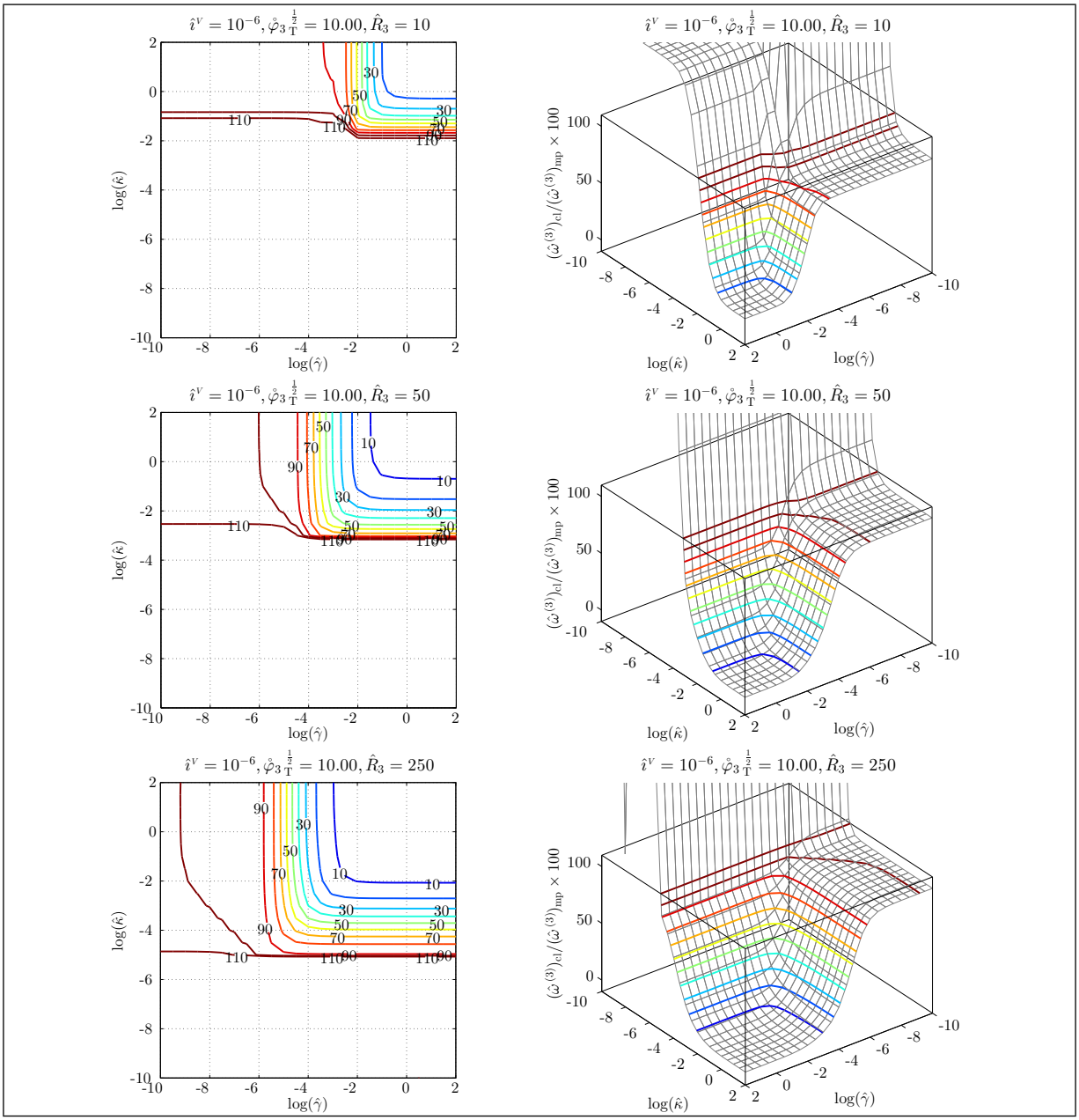

Figure 6.3: Relative 3rd natural frequency $(\hat{\omega}^{(3)})_{\mathrm{cl}}/(\hat{\omega}^{(3)})_{\mathrm{mp}}$ of micropolar gyrobeams with a small uniform axial gyricity vs. micropolar elastic constants.

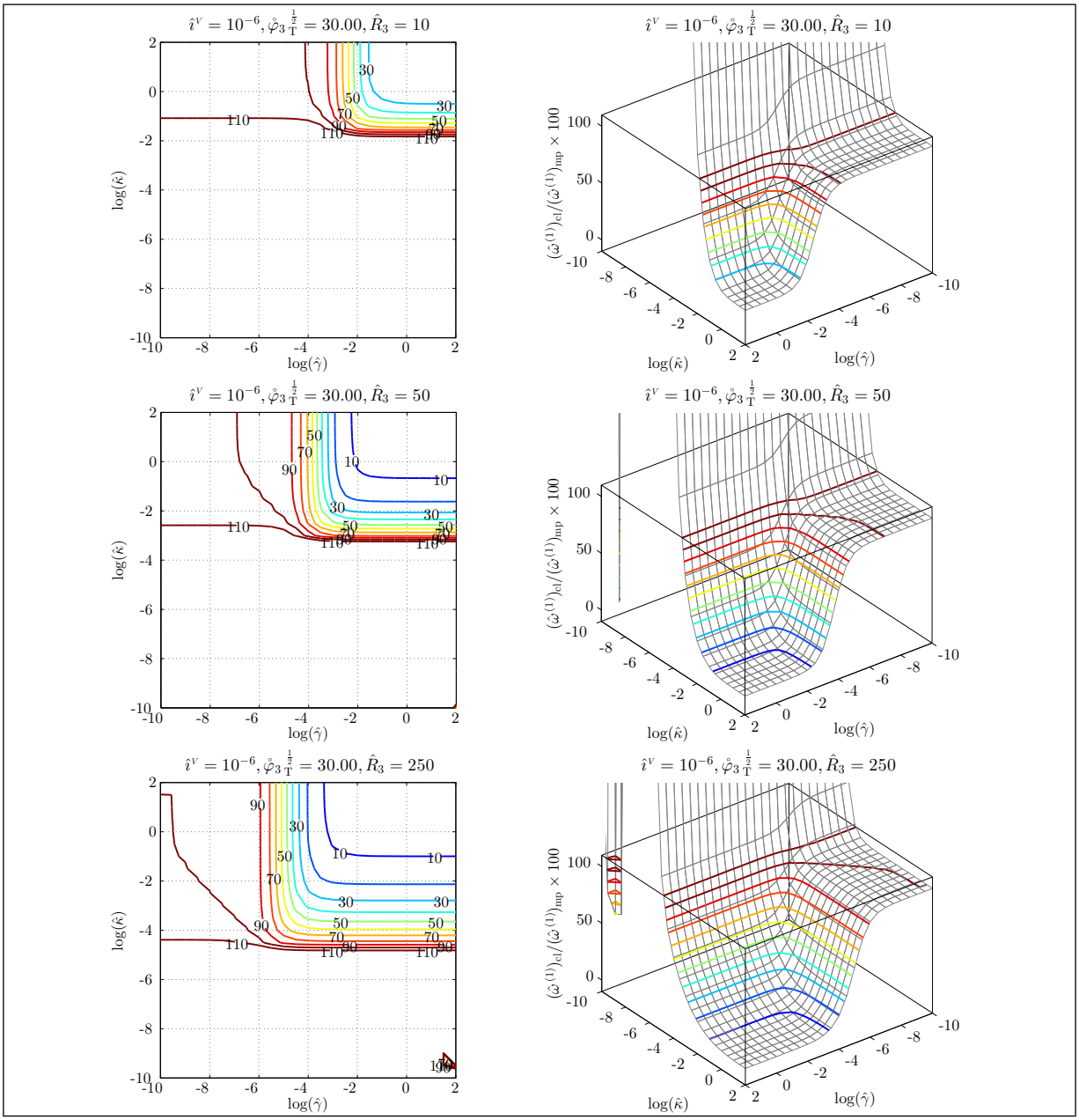

Figure 6.4: Relative 1st natural frequency $(\hat{\omega}^{(1)})_{\mathrm{cl}}/(\hat{\omega}^{(1)})_{\mathrm{mp}}$ of micropolar gyrobeams with a medium uniform axial gyricity vs. micropolar elastic constants.

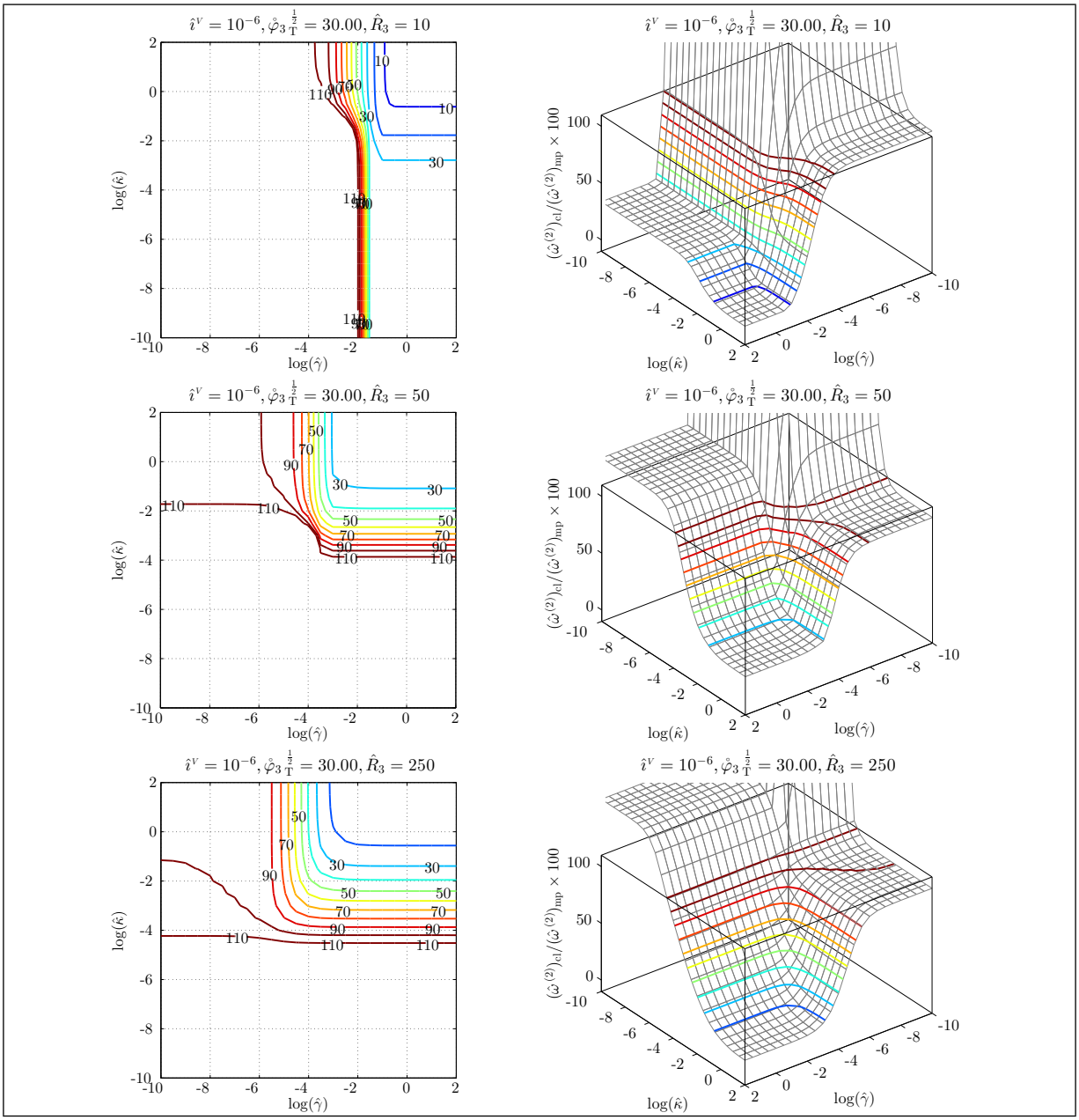

Figure 6.5: Relative 2nd natural frequency $(\hat{\omega}^{(2)})_{\mathrm{cl}}/(\hat{\omega}^{(2)})_{\mathrm{mp}}$ of micropolar gyrobeams with a medium uniform axial gyricity vs. micropolar elastic constants.

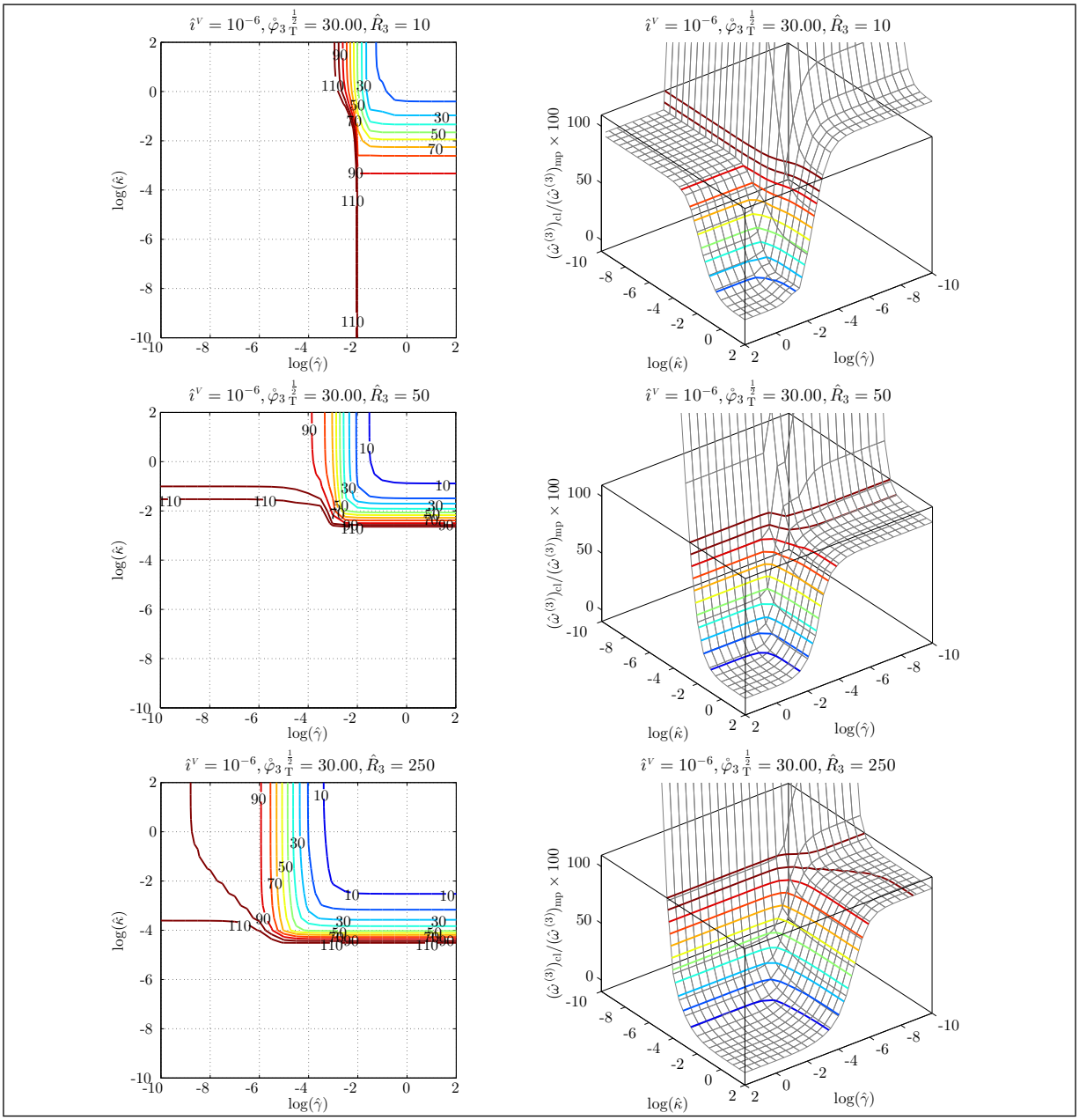

Figure 6.6: Relative 3rd natural frequency $(\hat{\omega}^{(3)})_{\mathrm{cl}}/(\hat{\omega}^{(3)})_{\mathrm{mp}}$ of micropolar gyrobeams with a medium uniform axial gyricity vs. micropolar elastic constants.

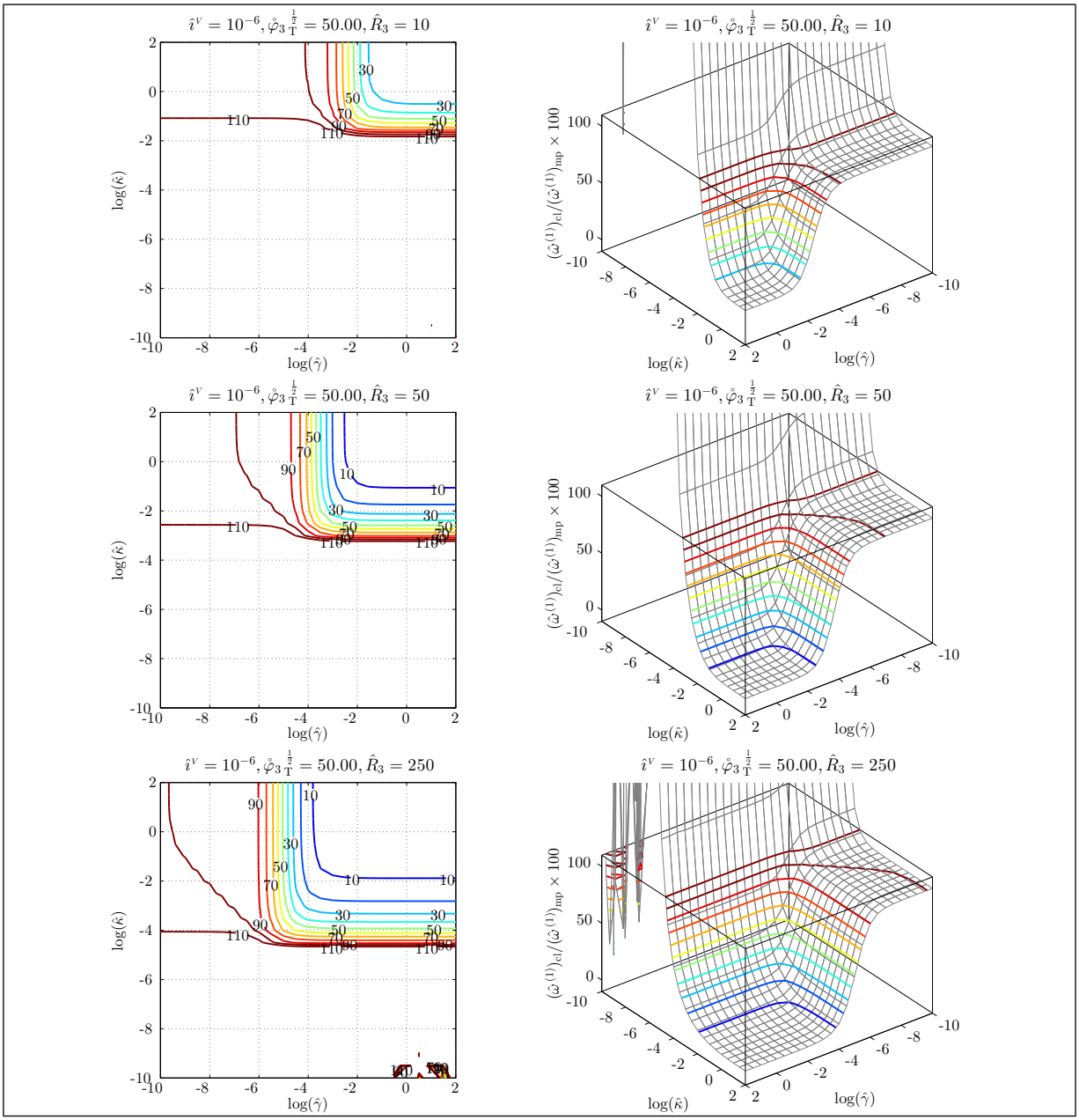

Figure 6.7: Relative 1st natural frequency $(\hat{\omega}^{(1)})_{\mathrm{cl}}/(\hat{\omega}^{(1)})_{\mathrm{mp}}$ of micropolar gyrobeams with a large uniform axial gyricity vs. micropolar elastic constants.

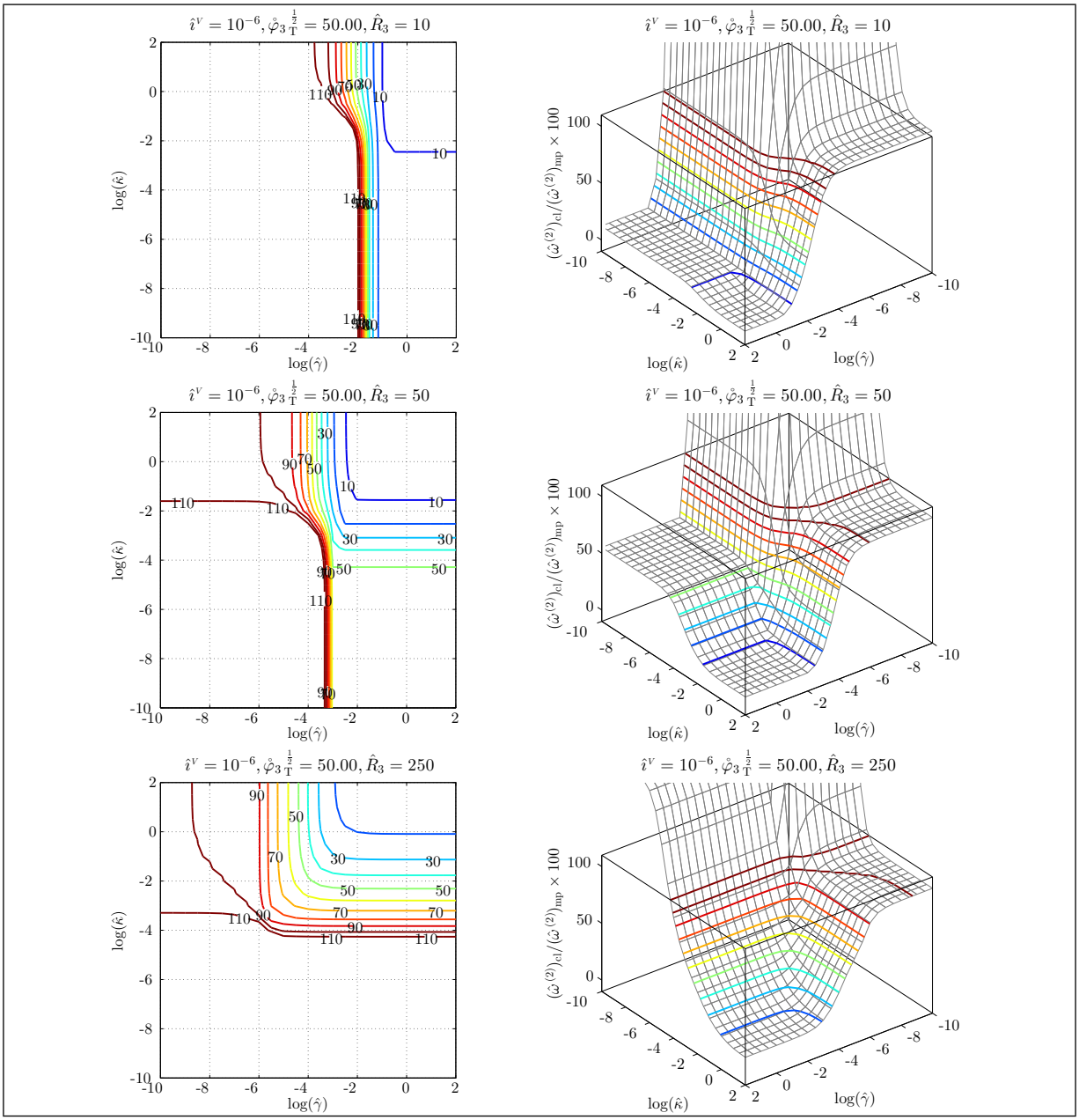

Figure 6.8: Relative 2nd natural frequency $(\hat{\omega}^{(2)})_{\mathrm{cl}}/(\hat{\omega}^{(2)})_{\mathrm{mp}}$ of micropolar gyrobeams with a large uniform axial gyricity vs. micropolar elastic constants.

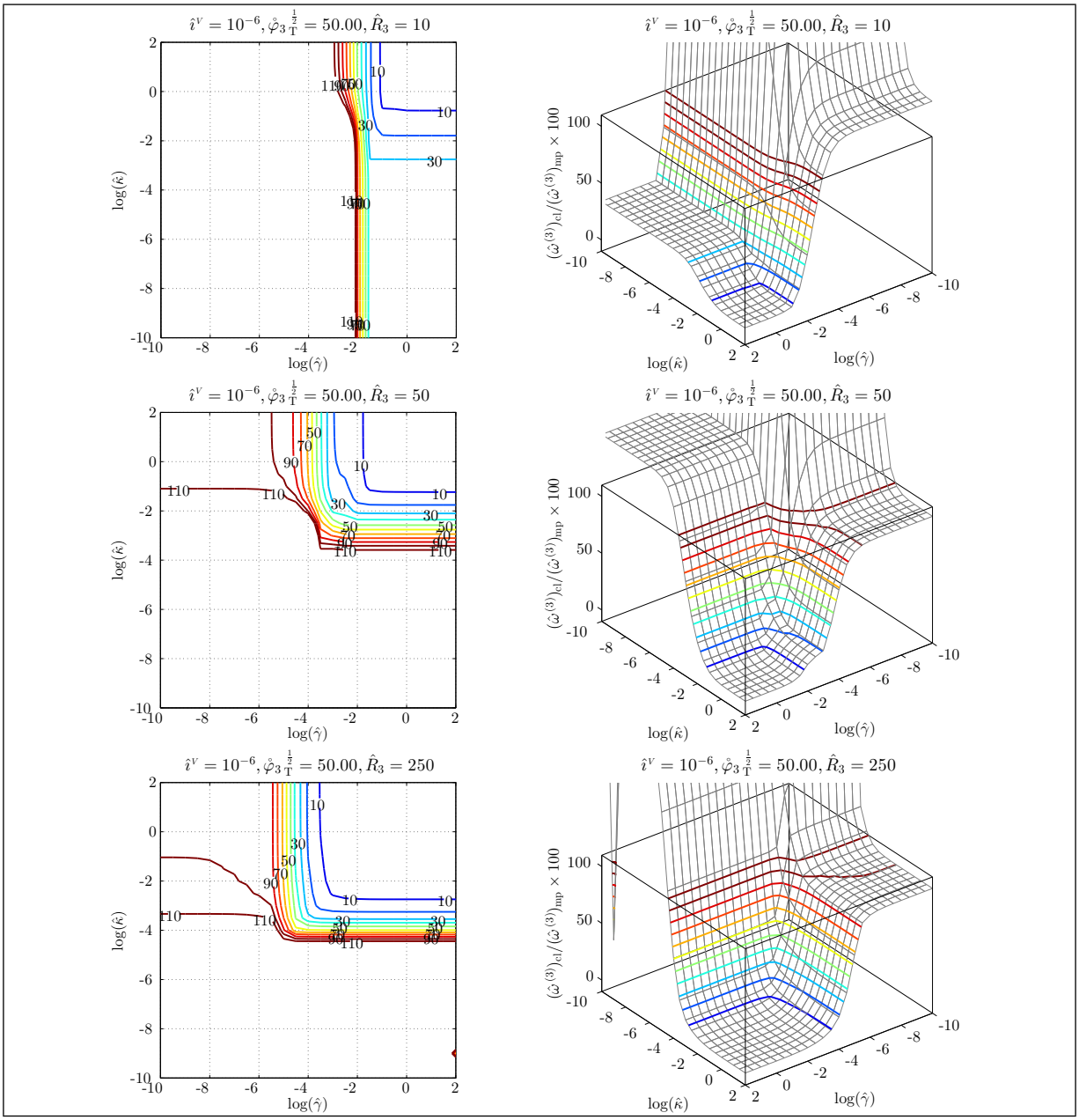

Figure 6.9: Relative 3rd natural frequency $(\hat{\omega}^{(3)})_{\mathrm{cl}}/(\hat{\omega}^{(3)})_{\mathrm{mp}}$ of micropolar gyrobeams with a large uniform axial gyricity vs. micropolar elastic constants.

It is also interesting to observe how the natural frequency loci and mode shapes in the micropolar gyrobeam model differ from those associated with the classical gyrobeam model. However, carrying out such an examination for the whole considered range of micropolar elastic constants $\hat{\kappa}$ and $\hat{\gamma}$ (*i.e.* continuous sweeping of the range $[10^{-10}, 10^{2}]$ for each constant) is impractical. In this text, out of the infinite number of possible choices, only four discrete combinations of micropolar elastic constants $\hat{\kappa}$ and $\hat{\gamma}$, as summarized in Table 6.3, are selected and used to study the natural frequencies and mode shapes of the general micropolar gyrobeam model.

The first specific micropolar gyrobeam model ($(\hat{\kappa}, \hat{\gamma}) = (10^{2}, 10^{-10})$) is selected as it is the closest match with the classical gyrobeam model. Note that, as shown in Appendix C, considering elastic beams with no gyricity the results of this model coincide with the classical model's results. The second specific micropolar gyrobeam model ($(\hat{\kappa}, \hat{\gamma}) = (10^{2}, 10^{-4})$) can reflect the the effect of changing $\hat{\gamma}$ on the natural frequency loci and mode shapes in the micropolar gyrobeam model (through the comparison with the first selected micropolar gyrobeam model). The third specific micropolar gyrobeam model ($(\hat{\kappa}, \hat{\gamma}) = (10^{-4}, 10^{-10})$) can be used to study how changing $\hat{\kappa}$ affects the natural frequency loci and mode shapes in the micropolar gyrobeam model (again if compared with the first selected micropolar gyrobeam model). Finally, the fourth specific micropolar gyrobeam model ($(\hat{\kappa}, \hat{\gamma}) = (10^{-1}, 10^{-7})$) can be regarded as a transition model when transforming from the first specific model to either the second or the third specific model. It is worth mentioning that insignificant differences can be seen between the results obtained from this fourth model and the results of a micropolar gyrobeam model with $(\hat{\kappa}, \hat{\gamma}) = (10^{2}, 10^{-7})$ or $(\hat{\kappa}, \hat{\gamma}) = (10^{-1}, 10^{-10})$.

Considering these four micropolar gyrobeam models (summarized in Table 6.3) the variations of their first 25 gyricity-affected natural frequencies with the variation of the total axial gyricity are depicted in the following figures. For each considered micropolar gyrobeam model, the natural frequency loci are plotted at three different values of slenderness ratio giving rise to three natural frequency figures. These three figures are followed by three mode shape figures, illustrating the first six gyricity-affected mode shapes of the medium-thickness micropolar gyrobeam model at three gyriciy values (*i.e.* small, medium, and large). An explanation of the results shown in the following figures, *i.e.* Figures 6.10–6.36, is reserved for after each set of figures for a specific micropolar gyrobeam model.

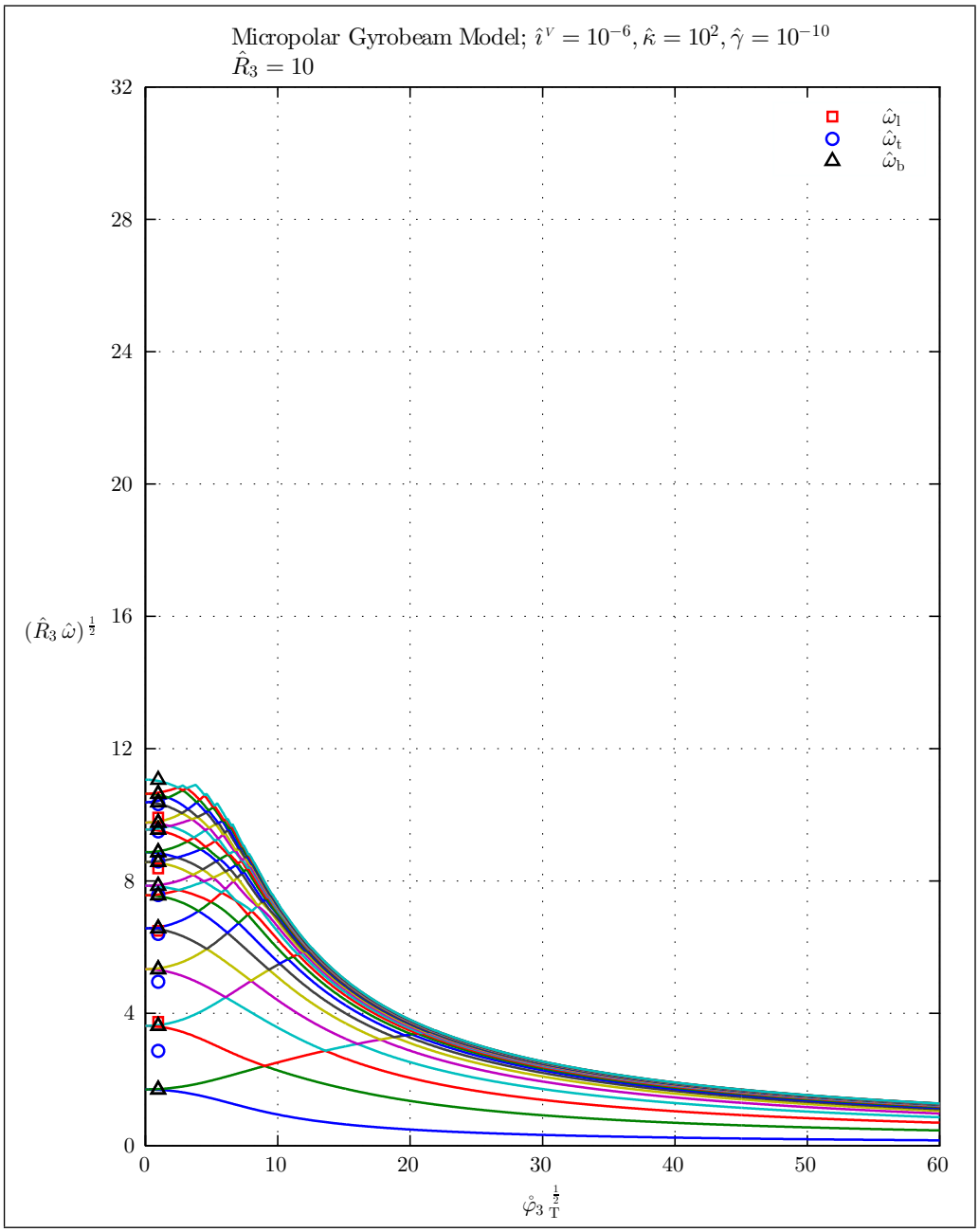

Figure 6.10: Natural frequencies of a thick micropolar gyrobeam with a uniform axial gyricity – Micropolar gyrobeam model 1.

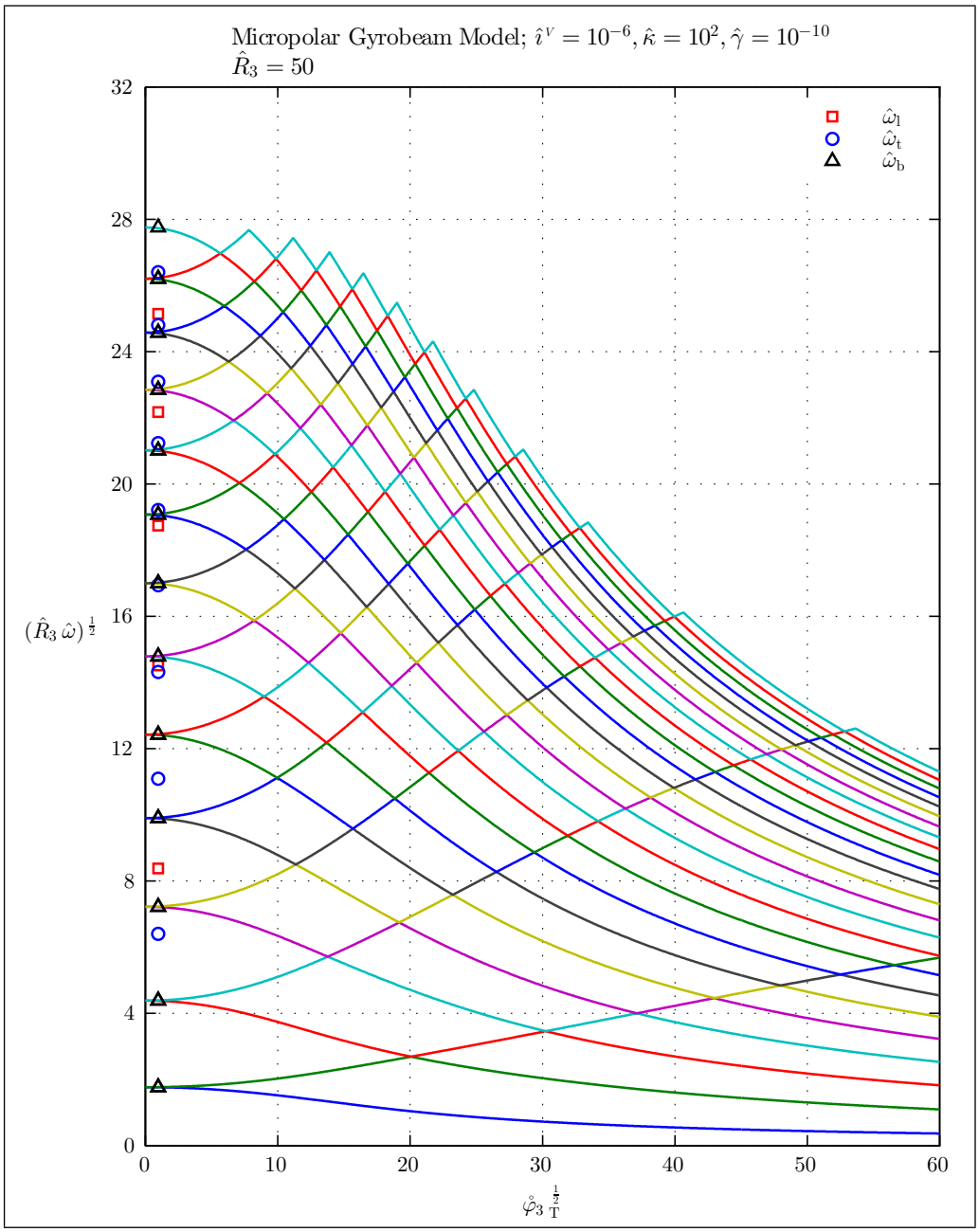

Figure 6.11: Natural frequencies of a medium micropolar gyrobeam with a uniform axial gyricity – Micropolar gyrobeam model 1.

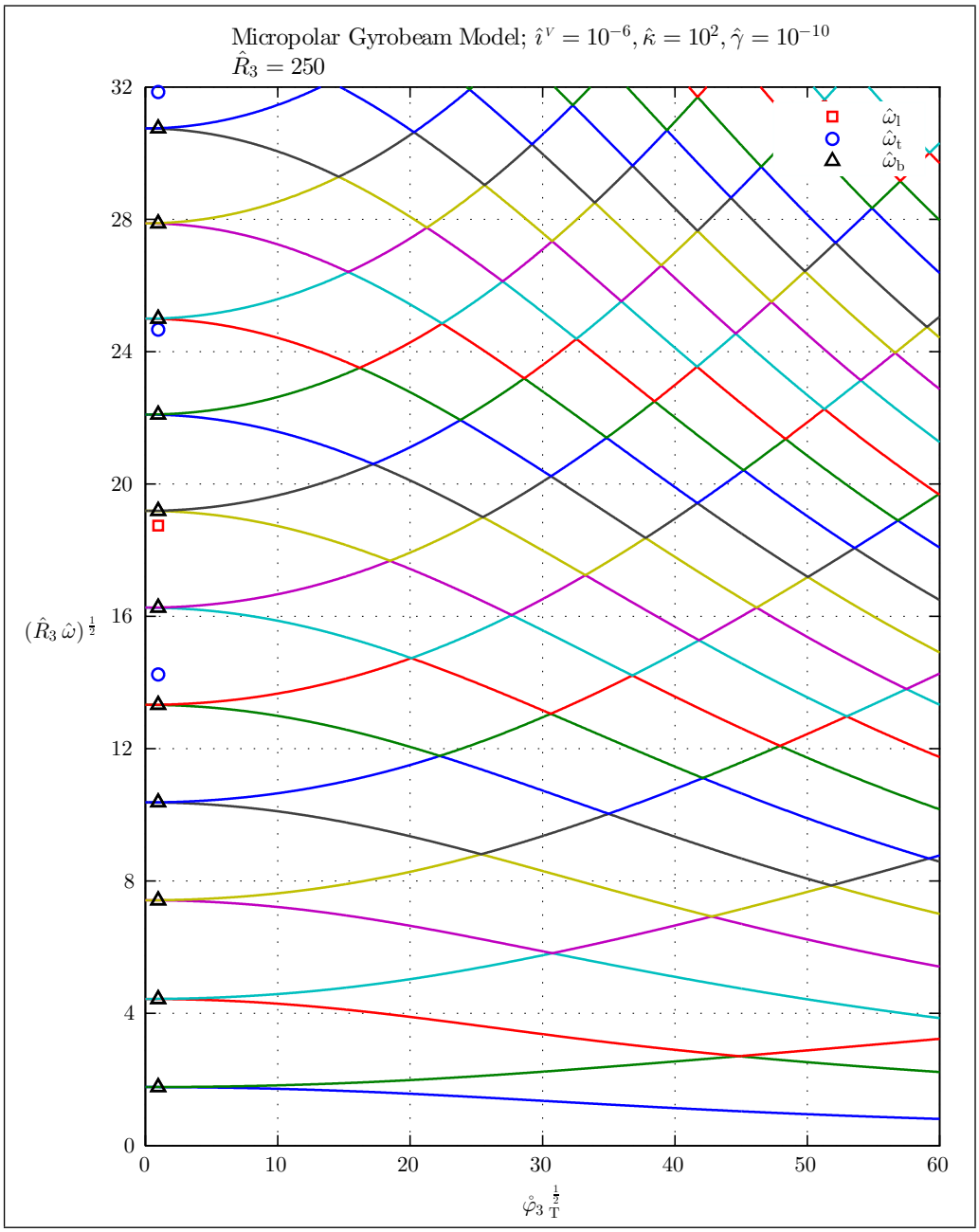

Figure 6.12: Natural frequencies of a thin micropolar gyrobeam with a uniform axial gyricity – Micropolar gyrobeam model 1.

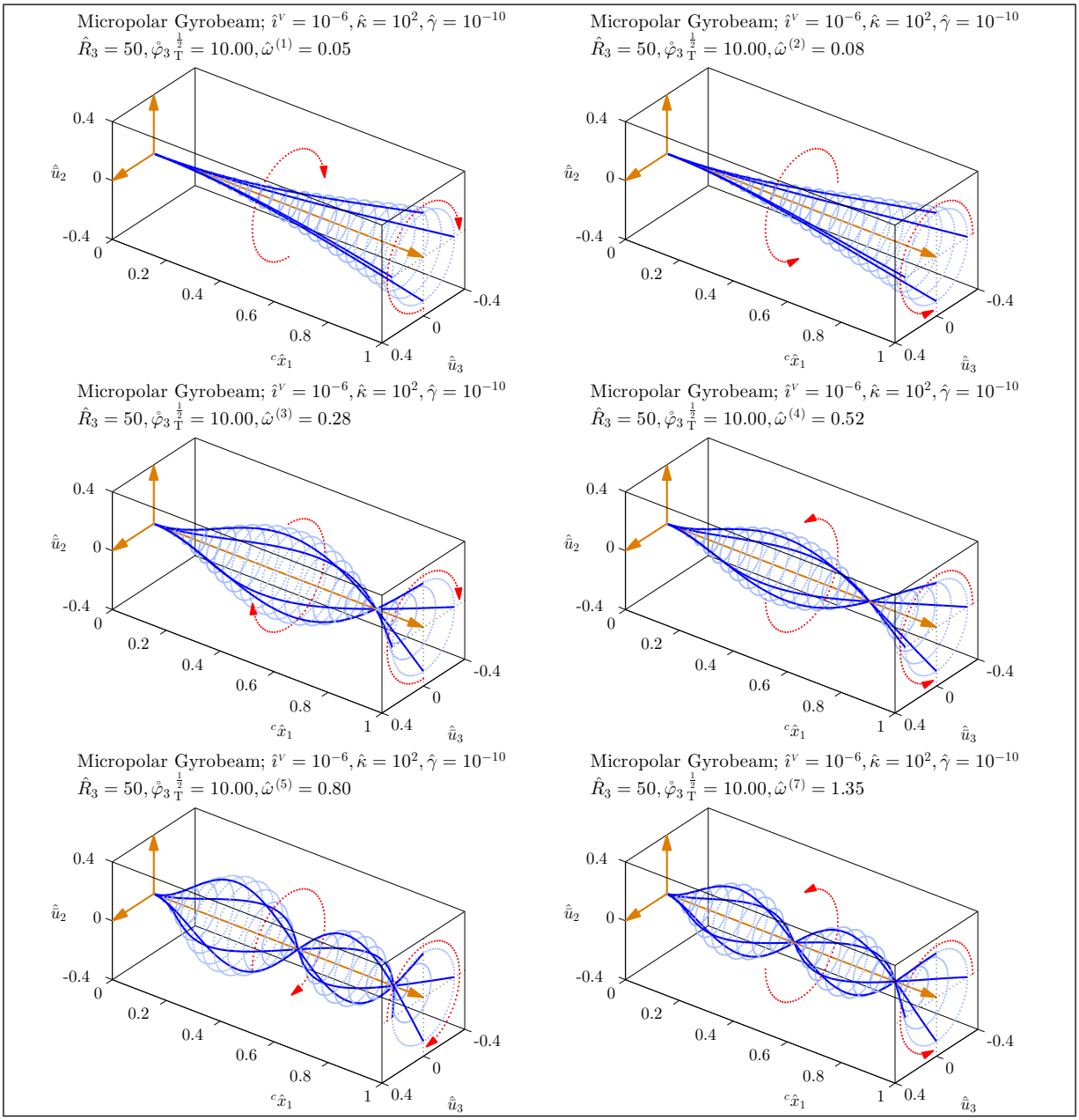

Figure 6.13: Mode shapes of a medium micropolar gyrobeam with a small uniform axial gyricity – Micropolar gyrobeam model 1.

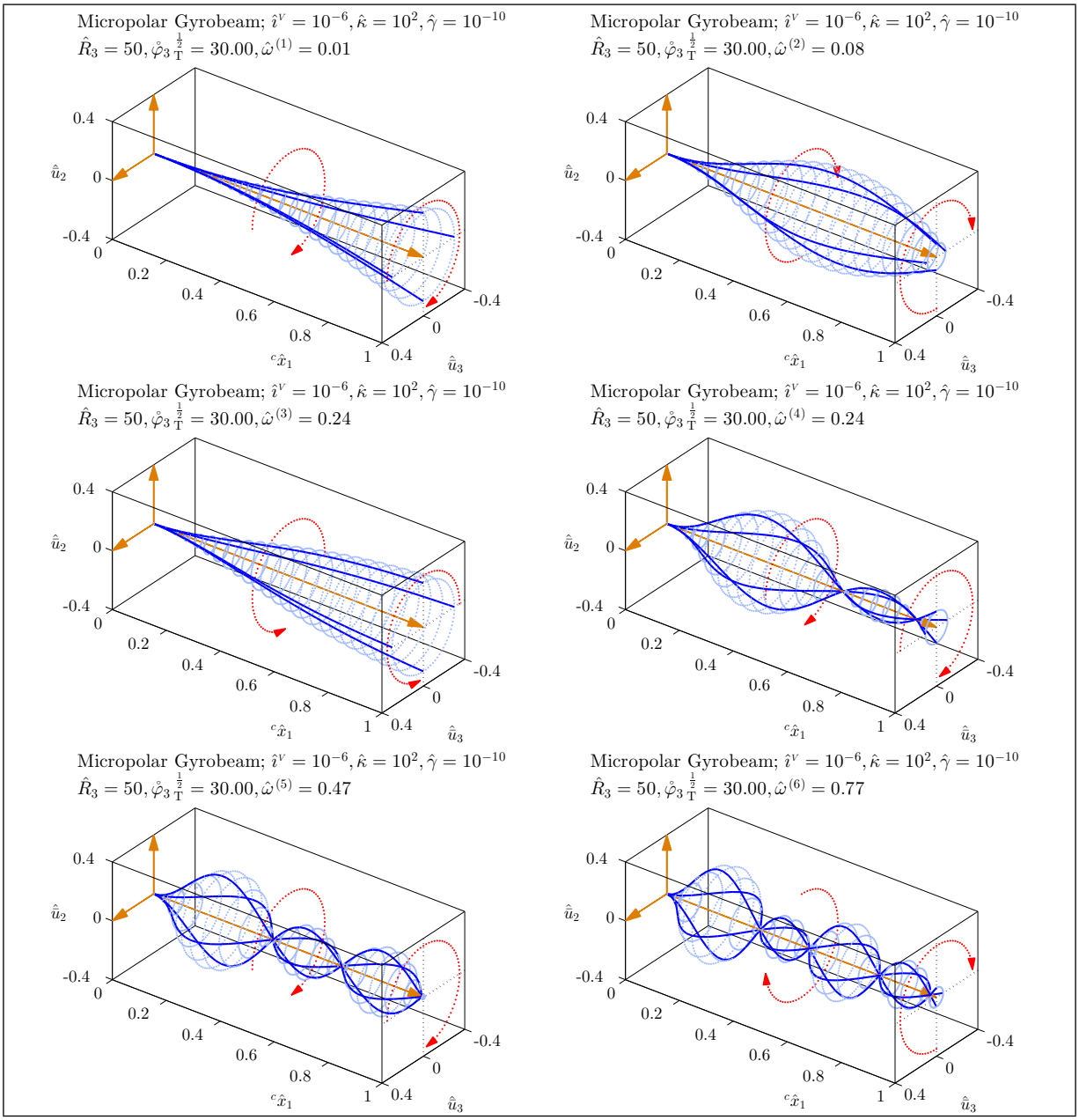

Figure 6.14: Mode shapes of a medium micropolar gyrobeam with a medium uniform axial gyricity – Micropolar gyrobeam model 1.

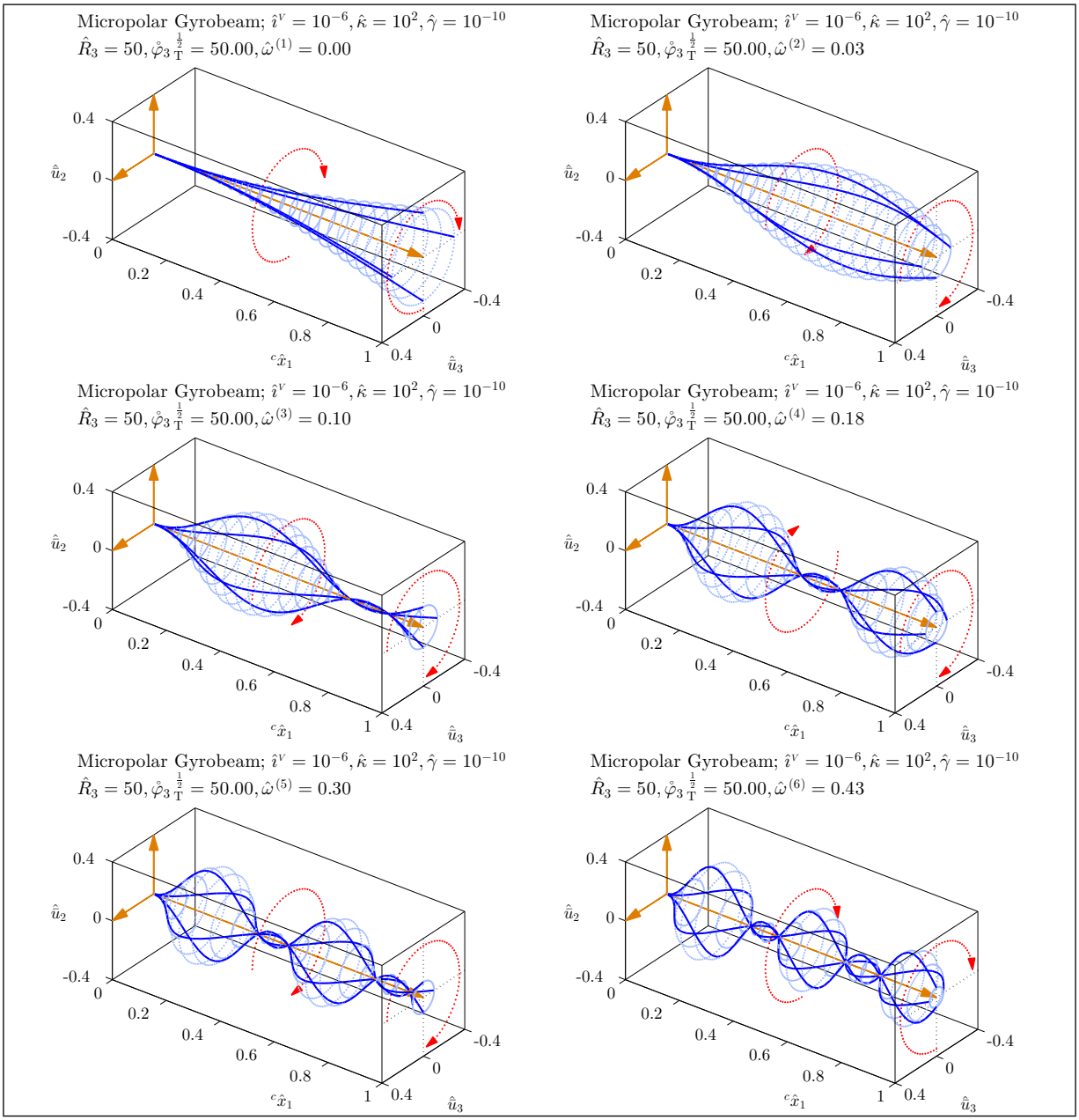

Figure 6.15: Mode shapes of a medium micropolar gyrobeam with a large uniform axial gyricity – Micropolar gyrobeam model 1.

The natural frequency loci and mode shapes of the first specific micropolar gyrobeam model are shown in Figures 6.10–6.15. Whereas the natural frequencies depicted in Figures 6.10, 6.11, and 6.12 are expected to be comparable to the corresponding results of the classical gyrobeam model, respectively given in Figures 5.5, 5.6, and 5.7, one may observe that this is only true for the very thin gyrobeams with $\hat{R}_3 = 250$. The natural frequency loci of the classical and micropolar gyrobeams with large and medium thicknesses (*i.e.* with $\hat{R}_3 = 10$ and $\hat{R}_3 = 50$), except for a few lower natural frequencies, have significant differences in general.

This is not a surprise because, as mentioned previously, the rotational inertia of the gyros is assumed to be proportional to the beam thickness and consequently thicker gyrobeams carry a larger gyricity compared to the thinner gyrobeams. Recall that a larger gyricity results in a bigger difference between the classical and micropolar gyrobeams specially when considering the higher natural frequencies. The weaker coupling effects in the thicker micropolar gyrobeams is another reason why their natural frequency loci deviate from the classical gyrobeams natural frequency loci.

It is interesting to observe that the natural frequencies of this micropolar gyrobeam model drop more quickly as the gyricity increases. This is opposite of what one may expect by just considering the size effects phenomenon (explained in Appendix A) which predicts a higher stiffness in a micropolar continuum compared to a classical one.

Finally, one may notice no significant differences between the mode shapes of the first micropolar gyrobeam model at medium thickness, shown in Figures 6.13, 6.14, and 6.15, and the corresponding mode shapes of the classical gyrobeam model, given in Figures 5.11, 5.12, and 5.13. The only exception is the last mode shape shown in Figure 6.15 which significantly deviates from the last mode shape in Figure 5.13. This disagreement is due to a curve veering point on the sixth natural frequency locus at around $\mathring{\varphi}_{3_\Gamma}^{\frac{1}{2}} = 50$ which is located differently in the two models (whereas in the classical gyrobeam model it occurs before $\mathring{\varphi}_{3_\Gamma}^{\frac{1}{2}} = 50$, in the first micropolar gyrobeam model it occurs after $\mathring{\varphi}_{3_\Gamma}^{\frac{1}{2}} = 50$).

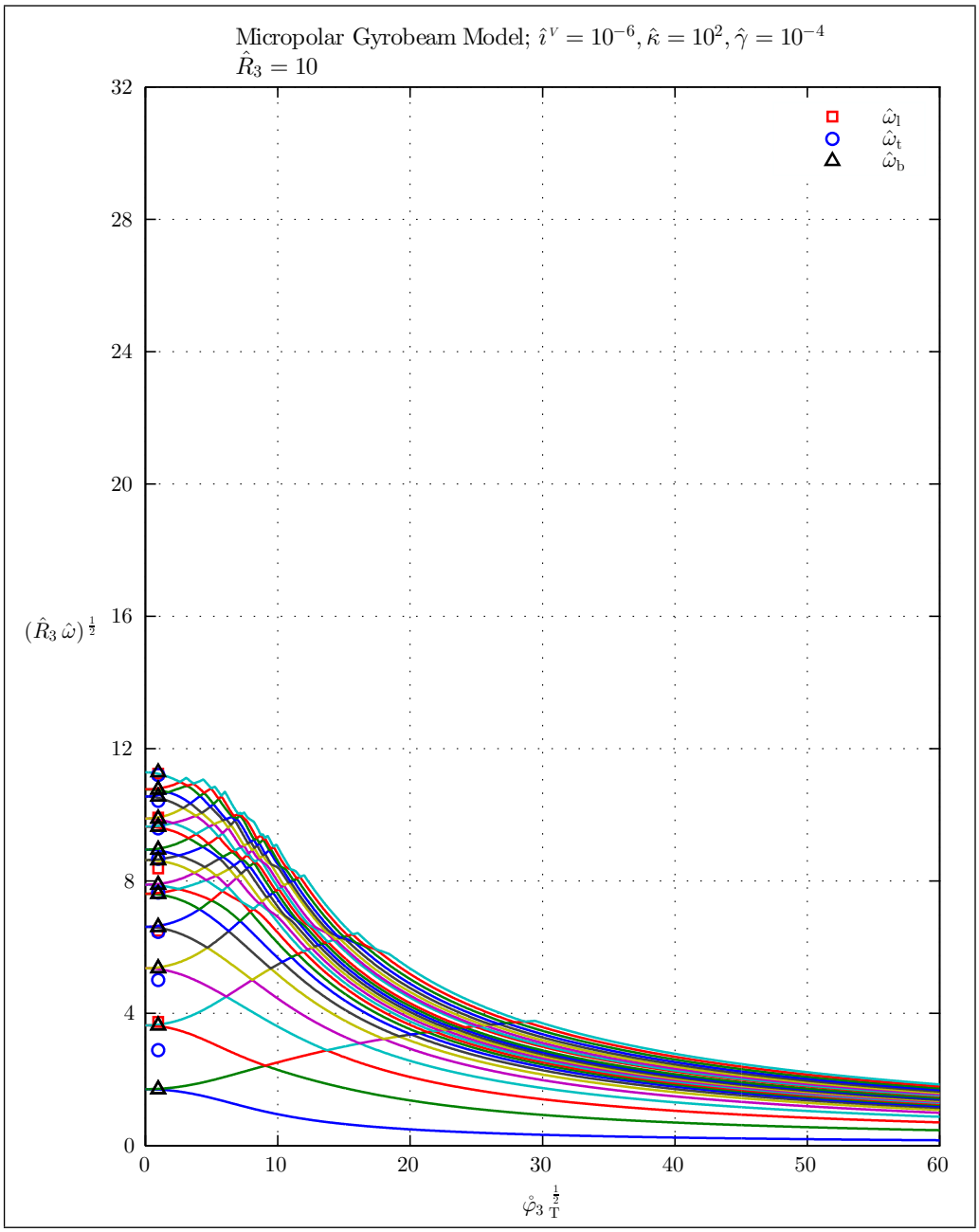

Figure 6.16: Natural frequencies of a thick micropolar gyrobeam with a uniform axial gyricity – Micropolar gyrobeam model 2.

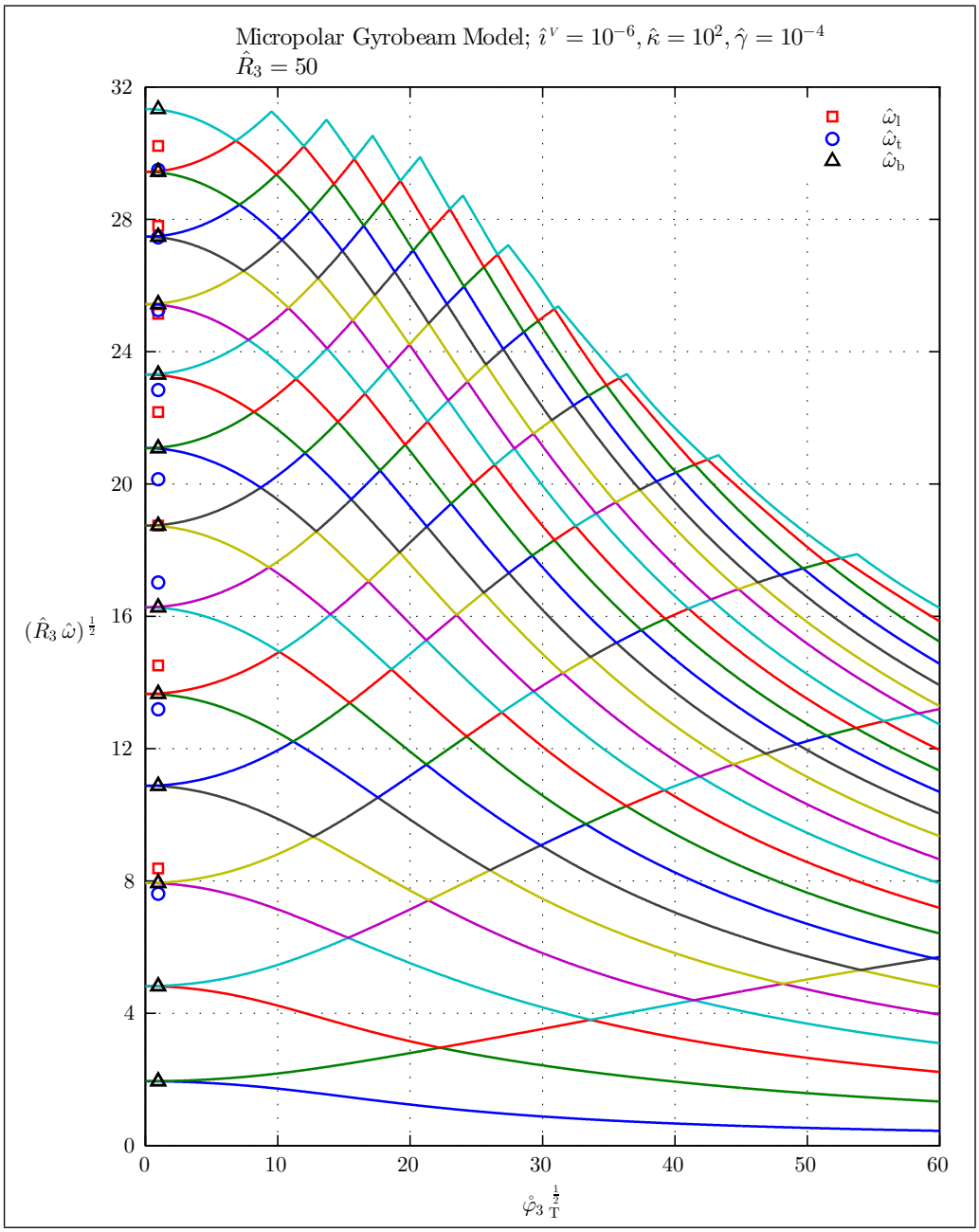

Figure 6.17: Natural frequencies of a medium micropolar gyrobeam with a uniform axial gyricity – Micropolar gyrobeam model 2.

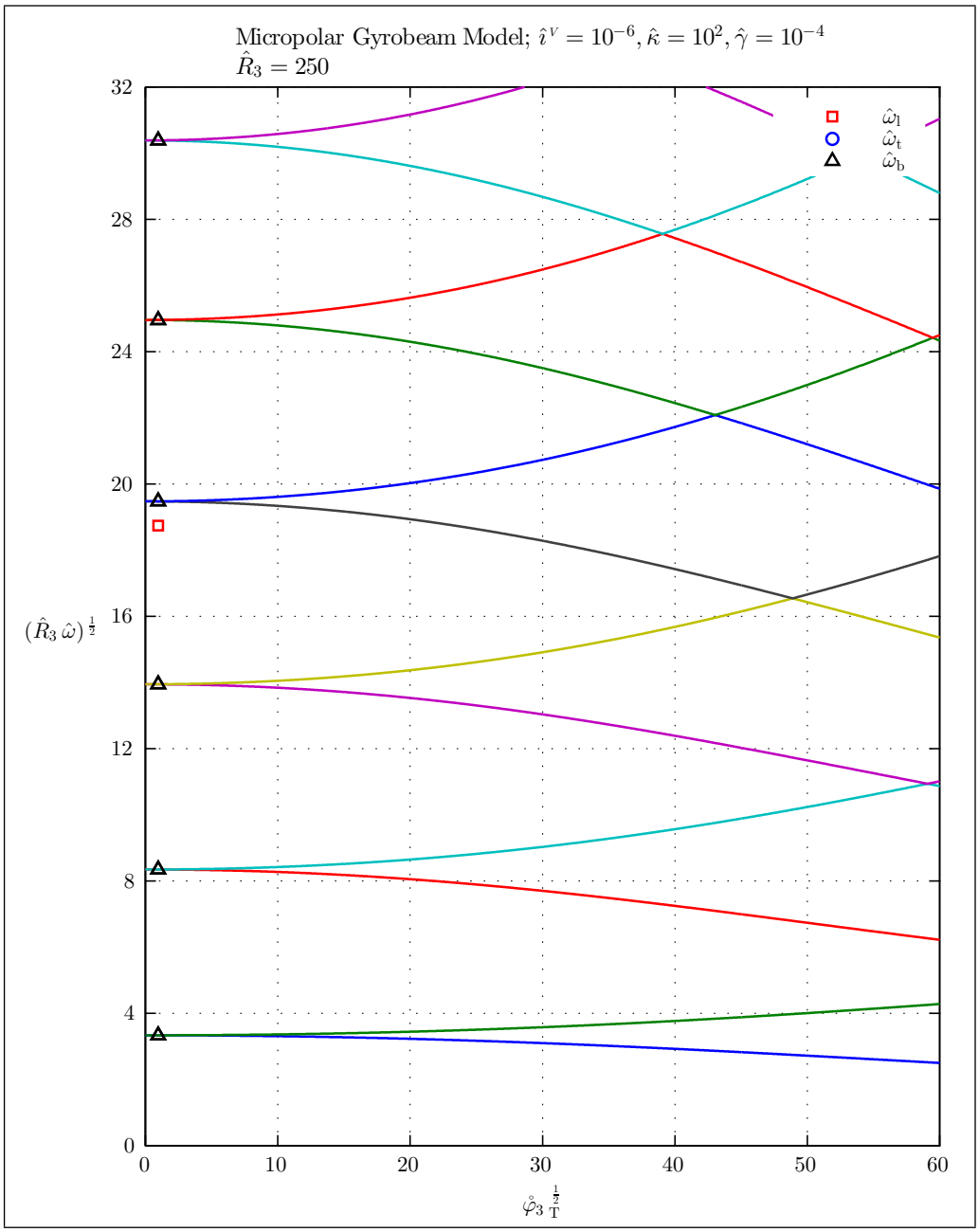

Figure 6.18: Natural frequencies of a thin micropolar gyrobeam with a uniform axial gyricity – Micropolar gyrobeam model 2.

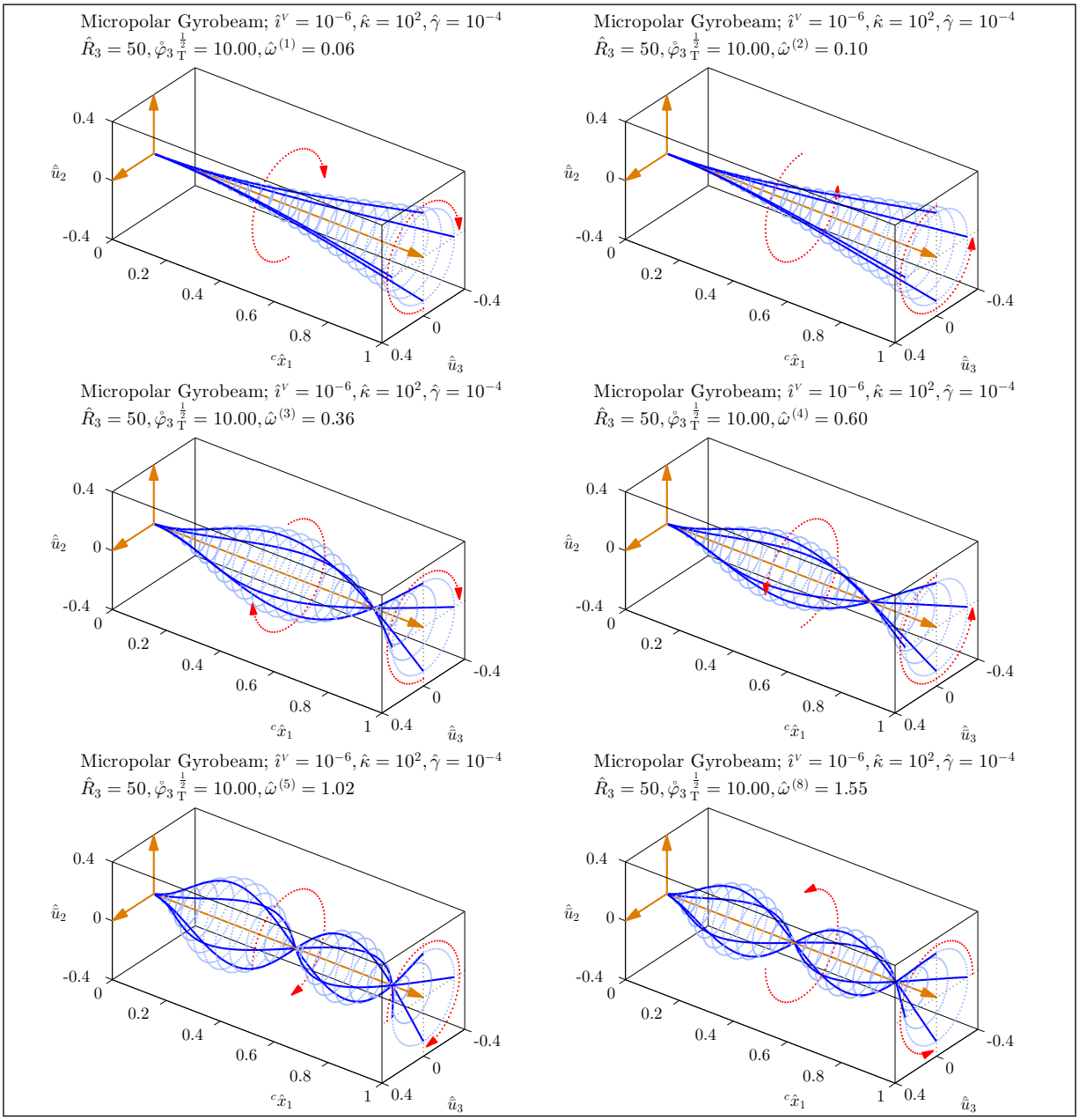

Figure 6.19: Mode shapes of a medium micropolar gyrobeam with a small uniform axial gyricity – Micropolar gyrobeam model 2.

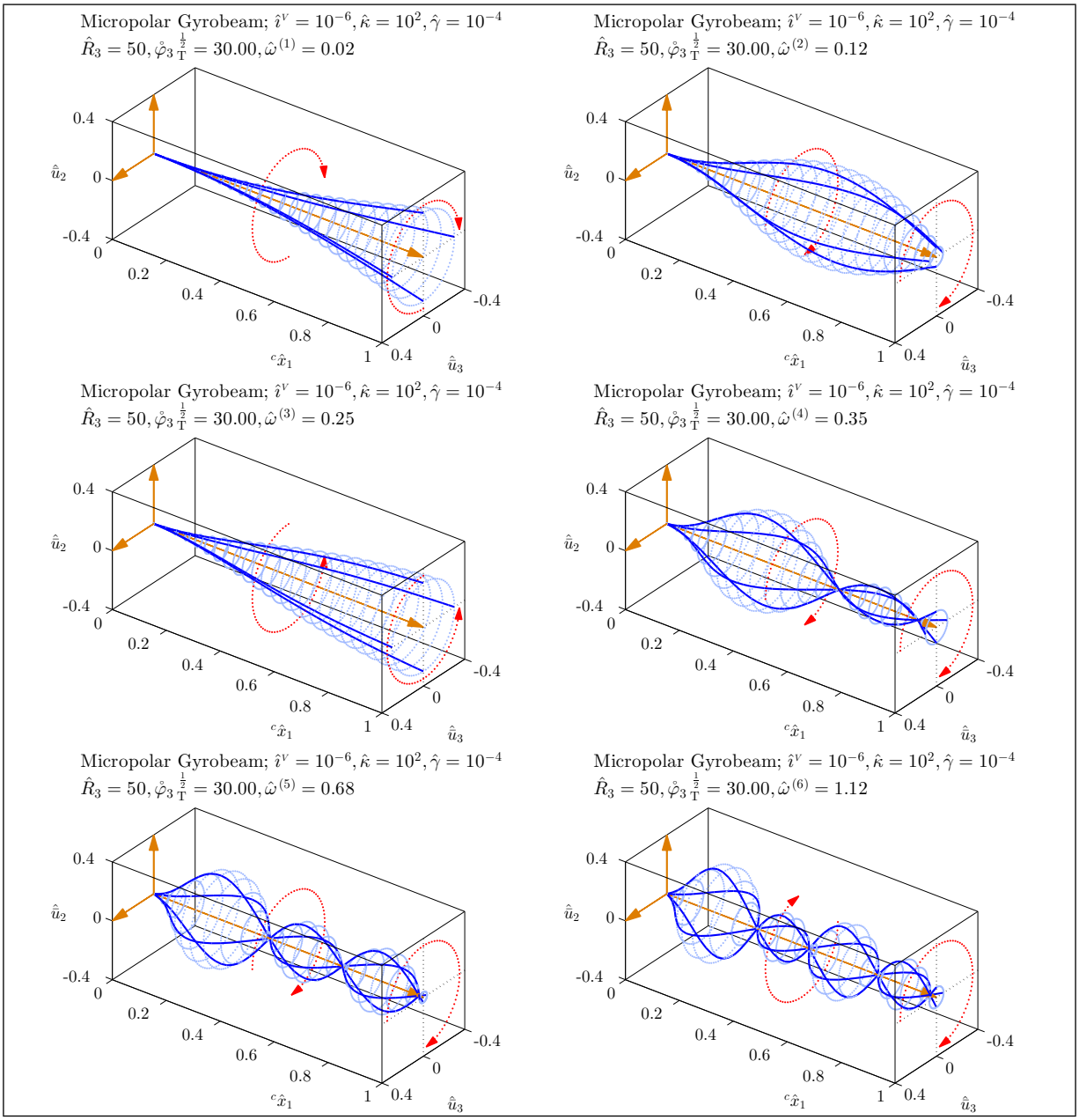

Figure 6.20: Mode shapes of a medium micropolar gyrobeam with a medium uniform axial gyricity – Micropolar gyrobeam model 2.

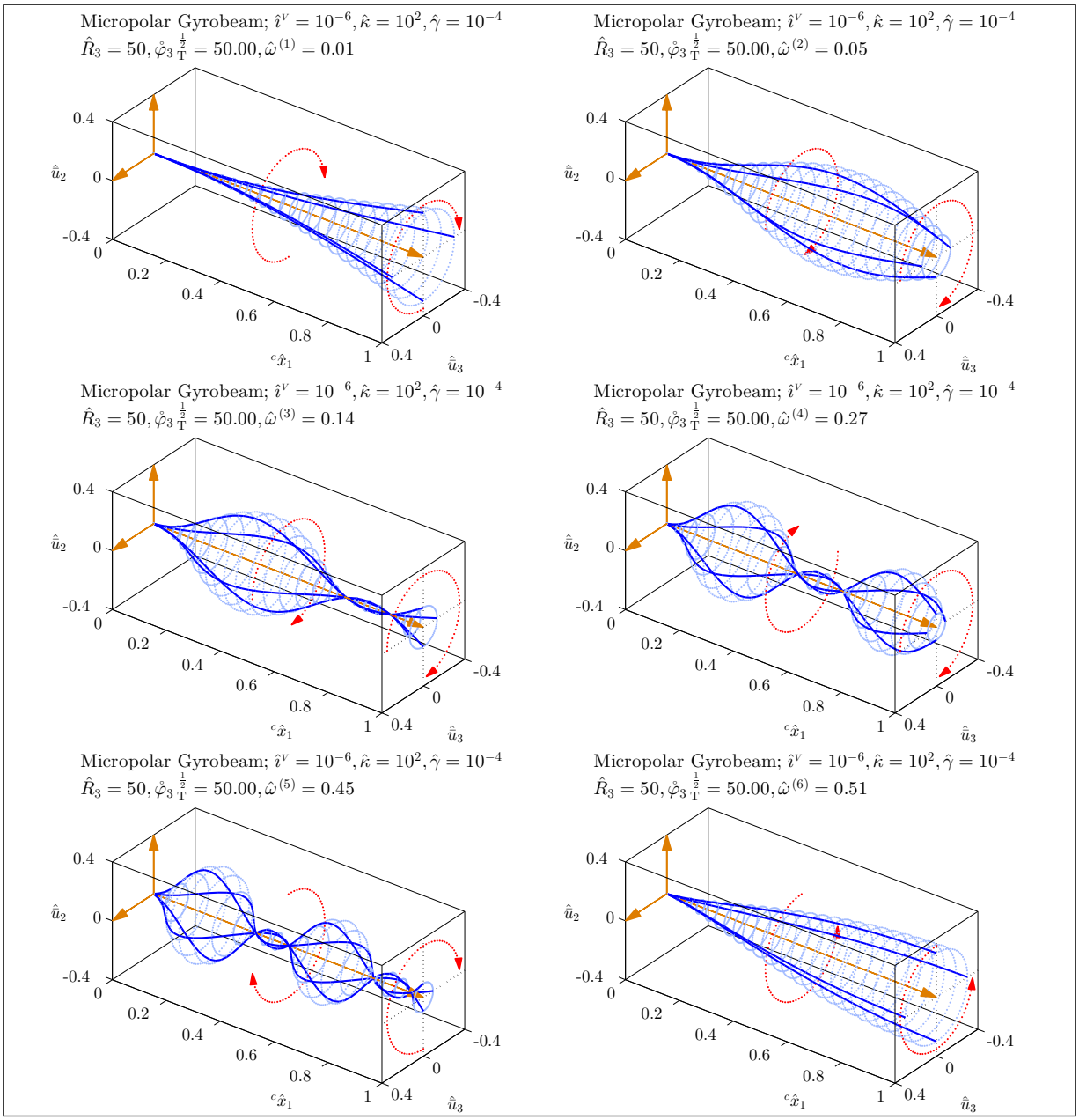

Figure 6.21: Mode shapes of a medium micropolar gyrobeam with a large uniform axial gyricity – Micropolar gyrobeam model 2.

Comparing the natural frequency loci and mode shapes of the second specific micropolar gyrobeam model, given in Figures 6.16–6.21, with those of the first micropolar gyrobeam model reveals the effect of increasing the micropolar elastic constant $\hat{\gamma}$ in the micropolar gyrobeam model. By looking at the natural frequency loci in Figures 6.16, 6.17, and 6.18 and comparing them with Figures 6.10, 6.11, and 6.12, one may expectantly note that in a micropolar gyrobeam model with a large enough value for $\hat{\kappa}$ (which is the case in here), a larger value for $\hat{\gamma}$ results in a higher stiffness and consequently higher natural frequencies. As suggested by the size effects phenomenon this is more pronounced in the thinnest micropolar gyrobeam. Considering Figures 6.12 and 6.18, it is interesting how the increase of $\hat{\gamma}$ can eliminate, or move to very high values of gyricity, most of the curve veering points.

For the gyrobeams with medium thickness, however, the differences between the mode shapes of the second micropolar gyrobeam model, shown in Figures 6.19, 6.20, and 6.21, and those of the first micropolar gyrobeam model are not significant. The only exception is the last mode shape shown in Figure 6.21 which due to a different curve veering of the sixth natural frequency locus is noticeably different than the last mode shape in Figure 6.15.

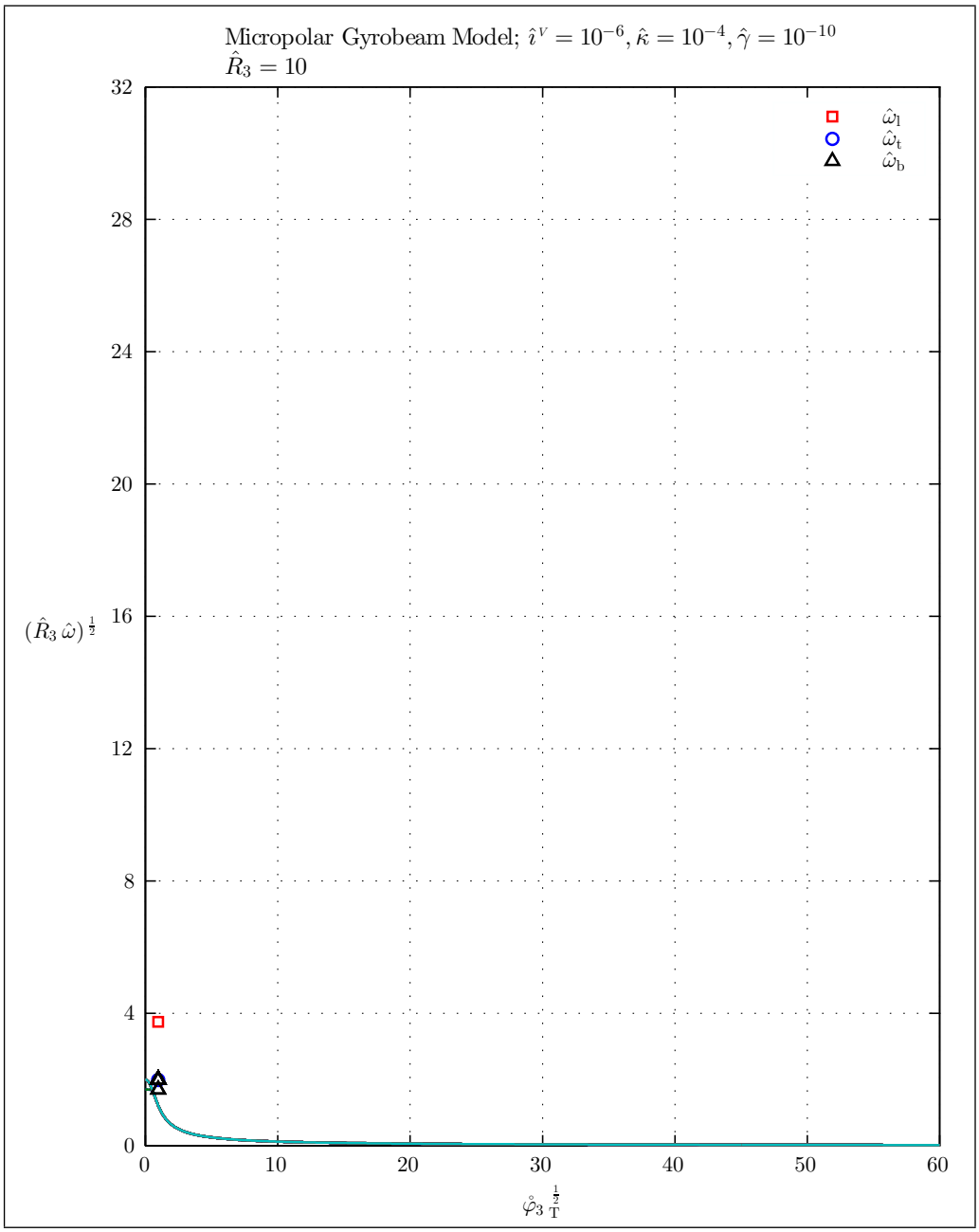

Figure 6.22: Natural frequencies of a thick micropolar gyrobeam with a uniform axial gyricity – Micropolar gyrobeam model 3.

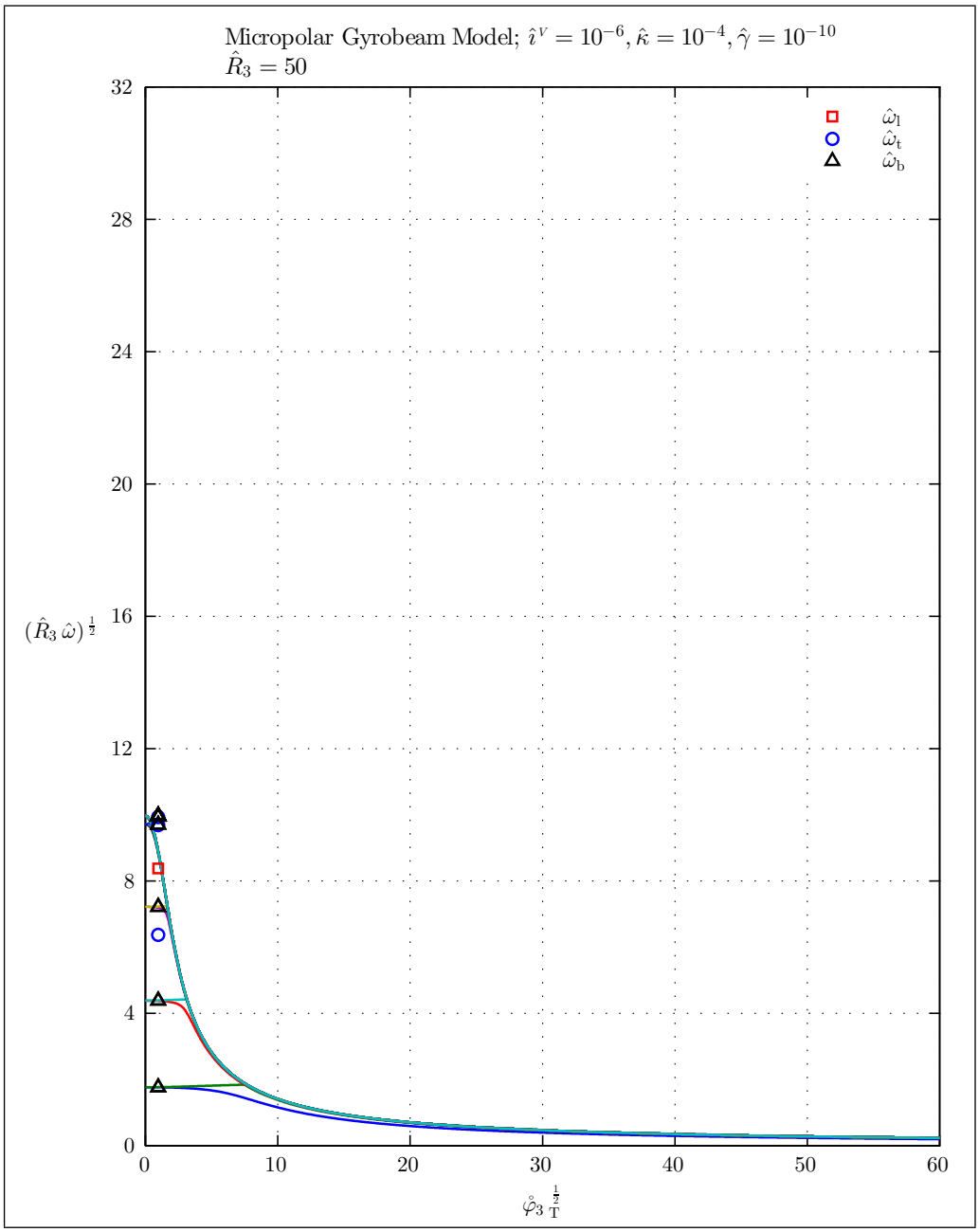

Figure 6.23: Natural frequencies of a medium micropolar gyrobeam with a uniform axial gyricity – Micropolar gyrobeam model 3.

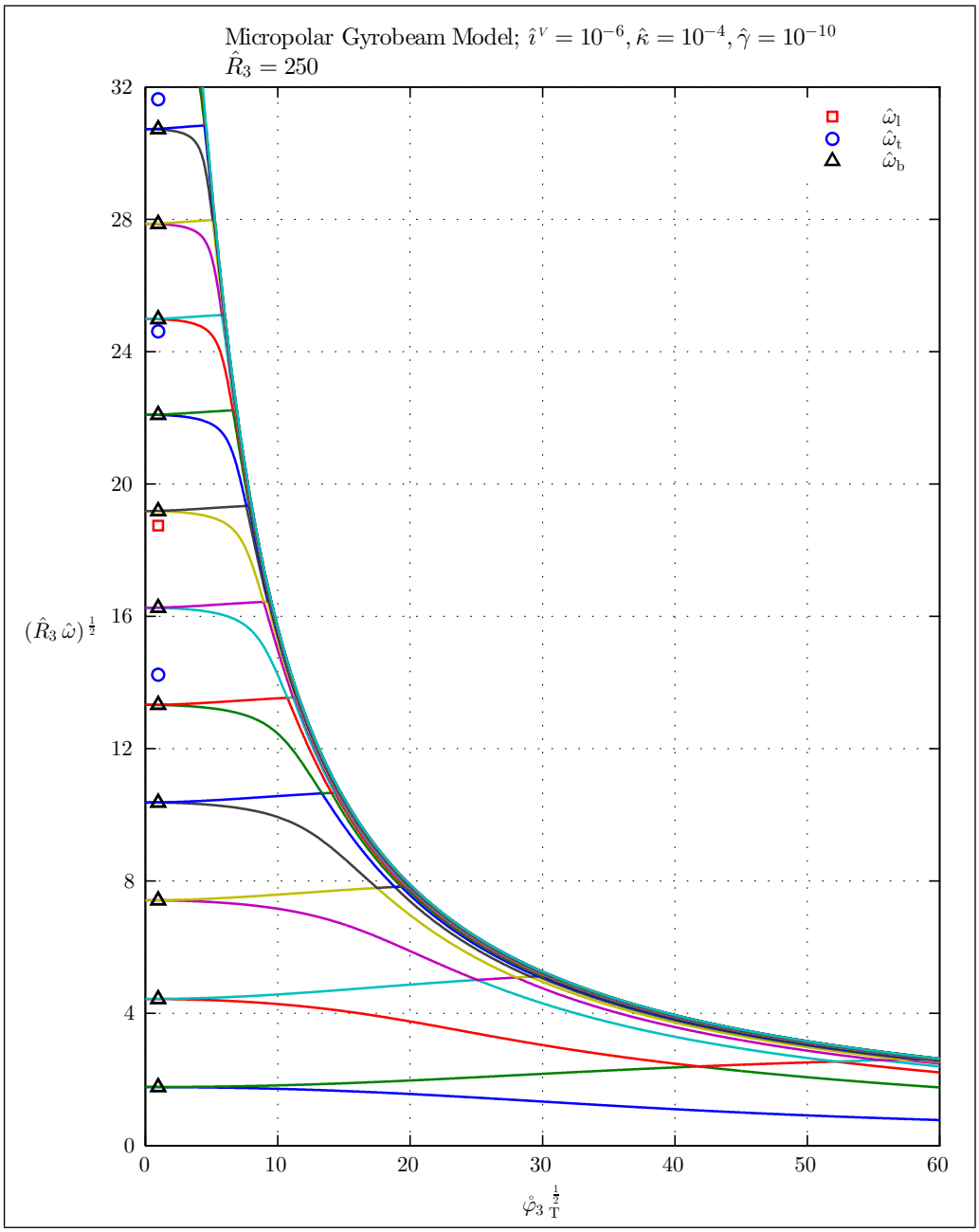

Figure 6.24: Natural frequencies of a thin micropolar gyrobeam with a uniform axial gyricity – Micropolar gyrobeam model 3.

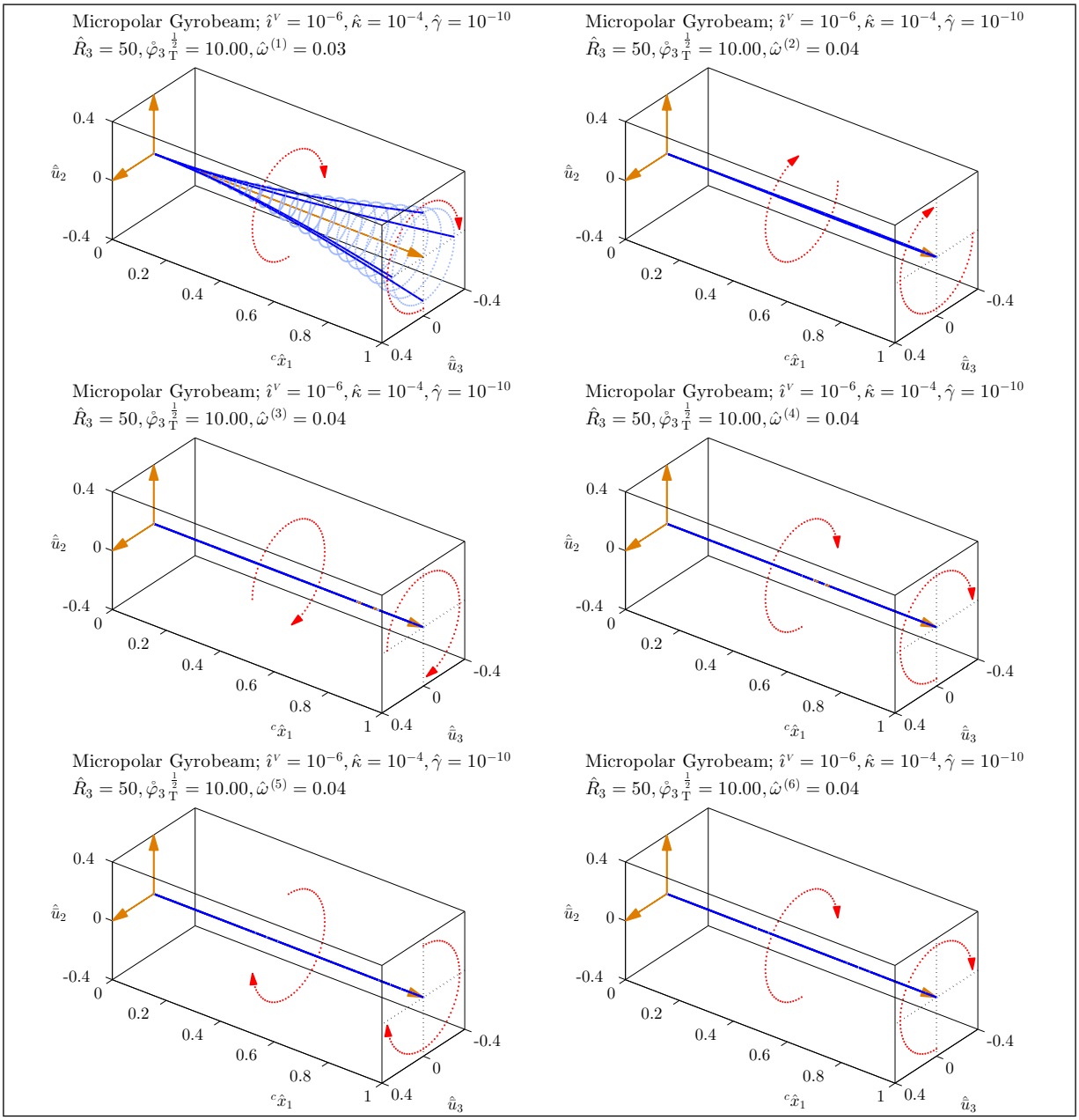

Figure 6.25: Mode shapes of a medium micropolar gyrobeam with a small uniform axial gyricity – Micropolar gyrobeam model 3.

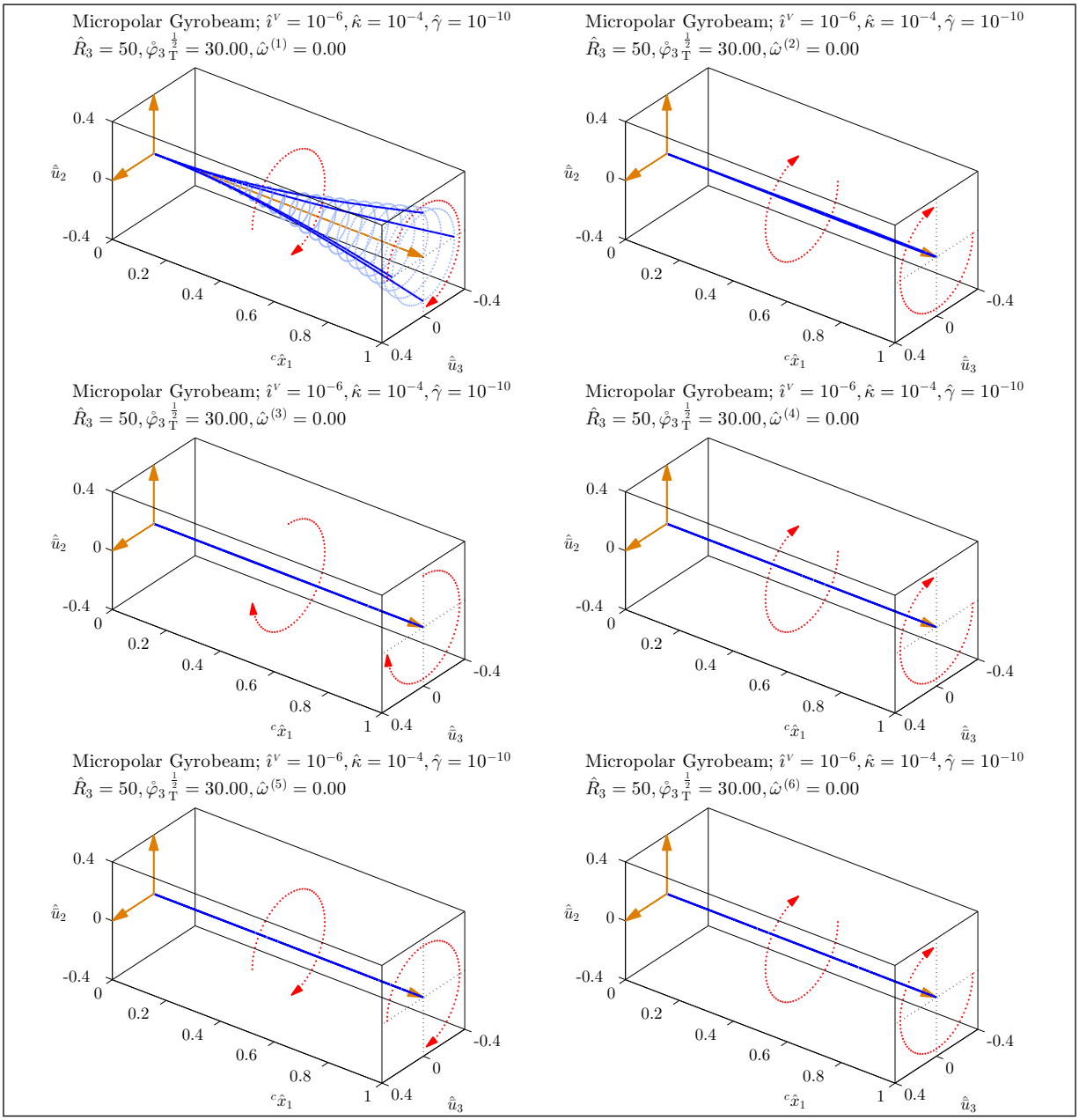

Figure 6.26: Mode shapes of a medium micropolar gyrobeam with a medium uniform axial gyricity – Micropolar gyrobeam model 3.

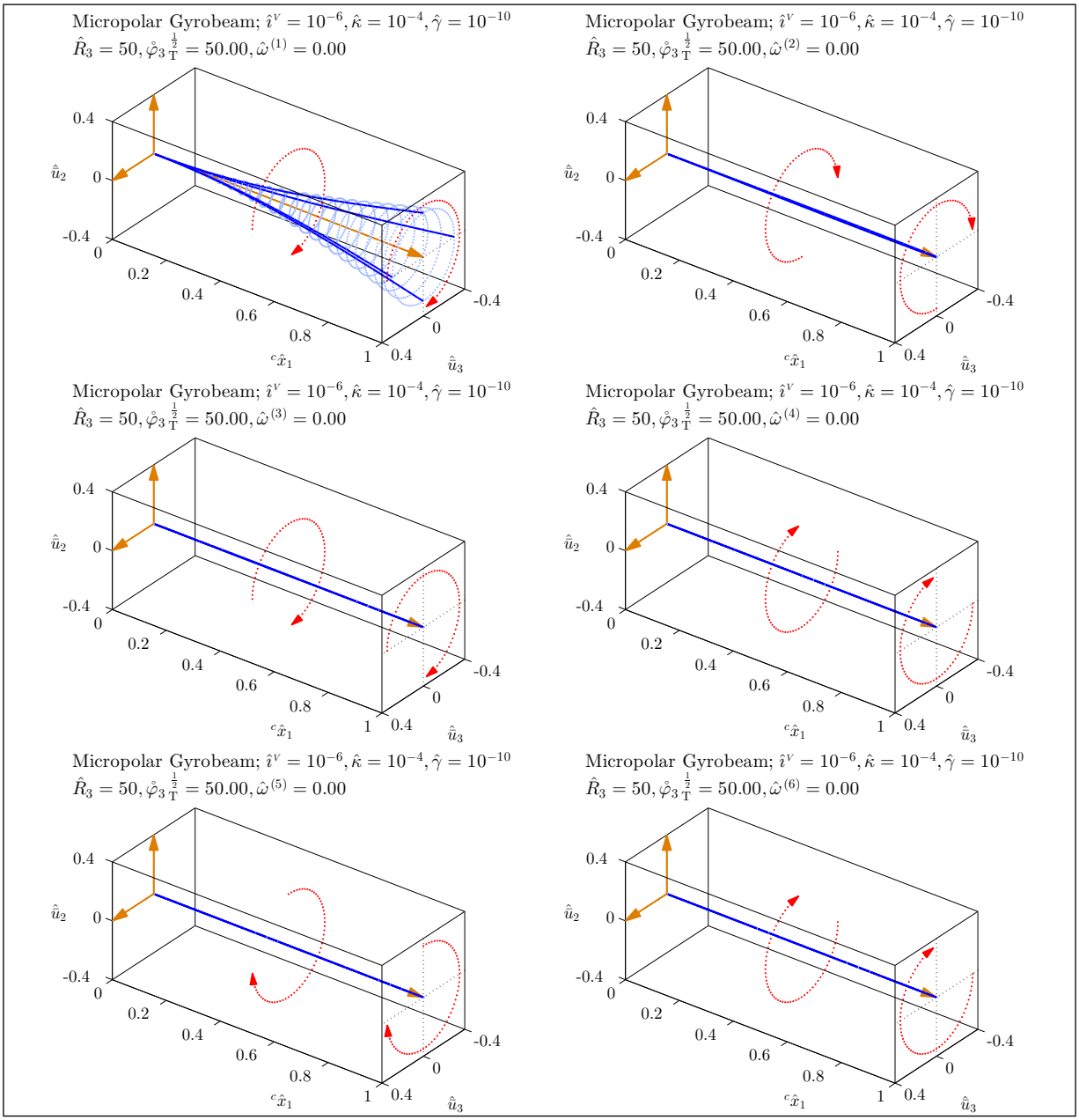

Figure 6.27: Mode shapes of a medium micropolar gyrobeam with a large uniform axial gyricity – Micropolar gyrobeam model 3.

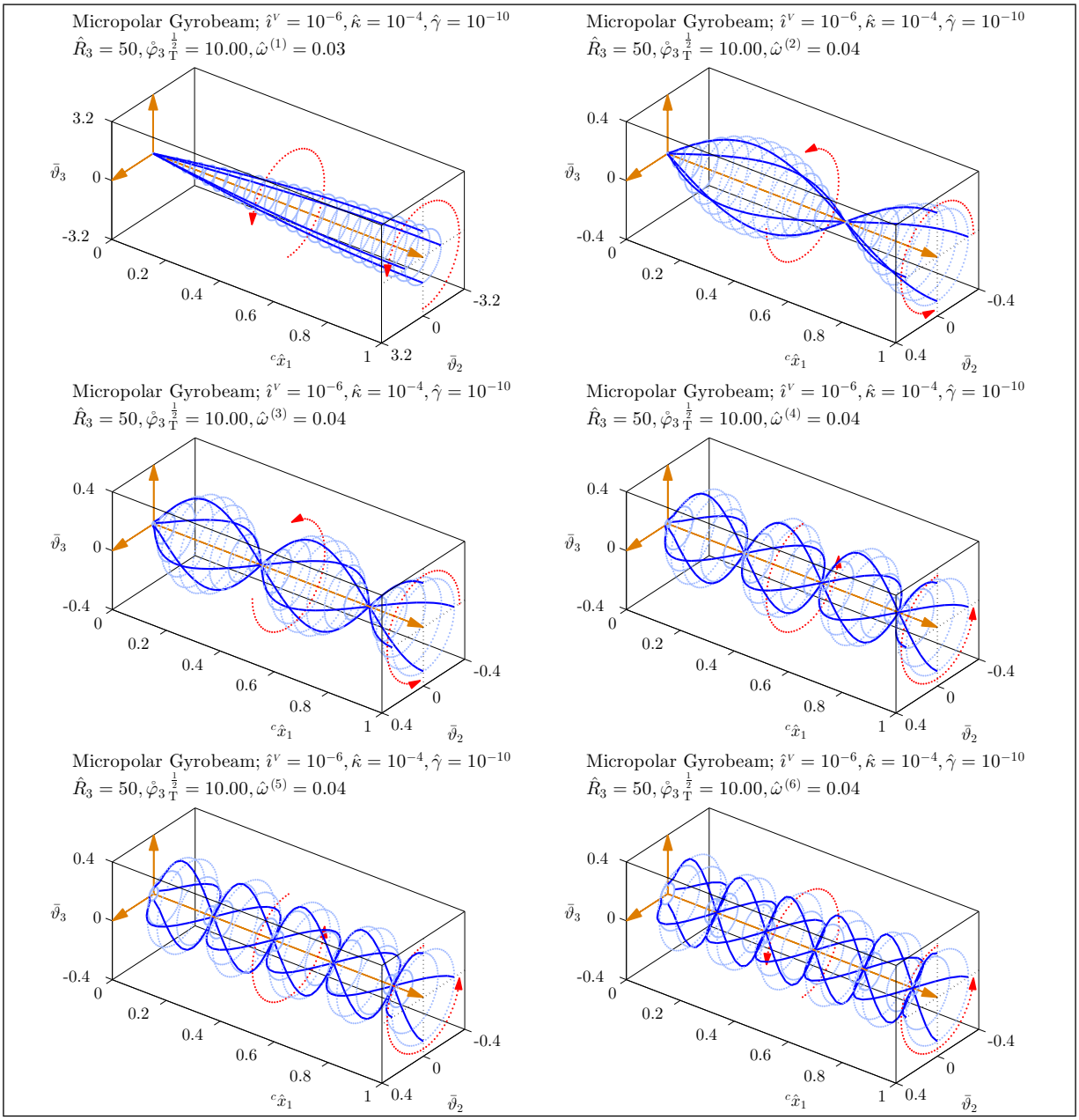

Figure 6.28: Mode shapes of a medium micropolar gyrobeam with a small uniform axial gyricity – Micropolar gyrobeam model 3.

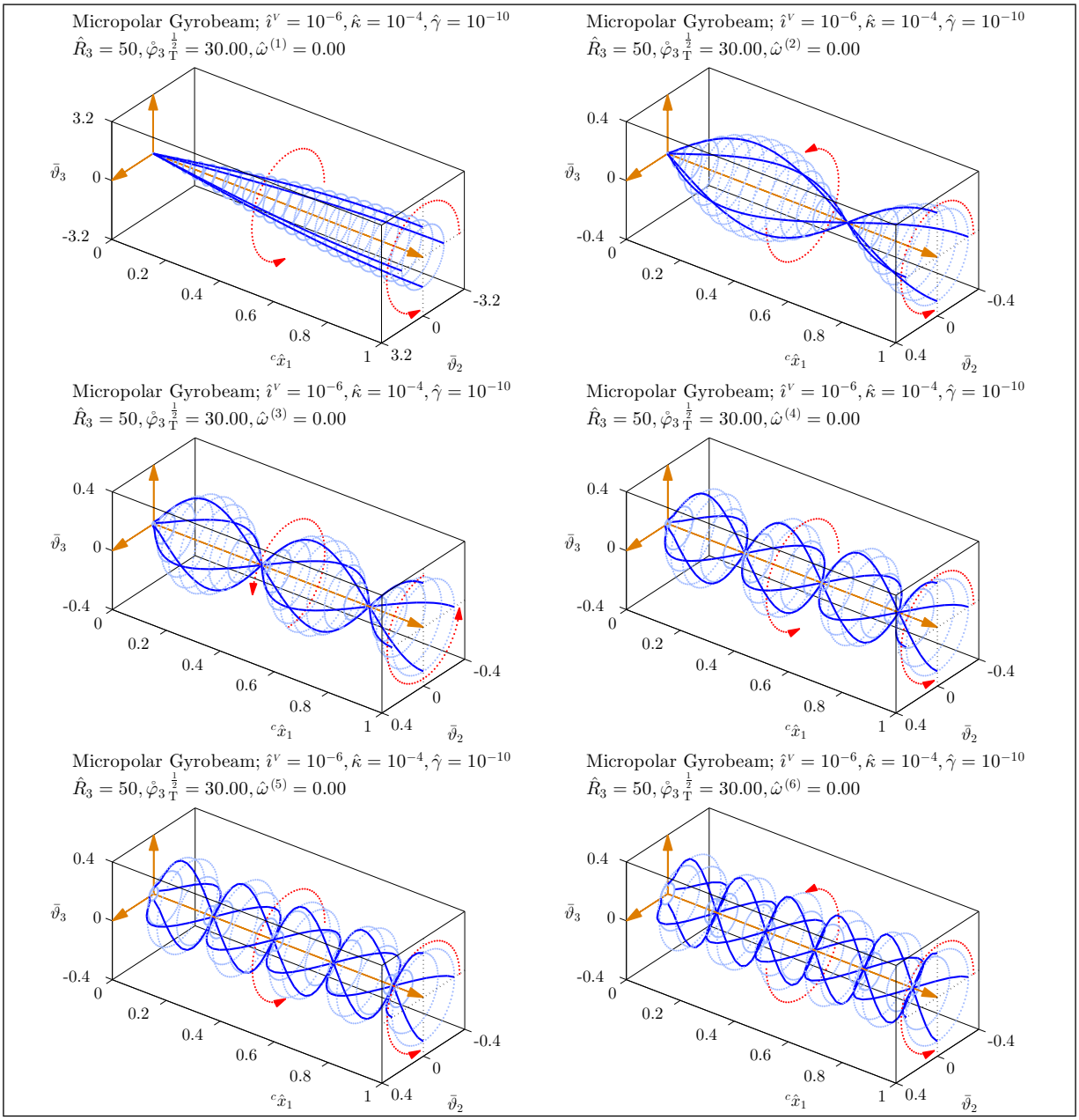

Figure 6.29: Mode shapes of a medium micropolar gyrobeam with a medium uniform axial gyricity – Micropolar gyrobeam model 3.

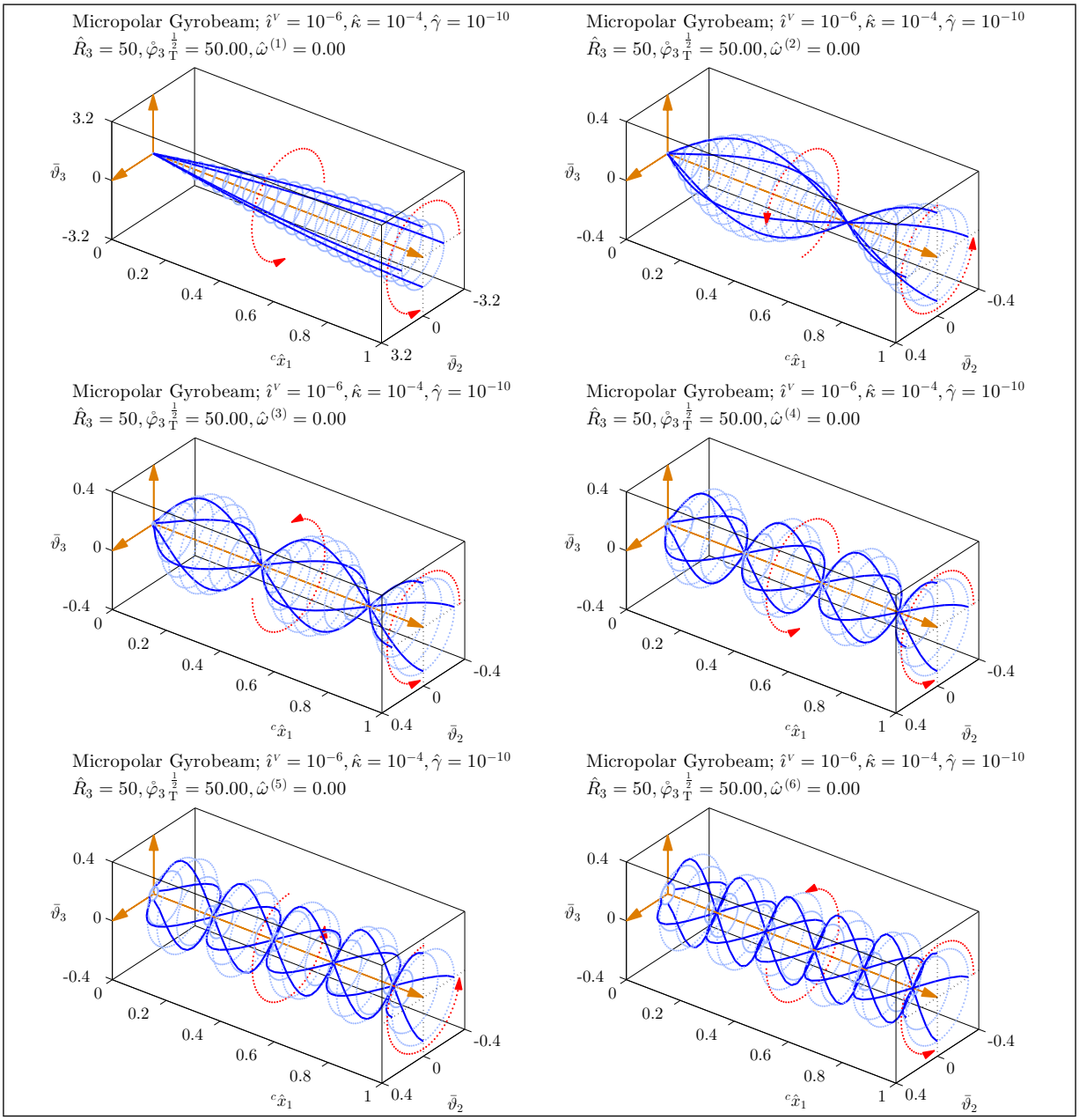

Figure 6.30: Mode shapes of a medium micropolar gyrobeam with a large uniform axial gyricity – Micropolar gyrobeam model 3.

The natural frequency loci and mode shapes of the third specific micropolar gyrobeam model are shown in Figures 6.22–6.30. These figures can be used to study the effect of decreasing the micropolar elastic constant $\hat{\kappa}$ in the micropolar gyrobeam model. One may notice from the natural frequency loci plots shown in Figures 6.22, 6.23, and 6.24 that the third micropolar gorobeam model with $\hat{\kappa} = 10^{-4}$ is close to being singular. Being more precise, for the thick and medium gyrobeams all the (first 25) natural frequency loci coincide and appear as a single curve (specially as the gyricity value increases) which indicates very small natural frequencies for the third micropolar gyrobeam model compared to the natural frequencies of the first gyrobeam model. This behavior is improved in the thinnest gyrobeam since (as noted in Appendix C) the coupling effects in a micropolar beam become stronger as the beam gets thinner.

In the natural frequency loci of the thinnest gyrobeam, given by Figure 6.24, it is interesting how the natural frequencies of the third micropolar gyrobeam model, which are initially equal to the natural frequencies of the first micropolar gyrobeam model, suddenly drop and the initially nonsingular micropolar gyrobeam model shows a singularity at higher gyricity values. Also note how the higher natural frequency curves gather as a single curve as the gyricity increases.

For this third micropolar gyrobeam model, due to the decoupling between the microrotations and the classical DOFs, in addition to the (classical) displacements it is essential to include the (micropolar) microrotations in the mode shape plots. The classical or displacement portions of the mode shapes for this micropolar gyrobeam model are depicted in Figures 6.25, 6.26, and 6.27, and the micropolar or microrotation portions are illustrated in Figures 6.28, 6.29, and 6.30.

Since the microrotations are decoupled from the displacements and the gyricity terms are directly affecting the microrotations, it is not a surprise that the displacement portions are mostly negligible compared to the microrotation portions and the mode shapes (except the first one) are pure micropolar modes. The coupling between the classical and micropolar DOFs is however strong enough to force these microrotation portions to follow the BCs of the classically cantilevered gyrobeam. Finally, one may notice that, at all the three gyricity values, all the mode shapes precess (or rotate) with a sense opposite to that of the gyricity.

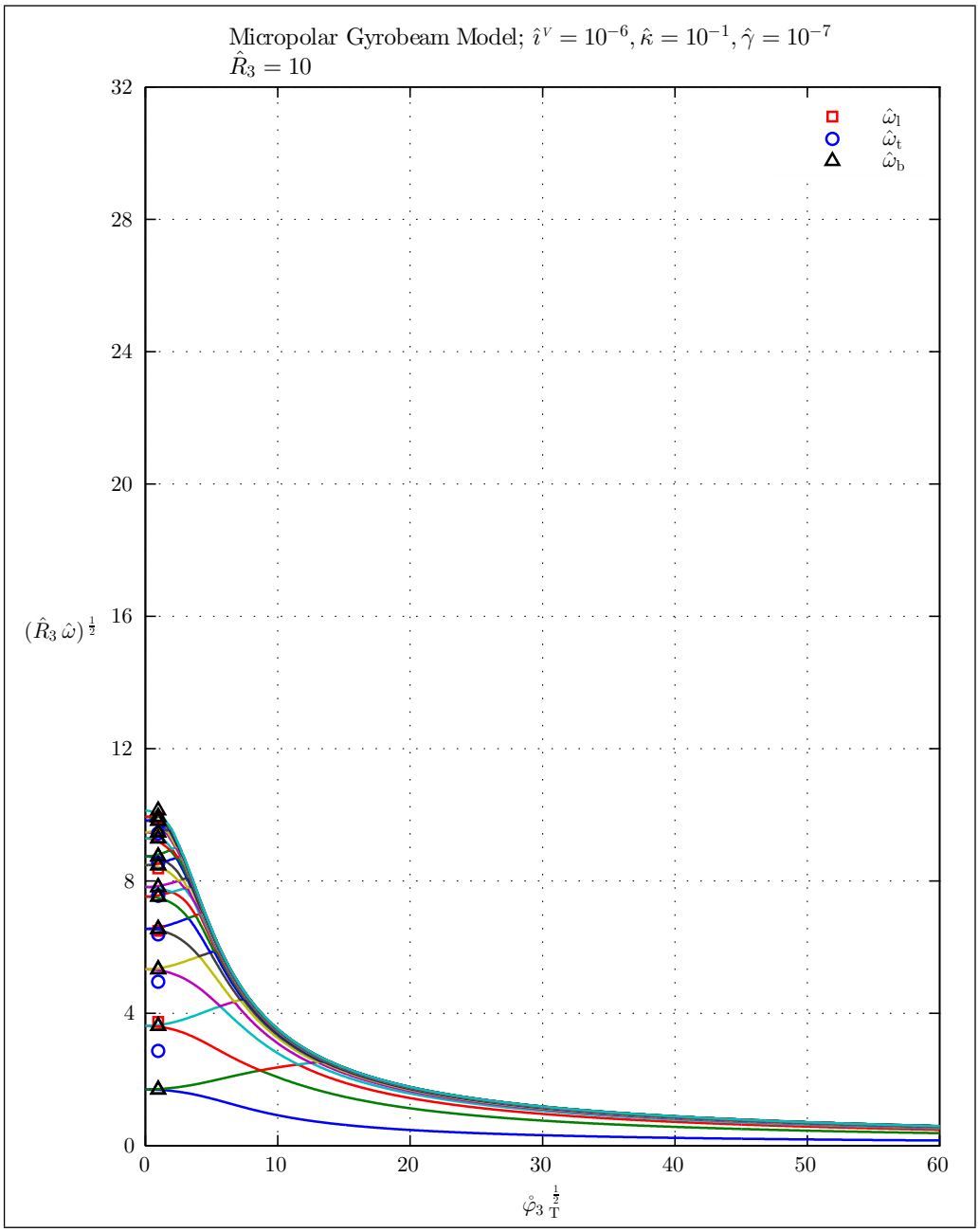

Figure 6.31: Natural frequencies of a thick micropolar gyrobeam with a uniform axial gyricity – Micropolar gyrobeam model 4.

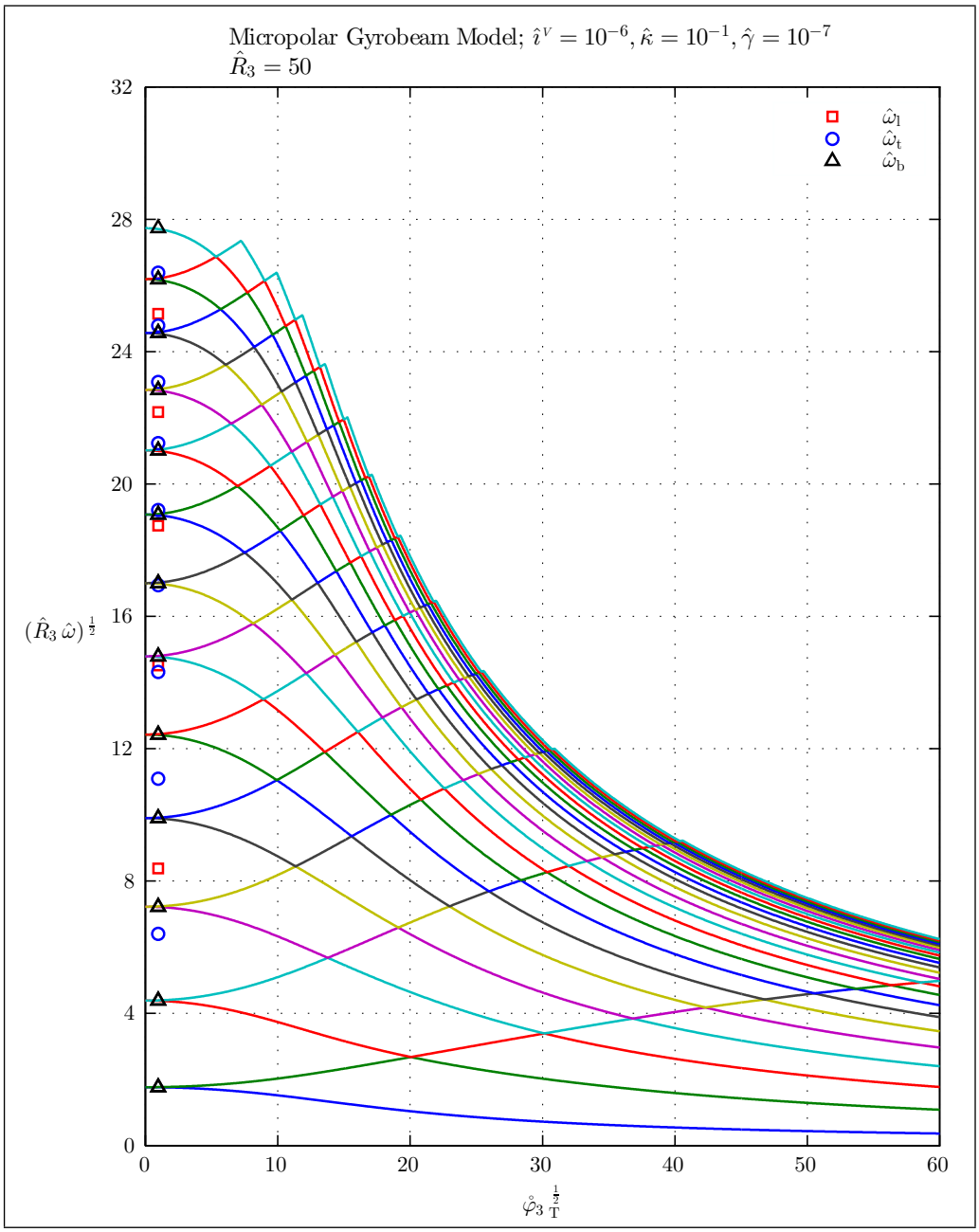

Figure 6.32: Natural frequencies of a medium micropolar gyrobeam with a uniform axial gyricity – Micropolar gyrobeam model 4.

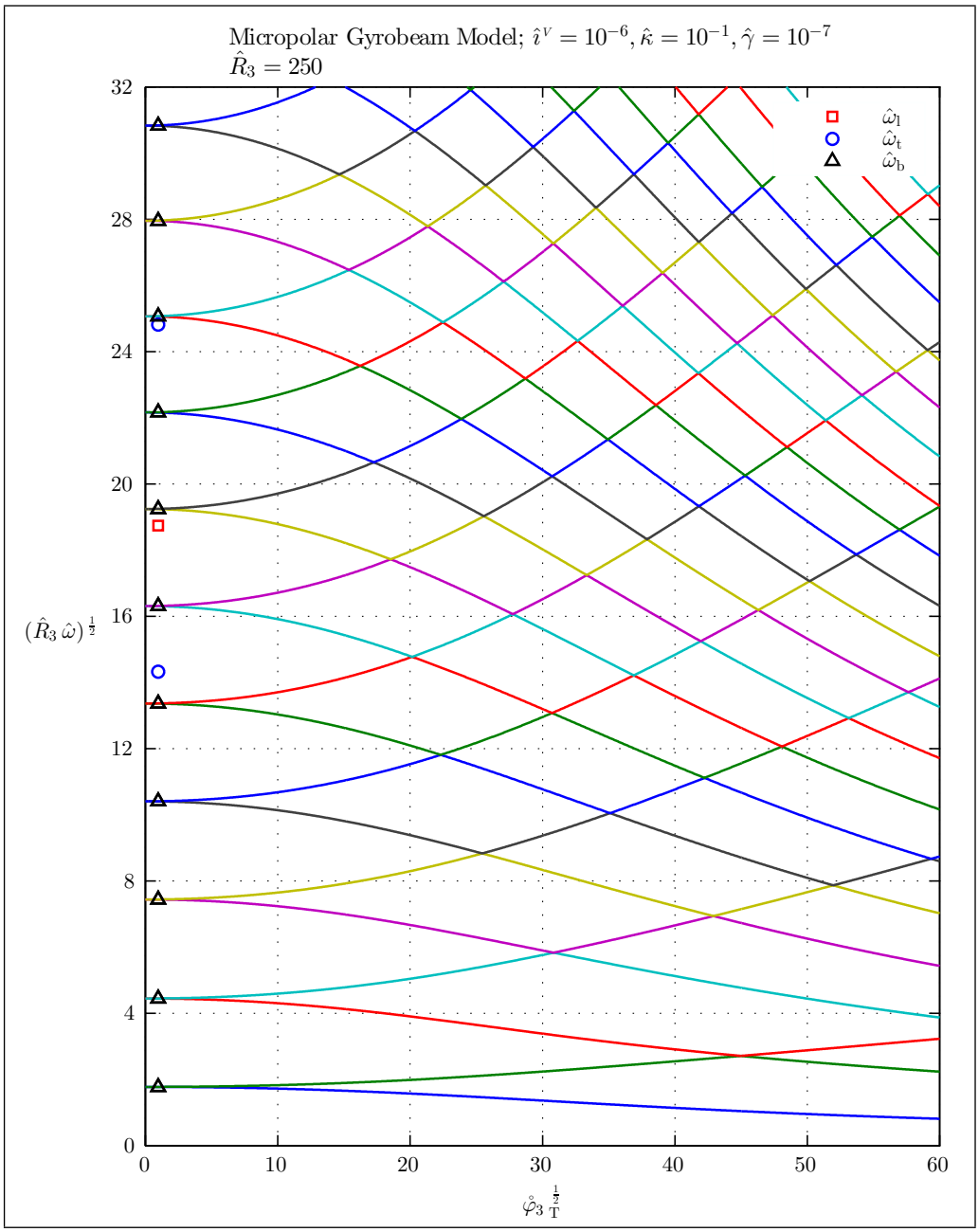

Figure 6.33: Natural frequencies of a thin micropolar gyrobeam with a uniform axial gyricity – Micropolar gyrobeam model 4.

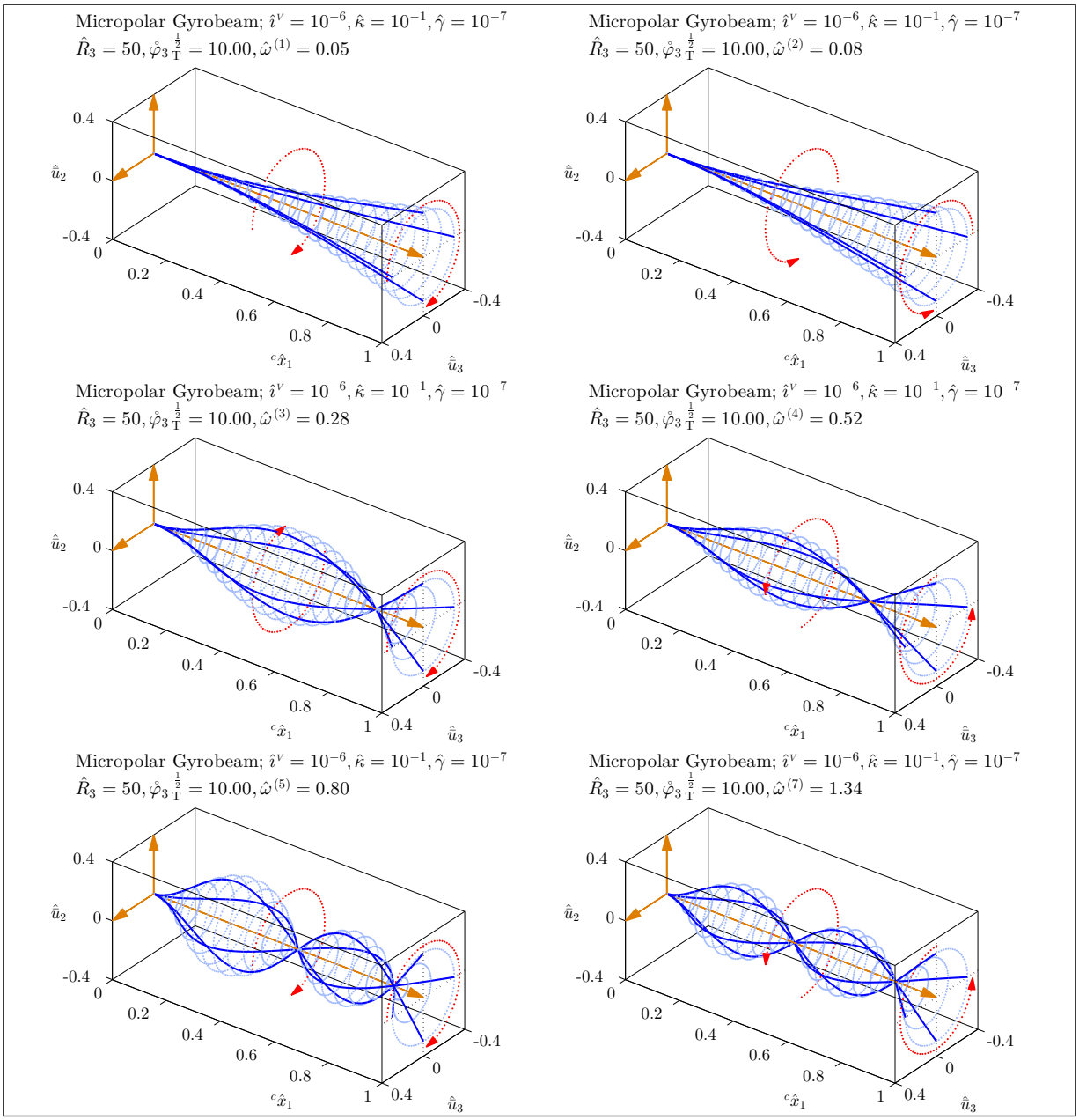

Figure 6.34: Mode shapes of a medium micropolar gyrobeam with a small uniform axial gyricity – Micropolar gyrobeam model 4.

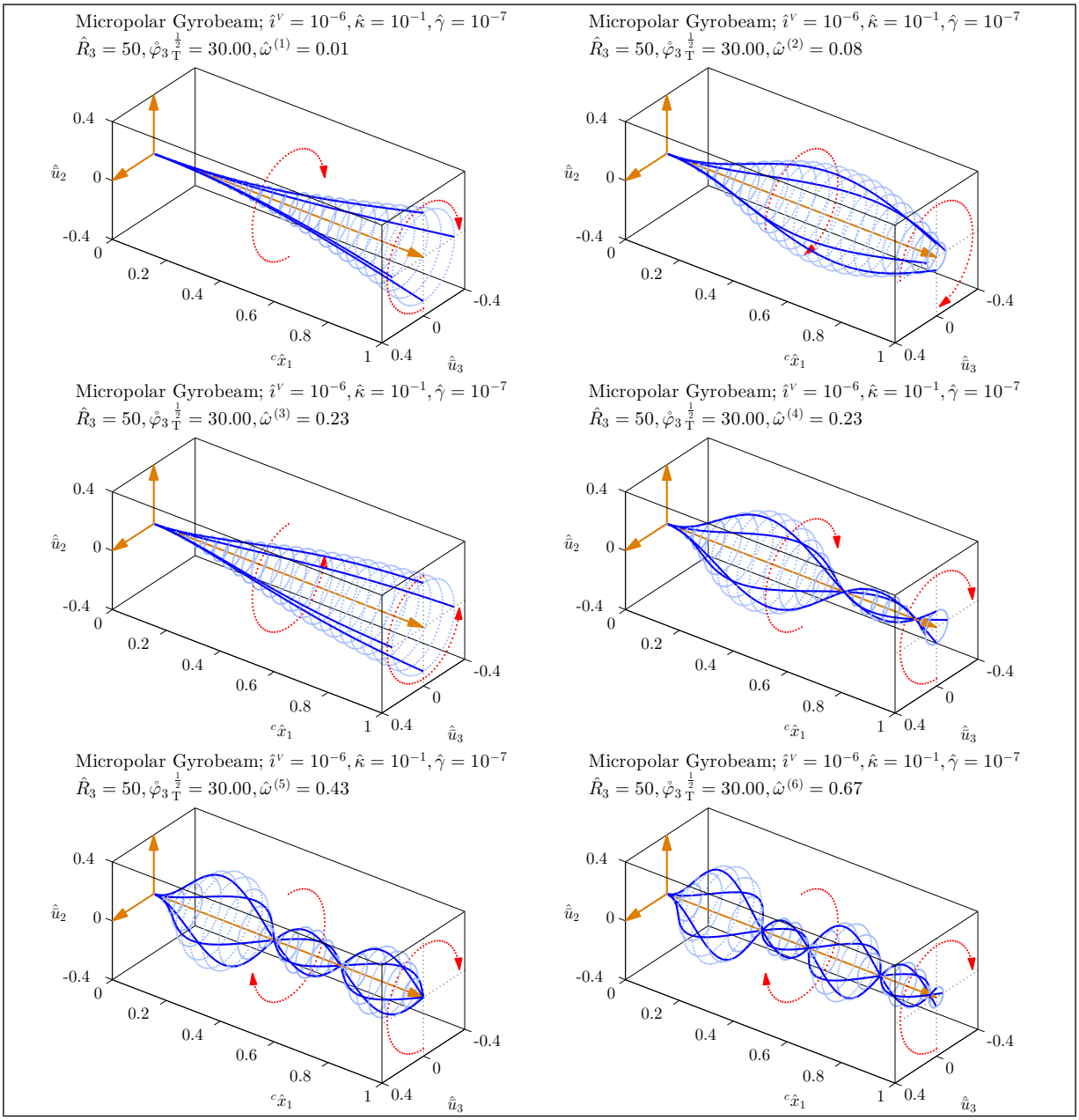

Figure 6.35: Mode shapes of a medium micropolar gyrobeam with a medium uniform axial gyricity – Micropolar gyrobeam model 4.

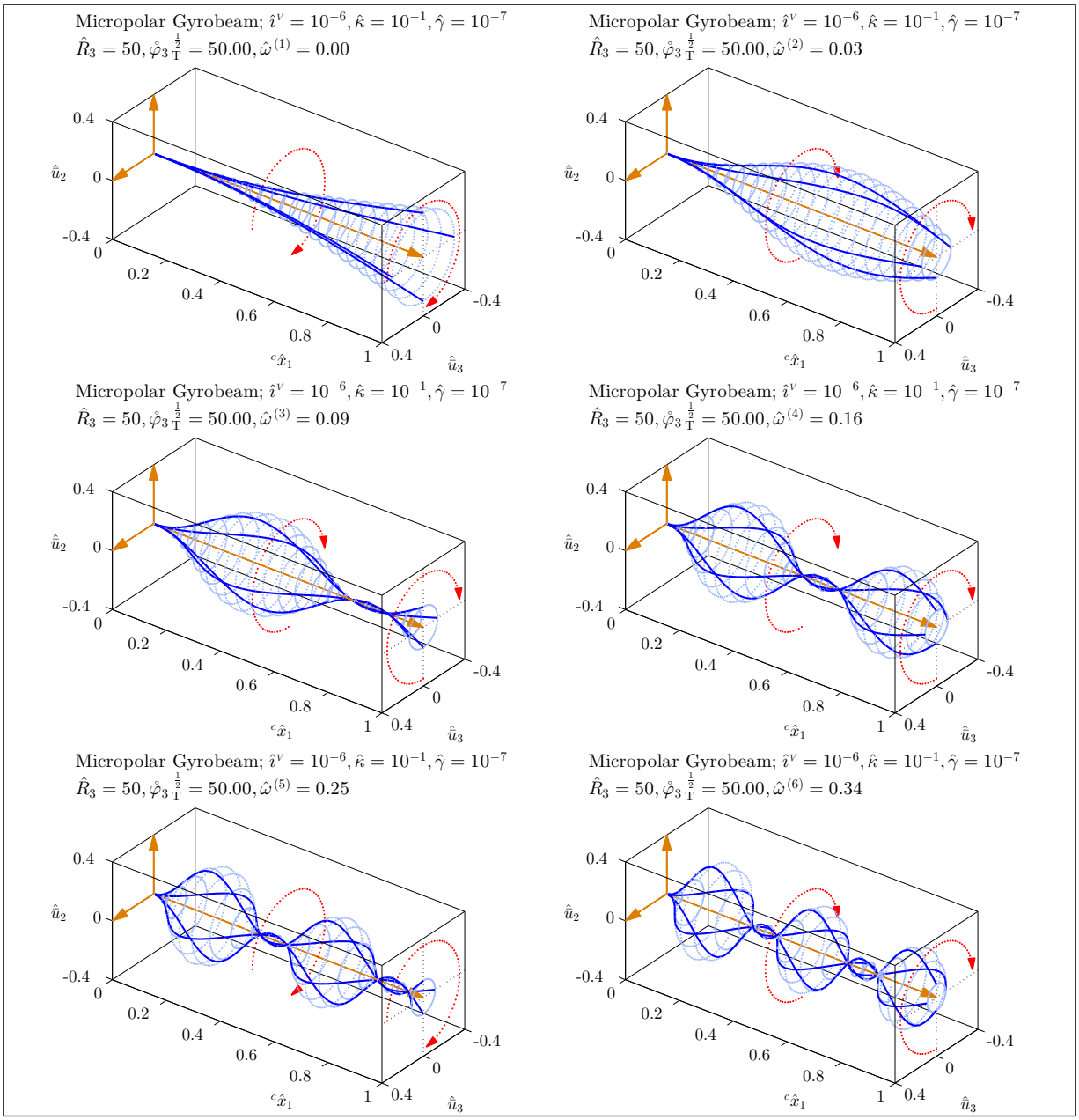

Figure 6.36: Mode shapes of a medium micropolar gyrobeam with a large uniform axial gyricity – Micropolar gyrobeam model 4.

The natural frequency loci and mode shapes shown in Figures 6.31–6.36 correspond to the fourth specific micropolar gyrobeam model. As noted previously, these figures can also qualitatively represent the results which one may obtain from a micropolar gyrobeam model with $(\hat{\kappa}, \hat{\gamma}) = (10^2, 10^{-7})$ or $(\hat{\kappa}, \hat{\gamma}) = (10^{-1}, 10^{-10})$. Overall, by comparing the natural frequency loci of this fourth micropolar gyrobeam model, shown in Figures 6.31, 6.32, and 6.33, with those of the first three micropolar gyrobeam models one can conclude that the effect of decreasing $\hat{\kappa}$ (in general resulting in lower natural frequencies) is more dominant than the effect of increasing $\hat{\gamma}$ (in general resulting in higher natural frequencies). Specially one may observe how the higher natural frequency curves of a thick gyrobeam are gathered as shown in Figure 6.31 which indicate the closeness of this micropolar gyrobeam model to being singular.

Finally, as shown in Figures 6.34, 6.35, and 6.36 for gyrobeams with medium thickness one may notice no significant differences between the mode shapes of this micropolar gyrobeam model and those corresponding to the first micropolar gyrobeam model.

6.3 Uniform transverse gyricity

Similar to the axial gyricity case, the comparison between classical and micropolar gyrobeams with a uniform transverse gyricity starts with drawing the first three gyricity-affected relative (classical to micropolar) gyrobeams' natural frequencies which are shown in Figures 6.37–6.45. Again, three slenderness ratios and three transverse gyricity values are taken into account to draw the natural frequency surfaces vs. the micropolar elastic constants $\hat{\kappa}$ and $\hat{\gamma}$. The scales in the figures are log-log-percentage and for each slenderness ratio a 2D contour plot and a 3D surface plot are provided.

Unsurprisingly, the same behaviors as those observed in the previous section for the axial gyricity case, can be seen in Figures 6.37–6.45 corresponding to the uniform transverse gyricity case which are summarized as follows.

The source of the noisy behavior of the natural frequency surfaces for very small $\hat{\kappa}$ and very large $\hat{\gamma}$, seen in some of the plots, is the ill-conditionedness of the micropolar gyrobeam's FEM stiffness matrix (see Figure C.21).

The singularity of the micropolar gyrobeam model with small $\hat{\kappa}$ is observable as abrupt jumps of the natural frequency surfaces (to very large values) which are more severe when compared to those corresponding to the natural frequency surfaces of micropolar elastic beams with no gyricity illustrated in Appendix C.

In each of Figures 6.37–6.45, increasing the gyrobeam slenderness ratio changes the shape of the plateau of agreement between the classical and micropolar gyrobeams, in the upper right corner of the 2D plots, from a horizontal rectangle for a thick gyrobeam to a vertical rectangle for a thin gyrobeam.

For different vibration modes, the gyricity effect on higher natural frequencies is more noteworthy. Consequently, in higher vibration modes the region where the micropolar gyrobeams show singular behaviors is larger and the region where the classical and micropolar gyrobeam models are in agreement is smaller. As noted in Appendix C, for micropolar elastic beams, the size effects are almost the same on different vibration modes and the coupling effects are slightly more evident at lower vibration modes; the same behaviors with minor influences from the gyricity terms can be observed for micropolar gyrobeams.

Again, the effect of increasing the gyricity value in Figures 6.37–6.45 is to embolden the differences between the classical and micropolar beam models and accordingly shrink or even completely remove the plateau of agreement between the classical and micropolar gyrobeam models in the natural frequency surfaces.

Finally, the same results and behaviors (including the singularities of the micropolar gyrobeam model with a small $\hat{\kappa}$), as those shown in Figures 6.37–6.45 corresponding to a small microinertia case, are expected to be seen for micropolar gyrobeams with a zero microinertia (while the ratio of body microinertia to gyros rotational inertia may differ by up to 25 percent).

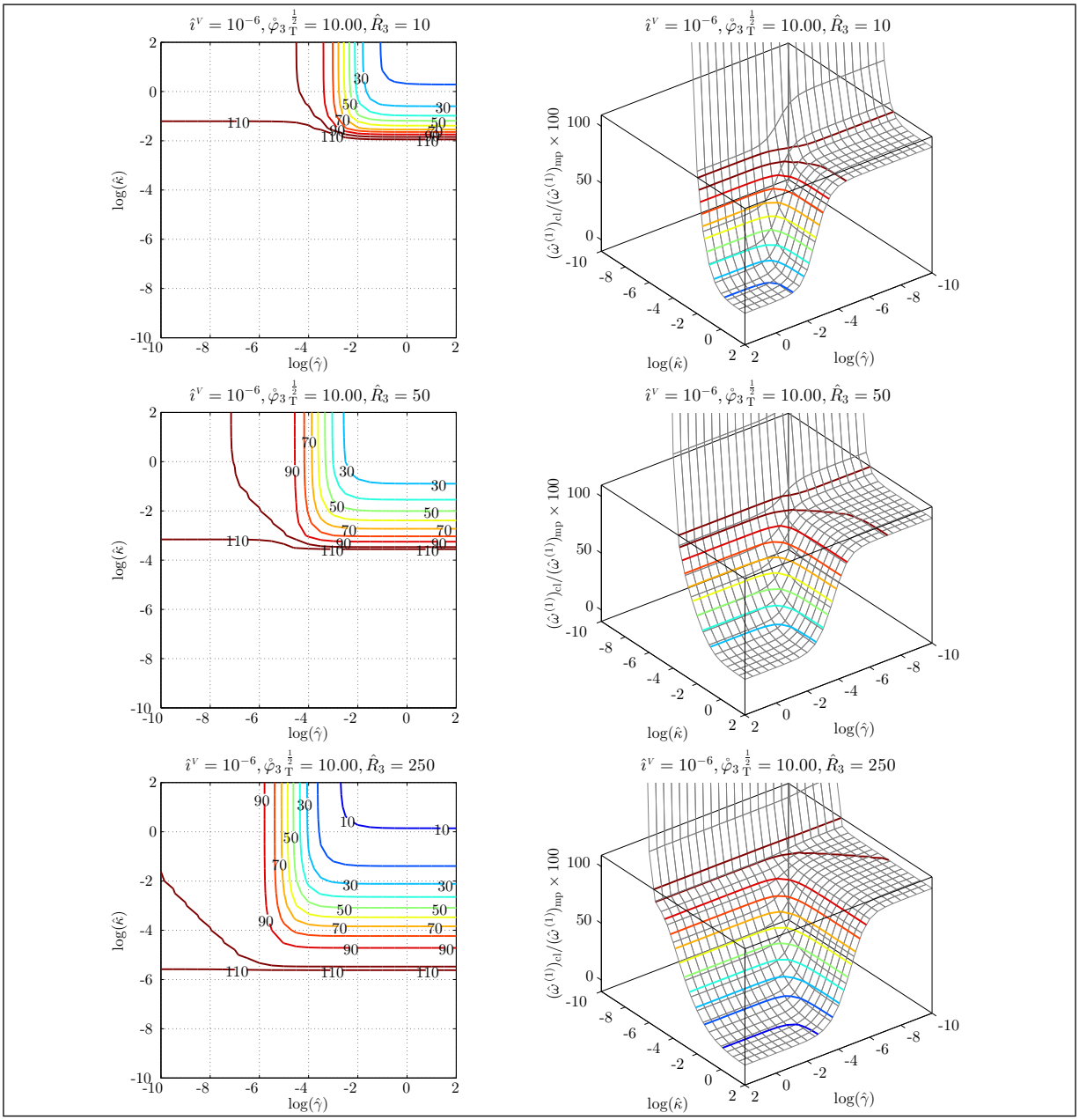

Figure 6.37: Relative 1st natural frequency $(\hat{\omega}^{(1)})_{\mathrm{cl}}/(\hat{\omega}^{(1)})_{\mathrm{mp}}$ of micropolar gyrobeams with a small uniform transverse gyricity vs. micropolar elastic constants.

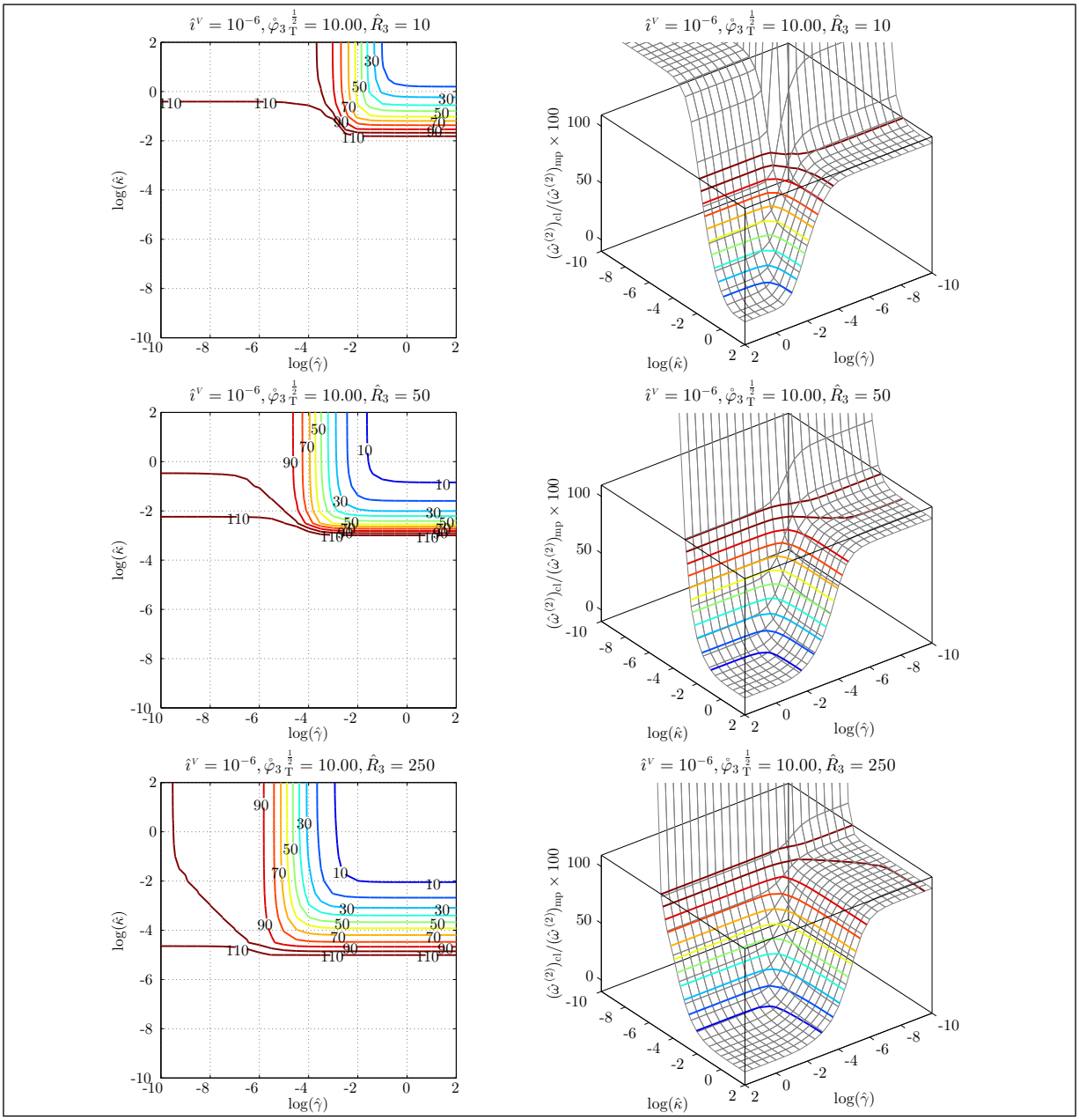

Figure 6.38: Relative 2nd natural frequency $(\hat{\omega}^{(2)})_{\mathrm{cl}}/(\hat{\omega}^{(2)})_{\mathrm{mp}}$ of micropolar gyrobeams with a small uniform transverse gyricity vs. micropolar elastic constants.

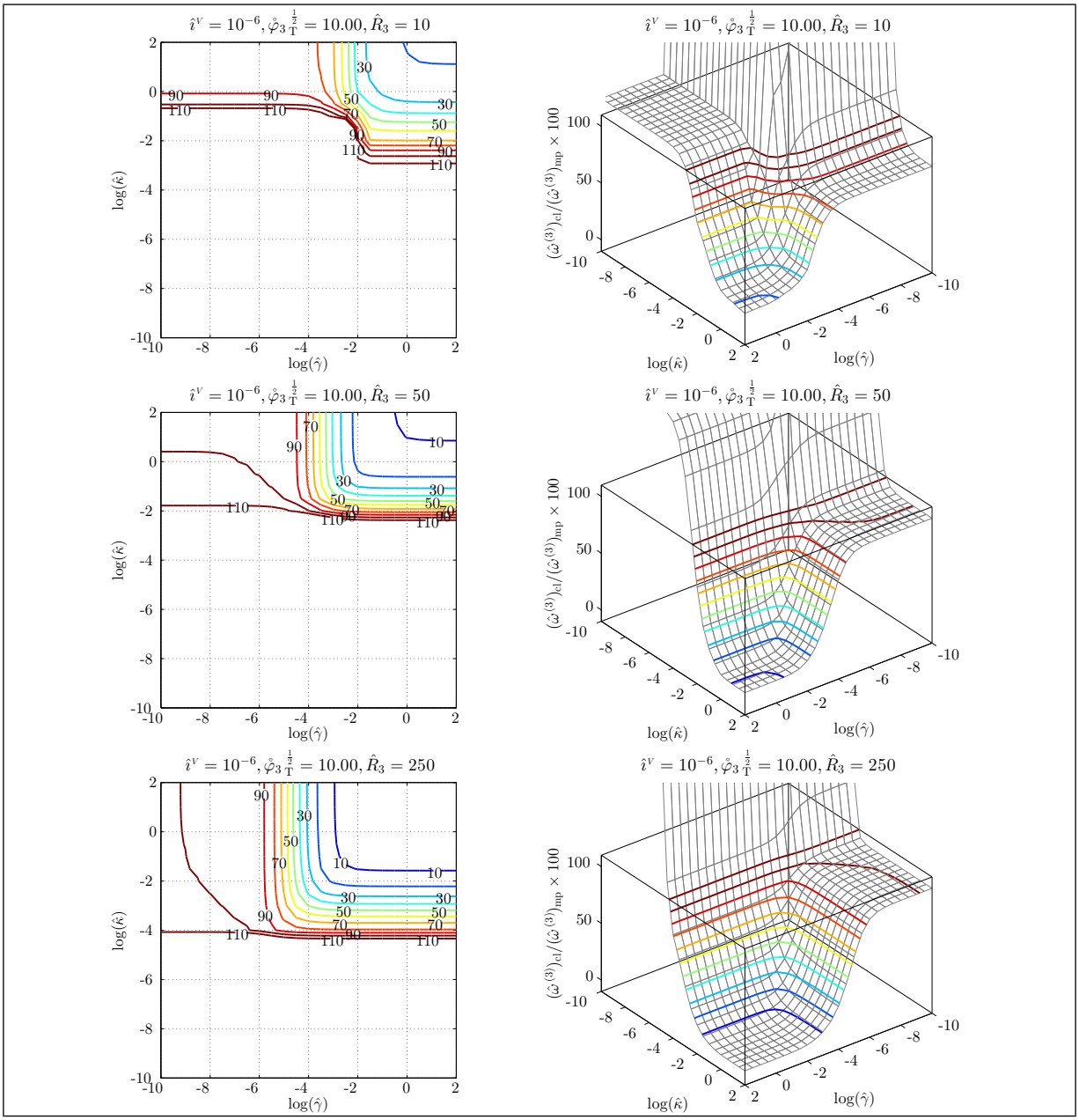

Figure 6.39: Relative 3rd natural frequency $(\hat{\omega}^{(3)})_{\mathrm{cl}}/(\hat{\omega}^{(3)})_{\mathrm{mp}}$ of micropolar gyrobeams with a small uniform transverse gyricity vs. micropolar elastic constants.

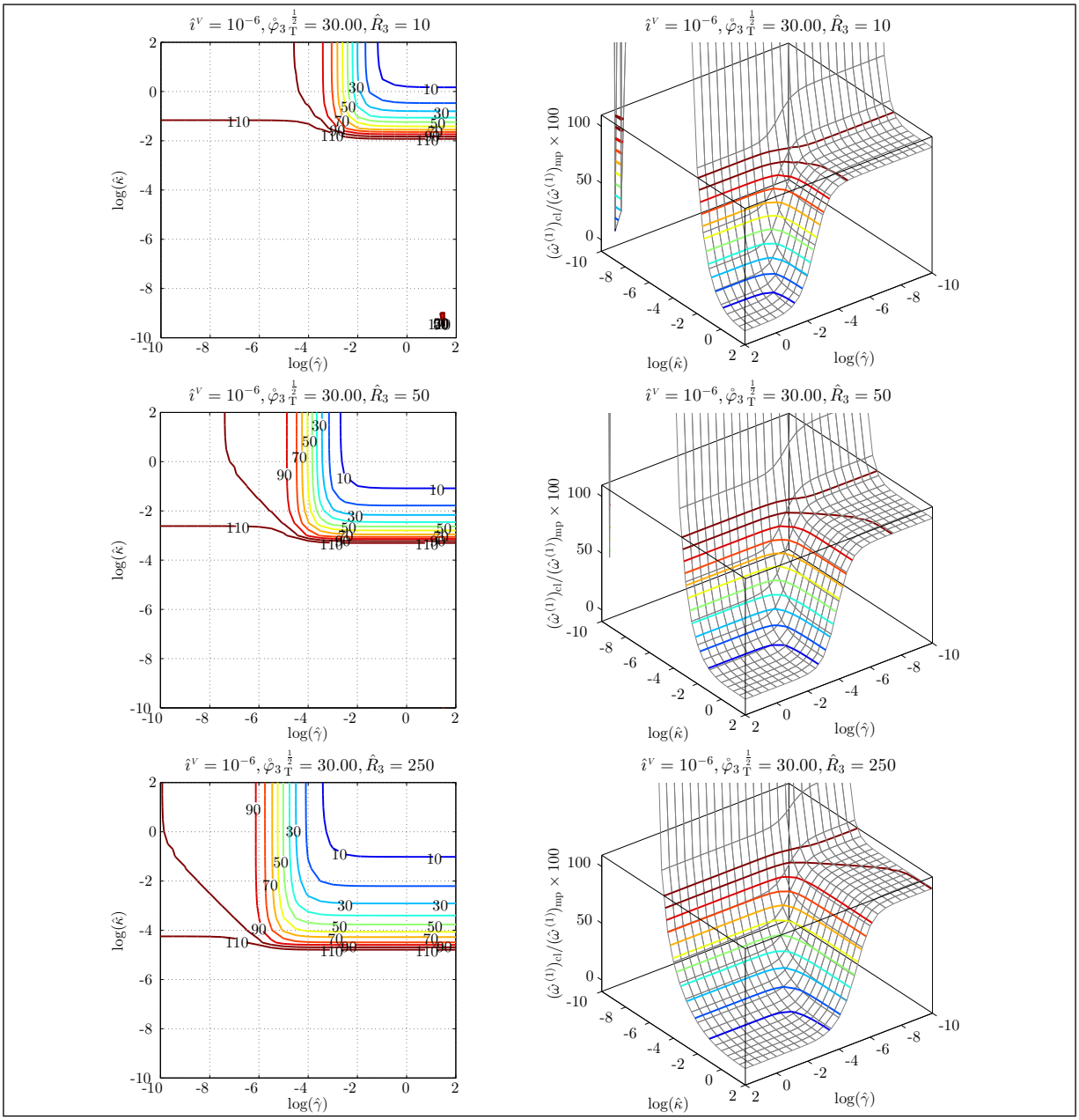

Figure 6.40: Relative 1st natural frequency $(\hat{\omega}^{(1)})_{\mathrm{cl}}/(\hat{\omega}^{(1)})_{\mathrm{mp}}$ of micropolar gyrobeams with a medium uniform transverse gyricity vs. micropolar elastic constants.

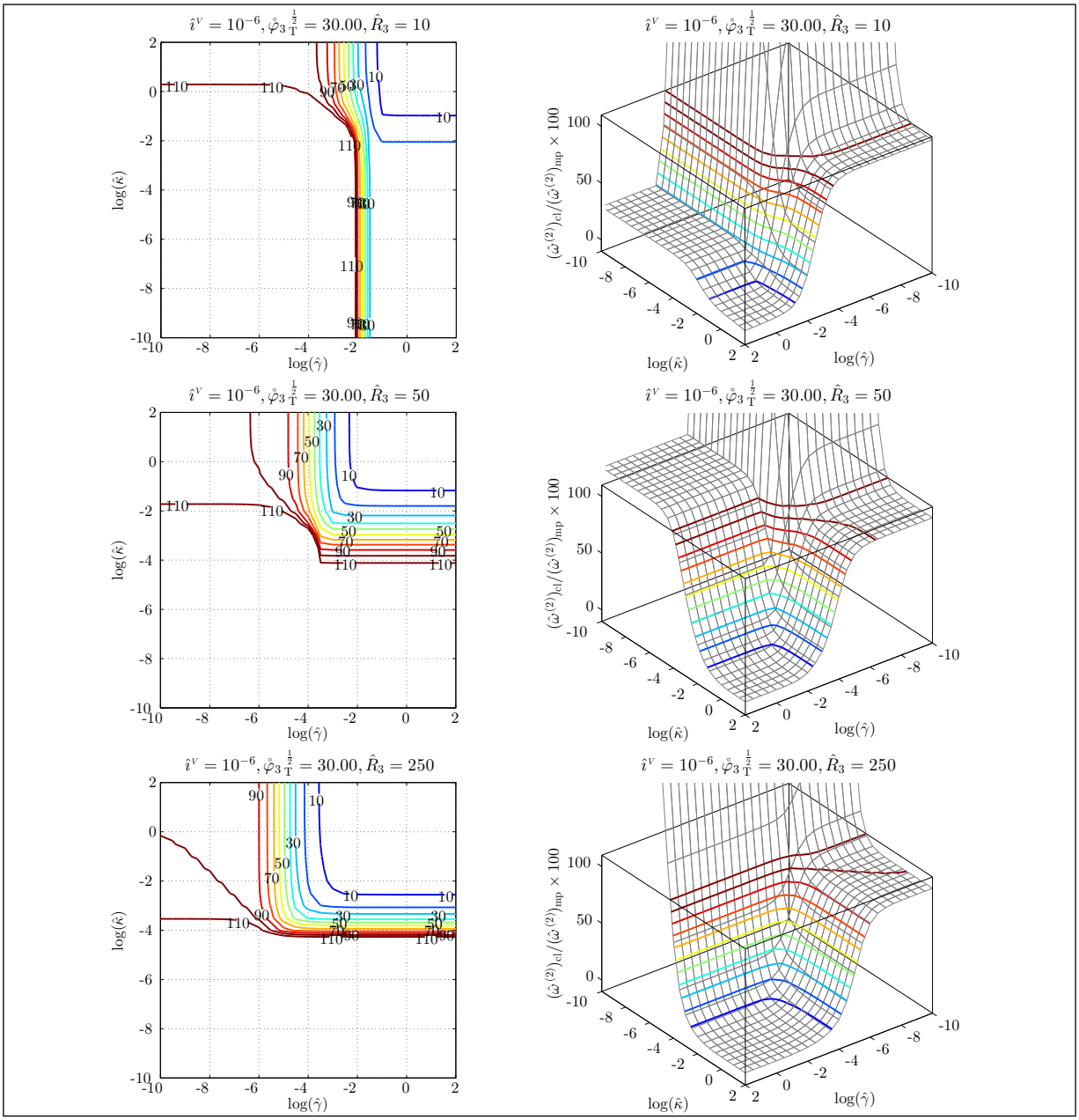

Figure 6.41: Relative 2nd natural frequency $(\hat{\omega}^{(2)})_{\mathrm{cl}}/(\hat{\omega}^{(2)})_{\mathrm{mp}}$ of micropolar gyrobeams with a medium uniform transverse gyricity vs. micropolar elastic constants.

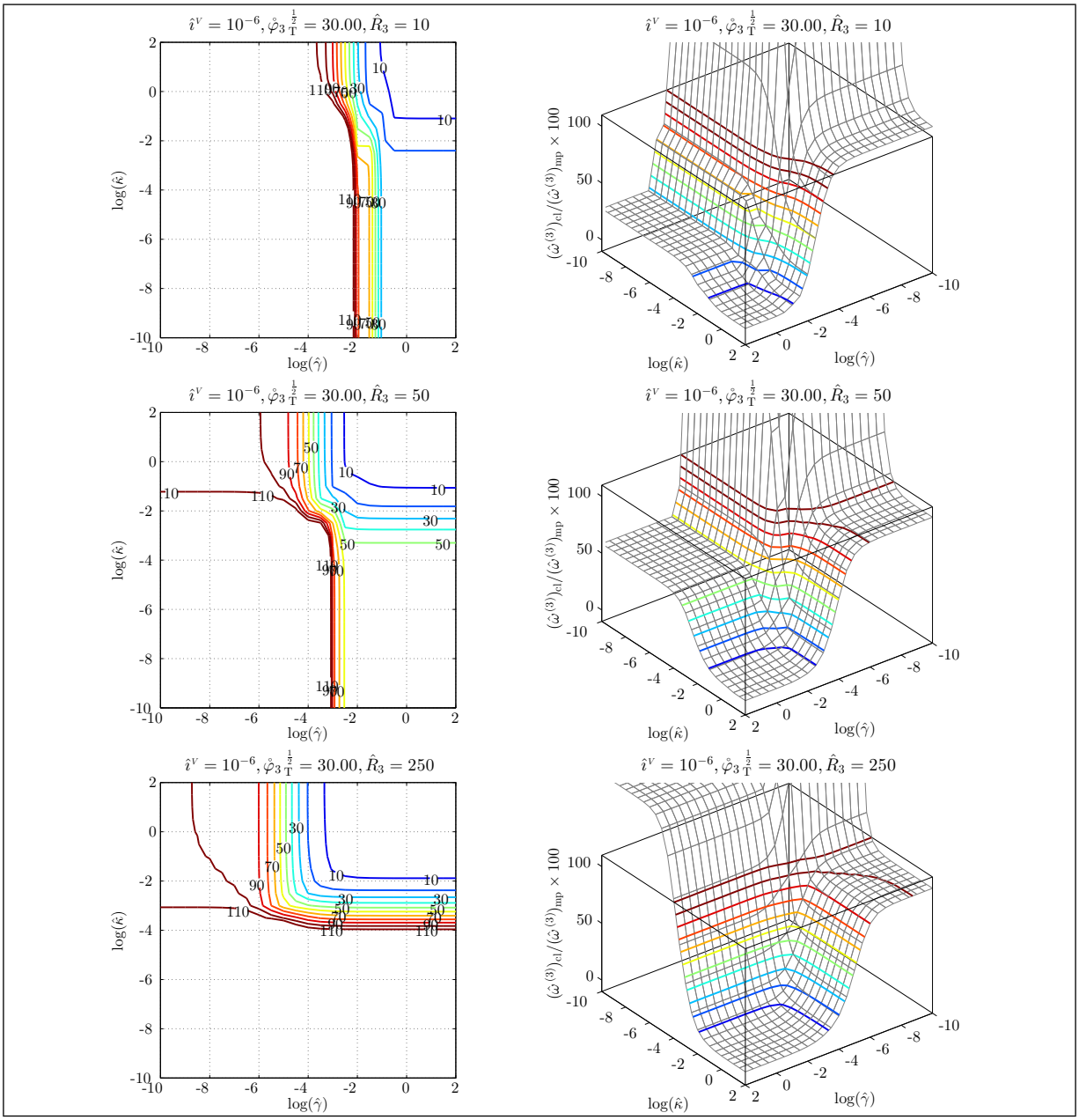

Figure 6.42: Relative 3rd natural frequency $(\hat{\omega}^{(3)})_{\mathrm{cl}}/(\hat{\omega}^{(3)})_{\mathrm{mp}}$ of micropolar gyrobeams with a medium uniform transverse gyricity vs. micropolar elastic constants.

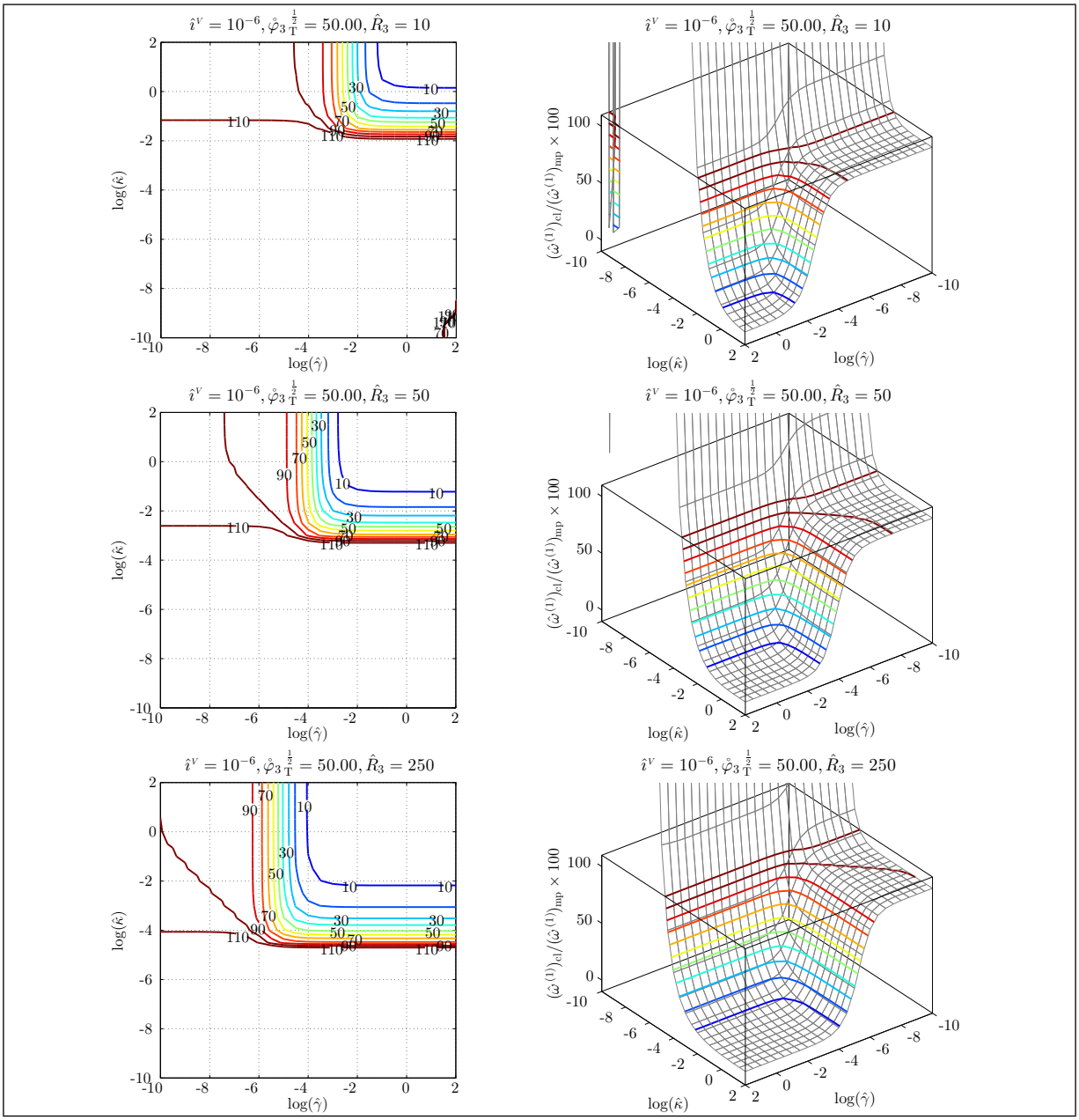

Figure 6.43: Relative 1st natural frequency $(\hat{\omega}^{(1)})_{\mathrm{cl}}/(\hat{\omega}^{(1)})_{\mathrm{mp}}$ of micropolar gyrobeams with a large uniform transverse gyricity vs. micropolar elastic constants.

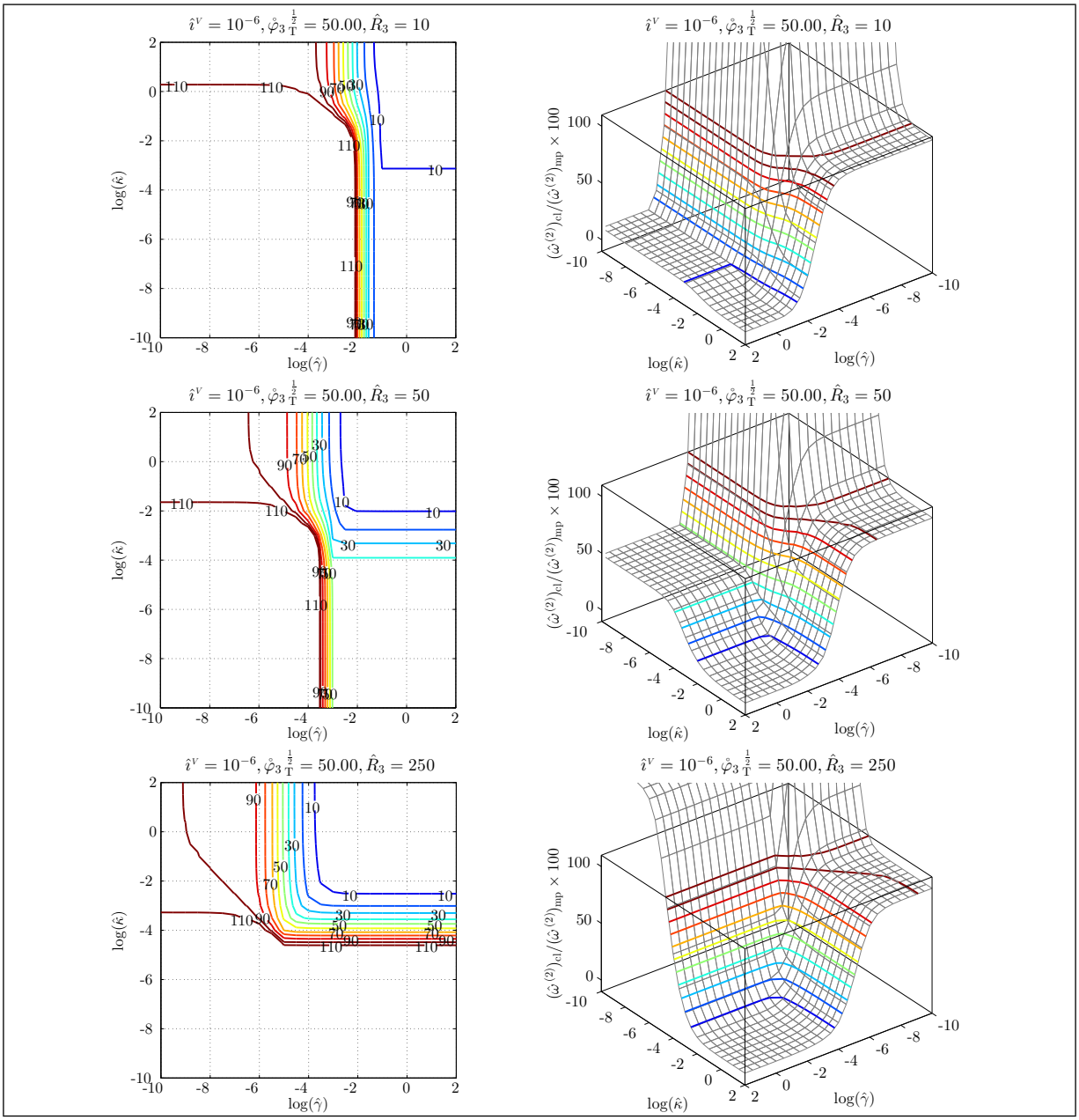

Figure 6.44: Relative 2nd natural frequency $(\hat{\omega}^{(2)})_{\mathrm{cl}}/(\hat{\omega}^{(2)})_{\mathrm{mp}}$ of micropolar gyrobeams with a large uniform transverse gyricity vs. micropolar elastic constants.

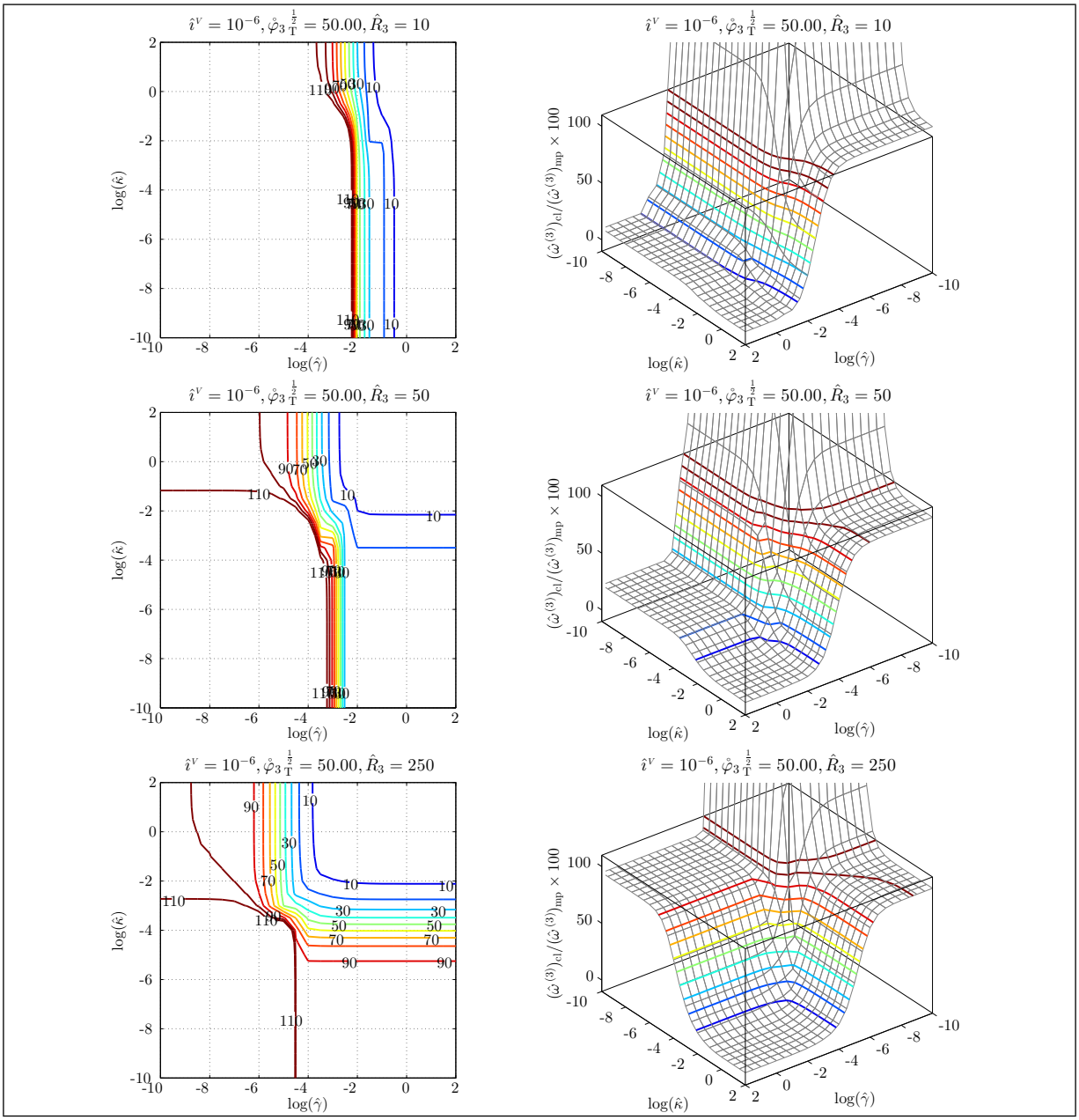

Figure 6.45: Relative 3rd natural frequency $(\hat{\omega}^{(3)})_{\mathrm{cl}}/(\hat{\omega}^{(3)})_{\mathrm{mp}}$ of micropolar gyrobeams with a large uniform transverse gyricity vs. micropolar elastic constants.

Analogous to the axial gyricity case, it is also appealing to observe how the natural frequency loci and mode shapes in the micropolar gyrobeam model with a transverse gyricity distribution differ from those associated with the classical gyrobeam model. Again this is done by considering just the four specific micropolar gyrobeam model summarized in Table 6.3. Recall that the first model is selected as a close match to the classical model, the second and third models are selected to respectively study the effects of the micropolar elastic constants $\hat{\gamma}$ and $\hat{\kappa}$, and the fourth model can be regarded as a transition model when toggling between the first three models.

For these four specific micropolar gyrobeam models, the variations of the first 25 gyricity-affected natural frequencies with the variation of the total transverse gyricity and also the first six gyricity-affected mode shapes are shown in Figures 6.46–6.72. The natural frequency loci are plotted at three different values of slenderness ratio and the mode shapes are drawn for the medium-thickness micropolar gyrobeam at three gyriciy values. The results of each specific micropolar gyrobeam model are explained briefly before the set of figures for that specific model.

From the results shown in Figures 6.46–6.51 one can conclude that the differences between the first micropolar gyrobeam model and the classical gyrobeam model is more significant when the gyricity is transverse.

In Figures 6.46, 6.47, and 6.48 it is interesting that the curve veering between the natural frequency loci are eliminated or smoothed in the first micropolar gyrobeam model (compared to the curve veering observed in the classical gyrobeam model).

In Figures 6.49, 6.50, and 6.51 one may notice that the differences between the mode shapes of the first micropolar gyrobeam model and those of the classical gyrobeam model are insignificant. There are only the last two mode shapes in Figure 6.50 which look different than the classical ones. This is since their corresponding natural frequency curves shown in Figure 6.47 experience a different curve veering before the $\mathring{\varphi}_{3_{\mathrm{T}}}^{\frac{1}{2}} = 30$ point than do the corresponding classical curves shown in Figure 5.21.

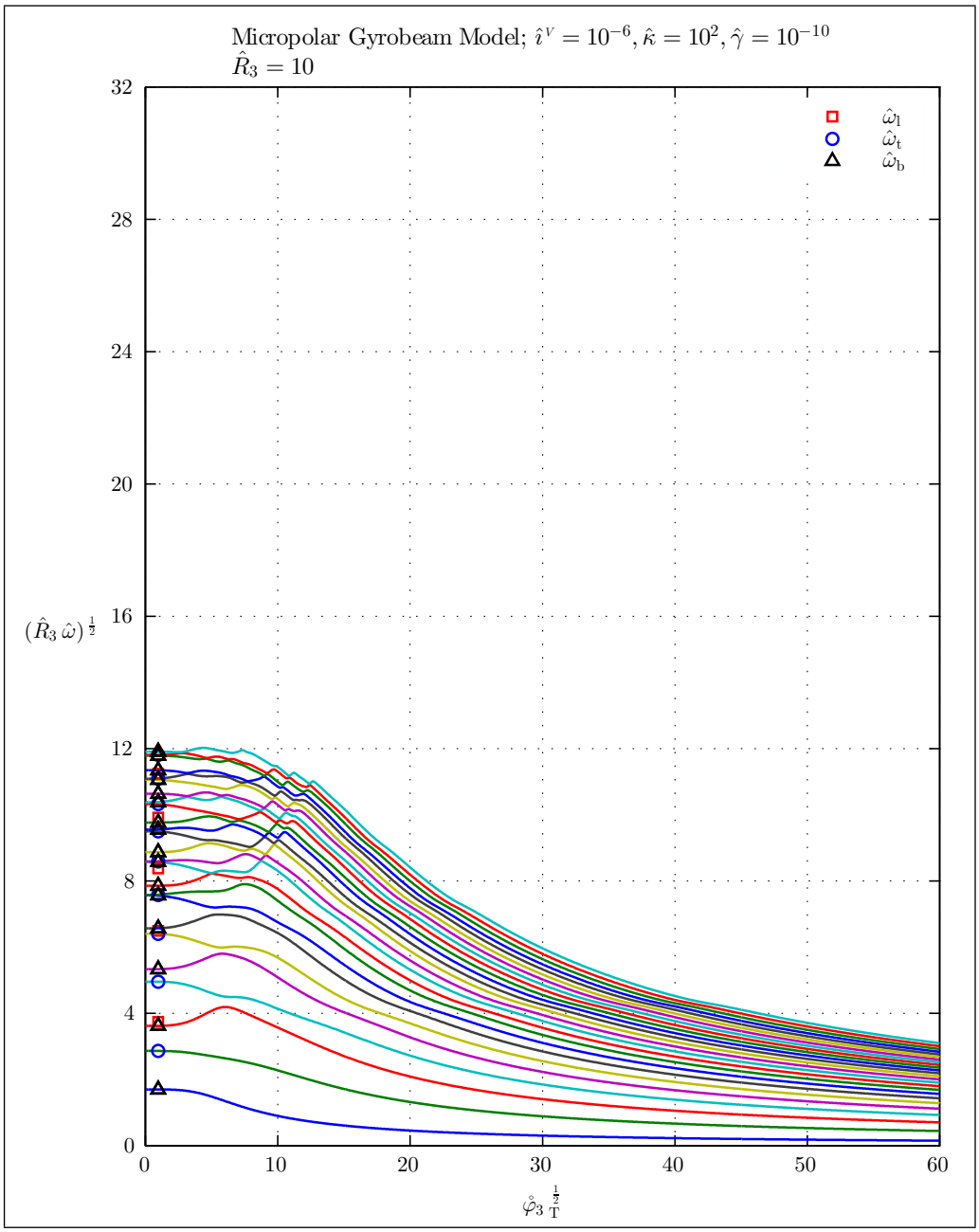

Figure 6.46: Natural frequencies of a thick micropolar gyrobeam with a uniform transverse gyricity – Micropolar gyrobeam model 1.

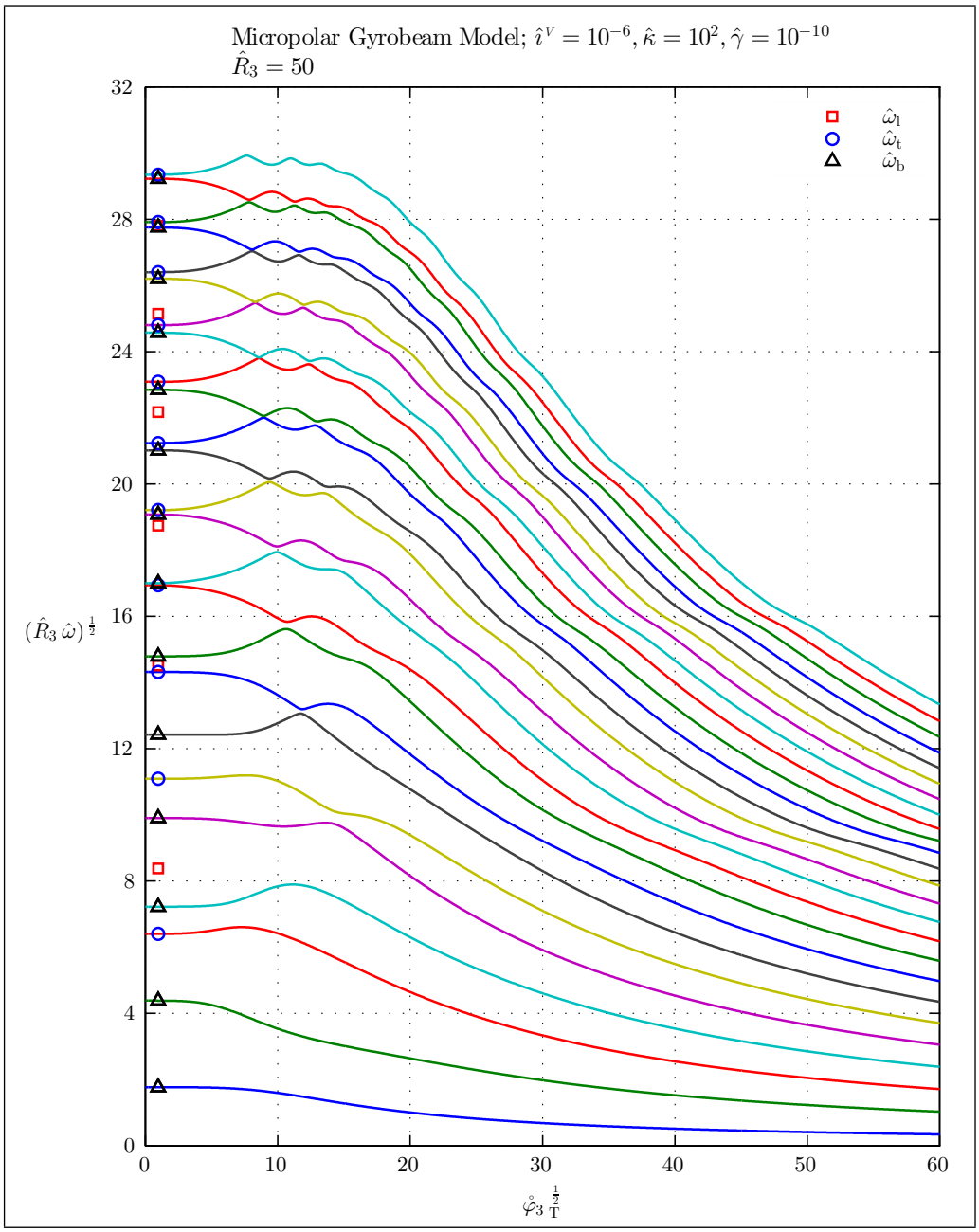

Figure 6.47: Natural frequencies of a medium micropolar gyrobeam with a uniform transverse gyricity – Micropolar gyrobeam model 1.

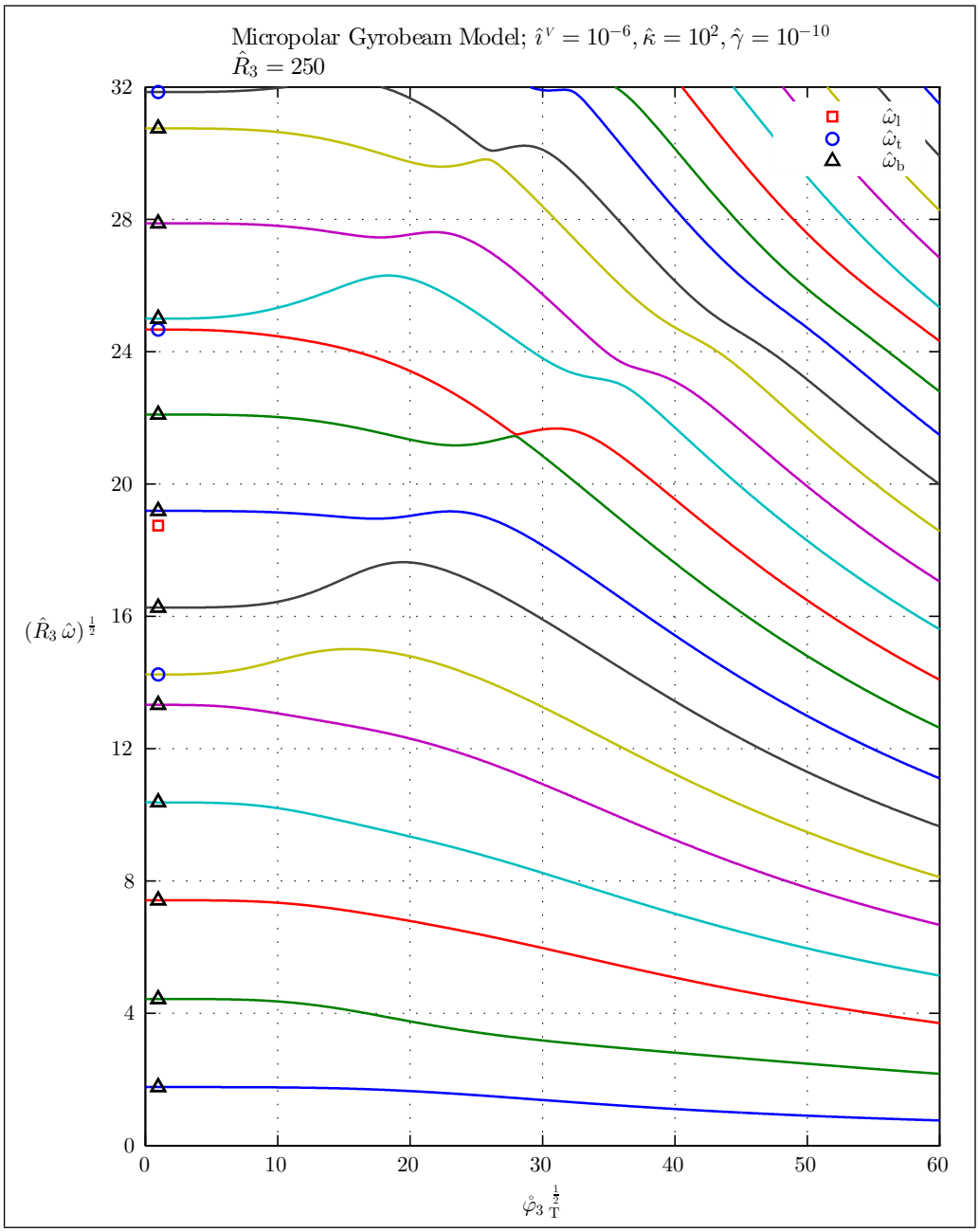

Figure 6.48: Natural frequencies of a thin micropolar gyrobeam with a uniform transverse gyricity – Micropolar gyrobeam model 1.

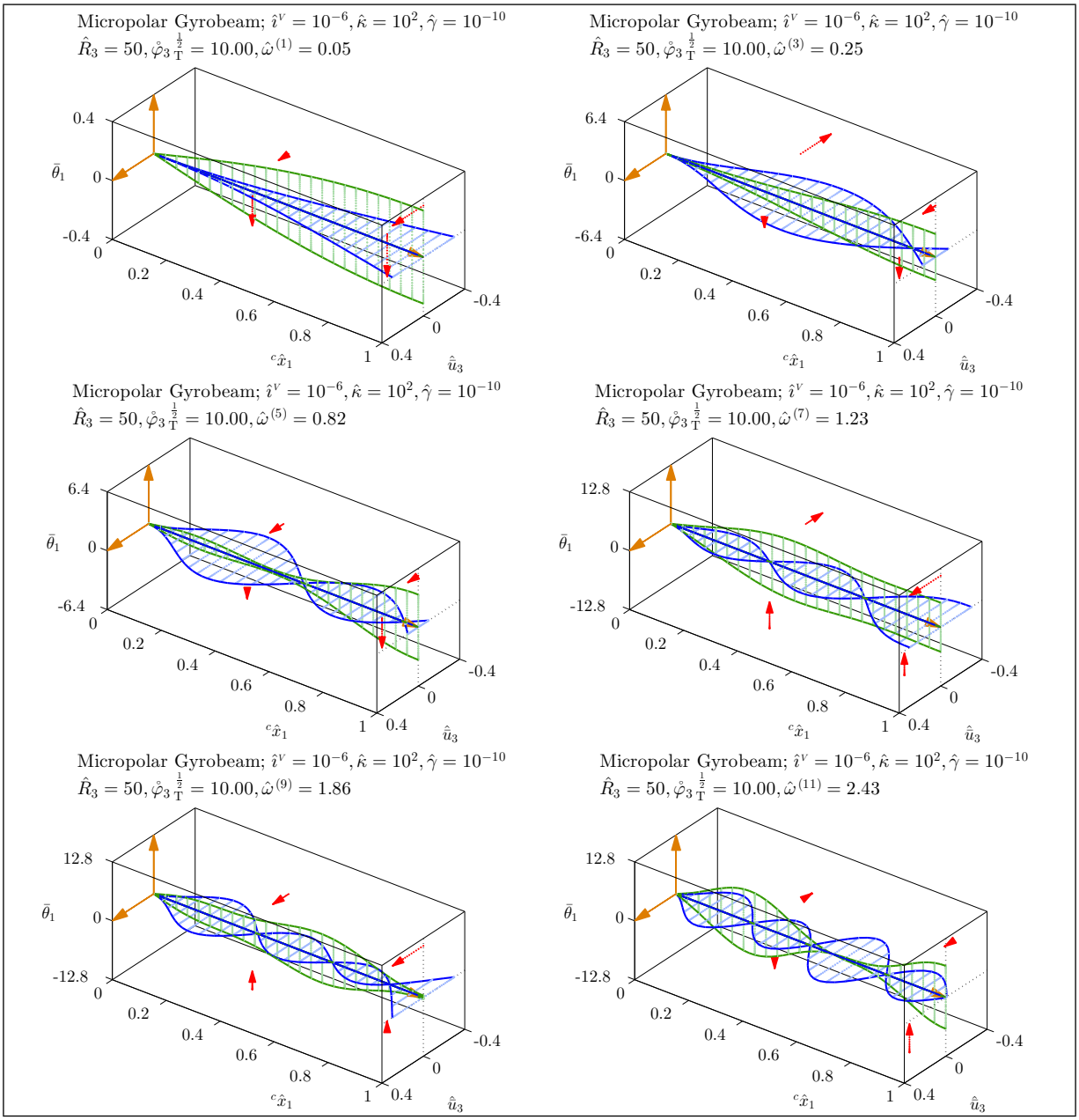

Figure 6.49: Mode shapes of a medium micropolar gyrobeam with a small uniform transverse gyricity – Micropolar gyrobeam model 1.

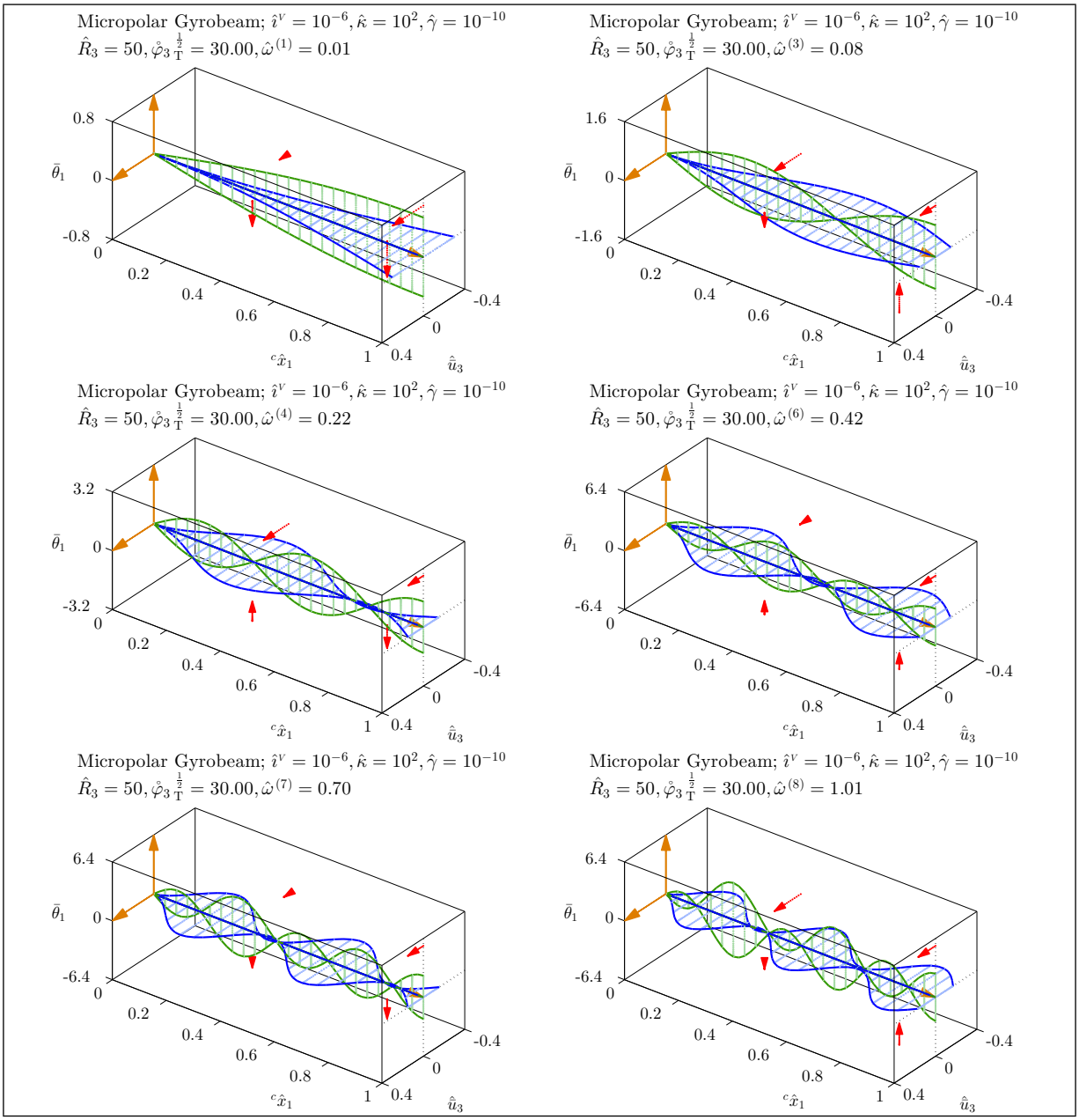

Figure 6.50: Mode shapes of a medium micropolar gyrobeam with a medium uniform transverse gyricity – Micropolar gyrobeam model 1.

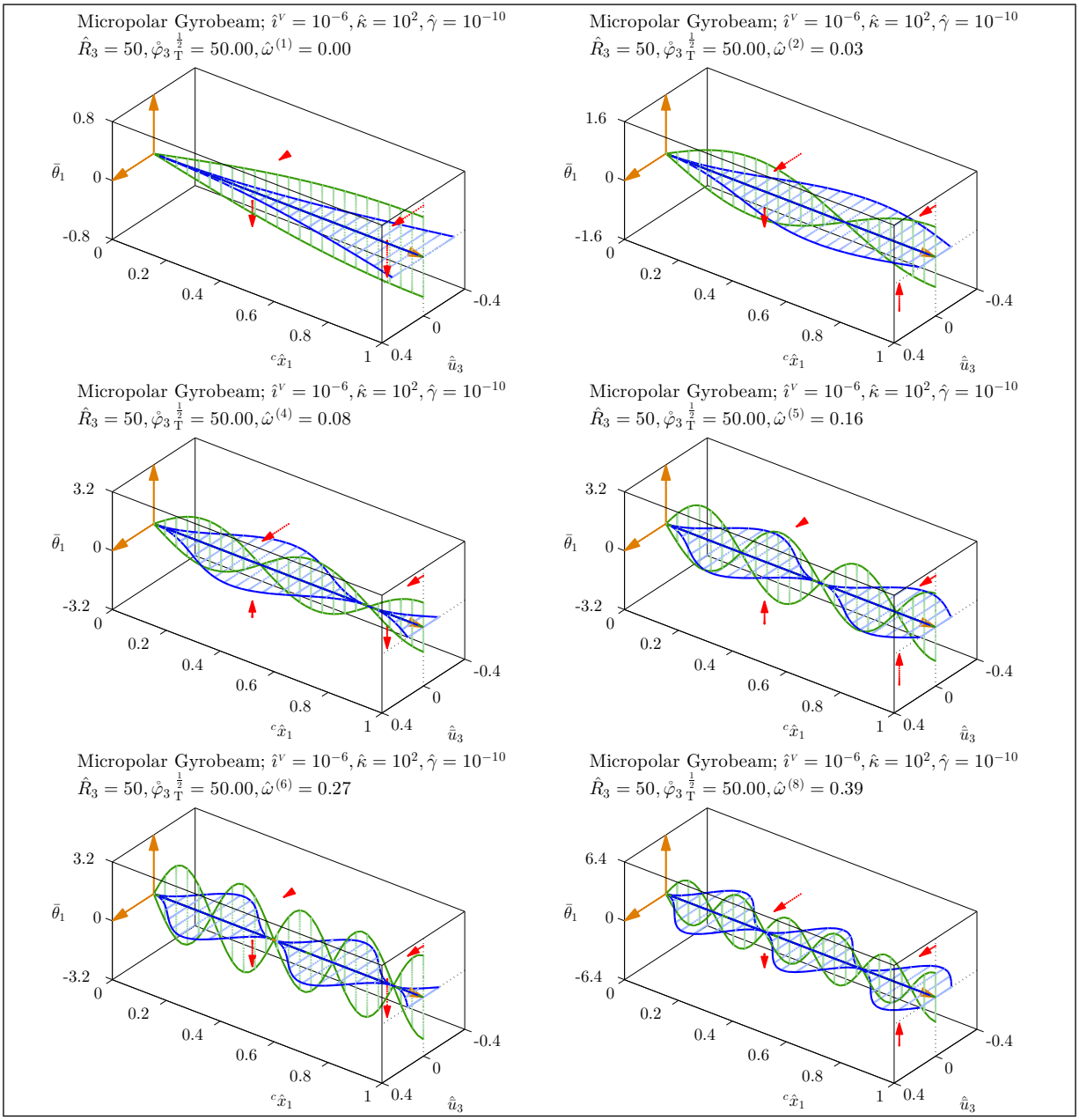

Figure 6.51: Mode shapes of a medium micropolar gyrobeam with a large uniform transverse gyricity – Micropolar gyrobeam model 1.

As expected the natural frequencies of the second specific micropolar gyrobeam model shown in Figures 6.52, 6.53, and 6.54 are generally higher than those of the first micropolar gyrobeam model and this is more pronounced in the thinnest gyrobeam. Specially, it is interesting how all the curve veering points are eliminated in Figure 6.54.

Considering the mode shapes of the second micropolar gyrobeam model depicted in Figures 6.55, 6.56, and 6.57 one may see no significant differences between them and those of the first micropolar gyrobeam model. The only exception is the last mode shape shown in Figure 6.56 which looks slightly different than the last mode shape in Figure 6.50. This can be again due to different curve veering history of the corresponding natural frequency loci in the two models (compare the sixth locus in Figure 6.53 to the sixth locus in Figure 6.47).

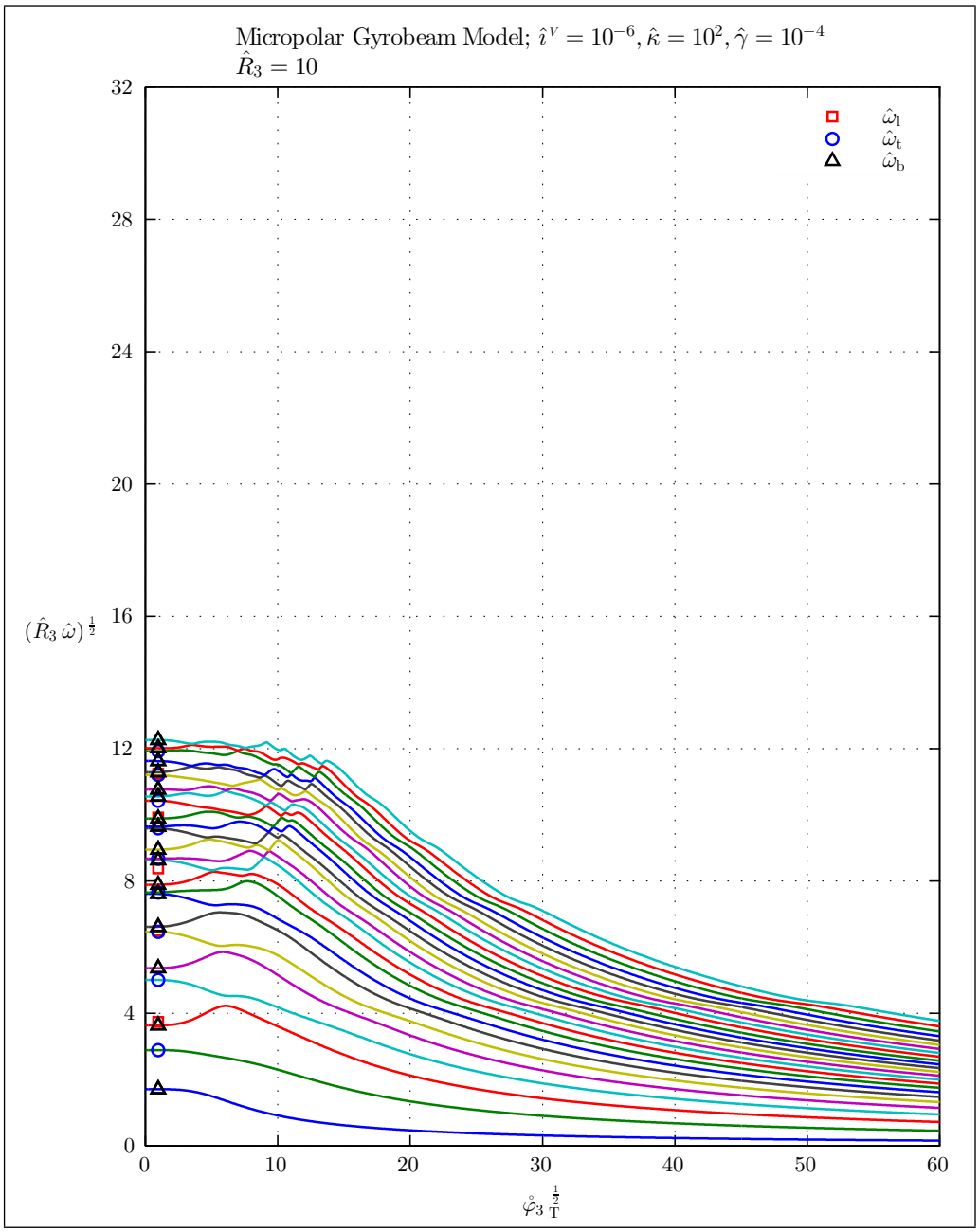

Figure 6.52: Natural frequencies of a thick micropolar gyrobeam with a uniform transverse gyricity – Micropolar gyrobeam model 2.

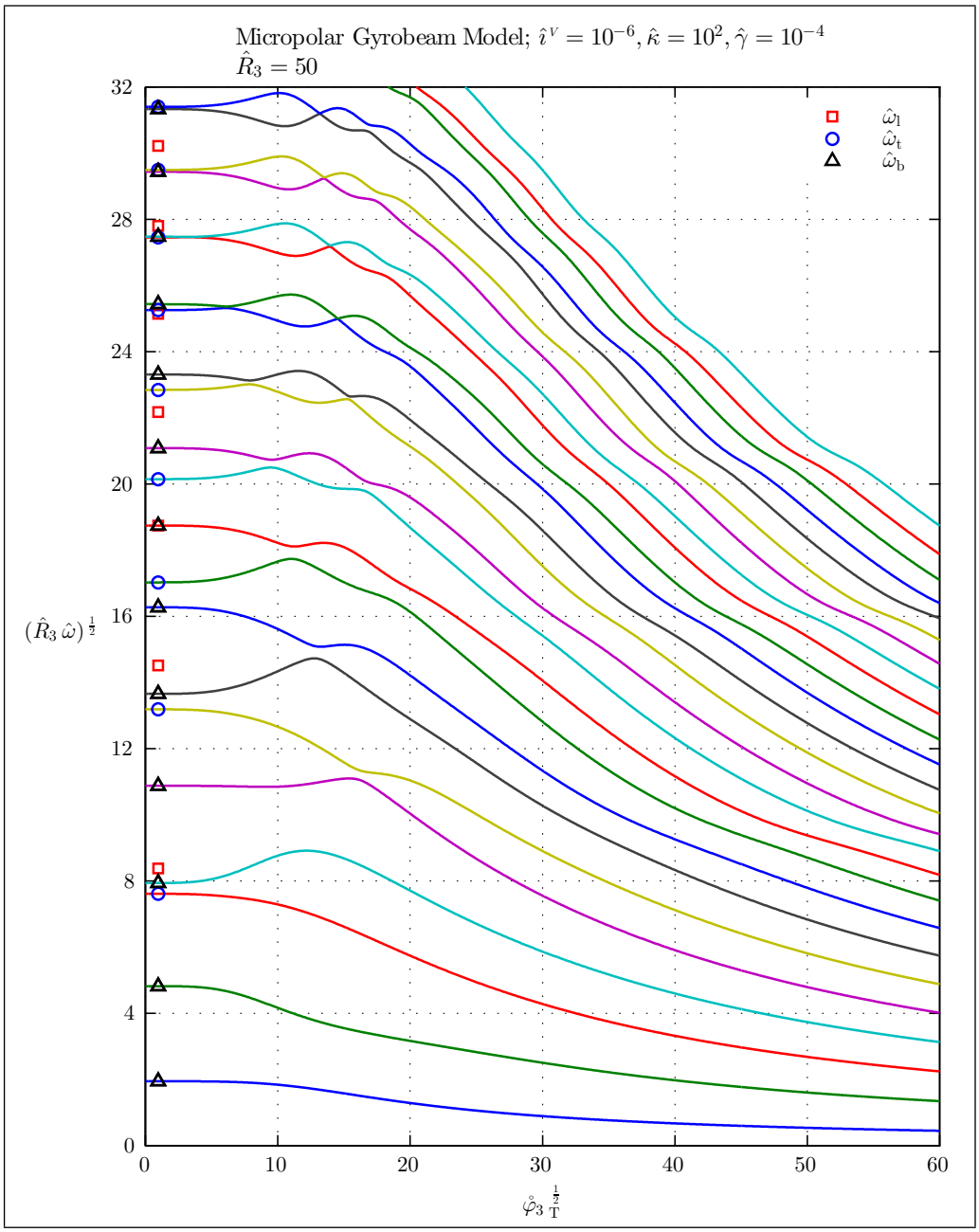

Figure 6.53: Natural frequencies of a medium micropolar gyrobeam with a uniform transverse gyricity – Micropolar gyrobeam model 2.

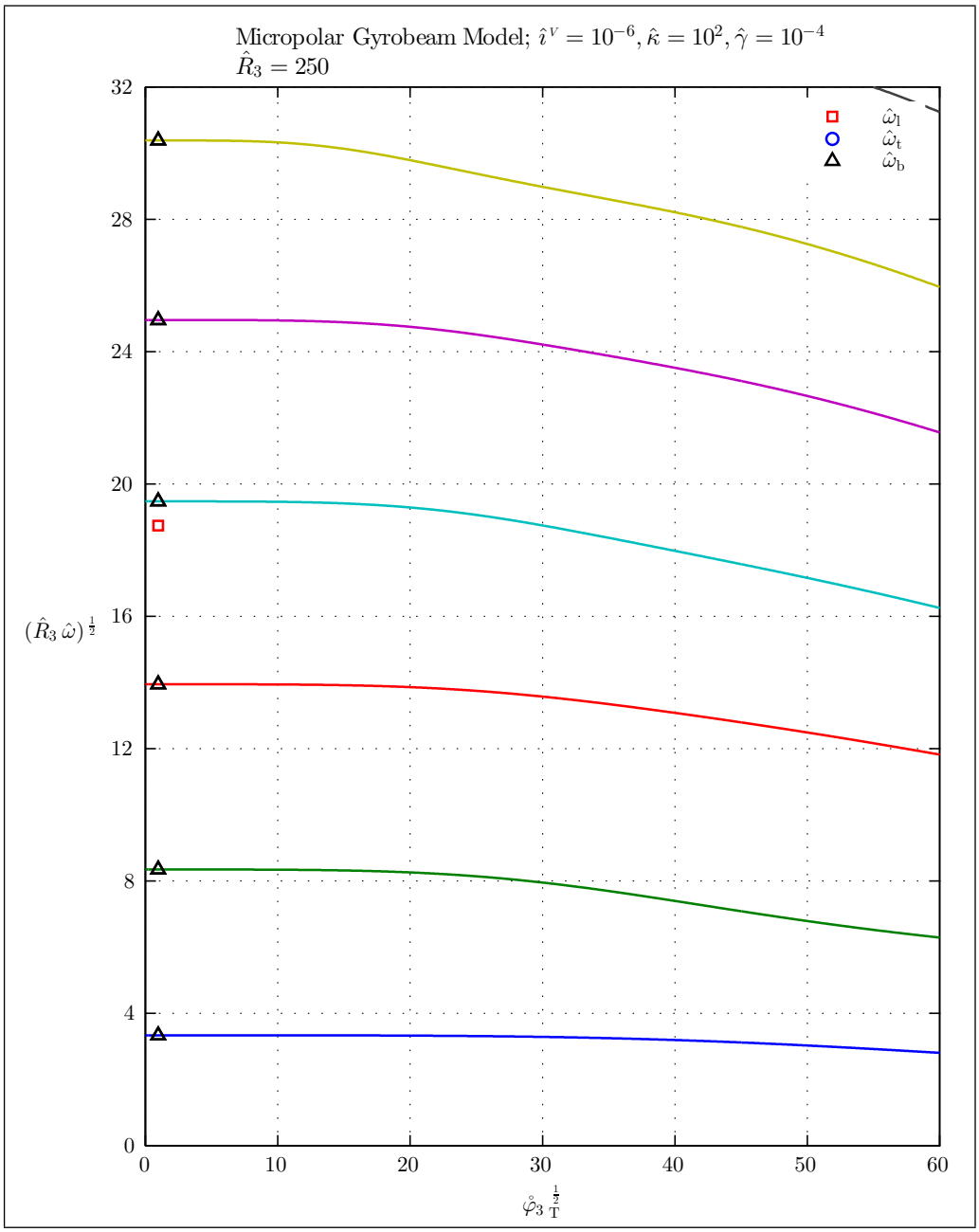

Figure 6.54: Natural frequencies of a thin micropolar gyrobeam with a uniform transverse gyricity – Micropolar gyrobeam model 2.

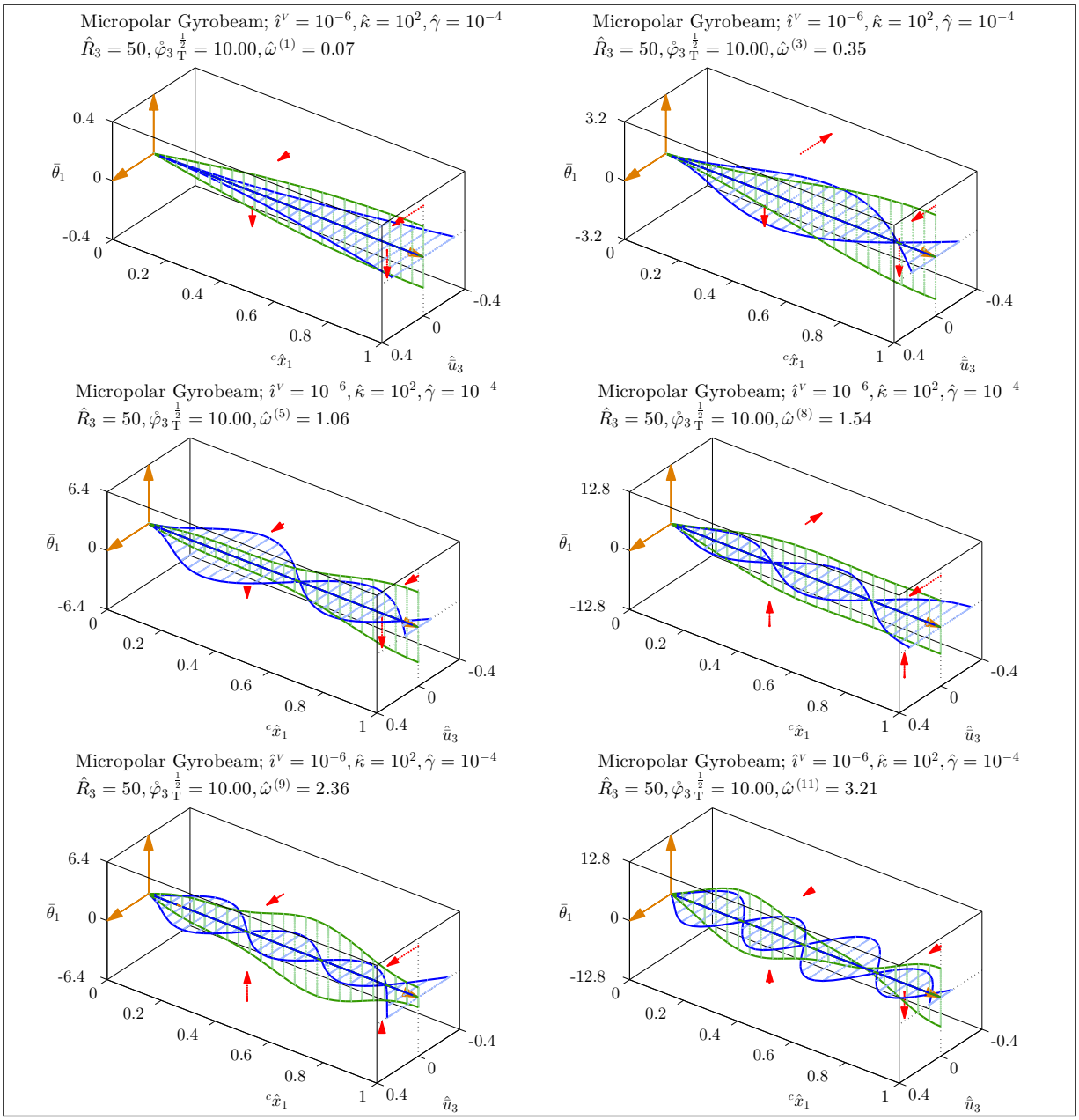

Figure 6.55: Mode shapes of a medium micropolar gyrobeam with a small uniform transverse gyricity – Micropolar gyrobeam model 2.

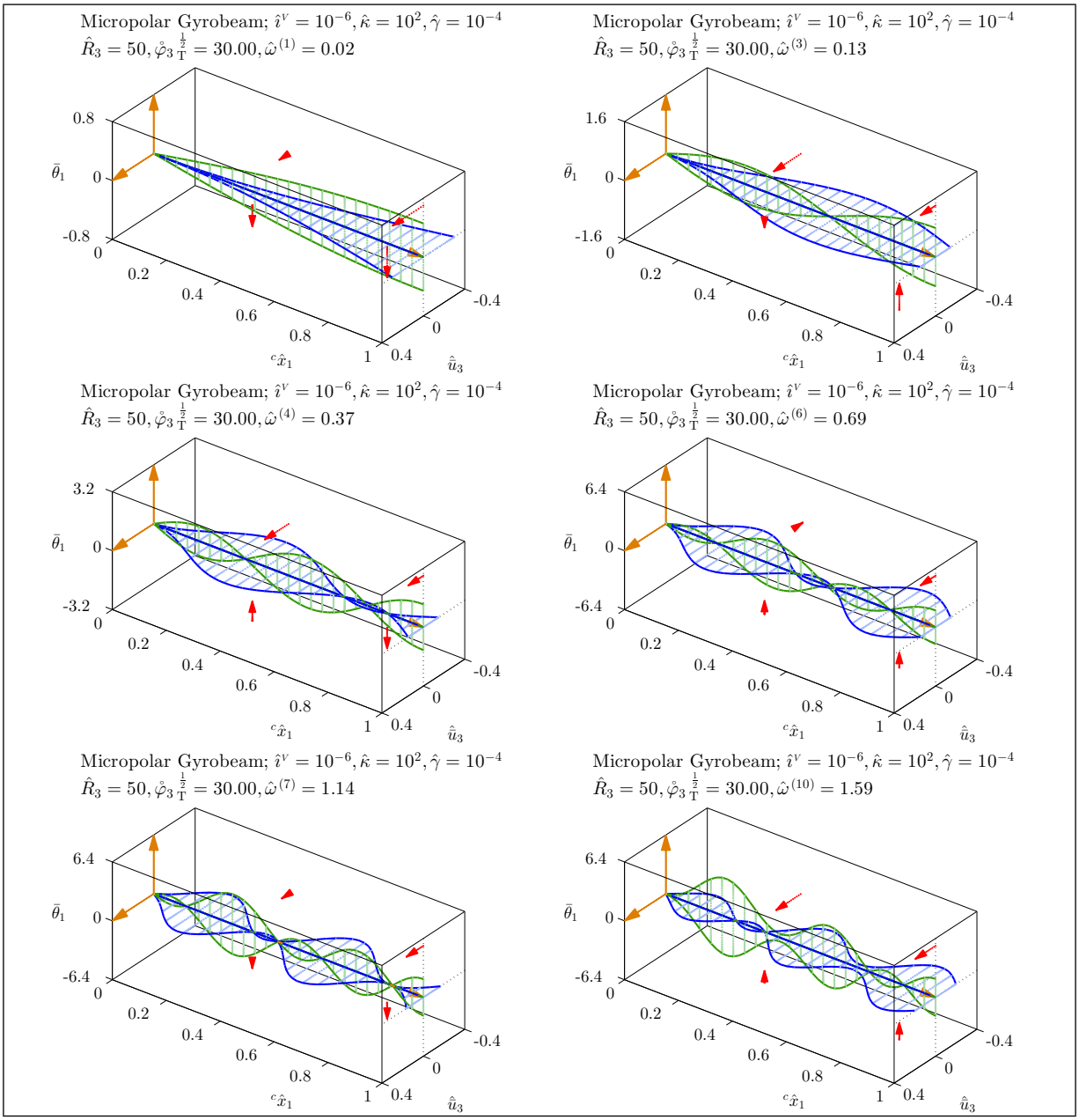

Figure 6.56: Mode shapes of a medium micropolar gyrobeam with a medium uniform transverse gyricity – Micropolar gyrobeam model 2.

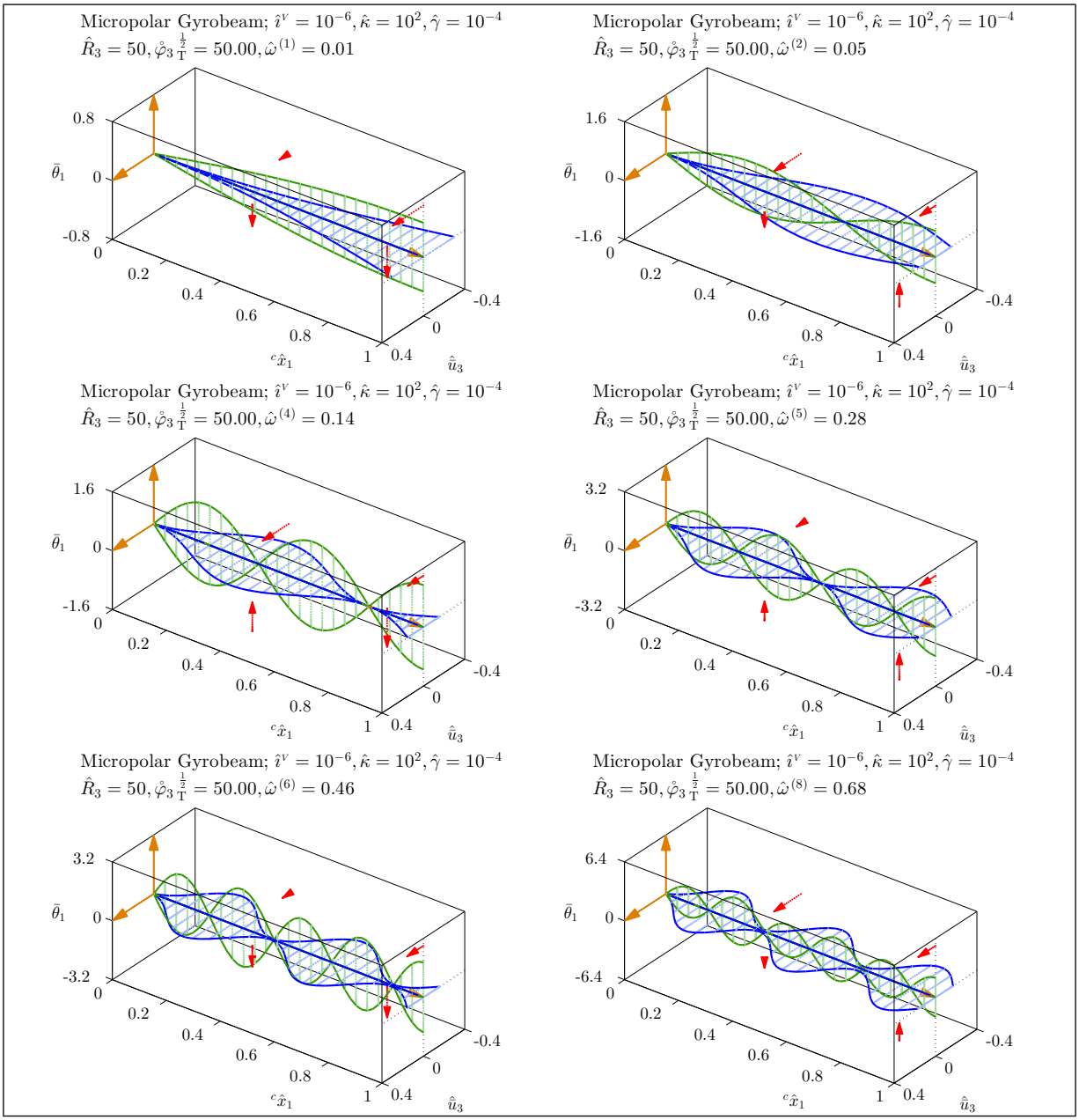

Figure 6.57: Mode shapes of a medium micropolar gyrobeam with a large uniform transverse gyricity – Micropolar gyrobeam model 2.

Again the singularity of the third specific micropolar gyrobeam model is obvious by looking at its natural frequencies and mode shapes shown in Figures 6.58–6.66.

The natural frequencies of the third micropolar gyrobeam model are much lower than those of the first micropolar gyrobeam model. In the natural frequency plots, *i.e.* in Figures 6.58, 6.59, and 6.60, the natural frequency loci gather together as a single curve which drops to lower values as the gyricity increases. Note that the singularity of this third model in the thinnest gyrobeam is not however visible at very low gyricity values.

Again for this micropolar gyrobeam model it is essential to draw the micropolar portions (*i.e.* the bending and torsional microrotations) of the mode shapes in addition to their classical portions (*i.e.* the bending displacement and torsional plane rotation). The classical and micropolar portions of the first six gyricity-affected mod shapes for a medium thickness gyrobeam are illustrated in Figures 6.61, 6.62, and 6.63 and Figures 6.64, 6.65, and 6.66 respectively.

One may note that analogous to the axial gyricity case the classical portions are mostly negligible compared to the micropolar portions and the mode shapes (except the first one) are pure micropolar modes. However, this time the coupling between the classical and micropolar DOFs is not strong enough to enforce the BCs of the classically cantilevered gyrobeam to the micrortation portions of the mode shapes. Interestingly in Figures 6.64, 6.65, and 6.66 the microrotations at the clamped end of the beam (beam's left end) are nonzero and even may become larger than the microrotations at the clamped end.

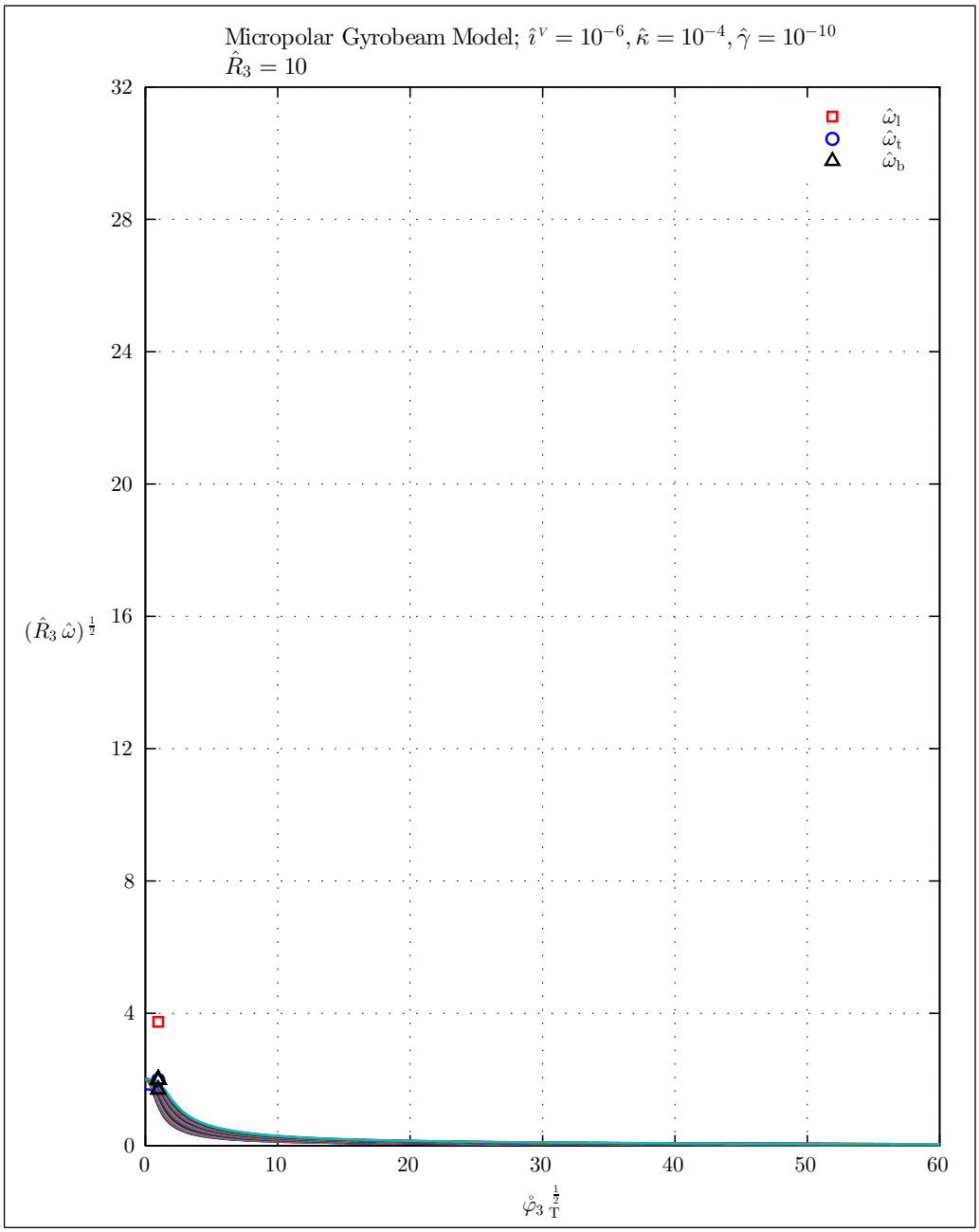

Figure 6.58: Natural frequencies of a thick micropolar gyrobeam with a uniform transverse gyricity – Micropolar gyrobeam model 3.

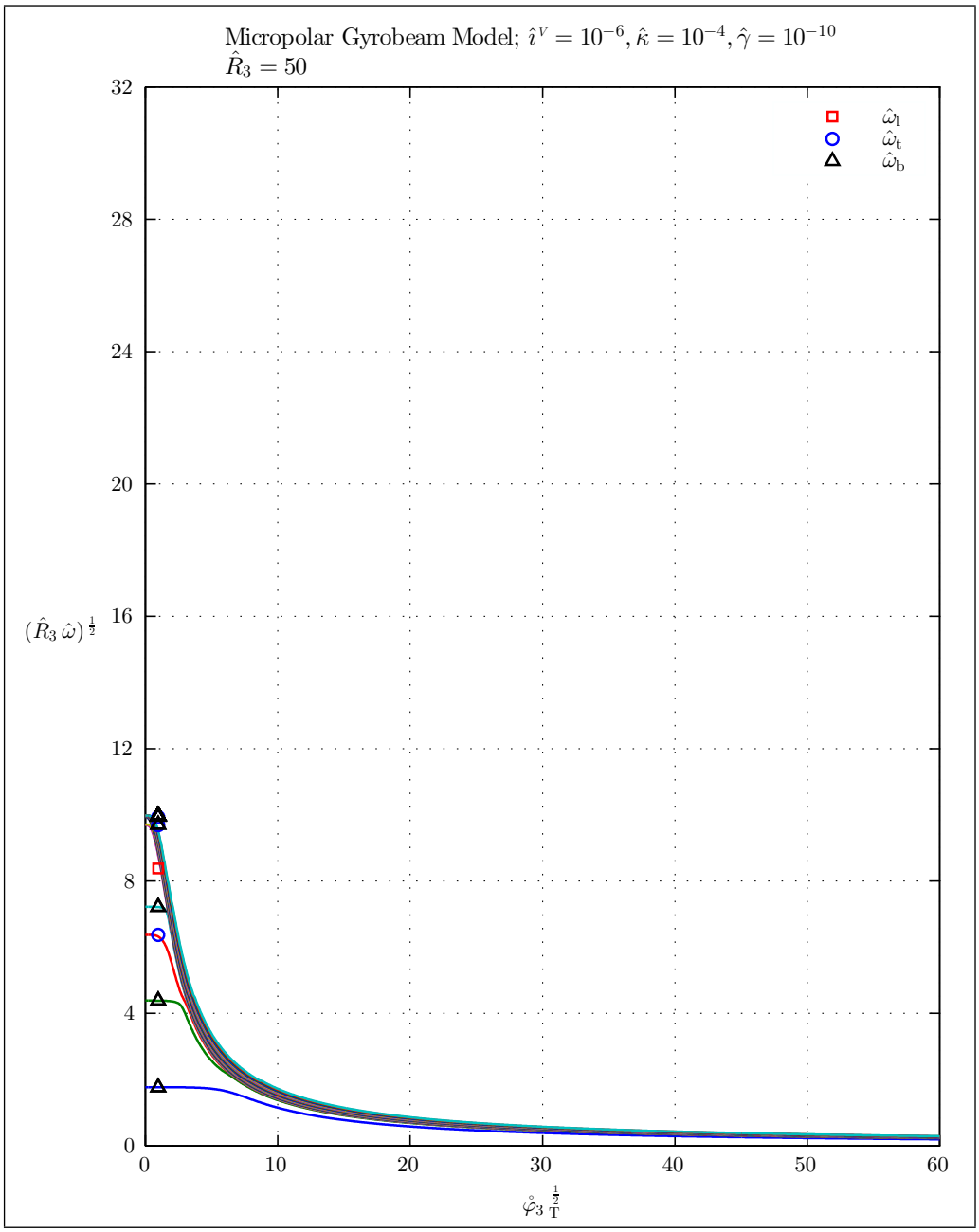

Figure 6.59: Natural frequencies of a medium micropolar gyrobeam with a uniform transverse gyricity – Micropolar gyrobeam model 3.

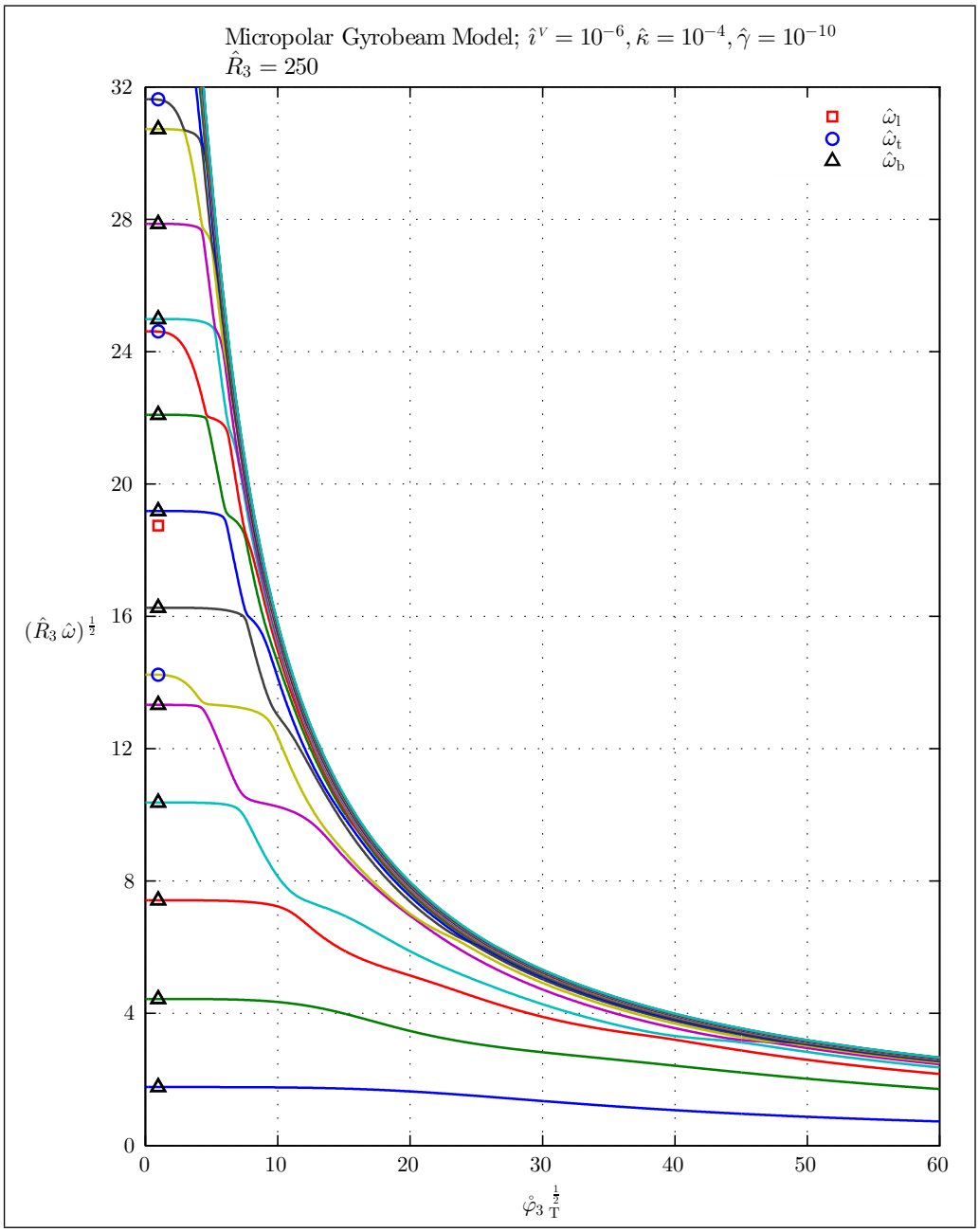

Figure 6.60: Natural frequencies of a thin micropolar gyrobeam with a uniform transverse gyricity – Micropolar gyrobeam model 3.

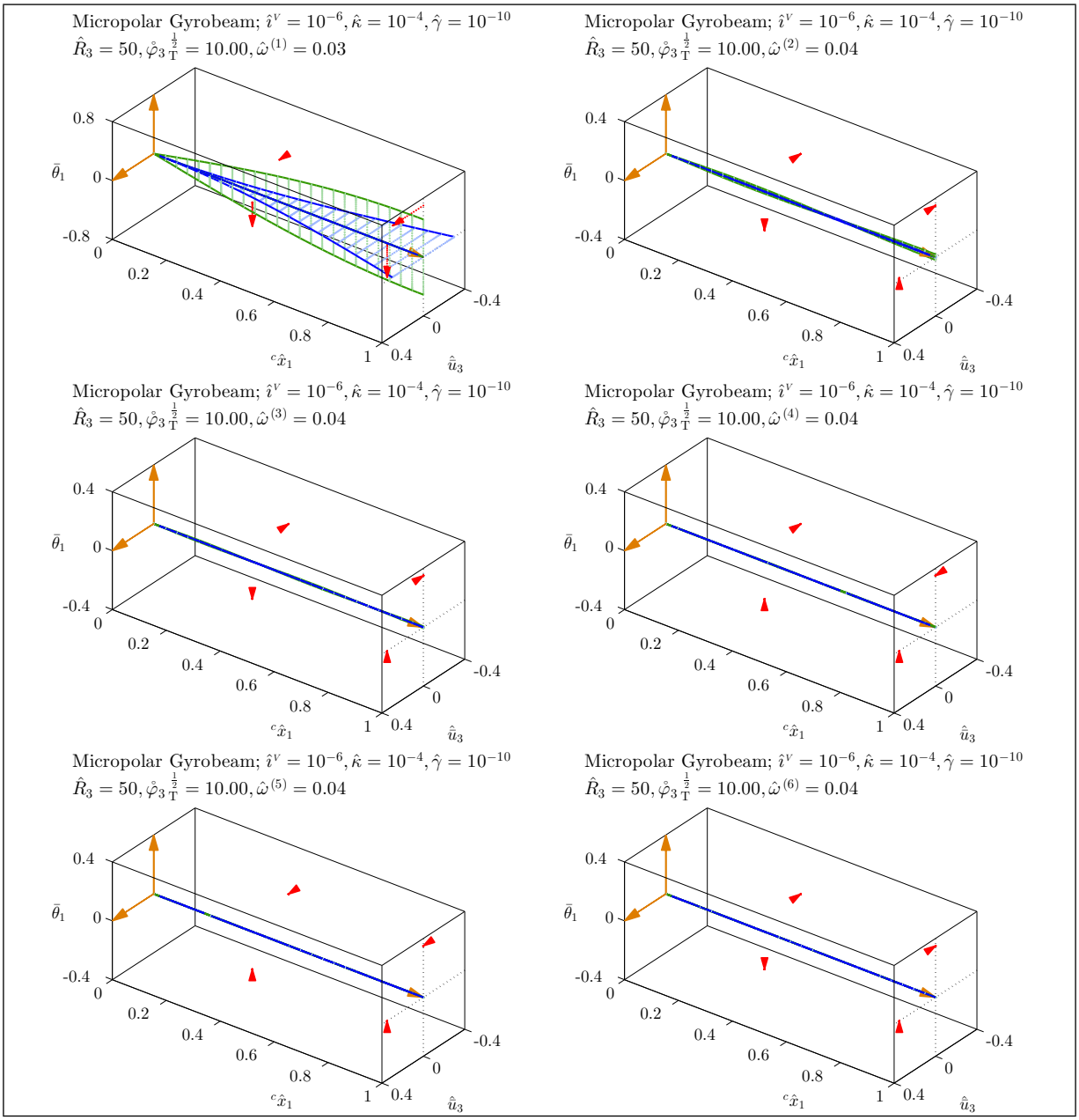

Figure 6.61: Mode shapes of a medium micropolar gyrobeam with a small uniform transverse gyricity – Micropolar gyrobeam model 3.

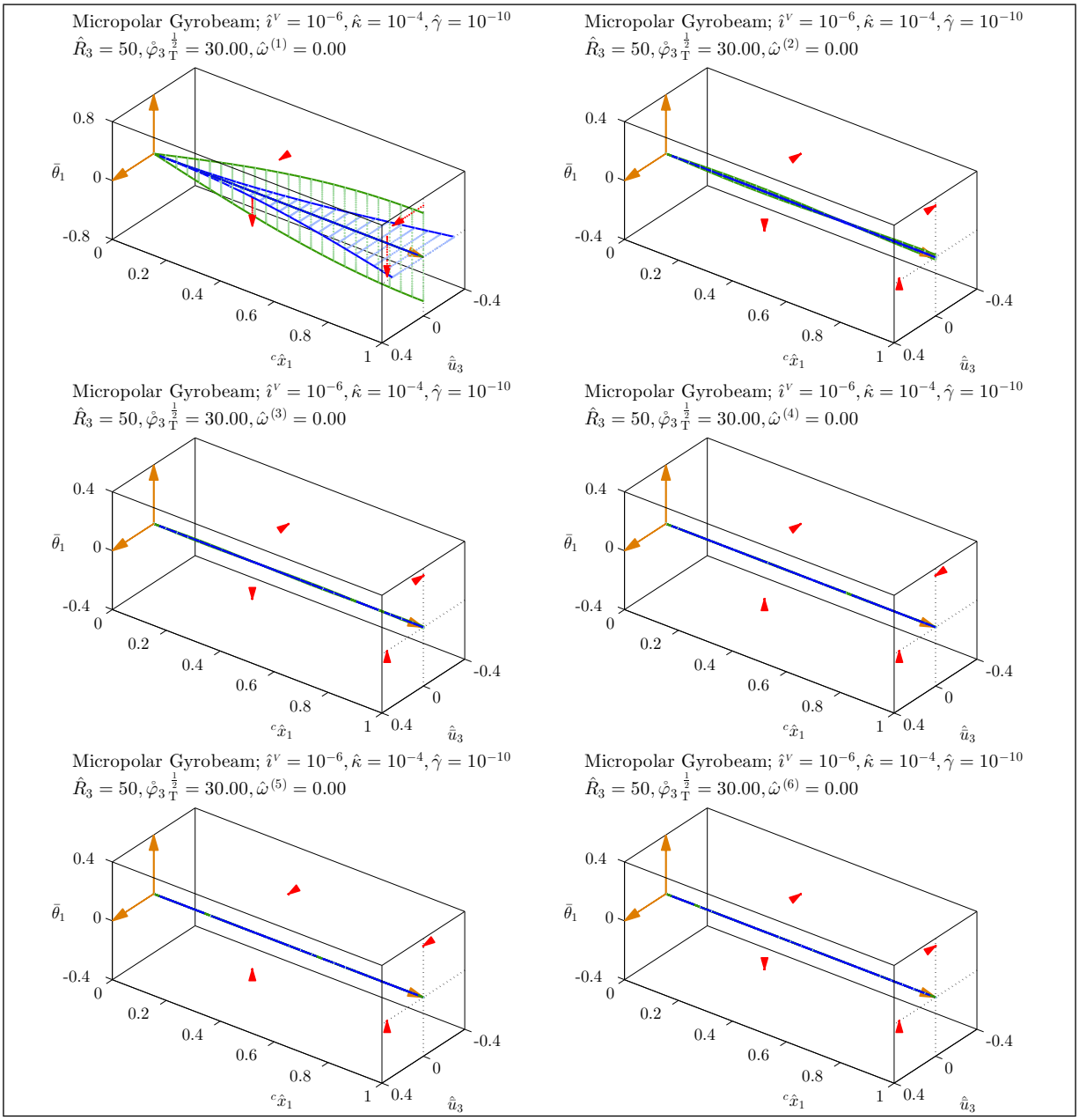

Figure 6.62: Mode shapes of a medium micropolar gyrobeam with a medium uniform transverse gyricity – Micropolar gyrobeam model 3.

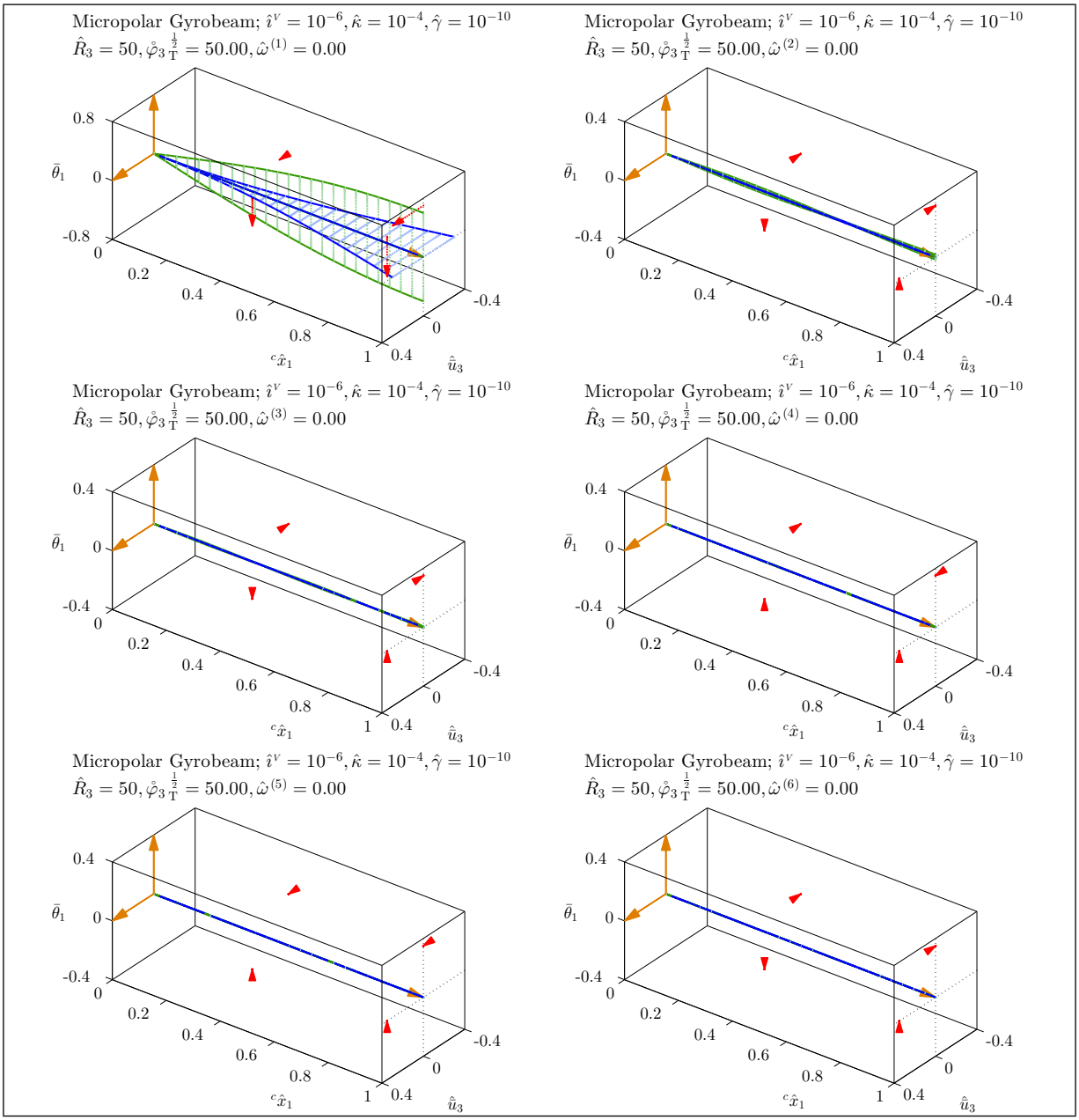

Figure 6.63: Mode shapes of a medium micropolar gyrobeam with a large uniform transverse gyricity – Micropolar gyrobeam model 3.

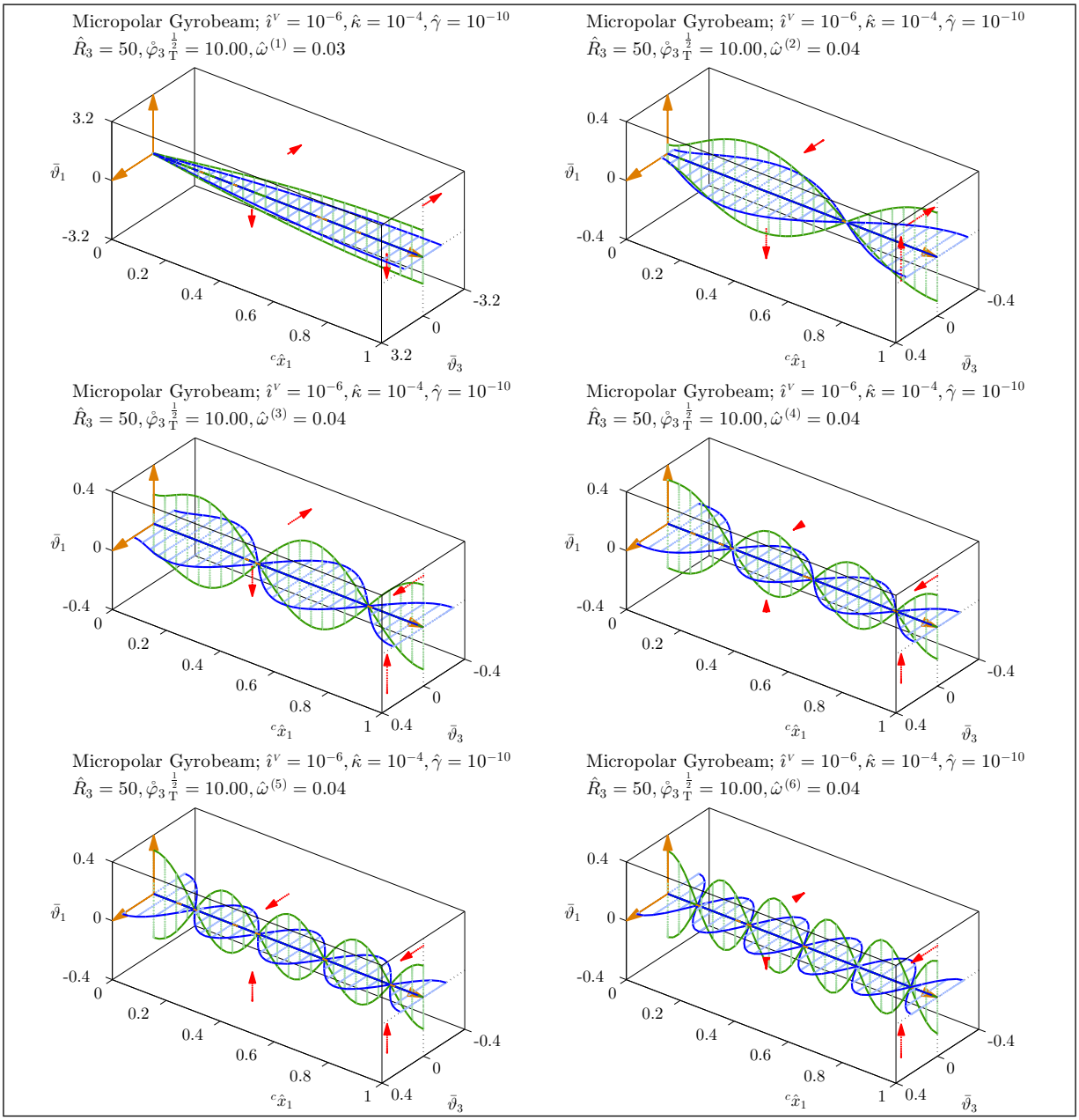

Figure 6.64: Mode shapes of a medium micropolar gyrobeam with a small uniform transverse gyricity – Micropolar gyrobeam model 3.

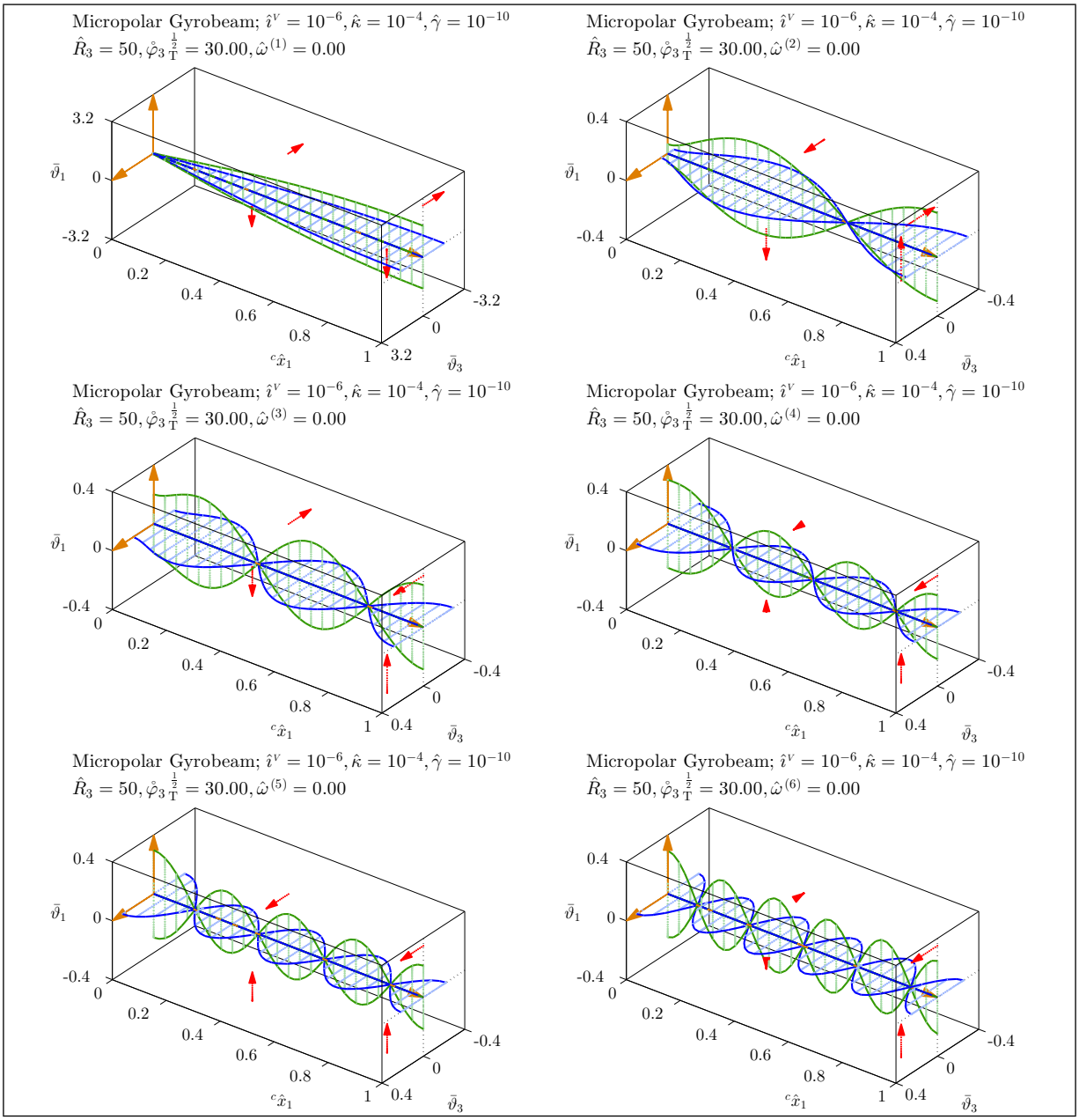

Figure 6.65: Mode shapes of a medium micropolar gyrobeam with a medium uniform transverse gyricity – Micropolar gyrobeam model 3.

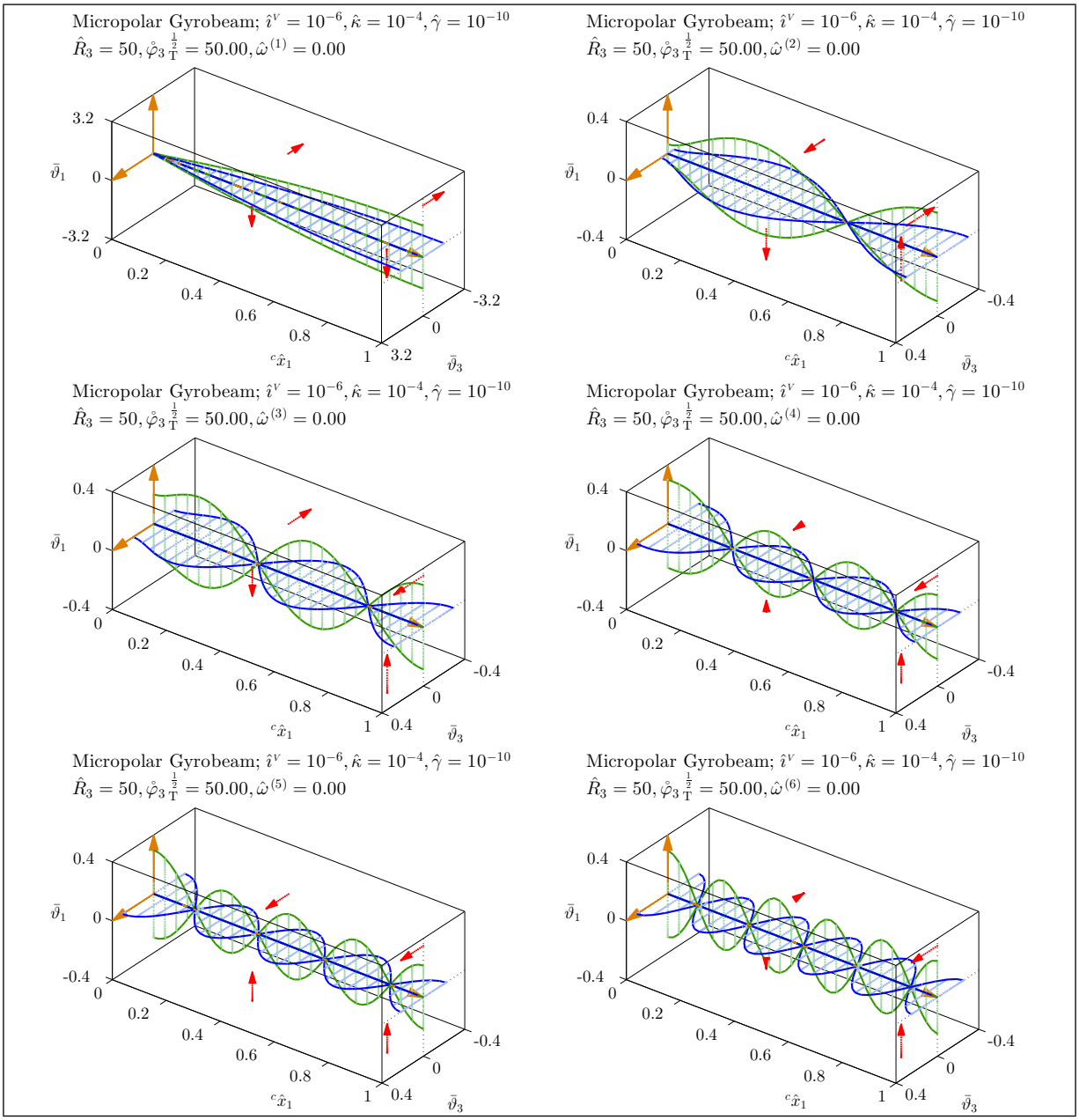

Figure 6.66: Mode shapes of a medium micropolar gyrobeam with a large uniform transverse gyricity – Micropolar gyrobeam model 3.

The natural frequency loci and mode shapes of the fourth specific micropolar gyrobeam model are shown in Figures 6.67–6.72. Overall, one can conclude that the effect of decreasing $\hat{\kappa}$ (in general resulting in lower natural frequencies) overrides the effect of increasing $\hat{\gamma}$ (in general resulting in higher natural frequencies).

It is interesting that in this model the curve veering between the natural frequency loci are more evident compared to the first specific micropolar gyrobeam model (or even the second and third ones). This can be seen more clearly in Figures 6.67 and 6.68 which can be compared to Figures 6.46 and 6.47. This is probably the main reason why the the last mode shapes shown in Figure 6.71 looks different than the last mode shape in Figure 6.50. The rest of the depicted mode shapes of the fourth micropolar gyrobeam are however analogous to the mode shapes of the first micropolar gyrobeam model.

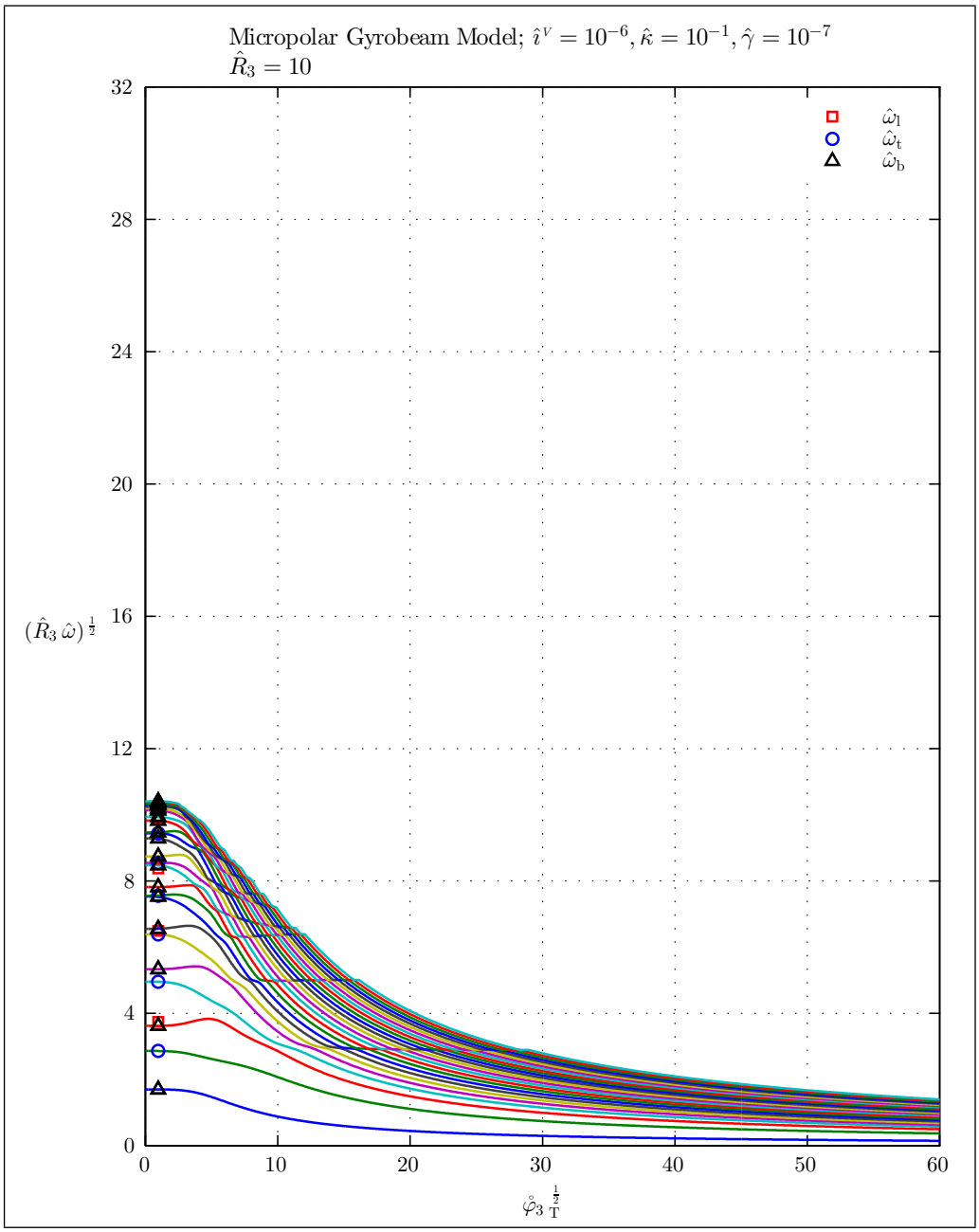

Figure 6.67: Natural frequencies of a thick micropolar gyrobeam with a uniform transverse gyricity – Micropolar gyrobeam model 4.

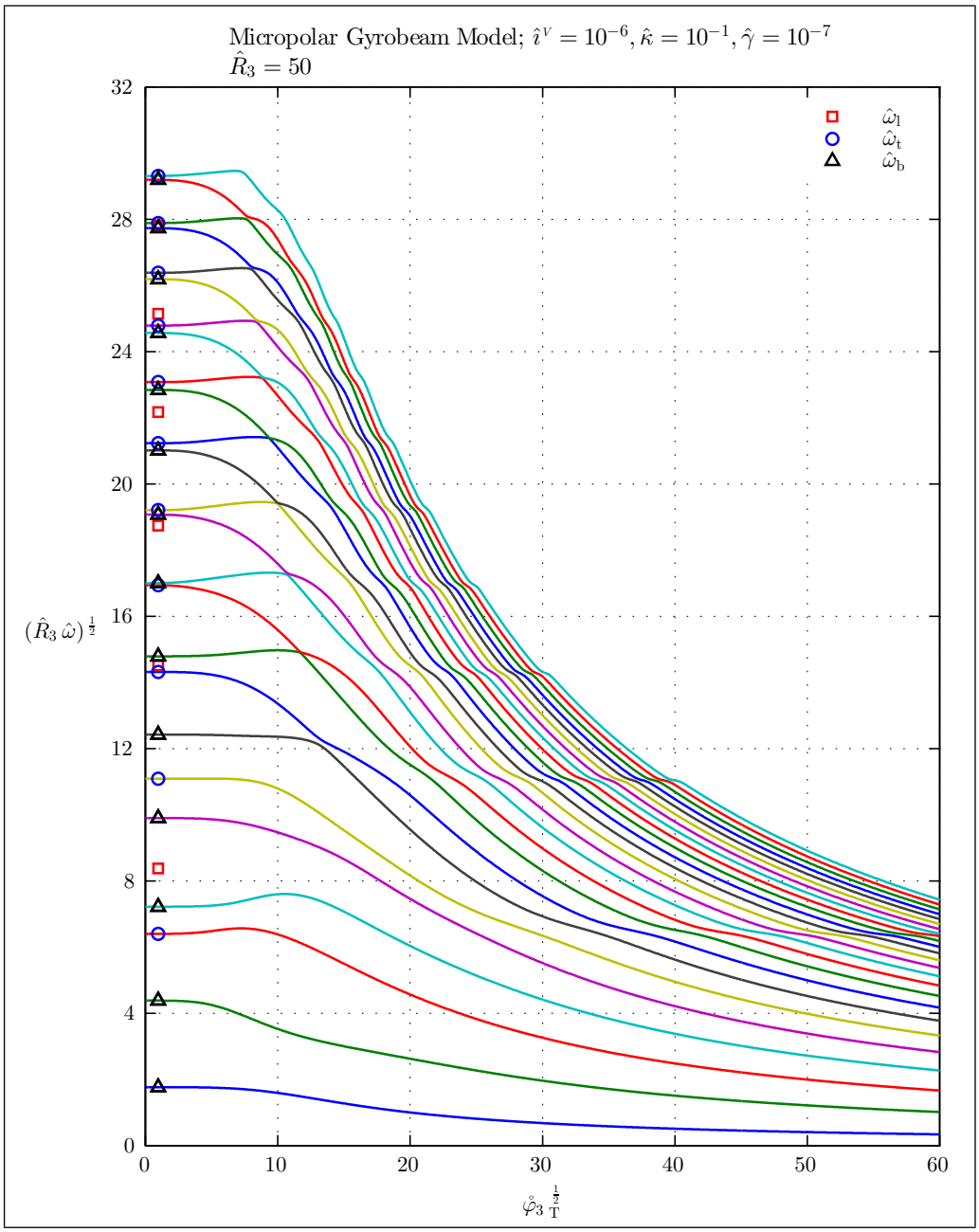

Figure 6.68: Natural frequencies of a medium micropolar gyrobeam with a uniform transverse gyricity – Micropolar gyrobeam model 4.

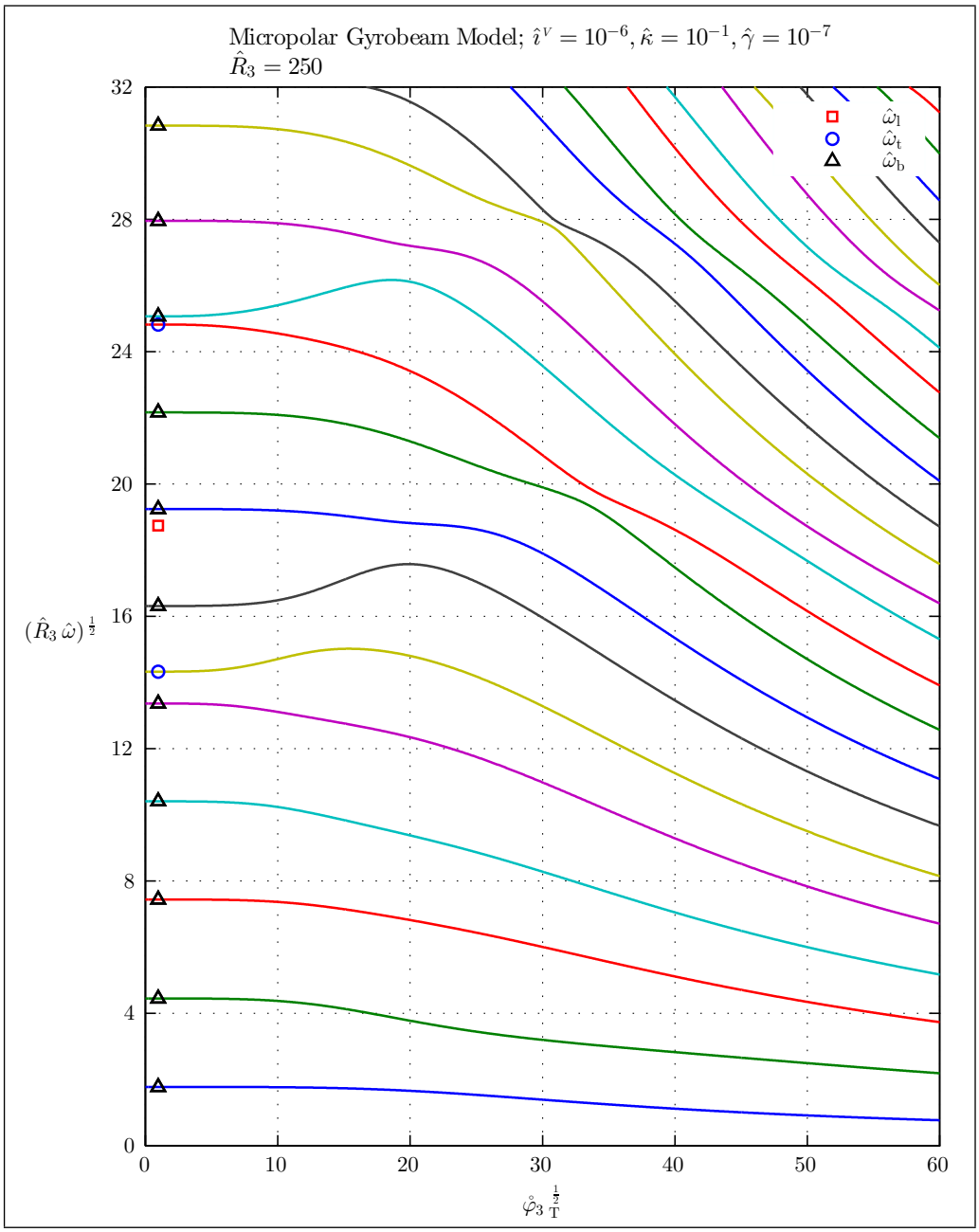

Figure 6.69: Natural frequencies of a thin micropolar gyrobeam with a uniform transverse gyricity – Micropolar gyrobeam model 4.

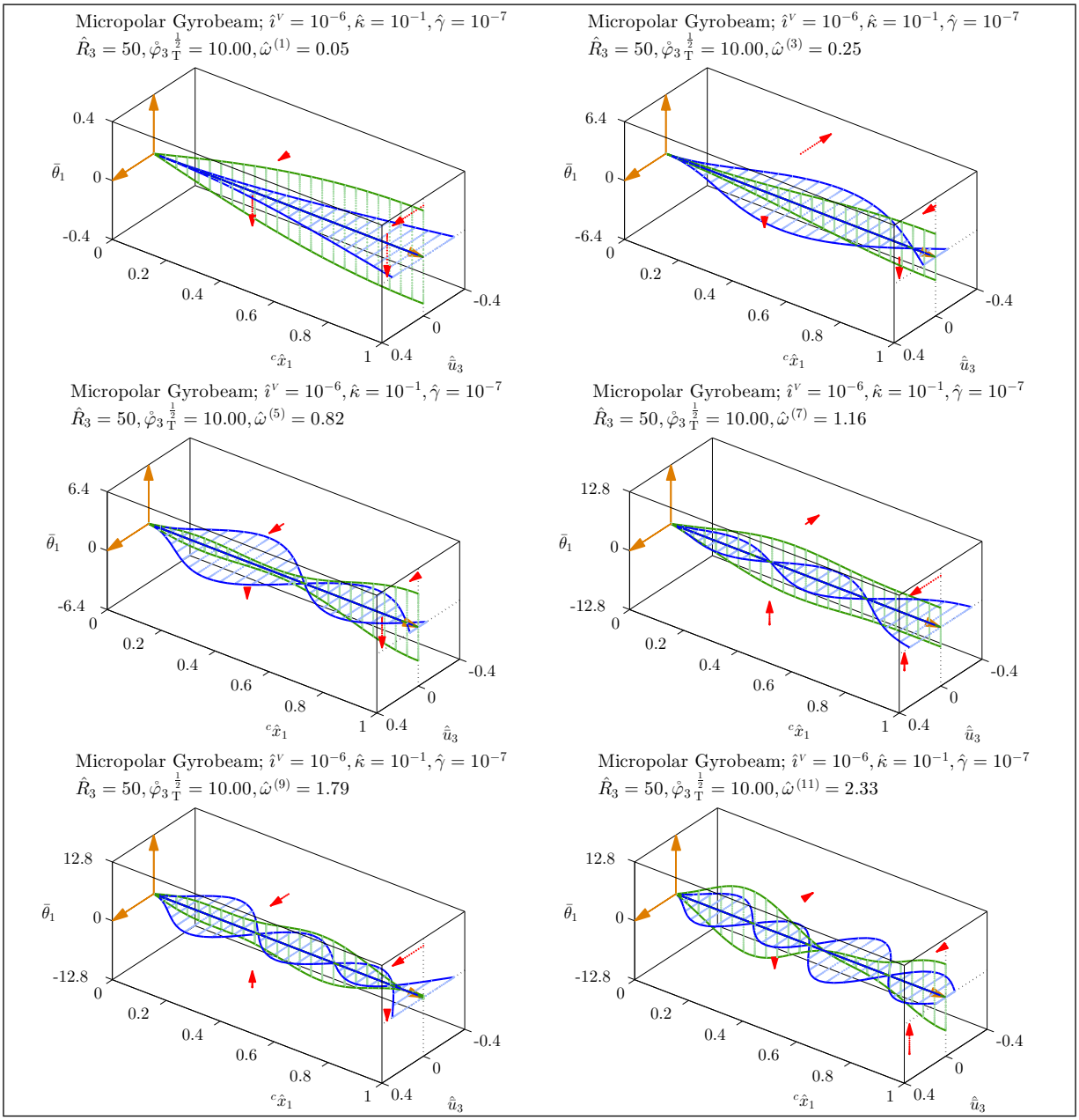

Figure 6.70: Mode shapes of a medium micropolar gyrobeam with a small uniform transverse gyricity – Micropolar gyrobeam model 4.

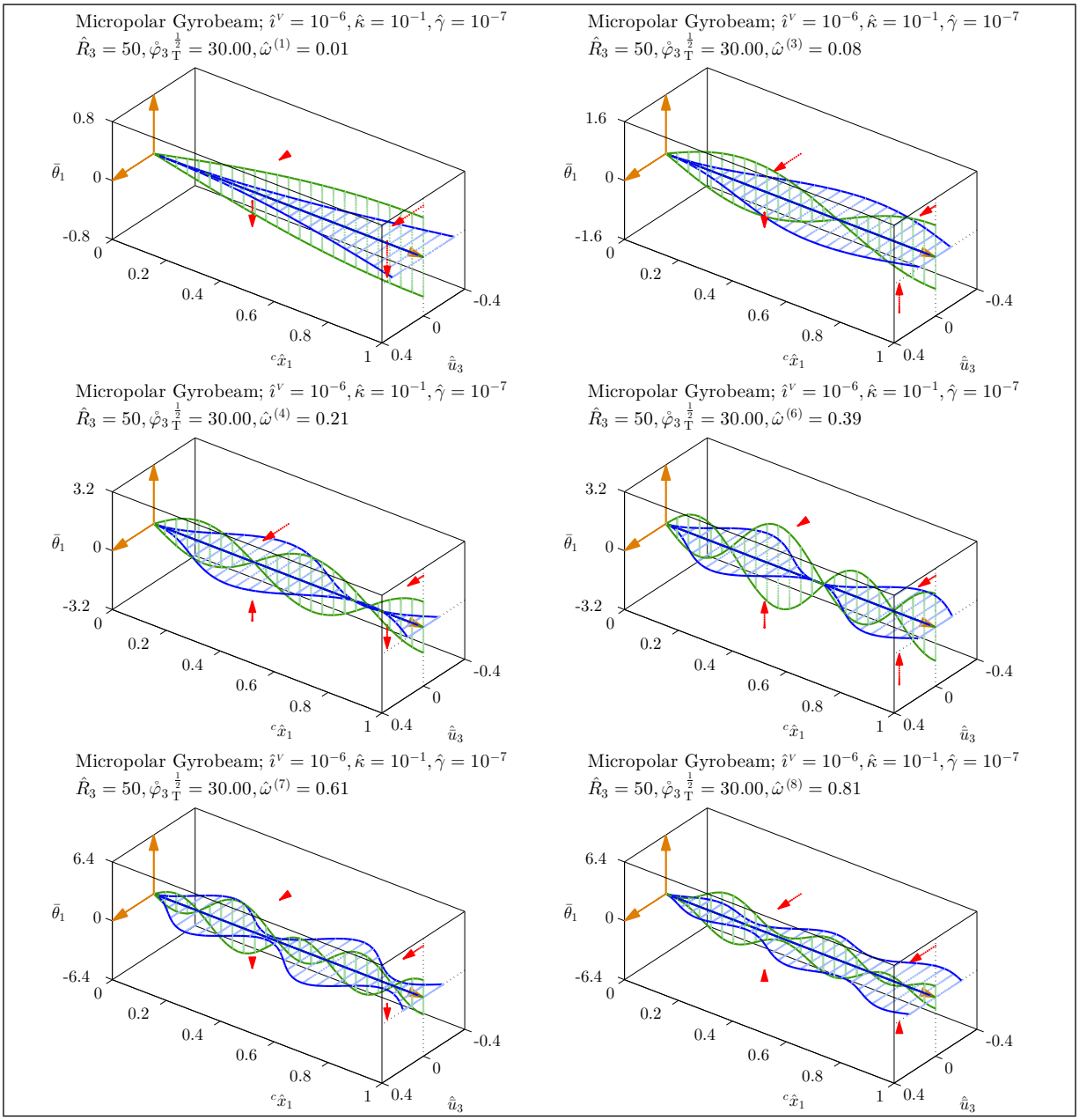

Figure 6.71: Mode shapes of a medium micropolar gyrobeam with a medium uniform transverse gyricity – Micropolar gyrobeam model 4.

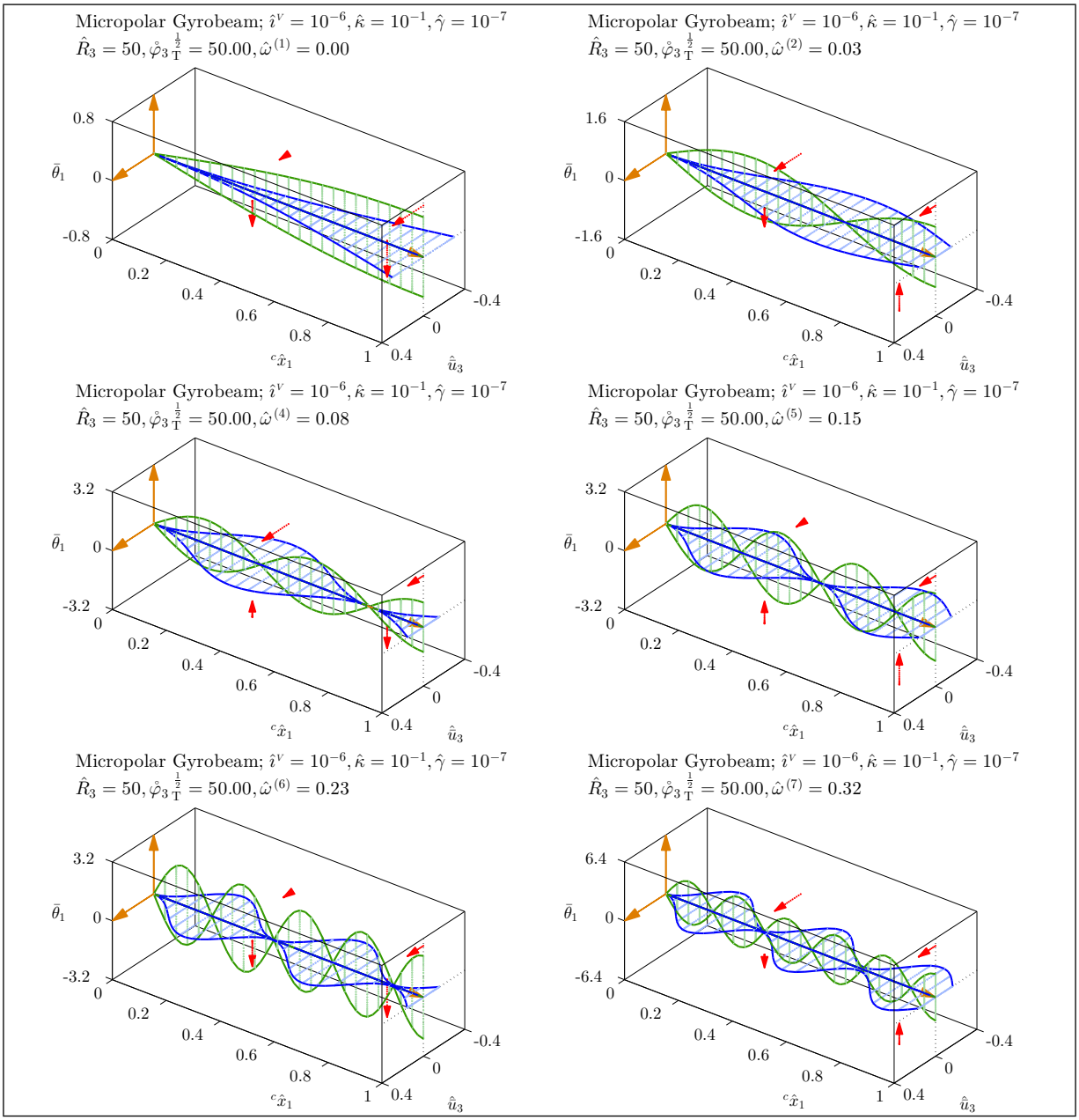

Figure 6.72: Mode shapes of a medium micropolar gyrobeam with a large uniform transverse gyricity – Micropolar gyrobeam model 4.

Chapter 7

Summary and Recommendations

7.1 Introduction

As the final chapter, this chapter presents a summary and reviews the work done. The main achievements and conclusions of the thesis are addressed. Finally, the recommendations for future work are reviewed.

7.2 Summary

The equations of motion for classical gyrocontinua without/with damping and considering small rotation angles for the gyros' axes were previously derived in the literature. In this work, the general (or unrestricted) equations of motion for undamped 3D classical and micropolar gyrocontinua have been derived. The equations are general in the sense that there has been no restriction on the rotational motion of the gyros. In addition, the potential energy, kinetic energy, and virtual work expressions for both the classical and the micropolar gyrocontinua have been obtained.

Gyroelastic beams or gyrobeams as a special case of general gyrocontinua have been formulated based on the classical and micropolar elastic beam theories. Numerical analysis and comparison of the micropolar and classical gyrobeams have been carried out using

FEM-based numerical models built in MATLAB®. It has been shown through the numerical examples that there are significant differences between the Timoshenko-based and Euler-Bernoulli-based classical gyrobeam models specially when the gyrobeam is thicker and the gyricity distribution is transverse. The numerical examples have also indicated that the unrestricted classical and micropolar gyrobeam models behave very diversely in a wide range of micropolar elastic constants even where the classical and micropolar elasticity models (with no gyricity effects) are expected to coincide. A detailed discussion of the results can be found in Chapters 5 and 6 and also Appendix C.

Overall, the micropolar gyroelastic continuum model with extra coefficients and degrees of freedom has been proved to be beneficial first, for including the asymmetry of the stress and strain tensors in the presence of a gyricity distribution and second, for describing the actual gyroscopic system or structure more comprehensively compared to the previously derived gyroelastic continuum models.

The thesis outlines as well as the reason(s) for and the outcome(s) of accomplishing each outlined work are summarized in Tables 7.1 and 7.2.

Table 7.1: The outlines of the main work done to date and the reason(s) for and the outcome(s) of each.

Main Work Done	**Reason(s)**	**Outcome(s)**
Allowing for unrestricted (non-small) rotations of gyros' axes with respect to the gyrocontinua.	Generalizes the existing restricted model of classical gyrocontinua where gyros' axis is allowed to rotate just through small angles.	A mathematical continuous model of unrestricted classical gyrocontinua.
Considering (asymmetric) micropolar elasticity for modeling the elasticity of gyrocontinua.	Asymmetric nature of the stress field inside the continua due to the presence of gyricity moments.	A mathematical continuous model of unrestricted micropolar gyrocontinua.
Considering a full 3D Timoshenko beam (with both torsional and bending deformations) for modeling classical gyrobeams.	Allow for the possibility of the occurrence of torsion, bending, and coupled torsion-bending deformations in the presence of a general gyricity distribution and therefore completing the existing model of Euler-Bernoulli gyrobeams with only bending deformations.	Mathematical model (Dynamic equations) of 3D classical (Timoshenko) unrestricted gyrobeams.
Constructing simple micropolar beam torsion and bending theories.	Lack of such simple theories which can be used to model a micropolar gyrobeam.	Mathematical model (Dynamic equations) of 3D micropolar unrestricted gyrobeams.
Building an FEM-based numerical simulation tool capable of solving the dynamics of both classical and micropolar gyrobeams.	Discretization of the continuous dynamic equations of gyrobeams (conversion of the continuous dynamic PDEs into a simpler-to-solve semi-discrete system of ODEs).	Semi-discrete dynamic equations in terms of FEM stiffness, mass, gyricity, circulatory, generalized moment, and generalized force matrices.

Continued on next page ...

Table 7.1: (continued)

Main Work Done	**Reason(s)**	**Outcome(s)**
Numerical examples.	Comparison between classical and micropolar beams (carrying no gyros) and comparison between classical and micropolar gyrobeams.	Figures illustrating the differences between classical and micropolar gyrobeams, importance of shear and torsion deformations inclusion, and the significant effect of the gyros mounting system stiffness which can be modeled as micropolar coupling constant κ in a micropolar gyrobeam.

Table 7.2: The outlines of the side work done to date and the reason(s) for and the outcome(s) of each.

Side Work Done	**Reason(s)**	**Outcome(s)**
A correct step-by-step simplification of micropolar elasticity to couple-stress theory and classical elasticity theory.	Finding the correct range for micropolar elastic constants when comparing with classical elasticity as there were numerous flawed works on this subject.	Correct values of micropolar elastic constants for reduction of micropolar elasticity to classical elasticity.
Presenting the correct approximation of microrotations in problems containing small rotations.	To be used for modeling the elastic continua microrotations as there were a few imperfect works with improper approximation of microrotations.	A correct first-order approximation of continua microrotations when deriving the dynamic equations by applying the calculus of variations on the system Lagrangian.

7.3 Future work

Whereas developing and analyzing more comprehensive gyrobeam models, as usual, come out as the first emerging recommendation for future work, there are plenty of possibilities which one can pursue using the herein developed micropolar gyrobeam models. These possibilities can be summarized as:

- Derivation of modal identities in the same way as suggested in [2].
- Dynamic analysis, especially energy diversion from one mode into others.
- Dynamic comparison of different gyrobeams in the presence of gyricity-induced damping.
- Inclusion and study of damping effects (non-gyricity-based dampings).
- Mode shape and natural frequency analysis in vicinity of curve veering points (for both symmetric and asymmetric beams when considering torsion, bending, and coupled torsion-bending modes).
- Feasibility study of finding analytical solutions for the modal and dynamic analyses.
- Stability analysis.
- Building (*i.e.* defining, designing, and manufacturing) an experimental setup for real examination of the gyrobeams behavior, *e.g.* natural frequencies and mode shapes, stability, and curve veering.
- Derivation and examination of more advanced classical and micropolar models capable of undertaking large elastic deformations.
- Examination of gyrobeams with nonuniform gyricity distributions in different directions.
- Optimization of gyricity distribution shape to achieve desired natural frequency loci and mode shapes.

- Full analysis of unconstrained gyrobeams.

Also the more comprehensive gyrobeam models developed in the current thesis can be used for undertaking studies on the following subjects:

- Equivalent continuum modeling of very large beam-like structures specially those with regular repetitive lattices and stored angular momentum or gyros distribution.
- Modeling and study of beam-like structures with imperfect mounting mechanisms for installing the gyros where the mounting mechanisms are non-rigid and have their own inertia.
- Application of gyros for stabilization/control of very large beam-like structures.
- Optimized placement of gyro actuators in the sense of the best stabilization/shape control with minimum number of actuators.
- Performance comparison of gyro actuation and piezo (piezoelectric) actuation for stabilization/control purposes.
- Application feasibility and fabrication of gyrobeams at micro scales.

A very broad aspect of future work can be considered as repeating this thesis studies (and of course the aforementioned possible future studies) for other simplified cases of gyrocontinua (*e.g.* different classical and micropolar gyroplates) or even for the very general 3D gyrocontinua.

Finally, the materials covered in this thesis and those mentioned as future work can be specialized and used in other fields where an angular momentum device (any rotating inertia) as gyro is interacting with an elastic structure (a or some flexible bodies) as elastic continuum. Examples of such systems are helicopters, airplanes (more specifically engine-mounted airplane wings), and (high-precision) machining tools.

Appendix A

Theory of Micropolar Elasticity

A.1 Introduction

The linear theory of micropolar elasticity is a generalized form of the couple-stress theory which itself is an extended form of the classical theory of elasticity [71]. Indeed, Voigt generalized the classical theory of (asymmetric) elasticity to take into account the effects of couple stresses and introduced the couple-stress theory (of asymmetric elasticity) [42,43]. Then, the Cosserat brothers extended the Voigt couple-stress theory to their own theory, *i.e.* the Cosserat elasticity model, by considering a microrotation field inside the elastic body which is independent of the body displacement field [42]. The Cosserat theory was further developed by Eringen via including the body microinertia and was renamed as the micropolar theory of (asymmetric) elasticity [72]. An extensive description of the linear theory of micropolar elasticity is presented by Nowacki [42].

In this appendix the linear theory of micropolar elasticity applied to a homogeneous, isotropic, and centrally symmetric material will be considered. The kinematics (deformation tensors and compatibility conditions), kinetics (load tensors and balance of momenta), constitutive relations, equations of motion, and internal energy will be formulated. Then the inconsistencies in the micropolar theory of elasticity and the resolution of them will be presented. Finally, the recovery of couple-stress theory and classical elasticity theory from the micropolar elasticity theory will be addressed.

A.2 Kinematics

In a micropolar continuum, the (classical) displacement field vector $\underset{\rightarrow}{u}$ is complemented by a microrotation field vector $\underset{\rightarrow}{\vartheta}$ (independent of the displacement field). Consequently, the translational velocity and acceleration field vectors are $\underset{\rightarrow}{\dot{u}}$ and $\underset{\rightarrow}{\ddot{u}}$, and the angular velocity and acceleration field vectors are $\underset{\rightarrow}{\dot{\vartheta}}$ and $\underset{\rightarrow}{\ddot{\vartheta}}$ (see Appendix B).

The micropolar deformation is fully described by (asymmetric) strain and twist tensors, $\underset{\leftrightarrow}{\varepsilon}$ and $\underset{\leftrightarrow}{\tau}$, which are defined as:

$$\begin{aligned} \varepsilon_{ij} &= u_{j,i} - \epsilon_{ijk}\,\vartheta_k \\ \tau_{ij} &= \vartheta_{j,i} \end{aligned} \tag{A.1}$$

Based on these definitions the following relations can be derived:

$$\begin{aligned} \vartheta_i &= \frac{1}{2}\,\epsilon_{ijk}\Big(u_{k,j} - \varepsilon_{jk}\Big) \\ \tau_{ij} &= \frac{1}{2}\,\epsilon_{jkl}\Big(u_{l,ki} - \varepsilon_{kl,i}\Big) \\ \tau_{ii} &= -\frac{1}{2}\,\epsilon_{ijk}\,\varepsilon_{jk,i} \end{aligned} \tag{A.2}$$

It is also useful to define the (classical) macrorotation vector $\underset{\rightarrow}{\theta}$ and the (classical) macrorotation tensor $\underset{\leftrightarrow}{\theta}^{\times}$ such that:

$$\begin{aligned} \theta_i &= \frac{1}{2}\epsilon_{ijk}u_{k,j} \\ \theta^{\times}_{ij} &= -\epsilon_{ijk}\,\theta_k = -\frac{1}{2}\Big(u_{j,i} - u_{i,j}\Big) \end{aligned} \tag{A.3}$$

Then the strain and twist tensors can be decomposed into their symmetric and anti-symmetric (skew-symmetric) parts as:

$$\begin{aligned} \varepsilon_{ij} &= \varepsilon^{\mathrm{s}}_{ij} + \varepsilon^{\mathrm{a}}_{ij} \\ \varepsilon^{\mathrm{s}}_{ij} &= \frac{1}{2}\Big(u_{j,i} + u_{i,j}\Big) \\ \varepsilon^{\mathrm{a}}_{ij} &= \frac{1}{2}\Big(u_{j,i} - u_{i,j}\Big) - \epsilon_{ijk}\vartheta_k = \epsilon_{ijk}\Big(\theta_k - \vartheta_k\Big) \end{aligned} \tag{A.4}$$

and:

$$\begin{aligned}\tau_{ij} &= \tau_{ij}^{\mathrm{s}} + \tau_{ij}^{\mathrm{a}} \\ \tau_{ij}^{\mathrm{s}} &= \frac{1}{2}\left(\vartheta_{j,i} + \vartheta_{i,j}\right) \\ \tau_{ij}^{\mathrm{a}} &= \frac{1}{2}\left(\vartheta_{j,i} - \vartheta_{i,j}\right)\end{aligned} \tag{A.5}$$

where note that $\underset{\leftrightarrow}{\varepsilon}^{\mathrm{a}}$ is a representation of the difference between the (classical) macrorotation and the (micropolar) microrotation.

Finally, the compatibility conditions (necessary conditions for continuity) that elements of the strain and twist tensors in micropolar elasticity should satisfy are:

$$\begin{aligned}&\varepsilon_{ij,k} - \varepsilon_{kj,i} + \epsilon_{ijl}\,\tau_{kl} - \epsilon_{kjl}\,\tau_{il} = 0 \\ &\tau_{ij,k} - \tau_{kj,i} = 0\end{aligned} \tag{A.6}$$

or equivalently:

$$\begin{aligned}&\epsilon_{ikl}\left(\varepsilon_{kj,l} + \epsilon_{kjm}\,\tau_{lm}\right) = 0 \\ &\epsilon_{ikl}\,\tau_{kj,l} = 0\end{aligned} \tag{A.7}$$

A.3 Kinetics

In a micropolar continuum, the (classical force) stress field tensor $\underset{\leftrightarrow}{\sigma}$ is completed by a (micropolar) couple stress field tensor $\underset{\leftrightarrow}{\chi}$. For a micropolar elastic body under the action of a general volume force $\underset{\rightarrow}{f}^{V}$ and a general volume moment $\underset{\rightarrow}{m}^{V}$ the balance of linear and angular momenta can be written in the following differential form:

$$\begin{aligned}\sigma_{ji,j} + f_i^V &= \rho^V \ddot{u}_i \\ \chi_{ji,j} + \epsilon_{ijk}\,\sigma_{jk} + m_i^V &= \imath^V \ddot{\vartheta}_i\end{aligned} \tag{A.8}$$

where ρ^V is the material mass density (translational inertia per unit volume) and $\imath^V$ is the material microinertia density (microrotational inertia per unit volume). Note that a more general case is when the material has a tensor of microinertia density $\underset{\leftrightarrow}{\imath}^{V}$, however this appendix is confined to the isotropic case where $\underset{\leftrightarrow}{\imath}^{V} = \imath^V \underset{\leftrightarrow}{\mathbb{1}}$ [42].

Analogous to the decomposition of strain and twist tensors, the force and couple stress tensors can be decomposed into their symmetric and antisymmetric parts as:

$$\begin{aligned}\sigma_{ij} &= \sigma^{\mathrm{s}}_{ij} + \sigma^{\mathrm{a}}_{ij} \\ \sigma^{\mathrm{s}}_{ij} &= \frac{1}{2}\Big(\sigma_{ij} + \sigma_{ji}\Big) \\ \sigma^{\mathrm{a}}_{ij} &= \frac{1}{2}\Big(\sigma_{ij} - \sigma_{ji}\Big)\end{aligned} \tag{A.9}$$

and:

$$\begin{aligned}\chi_{ij} &= \chi^{\mathrm{s}}_{ij} + \chi^{\mathrm{a}}_{ij} \\ \chi^{\mathrm{s}}_{ij} &= \frac{1}{2}\Big(\chi_{ij} + \chi_{ji}\Big) \\ \chi^{\mathrm{a}}_{ij} &= \frac{1}{2}\Big(\chi_{ij} - \chi_{ji}\Big)\end{aligned} \tag{A.10}$$

Utilizing Eq. (A.9) and the fact that for any symmetric second-order tensor $\underset{\leftrightarrow}{d}$:

$$\epsilon_{ijk} d_{jk} = 0 \tag{A.11}$$

the balance of momenta relations in Eq. (A.8) can be rewritten as:

$$\begin{aligned}\sigma^{\mathrm{s}}_{ji,j} + \sigma^{\mathrm{a}}_{ji,j} + f^{V}_{i} &= \rho^{V}\,\ddot{u}_i \\ \chi_{ji,j} + \epsilon_{ijk}\,\sigma^{\mathrm{a}}_{jk} + m^{V}_{i} &= \imath^{V}\,\ddot{\vartheta}_i\end{aligned} \tag{A.12}$$

Solving the second relation of Eq. (A.12) for the antisymmetric force stress tensor $\underset{\leftrightarrow}{\sigma}^{\mathrm{a}}$ and substituting into the first relation of Eq. (A.12) one can rewrite the balance relations as:

$$\begin{aligned}\sigma^{\mathrm{s}}_{ji,j} + \frac{1}{2}\,\epsilon_{ijk}\Big(\chi_{lk,lj} + m^{V}_{k\,,j} - \imath^{V}\,\ddot{\vartheta}_{k,j}\Big) + f^{V}_{i} &= \rho^{V}\ddot{u}_i \\ \epsilon_{ijk}\Big(\chi_{lk,l} + m^{V}_{k} - \imath^{V}\,\ddot{\vartheta}_{k}\Big) &= 2\,\sigma^{\mathrm{a}}_{ji}\end{aligned} \tag{A.13}$$

As can be concluded from Eq. (A.12) the antisymmetric part of the force stress tensor, $\underset{\leftrightarrow}{\sigma}^{\mathrm{a}}$, couples the linear and angular momenta balance relations.

A.4 Constitutive relations

The linear theory of micropolar elasticity proposed by Eringen results in a set of two constitutive relations with six elastic constants for a general homogeneous, isotropic, and

centrally symmetric elastic body. These relations (relating the force and couple stress tensors to the strain and twist tensors) have the following form:

$$\begin{aligned}\sigma_{ij} &= \Big(\mu + \kappa\Big)\,\varepsilon_{ij} + \Big(\mu - \kappa\Big)\,\varepsilon_{ji} + \lambda\,\varepsilon_{kk}\,\mathbb{1}_{ij} \\ \chi_{ij} &= \Big(\gamma + \beta\Big)\,\tau_{ij} + \Big(\gamma - \beta\Big)\,\tau_{ji} + \alpha\,\tau_{kk}\,\mathbb{1}_{ij}\end{aligned} \tag{A.14}$$

Among the six elastic constants denoted in Eq. (A.14), μ and λ are the well-known classical Lamé parameters (μ is also called Lamé shear modulus or briefly shear modulus). The other four constants, *i.e.* κ, γ, β, and α, are the new elastic constants usually referred to as the micropolar or Cosserat elastic constants. The micropolar constants represent the contribution of the material microstructure to the elastic properties of the body.

By decomposing the strain and twist tensors, as given by Eqs. (A.4) and (A.5), the constitutive relations in Eq. (A.14) can be rewritten as:

$$\begin{aligned}\sigma_{ij} &= 2\,\mu\,\varepsilon^{\mathrm{s}}_{ij} + \lambda\,\varepsilon_{kk}\,\mathbb{1}_{ij} + 2\,\kappa\,\varepsilon^{\mathrm{a}}_{ij} \\ \chi_{ij} &= 2\,\gamma\,\tau^{\mathrm{s}}_{ij} + \alpha\,\tau_{kk}\,\mathbb{1}_{ij} + 2\,\beta\,\tau^{\mathrm{a}}_{ij}\end{aligned} \tag{A.15}$$

Now a similar decomposition for the force and couple stress tensors, as given by Eqs. (A.9) and (A.10), gives rise to the following relations:

$$\begin{aligned}\sigma^{\mathrm{s}}_{ij} &= 2\,\mu\,\varepsilon^{\mathrm{s}}_{ij} + \lambda\,\varepsilon_{kk}\,\mathbb{1}_{ij}, \qquad & \sigma^{\mathrm{a}}_{ij} &= 2\,\kappa\,\varepsilon^{\mathrm{a}}_{ij} \\ \chi^{\mathrm{s}}_{ij} &= 2\,\gamma\,\tau^{\mathrm{s}}_{ij} + \alpha\,\tau_{kk}\,\mathbb{1}_{ij}, \qquad & \chi^{\mathrm{a}}_{ij} &= 2\,\beta\,\tau^{\mathrm{a}}_{ij}\end{aligned} \tag{A.16}$$

where the first relation is identical with the constitutive relation of classical elasticity.

Considering the original constitutive relations in Eq. (A.14) and applying the Einstein summation convention on stress tensors, $\underset{\leftrightarrow}{\sigma}$ and $\underset{\leftrightarrow}{\chi}$, it can be shown that:

$$\begin{aligned}\sigma_{kk} &= 3\,B\,\varepsilon_{kk}, \qquad & B &= \lambda + \frac{2}{3}\,\mu \\ \chi_{kk} &= 3\,\mathcal{B}\,\tau_{kk}, \qquad & \mathcal{B} &= \alpha + \frac{2}{3}\,\gamma\end{aligned} \tag{A.17}$$

where B is known as the (classical) tensile bulk modulus, and $\mathcal{B}$ as dual of the tensile bulk modulus can be called the (micropolar) tortile or torsional bulk modulus.

Simplifying the first constitutive relation given by Eq. (A.14) for the simple force stress state of uniform tension along axis ${}^{o}x_1$, where the only nonzero element of the force stress tensor is σ_{11}, results in definitions of the (classical) strain Poisson's ratio ν and the (classical) tensile or Young's modulus E as:

$$\begin{aligned} \nu &= -\frac{\varepsilon_{22}}{\varepsilon_{11}} = -\frac{\varepsilon_{33}}{\varepsilon_{11}} = \frac{\lambda}{2\left(\mu+\lambda\right)} \\ E &= \frac{\sigma_{11}}{\varepsilon_{11}} = \frac{\mu\left(2\,\mu+3\,\lambda\right)}{\mu+\lambda} = 2\,\mu\left(1+\nu\right) \end{aligned} \tag{A.18}$$

Analogously, the second constitutive relation in Eq. (A.14) can be simplified to account for the simple couple stress state of uniform torsion along axis ${}^{o}x_1$, where the only nonzero element of the couple stress tensor is χ_{11}. Then the (micropolar) twist Poisson's ratio ξ and the (micropolar) tortile or torsional modulus $\mathcal{E}$ can be defined as:

$$\begin{aligned} \xi &= -\frac{\tau_{22}}{\tau_{11}} = -\frac{\tau_{33}}{\tau_{11}} = \frac{\alpha}{2\left(\gamma+\alpha\right)} \\ \mathcal{E} &= \frac{\chi_{11}}{\tau_{11}} = \frac{\gamma\left(2\,\gamma+3\,\alpha\right)}{\gamma+\alpha} = 2\,\gamma\left(1+\xi\right) \end{aligned} \tag{A.19}$$

A.5 Equations of motion

Utilizing the constitutive relations in Eq. (A.14) and the definitions of the strain and twist tensors in Eq. (A.1) to replace the force and couple stresses in the balance of momenta relations given by Eq. (A.8), the system of PDEs representing the equations of motion for a micropolar continuum are derived as:

$$\begin{aligned} \left(\mu+\kappa\right)u_{i,jj} + \left(\mu-\kappa+\lambda\right)u_{j,ji} + 2\,\kappa\,\epsilon_{ijk}\,\vartheta_{k,j} + f_i^V &= \rho^V\,\ddot{u}_i \\ \left(\gamma+\beta\right)\vartheta_{i,jj} + \left(\gamma-\beta+\alpha\right)\vartheta_{j,ji} + 2\,\kappa\left(\epsilon_{ijk}\,u_{k,j} - 2\,\vartheta_i\right) + m_i^V &= \imath^V\,\ddot{\vartheta}_i \end{aligned} \tag{A.20}$$

Considering Eqs. (A.12) and (A.13) and substituting from the associated constitutive equations and the definitions of the strain and twist tensors into them, the following alter-

native forms for the dynamic equations can be attained respectively:

$$\begin{aligned} \mu\, u_{i,jj} + \Big(\mu + \lambda\Big)\, u_{j,ji} - 2\,\kappa\,\epsilon_{ijk}\,\Big(\theta_{k,j} - \vartheta_{k,j}\Big) + f_i^{\,V} &= \rho^{V}\,\ddot{u}_i \\ \Big(\gamma + \beta\Big)\,\vartheta_{i,jj} + \Big(\gamma - \beta + \alpha\Big)\,\vartheta_{j,ji} + 4\,\kappa\,\Big(\theta_i - \vartheta_i\Big) + m_i^{\,V} &= \imath^{\,V}\,\ddot{\vartheta}_i \end{aligned} \tag{A.21}$$

and:

$$\begin{aligned} \mu\, u_{i,jj} + \Big(\mu + \lambda\Big)\, u_{j,ji} + \frac{1}{2}\,\epsilon_{ijk}\,\Big(\Big(\gamma + \beta\Big)\,\vartheta_{k,llj} + m_{k\,,j}^{\,V} - \imath^{\,V}\,\ddot{\vartheta}_{k,j}\Big) + f_i^{\,V} &= \rho^{V}\,\ddot{u}_i \\ \Big(\gamma + \beta\Big)\,\vartheta_{i,jj} + \Big(\gamma - \beta + \alpha\Big)\,\vartheta_{j,ji} + m_i^{\,V} - \imath^{\,V}\,\ddot{\vartheta}_i = -\,4\,\kappa\,\Big(\theta_i - \vartheta_i\Big) \end{aligned} \tag{A.22}$$

where the relation given by Eq. (A.11) is recalled.

Note that in theories of elasticity the equations of motion are usually written in the vector form. The vector form of the motion equations given by Eqs. (A.20)–(A.22) are:

$$\begin{aligned} \Big(\mu + \kappa\Big)\,\Big(\underset{\rightarrow}{\nabla}\cdot\underset{\rightarrow}{\nabla}\Big)\,\underset{\rightarrow}{u} + \Big(\mu - \kappa + \lambda\Big)\,\underset{\rightarrow}{\nabla}\,\Big(\underset{\rightarrow}{\nabla}\cdot\underset{\rightarrow}{u}\Big) + 2\,\kappa\,\underset{\leftrightarrow}{\nabla}^{\times}\cdot\underset{\rightarrow}{\vartheta} + \underset{\rightarrow}{f}^{\,V} &= \rho^{V}\,\underset{\rightarrow}{\ddot{u}} \\ \Big(\gamma + \beta\Big)\,\Big(\underset{\rightarrow}{\nabla}\cdot\underset{\rightarrow}{\nabla}\Big)\,\underset{\rightarrow}{\vartheta} + \Big(\gamma - \beta + \alpha\Big)\,\underset{\rightarrow}{\nabla}\,\Big(\underset{\rightarrow}{\nabla}\cdot\underset{\rightarrow}{\vartheta}\Big) + 2\,\kappa\,\underset{\leftrightarrow}{\nabla}^{\times}\cdot\underset{\rightarrow}{u} - 4\,\underset{\rightarrow}{\vartheta} + \underset{\rightarrow}{m}^{\,V} &= \imath^{\,V}\,\underset{\rightarrow}{\ddot{\vartheta}} \end{aligned} \tag{A.23}$$

$$\begin{aligned} \mu\,\Big(\underset{\rightarrow}{\nabla}\cdot\underset{\rightarrow}{\nabla}\Big)\,\underset{\rightarrow}{u} + \Big(\mu + \lambda\Big)\,\underset{\rightarrow}{\nabla}\,\Big(\underset{\rightarrow}{\nabla}\cdot\underset{\rightarrow}{u}\Big) - 2\,\kappa\,\underset{\leftrightarrow}{\nabla}^{\times}\cdot\Big(\underset{\rightarrow}{\theta} - \underset{\rightarrow}{\vartheta}\Big) + \underset{\rightarrow}{f}^{\,V} &= \rho^{V}\,\underset{\rightarrow}{\ddot{u}} \\ \Big(\gamma + \beta\Big)\,\Big(\underset{\rightarrow}{\nabla}\cdot\underset{\rightarrow}{\nabla}\Big)\,\underset{\rightarrow}{\vartheta} + \Big(\gamma - \beta + \alpha\Big)\,\underset{\rightarrow}{\nabla}\,\Big(\underset{\rightarrow}{\nabla}\cdot\underset{\rightarrow}{\vartheta}\Big) + 4\,\kappa\,\Big(\underset{\rightarrow}{\theta} - \underset{\rightarrow}{\vartheta}\Big) + \underset{\rightarrow}{m}^{\,V} &= \imath^{\,V}\,\underset{\rightarrow}{\ddot{\vartheta}} \end{aligned} \tag{A.24}$$

$$\begin{aligned} \mu\,\Big(\underset{\rightarrow}{\nabla}\cdot\underset{\rightarrow}{\nabla}\Big)\,\underset{\rightarrow}{u} + \Big(\mu + \lambda\Big)\,\underset{\rightarrow}{\nabla}\,\Big(\underset{\rightarrow}{\nabla}\cdot\underset{\rightarrow}{u}\Big) + \frac{1}{2}\,\underset{\leftrightarrow}{\nabla}^{\times}\cdot\Big(\Big(\gamma + \beta\Big)\,\Big(\underset{\rightarrow}{\nabla}\cdot\underset{\rightarrow}{\nabla}\Big)\,\underset{\rightarrow}{\vartheta} + \underset{\rightarrow}{m}^{\,V} - \imath^{\,V}\,\underset{\rightarrow}{\ddot{\vartheta}}\Big) & \\ + \underset{\rightarrow}{f}^{\,V} = \rho^{V}\,\underset{\rightarrow}{\ddot{u}} & \\ \Big(\gamma + \beta\Big)\,\Big(\underset{\rightarrow}{\nabla}\cdot\underset{\rightarrow}{\nabla}\Big)\,\underset{\rightarrow}{\vartheta} + \Big(\gamma - \beta + \alpha\Big)\,\underset{\rightarrow}{\nabla}\,\Big(\underset{\rightarrow}{\nabla}\cdot\underset{\rightarrow}{\vartheta}\Big) + \underset{\rightarrow}{m}^{\,V} - \imath^{\,V}\,\underset{\rightarrow}{\ddot{\vartheta}} = -\,4\,\kappa\,\Big(\underset{\rightarrow}{\theta} - \underset{\rightarrow}{\vartheta}\Big) & \end{aligned} \tag{A.25}$$

where note that for any scalar z:

$$\underset{\leftrightarrow}{\nabla}^{\times}\cdot\underset{\rightarrow}{\nabla} z = \underset{\rightarrow}{0} \tag{A.26}$$

A.6 Internal energy

In the linear micropolar elasticity theory the strain energy density $\mathcal{U}_{\mathrm{e}}^{\,V}$ is expressed as:

$$2\,\mathcal{U}_{\mathrm{e}}^{\,V} = \sigma_{ij}\,\varepsilon_{ij} + \chi_{ij}\,\tau_{ij} \tag{A.27}$$

By decomposing the force stress, couple stress, strain, and twist tensors into their symmetric and antisymmetric parts this expression can be rewritten as:

$$2\mathcal{U}_{\mathrm{e}}^{V} = \sigma_{ij}^{\mathrm{s}}\,\varepsilon_{ij}^{\mathrm{s}} + \sigma_{ij}^{\mathrm{a}}\,\varepsilon_{ij}^{\mathrm{a}} + \chi_{ij}^{\mathrm{s}}\,\tau_{ij}^{\mathrm{s}} + \chi_{ij}^{\mathrm{a}}\,\tau_{ij}^{\mathrm{a}} \tag{A.28}$$

Correspondingly substitutions from the constitutive relations in Eqs. (A.14) and (A.16) into Eqs. (A.27) and (A.28) result in the following strain energy density expressions:

$$\begin{aligned} 2\mathcal{U}_{\mathrm{e}}^{V} = &\Big(\mu+\kappa\Big)\,\varepsilon_{ij}\,\varepsilon_{ij} + \Big(\mu-\kappa\Big)\,\varepsilon_{ji}\,\varepsilon_{ij} + \lambda\,\varepsilon_{ii}\,\varepsilon_{jj} \\ &+ \Big(\gamma+\beta\Big)\,\tau_{ij}\,\tau_{ij} + \Big(\gamma-\beta\Big)\,\tau_{ji}\,\tau_{ij} + \alpha\,\tau_{ii}\,\tau_{jj} \end{aligned} \tag{A.29}$$

and:

$$\begin{aligned} 2\mathcal{U}_{\mathrm{e}}^{V} = &\,2\,\mu\varepsilon_{ij}^{\mathrm{s}}\,\varepsilon_{ij}^{\mathrm{s}} + \lambda\,\varepsilon_{ii}\,\varepsilon_{jj} + 2\,\kappa\varepsilon_{ij}^{\mathrm{a}}\,\varepsilon_{ij}^{\mathrm{a}} \\ &+ 2\,\gamma\,\tau_{ij}^{\mathrm{s}}\,\tau_{ij}^{\mathrm{s}} + \alpha\,\tau_{ii}\,\tau_{jj} + 2\,\beta\tau_{ij}^{\mathrm{a}}\,\tau_{ij}^{\mathrm{a}} \end{aligned} \tag{A.30}$$

The fact that the strain energy density expression should have a positive definite quadratic form imposes the following restrictions on the material elastic constants [42]:

$$\begin{aligned} &\mu > 0, \qquad \kappa > 0, \qquad 2\,\mu + 3\,\lambda > 0 \\ &\gamma > 0, \qquad \beta > 0, \qquad 2\,\gamma + 3\,\alpha > 0 \end{aligned} \tag{A.31}$$

Note that from a purely physical point of view the strain energy is only non-negative (not necessarily positive) and, allowing for the possibility of $\mathcal{U}_{\mathrm{e}}^{V} = 0$, the restrictions given in Eq. (A.31) can weaken to [73, 74]:

$$\begin{aligned} &\mu \geq 0, \qquad \kappa \geq 0, \qquad 2\,\mu + 3\,\lambda \geq 0 \\ &\gamma \geq 0, \qquad \beta \geq 0, \qquad 2\,\gamma + 3\,\alpha \geq 0 \end{aligned} \tag{A.32}$$

The conditions given in Eq. (A.31) are also invoked to prove the uniqueness of the solution in a static micropolar elasticity problem [74].

A.7 Experimental investigations

In the context of micropolar elasticity, a great deal of effort has been put into determining the micropolar properties of materials which can be understood via micropolar elasticity,

e.g. composite materials, cellular solids, and biological materials [54, 71, 75–78]. Most of such effort is experimental in nature and is founded on the method of "size effects" [71, 72, 78–82]. In the method of size effects the analytic solutions obtained for simple 3D micropolar boundary value problems are investigated against the experimental results for specimens with different sizes to determine the micropolar parameters. Note that the size effects, expressing that small samples behave more stiffly than would be expected classically, are taken into account by the micropolar theory of elasticity in a natural way. These effects are attracting attention in conjunction with micro and nano devices [73].

The classical and micropolar properties measured experimentally for a few materials (*i.e.* human bone and three foams) are given in Table A.1 [72, 81]. It is noteworthy that in the literature on micropolar elastic constants the results are frequently illustrated in terms of the shear modulus, strain Poisson's ratio, Young's modulus, and the following technical constants [81]:

$$\begin{aligned} &\text{polar ratio:} && \Psi = \frac{2\,\gamma}{2\,\gamma + \alpha} \\ &\text{characteristic length for torsion:} && \ell_t^2 = \frac{\gamma}{\mu} \\ &\text{characteristic length for bending:} && \ell_b^2 = \frac{\gamma + \beta}{4\,\mu} \\ &\text{coupling number:} && N^2 = \frac{\kappa}{\mu + \kappa} \end{aligned} \tag{A.33}$$

However, in Table A.1 they are translated into the more fundamental elastic constants appearing in the constitutive relations given in Eq. (A.14) and the supplementary elastic constants defined by Eqs. (A.17)–(A.19). This translation is done using the following relations (the shear modulus, strain Poisson's ratio, and Young's modulus are retained):

$$\begin{aligned} &\lambda = \frac{2\,\nu}{1 - 2\,\nu}\,\mu, && \kappa = \frac{N^2}{1 - N^2}\,\mu, && B = \lambda + \frac{2}{3}\,\mu \\ &\gamma = \ell_t^2\,\mu, && \beta = 4\,\ell_b^2\,\mu - \gamma, && \alpha = 2\left(\frac{1}{\Psi} - 1\right)\gamma \\ &\xi = \frac{\alpha}{2\left(\gamma + \alpha\right)}, && \mathcal{E} = 2\left(1 + \xi\right)\gamma, && \mathcal{B} = \alpha + \frac{2}{3}\,\gamma \end{aligned} \tag{A.34}$$

Table A.1: Classical and micropolar properties of some materials [72, 81].

Property Group/Name	**Material**			
	Human Bone	Polystyrene Foam	Polyurethane Foam	Syntactic Foam
Classical/				
Lamé Shear Modulus μ (MPa)	4000	0.6	104	1033
Strain Poisson's Ratio ν	†	0.07	0.44	0.34
Lamé Coefficient λ (MPa)	‡	0.1	763	2195
Tensile Modulus E (MPa)	12 000	1.3	300	2758
Tensile Bulk Modulus B (MPa)	‡	0.5	832	2884
Mass Density ρ^V (kg/m^3)	2000	37	340	585
Micropolar/				
Cosserat Couple Modulus κ (MPa)	4000	0.06	4.33	115
Cosserat Twist Coefficient γ (N)	194	8.66	40.0	4.36
Cosserat Twist Coefficient β (N)	3046	51.3	5.30	−0.13
Cosserat Twist Coefficient α (N)	−129	−5.77	−26.7	−2.91
Twist Poisson's Ratio ξ	−1	−1	−1	−1
Tortile Modulus $\mathcal{E}$ (N)	0	0	0	0
Tortile Bulk Modulus $\mathcal{B}$ (N)	0	0	0	0
Microinertia Density $\imath^V$ (kg/m)	†	†	†	†

†: Not reported in the reference. ‡: Not calculable.

A.8 Discrepancies

Through its development, the micropolar elasticity theory has been represented using different notations; one has to be very careful about the symbols used by different authors to denote the material elastic constants. It is not too much to say "as often the case, notation is a nightmare" [83]. Cowin, for example, compared the notations used by some authors [84]. A similar comparison containing the equivalent notation used in the present text can be found in Table A.2. In this table, the reader's attention is directed to the different representations of the material elastic constants.

Eringen is known as one of the main developers of the Cosserat (micropolar) theory of elasticity and the person from whom the name "Micropolar Elasticity" has originated. His derivation of the linear theory of micropolar elasticity [85] is probably one of the most cited works in the field of linear micropolar elasticity. Therefore, it is not a surprise that Eringen's notation, summarized in Table A.2, is also the most popular one used by other authors on micropolar elasticity.

Despite its popularity, Eringen's notation, especially his representation of the micropolar elastic constants, is not the best one. In effect, it is a misleading notation as it may result in mistaking Eringen's symbol μ for the classical Lamé coefficient (shear modulus) often denoted as μ in the classical theory of elasticity. Actually, this is a common mistake appearing in many papers that follow Eringen's notation; a mistake which gives rise to erroneous conclusions (to be addressed later in this text). The difference between Eringen's symbol μ and the Lamé coefficient μ which can be understood from a study of Eringen's preliminary work on linear micropolar elasticity [85] is clarified in Table A.2.

The first erroneous conclusion following Eringen's notation appears in his own preliminary work on the derivation of the linear micropolar elasticity [85]. As mentioned by Cowin [86], mistaking his symbol μ for the Lamé shear modulus, Eringen has deduced an incorrect thermodynamic inequality in [85]. This incorrect inequality further misled some other authors to incorrectly compare the couple-stress theory and the micropolar elasticity theory as two independent theories (without realizing that the couple-stress theory is a special case of the micropolar elasticity theory) and also to wrongly remark that the couple-stress theory contradicts thermodynamic restrictions [86].

Table A.2: Comparison of notations used for representation of micropolar elasticity [84].

Notation Group/Description	**Representative Symbol Used by**				
	Present Author	Nowacki [42]	Eringen [85]	Cowin [84]	Neff [73]
Kinematics and Kinetics/					
Displacement Vector	u_i	u_i	u_i	u_i	u
Microrotation Vector	ϑ_i	φ_i	φ_i	$\hat{\psi}_i$	ϕ
Macrorotation Vector	θ_i	$\frac{1}{2}\,\epsilon_{ijk}\,u_{k,j}$ †	r_i	$-\,\hat{\omega}_i$	$\frac{1}{2}\,\mathrm{curl}\,u$ †
Strain Tensor	ε_{ij}	γ_{ij}	ϵ_{ji} ‡	$\varepsilon_{ij}+\gamma_{ij}$ †	$\bar{\varepsilon}$
Force Stress Tensor	σ_{ij}	σ_{ij}	t_{ij}	$\tau_{ij}+\sigma_{ij}$ †	σ
Twist Tensor	τ_{ij}	$\varkappa_{ij}$	$\varphi_{j,i}$	$\hat{\kappa}_{ij}$	$\nabla\phi$
Couple Stress Tensor	χ_{ij}	μ_{ij}	m_{ij}	$\hat{\mu}_{ij}$	m
Elastic Constants/					
Lamé Shear Modulus	μ	μ	$\mu+\frac{1}{2}\,\kappa$	μ	μ
Lamé Coefficient	λ	λ	λ	λ	λ
Cosserat Couple Modulus	κ	α	$\frac{1}{2}\,\kappa$	τ	μ_c
Cosserat Twist Coefficient	γ	γ	$\frac{1}{2}\,(\gamma+\beta)$	$\eta+\eta'$	$\frac{1}{2}\,(\gamma+\beta)$
Cosserat Twist Coefficient	β	ε	$\frac{1}{2}\,(\gamma-\beta)$	$\eta-\eta'$	$\frac{1}{2}\,(\gamma-\beta)$
Cosserat Twist Coefficient	α	β	α	$\frac{1}{2}\,\alpha$	α

†: No explicit symbol assigned. ‡: Note that subscript is ji and not ij.

To facilitate addressing the problems related to Eringen's notation, from now on, Eringen's symbols representing the elastic constants will be shown with a subscript E. Cowin [86] has shown that the Lamé shear modulus μ and the micropolar couple modulus κ are related to Eringen's symbols μ_{E} and κ_{E} according to:

$$\mu = \mu_{\text{E}} + \frac{1}{2}\,\kappa_{\text{E}}, \qquad \kappa = \frac{1}{2}\,\kappa_{\text{E}} \tag{A.35}$$

He also has shown that the incorrect inequalities presented by Eringen as [85]:

$$\mu_{\text{E}} \geq 0, \qquad \kappa_{\text{E}} \geq 0$$

should be replaced with the following correct inequalities [86]:

$$\mu = \mu_{\text{E}} + \frac{1}{2}\,\kappa_{\text{E}} \geq 0, \qquad \kappa = \frac{1}{2}\,\kappa_{\text{E}} \geq 0 \tag{A.36}$$

Whereas Eringen's incorrect inequality has been replaced by the correct form as early as its discovery by Cowin, the usage of Eringen's notation, leading to this mistake, continued in other works on micropolar elasticity. Unsurprisingly, erroneous statements regarding the micropolar theory of elasticity continued to be addressed. In fact, to the best of this author's knowledge, no one has paid attention to the origin of the incorrect inequality, and the confusing nature of Eringen's notation has not been discussed.

The relationship between the Lamé shear modulus μ and Eringen's symbols μ_{E} and κ_{E} as given by Eq. (A.35) has deceived authors using Eringen's notation to think of the classical theory of elasticity as a special case of micropolar elasticity when Eringen's elastic constant κ_{E} tends to zero. This conclusion, however, is incorrect and results in (physical) difficulties [87] and singularities which will be mentioned later in the present text.

Additionally, in Eringen's notation the classical Lamé shear modulus μ is dependent on both μ_{E} and κ_{E} as given by Eq. (A.35). Therefore, by varying κ_{E} both classical and micropolar elastic properties are being changed simultaneously. This dependency of the classical Lamé shear modulus μ on the symbol κ_{E} which is included to represent the micropolar effects is equivalent to a dependency of the classical parameters on the micropolar elastic constants which is not correct. In other words, a comparison between an elastic body with nonzero κ_{E} and an elastic body where κ_{E} is set to zero cannot reveal the

micropolar effects in the latter as the two elastic bodies are also different in terms of their classical properties. This coupling between the classical and micropolar elastic constants in Eringen's notation causes a similar problem when one is comparing the micropolar theory of elasticity with the couple-stress theory (of elasticity) by varying κ_{E} or more precisely letting κ_{E} go to infinity. Note that the couple-stress theory is known to be a special case of micropolar elasticity when κ_{E} tends to infinity.

In this regard notations utilizing single symbols for the classical Lamé parameters and representing the extra micropolar elastic constants with completely separate (uncoupled) symbols, such as the one used by Nowacki [42] as summarized in Table A.2, are superior choices to characterize the elastic properties of a micropolar material. The notation used in the present text is inspired by Nowacki's notation (see Table A.2). However, relating their notations with Eringen's symbols, even authors using more appropriate notations (with uncoupled classical and micropolar elastic constants) have been also misled to repeat the incorrect statement that the classical elasticity is a special case of the micropolar elasticity when the micropolar couple modulus κ is zero.

Indeed, making a literature survey, three groups of authors presenting flawed statements on micropolar elasticity can be identified:

- Authors who used Eringen's notation and did not realize the difference between Eringen's usage of the symbol μ_{E} and the conventional Lamé shear modulus μ. It is not a surprise to see mistaken conclusions in the works by these authors [54, 57, 59, 61, 71, 75, 82, 88].

- Authors who, while using the Eringen's notation, realized the difference between Eringen's usage of the symbol μ_{E} and the conventional Lamé parameter μ. These authors were probably misled by the improper notation towards incorrect statements in their works [49, 60].

- Authors who used a different notation than Eringen's. Unexpectedly, these authors repeated the erroneous declarations of authors using Eringen's notation in their works [73, 74, 84, 86, 89–91].

Also, in general there are six erroneous declarations or conclusions which have been frequently addressed by the authors on micropolar elasticity. They are as follows:

1. The symbol μ_{E} in Eringen's notation represents the Lamé shear modulus and is therefore necessarily a positive number [54, 57, 61, 71, 75, 82, 88].

2. Corresponding to Young's modulus, Poisson's ratio, and the shear modulus of classical elasticity, in micropolar elasticity one can define a micropolar Young's modulus, micropolar Poisson's ratio, and micropolar shear modulus as three unique elastic constants of a micropolar material [54, 57, 59, 61, 71, 75, 78]. These micropolar constants will be equal to the corresponding classical constants in the limit as κ_{E} tends to zero.

3. Classical elasticity as a special case of micropolar elasticity can be obtained from micropolar elasticity by letting κ_{E} (and other micropolar elastic constants) go to zero [49, 54, 55, 57, 59–61, 71–75, 78, 80–83, 87, 89–93]. This is equivalent to mentioning that the micropolar couple modulus κ or the coupling number N^2 (defined by the last relation of Eq. (A.33)) should vanish to recover the classical theory of elasticity. Note that using Eringen's notation the coupling number is defined as $N^2 = \dfrac{\kappa_{\mathrm{E}}}{2(\mu_{\mathrm{E}} + \kappa_{\mathrm{E}})}$.

4. In reality the value of κ_{E} (or κ) is very small compared to μ_{E} (or μ) for any elastic continuum and one can use the assumption that $\kappa_{\mathrm{E}} \ll 1$ or $\dfrac{\kappa_{\mathrm{E}}}{\mu_{\mathrm{E}}} \ll 1$ ($\kappa \ll 1$ or $\dfrac{\kappa}{\mu} \ll 1$) when solving a micropolar elasticity problem [55, 61, 75, 93]. In other words, a very small value for κ_{E} (or κ) is expected from experimental investigation of any real elastic material.

5. Couple-stress theory is recovered from micropolar elasticity as just κ_{E} goes to infinity (not mentioning that at the same time $\mu_{\mathrm{E}} + \frac{1}{2}\kappa_{\mathrm{E}}$ should remain limited and equal to the Lamé shear modulus) [72, 81].

6. Classical elasticity and couple-stress theory are two different (independent) special cases of micropolar elasticity where $N^2 = 0$ ($\kappa_{\mathrm{E}} \to 0$ or $\kappa \to 0$) and $N^2 = 1$ ($\kappa_{\mathrm{E}} \to \infty$ or $\kappa \to \infty$), respectively [71–73, 78, 80, 81, 83, 84, 86, 87, 89–91]. This implies that the classical elasticity theory and the couple-stress theory are two separate and

independent simplifications of the micropolar stress theory as shown in Figure A.1. In other words, it covers the fact that the micropolar elasticity theory, the couple-stress theory, and the classical elasticity theory can be arranged into a linear hierarchy structure like the one depicted in Figure A.2.

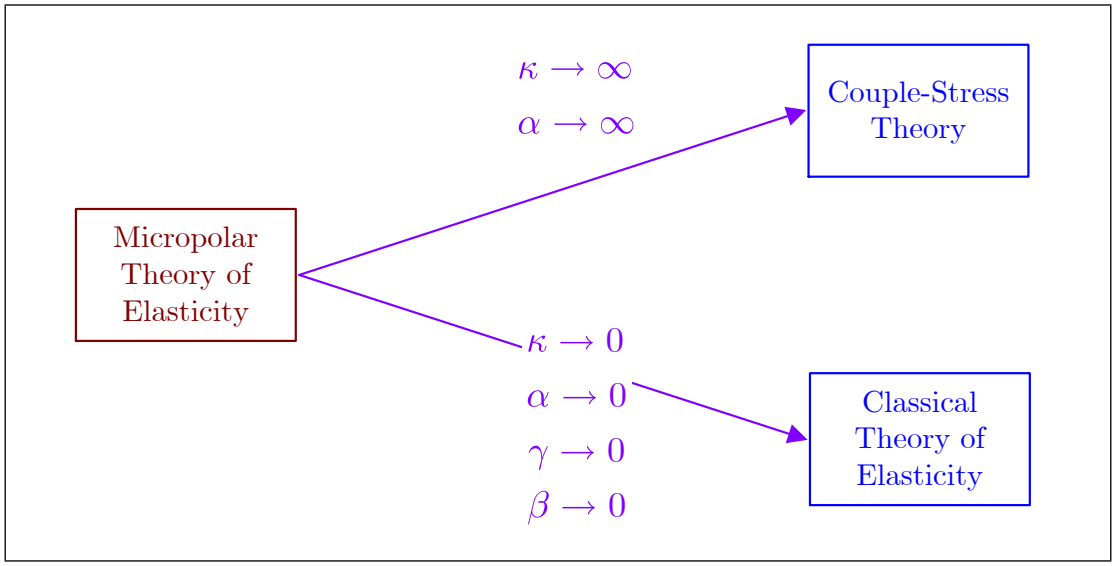

Figure A.1: The incorrect parallel structure for simplification of the micropolar theory of elasticity to the couple-stress theory and the classical theory of elasticity.

Considering these incorrect statements one can conclude that the main problem is how to simplify the micropolar elasticity model to recover the couple-stress theory and the classical elasticity theory as two special cases. In particular, recovering the classical theory of elasticity by letting κ_{E} or κ (and other micropolar elastic constants) go to zero is wrong and results in (physical) difficulties [87] and singularities. Here, one should note that Eringen's elastic constant κ_{E} (or the micropolar couple modulus κ) determines the strength of coupling between the displacement and local rotation fields [78]. Though, simplifying the micropolar elasticity for the case $\kappa_{\mathrm{E}} = 0$ (or $\kappa = 0$) is more straightforward, this corresponds to a decoupling of the rotational and translational DOFs [72]. Therefore, a micropolar elasticity model with $\kappa_{\mathrm{E}} = 0$ (or $\kappa = 0$) corresponds to an elastic continuum in

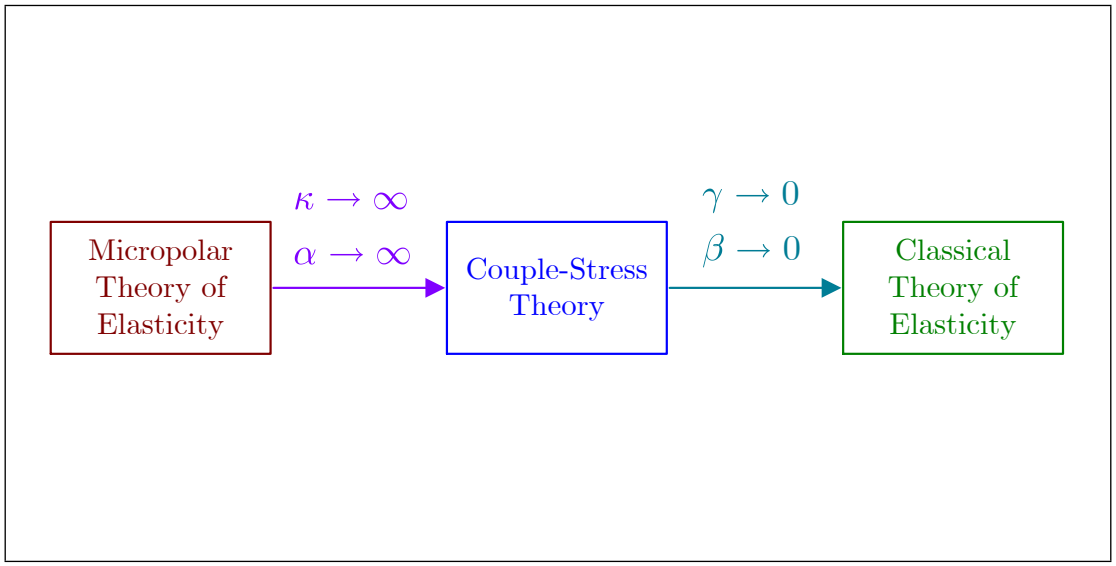

Figure A.2: The correct sequential structure for simplification of the micropolar theory of elasticity to the couple-stress theory and the classical theory of elasticity.

which the constitutive particles or cells are free to rotate and indeed in the presence of a volume moment rotate infinitely (a singularity occurs in the presence of a volume moment). The correct approach for simplifying the micropolar elasticity model will be addressed in the next section. What follows in the next section will clarify why the aforementioned statements are erroneous.

Here it is noteworthy that Neff [73, 74, 83, 90, 91] has addressed another physical inconsistency for the linear micropolar elasticity which is not pursued here. He has shown that, in the linear micropolar elasticity applied to continuous solids, the usually adopted positive definiteness condition for the internal energy results in restrictions on material elastic constants which (based on analytic solutions obtained for micropolar torsion and bending problems) are not enough to avoid (unphysical) unbounded stiffening behavior of very small samples (are not consistent with the physical expectation that small specimens should still have bounded rigidity). However, to the best of this author's knowledge, this is an incorrect conclusion founded on first, the mistaken statement that classical elasticity is recovered from micropolar elasticity as the micropolar couple modulus tends to zero (as

discussed previously), and second, a flawed definition for boundedness of stiffness.

A.9 Simplification

Before addressing the simplification of micropolar elasticity to special cases, *i.e.* couple-stress theory and classical elasticity, it is useful to recall the problem of recovering the Euler-Bernoulli beam equations from the more general Timoshenko beam theory. Whereas in the very beginning it was suggested that this can be done by setting the shear modulus in the Timoshenko equations equal to zero, nowadays it is well-known that this causes a singularity and a more sensible solution is to recover the Euler-Bernoulli equations in the limit as the shear modulus goes to infinity. In fact, a more detailed study of the Timoshenko beam theory reveals that Euler-Bernoulli beam equations can be recovered by taking any of the following four different points of view:

Kinematic: by neglecting the shear strains,

Kinetic: by neglecting the shear stresses,

Geometric: by letting the beam slenderness ratio go to infinity (*i.e.* considering a very thin long beam),

Mathematical: (as the most general and interesting approach) by letting the material shear modulus tend to infinity.

Analogously, one can simplify the micropolar theory of elasticity to couple-stress theory and then from couple-stress theory to classical theory of elasticity by taking a kinematic, kinetic, geometric, or mathematical point of view:

Kinematic: one can assume that the body motion is constrained such that the antisymmetric part of the strain tensor is negligible and consequently the microrotation field is identical with the macrorotation field (resulting in only three DOFs for any body particle). This implies a symmetric force stress tensor and simplifies the (asymmetric) micropolar elasticity theory to the (symmetric) couple-stress theory. Further,

by considering small deformations and neglecting the higher order differentials of displacement field one will be left with the (symmetric) classical elasticity theory.

Kinetic: it can be assumed that the loads applied on the body are constrained to result in a symmetric force stress tensor (the antisymmetric part is insignificant). This entails a symmetric strain tensor and again reduces the (asymmetric) micropolar elasticity theory to the (symmetric) couple-stress theory. Then, the (symmetric) classical elasticity can be recovered by ignoring the effects of couple stresses.

Geometric: while it is not clear yet how one can reduce the micropolar elasticity theory to the couple-stress theory, it is known that results of both micropolar elasticity and couple-stress theory merge to the classical elasticity results in the limit when the elastic body dimensions are order of magnitudes larger than (potentially definable and probably problem-specific) material characteristic length(s) (which are physically expected to be of the order of cell or grain size).

Mathematical: by letting the micropolar couple modulus κ go to infinity one can constrain the strain tensor without adding any restriction on the force stress tensor [73, 86, 89–91]. More specifically, as the micropolar couple modulus tends to infinity the strain tensor is constrained to be symmetric while the force stress tensor can maintain its generality as an asymmetric tensor. This condition will imply coupling between the displacement and microrotation fields and reduce the (asymmetric) micropolar elasticity to (asymmetric) couple-stress theory. To keep the generality of the loading mechanism inside the body it is also essential to set the micropolar twist coefficient α equal to infinity (to be shown later) [89]. By setting the remaining two micropolar twist coefficients γ and β equal to zero, one can recover the (asymmetric) classical elasticity as a special case of (asymmetric) couple-stress theory [94].

Since it has been frequently addressed in an erroneous way (see the references cited in the aforementioned list of erroneous statements) and also due to its generality and interesting nature, the mathematical approach will be studied in more detail in the following.

Consider a general homogeneous, isotropic, and centrally symmetric elastic body under the action of (finite) body volume force $\underset{\rightarrow}{f}^{V}$ and moment $\underset{\rightarrow}{m}^{V}$. For such a body, utilizing

the linear micropolar theory of elasticity results in the relations and definitions given by Eqs. (A.1)–(A.32).

Now taking into account the constitutive relations, especially the first relation given in Eq. (A.15), and letting the micropolar couple modulus κ tend to infinity while noting that the force stress tensor $\underset{\leftrightarrow}{\sigma}$ should remain finite, one can conclude that the antisymmetric strain tensor $\underset{\leftrightarrow}{\varepsilon}^{\mathrm{a}}$ should vanish:

$$\begin{aligned} \varepsilon^{\mathrm{a}}_{ij} &= \epsilon_{ijk}\left(\theta_k - \vartheta_k\right) = 0 \\ \vartheta_i &= \theta_i = \frac{1}{2}\,\epsilon_{ijk}\,u_{k,j} \end{aligned} \tag{A.37}$$

Consequently, the kinematic relations given by Eqs. (A.1)–(A.5) can be simplified to:

$$\begin{aligned} \varepsilon_{ij} &= \varepsilon^{\mathrm{s}}_{ij} + \varepsilon^{\mathrm{a}}_{ij} = \frac{1}{2}\left(u_{j,i} + u_{i,j}\right) \\ \varepsilon^{\mathrm{s}}_{ij} &= \frac{1}{2}\left(u_{j,i} + u_{i,j}\right) \\ \varepsilon^{\mathrm{a}}_{ij} &= 0 \\ \tau_{ij} &= \tau^{\mathrm{s}}_{ij} + \tau^{\mathrm{a}}_{ij} = \frac{1}{2}\,\epsilon_{jkl}\,u_{l,ki} \\ \tau^{\mathrm{s}}_{ij} &= \frac{1}{4}\,\epsilon_{jkl}\,u_{l,ki} + \frac{1}{4}\,\epsilon_{ikl}\,u_{l,kj} \\ \tau^{\mathrm{a}}_{ij} &= \frac{1}{4}\,\epsilon_{jkl}\,u_{l,ki} - \frac{1}{4}\,\epsilon_{ikl}\,u_{l,kj} \\ \tau_{ii} &= 0 \end{aligned} \tag{A.38}$$

Also, the compatibility conditions given by Eq. (A.7) can be modified to the following form:

$$\begin{aligned} &\epsilon_{ikl}\left(\varepsilon_{kj,l} + \epsilon_{kjm}\,\tau_{lm}\right) = 0 \\ &\epsilon_{ikl}\,\tau_{kj,l} = 0 \\ &\epsilon_{ijk}\,\varepsilon_{jk} = 0 \end{aligned} \tag{A.39}$$

or equivalently:

$$\begin{aligned} &\epsilon_{ikm}\,\epsilon_{jln}\,\varepsilon_{ij,kl} = 0 \\ &\epsilon_{ikl}\,\tau_{kj,l} = 0 \\ &\tau_{ii} = 0 \end{aligned} \tag{A.40}$$

For such a case (*i.e.* when $\kappa \to \infty$ and thus $\varepsilon^{\mathrm{a}}_{ij} = 0$ and $\tau_{ii} = 0$), the constitutive relations given by Eq. (A.16) take the form:

$$\begin{aligned}
\sigma^{\mathrm{s}}_{ij} &= 2\,\mu\,\varepsilon_{ij} + \lambda\,\varepsilon_{kk}\,\mathbb{1}_{ij} \\
\sigma^{\mathrm{a}}_{ij} &= \infty \times 0 = ¿ \\
\chi^{\mathrm{s}}_{ij} &= 2\,\gamma\,\tau^{\mathrm{s}}_{ij} \\
\chi^{\mathrm{a}}_{ij} &= 2\,\beta\,\tau^{\mathrm{a}}_{ij}
\end{aligned}$$

where ¿ is a symbol that represents a numerical quantity whose magnitude cannot be determined (an indeterminate quantity). However, as $\tau_{ii} = 0$ this form impose an unnecessary constraint on couple stress tensor, that is:

$$\chi_{ii} = 0$$

To remove this constraint it can be assumed that in the constitutive relations given by Eq. (A.16) (in addition to the micropolar couple modulus κ) the micropolar twist coefficient α also goes to infinity. Using the second relation of Eq. (A.17), this assumption gives rise to the following form for the constitutive relations in Eq. (A.16):

$$\begin{aligned}
\sigma^{\mathrm{s}}_{ij} &= 2\,\mu\,\varepsilon_{ij} + \lambda\,\varepsilon_{kk}\,\mathbb{1}_{ij} \\
\sigma^{\mathrm{a}}_{ij} &= \infty \times 0 = ¿ \\
\chi_{ii} &= \infty \times 0 = ¿ \\
\chi^{\mathrm{s}}_{ij} - \frac{1}{3}\,\chi_{kk}\,\mathbb{1}_{ij} &= 2\,\gamma\,\tau^{\mathrm{s}}_{ij} \\
\chi^{\mathrm{a}}_{ij} &= 2\,\beta\,\tau^{\mathrm{a}}_{ij}
\end{aligned} \tag{A.41}$$

or equivalently:

$$\begin{aligned}
\sigma_{ij} - \sigma^{\mathrm{a}}_{ij} &= 2\,\mu\,\varepsilon_{ij} + \lambda\,\varepsilon_{kk}\,\mathbb{1}_{ij} \\
\chi_{ij} - \frac{1}{3}\,\chi_{kk}\,\mathbb{1}_{ij} &= \Big(\gamma + \beta\Big)\tau_{ij} + \Big(\gamma - \beta\Big)\tau_{ij} \\
\sigma^{\mathrm{a}}_{ij} &= \infty \times 0 = ¿ \\
\chi_{ii} &= \infty \times 0 = ¿
\end{aligned} \tag{A.42}$$

It is worthwhile to note here that the indeterminacy of the asymmetric force stress tensor $\underset{\leftrightarrow}{\sigma}^{\mathrm{a}}$ and the summation of normal couple stresses χ_{ii} means they cannot be obtained from

the constitutive relations and (if possible) one should use the kinetic balance relations to determine them.

Whereas the tensile bulk modulus B, strain Poisson's ratio ν, and tensile modulus E defined in Eqs. (A.17) and (A.18) remain unchanged as κ and α tend to infinity, by letting α in Eqs. (A.17) and (A.19) go to infinity one can derive the tortile bulk modulus $\mathcal{B}$, twist Poisson's ratio ξ, and tortile modulus $\mathcal{E}$ which correspond to the current case, that is:

$$\begin{aligned} B &= \lambda + \frac{2}{3}\,\mu \\ \nu &= \frac{\lambda}{2\left(\mu+\lambda\right)} \\ E &= \frac{\mu\left(2\,\mu+3\,\lambda\right)}{\mu+\lambda} = 2\,\mu\left(1+\nu\right) \\ \mathcal{B} &= \infty \\ \xi &= \frac{1}{2} \\ \mathcal{E} &= 3\,\gamma \end{aligned} \tag{A.43}$$

By letting κ and α go to infinity, however, the kinetic relations will remain unchanged as no restriction is imposed on the force and couple stress tensors and, therefore, one can repeat, for example, the equilibrium relations given by Eq. (A.8):

$$\begin{aligned} \sigma_{ji,j} + f_i^{V} &= \rho^{V}\,\ddot{u}_i \\ \chi_{ji,j} + \epsilon_{ijk}\,\sigma_{jk} + m_i^{V} &= \imath^{V}\,\epsilon_{ijk}\,\ddot{u}_{k,j} \end{aligned} \tag{A.44}$$

or more properly the equilibrium relations in Eq. (A.13):

$$\begin{aligned} \sigma^{\mathrm{s}}_{ji,j} + \frac{1}{2}\,\epsilon_{ijk}\left(\chi_{lk,lj} + m^{V}_{k\,,j} - \imath^{V}\,\epsilon_{klm}\,\ddot{u}_{m,lj}\right) + f_i^{V} &= \rho^{V}\,\ddot{u}_i \\ \epsilon_{ijk}\left(\chi_{lk,l} + m^{V}_{k} - \imath^{V}\,\epsilon_{klm}\,\ddot{u}_{m,l}\right) &= 2\,\sigma^{\mathrm{a}}_{ji} \end{aligned} \tag{A.45}$$

Substitution from the constitutive relations of Eq. (A.42) into the balance relations given by Eq. (A.45) (or revision of the motion equations in Eq. (A.22) for the case when

$\kappa \to \infty$ and $\alpha \to \infty$) results in the corresponding equations of motion:

$$\begin{aligned} \mu\, u_{i,jj} + \Big(\mu + \lambda\Big)\, u_{j,ji} + \frac{1}{4}\,\epsilon_{ijk}\,\Big(\Big(\gamma + \beta\Big)\,\epsilon_{klm}\, u_{m,lnnj} + 2\, m^{V}_{k\,,j} - \imath^{V}\,\epsilon_{klm}\,\ddot{u}_{m,lj}\Big) \\ + f^{V}_{i} = \rho^{V}\,\ddot{u}_{i} \qquad \text{(A.46)} \\ 2\,\sigma^{\mathrm{a}}_{ji} - \frac{1}{3}\,\epsilon_{ijk}\,\chi_{ll,k} = \frac{1}{2}\,\epsilon_{ijk}\,\Big(\Big(\gamma + \beta\Big)\,\epsilon_{klm}\, u_{m,lnn} + 2\, m^{V}_{k} - \imath^{V}\,\epsilon_{klm}\,\ddot{u}_{m,l}\Big) \end{aligned}$$

Here the first relation of Eq. (A.46) corresponds to a set of three PDEs, enough for determination of the displacement field vector. However, the second relation of Eq. (A.46) also corresponding to a set of three PDEs does not provide enough information to compute the undetermined parts of the force and couple stress tensors, *i.e.* $\underset{\leftrightarrow}{\varrho}^{\mathrm{a}}$ and χ_{ii}, from a known displacement field vector. Indeed, there are only three equations that should be used to determine four unknowns (three elements of $\underset{\leftrightarrow}{\varrho}^{\mathrm{a}}$ and the scalar χ_{ii}).

Finally when $\kappa \to \infty$ and $\alpha \to \infty$, the strain energy density $\mathcal{U}^{V}_{\mathrm{e}}$ can be written as (compare this to Eqs. (A.27) and (A.28) given previously for a general micropolar case):

$$\begin{aligned} 2\,\mathcal{U}^{V}_{\mathrm{e}} &= \Big(\sigma_{ij} - \sigma^{\mathrm{a}}_{ij}\Big)\,\varepsilon_{ij} + \Big(\chi_{ij} - \frac{1}{3}\,\chi_{kk}\,\mathbb{1}_{ij}\Big)\,\tau_{ij} \\ &= \sigma^{\mathrm{s}}_{ij}\,\varepsilon_{ij} + \Big(\chi^{\mathrm{s}}_{ij} - \frac{1}{3}\,\chi_{kk}\,\mathbb{1}_{ij}\Big)\,\tau^{\mathrm{s}}_{ij} + \chi^{\mathrm{a}}_{ij}\,\tau^{\mathrm{a}}_{ij} \end{aligned} \qquad \text{(A.47)}$$

Now substituting from Eq. (A.41) or (A.42) into Eq. (A.47) results in the following expression for strain energy density $\mathcal{U}^{V}_{\mathrm{e}}$ (in comparison with Eq. (A.29) or (A.30)):

$$\begin{aligned} 2\,\mathcal{U}^{V}_{\mathrm{e}} &= 2\,\mu\varepsilon_{ij}\,\varepsilon_{ij} + \lambda\,\varepsilon_{ii}\,\varepsilon_{jj} + \Big(\gamma + \beta\Big)\,\tau_{ij}\,\tau_{ij} + \Big(\gamma - \beta\Big)\,\tau_{ji}\,\tau_{ij} \\ &= 2\,\mu\varepsilon_{ij}\,\varepsilon_{ij} + \lambda\,\varepsilon_{ii}\,\varepsilon_{jj} + 2\,\gamma\,\tau^{\mathrm{s}}_{ij}\,\tau^{\mathrm{s}}_{ij} + 2\,\beta\tau^{\mathrm{a}}_{ij}\,\tau^{\mathrm{a}}_{ij} \end{aligned} \qquad \text{(A.48)}$$

which have a positive definite form provided (compared to the conditions in Eq. (A.31)):

$$\begin{aligned} &\mu > 0, \qquad 2\,\mu + 3\,\lambda > 0 \\ &\gamma > 0, \qquad \beta > 0 \end{aligned} \qquad \text{(A.49)}$$

The relations given by Eqs. (A.37)–(A.49) (especially after ignoring the terms containing the material microinertia density $\imath^{V}$) are known as the relations of the indeterminate couple-stress theory [43] (since, as mentioned previously, the number of equations in

Eq. (A.46) are not enough for complete determination of engaged unknowns, the couple-stress theory is also called the indeterminate couple-stress theory).

To sum up, one can conclude that the couple-stress theory with four material elastic constants μ, λ, γ, and β is a special case of the more general micropolar theory of elasticity requiring six material elastic constants μ, κ, λ, γ, β, and α which can be obtained mathematically as $\kappa \to \infty$ and $\alpha \to \infty$ (it is also usual to neglect the microinertia effects by assuming $\imath^V \to 0$).

Taking another step by letting the micropolar twist coefficients γ and β and the microinertia density $\imath^V$ go to zero, the couple-stress theory relations, *i.e.* Eqs. (A.37)–(A.49), will further simplify to a set of relations in which the effects of the couple stresses are almost negligible. For such a case the constitutive relations will be:

$$\begin{aligned} \sigma_{ij} - \sigma^{\mathrm{a}}_{ij} &= 2\,\mu\,\varepsilon_{ij} + \lambda\,\varepsilon_{kk}\,\mathbb{1}_{ij} \\ \chi_{ij} - \frac{1}{3}\,\chi_{kk}\,\mathbb{1}_{ij} &= 0 \\ \sigma^{\mathrm{a}}_{ij} &= \text{¿} \\ \chi_{ii} &= \text{¿} \end{aligned}$$

Although one can continue while keeping the indeterminate portion of the couple stress, *i.e.* χ_{ii}, it is more frequent to neglect the couple stresses completely (by assuming $\chi_{ii} \to 0$ or $\alpha \to 0$) and consequently writing the constitutive relations as:

$$\begin{aligned} \sigma_{ij} - \sigma^{\mathrm{a}}_{ij} &= 2\,\mu\,\varepsilon_{ij} + \lambda\,\varepsilon_{kk}\,\mathbb{1}_{ij} \\ \sigma^{\mathrm{a}}_{ij} &= \text{¿} \\ \chi_{ij} &= 0 \end{aligned} \tag{A.50}$$

This implies that there is no need to define the twist tensor and derive the equations related to it. One can accordingly obtain the following set of relations (corresponding to Eqs. (A.37)–(A.49) as the relations of couple-stress theory):

$$\begin{aligned} \varepsilon_{ij} &= \frac{1}{2}\left(u_{j,i} + u_{i,j}\right) \\ \vartheta_i = \theta_i &= \frac{1}{2}\,\epsilon_{ijk}\,u_{k,j} \end{aligned} \tag{A.51}$$

$$\epsilon_{ikm}\,\epsilon_{jln}\,\varepsilon_{ij,kl}=0 \tag{A.52}$$

$$\begin{aligned}\sigma^{\mathrm{s}}_{ij}&=\sigma_{ij}-\sigma^{\mathrm{a}}_{ij}=2\,\mu\,\varepsilon_{ij}+\lambda\,\varepsilon_{kk}\,\mathbb{1}_{ij}\\ \sigma^{\mathrm{a}}_{ij}&=¿\end{aligned} \tag{A.53}$$

$$\begin{aligned}B&=\lambda+\frac{2}{3}\,\mu\\ \nu&=\frac{\lambda}{2\left(\mu+\lambda\right)}\\ E&=\frac{\mu\left(2\,\mu+3\,\lambda\right)}{\mu+\lambda}=2\,\mu\left(1+\nu\right)\end{aligned} \tag{A.54}$$

$$\begin{aligned}\sigma_{ji,j}+f^{V}_{i}&=\rho^{V}\ddot{u}_{i}\\ \epsilon_{ijk}\,\sigma_{jk}+m^{V}_{i}&=0\end{aligned} \tag{A.55}$$

$$\begin{aligned}\sigma^{\mathrm{s}}_{ji,j}+f^{V}_{i}+\frac{1}{2}\,\epsilon_{ijk}\,m^{V}_{k\,,j}&=\rho^{V}\ddot{u}_{i}\\ \epsilon_{ijk}\,m^{V}_{k}&=2\,\sigma^{\mathrm{a}}_{ji}\end{aligned} \tag{A.56}$$

$$\begin{aligned}\mu\,u_{i,jj}+\left(\mu+\lambda\right)u_{j,ji}+\frac{1}{2}\,\epsilon_{ijk}\,m^{V}_{k\,,j}+f^{V}_{i}&=\rho^{V}\,\ddot{u}_{i}\\ 2\,\sigma^{\mathrm{a}}_{ji}&=\epsilon_{ijk}\,m^{V}_{k}\end{aligned} \tag{A.57}$$

$$2\,\mathcal{U}^{V}_{\mathrm{e}}=\left(\sigma_{ij}-\sigma^{\mathrm{a}}_{ij}\right)\varepsilon_{ij}=\sigma^{\mathrm{s}}_{ij}\,\varepsilon_{ij} \tag{A.58}$$

$$2\,\mathcal{U}^{V}_{\mathrm{e}}=2\,\mu\varepsilon_{ij}\,\varepsilon_{ij}+\lambda\,\varepsilon_{ii}\,\varepsilon_{jj} \tag{A.59}$$

$$\mu>0,\qquad 2\,\mu+3\,\lambda>0 \tag{A.60}$$

The set of relations given by Eqs. (A.51)–(A.60) correspond to the asymmetric theory of classical elasticity [38]. Compared to the (well-known) symmetric classical elasticity, in the asymmetric theory of classical elasticity, although the strain tensor is symmetric, the force stress tensor can be asymmetric in the presence of a volume moment distribution.

There is no constitutive relation for the antisymmetric part of the stress tensor (as given by Eq. (A.53)) and the antisymmetric stress tensor is instead determined by the angular momentum balance equation (as given by Eq. (A.56) or (A.57)). Also, the volume moment distribution appears as an equivalent force distribution in the linear momentum balance equation (as in Eq. (A.56) or (A.57)).

Accordingly, one can conclude that the asymmetric classical theory of elasticity with two material elastic constants μ and λ is a special case of the more general couple-stress theory suggesting four material elastic constants μ, λ, γ, and β which can be obtained mathematically as $\gamma \to 0$, $\beta \to 0$, and $\imath^V \to 0$ [94]. Recalling that couple-stress theory is a special case of micropolar theory of elasticity, one can obtain the classical theory of elasticity directly from the micropolar theory of elasticity by letting $\kappa, \alpha \to \infty$ and $\gamma, \beta, \imath^V \to 0$ (or more easily by letting $\kappa \to \infty$ and $\gamma, \beta, \alpha, \imath^V \to 0$). In other words, the couple-stress theory is an intermediate theory derived through the process of recovering the classical elasticity theory from the micropolar elasticity theory (see Figure A.2).

Appendix B

Rotational Kinematics

B.1 Introduction

One of the most fundamental concepts, dealt with in this thesis, is the kinematics of rotating frames and bodies. However, considering the fact that the rotation of a body is usually defined as the rotation of a frame attached to it (known as the body fixed frame), this appendix just addresses the kinematics of rotating frames. As the key parameter in a general rotation problem, the rotation matrix is defined first. Then expressions for angular velocity and virtual rotation vectors in terms of the rotation matrix are derived. Also, the calculus of variations when applied to a general rotation problem is characterized. Finally, the infinitesimal rotation as a special case is considered and approximate formulations corresponding to this case are derived.

B.2 Rotation matrix

The first step for confronting rotational kinematics is to describe the rotation (or orientation) of a frame as an elementary concept. For a rotating frame $\mathcal{F}_b$, its orientation with respect to a fixed reference frame $\mathcal{F}_a$ can be described by specifying the direction cosines between the basis vectors of this rotating frame, *i.e.* $\underrightarrow{b_i}$, and the basis vectors of the fixed

reference frame, *i.e.* $\underset{\rightarrow}{a}_i$. These direction cosines are usually summarized in a rotation or transformation matrix [95,96], from frame $\mathcal{F}_b$ to frame $\mathcal{F}_a$, denoted by ${}^{ab}\underset{\sim}{\boldsymbol{C}}$ and defined as:

$$ {}^{ab}\underset{\sim}{\boldsymbol{C}} = \left[\begin{array}{ccc} {}^{a}\underline{\boldsymbol{b_1}} & {}^{a}\underline{\boldsymbol{b_2}} & {}^{a}\underline{\boldsymbol{b_3}} \end{array} \right] = \left[\begin{array}{ccc} {}^{ab}C_{11} & {}^{ab}C_{12} & {}^{ab}C_{13} \\ {}^{ab}C_{21} & {}^{ab}C_{22} & {}^{ab}C_{23} \\ {}^{ab}C_{31} & {}^{ab}C_{32} & {}^{ab}C_{33} \end{array} \right] = \left[{}^{ab}C_{ij} \right] \tag{B.1} $$

where ${}^{ab}C_{ij}$ is the cosine of the angle between the unit vectors $\underset{\rightarrow}{a}_i$ and $\underset{\rightarrow}{b}_j$. It is known that the rotation matrix defined by Eq. (B.1) is orthogonal, that is:

$$ \begin{aligned} {}^{ab}\underset{\sim}{\boldsymbol{C}} \, {}^{ab}\underset{\sim}{\boldsymbol{C}}^{\mathrm{T}} &= {}^{ab}\underset{\sim}{\boldsymbol{C}}^{\mathrm{T}} \, {}^{ab}\underset{\sim}{\boldsymbol{C}} = \underset{\equiv}{\mathbb{1}} \\ {}^{ab}\underset{\sim}{\boldsymbol{C}}^{\mathrm{T}} &= {}^{ab}\underset{\sim}{\boldsymbol{C}}^{-1} = {}^{ba}\underset{\sim}{\boldsymbol{C}} \end{aligned} \tag{B.2} $$

and that when dealing with more than two reference frames the following relation holds true for any set of three reference frames, *e.g.* frames $\mathcal{F}_a$, $\mathcal{F}_b$, and $\mathcal{F}_c$:

$$ {}^{ac}\underset{\sim}{\boldsymbol{C}} = {}^{ab}\underset{\sim}{\boldsymbol{C}} \, {}^{bc}\underset{\sim}{\boldsymbol{C}} \tag{B.3} $$

The 3×3 rotation matrix is a very important component in a rotation problem (usually used for tensor transformations between different frames) and hence, for any set of parameters used to identify the orientation, it is usually necessary to define the rotation matrix in terms of those parameters too.

In addition to the direction cosines, one can also define the orientation based on Euler's theorem and through the axis/angle variables. Based on Euler's theorem, the orientation of a frame $\mathcal{F}_b$ with respect to another frame $\mathcal{F}_a$ can be expressed in terms of a rotation by an angle ϑ around a screw axis (*i.e.* a unit vector) $\underset{\rightarrow}{s}$ [95,96]. In this representation, the rotation matrix from frame $\mathcal{F}_b$ to frame $\mathcal{F}_a$ will be:

$$ {}^{ab}\underset{\sim}{\boldsymbol{C}} = \underset{\sim}{\boldsymbol{C}}(\underset{\rightarrow}{s}, \vartheta) = \cos\vartheta \, \underset{\equiv}{\mathbb{1}} + \Big(1 - \cos\vartheta\Big) \, \underline{\boldsymbol{s}} \, \underline{\boldsymbol{s}}^{\mathrm{T}} + \sin\vartheta \, \underline{\tilde{\boldsymbol{s}}} \tag{B.4} $$

where $\underline{\boldsymbol{s}}$ is the component matrix of the screw axis (or rotation axis) in either $\mathcal{F}_b$ or $\mathcal{F}_a$:

$$ \underline{\boldsymbol{s}} = {}^{b}\underline{\boldsymbol{s}} = {}^{a}\underline{\boldsymbol{s}} \tag{B.5} $$

Euler's theorem, representing that rotation is describable via a rotation angle (a magnitude) and a rotation axis (a direction), might tempt one to define the rotation as a vector.

However, rotation is not a vector as it does not obey the parallelogram law of addition and when dealing with successive rotations the order in which the rotations are applied is important. Consequently, one may conclude that multiplication of rotation matrices is not commutative in general, *i.e.* for general rotations $(\underset{\rightarrow}{s_1}, \vartheta_1)$ and $(\underset{\rightarrow}{s_2}, \vartheta_2)$:

$$\underset{\sim}{\boldsymbol{C}}(\underset{\rightarrow}{s_1}, \vartheta_1)\, \underset{\sim}{\boldsymbol{C}}(\underset{\rightarrow}{s_2}, \vartheta_2) \neq \underset{\sim}{\boldsymbol{C}}(\underset{\rightarrow}{s_2}, \vartheta_2)\, \underset{\sim}{\boldsymbol{C}}(\underset{\rightarrow}{s_1}, \vartheta_1) \tag{B.6}$$

By setting the screw axis $\underset{\rightarrow}{s}$ in Eq. (B.4) to be the i$^{\text{th}}$ basis vector of either rotating frame $\mathcal{F}_b$ or fixed frame $\mathcal{F}_a$, that is:

$$\underset{}{\boldsymbol{s}} = \underset{}{\boldsymbol{b_1}} = \underset{}{\boldsymbol{a_1}} = \begin{bmatrix} 1 \\ 0 \\ 0 \end{bmatrix} \quad \text{or} \quad \underset{}{\boldsymbol{s}} = \underset{}{\boldsymbol{b_2}} = \underset{}{\boldsymbol{a_2}} = \begin{bmatrix} 0 \\ 1 \\ 0 \end{bmatrix} \quad \text{or} \quad \underset{}{\boldsymbol{s}} = \underset{}{\boldsymbol{b_3}} = \underset{}{\boldsymbol{a_3}} = \begin{bmatrix} 0 \\ 0 \\ 1 \end{bmatrix} \tag{B.7}$$

three particular single rotation matrices corresponding to the principal rotations ϑ_i about the basis vectors $\underset{\rightarrow}{b_i}$ or $\underset{\rightarrow}{a_i}$ will be obtained as:

$$\begin{aligned}
\underset{\sim}{\boldsymbol{C}}(\underset{\rightarrow}{b_1}, \vartheta_1) = \underset{\sim}{\boldsymbol{C}}(\underset{\rightarrow}{a_1}, \vartheta_1) &= \begin{bmatrix} 1 & 0 & 0 \\ 0 & \mathrm{c}_{\vartheta_1} & -\mathrm{s}_{\vartheta_1} \\ 0 & \mathrm{s}_{\vartheta_1} & \mathrm{c}_{\vartheta_1} \end{bmatrix} = \underset{\sim}{\boldsymbol{C_1}} \\
\underset{\sim}{\boldsymbol{C}}(\underset{\rightarrow}{b_2}, \vartheta_2) = \underset{\sim}{\boldsymbol{C}}(\underset{\rightarrow}{a_2}, \vartheta_2) &= \begin{bmatrix} \mathrm{c}_{\vartheta_2} & 0 & \mathrm{s}_{\vartheta_2} \\ 0 & 1 & 0 \\ -\mathrm{s}_{\vartheta_2} & 0 & \mathrm{c}_{\vartheta_2} \end{bmatrix} = \underset{\sim}{\boldsymbol{C_2}} \\
\underset{\sim}{\boldsymbol{C}}(\underset{\rightarrow}{b_3}, \vartheta_3) = \underset{\sim}{\boldsymbol{C}}(\underset{\rightarrow}{a_3}, \vartheta_3) &= \begin{bmatrix} \mathrm{c}_{\vartheta_3} & -\mathrm{s}_{\vartheta_3} & 0 \\ \mathrm{s}_{\vartheta_3} & \mathrm{c}_{\vartheta_3} & 0 \\ 0 & 0 & 1 \end{bmatrix} = \underset{\sim}{\boldsymbol{C_3}}
\end{aligned} \tag{B.8}$$

Any number of these principal rotation matrices can be multiplied in any order to produce a new rotation matrix. However, since a general rotation (angular displacement) has three DOFs and each principal rotation corresponds to one DOF, a minimum of three (independent) principal rotations about axes of either moving frame $\mathcal{F}_b$ or fixed frame $\mathcal{F}_a$ should combined to represent a general rotation or orientation.

In the first case, *i.e.* an orientation described by combining the principal rotations around axes of the moving frame, the corresponding rotation matrix will be a function

of three principal rotation angles, known as Euler angles, which denote the successive rotations of frame $\mathcal{F}_b$ about its rotating axes $\underset{\rightarrow}{b}_i$. Due to the fact that different rotation sequences result in different representations, in general there are 12 possible combinations of Euler angles to define the rotation matrix. In such representations, each rotation occurs about an axis whose location depends on the preceding rotation(s) and the rotation matrix is obtained by postmultiplying the corresponding principal rotation matrices.

The other option for description of a general orientation based on the principal rotations is to use a combination of principal rotations about axes of the fixed reference frame $\mathcal{F}_a$ (instead of axes of the moving frame $\mathcal{F}_b$) which results in a rotation matrix as a function of three principal rotation angles, known as fixed angles [97] (called Euler angles as well [96]). Again, there are 12 possible combinations of fixed angles to define the rotation matrix which are dual of the 12 possible sequences of Euler angles (*i.e.* principal rotations around axes of the moving frame $\mathcal{F}_b$). Indeed, each sequence of the principal rotations around the axes of the fixed frame gives rise to the same rotation matrix as the opposite sequence (same rotations occurring in opposite order) of the principal rotations around the axes of moving frame does. In this case, each rotation occurs about an axis whose location will change as the following rotation(s) occur(s) and the final rotation matrix will be obtained by premultiplying the corresponding principal rotation matrices.

As an example, the rotation matrix associated with the sequence $(\underset{\rightarrow}{b}_1, \vartheta_1)$, $(\underset{\rightarrow}{b}_2, \vartheta_2)$, and $(\underset{\rightarrow}{b}_3, \vartheta_3)$, shown in Figure B.1, is:

$$^{ab}\underset{\sim}{\boldsymbol{C}} = \underset{\sim}{\boldsymbol{C_1}}\,\underset{\sim}{\boldsymbol{C_2}}\,\underset{\sim}{\boldsymbol{C_3}} \tag{B.9}$$

which based on Eq. (B.8) is the same as the rotation matrix of the sequence $(\underset{\rightarrow}{a}_3, \vartheta_3)$, $(\underset{\rightarrow}{a}_2, \vartheta_2)$, and $(\underset{\rightarrow}{a}_1, \vartheta_1)$, shown in Figure B.2. Here, based on the first definition (*i.e.* three rotations around the basis vectors of the moving frame), the second and third rotations occur respectively around $\underset{\rightarrow}{b}_2$ rotated by $\underset{\sim}{\boldsymbol{C_1}}$ and $\underset{\rightarrow}{b}_3$ rotated by $\underset{\sim}{\boldsymbol{C_1}}\,\underset{\sim}{\boldsymbol{C_2}}$. However, based on the second definition (*i.e.* three rotations around the basis vectors of the fixed reference frame), the first and second rotation axes, *i.e.* $\underset{\rightarrow}{a}_3$ and $\underset{\rightarrow}{a}_2$, will be rotated by $\underset{\sim}{\boldsymbol{C_1}}\,\underset{\sim}{\boldsymbol{C_2}}$ and $\underset{\sim}{\boldsymbol{C_1}}$, respectively, as the second and the third rotations (*i.e.* $(\underset{\rightarrow}{a}_2, \vartheta_2)$ and $(\underset{\rightarrow}{a}_1, \vartheta_1)$) occur.

A general rotation can also be expressed as a combination of three nonprincipal rotations. An example is the rotation matrix corresponding to the sequence $(\underset{\rightarrow}{s}_1, \vartheta_1)$, $(\underset{\rightarrow}{s}_2, \vartheta_2)$,

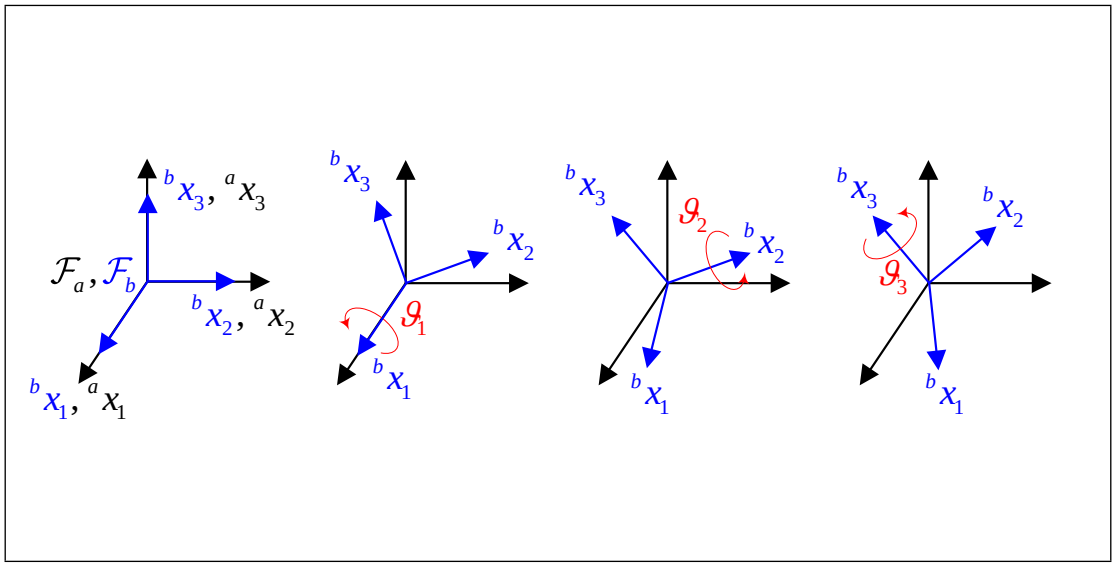

Figure B.1: Rotation of $\mathcal{F}_b$ with respect to $\mathcal{F}_a$ through Euler angles $(\underset{\rightarrow}{b_1}, \vartheta_1)$, $(\underset{\rightarrow}{b_2}, \vartheta_2)$, and $(\underset{\rightarrow}{b_3}, \vartheta_3)$.

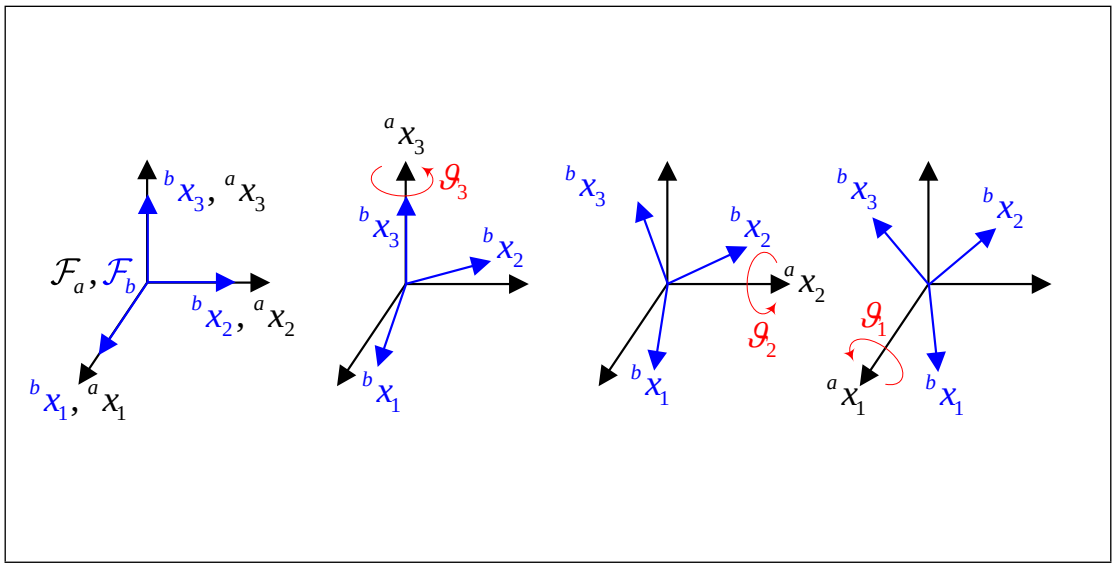

Figure B.2: Rotation of $\mathcal{F}_b$ with respect to $\mathcal{F}_a$ through fixed angles $(\underset{\rightarrow}{a_3}, \vartheta_3)$, $(\underset{\rightarrow}{a_2}, \vartheta_2)$, and $(\underset{\rightarrow}{a_1}, \vartheta_1)$.

and $(\underset{\rightarrow}{s_3}, \vartheta_3)$ representing the rotation of a frame $\mathcal{F}_b$ with respect to another frame $\mathcal{F}_a$ through arbitrary angles ϑ_1, ϑ_2, and ϑ_3, and around arbitrary axes $\underset{\rightarrow}{s_1}$, $\underset{\rightarrow}{s_2}$, and $\underset{\rightarrow}{s_3}$ which are fixed in $\mathcal{F}_b$. More precisely, there are three arbitrary axes $\underset{\rightarrow}{s_1}$, $\underset{\rightarrow}{s_2}$, and $\underset{\rightarrow}{s_3}$ affixed to $\mathcal{F}_b$ and the rotation of $\mathcal{F}_b$ occurs as follows; starting with the frame $\mathcal{F}_b$ coinciding with $\mathcal{F}_a$, frame $\mathcal{F}_b$ rotates by angle ϑ_1 around axis $\underset{\rightarrow}{s_1}$, followed by a second rotation of ϑ_2 about $\underset{\rightarrow}{s_2}$ (which is already rotated by ϑ_1), followed by a third rotation of ϑ_3 about $\underset{\rightarrow}{s_3}$ (which is already rotated by ϑ_1 and ϑ_2). The rotation matrix associated with this general case is:

$$\overset{ab}{\underset{\sim}{\boldsymbol{C}}} = \underset{\sim}{\boldsymbol{C_1}}\,\underset{\sim}{\boldsymbol{C_2}}\,\underset{\sim}{\boldsymbol{C_3}} \tag{B.10}$$

where this time:

$$\underset{\sim}{\boldsymbol{C_i}} = \underset{\sim}{\boldsymbol{C}}(\underset{\rightarrow}{s_i}, \vartheta_i), \qquad i = 1, 2, 3 \tag{B.11}$$

and $\underset{\sim}{\boldsymbol{C}}(\underset{\rightarrow}{s_i}, \vartheta_i)$ is calculated based on Eq. (B.4). The rotation angles ϑ_i can be considered as generalized Euler angles and the rotation problem defined here can be considered as a representative for a large group of rotation problems (including all those defined based on different combinations of Euler angles). From now on the symbol $\underset{\sim}{\boldsymbol{C_i}}$ will be used to represent the more general rotation matrix $\underset{\sim}{\boldsymbol{C}}(\underset{\rightarrow}{s_i}, \vartheta_i)$ instead of special rotation matrices $\underset{\sim}{\boldsymbol{C}}(\underset{\rightarrow}{a_i}, \vartheta_i)$ and $\underset{\sim}{\boldsymbol{C}}(\underset{\rightarrow}{b_i}, \vartheta_i)$.

Note that, in addition to the direction cosines, Euler axis/angle parameters, and Euler angles mentioned in this section, there are other parameter sets for orientation representation which are not used in this text and therefore reviewing them is worthless. Finally, having the rotation matrix between two reference frames $\mathcal{F}_a$ and $\mathcal{F}_b$, the following relations hold true for component matrices of a vector $\underset{\rightarrow}{v}$ and a dyadic $\underset{\leftrightarrow}{d}$:

$$\begin{aligned}
{}^a\underline{\boldsymbol{v}} &= {}^{ab}\underset{\sim}{\boldsymbol{C}}\,{}^b\underline{\boldsymbol{v}} \\
{}^a\underline{\underline{\boldsymbol{d}}} &= {}^{ab}\underset{\sim}{\boldsymbol{C}}\,{}^b\underline{\underline{\boldsymbol{d}}}\,{}^{ab}\underset{\sim}{\boldsymbol{C}}^{\mathrm{T}} = {}^{ab}\underset{\sim}{\boldsymbol{C}}\,{}^b\underline{\underline{\boldsymbol{d}}}\,{}^{ba}\underset{\sim}{\boldsymbol{C}} \\
{}^a\underline{\boldsymbol{v}}^{\times} &= \left({}^{ab}\underset{\sim}{\boldsymbol{C}}\,{}^b\underline{\boldsymbol{v}}\right)^{\times} = {}^{ab}\underset{\sim}{\boldsymbol{C}}\,{}^b\underline{\boldsymbol{v}}^{\times}\,{}^{ba}\underset{\sim}{\boldsymbol{C}}
\end{aligned} \tag{B.12}$$

B.3 Angular velocity

To formulate the angular velocity of a frame, consider the case in which the angular displacement of frame $\mathcal{F}_b$ evolves with time and thus the rotation matrix from frame $\mathcal{F}_b$ to

frame $\mathcal{F}_a$ is time dependent, *i.e.*:

$$ {}^{ab}\underset{\sim}{\boldsymbol{C}} = {}^{ab}\underset{\sim}{\boldsymbol{C}}(t) = \underset{\sim}{\boldsymbol{C}}(t) \tag{B.13} $$

where for brevity, symbol ${}^{ab}\underset{\sim}{\boldsymbol{C}}$ is simplified to symbol $\underset{\sim}{\boldsymbol{C}}$. It can be shown that such a rotation matrix obeys the following differential equation [95]:

$$ \dot{\underset{\sim}{\boldsymbol{C}}} - {}^{a}\underline{\underline{\boldsymbol{w}}}^{\times}\, \underset{\sim}{\boldsymbol{C}} = \underset{\sim}{\boldsymbol{0}} \tag{B.14} $$

or equivalently:

$$ \begin{aligned} {}^{a}\underline{\underline{\boldsymbol{w}}}^{\times} &= \dot{\underset{\sim}{\boldsymbol{C}}}\, \underset{\sim}{\boldsymbol{C}}^{\mathrm{T}} = -\underset{\sim}{\boldsymbol{C}}\, \dot{\underset{\sim}{\boldsymbol{C}}}^{\mathrm{T}} \\ {}^{b}\underline{\underline{\boldsymbol{w}}}^{\times} &= \underset{\sim}{\boldsymbol{C}}^{\mathrm{T}}\, \dot{\underset{\sim}{\boldsymbol{C}}} = -\dot{\underset{\sim}{\boldsymbol{C}}}^{\mathrm{T}}\, \underset{\sim}{\boldsymbol{C}} \end{aligned} \tag{B.15} $$

where $\underset{\rightarrow}{w}$ is the angular velocity vector of frame $\mathcal{F}_b$ with respect to frame $\mathcal{F}_a$. Note that time differentiating from the first relation in Eq. (B.2) gives rise to:

$$ \begin{aligned} \dot{\underset{\sim}{\boldsymbol{C}}}\, \underset{\sim}{\boldsymbol{C}}^{\mathrm{T}} + \underset{\sim}{\boldsymbol{C}}\, \dot{\underset{\sim}{\boldsymbol{C}}}^{\mathrm{T}} &= \underset{\sim}{\boldsymbol{0}} \\ \dot{\underset{\sim}{\boldsymbol{C}}}^{\mathrm{T}}\, \underset{\sim}{\boldsymbol{C}} + \underset{\sim}{\boldsymbol{C}}^{\mathrm{T}}\, \dot{\underset{\sim}{\boldsymbol{C}}} &= \underset{\sim}{\boldsymbol{0}} \end{aligned} \tag{B.16} $$

which means matrices $\dot{\underset{\sim}{\boldsymbol{C}}}\, \underset{\sim}{\boldsymbol{C}}^{\mathrm{T}}$ and $\dot{\underset{\sim}{\boldsymbol{C}}}^{\mathrm{T}}\, \underset{\sim}{\boldsymbol{C}}$ are antisymmetric and have the necessary form to be associated with cross product dyadic of a vector. Also, keep in mind that generally there is no rotation vector $\underset{\rightarrow}{\vartheta}$ such that its time derivative is an angular velocity vector $\underset{\rightarrow}{w}$. Time differentiating from relations in Eq. (B.15) will result in expressions for the angular acceleration of $\mathcal{F}_b$ relative to $\mathcal{F}_a$. In fact, the relative angular acceleration vector $\dot{\underset{\rightarrow}{w}}$ is:

$$ \dot{\underset{\rightarrow}{w}} = {}^{a}\frac{d}{dt}\left(\underset{\rightarrow}{w}\right) = {}^{b}\frac{d}{dt}\left(\underset{\rightarrow}{w}\right) \tag{B.17} $$

Before formulating the angular velocity in the general example mentioned in the previous section, it is beneficial to consider the specific rotation problem of a single rotation ϑ about axis $\underset{\rightarrow}{s}$. For such a problem whose rotation matrix is given in terms of Euler axis/angle parameters as Eq. (B.4), it can be shown that:

$$ \underset{\sim}{\boldsymbol{C}}(\underset{\rightarrow}{s}, \vartheta)\, \underline{\boldsymbol{s}} = \underset{\sim}{\boldsymbol{C}}^{\mathrm{T}}(\underset{\rightarrow}{s}, \vartheta)\, \underline{\boldsymbol{s}} = \underline{\boldsymbol{s}} \tag{B.18} $$

and more importantly:

$$ \underset{\sim}{\boldsymbol{C}}'(\underset{\rightarrow}{s}, \vartheta)\, \underset{\sim}{\boldsymbol{C}}^{\mathrm{T}}(\underset{\rightarrow}{s}, \vartheta) = \underline{\underline{\boldsymbol{s}}}^{\times} \tag{B.19} $$

where:

$$\underset{\sim}{\boldsymbol{C}}'(\underset{\rightarrow}{s},\vartheta)=\frac{\partial\underset{\sim}{\boldsymbol{C}}(\underset{\rightarrow}{s},\vartheta)}{\partial\vartheta}=-\sin\vartheta\,\underset{\equiv}{\mathbb{1}}+\sin\vartheta\,\underline{s}\,\underline{s}^{\mathrm{T}}-\cos\vartheta\,\underline{\underline{s}}^{\times} \tag{B.20}$$

One can use Eq. (B.19) to obtain the following relation between the time derivative of the rotation matrix given in Eq. (B.4) and the time derivative of the rotation angle (assuming that the angle ϑ is time dependent and the rotation axis $\underset{\rightarrow}{s}$ is constant):

$$\begin{aligned}{}^{ab}\dot{\underset{\sim}{\boldsymbol{C}}}(\underset{\rightarrow}{s},\vartheta)\,{}^{ab}\underset{\sim}{\boldsymbol{C}}^{\mathrm{T}}(\underset{\rightarrow}{s},\vartheta)&={}^{ab}\underset{\sim}{\boldsymbol{C}}'(\underset{\rightarrow}{s},\vartheta)\,\dot{\vartheta}\,{}^{ab}\underset{\sim}{\boldsymbol{C}}^{\mathrm{T}}(\underset{\rightarrow}{s},\vartheta)\\&={}^{ab}\underset{\sim}{\boldsymbol{C}}'(\underset{\rightarrow}{s},\vartheta)\,{}^{ab}\underset{\sim}{\boldsymbol{C}}^{\mathrm{T}}(\underset{\rightarrow}{s},\vartheta)\,\dot{\vartheta}\\&=\underline{\underline{s}}^{\times}\,\dot{\vartheta}=\left(\underline{s}\,\dot{\vartheta}\right)^{\times}\end{aligned} \tag{B.21}$$

Now, in the general example mentioned previously, *i.e.* successive rotations ϑ_i about rotating axes $\underset{\rightarrow}{s_i}$, where the time derivative of the rotation matrix is:

$$\dot{\underset{\sim}{\boldsymbol{C}}}=\dot{\underset{\sim}{\boldsymbol{C}}}_{\boldsymbol{1}}\,\underset{\sim}{\boldsymbol{C}}_{\boldsymbol{2}}\,\underset{\sim}{\boldsymbol{C}}_{\boldsymbol{3}}+\underset{\sim}{\boldsymbol{C}}_{\boldsymbol{1}}\,\dot{\underset{\sim}{\boldsymbol{C}}}_{\boldsymbol{2}}\,\underset{\sim}{\boldsymbol{C}}_{\boldsymbol{3}}+\underset{\sim}{\boldsymbol{C}}_{\boldsymbol{1}}\,\underset{\sim}{\boldsymbol{C}}_{\boldsymbol{2}}\,\dot{\underset{\sim}{\boldsymbol{C}}}_{\boldsymbol{3}} \tag{B.22}$$

the angular velocity of $\mathcal{F}_b$ with respect to $\mathcal{F}_a$ will be derived as:

$$\begin{aligned}{}^{a}\underline{\underline{\boldsymbol{w}}}^{\times}&=\dot{\underset{\sim}{\boldsymbol{C}}}\,\underset{\sim}{\boldsymbol{C}}^{\mathrm{T}}=\dot{\underset{\sim}{\boldsymbol{C}}}\left(\underset{\sim}{\boldsymbol{C}}_{\boldsymbol{3}}{}^{\mathrm{T}}\,\underset{\sim}{\boldsymbol{C}}_{\boldsymbol{2}}{}^{\mathrm{T}}\,\underset{\sim}{\boldsymbol{C}}_{\boldsymbol{1}}{}^{\mathrm{T}}\right)\\&=\dot{\underset{\sim}{\boldsymbol{C}}}_{\boldsymbol{1}}\,\underset{\sim}{\boldsymbol{C}}_{\boldsymbol{1}}{}^{\mathrm{T}}+\underset{\sim}{\boldsymbol{C}}_{\boldsymbol{1}}\,\dot{\underset{\sim}{\boldsymbol{C}}}_{\boldsymbol{2}}\,\underset{\sim}{\boldsymbol{C}}_{\boldsymbol{2}}{}^{\mathrm{T}}\,\underset{\sim}{\boldsymbol{C}}_{\boldsymbol{1}}{}^{\mathrm{T}}+\underset{\sim}{\boldsymbol{C}}_{\boldsymbol{1}}\,\underset{\sim}{\boldsymbol{C}}_{\boldsymbol{2}}\,\dot{\underset{\sim}{\boldsymbol{C}}}_{\boldsymbol{3}}\,\underset{\sim}{\boldsymbol{C}}_{\boldsymbol{3}}{}^{\mathrm{T}}\,\underset{\sim}{\boldsymbol{C}}_{\boldsymbol{2}}{}^{\mathrm{T}}\,\underset{\sim}{\boldsymbol{C}}_{\boldsymbol{1}}{}^{\mathrm{T}}\\&=\left(\underline{\boldsymbol{s}}_{\boldsymbol{1}}\,\dot{\vartheta}_1\right)^{\times}+\left(\underset{\sim}{\boldsymbol{C}}_{\boldsymbol{1}}\,\underline{\boldsymbol{s}}_{\boldsymbol{2}}\,\dot{\vartheta}_2\right)^{\times}+\left(\underset{\sim}{\boldsymbol{C}}_{\boldsymbol{1}}\,\underset{\sim}{\boldsymbol{C}}_{\boldsymbol{2}}\,\underline{\boldsymbol{s}}_{\boldsymbol{3}}\,\dot{\vartheta}_3\right)^{\times}\end{aligned} \tag{B.23}$$

or more desirably:

$${}^{a}\underline{\boldsymbol{w}}=\underline{\boldsymbol{s}}_{\boldsymbol{1}}\,\dot{\vartheta}_1+\underset{\sim}{\boldsymbol{C}}_{\boldsymbol{1}}\,\underline{\boldsymbol{s}}_{\boldsymbol{2}}\,\dot{\vartheta}_2+\underset{\sim}{\boldsymbol{C}}_{\boldsymbol{1}}\,\underset{\sim}{\boldsymbol{C}}_{\boldsymbol{2}}\,\underline{\boldsymbol{s}}_{\boldsymbol{3}}\,\dot{\vartheta}_3 \tag{B.24}$$

where matrices $\underline{\boldsymbol{s}}_{\boldsymbol{i}}$ are descriptions of the rotation vectors $\underset{\rightarrow}{s_i}$ in $\mathcal{F}_b$ or $\mathcal{F}_a$ before any rotation occurs (*i.e.* when $\mathcal{F}_b$ coincides with $\mathcal{F}_a$). Using Eqs. (B.10) and (B.24) one can get:

$${}^{b}\underline{\boldsymbol{w}}=\underset{\sim}{\boldsymbol{C}}^{\mathrm{T}}\,{}^{a}\underline{\boldsymbol{w}}=\underset{\sim}{\boldsymbol{C}}_{\boldsymbol{3}}{}^{\mathrm{T}}\,\underset{\sim}{\boldsymbol{C}}_{\boldsymbol{2}}{}^{\mathrm{T}}\,\underline{\boldsymbol{s}}_{\boldsymbol{1}}\,\dot{\vartheta}_1+\underset{\sim}{\boldsymbol{C}}_{\boldsymbol{3}}{}^{\mathrm{T}}\,\underline{\boldsymbol{s}}_{\boldsymbol{2}}\,\dot{\vartheta}_2+\underline{\boldsymbol{s}}_{\boldsymbol{3}}\,\dot{\vartheta}_3 \tag{B.25}$$

At the end of this section, having the angular velocity vector of frame $\mathcal{F}_b$ with respect to frame $\mathcal{F}_a$, *i.e.* having $\underset{\rightarrow}{w}$, the following relations hold true for time derivatives of a vector $\underset{\rightarrow}{v}$ and a dyadic $\underset{\leftrightarrow}{d}$:

$$\begin{aligned}{}^{a}\frac{d}{dt}\left(\underset{\rightarrow}{v}\right)&={}^{b}\frac{d}{dt}\left(\underset{\rightarrow}{v}\right)+\underset{\rightarrow}{w}\times\underset{\rightarrow}{v}={}^{b}\frac{d}{dt}\left(\underset{\rightarrow}{v}\right)+\underset{\leftrightarrow}{w}^{\times}\cdot\underset{\rightarrow}{v}\\{}^{a}\frac{d}{dt}\left(\underset{\leftrightarrow}{d}\right)&={}^{b}\frac{d}{dt}\left(\underset{\leftrightarrow}{d}\right)+\underset{\leftrightarrow}{w}^{\times}\cdot\underset{\leftrightarrow}{d}-\underset{\leftrightarrow}{d}\cdot\underset{\leftrightarrow}{w}^{\times}\end{aligned} \tag{B.26}$$

B.4 Virtual rotation

Analogous to the derivation of the angular velocity from the time derivative of a rotation matrix reviewed in the previous section it would be also pleasing if, in general, the virtual rotation or virtual angular displacement can be related to the variation of the rotation matrix. Similar to the Eq. (B.15), the relation can be defined as [98]:

$$\begin{aligned} {}^{a}\delta\underline{\underline{\boldsymbol{\vartheta}}}^{\times} &= \Delta\underset{\sim}{\boldsymbol{C}}\,\underset{\sim}{\boldsymbol{C}}^{\mathrm{T}} = -\,\underset{\sim}{\boldsymbol{C}}\,\Delta\underset{\sim}{\boldsymbol{C}}^{\mathrm{T}} \\ {}^{b}\delta\underline{\underline{\boldsymbol{\vartheta}}}^{\times} &= \underset{\sim}{\boldsymbol{C}}^{\mathrm{T}}\,\Delta\underset{\sim}{\boldsymbol{C}} = -\,\Delta\underset{\sim}{\boldsymbol{C}}^{\mathrm{T}}\,\underset{\sim}{\boldsymbol{C}} \end{aligned} \tag{B.27}$$

where $\delta\underset{\rightarrow}{\vartheta}$ is the virtual rotation vector of frame $\mathcal{F}_b$ with respect to frame $\mathcal{F}_a$. Note that taking the variation from the first relation in Eq. (B.2) results in the following relations:

$$\begin{aligned} \Delta\underset{\sim}{\boldsymbol{C}}\,\underset{\sim}{\boldsymbol{C}}^{\mathrm{T}} + \underset{\sim}{\boldsymbol{C}}\,\Delta\underset{\sim}{\boldsymbol{C}}^{\mathrm{T}} &= \underset{\sim}{\boldsymbol{0}} \\ \Delta\underset{\sim}{\boldsymbol{C}}^{\mathrm{T}}\,\underset{\sim}{\boldsymbol{C}} + \underset{\sim}{\boldsymbol{C}}^{\mathrm{T}}\,\Delta\underset{\sim}{\boldsymbol{C}} &= \underset{\sim}{\boldsymbol{0}} \end{aligned} \tag{B.28}$$

which illustrate the antisymmetry of matrices $\Delta\underset{\sim}{\boldsymbol{C}}\,\underset{\sim}{\boldsymbol{C}}^{\mathrm{T}}$ and $\Delta\underset{\sim}{\boldsymbol{C}}^{\mathrm{T}}\,\underset{\sim}{\boldsymbol{C}}$. In addition, it is noteworthy that although talking about a rotation vector is not meaningful in general, the infinitesimal virtual rotations can be always combined as a vector (this will be shown later in this appendix). Thus, in general, there is no rotation vector $\underset{\rightarrow}{\vartheta}$ such that its variation is a virtual rotation vector $\delta\underset{\rightarrow}{\vartheta}$ [98].

For the case of a single rotation about a fixed axis, the relation between the variation of the rotation matrix and the variation of the rotation angle or virtual rotation will be obtained as (the variation of the rotation axis is assumed to vanish):

$$\begin{aligned} \Delta\,{}^{ab}\underset{\sim}{\boldsymbol{C}}(\underset{\rightarrow}{s},\vartheta)\,{}^{ab}\underset{\sim}{\boldsymbol{C}}^{\mathrm{T}}(\underset{\rightarrow}{s},\vartheta) &= {}^{ab}\underset{\sim}{\boldsymbol{C}}'(\underset{\rightarrow}{s},\vartheta)\,\delta\vartheta\,{}^{ab}\underset{\sim}{\boldsymbol{C}}^{\mathrm{T}}(\underset{\rightarrow}{s},\vartheta) \\ &= {}^{ab}\underset{\sim}{\boldsymbol{C}}'(\underset{\rightarrow}{s},\vartheta)\,{}^{ab}\underset{\sim}{\boldsymbol{C}}^{\mathrm{T}}(\underset{\rightarrow}{s},\vartheta)\,\delta\vartheta \\ &= \underline{\underline{\boldsymbol{s}}}^{\times}\,\delta\vartheta = \left(\underset{\sim}{\boldsymbol{s}}\,\delta\vartheta\right)^{\times} \end{aligned} \tag{B.29}$$

Therefore, in the general example of successive rotations ϑ_i about axes $\underset{\rightarrow}{s_i}$, by using Eq. (B.29) the following relations will be derived for the variation of the rotation matrix and the virtual rotation vector:

$$\Delta\underset{\sim}{\boldsymbol{C}} = \Delta\underset{\sim}{\boldsymbol{C}}_{\boldsymbol{1}}\,\underset{\sim}{\boldsymbol{C}}_{\boldsymbol{2}}\,\underset{\sim}{\boldsymbol{C}}_{\boldsymbol{3}} + \underset{\sim}{\boldsymbol{C}}_{\boldsymbol{1}}\,\Delta\underset{\sim}{\boldsymbol{C}}_{\boldsymbol{2}}\,\underset{\sim}{\boldsymbol{C}}_{\boldsymbol{3}} + \underset{\sim}{\boldsymbol{C}}_{\boldsymbol{1}}\,\underset{\sim}{\boldsymbol{C}}_{\boldsymbol{2}}\,\Delta\underset{\sim}{\boldsymbol{C}}_{\boldsymbol{3}} \tag{B.30}$$

$$
\begin{aligned}
{}^{a}\delta\underline{\underline{\boldsymbol{\vartheta}}}^{\times} &= \Delta\underset{\sim}{\boldsymbol{C}}\,\underset{\sim}{\boldsymbol{C}}^{\mathrm{T}} = \Delta\underset{\sim}{\boldsymbol{C}}\left(\underset{\sim}{\boldsymbol{C_3}}^{\mathrm{T}}\,\underset{\sim}{\boldsymbol{C_2}}^{\mathrm{T}}\,\underset{\sim}{\boldsymbol{C_1}}^{\mathrm{T}}\right) \\
&= \Delta\underset{\sim}{\boldsymbol{C_1}}\,\underset{\sim}{\boldsymbol{C_1}}^{\mathrm{T}} + \underset{\sim}{\boldsymbol{C_1}}\,\Delta\underset{\sim}{\boldsymbol{C_2}}\,\underset{\sim}{\boldsymbol{C_2}}^{\mathrm{T}}\,\underset{\sim}{\boldsymbol{C_1}}^{\mathrm{T}} + \underset{\sim}{\boldsymbol{C_1}}\,\underset{\sim}{\boldsymbol{C_2}}\,\Delta\underset{\sim}{\boldsymbol{C_3}}\,\underset{\sim}{\boldsymbol{C_3}}^{\mathrm{T}}\,\underset{\sim}{\boldsymbol{C_2}}^{\mathrm{T}}\,\underset{\sim}{\boldsymbol{C_1}}^{\mathrm{T}} \\
&= \left(\underset{\_}{\boldsymbol{s_1}}\,\delta\vartheta_1\right)^{\times} + \left(\underset{\sim}{\boldsymbol{C_1}}\,\underset{\_}{\boldsymbol{s_2}}\,\delta\vartheta_2\right)^{\times} + \left(\underset{\sim}{\boldsymbol{C_1}}\,\underset{\sim}{\boldsymbol{C_2}}\,\underset{\_}{\boldsymbol{s_3}}\,\delta\vartheta_3\right)^{\times}
\end{aligned}
\tag{B.31}
$$

$$
{}^{a}\delta\underline{\boldsymbol{\vartheta}} = \underset{\_}{\boldsymbol{s_1}}\,\delta\vartheta_1 + \underset{\sim}{\boldsymbol{C_1}}\,\underset{\_}{\boldsymbol{s_2}}\,\delta\vartheta_2 + \underset{\sim}{\boldsymbol{C_1}}\,\underset{\sim}{\boldsymbol{C_2}}\,\underset{\_}{\boldsymbol{s_3}}\,\delta\vartheta_3 \tag{B.32}
$$

$$
{}^{b}\delta\underline{\boldsymbol{\vartheta}} = \underset{\sim}{\boldsymbol{C}}^{\mathrm{T}}\,{}^{a}\delta\underline{\boldsymbol{\vartheta}} = \underset{\sim}{\boldsymbol{C_3}}^{\mathrm{T}}\,\underset{\sim}{\boldsymbol{C_2}}^{\mathrm{T}}\underset{\_}{\boldsymbol{s_1}}\,\delta\vartheta_1 + \underset{\sim}{\boldsymbol{C_3}}^{\mathrm{T}}\,\underset{\_}{\boldsymbol{s_2}}\,\delta\vartheta_2 + \underset{\_}{\boldsymbol{s_3}}\,\delta\vartheta_3 \tag{B.33}
$$

Note that in the above equations $\delta\vartheta_i$ is the i$^{\text{th}}$ infinitesimal virtual rotation around axis $\underset{\rightarrow}{s_i}$ and not the i$^{\text{th}}$ element of the virtual rotation component matrix $\delta\underline{\boldsymbol{\vartheta}}$.

At the end of this section, it is useful to define the variation of a variable with respect to a frame as the variation of the variable description in that frame, *i.e.*:

$$
\begin{aligned}
{}^{a}\Delta z &= \Delta\left({}^{a}z\right) = \Delta^{a}z \\
{}^{b}\Delta z &= \Delta\left({}^{b}z\right) = \Delta^{b}z
\end{aligned}
\tag{B.34}
$$

In this way, having the virtual rotation vector of $\mathcal{F}_b$ with respect to $\mathcal{F}_a$, *i.e.* having $\delta\underset{\rightarrow}{\vartheta}$, the following relations can be obtained for variations of a vector $\underset{\rightarrow}{v}$ and a dyadic $\underset{\leftrightarrow}{d}$:

$$
\begin{aligned}
{}^{a}\Delta\underset{\rightarrow}{v} &= {}^{b}\Delta\underset{\rightarrow}{v} + \delta\underset{\rightarrow}{\vartheta}\times\underset{\rightarrow}{v} = {}^{b}\Delta\underset{\rightarrow}{v} + \delta\underset{\leftrightarrow}{\vartheta}^{\times}\cdot\underset{\rightarrow}{v} \\
{}^{a}\Delta\underset{\leftrightarrow}{d} &= {}^{b}\Delta\underset{\leftrightarrow}{d} + \delta\underset{\leftrightarrow}{\vartheta}^{\times}\cdot\underset{\leftrightarrow}{d} - \underset{\leftrightarrow}{d}\cdot\delta\underset{\leftrightarrow}{\vartheta}^{\times}
\end{aligned}
\tag{B.35}
$$

which are derived by considering the following relations:

$$
\begin{aligned}
\Delta\left({}^{a}\underline{\boldsymbol{v}}\right) &= \Delta\left(\underset{\sim}{\boldsymbol{C}}\,{}^{b}\underline{\boldsymbol{v}}\right) = \underset{\sim}{\boldsymbol{C}}\,\Delta\left({}^{b}\underline{\boldsymbol{v}}\right) + \Delta\underset{\sim}{\boldsymbol{C}}\,{}^{b}\underline{\boldsymbol{v}} \\
&= \underset{\sim}{\boldsymbol{C}}\,\Delta\left({}^{b}\underline{\boldsymbol{v}}\right) + \Delta\underset{\sim}{\boldsymbol{C}}\,\underset{\sim}{\boldsymbol{C}}^{\mathrm{T}}\,\underset{\sim}{\boldsymbol{C}}\,{}^{b}\underline{\boldsymbol{v}} \\
&= \underset{\sim}{\boldsymbol{C}}\,\Delta\left({}^{b}\underline{\boldsymbol{v}}\right) + {}^{a}\delta\underline{\underline{\boldsymbol{\vartheta}}}^{\times}\,{}^{a}\underline{\boldsymbol{v}}
\end{aligned}
\tag{B.36}
$$

$$
\begin{aligned}
\Delta\left({}^{a}\underline{\underline{\boldsymbol{d}}}\right) &= \Delta\left(\underset{\sim}{\boldsymbol{C}}\,{}^{b}\underline{\underline{\boldsymbol{d}}}\,\underset{\sim}{\boldsymbol{C}}^{\mathrm{T}}\right) = \underset{\sim}{\boldsymbol{C}}\,\Delta\left({}^{b}\underline{\underline{\boldsymbol{d}}}\right)\underset{\sim}{\boldsymbol{C}}^{\mathrm{T}} + \Delta\underset{\sim}{\boldsymbol{C}}\,{}^{b}\underline{\underline{\boldsymbol{d}}}\,\underset{\sim}{\boldsymbol{C}}^{\mathrm{T}} + \underset{\sim}{\boldsymbol{C}}\,{}^{b}\underline{\underline{\boldsymbol{d}}}\,\Delta\underset{\sim}{\boldsymbol{C}}^{\mathrm{T}} \\
&= \underset{\sim}{\boldsymbol{C}}\,\Delta\left({}^{b}\underline{\underline{\boldsymbol{d}}}\right)\underset{\sim}{\boldsymbol{C}}^{\mathrm{T}} + \Delta\underset{\sim}{\boldsymbol{C}}\,\underset{\sim}{\boldsymbol{C}}^{\mathrm{T}}\,\underset{\sim}{\boldsymbol{C}}\,{}^{b}\underline{\underline{\boldsymbol{d}}}\,\underset{\sim}{\boldsymbol{C}}^{\mathrm{T}} + \underset{\sim}{\boldsymbol{C}}\,{}^{b}\underline{\underline{\boldsymbol{d}}}\,\underset{\sim}{\boldsymbol{C}}^{\mathrm{T}}\,\underset{\sim}{\boldsymbol{C}}\,\Delta\underset{\sim}{\boldsymbol{C}}^{\mathrm{T}} \\
&= \underset{\sim}{\boldsymbol{C}}\,\Delta\left({}^{b}\underline{\underline{\boldsymbol{d}}}\right)\underset{\sim}{\boldsymbol{C}}^{\mathrm{T}} + {}^{a}\delta\underline{\underline{\boldsymbol{\vartheta}}}^{\times}\,{}^{a}\underline{\underline{\boldsymbol{d}}} - {}^{a}\underline{\underline{\boldsymbol{d}}}\,{}^{a}\delta\underline{\underline{\boldsymbol{\vartheta}}}^{\times}
\end{aligned}
\tag{B.37}
$$

B.5 Calculus of variations

As a field of mathematics, the calculus of variations is a very useful tool, or technique of optimization, which deals with extremizing an integral involving unknown functions. It forms the basis of Hamilton's principle utilized in this thesis for dynamic modeling of gyroelastic systems where rotational displacements play a central role.

Derivation of the virtual work expression is one of the steps when Hamilton's principle is employed for dynamic modeling. Assuming that, in a dynamic problem containing rotational displacements, the rotational displacement at an arbitrary point is described as a rotation matrix $\underset{\sim}{\boldsymbol{C}}$ from a rotating frame $\mathcal{F}_b$ to a fixed frame $\mathcal{F}_a$ and the moment applied at the point is $\underset{\rightarrow}{m}$, the virtual work $\delta\mathcal{W}$ done by the moment can be expressed as:

$$\delta\mathcal{W} = \underset{\rightarrow}{\delta\vartheta} \cdot \underset{\rightarrow}{m} = {}^{b}\underset{\sim}{\delta\boldsymbol{\vartheta}}^{\mathrm{T}}\, {}^{b}\underset{\sim}{\boldsymbol{m}} = {}^{a}\underset{\sim}{\delta\boldsymbol{\vartheta}}^{\mathrm{T}}\, {}^{a}\underset{\sim}{\boldsymbol{m}} \tag{B.38}$$

where virtual rotation vector $\underset{\rightarrow}{\delta\vartheta}$ is calculated using Eq. (B.27).

Also, when utilizing Hamilton's principle in dynamic problems containing rotational displacements, important variational terms of the following general forms may appear during the procedure:

$$\begin{aligned}
\Delta\mathcal{A} &= \int_t {}^{a}\Delta\underset{\rightarrow}{w} \cdot \underset{\rightarrow}{v}\, dt = \int_t \Delta\left({}^{a}\underset{\sim}{\boldsymbol{w}}^{\mathrm{T}}\right) {}^{a}\underset{\sim}{\boldsymbol{v}}\, dt \\
\Delta\mathcal{A} &= \int_t {}^{b}\Delta\underset{\rightarrow}{w} \cdot \underset{\rightarrow}{v}\, dt = \int_t \Delta\left({}^{b}\underset{\sim}{\boldsymbol{w}}^{\mathrm{T}}\right) {}^{b}\underset{\sim}{\boldsymbol{v}}\, dt
\end{aligned} \tag{B.39}$$

where $\underset{\rightarrow}{v}$ is a general vector, and ${}^{a}\Delta\underset{\rightarrow}{w}$ and ${}^{b}\Delta\underset{\rightarrow}{w}$ are variations of the angular velocity vector (not virtual angular velocity vectors). Such variational terms can be handled by relating the variation of the angular velocity vector to the virtual rotation vector and its time derivative.

The desired expressions for the variation of the angular velocity vector can be obtained by taking the variation of the relations given by Eq. (B.15) which results in:

$$\begin{aligned}
\Delta\left({}^{a}\underset{\approx}{\boldsymbol{w}}^{\times}\right) &= \Delta\dot{\underset{\sim}{\boldsymbol{C}}}\,\underset{\sim}{\boldsymbol{C}}^{\mathrm{T}} + \dot{\underset{\sim}{\boldsymbol{C}}}\,\Delta\underset{\sim}{\boldsymbol{C}}^{\mathrm{T}} = \frac{d}{dt}\left(\Delta\underset{\sim}{\boldsymbol{C}}\,\underset{\sim}{\boldsymbol{C}}^{\mathrm{T}}\right) - \Delta\underset{\sim}{\boldsymbol{C}}\,\dot{\underset{\sim}{\boldsymbol{C}}}^{\mathrm{T}} + \dot{\underset{\sim}{\boldsymbol{C}}}\,\Delta\underset{\sim}{\boldsymbol{C}}^{\mathrm{T}} \\
\Delta\left({}^{b}\underset{\approx}{\boldsymbol{w}}^{\times}\right) &= \Delta\underset{\sim}{\boldsymbol{C}}^{\mathrm{T}}\,\dot{\underset{\sim}{\boldsymbol{C}}} + \underset{\sim}{\boldsymbol{C}}^{\mathrm{T}}\,\Delta\dot{\underset{\sim}{\boldsymbol{C}}} = \frac{d}{dt}\left(\underset{\sim}{\boldsymbol{C}}^{\mathrm{T}}\,\Delta\underset{\sim}{\boldsymbol{C}}\right) - \dot{\underset{\sim}{\boldsymbol{C}}}^{\mathrm{T}}\,\Delta\underset{\sim}{\boldsymbol{C}} + \Delta\underset{\sim}{\boldsymbol{C}}^{\mathrm{T}}\,\dot{\underset{\sim}{\boldsymbol{C}}}
\end{aligned} \tag{B.40}$$

Recalling that the rotation matrix is orthogonal and using Eq. (B.27), the expressions can be rewritten as:

$$\begin{aligned}
\Delta\left({}^{a}\underline{\underline{\boldsymbol{w}}}^{\times}\right) &= \frac{d}{dt}\left({}^{a}\underline{\underline{\delta\boldsymbol{\vartheta}}}^{\times}\right) - \Delta\underset{\sim}{\boldsymbol{C}}\,\underset{\sim}{\boldsymbol{C}}^{\mathrm{T}}\,\underset{\sim}{\boldsymbol{C}}\,\dot{\underset{\sim}{\boldsymbol{C}}}^{\mathrm{T}} + \dot{\underset{\sim}{\boldsymbol{C}}}\,\underset{\sim}{\boldsymbol{C}}^{\mathrm{T}}\,\underset{\sim}{\boldsymbol{C}}\,\Delta\underset{\sim}{\boldsymbol{C}}^{\mathrm{T}} \\
&= \frac{d}{dt}\left({}^{a}\underline{\underline{\delta\boldsymbol{\vartheta}}}^{\times}\right) + {}^{a}\underline{\underline{\delta\boldsymbol{\vartheta}}}^{\times}\,{}^{a}\underline{\underline{\boldsymbol{w}}}^{\times} - {}^{a}\underline{\underline{\boldsymbol{w}}}^{\times}\,{}^{a}\underline{\underline{\delta\boldsymbol{\vartheta}}}^{\times} \\
&= \frac{d}{dt}\left({}^{a}\underline{\underline{\delta\boldsymbol{\vartheta}}}^{\times}\right) - \left({}^{a}\underline{\underline{\boldsymbol{w}}}^{\times}\,{}^{a}\underline{\delta\boldsymbol{\vartheta}}\right)^{\times} \\
\Delta\left({}^{b}\underline{\underline{\boldsymbol{w}}}^{\times}\right) &= \frac{d}{dt}\left({}^{b}\underline{\underline{\delta\boldsymbol{\vartheta}}}^{\times}\right) - \dot{\underset{\sim}{\boldsymbol{C}}}^{\mathrm{T}}\,\underset{\sim}{\boldsymbol{C}}\,\underset{\sim}{\boldsymbol{C}}^{\mathrm{T}}\,\Delta\underset{\sim}{\boldsymbol{C}} + \Delta\underset{\sim}{\boldsymbol{C}}^{\mathrm{T}}\,\underset{\sim}{\boldsymbol{C}}\,\underset{\sim}{\boldsymbol{C}}^{\mathrm{T}}\,\dot{\underset{\sim}{\boldsymbol{C}}} \\
&= \frac{d}{dt}\left({}^{b}\underline{\underline{\delta\boldsymbol{\vartheta}}}^{\times}\right) + {}^{b}\underline{\underline{\boldsymbol{w}}}^{\times}\,{}^{b}\underline{\underline{\delta\boldsymbol{\vartheta}}}^{\times} - {}^{b}\underline{\underline{\delta\boldsymbol{\vartheta}}}^{\times}\,{}^{b}\underline{\underline{\boldsymbol{w}}}^{\times} \\
&= \frac{d}{dt}\left({}^{b}\underline{\underline{\delta\boldsymbol{\vartheta}}}^{\times}\right) + \left({}^{b}\underline{\underline{\boldsymbol{w}}}^{\times}\,{}^{b}\underline{\delta\boldsymbol{\vartheta}}\right)^{\times}
\end{aligned} \tag{B.41}$$

or more simply:

$$\begin{aligned}
\Delta\left({}^{a}\underline{\boldsymbol{w}}\right) &= \frac{d}{dt}\left({}^{a}\underline{\delta\boldsymbol{\vartheta}}\right) - {}^{a}\underline{\underline{\boldsymbol{w}}}^{\times}\,{}^{a}\underline{\delta\boldsymbol{\vartheta}} \\
\Delta\left({}^{b}\underline{\boldsymbol{w}}\right) &= \frac{d}{dt}\left({}^{b}\underline{\delta\boldsymbol{\vartheta}}\right) + {}^{b}\underline{\underline{\boldsymbol{w}}}^{\times}\,{}^{b}\underline{\delta\boldsymbol{\vartheta}}
\end{aligned} \tag{B.42}$$

which can also be written in the vector form as:

$$\begin{aligned}
{}^{a}\Delta\underset{\rightarrow}{w} &= {}^{a}\frac{d}{dt}\left(\underset{\rightarrow}{\delta\vartheta}\right) - \underset{\leftrightarrow}{w}^{\times}\cdot\underset{\rightarrow}{\delta\vartheta} = {}^{b}\frac{d}{dt}\left(\underset{\rightarrow}{\delta\vartheta}\right) \\
{}^{b}\Delta\underset{\rightarrow}{w} &= {}^{b}\frac{d}{dt}\left(\underset{\rightarrow}{\delta\vartheta}\right) + \underset{\leftrightarrow}{w}^{\times}\cdot\underset{\rightarrow}{\delta\vartheta} = {}^{a}\frac{d}{dt}\left(\underset{\rightarrow}{\delta\vartheta}\right)
\end{aligned} \tag{B.43}$$

In Eq. (B.43) the vectors ${}^{a}\frac{d}{dt}\left(\underset{\rightarrow}{\delta\vartheta}\right)$ and ${}^{b}\frac{d}{dt}\left(\underset{\rightarrow}{\delta\vartheta}\right)$ can be considered as the virtual angular velocity vectors [47], which are different in the meaning from the variations of the angular velocity vector ${}^{a}\Delta\underset{\rightarrow}{w}$ and ${}^{b}\Delta\underset{\rightarrow}{w}$. In fact, whereas the virtual velocity vectors must obey the problem BCs, the variations of the angular velocity vector can violate them.

Consequently, the variational terms of the general form given in Eq. (B.39) can be

rewritten as:

$$\begin{aligned}
\Delta\mathcal{A} &= \int_t {}^a\Delta\underset{\rightarrow}{w}\cdot\underset{\rightarrow}{v}\,dt = \int_t \Big({}^a\frac{d}{dt}\Big(\underset{\rightarrow}{\delta\vartheta}\Big) - \underset{\leftrightarrow}{w}^{\times}\cdot\underset{\rightarrow}{\delta\vartheta}\Big)\cdot\underset{\rightarrow}{v}\,dt = \int_t {}^b\frac{d}{dt}\Big(\underset{\rightarrow}{\delta\vartheta}\Big)\cdot\underset{\rightarrow}{v}\,dt \\
\Delta\mathcal{A} &= \int_t {}^b\Delta\underset{\rightarrow}{w}\cdot\underset{\rightarrow}{v}\,dt = \int_t \Big({}^b\frac{d}{dt}\Big(\underset{\rightarrow}{\delta\vartheta}\Big) + \underset{\leftrightarrow}{w}^{\times}\cdot\underset{\rightarrow}{\delta\vartheta}\Big)\cdot\underset{\rightarrow}{v}\,dt = \int_t {}^a\frac{d}{dt}\Big(\underset{\rightarrow}{\delta\vartheta}\Big)\cdot\underset{\rightarrow}{v}\,dt
\end{aligned} \tag{B.44}$$

which utilizing the integration by parts, take the following form:

$$\begin{aligned}
\Delta\mathcal{A} = \int_t {}^a\Delta\underset{\rightarrow}{w}\cdot\underset{\rightarrow}{v}\,dt &= -\int_t \underset{\rightarrow}{\delta\vartheta}\cdot\Big({}^a\frac{d}{dt}\Big(\underset{\rightarrow}{v}\Big) - \underset{\leftrightarrow}{w}^{\times}\cdot\underset{\rightarrow}{v}\Big)\,dt + \Big[\underset{\rightarrow}{\delta\vartheta}\cdot\underset{\rightarrow}{v}\Big]_{t_1}^{t_2} \\
&= -\int_t \underset{\rightarrow}{\delta\vartheta}\cdot{}^b\frac{d}{dt}\Big(\underset{\rightarrow}{v}\Big)\,dt + \Big[\underset{\rightarrow}{\delta\vartheta}\cdot\underset{\rightarrow}{v}\Big]_{t_1}^{t_2} \\
\Delta\mathcal{A} = \int_t {}^b\Delta\underset{\rightarrow}{w}\cdot\underset{\rightarrow}{v}\,dt &= -\int_t \underset{\rightarrow}{\delta\vartheta}\cdot\Big({}^b\frac{d}{dt}\Big(\underset{\rightarrow}{v}\Big) + \underset{\leftrightarrow}{w}^{\times}\cdot\underset{\rightarrow}{v}\Big)\,dt + \Big[\underset{\rightarrow}{\delta\vartheta}\cdot\underset{\rightarrow}{v}\Big]_{t_1}^{t_2} \\
&= -\int_t \underset{\rightarrow}{\delta\vartheta}\cdot{}^a\frac{d}{dt}\Big(\underset{\rightarrow}{v}\Big)\,dt + \Big[\underset{\rightarrow}{\delta\vartheta}\cdot\underset{\rightarrow}{v}\Big]_{t_1}^{t_2}
\end{aligned} \tag{B.45}$$

In the end, it is noteworthy that for scalar terms of the form:

$$\mathcal{A} = \int_t \underset{\rightarrow}{w}\cdot\underset{\rightarrow}{v}\,dt \tag{B.46}$$

its variation can be derived by two approaches as:

$$\Delta\mathcal{A} = {}^a\Delta\mathcal{A} = \int_t {}^a\Delta\underset{\rightarrow}{w}\cdot\underset{\rightarrow}{v}\,dt + \int_t \underset{\rightarrow}{w}\cdot{}^a\Delta\underset{\rightarrow}{v}\,dt \tag{B.47}$$

and:

$$\Delta\mathcal{A} = {}^b\Delta\mathcal{A} = \int_t {}^b\Delta\underset{\rightarrow}{w}\cdot\underset{\rightarrow}{v}\,dt + \int_t \underset{\rightarrow}{w}\cdot{}^b\Delta\underset{\rightarrow}{v}\,dt \tag{B.48}$$

The first approach is specially desired for the case:

$${}^a\Delta\underset{\rightarrow}{v} = 0 \tag{B.49}$$

where it will reduce to:

$$\Delta\mathcal{A} = {}^{a}\Delta\mathcal{A} = \int_{t} {}^{a}\Delta\underset{\rightarrow}{w} \cdot \underset{\rightarrow}{v}\, dt \tag{B.50}$$

Analogously, the second approach is more pleasing for the case:

$${}^{b}\Delta\underset{\rightarrow}{v} = 0 \tag{B.51}$$

and will simplify to:

$$\Delta\mathcal{A} = {}^{b}\Delta\mathcal{A} = \int_{t} {}^{b}\Delta\underset{\rightarrow}{w} \cdot \underset{\rightarrow}{v}\, dt \tag{B.52}$$

B.6 Infinitesimal rotation

Now consider rotation problems dealing with infinitesimal angular displacements (*i.e.* infinitesimal rotations or microrotations) where a first-order approximation is desired. For such problems the rotation matrix, described in terms of Euler axis/angle parameters as given by Eq. (B.4), can be approximated as:

$${}^{ab}\underset{\sim}{\boldsymbol{C}} = \underset{\sim}{\boldsymbol{C}}(\underset{\rightarrow}{s}, \vartheta) = \underset{=}{\mathbb{1}} + \vartheta\, \underset{=}{\boldsymbol{s}}^{\times} \tag{B.53}$$

to first order in ϑ. The orthogonality of this rotation matrix can be tested by computing:

$$\begin{aligned} {}^{ab}\underset{\sim}{\boldsymbol{C}}\, {}^{ab}\underset{\sim}{\boldsymbol{C}}^{\mathrm{T}} &= \left(\underset{=}{\mathbb{1}} + \vartheta\, \underset{=}{\boldsymbol{s}}^{\times}\right)\left(\underset{=}{\mathbb{1}} - \vartheta\, \underset{=}{\boldsymbol{s}}^{\times}\right) = \underset{=}{\mathbb{1}} - \vartheta^{2}\, \underset{=}{\boldsymbol{s}}^{\times}\, \underset{=}{\boldsymbol{s}}^{\times} \\ {}^{ab}\underset{\sim}{\boldsymbol{C}}^{\mathrm{T}}\, {}^{ab}\underset{\sim}{\boldsymbol{C}} &= \left(\underset{=}{\mathbb{1}} - \vartheta\, \underset{=}{\boldsymbol{s}}^{\times}\right)\left(\underset{=}{\mathbb{1}} + \vartheta\, \underset{=}{\boldsymbol{s}}^{\times}\right) = \underset{=}{\mathbb{1}} - \vartheta^{2}\, \underset{=}{\boldsymbol{s}}^{\times}\, \underset{=}{\boldsymbol{s}}^{\times} \end{aligned} \tag{B.54}$$

which differ from the identity matrix just by a (negligible) second-order term. Therefore, to first order the infinitesimal rotation matrix is orthogonal.

In addition, for a rotation problem containing two infinitesimal rotations $(\underset{\rightarrow}{s_1}, \vartheta_1)$ and $(\underset{\rightarrow}{s_2}, \vartheta_2)$, one can derive:

$$\begin{aligned} \underset{\sim}{\boldsymbol{C}}(\underset{\rightarrow}{s_1}, \vartheta_1)\, \underset{\sim}{\boldsymbol{C}}(\underset{\rightarrow}{s_2}, \vartheta_2) &= \left(\underset{=}{\mathbb{1}} + \vartheta_1\, \underset{=}{\boldsymbol{s_1}}^{\times}\right)\left(\underset{=}{\mathbb{1}} + \vartheta_2\, \underset{=}{\boldsymbol{s_2}}^{\times}\right) \\ &= \underset{=}{\mathbb{1}} + \vartheta_1\, \underset{=}{\boldsymbol{s_1}}^{\times} + \vartheta_2\, \underset{=}{\boldsymbol{s_2}}^{\times} + \vartheta_1\, \vartheta_2\, \underset{=}{\boldsymbol{s_1}}^{\times}\, \underset{=}{\boldsymbol{s_2}}^{\times} \\ \underset{\sim}{\boldsymbol{C}}(\underset{\rightarrow}{s_2}, \vartheta_2)\, \underset{\sim}{\boldsymbol{C}}(\underset{\rightarrow}{s_1}, \vartheta_1) &= \left(\underset{=}{\mathbb{1}} + \vartheta_2\, \underset{=}{\boldsymbol{s_2}}^{\times}\right)\left(\underset{=}{\mathbb{1}} + \vartheta_1\, \underset{=}{\boldsymbol{s_1}}^{\times}\right) \\ &= \underset{=}{\mathbb{1}} + \vartheta_2\, \underset{=}{\boldsymbol{s_2}}^{\times} + \vartheta_1\, \underset{=}{\boldsymbol{s_1}}^{\times} + \vartheta_2\, \vartheta_1\, \underset{=}{\boldsymbol{s_2}}^{\times}\, \underset{=}{\boldsymbol{s_1}}^{\times} \end{aligned} \tag{B.55}$$

which are equal to first order. Therefore, multiplication of infinitesimal rotation matrices is commutative to first order, that is:

$$\underset{\sim}{\boldsymbol{C}}(\underset{\rightarrow}{s_1}, \vartheta_1)\, \underset{\sim}{\boldsymbol{C}}(\underset{\rightarrow}{s_2}, \vartheta_2) = \underset{\sim}{\boldsymbol{C}}(\underset{\rightarrow}{s_2}, \vartheta_2)\, \underset{\sim}{\boldsymbol{C}}(\underset{\rightarrow}{s_1}, \vartheta_1) \tag{B.56}$$

Equivalently, the order in which infinitesimal rotations occur is irrelevant and infinitesimal rotations can be regarded as vectors (as they are describable by a rotation angle as a magnitude and a rotation axis as a direction, and also obey the parallelogram addition law). For such a case (when rotations are infinitesimal and a first-order approximation is used) the distinction between different rotation parameter sets (*e.g.* Euler axis/angle and Euler angles) tends to vanish [95].

Recalling the relation in Eq. (B.53), it is useful to define the infinitesimal rotation (or microrotation) vector as:

$$\begin{aligned} \underset{\rightarrow}{\vartheta} &= \vartheta\, \underset{\rightarrow}{s} \\ {}^{a}\underset{\sim}{\boldsymbol{\vartheta}} = {}^{b}\underset{\sim}{\boldsymbol{\vartheta}} &= \vartheta\, \underset{\sim}{\boldsymbol{s}} = \begin{bmatrix} \vartheta\, s_1 & \vartheta\, s_2 & \vartheta\, s_3 \end{bmatrix}^{\mathrm{T}} = \begin{bmatrix} \vartheta_1 & \vartheta_2 & \vartheta_3 \end{bmatrix}^{\mathrm{T}} = \underset{\sim}{\boldsymbol{\vartheta}} \end{aligned} \tag{B.57}$$

where ϑ_i represents the infinitesimal rotation of frame $\mathcal{F}_b$ with respect to $\mathcal{F}_a$ around axis $\underset{\rightarrow}{a_i}$ or $\underset{\rightarrow}{b_i}$. Afterwards, for microrotation problems, the rotation matrix from $\mathcal{F}_b$ to $\mathcal{F}_a$ can be written as:

$${}^{ab}\underset{\sim}{\boldsymbol{C}} = \underline{\underline{\mathbb{1}}} + \underline{\underline{\boldsymbol{\vartheta}}}^{\times} \tag{B.58}$$

and inversely:

$${}^{ba}\underset{\sim}{\boldsymbol{C}} = \underline{\underline{\mathbb{1}}} - \underline{\underline{\boldsymbol{\vartheta}}}^{\times} \tag{B.59}$$

Also, for a vector $\underset{\rightarrow}{v}$ and a dyadic $\underset{\leftrightarrow}{d}$:

$$\begin{aligned} {}^{a}\underset{\sim}{\boldsymbol{v}} &= {}^{b}\underset{\sim}{\boldsymbol{v}} + \underline{\underline{\boldsymbol{\vartheta}}}^{\times}\, {}^{b}\underset{\sim}{\boldsymbol{v}} \\ {}^{a}\underline{\underline{\boldsymbol{d}}} &= {}^{b}\underline{\underline{\boldsymbol{d}}} + \underline{\underline{\boldsymbol{\vartheta}}}^{\times}\, {}^{b}\underline{\underline{\boldsymbol{d}}} - {}^{b}\underline{\underline{\boldsymbol{d}}}\, \underline{\underline{\boldsymbol{\vartheta}}}^{\times} \\ {}^{a}\underline{\underline{\boldsymbol{v}}}^{\times} &= {}^{b}\underline{\underline{\boldsymbol{v}}}^{\times} + \underline{\underline{\boldsymbol{\vartheta}}}^{\times}\, {}^{b}\underline{\underline{\boldsymbol{v}}}^{\times} - {}^{b}\underline{\underline{\boldsymbol{v}}}^{\times}\, \underline{\underline{\boldsymbol{\vartheta}}}^{\times} \end{aligned} \tag{B.60}$$

Utilizing Eqs. (B.15) and (B.17), it can be shown that for microrotation problems the angular velocity and acceleration of frame $\mathcal{F}_b$ with respect to frame $\mathcal{F}_a$ are:

$$\begin{aligned} \underset{\rightarrow}{w} &= \dot{\underset{\rightarrow}{\vartheta}} \\ {}^{a}\underset{\sim}{\boldsymbol{w}} &= {}^{b}\underset{\sim}{\boldsymbol{w}} = \underset{\sim}{\boldsymbol{w}} = \dot{\underset{\sim}{\boldsymbol{\vartheta}}} \end{aligned} \tag{B.61}$$

where:

$$\begin{aligned} \dot{\underset{\rightarrow}{\vartheta}} &= {}^{a}\frac{d}{dt}\left(\underset{\rightarrow}{\vartheta}\right) = {}^{b}\frac{d}{dt}\left(\underset{\rightarrow}{\vartheta}\right) \\ \dot{\underline{\boldsymbol{\vartheta}}} &= \frac{d}{dt}\left(\underline{\boldsymbol{\vartheta}}\right) = \begin{bmatrix} \dot{\vartheta}_1 & \dot{\vartheta}_2 & \dot{\vartheta}_3 \end{bmatrix}^{\mathrm{T}} \end{aligned} \tag{B.62}$$

and:

$$\begin{aligned} \dot{\underset{\rightarrow}{w}} &= \ddot{\underset{\rightarrow}{\vartheta}} \\ {}^{a}\dot{\underline{\boldsymbol{w}}} &= {}^{b}\dot{\underline{\boldsymbol{w}}} = \dot{\underline{\boldsymbol{w}}} = \ddot{\underline{\boldsymbol{\vartheta}}} \end{aligned} \tag{B.63}$$

where:

$$\begin{aligned} \ddot{\underset{\rightarrow}{\vartheta}} &= {}^{a}\frac{d^2}{dt^2}\left(\underset{\rightarrow}{\vartheta}\right) = {}^{b}\frac{d^2}{dt^2}\left(\underset{\rightarrow}{\vartheta}\right) \\ \ddot{\underline{\boldsymbol{\vartheta}}} &= \frac{d^2}{dt^2}\left(\underline{\boldsymbol{\vartheta}}\right) = \begin{bmatrix} \ddot{\vartheta}_1 & \ddot{\vartheta}_2 & \ddot{\vartheta}_3 \end{bmatrix}^{\mathrm{T}} \end{aligned} \tag{B.64}$$

Note that here, the time integral of the angular velocity vector $\underset{\rightarrow}{w}$ is meaningful and is the same as the microrotation vector $\underset{\rightarrow}{\vartheta}$. Additionally, for the time derivative of a vector $\underset{\rightarrow}{v}$ and a dyadic $\underset{\leftrightarrow}{d}$, one can get:

$$\begin{aligned} {}^{a}\frac{d}{dt}\left(\underset{\rightarrow}{v}\right) &= {}^{b}\frac{d}{dt}\left(\underset{\rightarrow}{v}\right) + \dot{\underset{\leftrightarrow}{\vartheta}}^{\times} \cdot \underset{\rightarrow}{v} \\ {}^{a}\frac{d}{dt}\left(\underset{\leftrightarrow}{d}\right) &= {}^{b}\frac{d}{dt}\left(\underset{\leftrightarrow}{d}\right) + \dot{\underset{\leftrightarrow}{\vartheta}}^{\times} \cdot \underset{\leftrightarrow}{d} - \underset{\leftrightarrow}{d} \cdot \dot{\underset{\leftrightarrow}{\vartheta}}^{\times} \end{aligned} \tag{B.65}$$

The virtual rotation vector for the case of microrotations, *i.e.* $\delta\underset{\rightarrow}{\vartheta}$, can be derived from Eq. (B.27) as:

$$\begin{aligned} \delta\underset{\rightarrow}{\vartheta} &= \Delta\left(\underset{\rightarrow}{\vartheta}\right) \\ {}^{a}\delta\underline{\boldsymbol{\vartheta}} &= {}^{b}\delta\underline{\boldsymbol{\vartheta}} = \delta\underline{\boldsymbol{\vartheta}} = \Delta\left(\underline{\boldsymbol{\vartheta}}\right) \end{aligned} \tag{B.66}$$

where:

$$\begin{aligned} \Delta\left(\underset{\rightarrow}{\vartheta}\right) &= {}^{a}\Delta\underset{\rightarrow}{\vartheta} = {}^{b}\Delta\underset{\rightarrow}{\vartheta} \\ \Delta\left(\underline{\boldsymbol{\vartheta}}\right) &= \Delta\left(\begin{bmatrix} \vartheta_1 & \vartheta_2 & \vartheta_3 \end{bmatrix}^{\mathrm{T}}\right) = \begin{bmatrix} \delta\vartheta_1 & \delta\vartheta_2 & \delta\vartheta_3 \end{bmatrix}^{\mathrm{T}} \end{aligned} \tag{B.67}$$

Besides, the following relations can be obtained from Eqs. (B.43) and (B.45) for the case of microrotation problems (which might be useful when applying the calculus of variations

to them):

$$
\begin{aligned}
{}^{a}\Delta\underset{\rightarrow}{w} &= {}^{a}\frac{d}{dt}\left(\delta\underset{\rightarrow}{\vartheta}\right) - \dot{\underset{\leftrightarrow}{\vartheta}}^{\times}\cdot\delta\underset{\rightarrow}{\vartheta} = {}^{b}\frac{d}{dt}\left(\delta\underset{\rightarrow}{\vartheta}\right) \\
{}^{b}\Delta\underset{\rightarrow}{w} &= {}^{b}\frac{d}{dt}\left(\delta\underset{\rightarrow}{\vartheta}\right) + \dot{\underset{\leftrightarrow}{\vartheta}}^{\times}\cdot\delta\underset{\rightarrow}{\vartheta} = {}^{a}\frac{d}{dt}\left(\delta\underset{\rightarrow}{\vartheta}\right)
\end{aligned}
\tag{B.68}
$$

$$
\begin{aligned}
\Delta\mathcal{A} = \int_t {}^{a}\Delta\underset{\rightarrow}{w}\cdot\underset{\rightarrow}{v}\,dt &= -\int_t \delta\underset{\rightarrow}{\vartheta}\cdot\left({}^{a}\frac{d}{dt}\left(\underset{\rightarrow}{v}\right) - \dot{\underset{\leftrightarrow}{\vartheta}}^{\times}\cdot\underset{\rightarrow}{v}\right)dt + \left[\delta\underset{\rightarrow}{\vartheta}\cdot\underset{\rightarrow}{v}\right]_{t_1}^{t_2} \\
&= -\int_t \delta\underset{\rightarrow}{\vartheta}\cdot{}^{b}\frac{d}{dt}\left(\underset{\rightarrow}{v}\right)dt + \left[\delta\underset{\rightarrow}{\vartheta}\cdot\underset{\rightarrow}{v}\right]_{t_1}^{t_2} \\
\Delta\mathcal{A} = \int_t {}^{b}\Delta\underset{\rightarrow}{w}\cdot\underset{\rightarrow}{v}\,dt &= -\int_t \delta\underset{\rightarrow}{\vartheta}\cdot\left({}^{b}\frac{d}{dt}\left(\underset{\rightarrow}{v}\right) + \dot{\underset{\leftrightarrow}{\vartheta}}^{\times}\cdot\underset{\rightarrow}{v}\right)dt + \left[\delta\underset{\rightarrow}{\vartheta}\cdot\underset{\rightarrow}{v}\right]_{t_1}^{t_2} \\
&= -\int_t \delta\underset{\rightarrow}{\vartheta}\cdot{}^{a}\frac{d}{dt}\left(\underset{\rightarrow}{v}\right)dt + \left[\delta\underset{\rightarrow}{\vartheta}\cdot\underset{\rightarrow}{v}\right]_{t_1}^{t_2}
\end{aligned}
\tag{B.69}
$$

Considering Eq. (B.68), it is noteworthy that whereas Eqs. (B.61) and (B.66) hold true for microrotation problems, *i.e.* ${}^{a}\underline{\boldsymbol{w}} = {}^{b}\underline{\boldsymbol{w}} = \underline{\dot{\boldsymbol{\vartheta}}}$ and ${}^{a}\delta\underline{\boldsymbol{\vartheta}} = {}^{b}\delta\underline{\boldsymbol{\vartheta}} = \delta\underline{\boldsymbol{\vartheta}}$, the variation of the angular velocity in frame $\mathcal{F}_a$ is not the same as that in frame $\mathcal{F}_b$, *i.e.* ${}^{a}\Delta\underset{\rightarrow}{w} \neq {}^{b}\Delta\underset{\rightarrow}{w}$. In fact, considering:

$${}^{a}\Delta\underset{\rightarrow}{w} = {}^{b}\Delta\underset{\rightarrow}{w} = {}^{a}\frac{d}{dt}\left(\delta\underset{\rightarrow}{\vartheta}\right) = {}^{b}\frac{d}{dt}\left(\delta\underset{\rightarrow}{\vartheta}\right) = \delta\dot{\underset{\rightarrow}{\vartheta}}$$

will result in missing some important terms through the variational calculus procedure. Consequently, to prevent from any confusion when dealing with microrotations, where the angular velocity vector $\underset{\rightarrow}{w}$ is substituted with vector $\dot{\underset{\rightarrow}{\vartheta}}$, the following important relations are introduced and will be used:

$$
\begin{aligned}
{}^{a}\Delta\dot{\underset{\rightarrow}{\vartheta}} &= {}^{a}\frac{d}{dt}\left(\delta\underset{\rightarrow}{\vartheta}\right) - \dot{\underset{\leftrightarrow}{\vartheta}}^{\times}\cdot\delta\underset{\rightarrow}{\vartheta} = {}^{b}\frac{d}{dt}\left(\delta\underset{\rightarrow}{\vartheta}\right) \neq {}^{a}\frac{d}{dt}\left(\delta\underset{\rightarrow}{\vartheta}\right) \\
{}^{b}\Delta\dot{\underset{\rightarrow}{\vartheta}} &= {}^{b}\frac{d}{dt}\left(\delta\underset{\rightarrow}{\vartheta}\right) + \dot{\underset{\leftrightarrow}{\vartheta}}^{\times}\cdot\delta\underset{\rightarrow}{\vartheta} = {}^{a}\frac{d}{dt}\left(\delta\underset{\rightarrow}{\vartheta}\right) \neq {}^{b}\frac{d}{dt}\left(\delta\underset{\rightarrow}{\vartheta}\right)
\end{aligned}
\tag{B.70}
$$

In the end, the results obtained in this section for microrotation problems are summarized in Table B.1. The relations given in this table correspond to the infinitesimal angular displacement of a frame $\mathcal{F}_b$ with respect to another frame $\mathcal{F}_a$.

Table B.1: A summary of the useful relations for microrotation problems.

Relation	**Vector Form**	**Matrix Form (in $\mathcal{F}_a$ or $\mathcal{F}_b$)**
Rotation Vector	$\underset{\rightarrow}{\vartheta}$	$\underline{\boldsymbol{\vartheta}} = \left[\begin{array}{ccc} \vartheta_1 & \vartheta_2 & \vartheta_3 \end{array}\right]^{\mathrm{T}}$
Rotation Tensor (Rotation Dyadic)	$\underset{\leftrightarrow}{\vartheta}^{\times}$	$\underline{\underline{\boldsymbol{\vartheta}}}^{\times} = \left[\begin{array}{ccc} 0 & -\vartheta_3 & \vartheta_2 \\ \vartheta_3 & 0 & -\vartheta_1 \\ -\vartheta_2 & \vartheta_1 & 0 \end{array}\right]$
Rotation Matrix	not applicable	${}^{ab}\underset{\sim}{\boldsymbol{C}} = \underline{\underline{\mathbb{1}}} + \underline{\underline{\boldsymbol{\vartheta}}}^{\times}$ ${}^{ba}\underset{\sim}{\boldsymbol{C}} = \underline{\underline{\mathbb{1}}} - \underline{\underline{\boldsymbol{\vartheta}}}^{\times}$
Angular Velocity Vector $\underset{\rightarrow}{w}$	$\underset{\rightarrow}{\dot{\vartheta}} = {}^{a}\dfrac{d}{dt}\left(\underset{\rightarrow}{\vartheta}\right) = {}^{b}\dfrac{d}{dt}\left(\underset{\rightarrow}{\vartheta}\right)$	$\underline{\dot{\boldsymbol{\vartheta}}} = \dfrac{d}{dt}\left(\underline{\boldsymbol{\vartheta}}\right) = \left[\begin{array}{ccc} \dot{\vartheta}_1 & \dot{\vartheta}_2 & \dot{\vartheta}_3 \end{array}\right]^{\mathrm{T}}$
Angular Acceleration Vector $\underset{\rightarrow}{\dot{w}}$	$\underset{\rightarrow}{\ddot{\vartheta}} = {}^{a}\dfrac{d}{dt}\left(\underset{\rightarrow}{\dot{\vartheta}}\right) = {}^{b}\dfrac{d}{dt}\left(\underset{\rightarrow}{\dot{\vartheta}}\right)$	$\underline{\ddot{\boldsymbol{\vartheta}}} = \dfrac{d}{dt}\left(\underline{\dot{\boldsymbol{\vartheta}}}\right) = \left[\begin{array}{ccc} \ddot{\vartheta}_1 & \ddot{\vartheta}_2 & \ddot{\vartheta}_3 \end{array}\right]^{\mathrm{T}}$
Virtual Rotation Vector	$\delta\underset{\rightarrow}{\vartheta} = {}^{a}\Delta\underset{\rightarrow}{\vartheta} = {}^{b}\Delta\underset{\rightarrow}{\vartheta}$	$\delta\underline{\boldsymbol{\vartheta}} = \Delta\left(\underline{\boldsymbol{\vartheta}}\right) = \left[\begin{array}{ccc} \delta\vartheta_1 & \delta\vartheta_2 & \delta\vartheta_3 \end{array}\right]^{\mathrm{T}}$
Variation of Angular Velocity Vector	${}^{a}\Delta\underset{\rightarrow}{\dot{\vartheta}} = {}^{b}\dfrac{d}{dt}\left(\delta\underset{\rightarrow}{\vartheta}\right) = {}^{a}\dfrac{d}{dt}\left(\delta\underset{\rightarrow}{\vartheta}\right) - \underset{\leftrightarrow}{\dot{\vartheta}}^{\times}\cdot\delta\underset{\rightarrow}{\vartheta}$ ${}^{b}\Delta\underset{\rightarrow}{\dot{\vartheta}} = {}^{a}\dfrac{d}{dt}\left(\delta\underset{\rightarrow}{\vartheta}\right) = {}^{b}\dfrac{d}{dt}\left(\delta\underset{\rightarrow}{\vartheta}\right) + \underset{\leftrightarrow}{\dot{\vartheta}}^{\times}\cdot\delta\underset{\rightarrow}{\vartheta}$	${}^{a}\Delta\underline{\dot{\boldsymbol{\vartheta}}} = {}^{b}\dfrac{d}{dt}\left(\delta\underline{\boldsymbol{\vartheta}}\right) = {}^{a}\dfrac{d}{dt}\left(\delta\underline{\boldsymbol{\vartheta}}\right) - \underline{\underline{\dot{\boldsymbol{\vartheta}}}}^{\times}\,\delta\underline{\boldsymbol{\vartheta}}$ ${}^{b}\Delta\underline{\dot{\boldsymbol{\vartheta}}} = {}^{a}\dfrac{d}{dt}\left(\delta\underline{\boldsymbol{\vartheta}}\right) = {}^{b}\dfrac{d}{dt}\left(\delta\underline{\boldsymbol{\vartheta}}\right) + \underline{\underline{\dot{\boldsymbol{\vartheta}}}}^{\times}\,\delta\underline{\boldsymbol{\vartheta}}$
Miscellaneous	${}^{a}\Delta\underset{\rightarrow}{\dot{\vartheta}} \neq {}^{b}\Delta\underset{\rightarrow}{\dot{\vartheta}},\ {}^{a}\dfrac{d}{dt}\left(\delta\underset{\rightarrow}{\vartheta}\right) \neq {}^{b}\dfrac{d}{dt}\left(\delta\underset{\rightarrow}{\vartheta}\right)$	${}^{a}\Delta\underline{\dot{\boldsymbol{\vartheta}}} \neq {}^{b}\Delta\underline{\dot{\boldsymbol{\vartheta}}},\ {}^{a}\dfrac{d}{dt}\left(\delta\underline{\boldsymbol{\vartheta}}\right) \neq {}^{b}\dfrac{d}{dt}\left(\delta\underline{\boldsymbol{\vartheta}}\right)$

B.7 Discrepancies

When dealing with infinitesimal rotations some references suggested and used a second-order approximation while regarding the infinitesimal rotations as vectors [2, 23, 26–28, 30, 31, 33, 34, 95, 99]. However, it will be shown in this section that when using a second-order approximation the infinitesimal rotations cannot be defined as vectors. More precisely, infinitesimal rotations do not obey the parallelogram addition law if the second-order terms are taken into account.

The rotation matrix given by Eq. (B.4) can be written to second order as:

$$ {}^{ab}\underset{\sim}{\boldsymbol{C}} = \underset{\sim}{\boldsymbol{C}}(\underset{\rightarrow}{s}, \vartheta) = \underline{\underline{\mathbb{1}}} + \vartheta\, \underline{\underline{\boldsymbol{s}}}^{\times} + \frac{1}{2}\,\vartheta^2\, \underline{\underline{\boldsymbol{s}}}^{\times}\, \underline{\underline{\boldsymbol{s}}}^{\times} \tag{B.71} $$

which is orthogonal to second order as matrices:

$$ \begin{aligned} {}^{ab}\underset{\sim}{\boldsymbol{C}}\, {}^{ab}\underset{\sim}{\boldsymbol{C}}^{\mathrm{T}} &= \left(\underline{\underline{\mathbb{1}}} + \vartheta\, \underline{\underline{\boldsymbol{s}}}^{\times} + \frac{1}{2}\,\vartheta^2\, \underline{\underline{\boldsymbol{s}}}^{\times}\, \underline{\underline{\boldsymbol{s}}}^{\times}\right)\left(\underline{\underline{\mathbb{1}}} - \vartheta\, \underline{\underline{\boldsymbol{s}}}^{\times} + \frac{1}{2}\,\vartheta^2\, \underline{\underline{\boldsymbol{s}}}^{\times}\, \underline{\underline{\boldsymbol{s}}}^{\times}\right) \\ &= \underline{\underline{\mathbb{1}}} + \frac{1}{4}\,\vartheta^4\, \underline{\underline{\boldsymbol{s}}}^{\times}\, \underline{\underline{\boldsymbol{s}}}^{\times}\, \underline{\underline{\boldsymbol{s}}}^{\times}\, \underline{\underline{\boldsymbol{s}}}^{\times} \end{aligned} \tag{B.72} $$

and:

$$ \begin{aligned} {}^{ab}\underset{\sim}{\boldsymbol{C}}^{\mathrm{T}}\, {}^{ab}\underset{\sim}{\boldsymbol{C}} &= \left(\underline{\underline{\mathbb{1}}}_{\vartheta}\, \underline{\underline{\boldsymbol{s}}}^{\times} + \frac{1}{2}\,\vartheta^2\, \underline{\underline{\boldsymbol{s}}}^{\times}\, \underline{\underline{\boldsymbol{s}}}^{\times}\right)\left(\underline{\underline{\mathbb{1}}} + \vartheta\, \underline{\underline{\boldsymbol{s}}}^{\times} + \frac{1}{2}\,\vartheta^2\, \underline{\underline{\boldsymbol{s}}}^{\times}\, \underline{\underline{\boldsymbol{s}}}^{\times}\right) \\ &= \underline{\underline{\mathbb{1}}} + \frac{1}{4}\,\vartheta^4\, \underline{\underline{\boldsymbol{s}}}^{\times}\, \underline{\underline{\boldsymbol{s}}}^{\times}\, \underline{\underline{\boldsymbol{s}}}^{\times}\, \underline{\underline{\boldsymbol{s}}}^{\times} \end{aligned} \tag{B.73} $$

differ from the identity matrix just by a (negligible) fourth order term.

However, for a rotation problem containing two infinitesimal rotations $(\underset{\rightarrow}{s}_1, \vartheta_1)$ and $(\underset{\rightarrow}{s}_2, \vartheta_2)$, one can derive (to second order):

$$ \begin{aligned} \underset{\sim}{\boldsymbol{C}}(\underset{\rightarrow}{s}_1, \vartheta_1)\, \underset{\sim}{\boldsymbol{C}}(\underset{\rightarrow}{s}_2, \vartheta_2) &= \underline{\underline{\mathbb{1}}} + \vartheta_1\, \underline{\underline{\boldsymbol{s_1}}}^{\times} + \frac{1}{2}\,\vartheta_1^2\, \underline{\underline{\boldsymbol{s_1}}}^{\times}\, \underline{\underline{\boldsymbol{s_1}}}^{\times} + \vartheta_2\, \underline{\underline{\boldsymbol{s_2}}}^{\times} + \frac{1}{2}\,\vartheta_2^2\, \underline{\underline{\boldsymbol{s_2}}}^{\times}\, \underline{\underline{\boldsymbol{s_2}}}^{\times} \\ &\quad + \vartheta_1\,\vartheta_2\, \underline{\underline{\boldsymbol{s_1}}}^{\times}\, \underline{\underline{\boldsymbol{s_2}}}^{\times} \\ \underset{\sim}{\boldsymbol{C}}(\underset{\rightarrow}{s}_2, \vartheta_2)\, \underset{\sim}{\boldsymbol{C}}(\underset{\rightarrow}{s}_1, \vartheta_1) &= \underline{\underline{\mathbb{1}}} + \vartheta_2\, \underline{\underline{\boldsymbol{s_2}}}^{\times} + \frac{1}{2}\,\vartheta_2^2\, \underline{\underline{\boldsymbol{s_2}}}^{\times}\, \underline{\underline{\boldsymbol{s_2}}}^{\times} + \vartheta_1\, \underline{\underline{\boldsymbol{s_1}}}^{\times} + \frac{1}{2}\,\vartheta_1^2\, \underline{\underline{\boldsymbol{s_1}}}^{\times}\, \underline{\underline{\boldsymbol{s_1}}}^{\times} \\ &\quad + \vartheta_2\,\vartheta_1\, \underline{\underline{\boldsymbol{s_2}}}^{\times}\, \underline{\underline{\boldsymbol{s_1}}}^{\times} \end{aligned} \tag{B.74} $$

which are not equal to second order as in general:

$$ \underline{\underline{\boldsymbol{s_1}}}^{\times}\, \underline{\underline{\boldsymbol{s_2}}}^{\times} \neq \underline{\underline{\boldsymbol{s_2}}}^{\times}\, \underline{\underline{\boldsymbol{s_1}}}^{\times} \tag{B.75} $$

Therefore, multiplication of infinitesimal rotation matrices is not commutative to second order, that is:

$$\underset{\sim}{\boldsymbol{C}}(\underset{\rightarrow}{s_1}, \vartheta_1)\, \underset{\sim}{\boldsymbol{C}}(\underset{\rightarrow}{s_2}, \vartheta_2) \neq \underset{\sim}{\boldsymbol{C}}(\underset{\rightarrow}{s_2}, \vartheta_2)\, \underset{\sim}{\boldsymbol{C}}(\underset{\rightarrow}{s_1}, \vartheta_1) \tag{B.76}$$

Equivalently, the order in which infinitesimal rotations are applied is important and infinitesimal rotations cannot be considered as vectors (as they do not obey the parallelogram addition law).

It is worthwhile to note that to the best of this author's knowledge in the aforementioned references a simple incomplete variational calculus was considered for derivation of the dynamic equations from the system Lagrangian. However, by using this simple incomplete variational formulation where:

$$^{a}\Delta\underset{\rightarrow}{w} = {}^{b}\Delta\underset{\rightarrow}{w} = {}^{a}\frac{d}{dt}\Big(\delta\underset{\rightarrow}{\vartheta}\Big) = {}^{b}\frac{d}{dt}\Big(\delta\underset{\rightarrow}{\vartheta}\Big) = \delta\underset{\rightarrow}{\dot{\vartheta}}$$

some important terms will be missed from the dynamic equations provided a first-order approximation in infinitesimal rotations is used. This fact induced the authors to, while treating the infinitesimal rotations as vectors, utilize a second-order approximation in infinitesimal rotations (which is inconsistent). Recall that a more appropriate approach is using a first-order approximation for the infinitesimal rotations, regarding them as vectors, and using the complete variational formulation, derived in the previous section and summarized in Table B.1, for handling the variational terms including the infinitesimal rotations.

Appendix C

Numerical Analysis of Micropolar Elastic Beams

C.1 Introduction

Despite the classical gyrobeams which are based on the well-known classical torsion and bending theories (*i.e.* Duleau torsion theory [50] and Euler-Bernoulli or Timoshenko bending theory), the micropolar gyrobeams are founded on newly developed (unfamiliar) micropolar torsion and bending theories. Study of these new theories through examination of micropolar elastic beams (carrying no gyricity) is accordingly worth a few pages of this text. This examination, including a comparison of micropolar and classical elastic beams, lays a groundwork for a better understanding of the more complicated micropolar gyrobeams and their differences with the classical gyrobeams.

Due to the general lack of analytical solutions for static and dynamic problems of micropolar elastic beams, the 3D micropolar elastic beams are examined numerically via two sets of examples. The first set of numerical examples is aimed at focusing on the static behavior of micropolar elastic beams where this behavior is compared to the static behavior of classical elastic beams. The second set of examples compares the dynamic behavior of micropolar and classical elastic beams in terms of their natural frequencies

and mode shapes. The examples also reveal the effects of micropolar elastic constants on different behaviors of micropolar beams.

In the designed numerical examples the micropolar beams will be examined only against the classical beams which employ the Timoshenko theory to predict the bending deformations. The comparison of micropolar elastic beams with those classical elastic beams utilizing the Euler-Bernoulli bending theory will be made easily as the relationships between the Timoshenko and Euler-Bernoulli bending theories are extensively addressed in the literature. Henceforth, the term "classical beams" in this appendix will exclusively refer to those beams which are modeled employing the Timoshenko bending theory in addition to the simple longitudinal deformation theory (Hooke's law) and the Duleau torsion theory. The term "micropolar beams", on the other hand, refer to those beams founded on the micropolar torsion and bending theories (developed in this text) along with the simple longitudinal deformation theory.

The 3D micropolar and classical elastic beams selected for numerical analyses are classically cantilevered uniform beams along the first axis of the inertial reference frame (the principal axes of beams' cross sections are assumed to be parallel to the second and third coordinate axes of the inertial frame). The beams' properties (geometries, inertia densities, and elastic constants) are assumed constant over the beam length. The FEM-based numerical models of these beams are implemented in MATLAB® [66] using the parameters summarized in Tables C.1 and C.2.

The beams have four modes of deformation, *i.e.* longitudinal displacement along the ${}^{c}\hat{x}_1$ axis, torsional rotation around the ${}^{c}\hat{x}_1$ axis, bending deformation in the ${}^{c}\hat{x}_1{}^{c}\hat{x}_2$ plane, and bending deformation in the ${}^{c}\hat{x}_1{}^{c}\hat{x}_3$ plane; in the absence of gyricity terms these are decoupled and a full comparison of the micropolar and classical elastic beam models can be done in four stages, focusing only on one deformation mode at each stage. However, since the two models predict the same longitudinal displacements (the governing equations are identical) and the two bending modes in the ${}^{c}\hat{x}_1{}^{c}\hat{x}_2$ and ${}^{c}\hat{x}_1{}^{c}\hat{x}_3$ planes are similar, in this appendix only the torsional rotation around the ${}^{c}\hat{x}_1$ axis and bending deformations in the ${}^{c}\hat{x}_1{}^{c}\hat{x}_2$ plane are subjects of the analysis and comparison of micropolar and classical elastic beams.

Table C.1: Summary of the main dimensionless parameters used in the numerical micropolar and classical elastic beam models.

Parameter	**Value(s)**
$\hat{R}_3 = \hat{R}_2 = \sqrt{2}\,\hat{R}_1$	10, 50, and 250
$\hat{\mu}$	$\frac{3}{8}$
k_{t}	1
$k_{\mathrm{s}_2} = k_{\mathrm{s}_3}$	1
$\log(\hat{\kappa})$	$[-10, 2]$
$\log(\hat{\gamma}) = \log(\hat{\beta})$	$[-10, 2]$
ξ	$\frac{1}{2}$
$\hat{\imath}^V$ $({}^b\hat{\underline{\underline{\boldsymbol{\imath}}}}^V = \hat{\imath}^V\,\underline{\underline{\mathbb{1}}})$	0 and 1×10^{-6}

Table C.2: Summary of the main FEM parameters used in the numerical micropolar and classical elastic beam models.

Parameter	**Value**
Element Type	C^0 four-node
Basis Functions	cubic Lagrange polynomials
Number of Elements	16
Number of Nodes	49 (distributed evenly)
DOFs per Node	6 (for classical beams)
	9 (for micropolar beams)
Longitudinal BCs	fixed-free
Torsional BCs	classical fixed-free
Bending BCs	classical clamped-free

C.2 Static analysis

The static equations of micropolar and classical beams can be obtained by simplifying the micropolar and classical gyrobeam dynamic equations given by Eqs. (4.100) and (4.101) (*i.e.* by eliminating the inertia and gyricity related terms). In this section the static torsional deformations about the ${}^c\hat{x}_1$ axis and static bending deformations in the ${}^c\hat{x}_1{}^c\hat{x}_2$ plane are subjects of the comparison between micropolar and classical beam models. This means that the following set of micropolar beam static equations:

$$\begin{aligned}
\hat{\bar{m}}_1^{\,L} &= -k_{\mathrm{t}}\,\hat{\mu}\,\hat{I}_1\,\bar{\theta}_{1,\hat{1}\hat{1}} - \hat{\kappa}\,\hat{I}_1\left(\bar{\theta}_{1,\hat{1}\hat{1}} - 2\,\xi\,\bar{\vartheta}_{1,\hat{1}\hat{1}}\right) + 4\,\hat{\kappa}\left(\bar{\theta}_1 - \bar{\vartheta}_1\right)\\
\hat{\bar{m}}_1^{\,V} &= -\hat{\mathcal{E}}\,\bar{\vartheta}_{1,\hat{1}\hat{1}} + 2\,\xi\,\hat{\kappa}\,\hat{I}_1\left(\bar{\theta}_{1,\hat{1}\hat{1}} - 2\,\xi\,\bar{\vartheta}_{1,\hat{1}\hat{1}}\right) - 4\,\hat{\kappa}\left(\bar{\theta}_1 - \bar{\vartheta}_1\right)\\
\hat{\bar{f}}_2^{\,V} &= -k_{\mathrm{s}_2}\,\hat{\mu}\left(\hat{\bar{u}}_{2,\hat{1}\hat{1}} - \bar{\theta}_{3,\hat{1}}\right) - \hat{\kappa}\left(\hat{\bar{u}}_{2,\hat{1}\hat{1}} + \bar{\theta}_{3,\hat{1}} - 2\,\bar{\vartheta}_{3,\hat{1}}\right)\\
\hat{\bar{m}}_3^{\,L} &= -\hat{I}_3\,\bar{\theta}_{3,\hat{1}\hat{1}} - k_{\mathrm{s}_2}\,\hat{\mu}\left(\hat{\bar{u}}_{2,\hat{1}} - \bar{\theta}_3\right) + \hat{\kappa}\left(\hat{\bar{u}}_{2,\hat{1}} + \bar{\theta}_3 - 2\,\bar{\vartheta}_3\right)\\
\hat{\bar{m}}_3^{\,V} &= -\left(\hat{\gamma} + \hat{\beta}\right)\bar{\vartheta}_{3,\hat{1}\hat{1}} - 2\,\hat{\kappa}\left(\hat{\bar{u}}_{2,\hat{1}} + \bar{\theta}_3 - 2\,\bar{\vartheta}_3\right)
\end{aligned} \tag{C.1}$$

will be compared to the following set of classical beam static equations:

$$\begin{aligned}
\hat{\bar{m}}_1^{\,L} + \hat{\bar{m}}_1^{\,V} &= -k_{\mathrm{t}}\,\hat{\mu}\,\hat{I}_1\,\bar{\theta}_{1,\hat{1}\hat{1}}\\
\hat{\bar{f}}_2^{\,V} &= -k_{\mathrm{s}_2}\,\hat{\mu}\left(\hat{\bar{u}}_{2,\hat{1}\hat{1}} - \bar{\theta}_{3,\hat{1}}\right)\\
\hat{\bar{m}}_3^{\,L} + \hat{\bar{m}}_3^{\,V} &= -\hat{I}_3\,\bar{\theta}_{3,\hat{1}\hat{1}} - k_{\mathrm{s}_2}\,\hat{\mu}\left(\hat{\bar{u}}_{2,\hat{1}} - \bar{\theta}_3\right)
\end{aligned} \tag{C.2}$$

after imposing the classically cantilevered BCs (as described in Table C.2) on both.

The PDEs given by Eqs. (C.1) and (C.2), may be compared in terms of their homogeneous form characteristic equations and characteristic roots which exemplify the PDEs general homogeneous solution (without accounting for the BCs). Here, by rewriting the first two relations of Eq. (C.1), corresponding to the micropolar beam torsion, as:

$$\hat{\underset{\sim}{\mathcal{Q}}} = \hat{\underset{\sim}{\mathcal{K}}}_{\hat{1}\hat{1}}\,\hat{\underset{\sim}{q}}_{,\hat{1}\hat{1}} + \hat{\underset{\sim}{\mathcal{K}}}\,\hat{\underset{\sim}{q}} \tag{C.3}$$

where:

$$\begin{aligned}
\hat{\underset{\sim}{\mathcal{Q}}} &= \begin{bmatrix} \hat{\bar{m}}_1^{\,L} & \hat{\bar{m}}_1^{\,V} \end{bmatrix}^{\mathrm{T}}\\
\hat{\underset{\sim}{q}} &= \begin{bmatrix} \bar{\theta}_1 & \bar{\vartheta}_1 \end{bmatrix}^{\mathrm{T}}
\end{aligned} \tag{C.4}$$

$$\hat{\underset{\sim}{\boldsymbol{\mathcal{K}}}}_{\hat{1}\hat{1}} = \begin{bmatrix} -\left(k_{\mathrm{t}}\,\hat{\mu}+\hat{\kappa}\right)\hat{I}_1 & 2\,\xi\,\hat{\kappa}\,\hat{I}_1 \\ 2\,\xi\,\hat{\kappa}\,\hat{I}_1 & -\left(\hat{\mathcal{E}}+4\,\xi^2\,\hat{\kappa}\,\hat{I}_1\right) \end{bmatrix} \tag{C.5}$$

$$\hat{\underset{\sim}{\boldsymbol{\mathcal{K}}}} = \begin{bmatrix} 4\,\hat{\kappa} & -4\,\hat{\kappa} \\ -4\,\hat{\kappa} & 4\,\hat{\kappa} \end{bmatrix} \tag{C.6}$$

the characteristic equation of the micropolar beam torsion will be obtained as:

$$\hat{I}_1\left(k_{\mathrm{t}}\,\hat{\mu}\,\hat{\mathcal{E}}+\hat{\kappa}\,\hat{\mathcal{E}}+4\,\xi^2\,k_{\mathrm{t}}\,\hat{\mu}\,\hat{\kappa}\,\hat{I}_1\right)\hat{r}^4-4\,\hat{\kappa}\left(k_{\mathrm{t}}\,\hat{\mu}\,\hat{I}_1+\left(2\,\xi-1\right)^2\hat{\kappa}\,\hat{I}_1+\hat{\mathcal{E}}\right)\hat{r}^2=0 \tag{C.7}$$

which has four roots:

$$\begin{aligned} &\hat{r}_1=\hat{r}_2=0 \\ &\hat{r}_3=-\hat{r}_4=+2\sqrt{\frac{\hat{\kappa}\left(k_{\mathrm{t}}\,\hat{\mu}\,\hat{I}_1+\left(2\,\xi-1\right)^2\hat{\kappa}\,\hat{I}_1+\hat{\mathcal{E}}\right)}{\hat{I}_1\left(k_{\mathrm{t}}\,\hat{\mu}\,\hat{\mathcal{E}}+\hat{\kappa}\,\hat{\mathcal{E}}+4\,\xi^2\,k_{\mathrm{t}}\,\hat{\mu}\,\hat{\kappa}\,\hat{I}_1\right)}} \end{aligned} \tag{C.8}$$

Noting that the characteristic equation corresponding to the homogeneous classical torsion PDE, *i.e.* the first relation of Eq. (C.2), is:

$$k_{\mathrm{t}}\,\hat{\mu}\,\hat{I}_1\,\hat{r}^2=0 \tag{C.9}$$

with two repeated roots:

$$\hat{r}_1=\hat{r}_2=0 \tag{C.10}$$

the absolute value of the nonzero roots of the micropolar torsion characteristic equation (or equivalently the positive characteristic root), given by the second relation of Eq. (C.8), can be considered as an index for analysis of torsional behaviors in micropolar beams. It is worth mentioning that the general homogeneous solution corresponding to the micropolar and classical beam torsion problems respectively are:

$$\hat{\underset{\sim}{\boldsymbol{q}}}=z_1+z_2\,{}^{c}\hat{x}_1+z_3\,\exp(\hat{r}_3)+z_4\,\exp(\hat{r}_4) \tag{C.11}$$

and:

$$\hat{\underset{\sim}{\boldsymbol{q}}}=z_1+z_2\,{}^{c}\hat{x}_1 \tag{C.12}$$

where the reader's attention is directed to the two extra terms in Eq. (C.11) that the general homogeneous solution of the micropolar beam torsion has.

Analogously, the last three relations of Eq. (C.1), representing the micropolar beam bending, can be rewritten as:

$$\hat{\underset{\sim}{\mathcal{Q}}} = \hat{\underset{\sim}{\mathcal{K}}}_{\hat{1}\hat{1}}\, \hat{\underset{\sim}{q}}_{,\hat{1}\hat{1}} + \hat{\underset{\sim}{\mathcal{K}}}_{\hat{1}}\, \hat{\underset{\sim}{q}}_{,\hat{1}} + \hat{\underset{\sim}{\mathcal{K}}}\, \hat{\underset{\sim}{q}} \tag{C.13}$$

where:

$$\begin{aligned} \hat{\underset{\sim}{\mathcal{Q}}} &= \left[\begin{array}{ccc} \hat{\bar{f}}_2^{\,V} & \hat{\bar{m}}_3^{\,L} & \hat{\bar{m}}_3^{\,V} \end{array} \right]^{\mathrm{T}} \\ \hat{\underset{\sim}{q}} &= \left[\begin{array}{ccc} \hat{\bar{u}}_2 & \bar{\theta}_3 & \bar{\vartheta}_3 \end{array} \right]^{\mathrm{T}} \end{aligned} \tag{C.14}$$

$$\hat{\underset{\sim}{\mathcal{K}}}_{\hat{1}\hat{1}} = \left[\begin{array}{ccc} -\left(k_{s_2}\,\hat{\mu} + \hat{\kappa}\right) & 0 & 0 \\ 0 & -\hat{I}_3 & 0 \\ 0 & 0 & -\left(\hat{\gamma} + \hat{\beta}\right) \end{array} \right] \tag{C.15}$$

$$\hat{\underset{\sim}{\mathcal{K}}}_{\hat{1}} = \left[\begin{array}{ccc} 0 & \left(k_{s_2}\,\hat{\mu} - \hat{\kappa}\right) & 2\,\hat{\kappa} \\ -\left(k_{s_2}\,\hat{\mu} - \hat{\kappa}\right) & 0 & 0 \\ -2\,\hat{\kappa} & 0 & 0 \end{array} \right] \tag{C.16}$$

$$\hat{\underset{\sim}{\mathcal{K}}} = \left[\begin{array}{ccc} 0 & 0 & 0 \\ 0 & \left(k_{s_2}\,\hat{\mu} + \hat{\kappa}\right) & -2\,\hat{\kappa} \\ 0 & -2\,\hat{\kappa} & 4\,\hat{\kappa} \end{array} \right] \tag{C.17}$$

The characteristic equation corresponding to these PDEs is:

$$\hat{I}_3 \left(k_{s_2}\,\hat{\mu} + \hat{\kappa}\right) \left(\hat{\gamma} + \hat{\beta}\right) \hat{r}^{\,6} - 4\,k_{s_2}\,\hat{\mu}\,\hat{\kappa} \left(\hat{I}_3 + \hat{\gamma} + \hat{\beta}\right) \hat{r}^{\,4} = 0 \tag{C.18}$$

which has six roots:

$$\begin{aligned} &\hat{r}_1 = \hat{r}_2 = \hat{r}_3 = \hat{r}_4 = 0 \\ &\hat{r}_5 = -\hat{r}_6 = +2 \sqrt{\frac{k_{s_2}\,\hat{\mu}\,\hat{\kappa} \left(\hat{I}_3 + \hat{\gamma} + \hat{\beta}\right)}{\hat{I}_3 \left(k_{s_2}\,\hat{\mu} + \hat{\kappa}\right) \left(\hat{\gamma} + \hat{\beta}\right)}} \end{aligned} \tag{C.19}$$

Considering the characteristic equation corresponding to the classical bending PDEs (the last two relations of Eq. (C.2)), *i.e.*:

$$k_{s_2}\,\hat{\mu}\,\hat{I}_3\,\hat{r}^4 = 0 \tag{C.20}$$

and its four repeated roots:

$$\hat{r}_1 = \hat{r}_2 = \hat{r}_3 = \hat{r}_4 = 0 \tag{C.21}$$

the positive characteristic root of the micropolar bending equations, given by the second relation of Eq. (C.19), can be regarded as an index to examine the bending behavior of micropolar elastic beams. Again, note that the general homogeneous solution corresponding to the micropolar and classical beam bending problems respectively are:

$$\underset{\sim}{\hat{\boldsymbol{q}}} = z_1 + z_2\,{}^c\hat{x}_1 + z_3\,{}^c\hat{x}_1^2 + z_4\,{}^c\hat{x}_1^3 + z_5\,\exp(\hat{r}_5) + z_6\,\exp(\hat{r}_6) \tag{C.22}$$

and:

$$\underset{\sim}{\hat{\boldsymbol{q}}} = z_1 + z_2\,{}^c\hat{x}_1 + z_3\,{}^c\hat{x}_1^2 + z_4\,{}^c\hat{x}_1^3 \tag{C.23}$$

where one should notice the two extra terms of the micropolar beam bending general homogeneous solution given in Eq. (C.22).

Other indices for comparison of the static micropolar and classical beams can be the relative torsional and bending deformations defined as the micropolar beam deformation $(\hat{q}_i)_{\text{mp}}$ divided by the corresponding classical beam deformation $(\hat{q}_i)_{\text{cl}}$ (at a specific point and under a certain type of loading). Here, the micropolar torsional rotations $(\bar{\theta}_1)_{\text{mp}}$ and $(\bar{\vartheta}_1)_{\text{mp}}$ are compared against the classical torsional rotation $(\bar{\theta}_1)_{\text{cl}}$, the micropolar bending rotations $(\bar{\theta}_3)_{\text{mp}}$ and $(\bar{\vartheta}_3)_{\text{mp}}$ are weighed against the classical bending rotation $(\bar{\theta}_3)_{\text{cl}}$, and the micropolar bending displacement $(\hat{\bar{u}}_2)_{\text{mp}}$ is divided by the classical bending displacement $(\hat{\bar{u}}_2)_{\text{cl}}$; all measured at the free end of the beams.

The positive characteristic root of the micropolar torsion $\hat{r}_3$ (given by the second relation of Eq. (C.19)) vs. the dimensionless micropolar elastic constants $\hat{\gamma}$ and $\hat{\kappa}$ for three different beam slenderness ratios is depicted in Figure C.1. Similarly the positive characteristic root of the micropolar bending $\hat{r}_5$ is illustrated in Figure C.2. Note that the scales in these figures are log-log-log and for each slenderness ratio a 2D contour plot and a 3D surface

plot are provided; the 3D plot is obtained by looking at the 2D plot from a point over the 2D plot's upper right corner. A detailed discussion of Figures C.1 and C.2 follows.

The relative torsional deformations, *i.e.* the relative plane rotation $\frac{(\bar{\theta}_1)_{\text{mp}}}{(\theta_1)_{\text{cl}}}$ and relative microrotation $\frac{(\bar{\vartheta}_1)_{\text{mp}}}{(\theta_1)_{\text{cl}}}$, at the beam tip (the free end) and under the action of an external volume moment $\hat{\bar{m}}_1^{\,V}$ vs. the micropolar elastic constants are plotted in Figures C.3 and C.4. Similar graphs for the case when the beams are subject to an external line moment $\hat{\bar{m}}_1^{\,L}$ are shown in Figures C.5 and C.6. The relative bending deformations, *i.e.* the relative displacement $\frac{(\hat{\bar{u}}_2)_{\text{mp}}}{(\hat{\bar{u}}_2)_{\text{cl}}}$, relative plane rotation $\frac{(\bar{\theta}_3)_{\text{mp}}}{(\theta_3)_{\text{cl}}}$, and relative microrotation $\frac{(\bar{\vartheta}_3)_{\text{mp}}}{(\theta_3)_{\text{cl}}}$, measured at the beam tip vs. the micropolar elastic constants for different types of loading (*i.e.* volume force $\hat{\bar{f}}_2^{\,V}$, volume moment $\hat{\bar{m}}_3^{\,V}$, and line moment $\hat{\bar{m}}_3^{\,L}$) are shown in Figures C.7–C.15. In Figures C.3–C.15 note that scales are log-log-percentage. Again, for each slenderness ratio a 2D contour plot and a 3D surface plot are provided; the 3D plot is obtained by looking at the 2D plot from a point over the 2D plot's upper right corner. A more detailed discussion of these figures is reserved for later in this appendix.

Considering the beam with medium thickness or slenderness ratio (*i.e.* $\hat{R}_3 = 50$), its complete torsional and bending deformations under different types of loading are shown in Figures C.16–C.20. The six graphs included in each figure are obtained considering one classical beam model and five micropolar beam models. The micropolar beam models differ in the values used for the micropolar elastic constants $\hat{\kappa}$ and $\hat{\gamma}$ (recall that based on Table C.1 $\hat{\beta} = \hat{\gamma}$ and $\xi = \frac{1}{2}$). The magnitude of the applied load in each figure (set of six plots) is selected such that it results in a maximum torsional rotation or bending (nondimensional) displacement of 0.3 in the classical beam model.

Noting the noisy behavior of the contours in the lower right corner of the 2D plots in some of the figures, *e.g.* Figures C.3, C.9, and C.10, it is wise to check the finite element stiffness matrices for any possible numerical singularity or ill-conditionedness in that area (*i.e.* where $\hat{\kappa} \ll 1$ and $\hat{\gamma} \gg 1$). Here, the 1-norm condition number of the micropolar beams' finite element stiffness matrix $(K_{\underset{\sim}{\mathcal{K}}})_{\text{mp}}$ against the micropolar elastic constants $\hat{\kappa}$ and $\hat{\gamma}$ is plotted in Figure C.21 (alike the characteristic root figures scales are log-log-log and there are two plots for each slenderness ratio). Based on the accuracy of the MATLAB® utilized for numerical calculations of this thesis ($\epsilon_{\text{M}} = 2.22 \times 10^{-16}$ [66]), a condition number close

to $\frac{1}{\epsilon_M} \approx 5 \times 10^{15}$ implies that numerical errors may be included in the results corresponding to that area and those results are unreliable.

While a detailed discussion of the figures is reserved for later (after each set of figures), a general rule in all of these figures is that the dimensionless slenderness ratio $\hat{R}_3$ can be a measure of the beam thickness assuming that the beam length does not change from one plot to another. The dimensionless micropolar constant $\hat{\kappa}$ represents the extent of coupling between micropolar and classical deformation modes (or coupling between micropolar and classical stiffnesses). Also the dimensionless micropolar constant $\hat{\gamma}$ is a measure of the significance of micropolar deformations relative to classical deformations (or a measure of the micropolar stiffness relative to the classical stiffness as well as a measure of "size effects" significance). See Eqs. (4.82) and (4.80) for definitions of $\hat{R}_3$, $\hat{\kappa}$, and $\hat{\gamma}$.

More precisely, in the upper left quarter of the 2D plots due to a relatively large $\hat{\kappa}$ the micropolar deformations are coupled to the classical deformations and due to a relatively small $\hat{\gamma}$ the classical modes are dominant and characterize the beam total deformations (micropolar deformations follow the classical deformations). In the upper left quarter of the 2D plots the coupling between micropolar and classical deformations is maintained due to a relatively large $\hat{\kappa}$, however a relatively large $\hat{\gamma}$ makes the micropolar modes dominant over the classical modes and the beam total deformation is characterized by the micropolar modes (classical deformations follow the micropolar deformations). In the lower left and right quarters of the 2D plots (or more exactly the whole lower half of the 2D plots) the coupling between micropolar and classical modes weakens due to a relatively small $\hat{\kappa}$ and therefore the micropolar constant $\hat{\gamma}$ loses its meaning as a measure of the micropolar to classical relative stiffness. In this case, the contributions of the micropolar and classical modes into the beam total deformations depend on the relative values of $\hat{\kappa}$ and $\hat{\gamma}$ and also the type of external loads and boundary conditions (*e.g.* are they directly applied to the micropolar or classical DOFs?). The micropolar beam models with small $\hat{\kappa}$ can be called (analytically) singular due to an ill-conditioned stiffness operator which cannot guarantee the continuity of the beam as just one continuous system (this will be explained in more detail later in this appendix). The values of $\hat{\kappa}$ and $\hat{\gamma}$ at which the transition between these states occurs are dependent on the beam's thickness or the beam's slenderness ratio represented by $\hat{R}_3$.

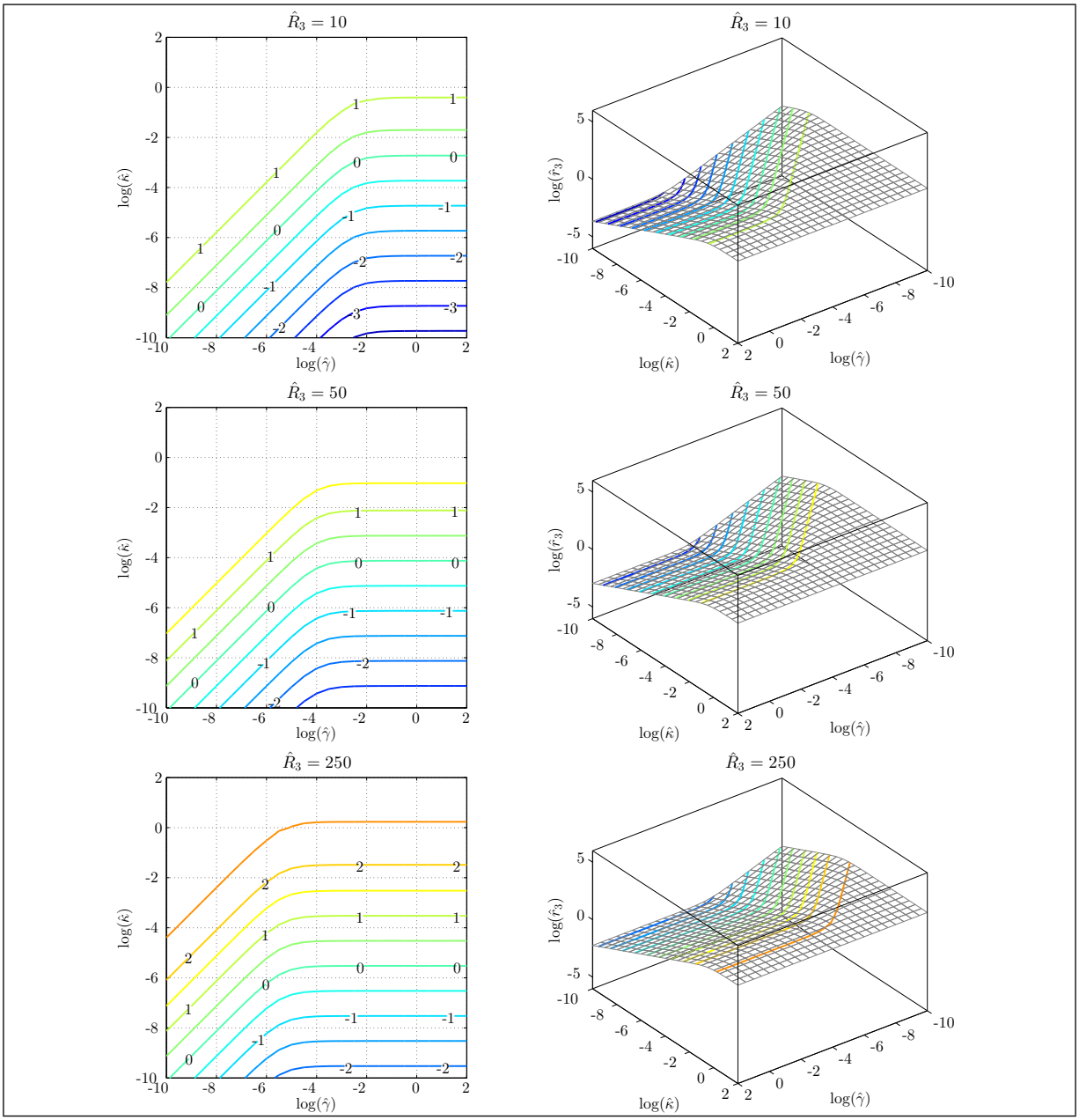

Figure C.1: Micropolar torsion positive characteristic root $\hat{r}_3$ vs. micropolar elastic constants.

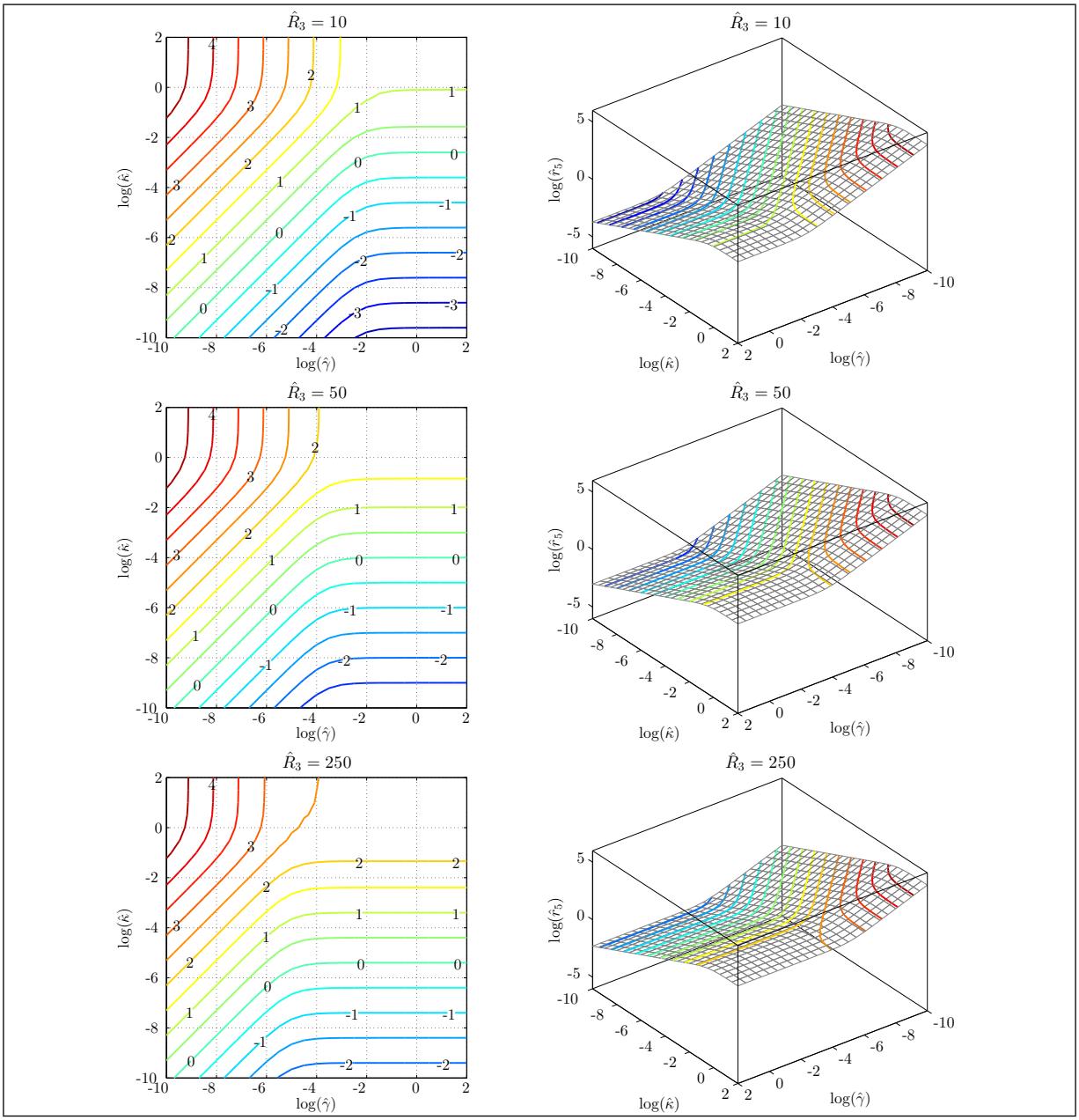

Figure C.2: Micropolar bending positive characteristic root $\hat{r}_5$ vs. micropolar elastic constants.

The nonzero torsion and bending characteristic roots are the spirit of the micropolar torsion and bending modes (they do not have a correspondent in the classical torsion and bending modes) and characterize the micropolar modes. Moreover, the micropolar modes are mainly related to the material microstructure and are expected to work similarly in torsion and bending. Therefore, one can expect to see comparable behaviors when examining the nonzero characteristic roots corresponding to the torsion and bending modes. However, for large $\hat{\kappa}$ and small $\hat{\gamma}$ the non-dominant micropolar modes are coupled to the dominant classical modes which have different natures in torsion and bending (the micropolar deformations will follow the classical torsional and bending deformations). Consequently, the nonzero characteristic roots of torsion and bending modes have different trends in the region where $\hat{\kappa}$ is large and $\hat{\gamma}$ is small. For other regions where $\hat{\kappa}$ is small or $\hat{\gamma}$ is large the nonzero torsion and bending characteristic roots act analogously.

Comparing the corresponding plots of Figures C.1 and C.2, one can notice that except for the upper left quarter of the 2D plots (*i.e.* where $\hat{\kappa} > 1 \times 10^{-4}$ and $\hat{\gamma} < 1 \times 10^{-4}$) the micropolar torsion and bending deformation modes behave similarly, that is, the nonzero characteristic roots of micropolar torsion and bending modes have analogous trends; this is in agreement with the above-mentioned theoretical observation.

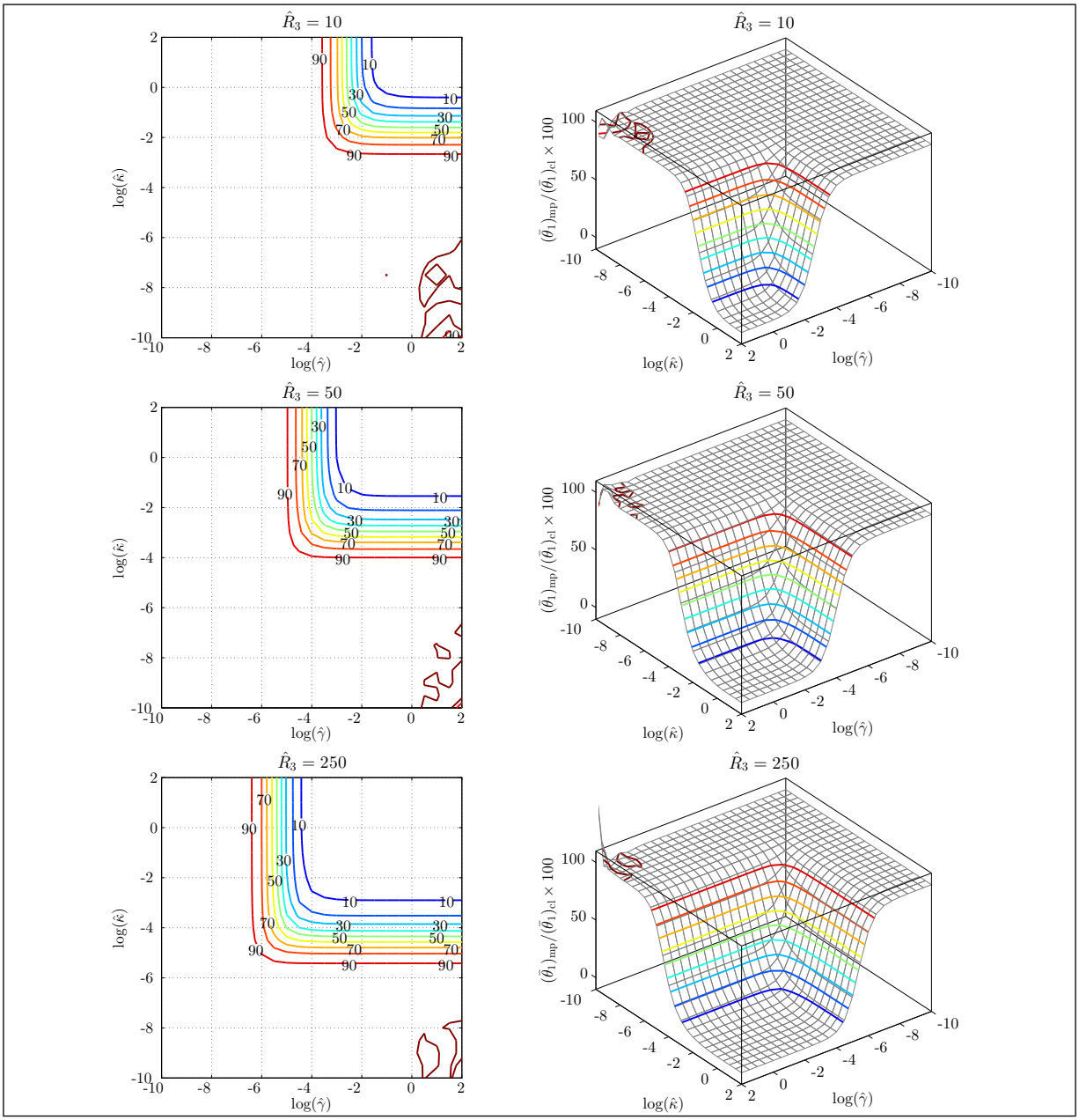

Figure C.3: Relative torsional plane rotation $(\bar{\theta}_1)_{\mathrm{mp}}/(\bar{\theta}_1)_{\mathrm{cl}}$ of micropolar beams under volume moment $\hat{\bar{m}}_1^{\,V}$ vs. micropolar elastic constants.

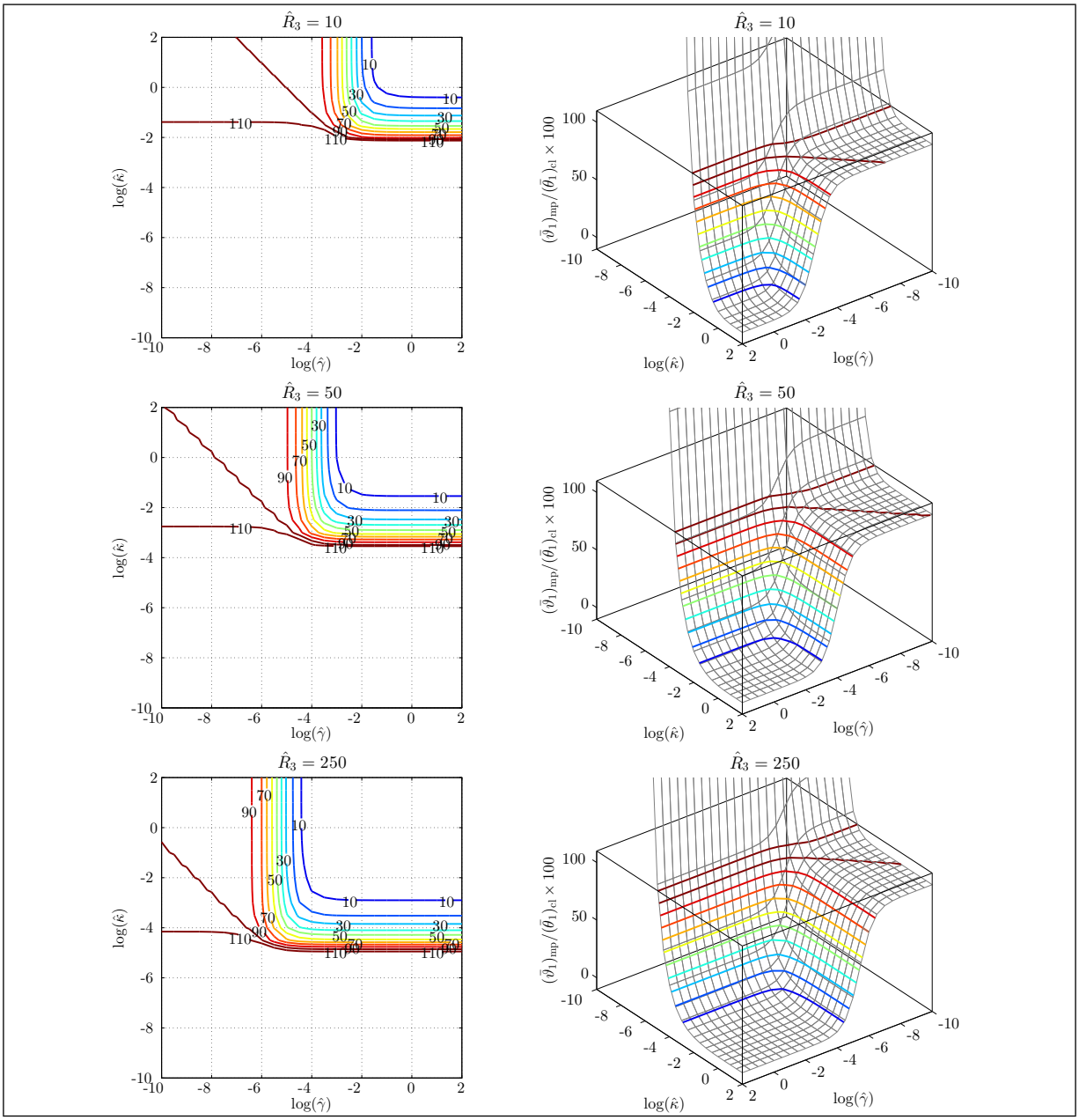

Figure C.4: Relative torsional microrotation $(\bar{\vartheta}_1)_{\mathrm{mp}}/(\bar{\theta}_1)_{\mathrm{cl}}$ of micropolar beams under volume moment $\hat{\bar{m}}_1^{\,V}$ vs. micropolar elastic constants.

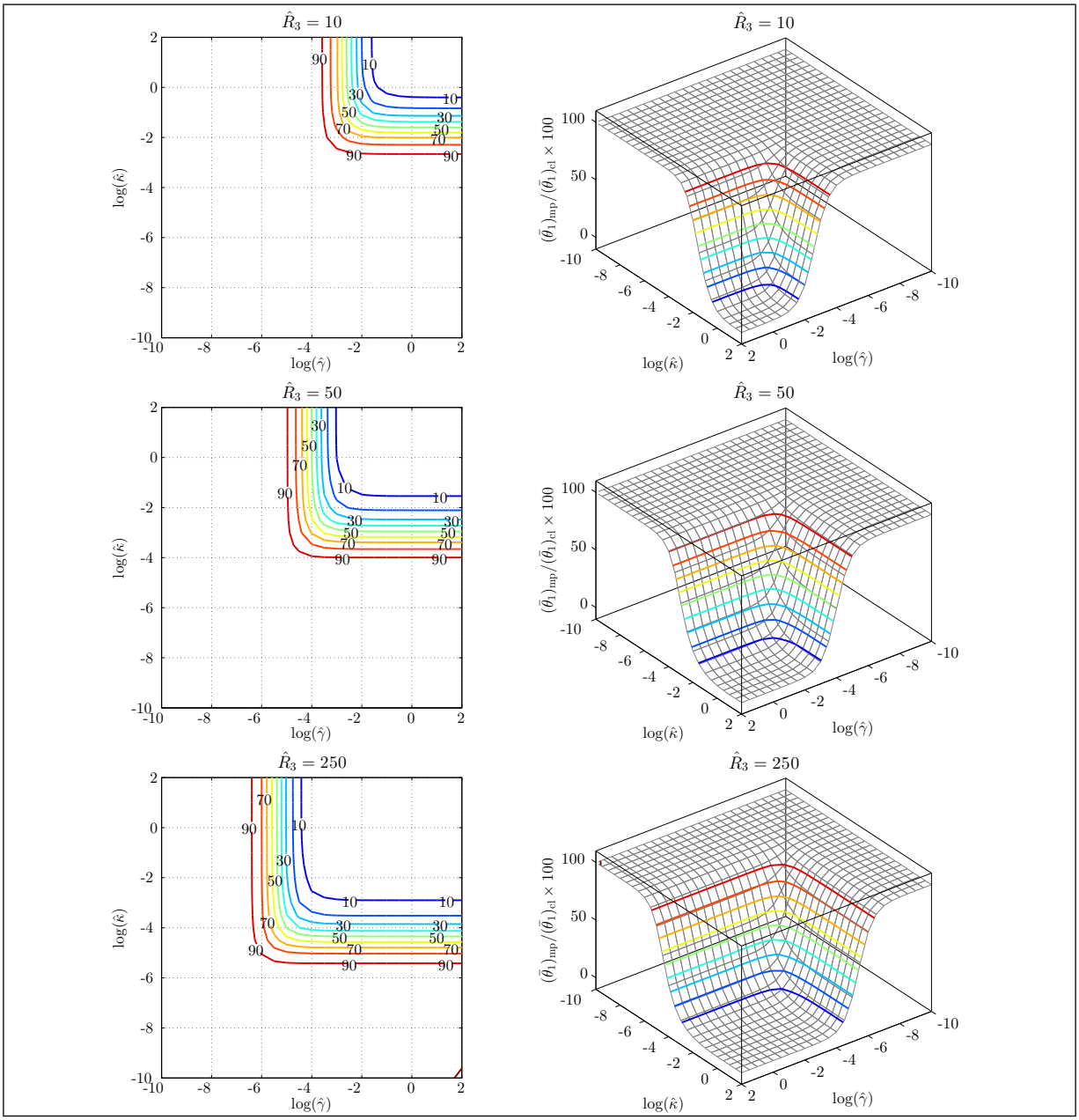

Figure C.5: Relative torsional plane rotation $(\bar{\theta}_1)_{\mathrm{mp}}/(\bar{\theta}_1)_{\mathrm{cl}}$ of micropolar beams under line moment $\hat{\bar{m}}_1^{\,L}$ vs. micropolar elastic constants.

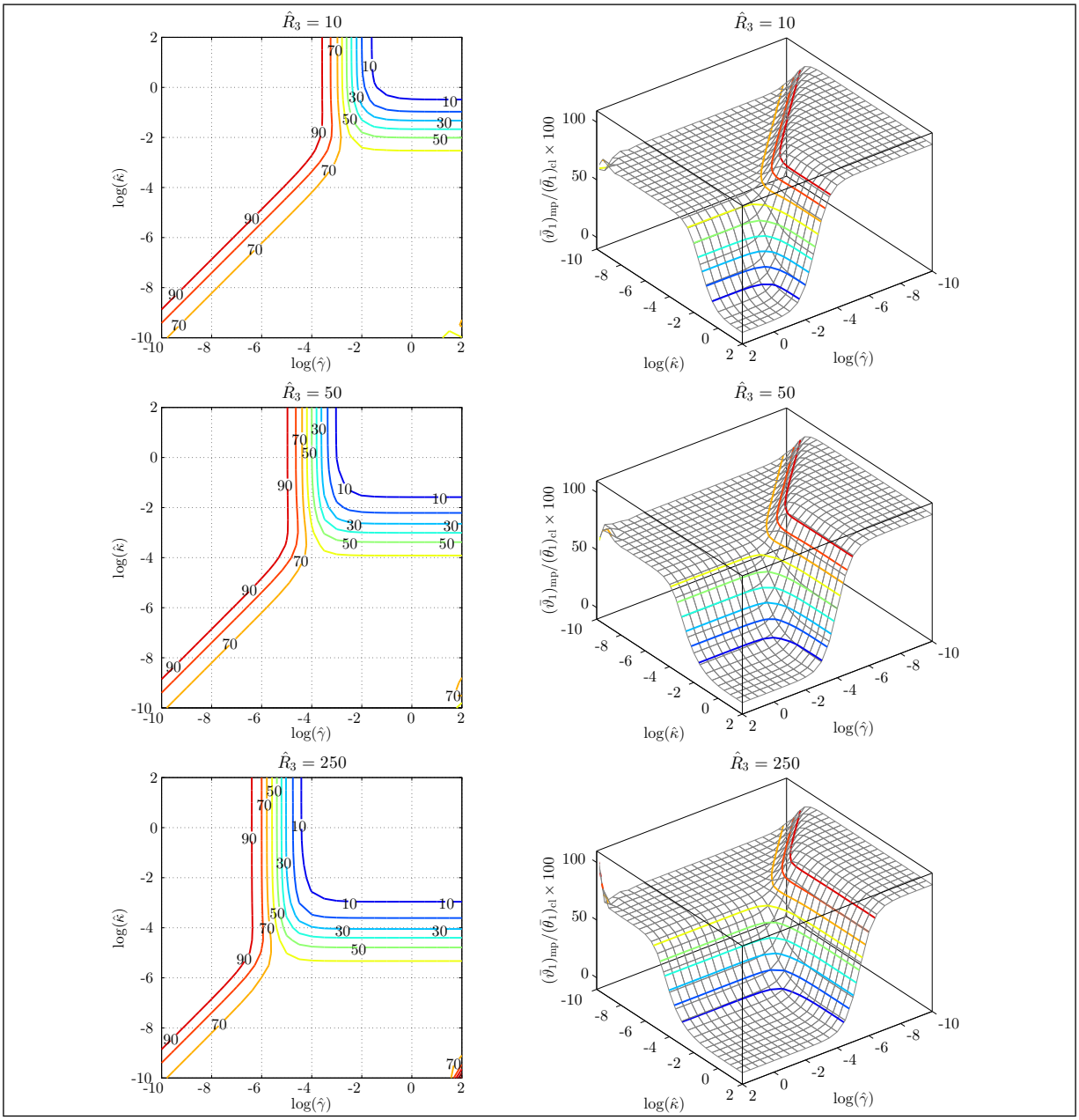

Figure C.6: Relative torsional microrotation $(\bar{\vartheta}_1)_{\mathrm{mp}}/(\bar{\theta}_1)_{\mathrm{cl}}$ of micropolar beams under line moment $\hat{\bar{m}}_1^{\,L}$ vs. micropolar elastic constants.

In Figures C.3–C.6 the torsional deformations of micropolar beams relative to the torsional deformations of classical beams are shown. Since the beams are under the same external load and the deformations are inversely proportional to the stiffness, they can also represent the classical stiffness relative to the micropolar stiffness.

The first point in the figures is that in the region where $\hat{\kappa}$ is very small and $\hat{\gamma}$ is very large (the lower right corner of the 2D plots) the results are not reliable; referring to Figure C.21, in this region the FEM stiffness matrix of micropolar beams is ill-conditioned. Numerical errors are sources of the noisy behavior seen in Figures C.3 and C.6.

As the next point one can notice that in the set of six plots in each figure, the region, where the micropolar effects are observable (in the upper right quarter of the 2D plots), becomes larger for thinner beams with larger slenderness ratios $\hat{R}_3$ (*i.e.* in the bottom plots of each set of six). Also in each plot, a larger $\hat{\gamma}$ which for constant slenderness ratio and constant material properties will correspond to a smaller beam length (refer to the definition of this dimensionless parameter in Eq. (4.80)) will result in a bigger difference between the micropolar and classical beam models. These results are in agreement with the size effects phenomenon known as a characteristic of the micropolar elasticity.

Also, as shown in Figure C.4, the micropolar beam torsion model predicts infinite deformations when the micropolar beams are subject to an external volume moment and the micropolar constant $\hat{\kappa}$ is very small. Indeed, a very small micropolar constant $\hat{\kappa}$ decouples the micropolar DOFs from the classical DOFs and if the micropolar constant $\hat{\gamma}$, illustrating the micropolar stiffness or the connection between the micropolar DOFs, is small or the micropolar DOFs are not constrained, an external volume moment which is directly affecting the micropolar DOFs may result in infinite micropolar deformations. The smaller singular region for the thinner beams implies that the coupling between the classical and micropolar DOFs improves (*i.e.* becomes stronger) as the beam slenderness ratio increases.

Finally, considering all the results obtained here, illustrating the relative torsional plane rotation and microrotation under different types of loading, it can be concluded that the results of micropolar and classical beam models will coincide in the region where $\hat{\kappa}$ is large and γ is small (*i.e.* in the upper left corner of the 2D plots).

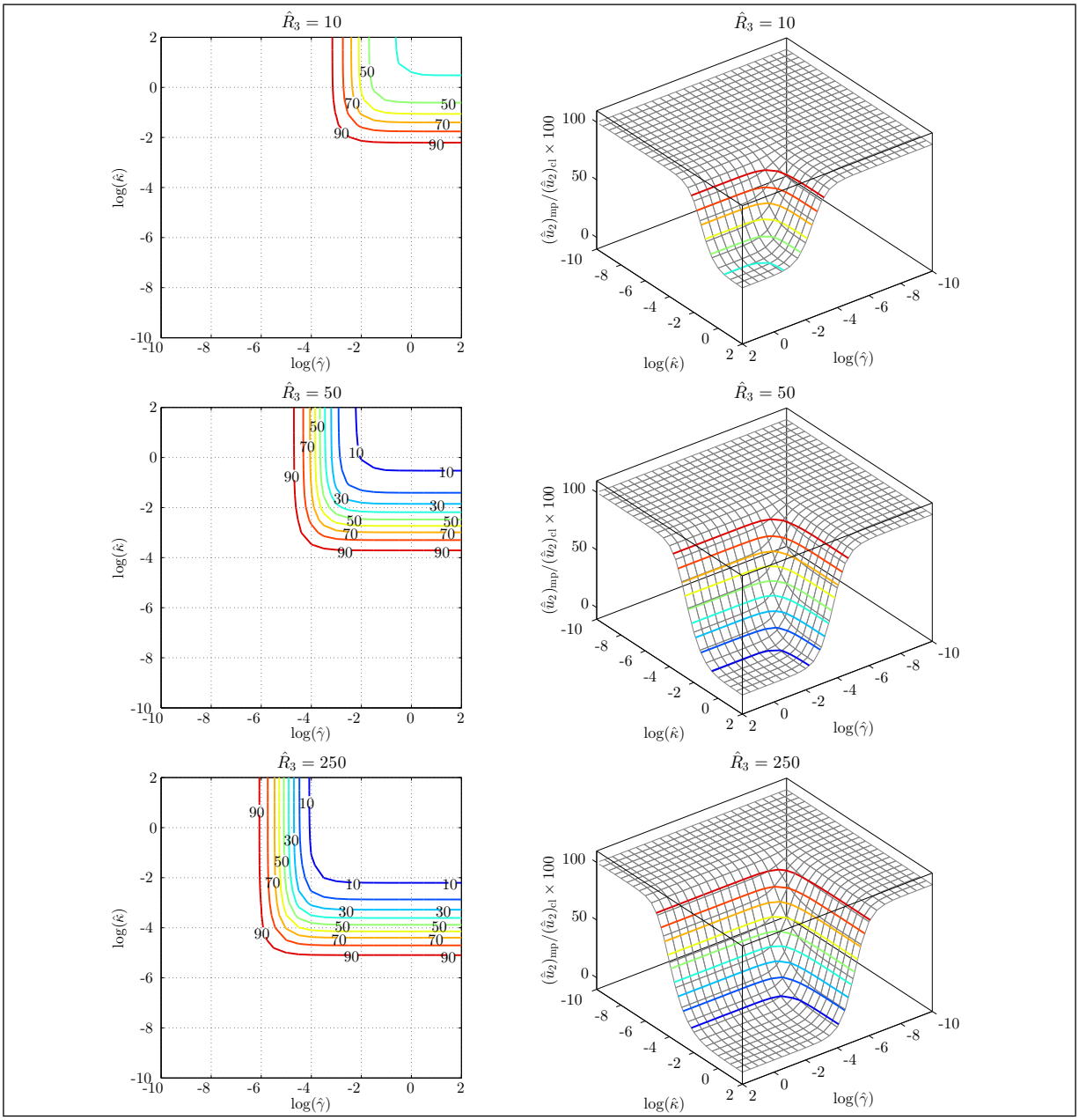

Figure C.7: Relative bending displacement $(\hat{\bar{u}}_2)_{\rm mp}/(\hat{\bar{u}}_2)_{\rm cl}$ of micropolar beams under volume force $\hat{\bar{f}}_2^V$ vs. micropolar elastic constants.

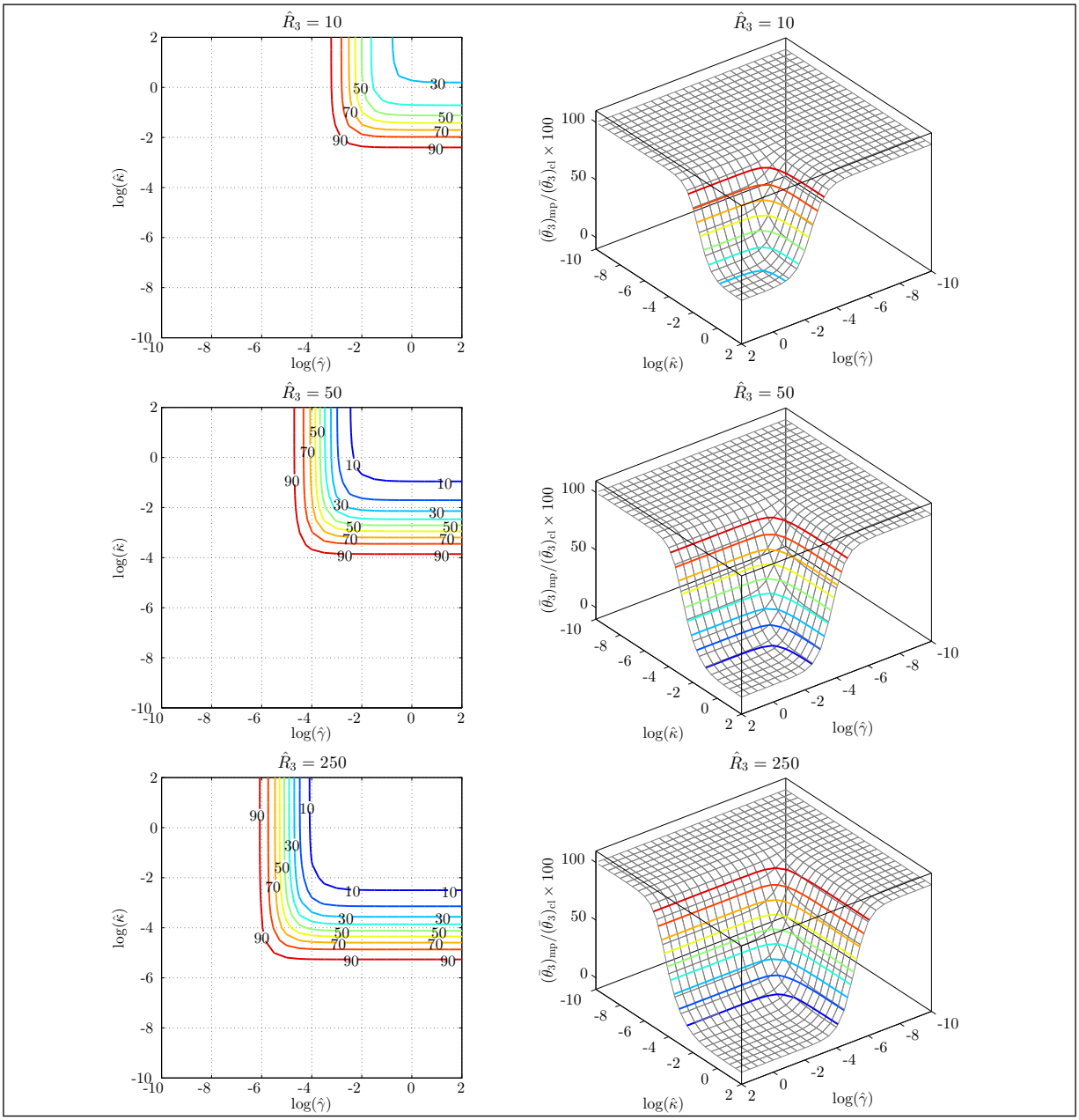

Figure C.8: Relative bending plane rotation $(\bar{\theta}_3)_{\rm mp}/(\bar{\theta}_3)_{\rm cl}$ of micropolar beams under volume force $\hat{\bar{f}}_2^V$ vs. micropolar elastic constants.

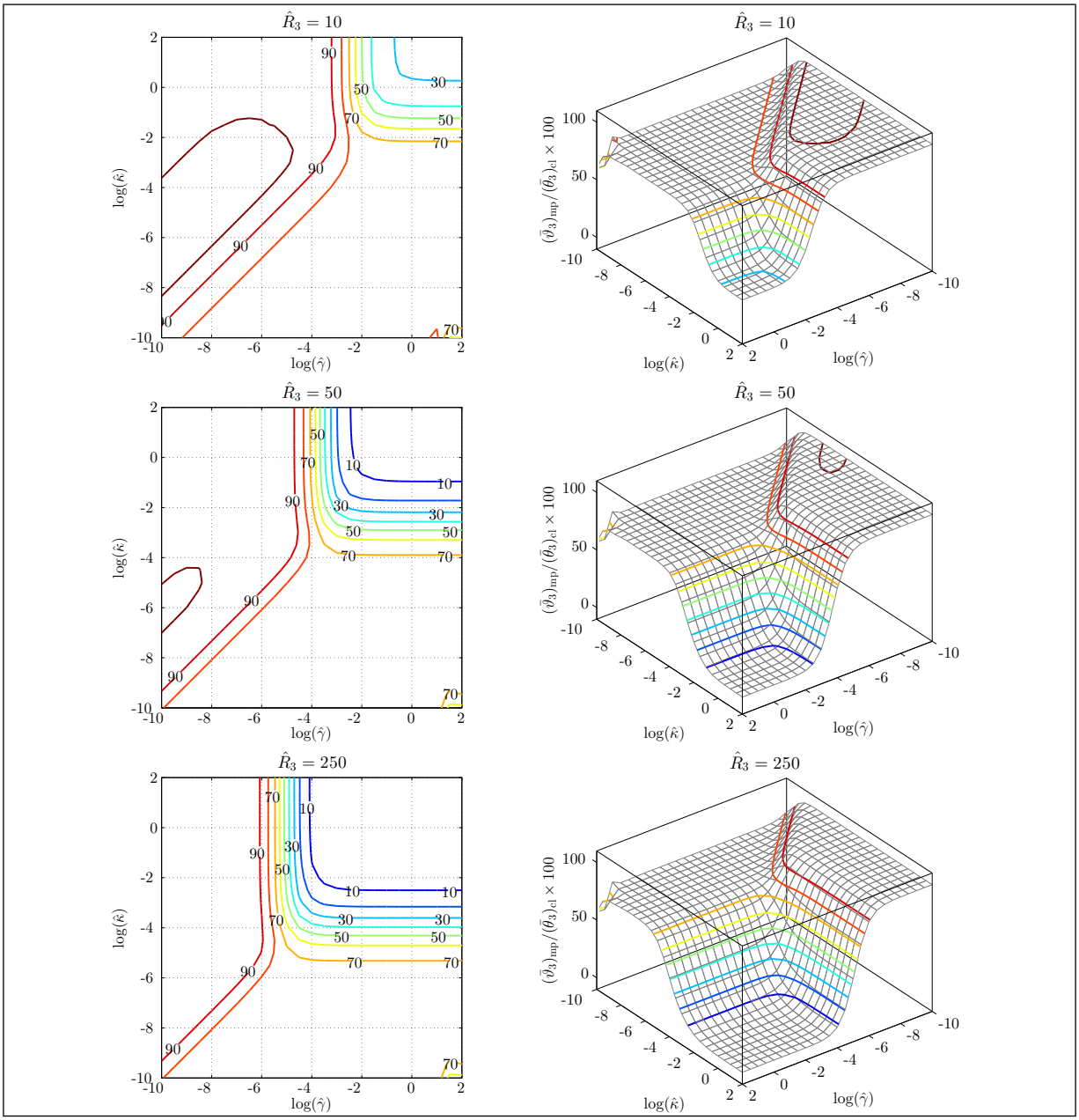

Figure C.9: Relative bending microrotation $(\bar{\vartheta}_3)_{\mathrm{mp}}/(\bar{\theta}_3)_{\mathrm{cl}}$ of micropolar beams under volume force $\hat{\bar{f}}_2^V$ vs. micropolar elastic constants.

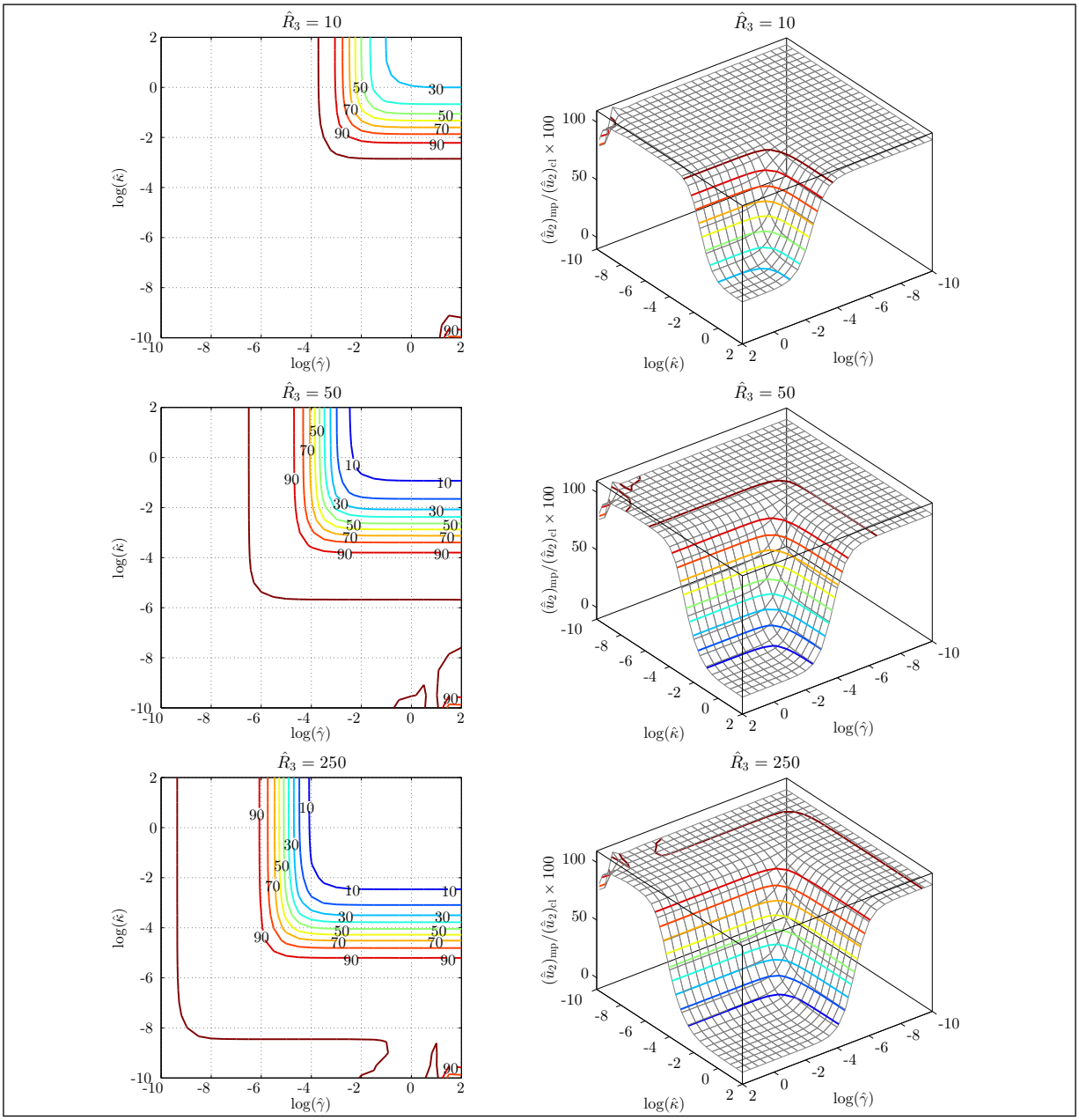

Figure C.10: Relative bending displacement $(\hat{\bar{u}}_2)_{\rm mp}/(\hat{\bar{u}}_2)_{\rm cl}$ of micropolar beams under volume moment $\hat{\bar{m}}_3^{\,V}$ vs. micropolar elastic constants.

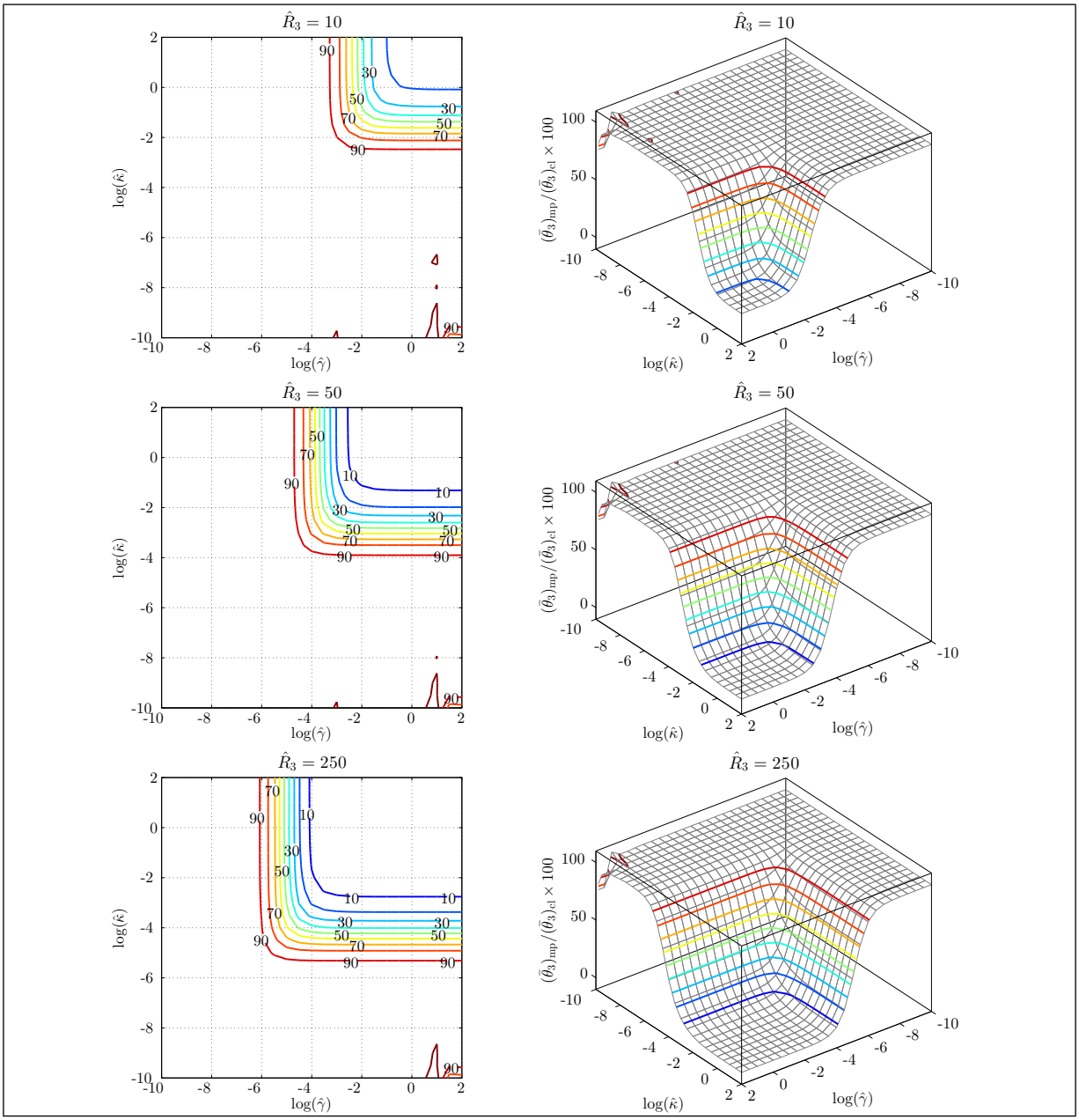

Figure C.11: Relative bending plane rotation $(\bar{\theta}_3)_{\rm mp}/(\bar{\theta}_3)_{\rm cl}$ of micropolar beams under volume moment $\hat{\bar{m}}_3^{\,V}$ vs. micropolar elastic constants.

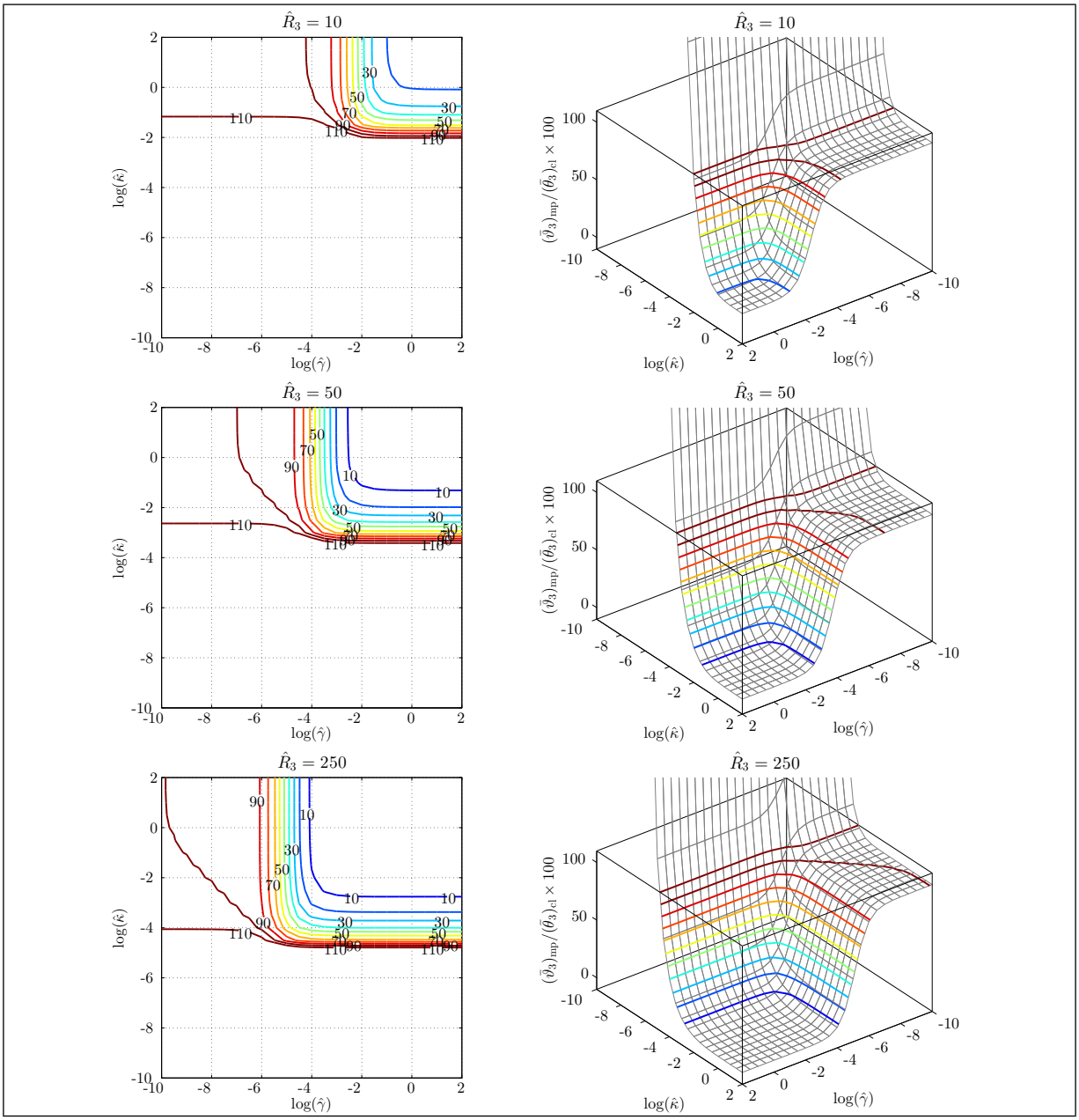

Figure C.12: Relative bending microrotation $(\bar{\vartheta}_3)_{\mathrm{mp}}/(\bar{\theta}_3)_{\mathrm{cl}}$ of micropolar beams under volume moment $\hat{\hat{m}}_3^{\,V}$ vs. micropolar elastic constants.

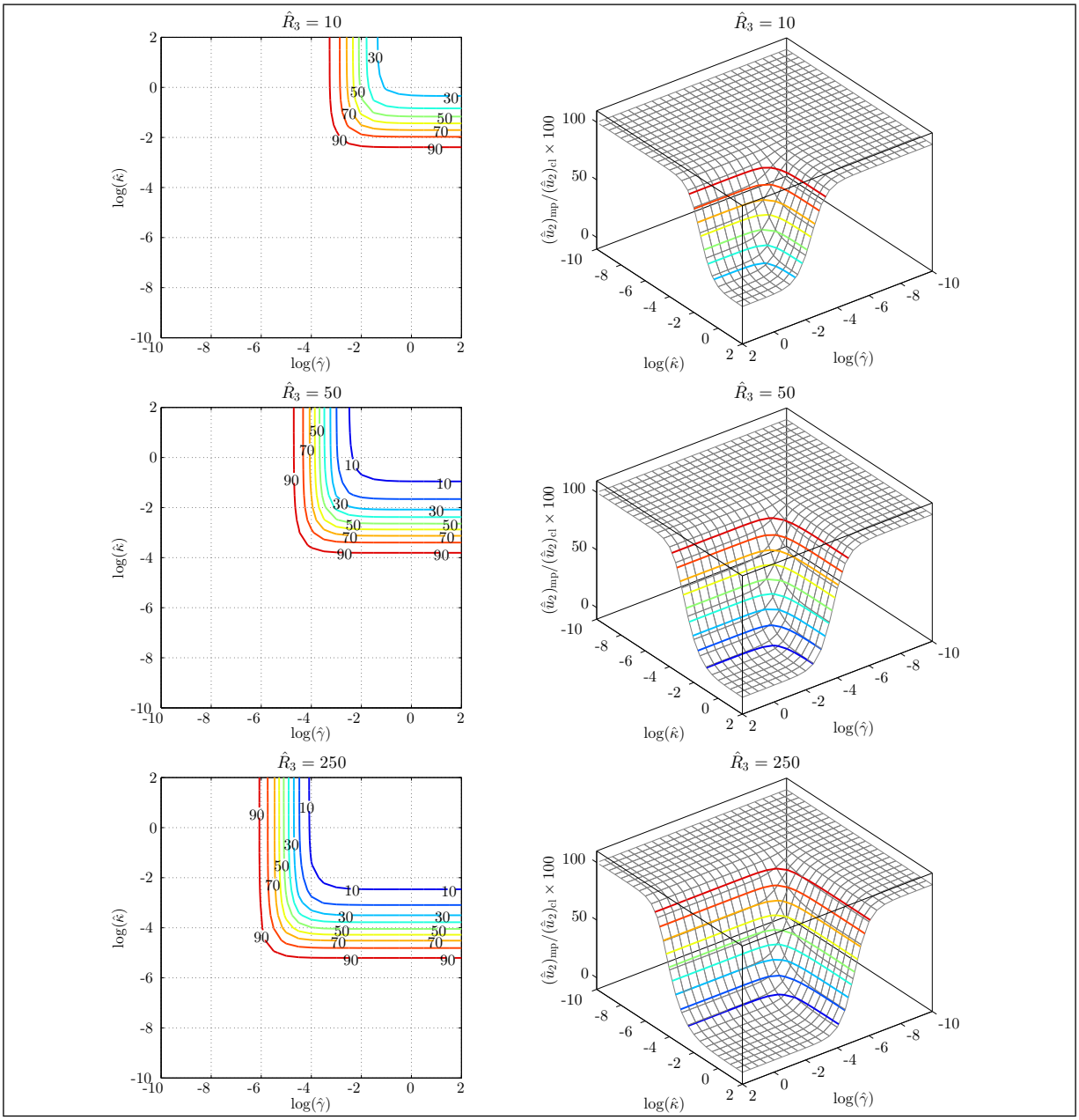

Figure C.13: Relative bending displacement $(\hat{\bar{u}}_2)_{\rm mp}/(\hat{\bar{u}}_2)_{\rm cl}$ of micropolar beams under line moment $\hat{\bar{m}}_3^{\,L}$ vs. micropolar elastic constants.

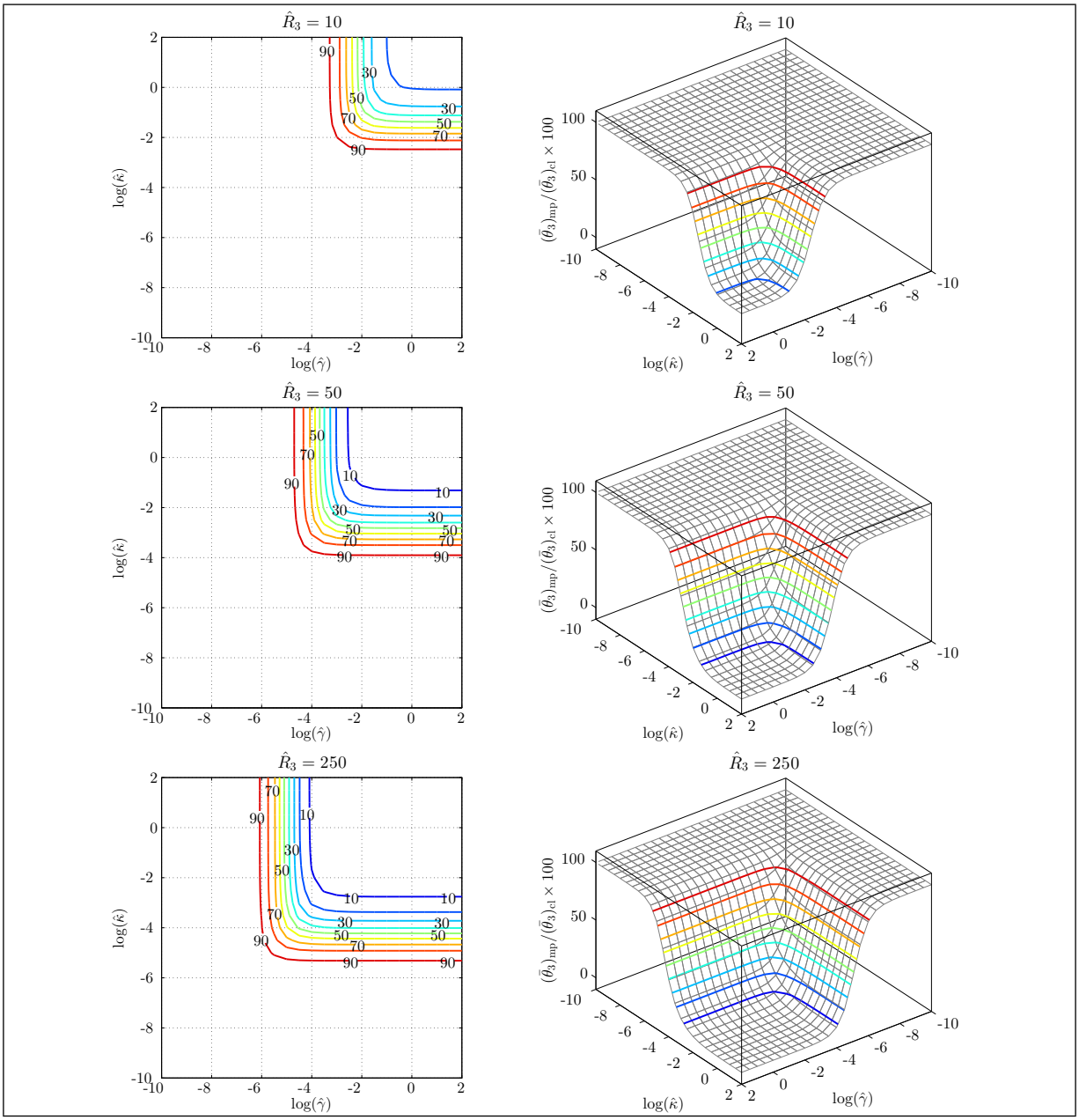

Figure C.14: Relative bending plane rotation $(\bar{\theta}_3)_{\mathrm{mp}}/(\bar{\theta}_3)_{\mathrm{cl}}$ of micropolar beams under line moment $\hat{\bar{m}}_3^{\,L}$ vs. micropolar elastic constants.

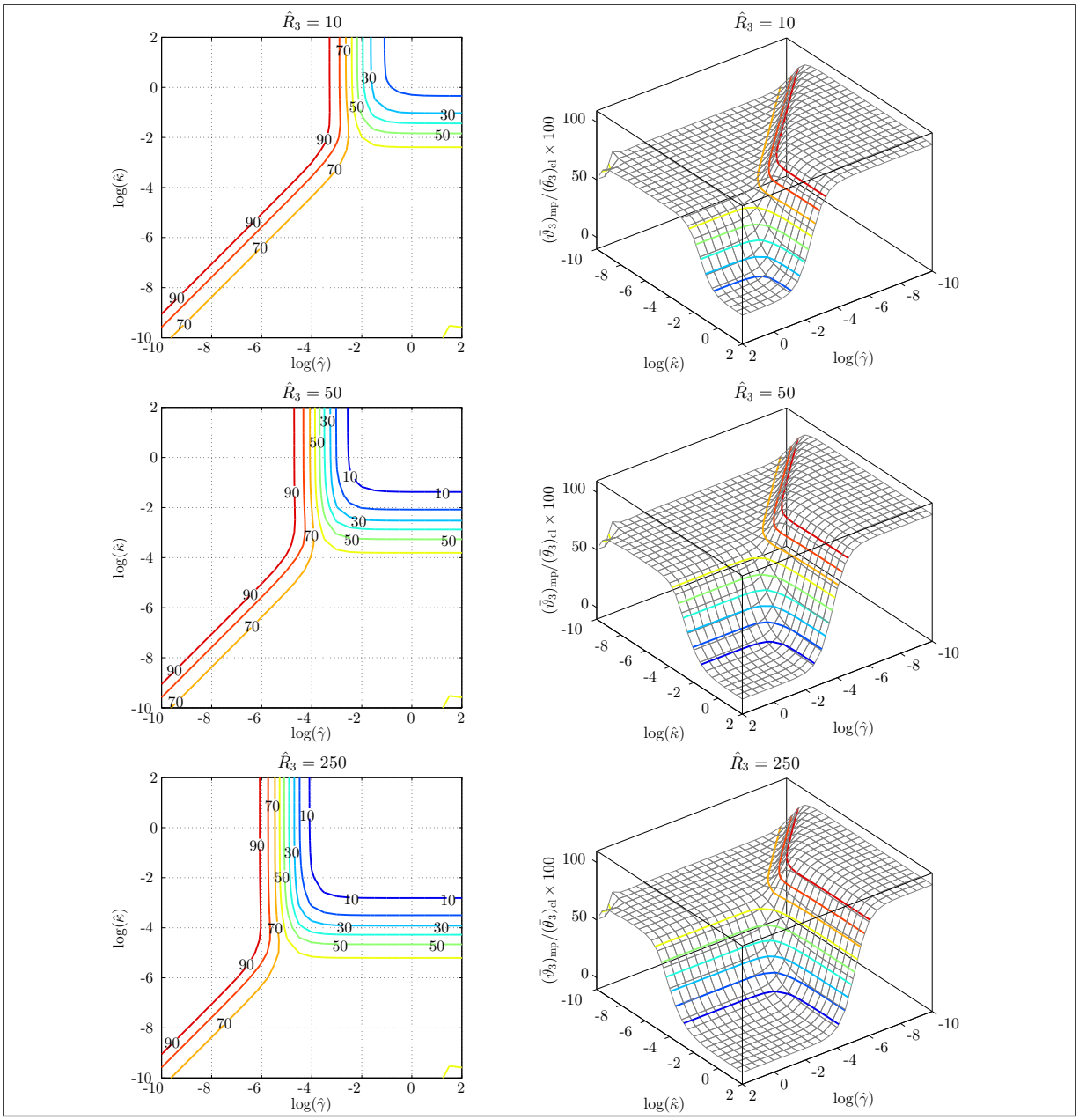

Figure C.15: Relative bending microrotation $(\bar{\vartheta}_3)_{\mathrm{mp}}/(\bar{\theta}_3)_{\mathrm{cl}}$ of micropolar beams under line moment $\hat{\bar{m}}_3^{\,L}$ vs. micropolar elastic constants.

The micropolar to classical relative bending deformations under different types of loading are shown in Figures C.7–C.15. Analogous to the torsion case, these figures also illustrate the (classical to micropolar) relative stiffness of the beam models.

As expected, the figures corresponding to the bending deformations show the same behaviors as those observed for torsional deformations. These behaviors are mentioned briefly in the following.

The noisy behavior in the region where $\hat{\kappa}$ is very small and $\hat{\gamma}$ is very large, which can be seen in Figures C.9–C.11 and Figure C.15, is due to an ill-conditioned FEM stiffness matrix of micropolar beams and the presence of numerical precision errors in the results.

Keeping the material unchanged, for a larger slenderness ratio $\hat{R}_3$ or a larger dimensionless micropolar constant $\hat{\gamma}$, which correspond to a thinner or shorter beam, the micropolar effects are more noticeable and the difference between micropolar and classical beam models is more evident. For very small $\hat{\kappa}$ the micropolar bending model is singular and as shown in Figure C.12 under the action of an external volume moment may result in an infinite bending microrotation $\bar{\vartheta}_3$. However, the stronger coupling between the classical and micropolar modes in thinner beams causes the singular region to become smaller as the beam gets thinner.

Finally, one can conclude when considering all the figures of relative bending deformations that the micropolar and classical beam models predict the same deformations again in the region where $\hat{\kappa}$ is large and $\hat{\gamma}$ is small (*i.e.* in the upper left corner of the 2D plots).

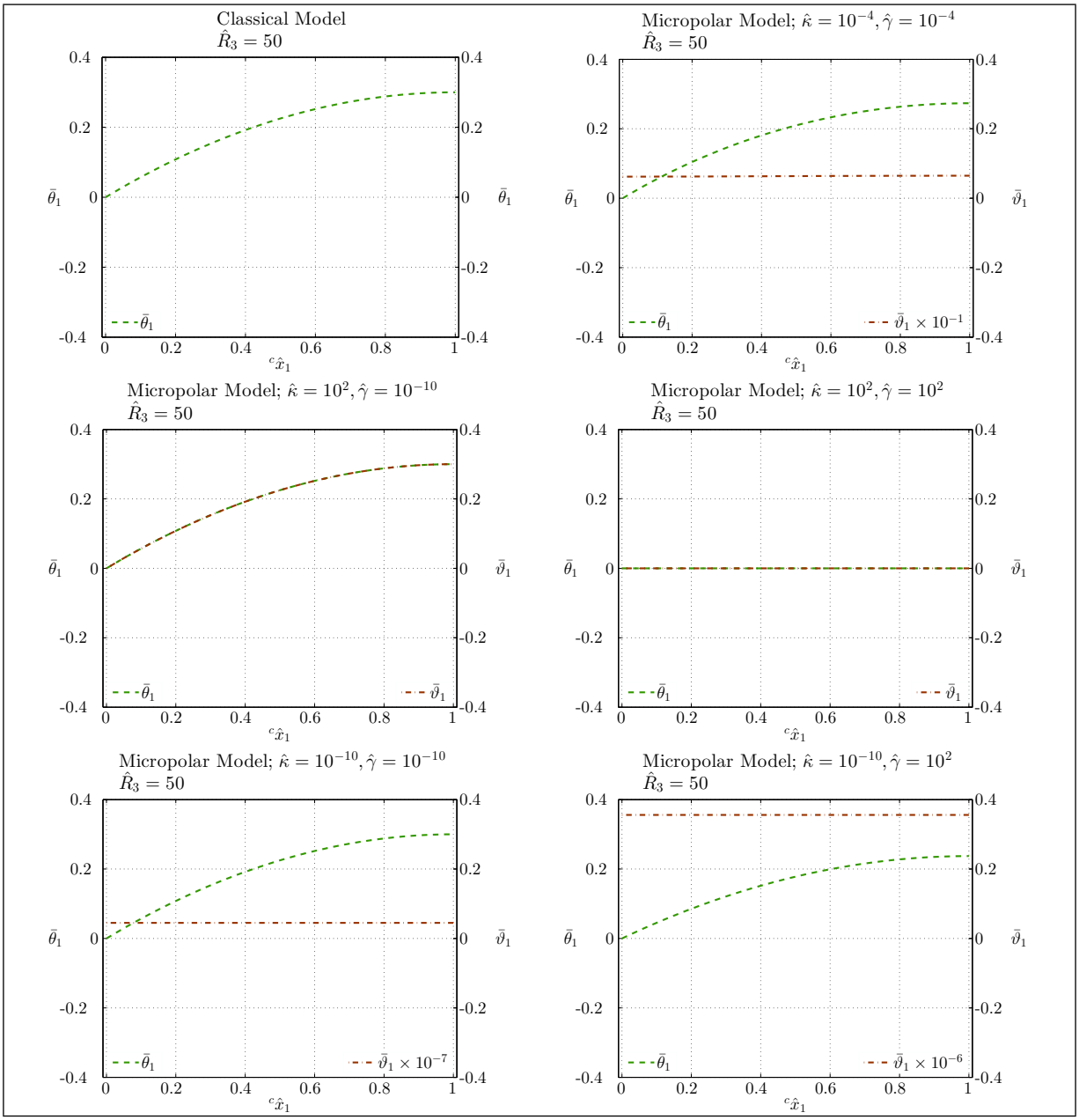

Figure C.16: Torsional deformations of beams with medium thickness under volume moment $\hat{\hat{m}}_1^{\,V}$.

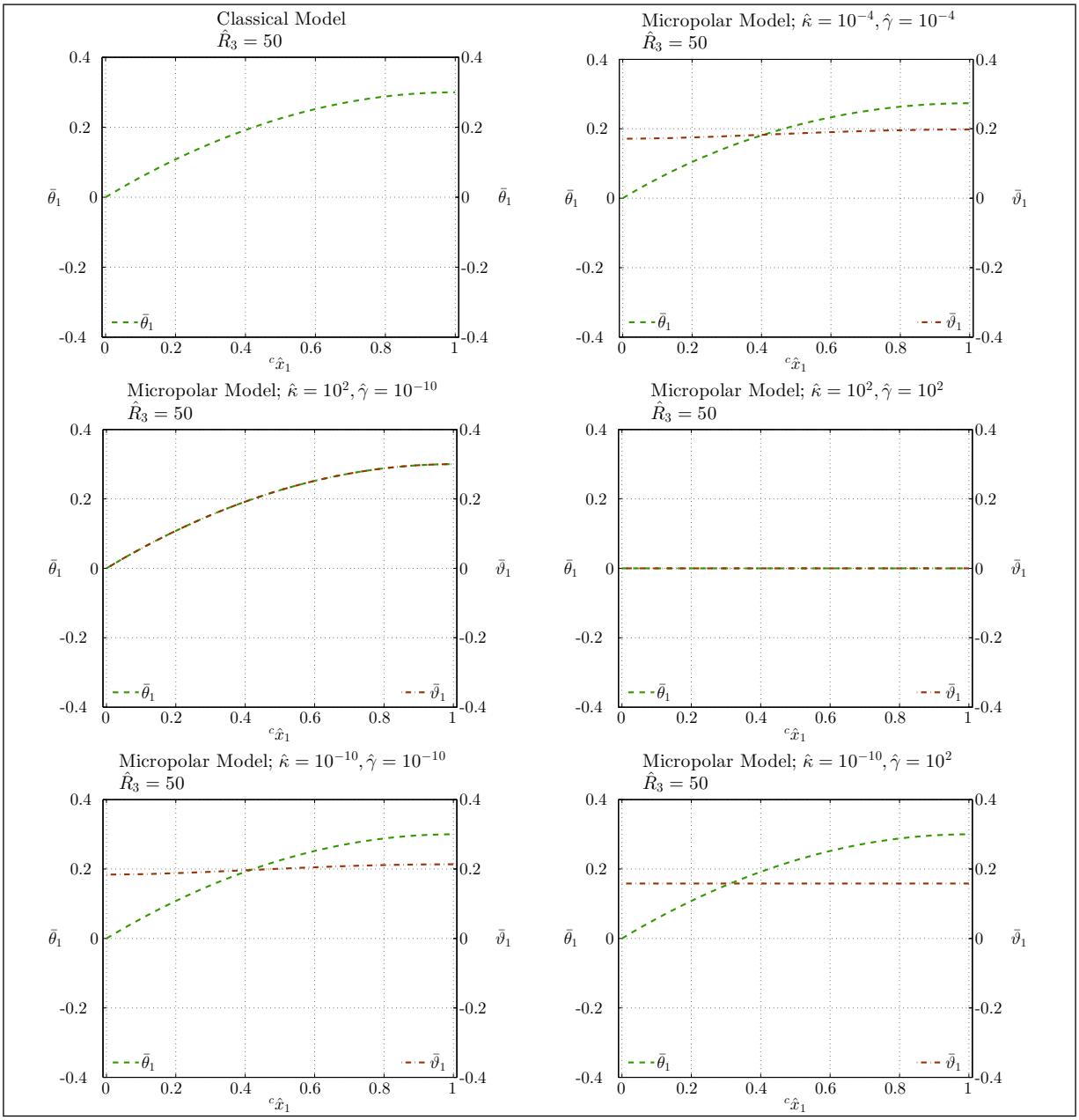

Figure C.17: Torsional deformations of beams with medium thickness under line moment $\hat{\hat{m}}_1^{\,L}$.

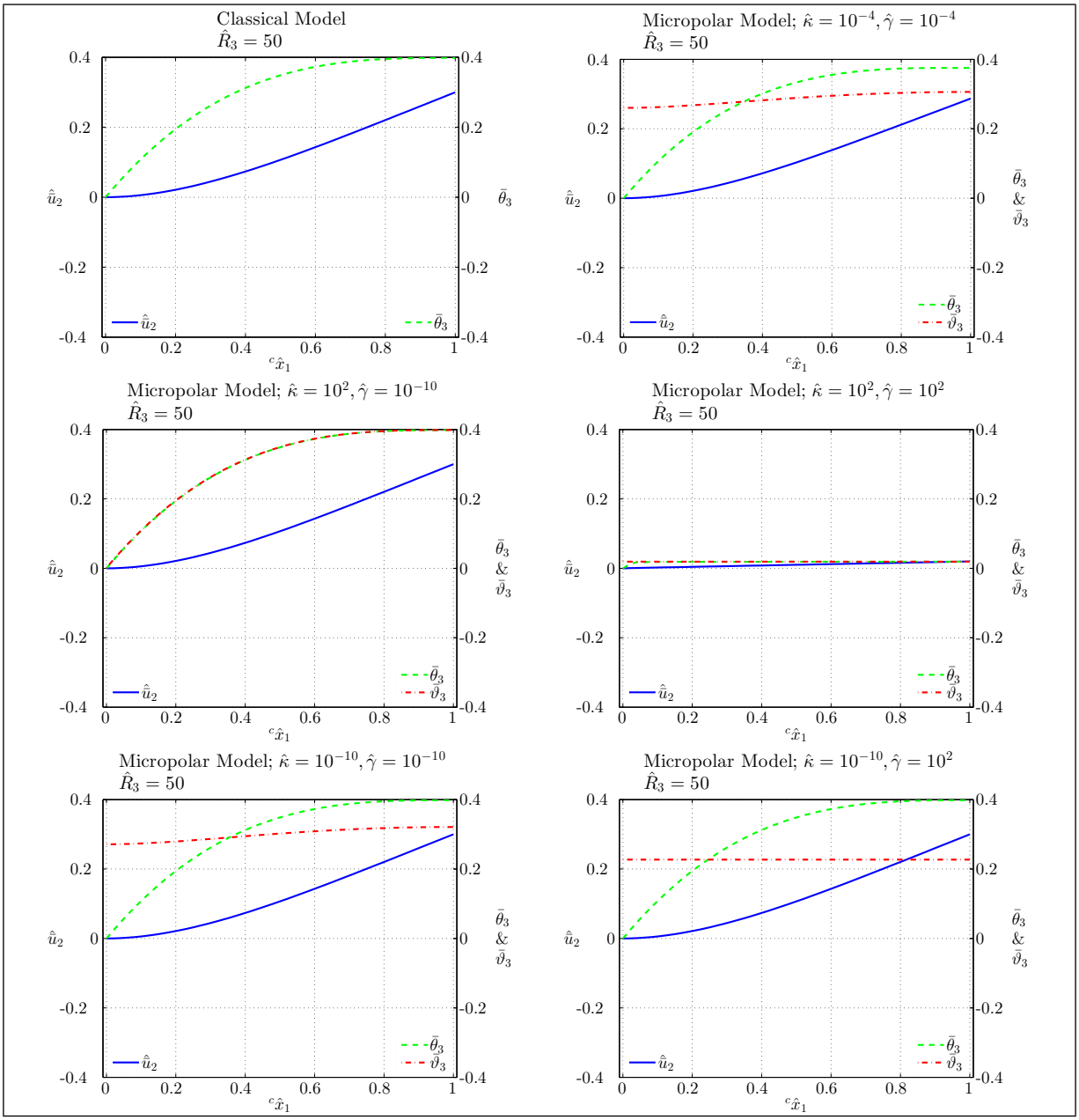

Figure C.18: Bending deformations of beams with medium thickness under volume force $\hat{\hat{f}}_2^V$.

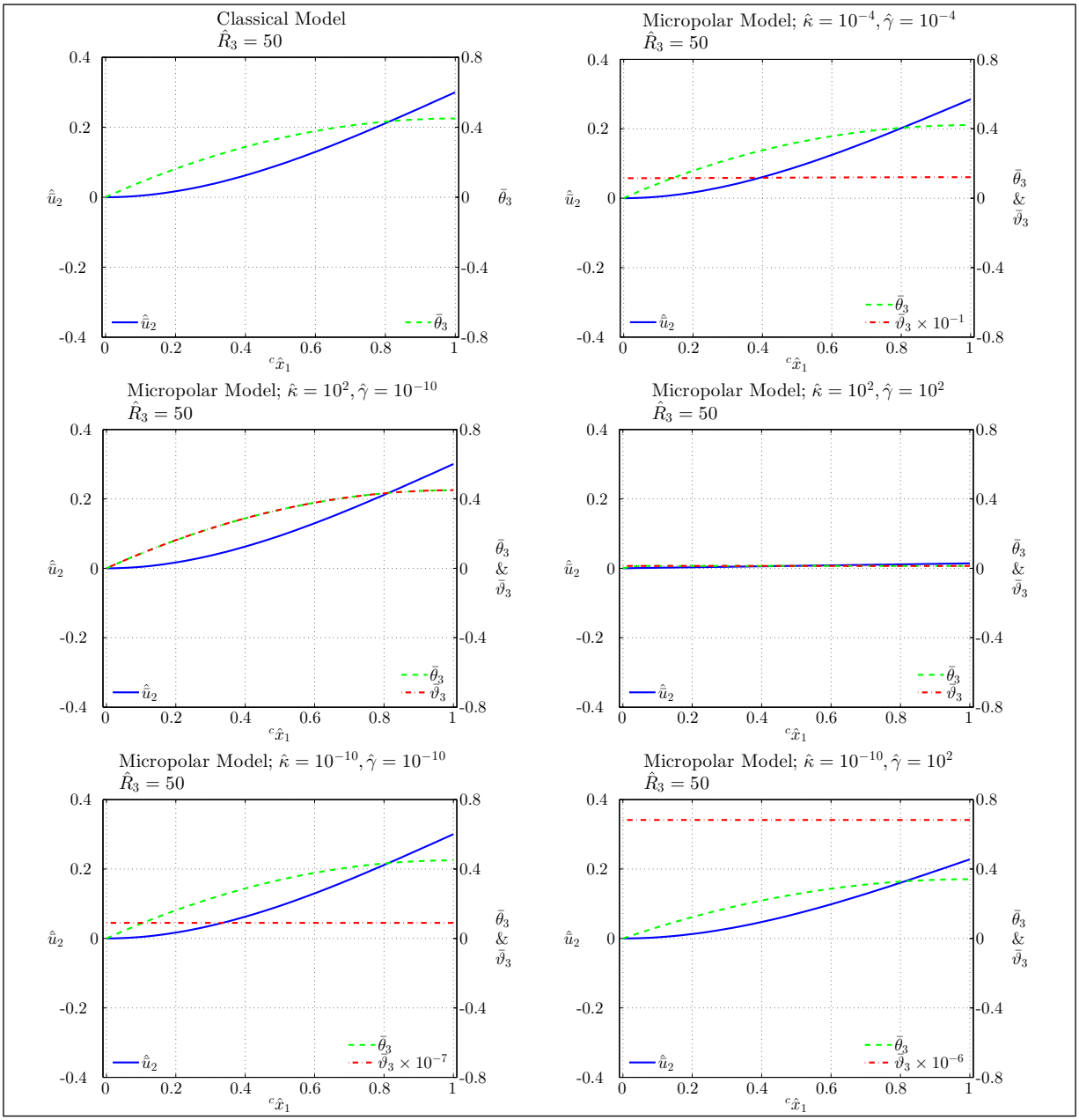

Figure C.19: Bending deformations of beams with medium thickness under volume moment $\hat{\hat{m}}_3^{\,V}$.

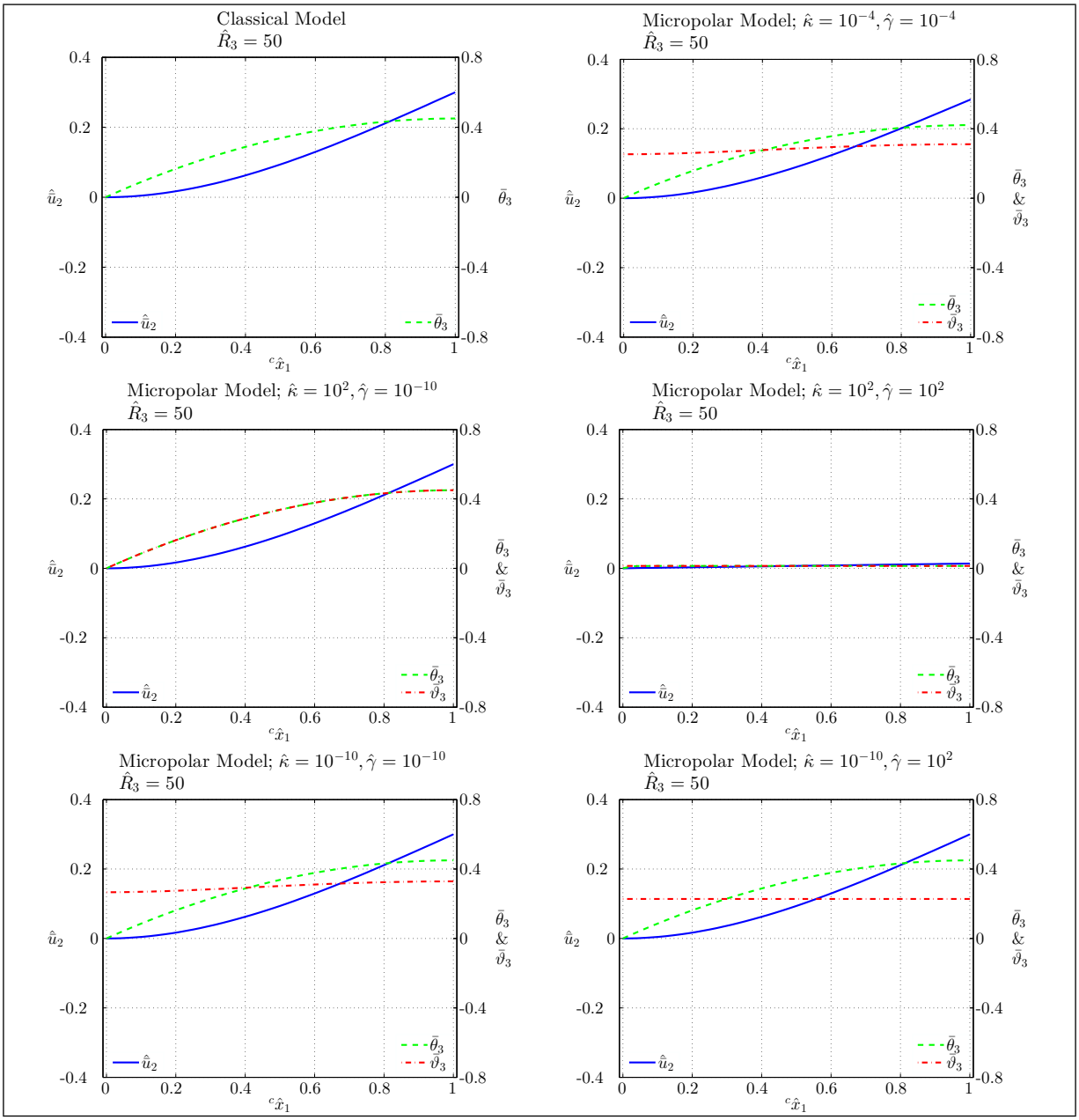

Figure C.20: Bending deformations of beams with medium thickness under line moment $\hat{\hat{m}}_3^L$.

The distribution of torsional and bending deformations along the beam length for a classical beam model and five selected micropolar beam models are plotted in Figures C.16–C.20. The five micropolar beam models which vary in the values assigned to the micropolar constants $\hat{\kappa}$ and $\hat{\gamma}$ correspond to the middle and corner points of the 2D plots in Figures C.3–C.15. The previously mentioned static behaviors of the micropolar beam model (in both torsion and bending), compared to the classical beam model, can be noticed more clearly in these plots.

In each plot of Figures C.16–C.20 there are two scales, one on the left and one on the right vertical axis. The vertical axes have their own legend, in the lower left and right corners of the plots, which note the variables measured on each axis. In the torsional deformation plots the left vertical axis quantifies the plane rotation $\bar{\theta}_1$ and the right vertical axis quantifies the microrotation $\bar{\vartheta}_1$. In the plots illustrating the bending deformations, the bending displacement $\hat{\bar{u}}_2$ is measured on the left vertical axis and the plane rotation $\bar{\theta}_3$ and the microrotation $\bar{\vartheta}_3$ are measured on the right vertical axis. Note that, as mentioned in their legends (in the lower left and right corners), in the two bottom plots of Figures C.16 and C.19 the microrotations are scaled separately to be visible in the plotted frame.

In each figure (for both torsion and bending cases) the top left plot corresponds to the classical beam model. This plot is a reference for examination of the selected micropolar beam models. In the case of torsion it contains the torsional plane rotation $\bar{\theta}_1$ and in the case of bending it contains the bending displacement $\hat{\bar{u}}_2$ and the bending plane rotation $\bar{\theta}_3$. Note that in addition to these classical DOFs, the micropolar beam models include the torsional and bending microrotations $\bar{\vartheta}_1$ and $\bar{\vartheta}_3$ in the torsion and bending cases, correspondingly.

The top right plot of each figure is obtained from a micropolar beam model with medium $\hat{\kappa}$ and $\hat{\gamma}$ which was represented as the middle point of the 2D plots in Figures C.3–C.15. As can be seen in this micropolar beam model a medium $\hat{\kappa}$ (*i.e.* $\hat{\kappa} = 1 \times 10^{-4}$) is not enough for complete coupling of the micropolar and classical DOFs. However, a medium $\hat{\gamma}$ (*i.e.* $\hat{\gamma} = 1 \times 10^{-4}$) is small enough to make the micropolar modes non-dominant and let the classical deformations of this micropolar beam model be relatively comparable with those obtained from the classical beam model.

The middle left plot of each figure corresponds to a micropolar beam model with a large $\hat{\kappa}$ and a small $\hat{\gamma}$, shown in the upper left corner of the 2D plots in Figures C.3–C.15. As noted previously, the results of this micropolar beam model match the classical beam model results with an acceptable accuracy and the extra torsional and bending microrotations of this model coincide (exactly) with the corresponding classical plane rotations.

The middle right plot in each figure, related to the upper right corner of the 2D plots in Figures C.3–C.15, illustrates a micropolar beam model with large $\hat{\kappa}$ and $\hat{\gamma}$. In this model the large $\hat{\kappa}$ couples the micropolar and classical modes and the large $\hat{\gamma}$ dominates the micropolar mode. However, in Figures C.16–C.20 the external load is not large enough to generate any significant micropolar deformations from this micropolar beam model (compared to the classical deformations obtained from the classical beam model).

The bottom left plot in each figure corresponds to a micropolar beam model with small $\hat{\kappa}$ and $\hat{\gamma}$ and was shown in the lower left corner of the 2D plots in Figures C.3–C.15. This is the case which was wrongly expected by some authors to have micropolar results coincide with the classical results (see Section A.8). However, as can be seen in Figures C.16 and C.19 this micropolar beam model is singular (*i.e.* predicts torsional and bending microrotations which are six to seven orders of magnitude larger than classical deformations) in the presence of an external volume moment and cannot be considered as the case where the micropolar and classical models are equivalent. In this micropolar beam model there is not enough connection, or coupling, between the micropolar and classical DOFs (due to a small $\hat{\kappa}$) and whereas the model is able to reproduce the classical deformations (due to a small $\hat{\gamma}$), the micropolar deformations do not follow the classical ones and may even tend to infinity. This model can correspond to a micropolar material in which the grains or particles are free to rotate independent of the lattices or cells (or the material structure as a whole).

Finally, in each figure the bottom right plot corresponds to a micropolar beam model with a small $\hat{\kappa}$ and a large $\hat{\gamma}$ which was represented as the lower right corner of the 2D plots in Figures C.3–C.15. As noted previously the results obtained from this model might be erroneous due to an ill-conditioned FEM stiffness matrix. However, overall one can notice the singular behavior of this model under the action of external volume moments which is due to a loose connection between the micropolar and classical DOFs.

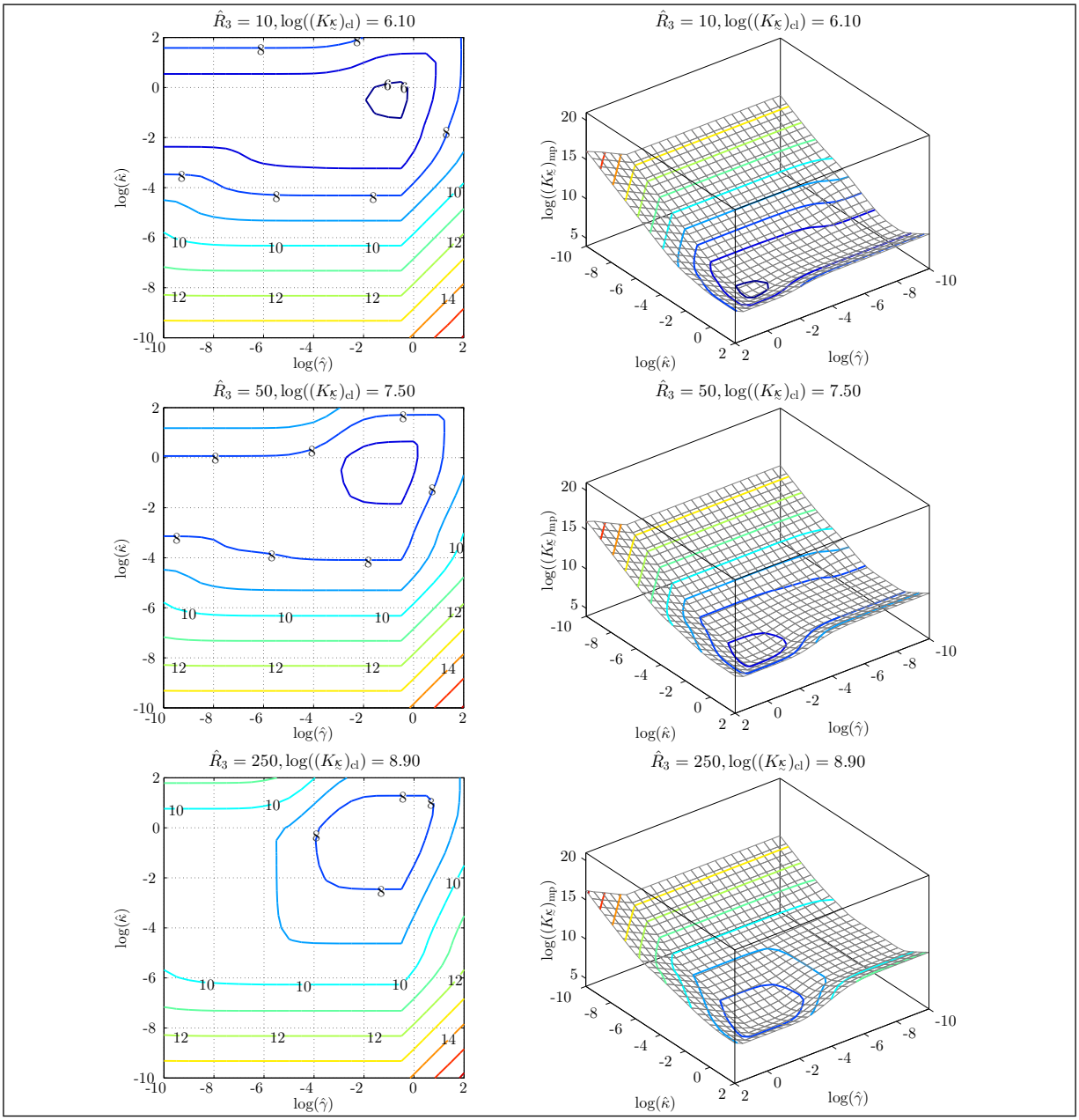

Figure C.21: Condition number of FEM stiffness matrix $(K_{\underset{\sim}{\boldsymbol{\kappa}}})_{\rm mp}$ of micropolar beams vs. micropolar elastic constants.

The plots of Figure C.21 illustrate the variation of the 1-norm condition number of the micropolar beams' FEM stiffness matrix (including both torsional and bending stiffnesses) vs. the variation of the micropolar elastic constants $\hat{\kappa}$ and $\hat{\gamma}$. Note that the condition number of the FEM stiffness matrix also depends on the number of nodes or elements and these plots correspond to a FEM with 49 nodes or 16 elements.

For comparison, the 1-norm condition number of the classical beam FEM stiffness matrix (using the same number of nodes) for different slenderness ratios is given in the title of each plot. Here one should be careful not to expect the same condition number from micropolar and classical beam models in the region where the models are supposed to coincide. This is due to the fact that whereas the number of nodes is the same for both micropolar and classical FEMs, their corresponding stiffness matrices have totally different dimensions as they are based on different finite elements with different number of DOFs per node (respectively nine and six DOFs per node in micropolar and classical FEM).

As mentioned previously, based on the plots shown in Figure C.21 and considering the accuracy of numerical calculations in MATLAB®, all the results reported or plotted previously for a micropolar beam model with roughly $\hat{\kappa} < 1 \times 10^{-8}$ and $\hat{\gamma} > 1$ are unreliable as they might include numerical precision errors.

Whereas more study can be performed on the static behavior of micropolar elastic beams (with different types of BCs and external loadings), this will not be pursued here and this appendix will proceed with modal analysis and comparison of classically cantilevered micropolar and classical elastic beams.

C.3 Dynamic analysis

To complement the static analysis addressed in the previous section, the dynamic analysis of micropolar beams is presented in this section. This dynamic analysis is accomplished through a natural frequencies and mode shapes comparison between the micropolar and classical beam models.

Again, the comparison is done considering just the beam torsional deformations around the ${}^{c}\hat{x}_1$ axis and the beam bending deformations in the ${}^{c}\hat{x}_1{}^{c}\hat{x}_2$ plane. In other words, the

natural frequencies and mode shapes corresponding to the homogeneous micropolar beam dynamic equations:

$$
\begin{aligned}
0 &= \hat{I}_1 \, \overset{\circ\circ}{\bar{\theta}}_1 - k_{\mathrm{t}} \, \hat{\mu} \, \hat{I}_1 \, \bar{\theta}_{1,\hat{1}\hat{1}} - \hat{\kappa} \, \hat{I}_1 \left(\bar{\theta}_{1,\hat{1}\hat{1}} - 2 \, \xi \, \bar{\vartheta}_{1,\hat{1}\hat{1}} \right) + 4 \, \hat{\kappa} \left(\bar{\theta}_1 - \bar{\vartheta}_1 \right) \\
0 &= \overset{\circ}{\hat{\mathcal{I}}}_1^{\,V} - \hat{\mathcal{E}} \, \bar{\vartheta}_{1,\hat{1}\hat{1}} + 2 \, \xi \, \hat{\kappa} \, \hat{I}_1 \left(\bar{\theta}_{1,\hat{1}\hat{1}} - 2 \, \xi \, \bar{\vartheta}_{1,\hat{1}\hat{1}} \right) - 4 \, \hat{\kappa} \left(\bar{\theta}_1 - \bar{\vartheta}_1 \right) \\
0 &= \overset{\circ\circ}{\hat{\bar{u}}}_2 - k_{\mathrm{s}_2} \, \hat{\mu} \left(\hat{\bar{u}}_{2,\hat{1}\hat{1}} - \bar{\theta}_{3,\hat{1}} \right) - \hat{\kappa} \left(\hat{\bar{u}}_{2,\hat{1}\hat{1}} + \bar{\theta}_{3,\hat{1}} - 2 \, \bar{\vartheta}_{3,\hat{1}} \right) \\
0 &= \hat{I}_3 \, \overset{\circ\circ}{\bar{\theta}}_3 - \hat{I}_3 \, \bar{\theta}_{3,\hat{1}\hat{1}} - k_{\mathrm{s}_2} \, \hat{\mu} \left(\hat{\bar{u}}_{2,\hat{1}} - \bar{\theta}_3 \right) + \hat{\kappa} \left(\hat{\bar{u}}_{2,\hat{1}} + \bar{\theta}_3 - 2 \, \bar{\vartheta}_3 \right) \\
0 &= \overset{\circ}{\hat{\mathcal{I}}}_3^{\,V} - \left(\hat{\gamma} + \hat{\beta} \right) \bar{\vartheta}_{3,\hat{1}\hat{1}} - 2 \, \hat{\kappa} \left(\hat{\bar{u}}_{2,\hat{1}} + \bar{\theta}_3 - 2 \, \bar{\vartheta}_3 \right)
\end{aligned}
\tag{C.24}
$$

will be compared against the natural frequencies and mode shapes obtained from the following homogeneous classical beam dynamic equations:

$$
\begin{aligned}
0 &= \hat{I}_1 \, \overset{\circ\circ}{\bar{\theta}}_1 - k_{\mathrm{t}} \, \hat{\mu} \, \hat{I}_1 \, \bar{\theta}_{1,\hat{1}\hat{1}} \\
0 &= \overset{\circ\circ}{\hat{\bar{u}}}_2 - k_{\mathrm{s}_2} \, \hat{\mu} \left(\hat{\bar{u}}_{2,\hat{1}\hat{1}} - \bar{\theta}_{3,\hat{1}} \right) \\
0 &= \hat{I}_3 \, \overset{\circ\circ}{\bar{\theta}}_3 - \hat{I}_3 \, \bar{\theta}_{3,\hat{1}\hat{1}} - k_{\mathrm{s}_2} \, \hat{\mu} \left(\hat{\bar{u}}_{2,\hat{1}} - \bar{\theta}_3 \right)
\end{aligned}
\tag{C.25}
$$

after considering the classically cantilevered BCs (as described in Table C.2) for both cases.

It is worth mentioning that analogous to the characteristic roots corresponding to the homogeneous form of a set of PDEs (exemplifying the PDEs general homogeneous solution), the natural frequencies and mode shapes obtained from the homogenized dynamic PDEs (or dynamic equations) characterize the general dynamic solution of the PDEs exposed to different I/BCs and external (time-varying) loadings. They also carry the BC information with themselves (despite the characteristic roots which do not). Therefore, a comparison of the natural frequencies and mode shapes would be enough for a fairly comprehensive dynamic comparison between micropolar and classical beams.

Now recall that the static comparison of the previous section is based on the micropolar to classical deformation ratios which also reveal the classical to micropolar beam stiffness ratios as the static deformations are inversely related to the beam stiffness. To be consistent with these static results and to have a measure of the classical to micropolar beam stiffness

ratios once more, in this section the dynamic comparison will be carried out based on the classical to micropolar natural frequency ratios as the natural frequencies are directly related to the (square root of) beam stiffness.

Therefore, in this section the indices of dynamic comparison are considered to be the relative torsional and bending natural frequencies identified as the classical beam natural frequency $(\hat{\omega}^{(i)})_{\text{cl}}$ divided by the micropolar beam natural frequency $(\hat{\omega}^{(i)})_{\text{mp}}$ of the same type and the same rank. To be more precise, the classical torsional natural frequencies $(\hat{\omega}_{\text{t}}^{(i)})_{\text{cl}}$ are divided by the micropolar torsional natural frequencies $(\hat{\omega}_{\text{t}}^{(i)})_{\text{mp}}$ and the classical bending natural frequencies $(\hat{\omega}_{\text{b}}^{(i)})_{\text{cl}}$ are weighted against the micropolar bending natural frequencies $(\hat{\omega}_{\text{b}}^{(i)})_{\text{mp}}$.

The natural frequencies comparison is complemented by a mode shape comparison of the micropolar and classical beams. In the mode shape comparison five micropolar beam models are selected (in the same way as in the previous section for plotting the complete torsional and bending deformations) and their torsional and bending mode shapes are plotted next to the same-type and same-rank classical torsional and bending mode shapes. This reveals the nature of natural frequencies and the modal behavior of different micropolar beam models.

The first three relative classical to micropolar torsional natural frequencies vs. the micropolar elastic constants are given in Figures C.22–C.27. Similar graphs for the first three relative bending natural frequencies are shown in Figures C.28–C.33. These figures show how the micropolar natural frequencies $(\hat{\omega}^{(i)})_{\text{mp}}$ vary with the changes in the micropolar elastic constants $\hat{\kappa}$ and $\hat{\gamma}$, as well as the changes in the beam slenderness ratio $\hat{R}_3$ and the micropolar microinertia $\hat{\imath}^V$.

In Figures C.22–C.33 note that scales are log-log-percentage. Also, for each slenderness ratio a 2D contour plot and a 3D surface plot are provided; the 3D plot is obtained by looking at the 2D plot from a point over the 2D plot's upper right corner.

The first three torsional and bending mode shapes for the beam with medium thickness (*i.e.* $\hat{R}_3 = 50$) are plotted in Figures C.34–C.45. All the torsional and bending mode shapes corresponding to the classical beam model are normalized (or scaled) such that the maximum torsional plane rotation or bending (nondimensional) displacement of the mode

shape does not exceed 0.3. The torsional and bending mode shapes of the micropolar beam models are scaled accordingly except the pure micropolar modeshapes which are scaled such that the the maximum microrotation ($\bar{\vartheta}_1$ or $\bar{\vartheta}_3$) does not exceed 0.3.

Whereas only the first three torsional and bending vibration modes are illustrated in the figures of this section, the explanations and conclusions are based on considering the first 10 torsional and bending vibration modes. A brief discussion of what the figures show and mean will be given later, after each set of figures. However, as a general rule the dimensionless (micropolar) microinertia density $\hat{\imath}^V$ is a measure of the material grain (or particle) size relative to the beam length (refer to the definition of $\hat{\imath}^V$ in Eq. (4.83)). A zero microinertia corresponds to a material with no grain or a zero grain size. Analogous to the static case, the slenderness ratio $\hat{R}_3$ represents the beam thickness, the micropolar constant $\hat{\kappa}$ represents the extent of coupling between micropolar and classical deformations, and the micropolar constant $\hat{\gamma}$ is a measure of the significance of micropolar deformations relative to classical deformations or a measure of size effects significance. Recall that the micropolar beam model with small $\hat{\kappa}$ are analytically singular due to an ill-conditioned stiffness operator which cannot guarantee the continuity of the beam.

It is worth mentioning that, again, in the region where $\hat{\kappa}$ is very small and $\hat{\gamma}$ is very large (*i.e.* in the lower right corner of the 2D plots) the plotted results are unreliable as the FEM stiffness matrices of micropolar beams are numerically ill-conditioned in this region (refer to Figure C.21).

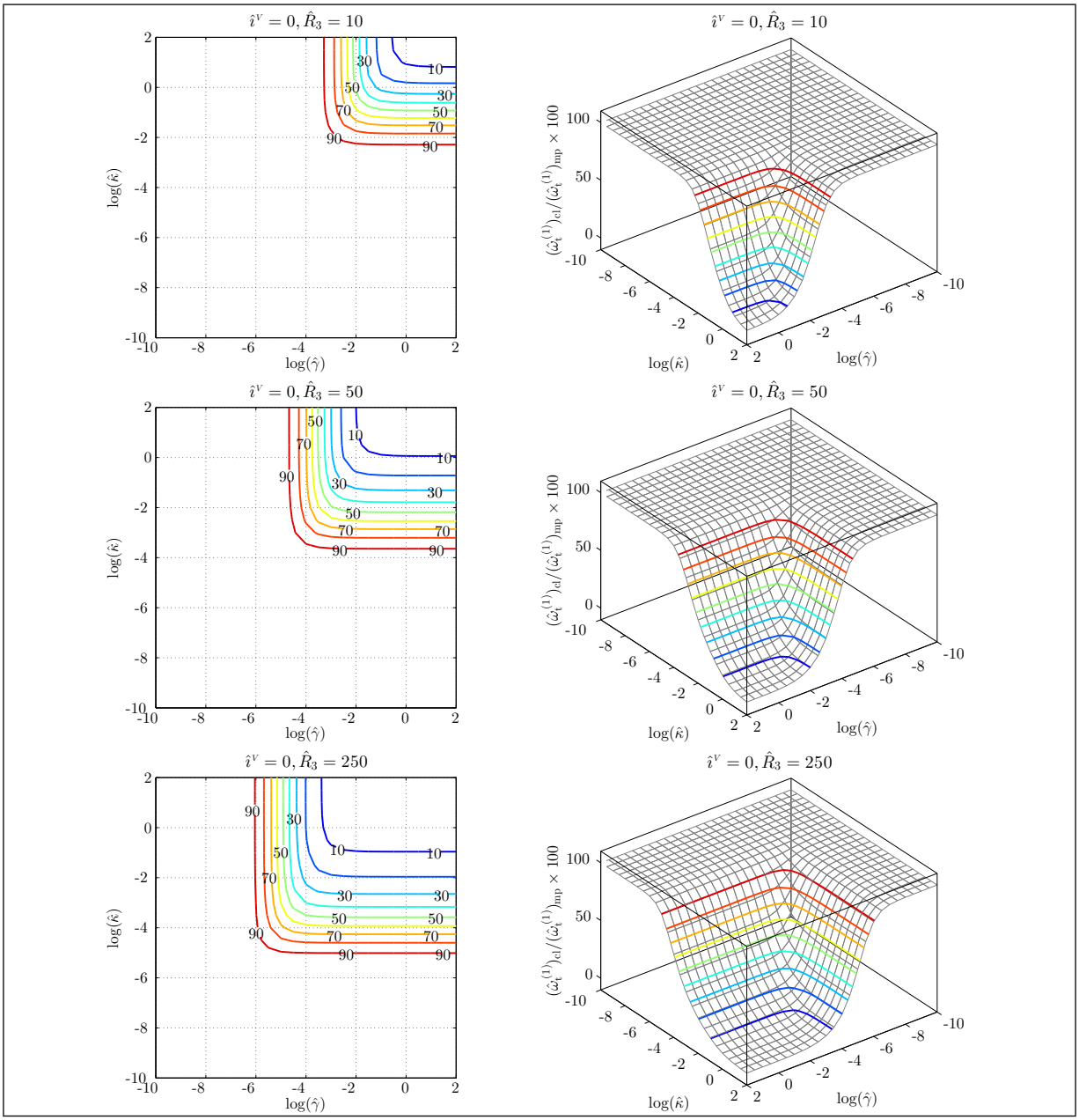

Figure C.22: Relative 1$^{\mathrm{st}}$ natural frequency of torsion $(\hat{\omega}_{\mathrm{t}}^{(1)})_{\mathrm{cl}}/(\hat{\omega}_{\mathrm{t}}^{(1)})_{\mathrm{mp}}$ for micropolar beams with a zero microinertia vs. micropolar elastic constants.

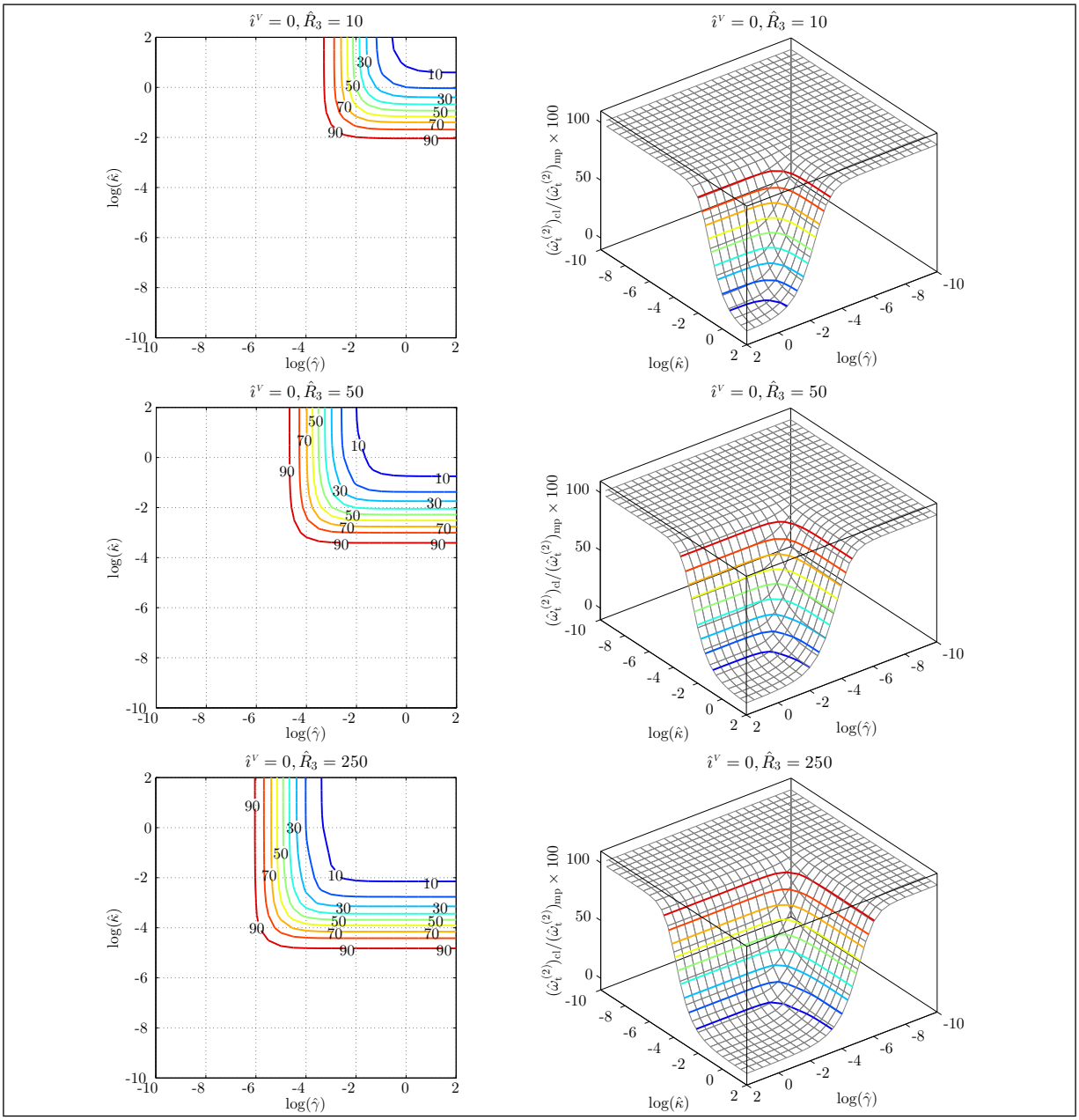

Figure C.23: Relative 2nd natural frequency of torsion $(\hat{\omega}_t^{(2)})_{cl}/(\hat{\omega}_t^{(2)})_{mp}$ for micropolar beams with a zero microinertia vs. micropolar elastic constants.

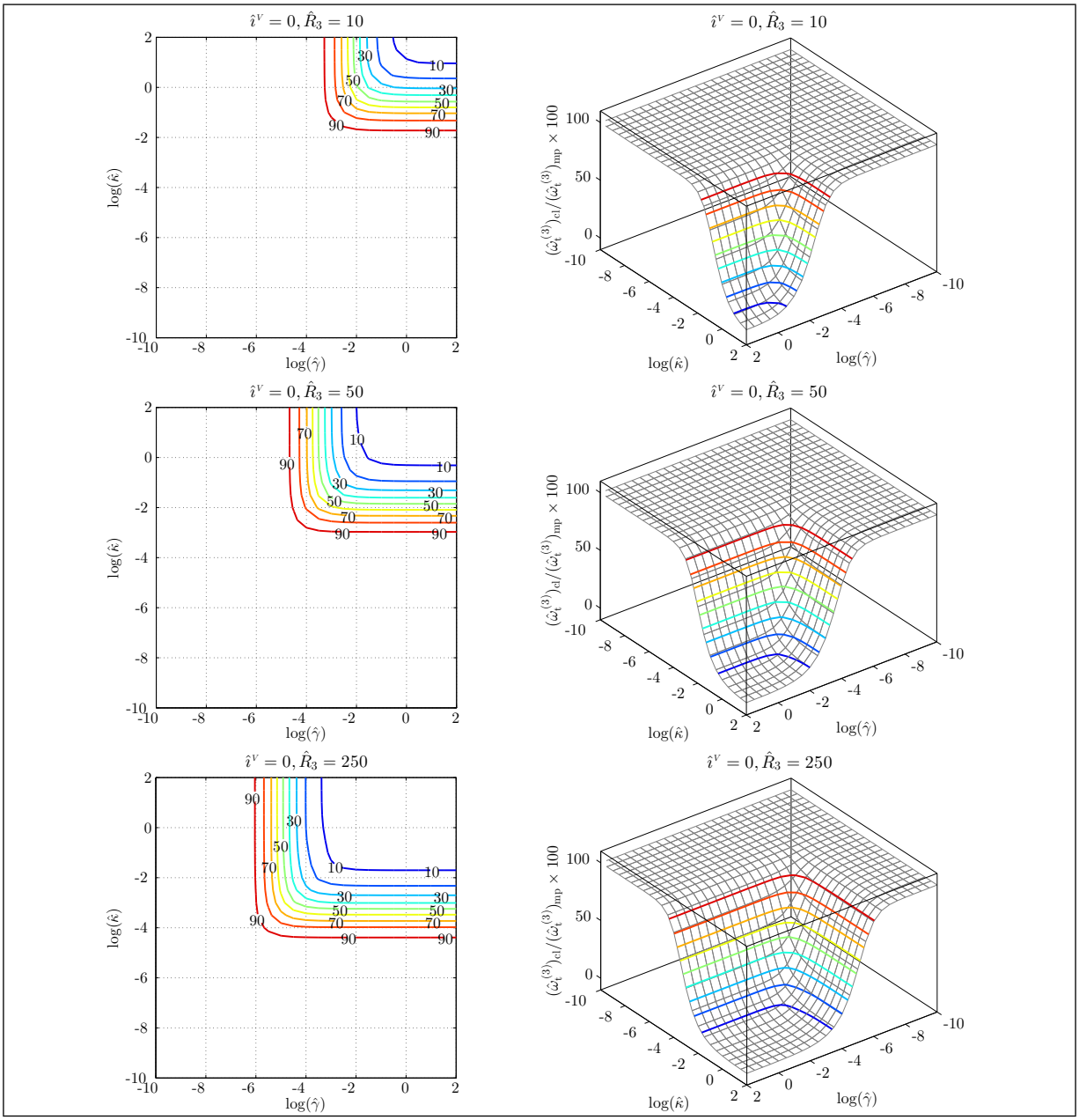

Figure C.24: Relative 3rd natural frequency of torsion $(\hat{\omega}_t^{(3)})_{cl}/(\hat{\omega}_t^{(3)})_{mp}$ for micropolar beams with a zero microinertia vs. micropolar elastic constants.

The plots shown in Figures C.22–C.24 illustrate the variations of the first three torsional natural frequencies of micropolar beams when the microinertia is zero ($\hat{\imath}^V = 0$).

As the first point one can notice the size effects phenomenon in these figures, that is the difference between micropolar and classical beam models is more apparent for larger $\hat{R}_3$ and $\hat{\gamma}$ (equivalent to a thinner and shorter beam, respectively).

Comparing the plots of different natural frequencies one can conclude that the effects of the micropolar constant $\hat{\kappa}$, representing the coupling between micropolar and classical DOFs, are slightly more evident in lower vibration modes (*i.e.* the higher the mode the larger the value of $\hat{\kappa}$ at which the natural frequency surface drops). However, the effects of the micropolar constant $\hat{\gamma}$, representing the relative significance of micropolar deformations, are almost the same in different vibration modes (*i.e.* for different modes the natural frequency surface drops at the same value of $\hat{\gamma}$).

In Figures C.22–C.24 the singularity of the micropolar beam model for small $\hat{\kappa}$ where the micropolar and classical DOFs are decoupled is not visible due to a zero microinertia. Indeed, the singularity of the micropolar beam model with zero microinertia $\hat{\imath}^V$ and small $\hat{\kappa}$ will be disclosed as infinite natural frequencies (corresponding to the decoupled micropolar deformation modes) which sorting the natural frequencies will place them among the very high vibration modes, outside the span of few lower vibration modes considered here. This is analogous to the simple case of a zero mass attached to an ideal (massless) soft spring which has an infinite natural frequency.

The unseen (or hidden) singularity of micropolar beam models with zero microinertia and small $\hat{\kappa}$ may deceive one to conclude that except the region where $\hat{\kappa}$ and $\hat{\gamma}$ are large (*i.e.* the upper right quarter of the 2D plots), the micropolar and classical beam models coincide in terms of vibration modes. However, as mentioned before this is not true and the micropolar beams with small $\hat{\kappa}$ have vibration modes which do not match any of the vibration modes in a corresponding classical beam. Therefore, similar to the static case, the micropolar and classical beam models coincide only when $\hat{\kappa}$ is large and $\hat{\gamma}$ is small. The next three figures, illustrating the first three torsional natural frequencies of micropolar beams with a small microinertia, will show this more clearly.

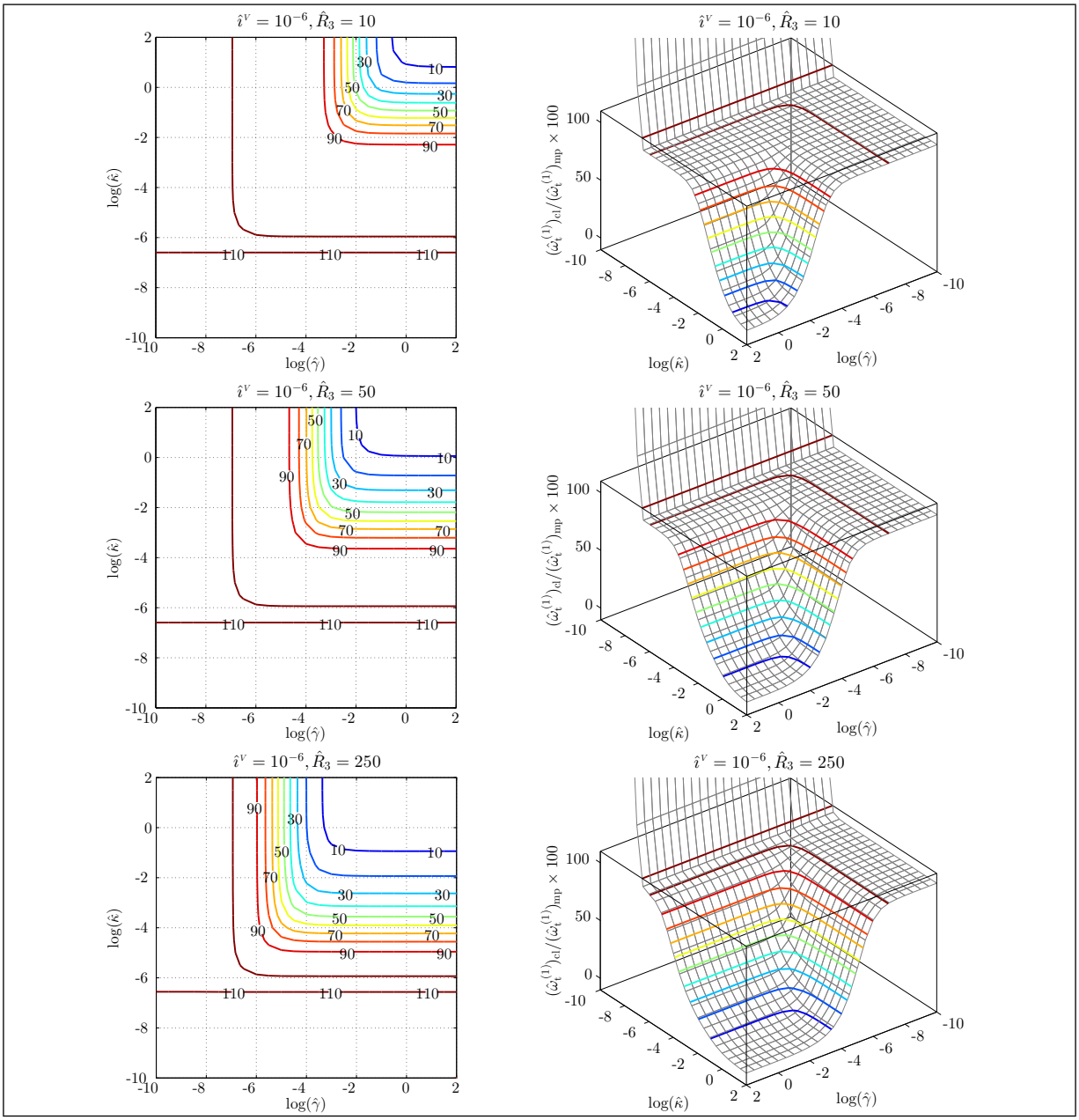

Figure C.25: Relative 1st natural frequency of torsion $(\hat{\omega}_t^{(1)})_{cl}/(\hat{\omega}_t^{(1)})_{mp}$ for micropolar beams with a small microinertia vs. micropolar elastic constants.

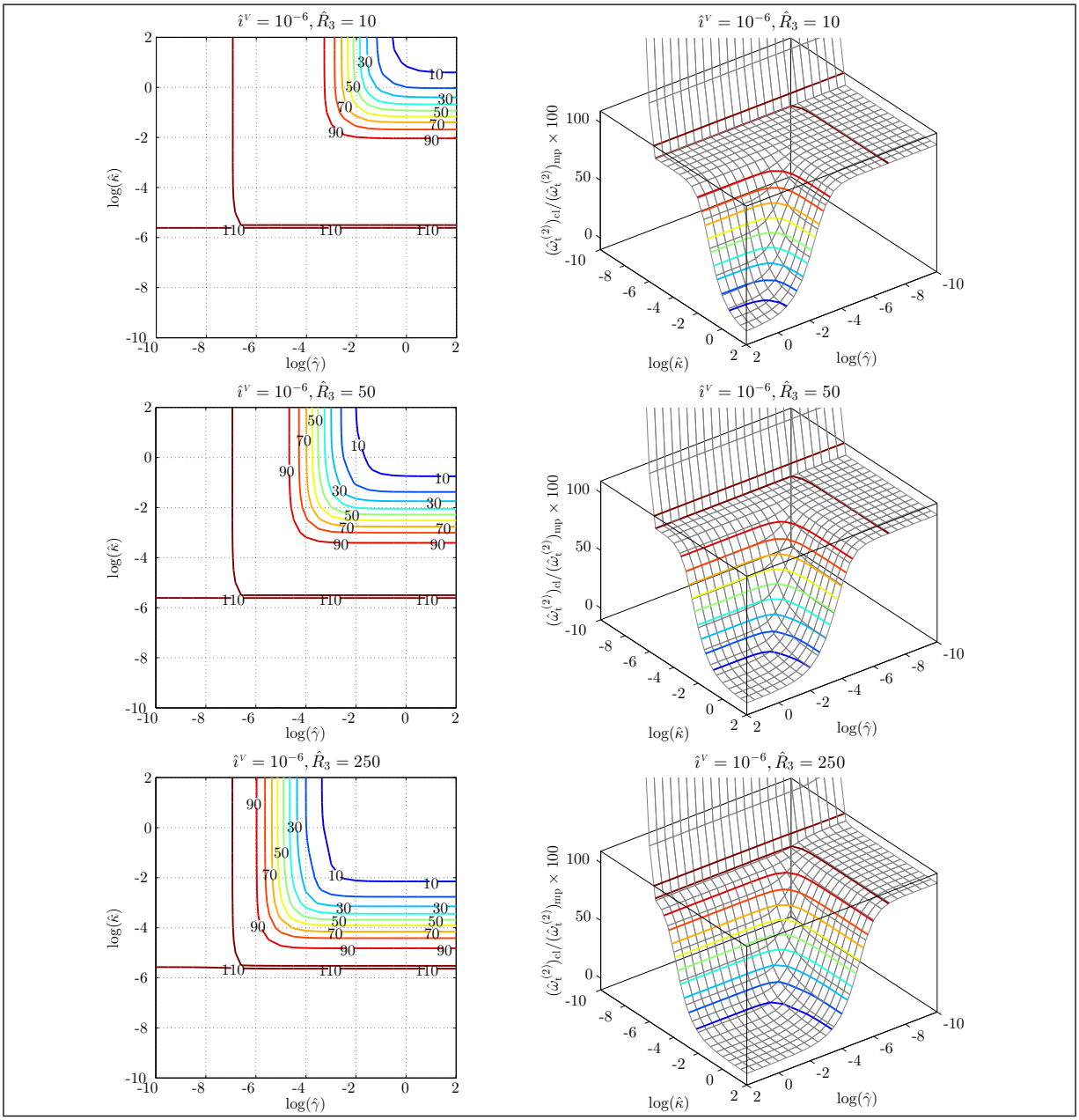

Figure C.26: Relative 2nd natural frequency of torsion $(\hat{\omega}_t^{(2)})_{cl}/(\hat{\omega}_t^{(2)})_{mp}$ for micropolar beams with a small microinertia vs. micropolar elastic constants.

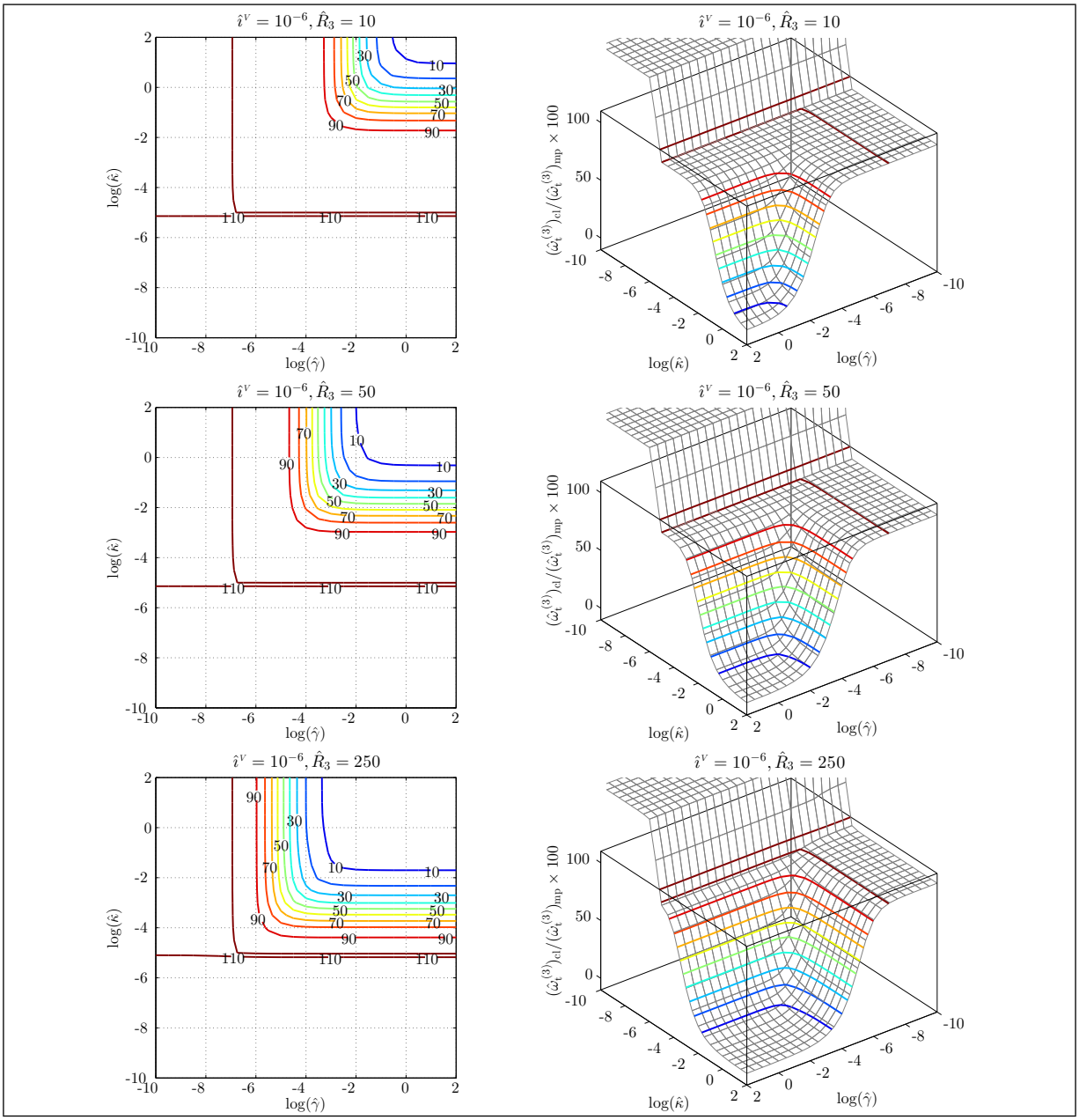

Figure C.27: Relative 3rd natural frequency of torsion $(\hat{\omega}_t^{(3)})_{cl}/(\hat{\omega}_t^{(3)})_{mp}$ for micropolar beams with a small microinertia vs. micropolar elastic constants.

The plots of Figures C.25–C.27 show the first three torsional natural frequencies of the micropolar beams with a small microinertia ($\hat{\imath}^V = 1 \times 10^{-6}$). Most of the behaviors seen for the zero-microinertia case can be seen again in these plots. The difference between micropolar and classical beam models is more apparent for larger $\hat{R}_3$ and $\hat{\gamma}$ (equivalent to a thinner and shorter beam, respectively). This confirms the size effects phenomenon. The effects of the micropolar constant $\hat{\kappa}$ is slightly more significant on lower natural frequencies. The micropolar constant $\hat{\gamma}$ has almost the same effects on different natural frequencies.

Here, in the region where $\hat{\kappa}$ is small one can see a jump in the plots of natural frequencies which is a representation of the singularity in the micropolar beam model with small $\hat{\kappa}$. Indeed, the small (but nonzero) microinertia ($\hat{\imath}^V = 1 \times 10^{-6}$) is enough to place the decoupled micropolar deformation modes among the few lower vibration modes considered in this section for the comparison between micropolar and classical beams. In other words, despite the zero-microinertia micropolar beams which have infinite natural frequencies corresponding to the decoupled micropolar vibration modes, the micropolar beams with a small microinertia $\hat{\imath}^V$ may have small natural frequencies corresponding to the decoupled micropolar vibration modes depending on the relative magnitude of $\hat{\imath}^V$ and $\hat{\kappa}$ (as is the case in here). One may interpret this as the case of a small mass attached to a massless soft spring which can result in a small natural frequency as long as the mass to stiffness ratio is large enough.

Note that the inclusion of the decoupled micropolar vibration modes (with small natural frequencies) in the selected lower vibration modes causes the subsequent micropolar natural frequencies to be compared against the (same-rank but) non-corresponding classical ones and this is the source for the observed jumps in the plots. When comparing the plots of different vibration modes (for the same slenderness ratio) one can notice that at higher vibration modes these jumps happen at larger values of $\hat{\kappa}$. However, comparing the plots of one figure it can be concluded that the singular region does not change its size as the beam thickness varies. The reason is that while the beam thickness decreases the increasing microinertia effects work against the growing coupling effects and do not allow the singular region to shrink.

Again, the micropolar and classical beam models coincide in terms of vibration modes when $\hat{\kappa}$ is large and $\hat{\gamma}$ is small.

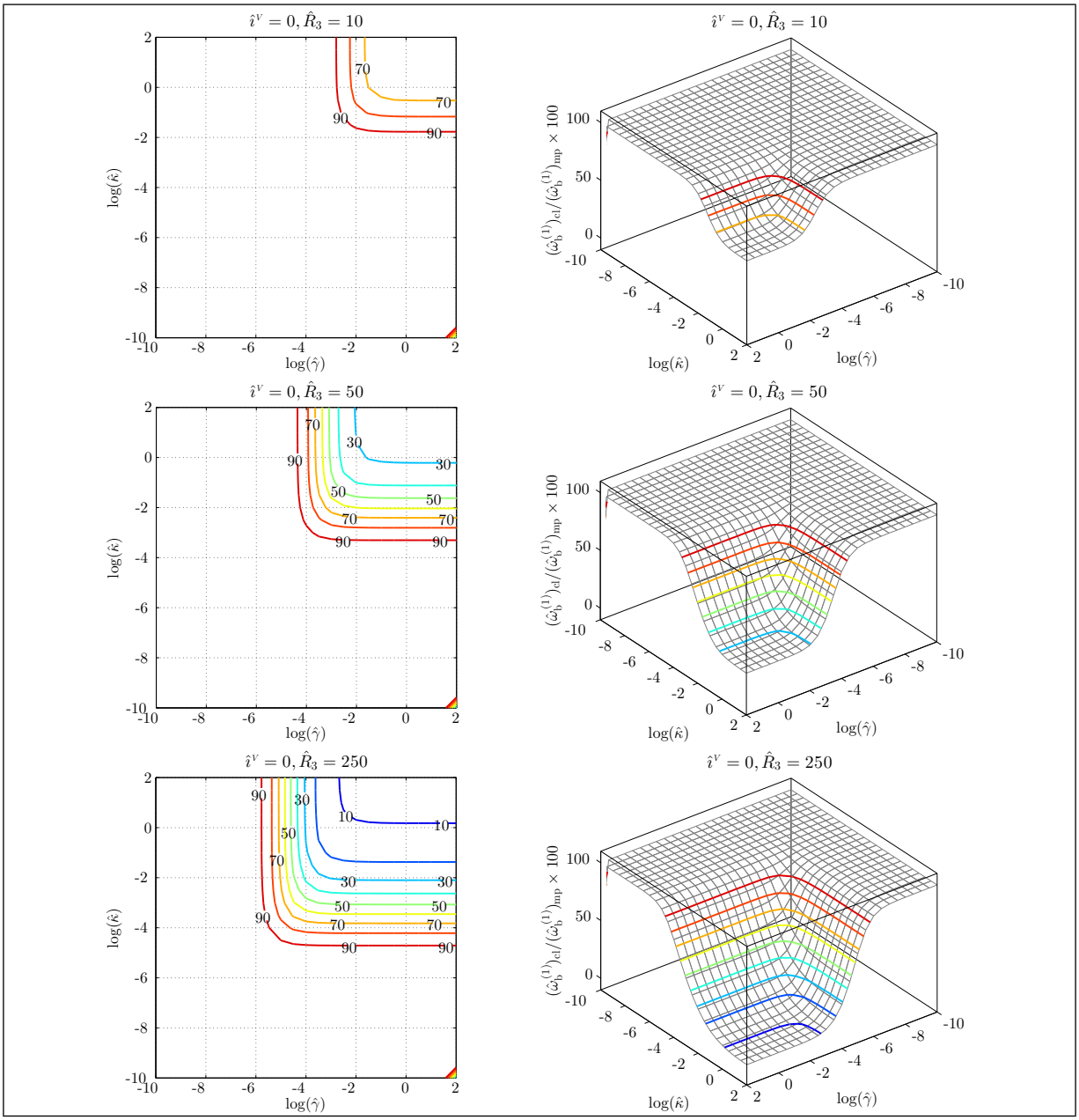

Figure C.28: Relative 1st natural frequency of bending $(\hat{\omega}_{\mathrm{b}}^{(1)})_{\mathrm{cl}}/(\hat{\omega}_{\mathrm{b}}^{(1)})_{\mathrm{mp}}$ for micropolar beams with a zero microinertia vs. micropolar elastic constants.

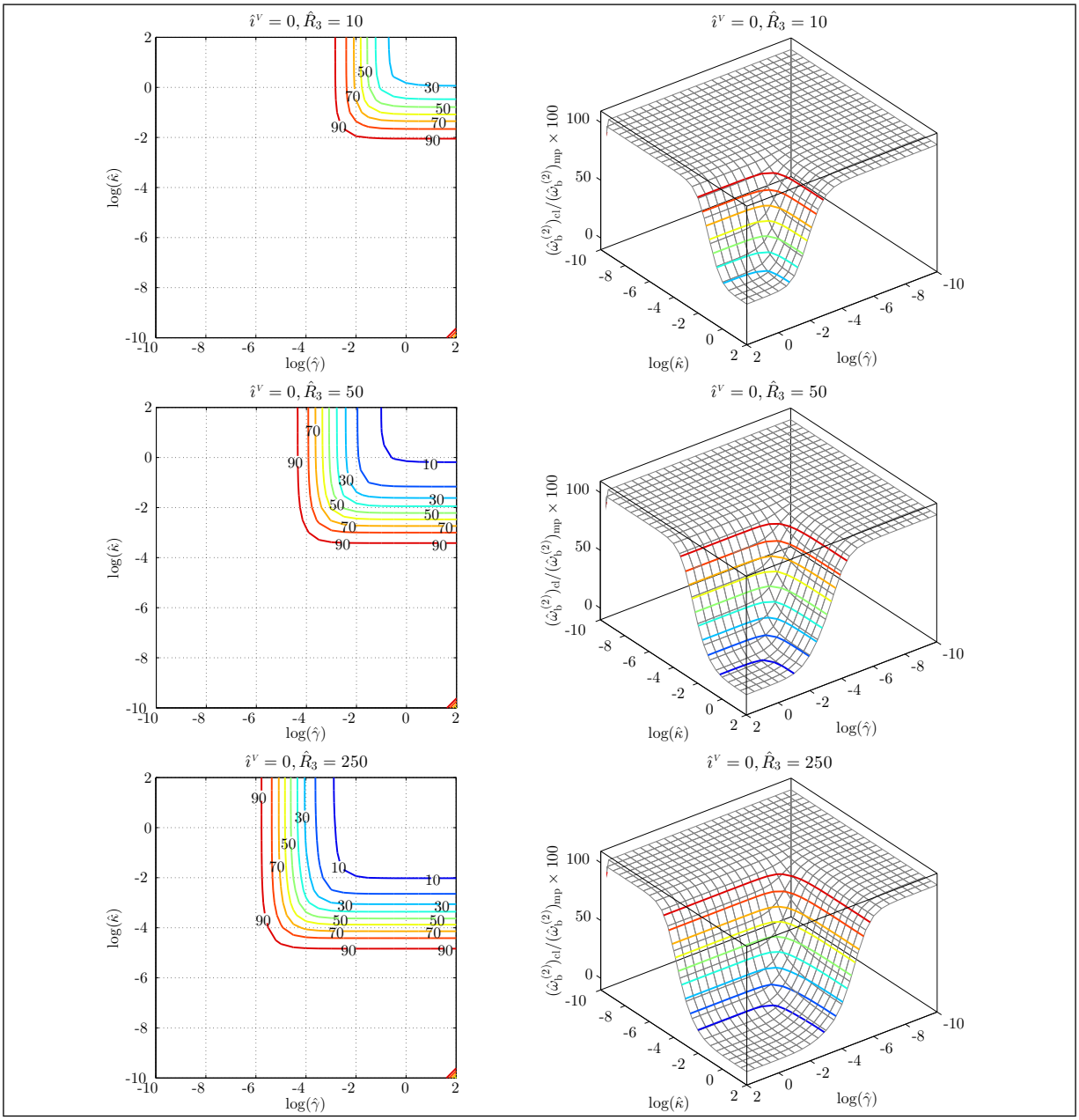

Figure C.29: Relative 2nd natural frequency of bending $(\hat{\omega}_{\mathrm{b}}^{(2)})_{\mathrm{cl}}/(\hat{\omega}_{\mathrm{b}}^{(2)})_{\mathrm{mp}}$ for micropolar beams with a zero microinertia vs. micropolar elastic constants.

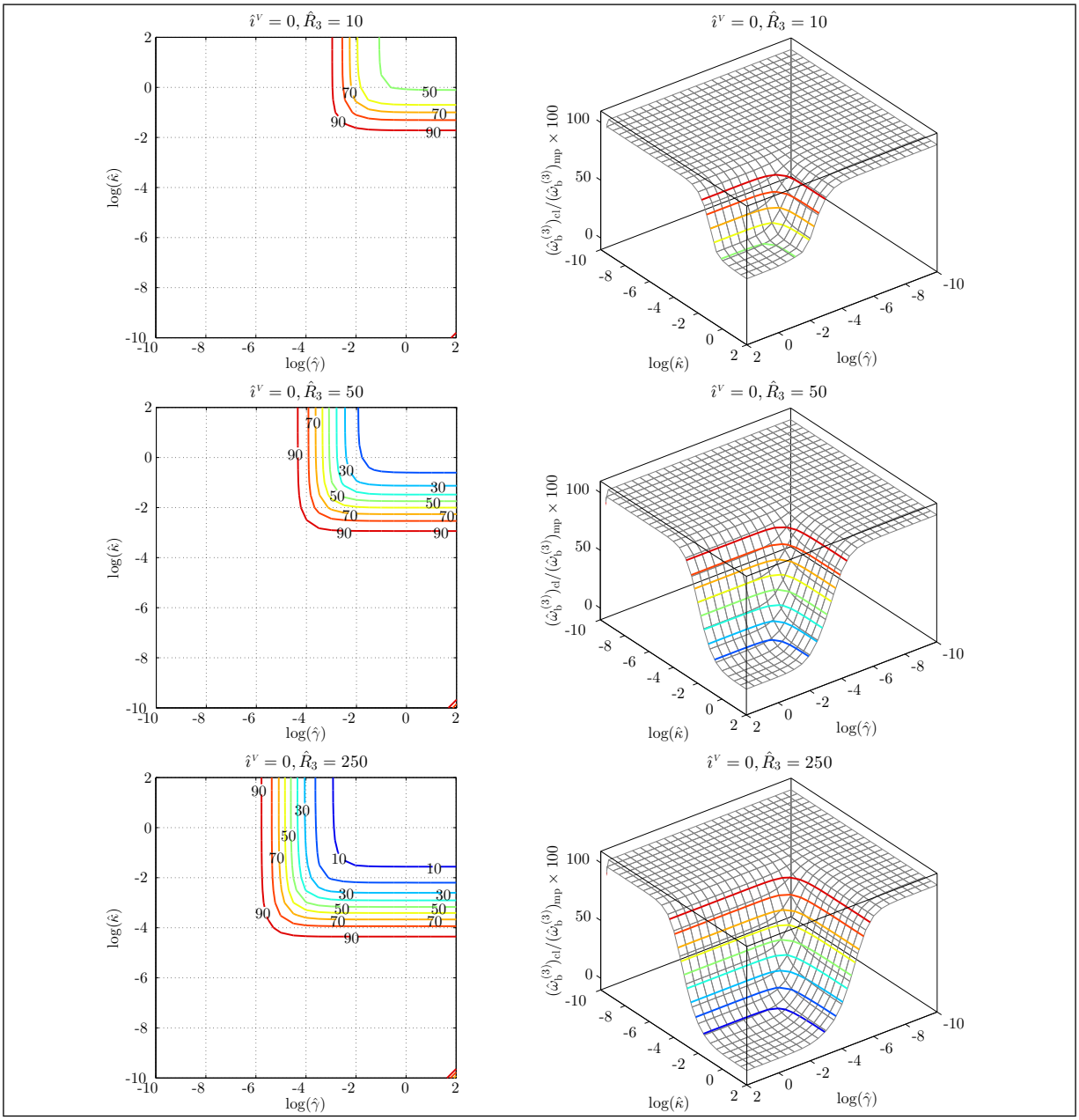

Figure C.30: Relative 3rd natural frequency of bending $(\hat{\omega}_b^{(3)})_{cl}/(\hat{\omega}_b^{(3)})_{mp}$ for micropolar beams with a zero microinertia vs. micropolar elastic constants.

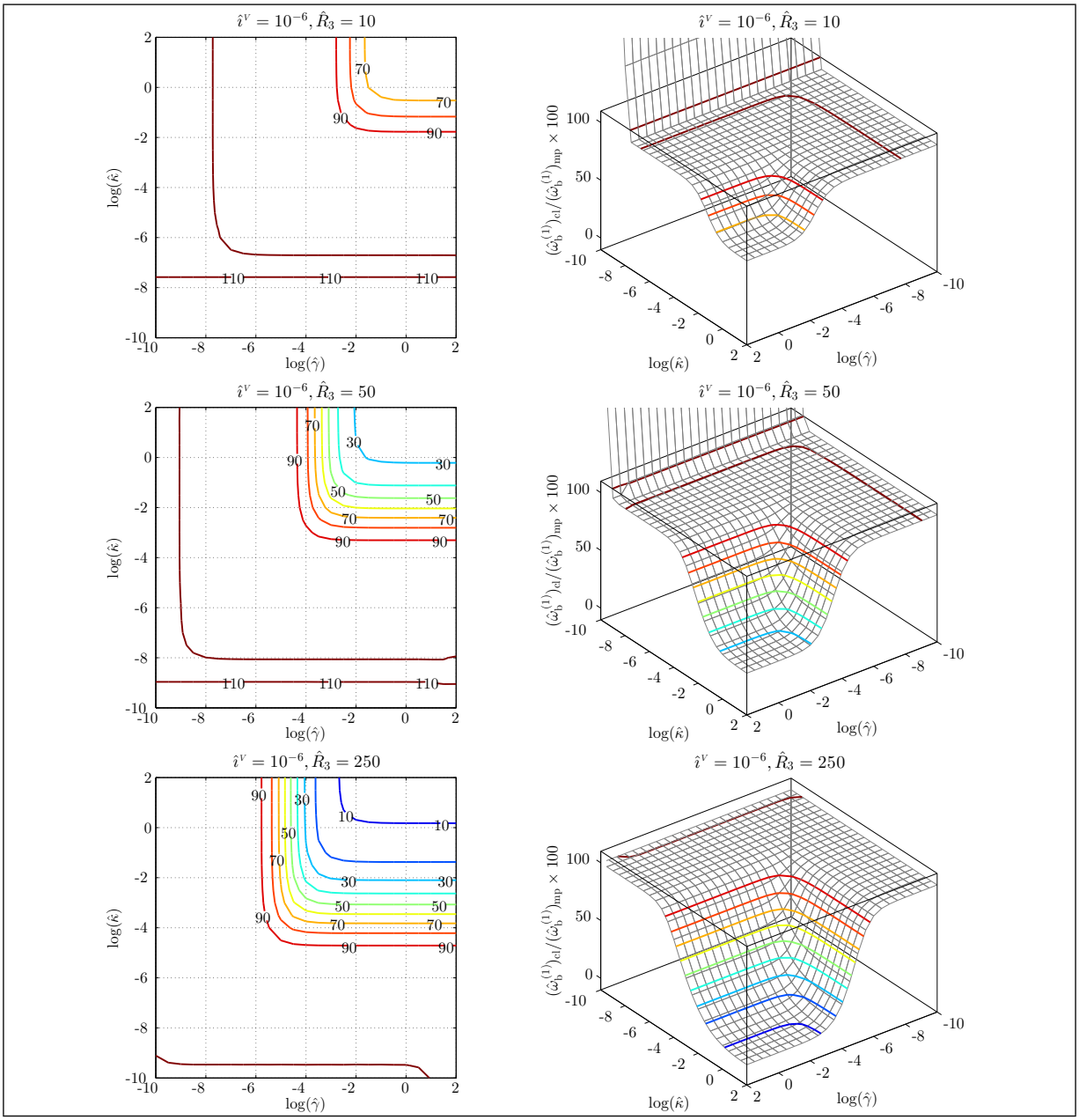

Figure C.31: Relative 1st natural frequency of bending $(\hat{\omega}_{\mathrm{b}}^{(1)})_{\mathrm{cl}}/(\hat{\omega}_{\mathrm{b}}^{(1)})_{\mathrm{mp}}$ for micropolar beams with a small microinertia vs. micropolar elastic constants.

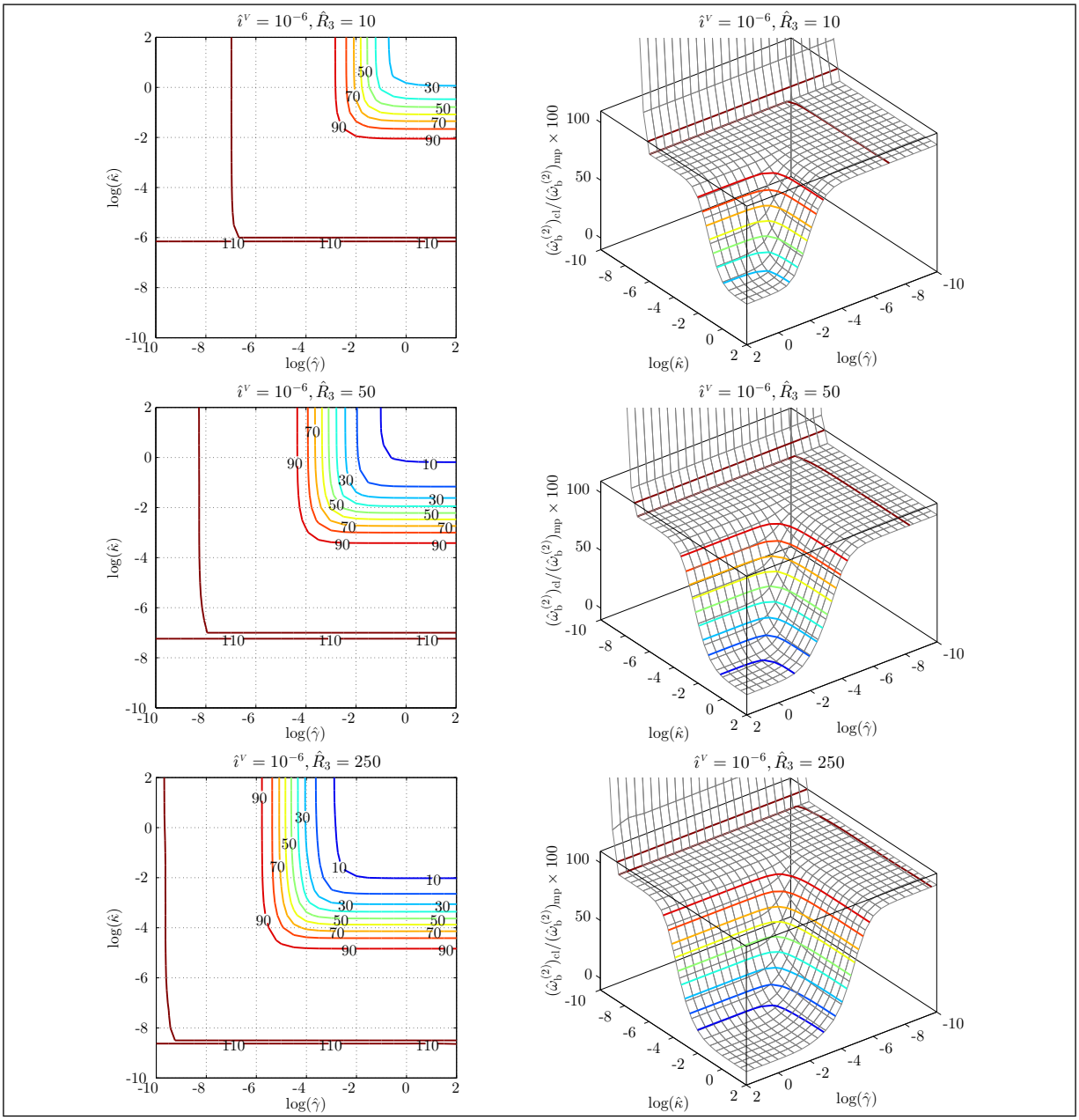

Figure C.32: Relative 2nd natural frequency of bending $(\hat{\omega}_{\mathrm{b}}^{(2)})_{\mathrm{cl}}/(\hat{\omega}_{\mathrm{b}}^{(2)})_{\mathrm{mp}}$ for micropolar beams with a small microinertia vs. micropolar elastic constants.

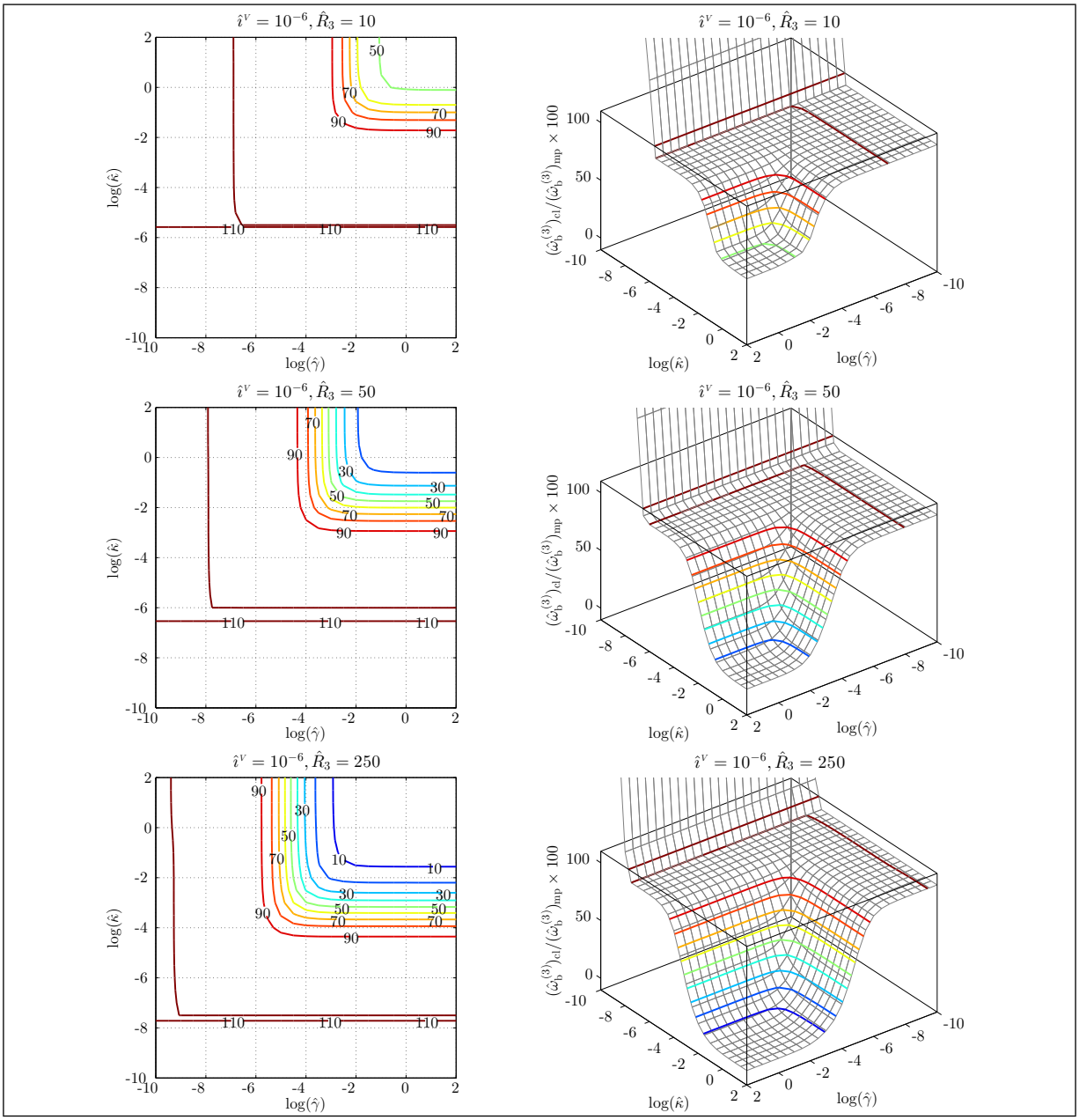

Figure C.33: Relative 3$^{\mathrm{rd}}$ natural frequency of bending $(\hat{\omega}_{\mathrm{b}}^{(3)})_{\mathrm{cl}}/(\hat{\omega}_{\mathrm{b}}^{(3)})_{\mathrm{mp}}$ for micropolar beams with a small microinertia vs. micropolar elastic constants.

Figures C.28–C.33 show the first three bending natural frequencies of micropolar beams with zero and small microinertia ($\hat{\imath}^V = 0$ and $\hat{\imath}^V = 1 \times 10^{-6}$). Almost the same behaviors as those observed for torsional natural frequencies can be seen in these plots.

For larger $\hat{R}_3$ and $\hat{\gamma}$ the difference between the micropolar and classical beam models is more apparent. In addition, whereas the effects of $\hat{\gamma}$ on different vibration modes seems to be the same, the effects of $\hat{\kappa}$ is slightly more significant on lower vibration modes. This latter conclusion is obtained by considering the first 10 bending natural frequencies and may not hold true for every one of them. For example, comparing the first and the second bending natural frequencies (respectively shown in plots of Figures C.28 and C.31 and plots of Figures C.29 and C.32), $\hat{\kappa}$ has a more significant effect on the latter.

Again, the singularity of micropolar beam models with small $\hat{\kappa}$ is not clear in plots of Figures C.28–C.30 for which the microinertia is zero (the natural frequencies corresponding to the decoupled micropolar vibration modes are infinite and out of the scope when taking into account just a few lower vibration modes). However, for the nonzero-microinertia case, shown in Figures C.31–C.33, this singularity can be seen as the jumps which exist in the region where $\hat{\kappa}$ is small (the natural frequencies corresponding to the decoupled micropolar vibration modes are now small enough to rest among the few considered lower vibration modes). Recall that the placement of the decoupled micropolar vibration modes among the selected lower vibration modes causes the subsequent micropolar natural frequencies to be compared against the (same-rank but) non-corresponding classical natural frequencies.

When comparing the plots of different natural frequencies for the case of nonzero microinertia, one can notice that, keeping the slenderness ratio constant, the higher the vibration mode the larger the value of $\hat{\kappa}$ at which the natural frequency surfaces jump. Also considering the plots of each figure for the case of nonzero microinertia, it can be concluded that for thinner beams the jumps occur at lower values of $\hat{\kappa}$. Here, the increase of microinertia effects is not as fast as the growth of coupling effects as the beam becomes thinner and therefore the improvement of coupling is dominant resulting in a smaller singular region for thinner beams.

Finally, for both cases of zero and small microinertia the micropolar and classical beam models coincide when $\hat{\kappa}$ is large and $\hat{\gamma}$ is small.

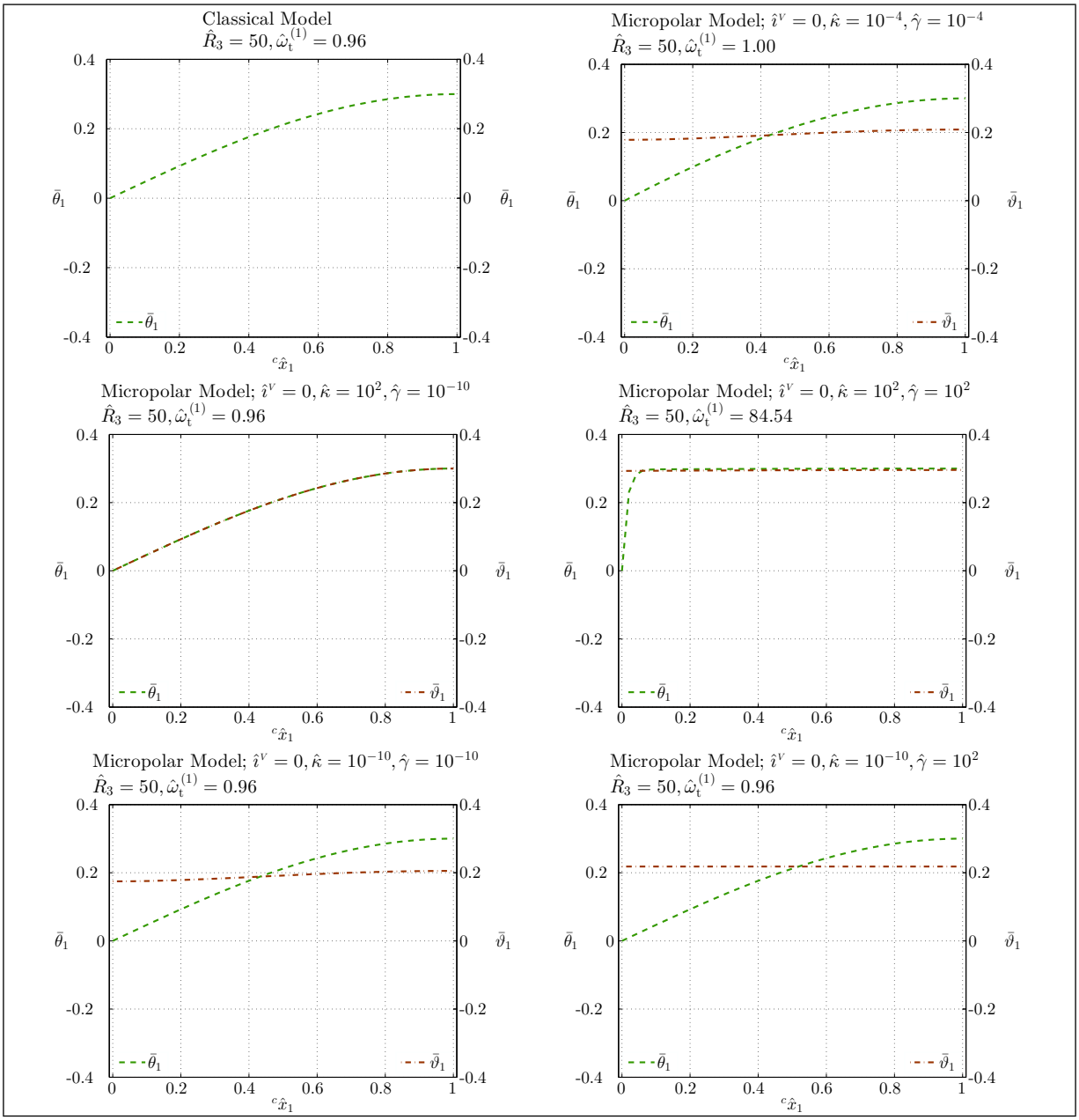

Figure C.34: 1st mode shape of torsion $\underset{\sim}{\hat{\boldsymbol{q}}}_{\mathrm{t}}^{(1)}$ for beams with a zero microinertia and medium thickness.

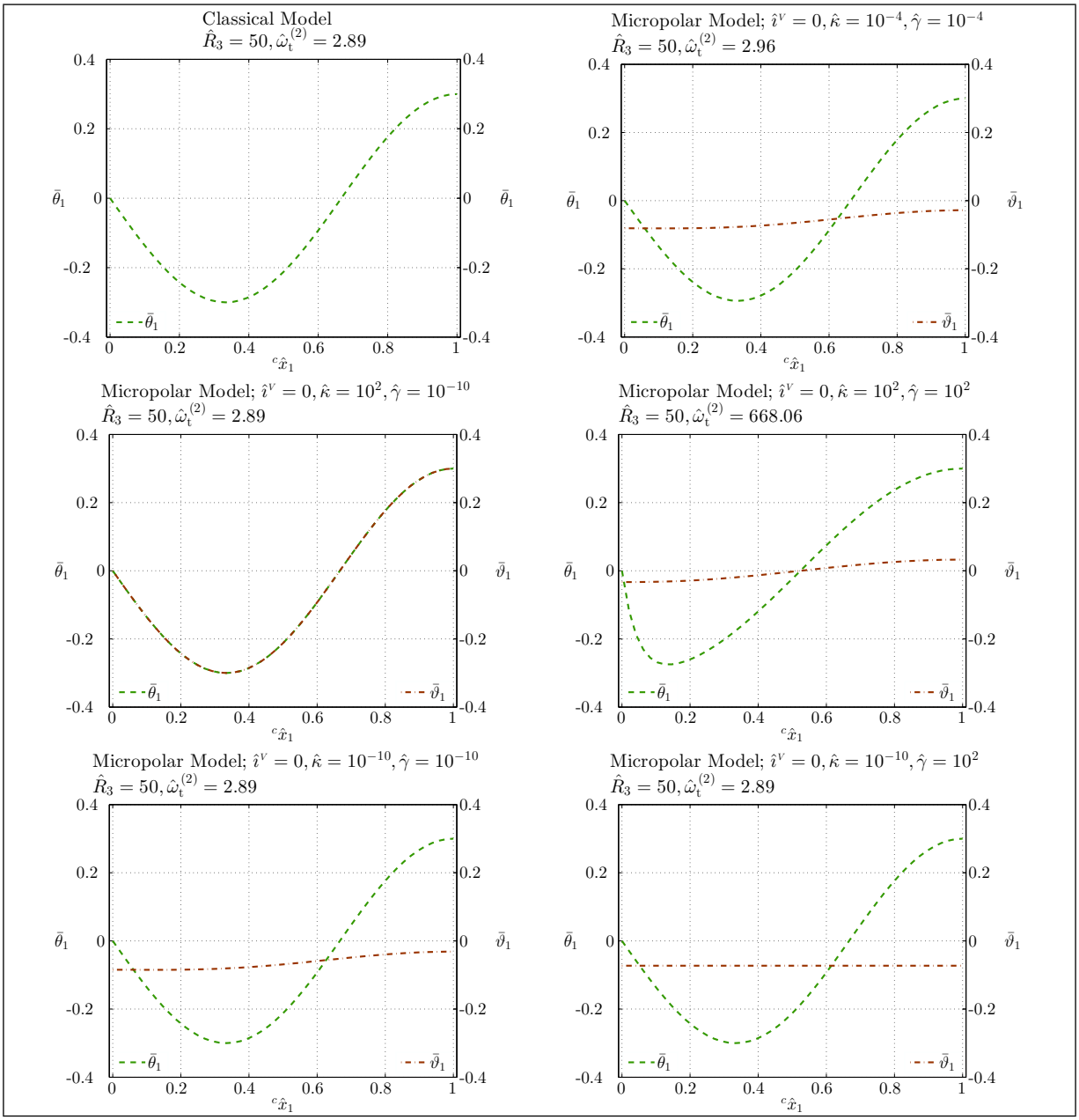

Figure C.35: 2nd mode shape of torsion $\underset{\sim}{\hat{\boldsymbol{q}}}_{\mathrm{t}}^{(2)}$ for beams with a zero microinertia and medium thickness.

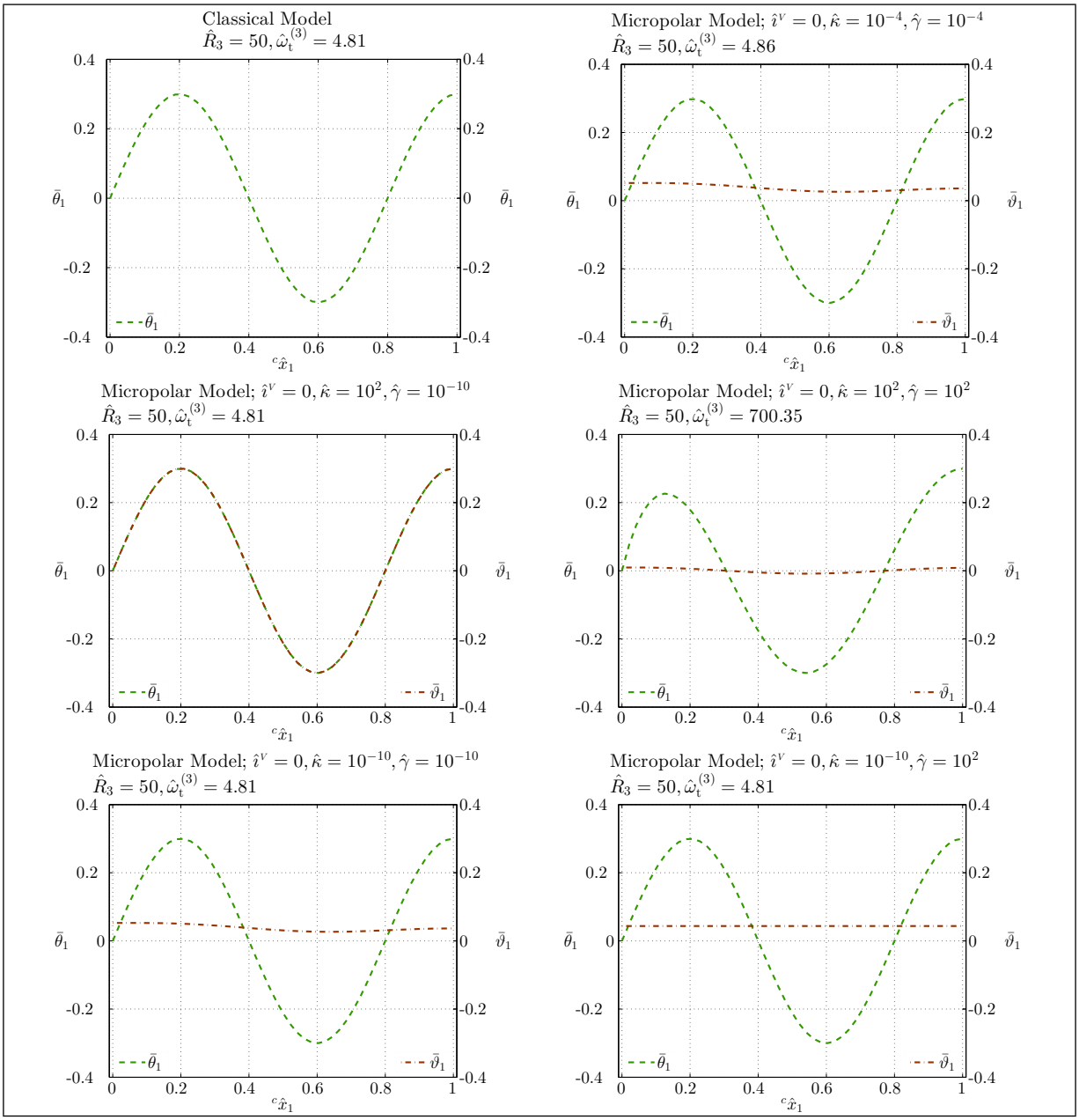

Figure C.36: 3rd mode shape of torsion $\underset{\sim}{\hat{\boldsymbol{q}}}_t^{(3)}$ for beams with a zero microinertia and medium thickness.

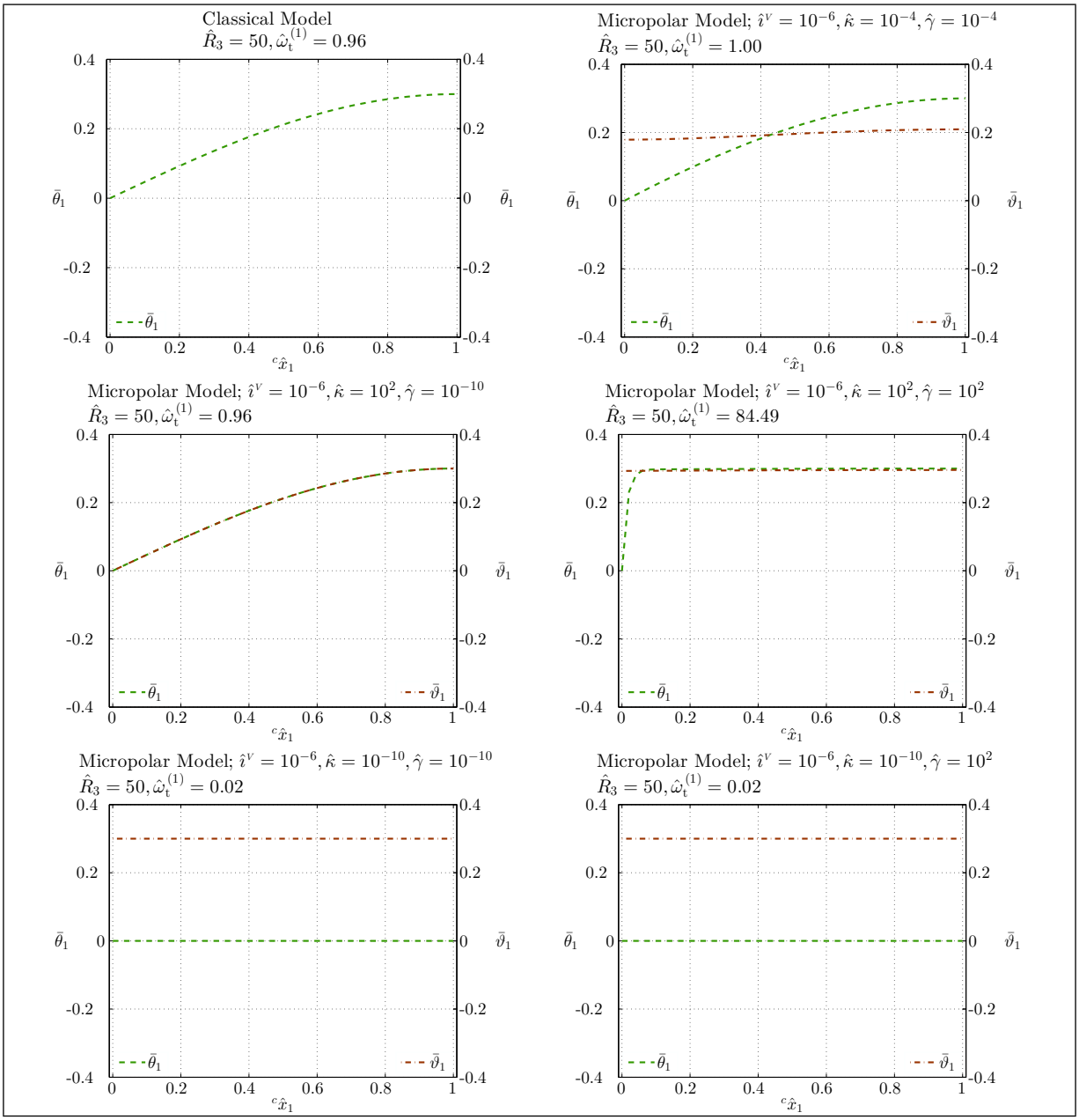

Figure C.37: 1st mode shape of torsion $\underset{\sim}{\hat{\boldsymbol{q}}}_{\mathrm{t}}^{(1)}$ for beams with a small microinertia and medium thickness.

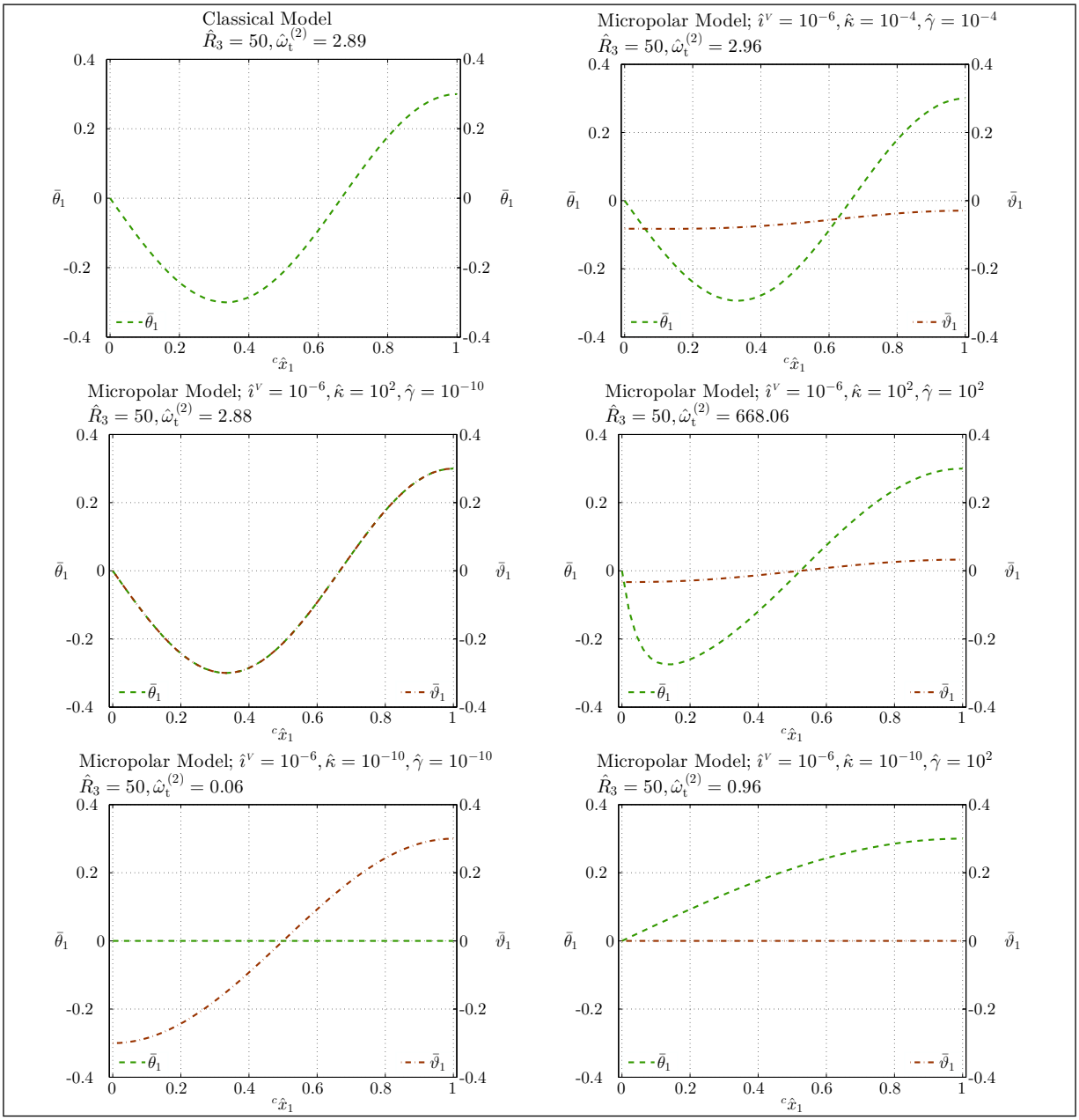

Figure C.38: 2nd mode shape of torsion $\underset{\sim}{\hat{\boldsymbol{q}}}_{\mathrm{t}}^{(2)}$ for beams with a small microinertia and medium thickness.

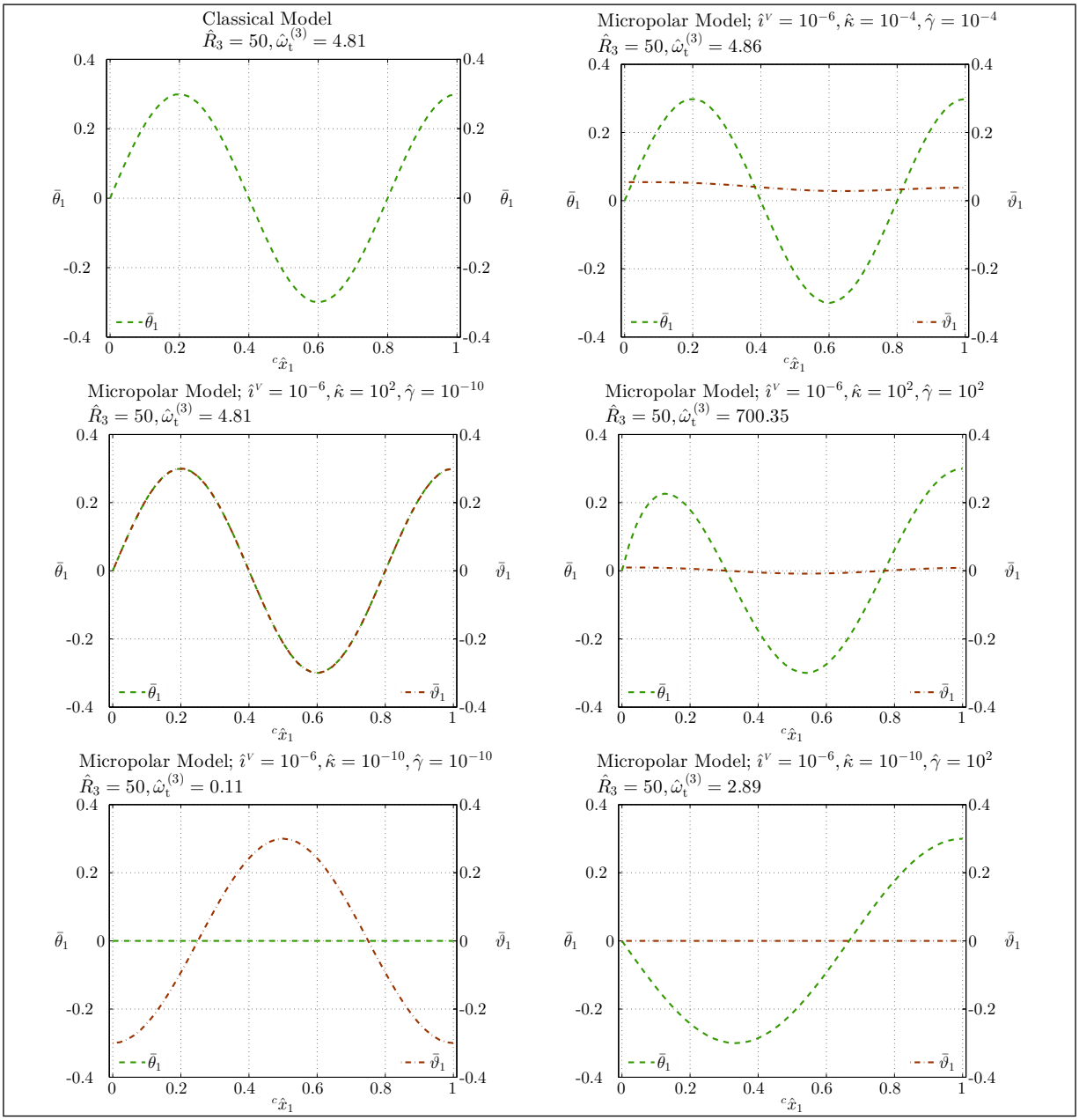

Figure C.39: 3rd mode shape of torsion $\hat{\underset{\sim}{\boldsymbol{q}}}_{\mathrm{t}}^{(3)}$ for beams with a small microinertia and medium thickness.

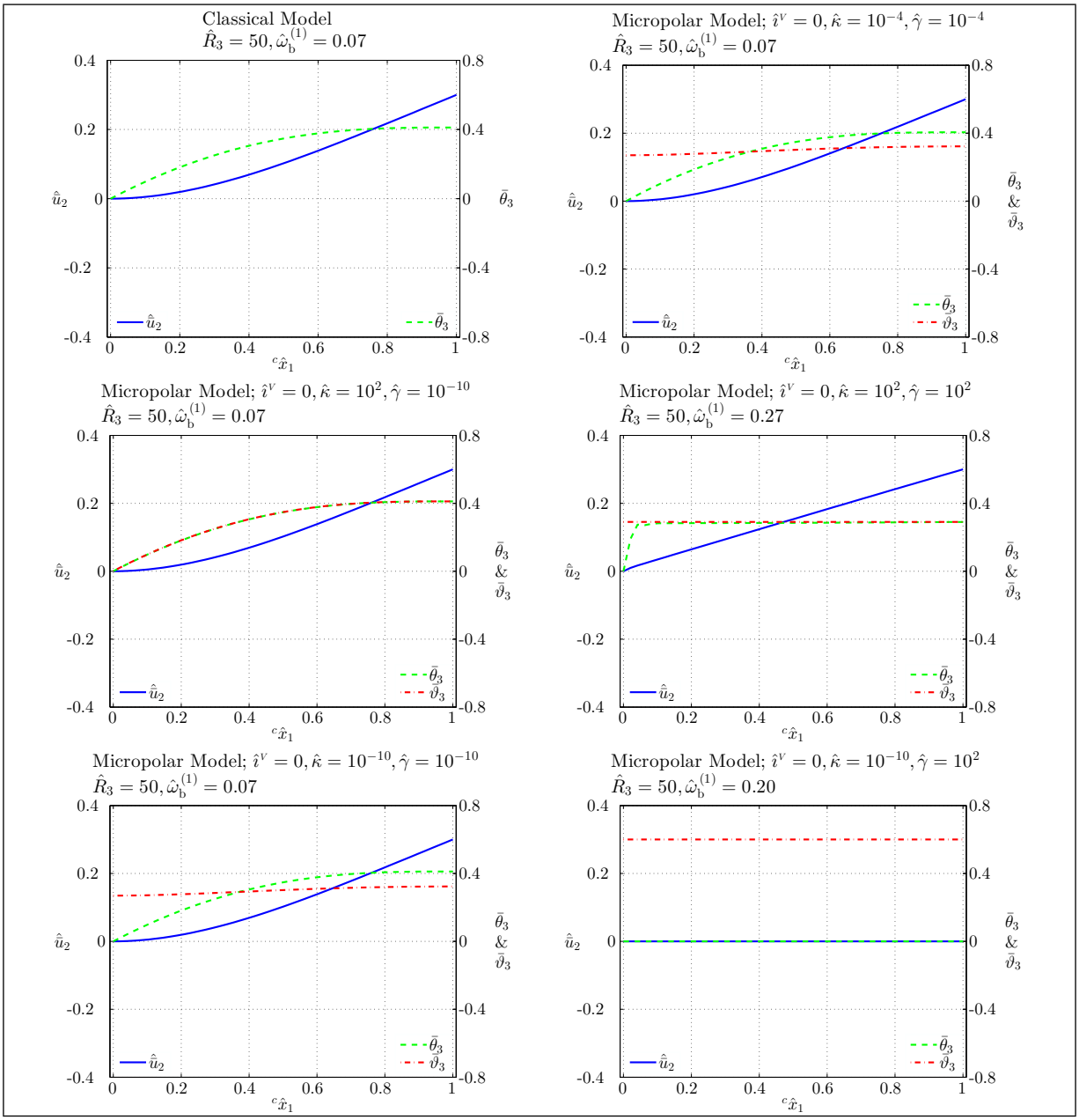

Figure C.40: 1st mode shape of bending $\underset{\sim}{\hat{\boldsymbol{q}}}_{\mathrm{b}}^{(1)}$ for beams with a zero microinertia and medium thickness.

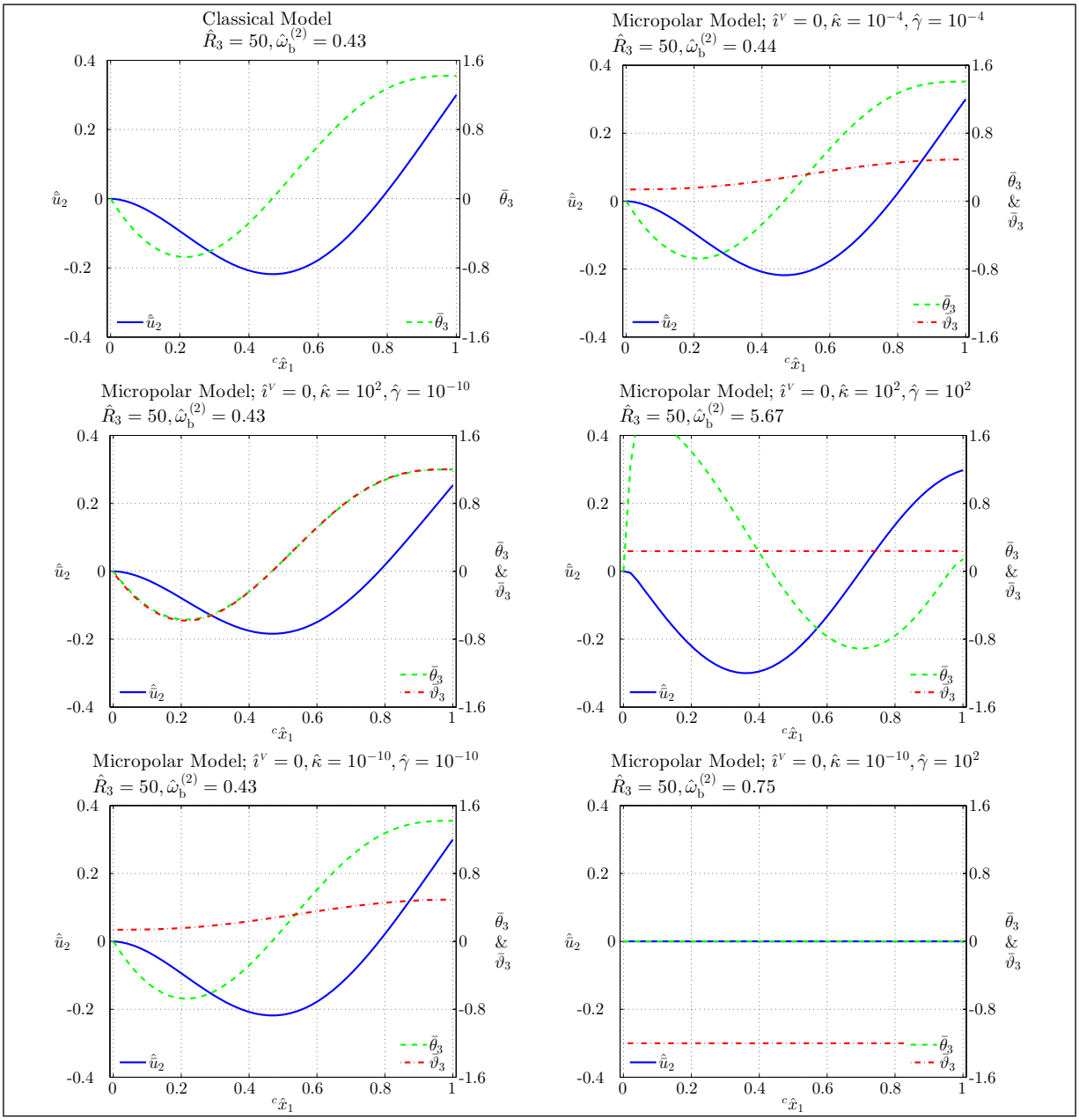

Figure C.41: 2nd mode shape of bending $\underset{\sim}{\hat{\boldsymbol{q}}}_{\mathrm{b}}^{(2)}$ for beams with a zero microinertia and medium thickness.

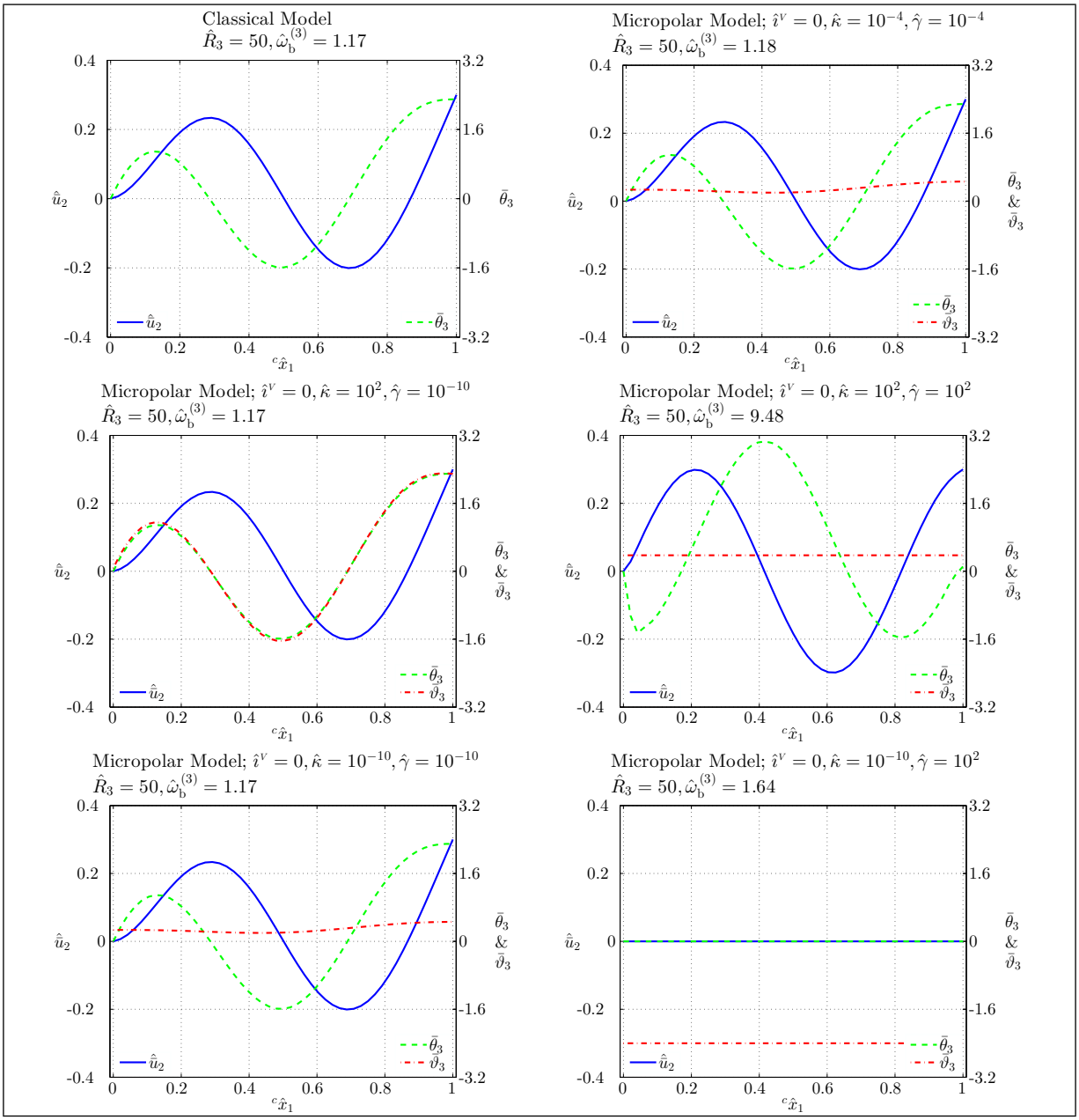

Figure C.42: 3rd mode shape of bending $\underset{\sim}{\hat{\boldsymbol{q}}}_{\mathrm{b}}^{(3)}$ for beams with a zero microinertia and medium thickness.

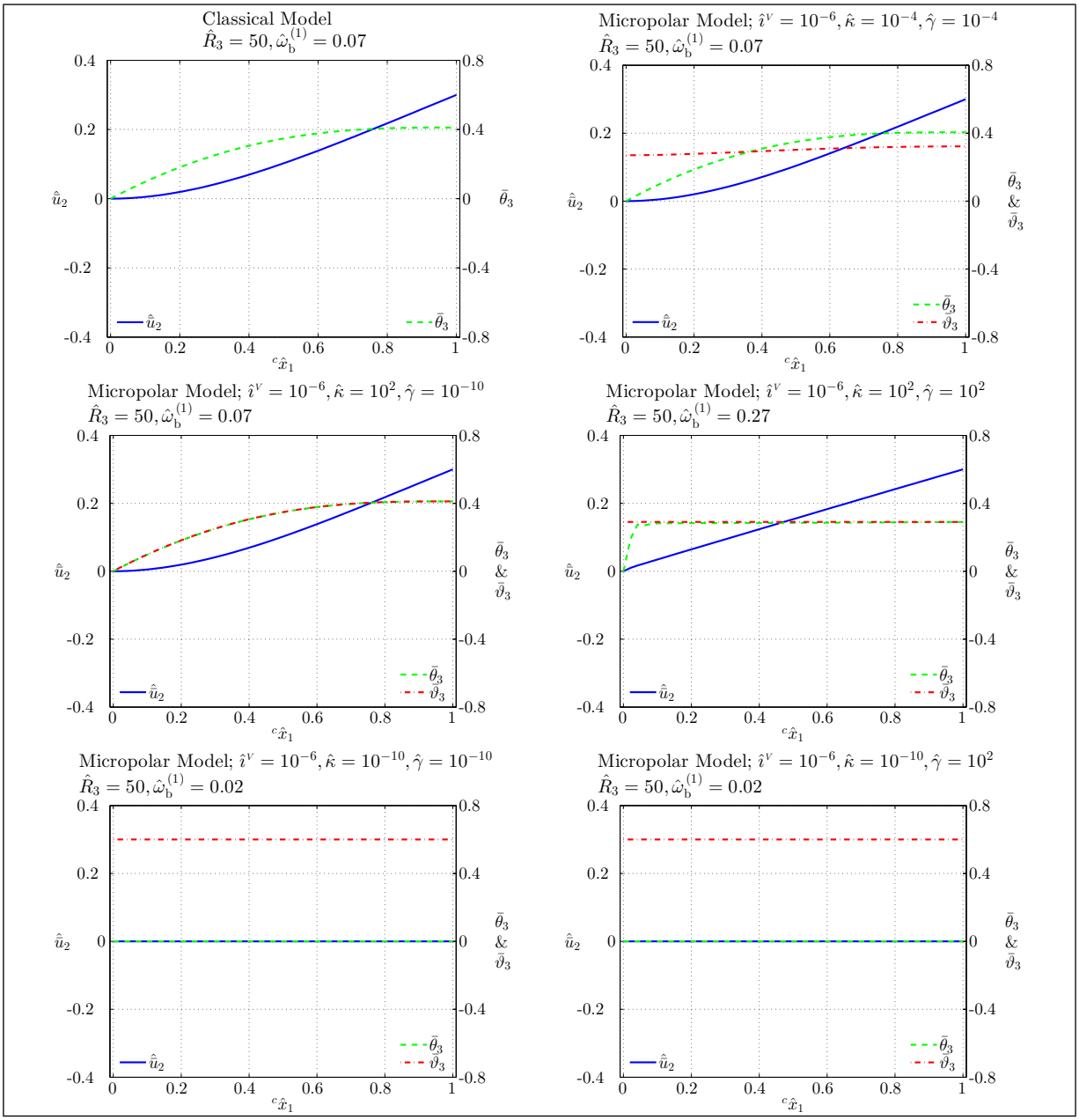

Figure C.43: 1st mode shape of bending $\hat{\underset{\sim}{\boldsymbol{q}}}_{\mathrm{b}}^{(1)}$ for beams with a small microinertia and medium thickness.

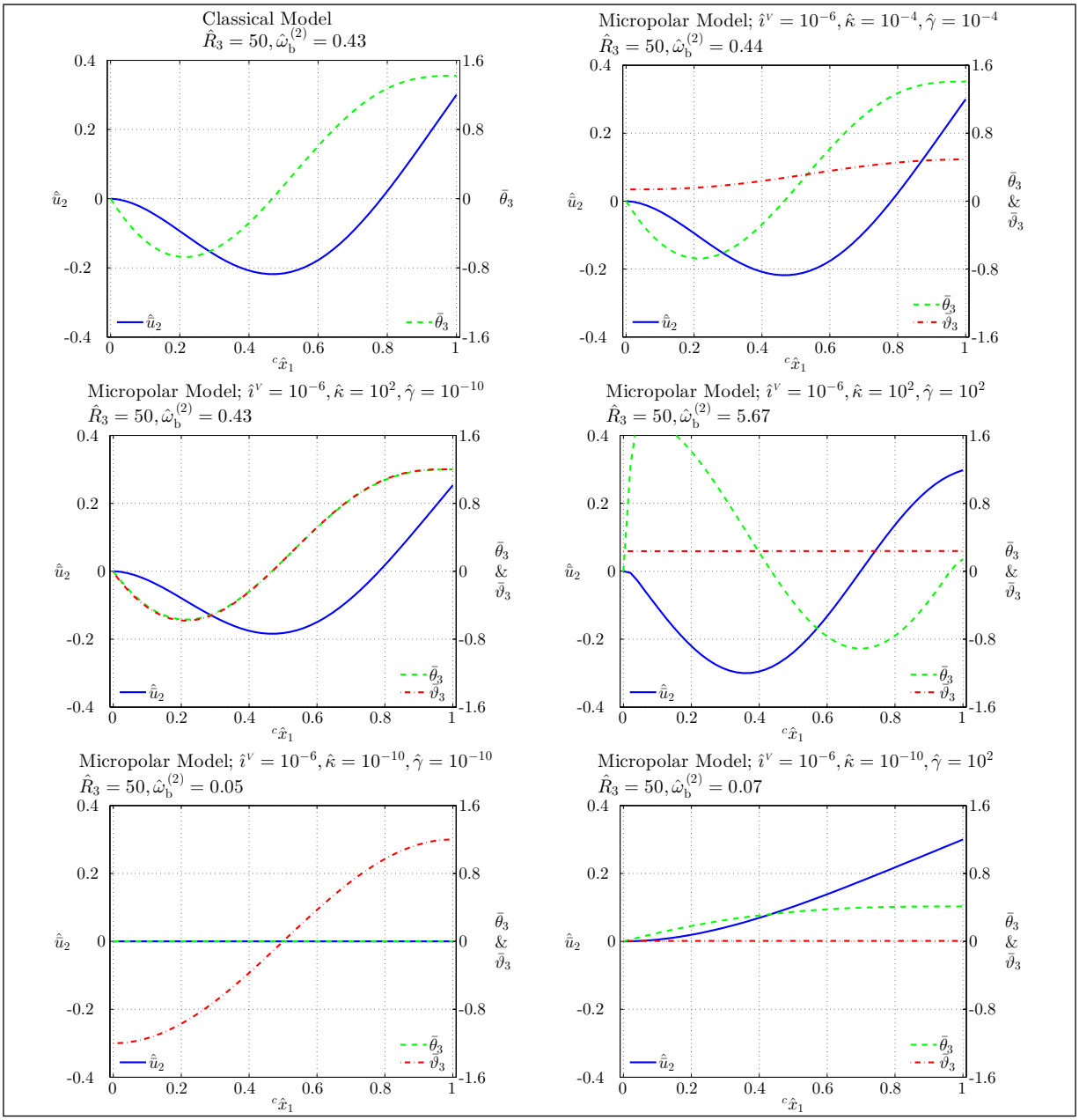

Figure C.44: 2^{nd} mode shape of bending $\underset{\sim}{\hat{\boldsymbol{q}}}_{\mathrm{b}}^{(2)}$ for beams with a small microinertia and medium thickness.

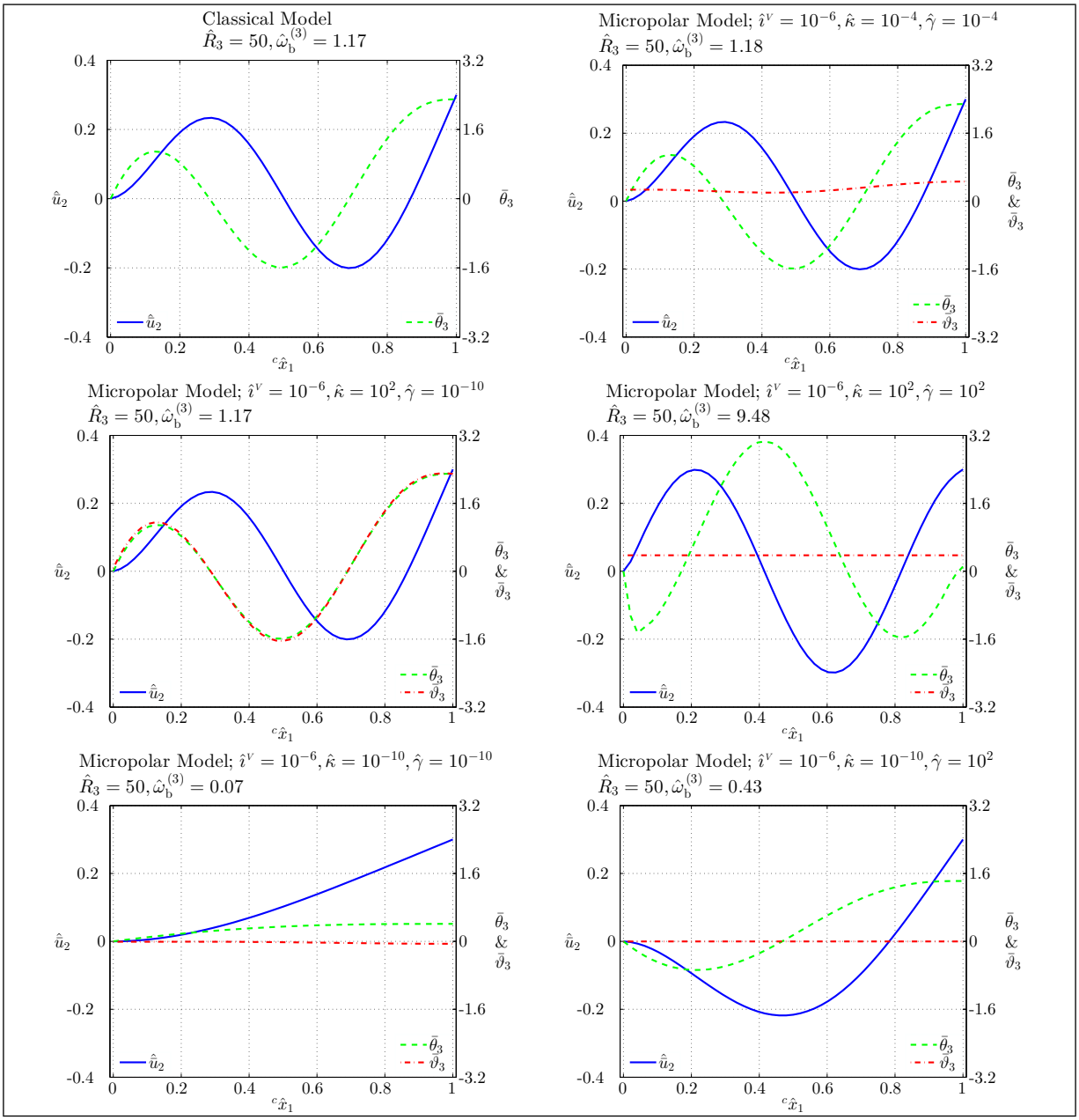

Figure C.45: 3rd mode shape of bending $\underset{\sim}{\hat{\boldsymbol{q}}}_{\mathrm{b}}^{(3)}$ for beams with a small microinertia and medium thickness.

The first three torsional and bending mode shapes for a classical beam model and five selected micropolar beam models with zero and small microinertia are plotted in Figures C.34–C.45. The five micropolar beam models are those previously selected for showing the static torsional and bending deformations along the beam length and correspond to the middle and corner points of the 2D plots in Figures C.22–C.33. These mode shape plots complement the natural frequencies plots and more clearly illustrate most of the previously mentioned modal behaviors of the micropolar beam models (in both torsion and bending).

Similar to the plots of static deformations, in each plot of Figures C.34–C.45 there are two scales, one on the left and one on the right vertical axis and the vertical axes have their own legend, in the lower left and right corners of the plots, noting the variables measured on the axes.

In the torsional mode shape plots the left vertical axis measures the plane rotation $\bar{\theta}_1$ and the right vertical axis measures the microrotation $\bar{\vartheta}_1$. In the plots illustrating the bending mode shapes, the bending displacement $\hat{\bar{u}}_2$ is scaled on the right vertical axis and the plane rotation $\bar{\theta}_3$ and the microrotation $\bar{\vartheta}_3$ are scaled on the right vertical axis.

In each figure the top left plot corresponds to the classical beam model. This plot is a reference for the examination of the selected micropolar beam models.

The top right plot of each figure is obtained from a micropolar beam model with medium $\hat{\kappa}$ and $\hat{\gamma}$. In this micropolar beam model a medium $\hat{\kappa}$ is not enough for complete coupling of the micropolar and classical DOFs, however, a medium $\hat{\gamma}$ is small enough to make the micropolar effects negligible.

The middle left plot of each figure corresponds to a micropolar beam model with a large $\hat{\kappa}$ and a small $\hat{\gamma}$. For both cases of zero and small microinertia the results of this micropolar beam model match the classical beam model results. In each mode shape of this model, the extra torsional and bending microrotations follow the corresponding classical plane rotations.

The middle right plot in each figure illustrates a micropolar beam model with large $\hat{\kappa}$ and $\hat{\gamma}$. In this model the large $\hat{\kappa}$ couples the micropolar and classical DOFs and the large $\hat{\gamma}$ dominates the micropolar modes. However, as mentioned previously the coupling effects

weaken in higher vibration modes and for $\hat{\kappa} = 1 \times 10^2$ it is just in the first vibration mode that the classical plane rotations follow the micropolar microrotations.

The bottom left plot in each figure corresponds to a micropolar beam model with small $\hat{\kappa}$ and $\hat{\gamma}$. For a zero microinertia the results of this micropolar beam model match the results of classical beam model if the decoupled microrotations are completely ignored (which is not a correct approach). However, for a nonzero microinertia the lower mode shapes are pure micropolar vibration modes which do not correspond to the lower mode shapes of the classical beam model. This model was wrongly mentioned by some authors as the case where the classical results can be reproduced.

Finally, in each figure the bottom right plot corresponds to a micropolar beam model with a small $\hat{\kappa}$ and a large $\hat{\gamma}$ which as mentioned previously may be erroneous due to an ill-conditioned FEM stiffness matrix. Overall in this model one can notice the existence of pure micropolar mode shapes among the considered lower vibration modes which is due to the decoupling between micropolar and classical DOFs.

A more detailed study on the dynamic behavior of micropolar elastic beams is reserved as a possible future work.

Appendix D

Euler-Bernoulli Gyroelastic Beams

D.1 Introduction

This appendix is devoted to a brief review of the 3D Euler-Bernoulli gyrobeam model in which the simple longitudinal deformation theory, Duleau torsion theory [50], and Euler-Bernoulli bending theory are combined for modeling the beam elasticity. The Euler-Bernoulli gyrobeam model, mainly studied by D'Eleuterio [2, 16] and Zee [33], can be considered as an elementary classical gyrobeam model due to the fact that in this model (in comparison to the Timoshenko gyrobeam model) the less inclusive classical Euler-Bernoulli bending theory is employed to characterize the elastic beam. As it is more studied, this model of gyrobeams is however useful for comparison, verification, and examination of the two (more advanced) models of gyrobeams developed in this text, *i.e.* the Timoshenko-based classical gyrobeam model and the micropolar gyrobeam model.

Considering a 3D Euler-Bernoulli gyrobeam, in the following sections the system Lagrangian and virtual work expressions are obtained. Hamilton's principle is then applied to these expressions to derive the equations of motion along with the initial and boundary conditions (I/BCs). The so-obtained dynamic equations are nondimensionalized and a FEM-based discretization is presented. Finally, the derived 3D Euler-Bernoulli gyrobeam model and its corresponding FEM formulation are verified.

Note that whereas the Euler-Bernoulli gyrobeam model developed by D'Eleuterio [2,16] and Zee [33] is based on assuming small attitude changes for the gyros and applying a zero-order approximation, in this appendix the Euler-Bernoulli gyrobeam equations will be derived by considering unrestricted (large) attitude changes for the axes of the gyros without imposing any approximation.

D.2 Kinematics

Consider a linear elastic beam deformed in 3D space (as a result of longitudinal, axial torsional, and lateral bending deformations), like the one shown in Figure 4.1 or 4.2. The beam's neutral axis with boundary points P_1 and P_2 is along the first coordinate axis of the inertial reference frame ${}^{o}x_1$, and the principal axes of the beam's cross section are parallel to the other coordinate axes of the inertial reference frame ${}^{o}x_2$ and ${}^{o}x_3$. A beam fixed frame $\mathcal{F}_c$ (different than the body frames $\mathcal{F}_b$ attached to every infinitesimal element of the beam) is located at the boundary point P_1. The beam's length, cross sectional area, and cross sectional area moments are L, A, and I_i $(i = 1, 2, 3)$, respectively.

Assuming small deformations through which plane sections of the beam remain plane and perpendicular to the beam's neutral axis (*i.e.* neglecting torsional warping and shear effects) the total deformation of an Euler-Bernoulli elastic beam can be characterized by a displacement field of the form:

$$\begin{aligned} u_1 &= \bar{u}_1(t, {}^{c}x_1) - {}^{c}x_2\,\bar{\theta}_3(t, {}^{c}x_1) + {}^{c}x_3\,\bar{\theta}_2(t, {}^{c}x_1) \\ u_2 &= \bar{u}_2(t, {}^{c}x_1) - {}^{c}x_3\,\bar{\theta}_1(t, {}^{c}x_1) \\ u_3 &= \bar{u}_3(t, {}^{c}x_1) + {}^{c}x_2\,\bar{\theta}_1(t, {}^{c}x_1) \end{aligned} \tag{D.1}$$

where $\bar{u}_i$ and $\bar{\theta}_i$ $(i = 1, 2, 3)$ are respectively displacements of the beam's neutral axis and rotations of the beam's plane sections. However, from the perpendicularity of the beam plane section to the beam's neutral axis (due to assuming negligible shear deflections) one can derive:

$$\begin{aligned} \bar{\theta}_2(t, {}^{c}x_1) &= -\,\bar{u}_{3,1}(t, {}^{c}x_1) \\ \bar{\theta}_3(t, {}^{c}x_1) &= +\,\bar{u}_{2,1}(t, {}^{c}x_1) \end{aligned} \tag{D.2}$$

Now by considering the beam deformation problem as a plane stress problem and recalling the fact that:

$$\frac{d}{dx_i} = {}^{c}\frac{d}{dx_i} \tag{D.3}$$

the elements of the strain tensor will be:

$$\begin{aligned}
\varepsilon_{11} &= \bar{u}_{1,1} - {}^{c}x_2\,\bar{u}_{2,11} - {}^{c}x_3\,\bar{u}_{3,11} \\
\varepsilon_{22} &= \varepsilon_{33} = -\nu\,\varepsilon_{11} \\
\varepsilon_{12} &= \varepsilon_{21} = -\frac{1}{2}\,{}^{c}x_3\,\bar{\theta}_{1,1} \\
\varepsilon_{13} &= \varepsilon_{31} = \frac{1}{2}\,{}^{c}x_2\,\bar{\theta}_{1,1} \\
\varepsilon_{23} &= \varepsilon_{32} = 0
\end{aligned} \tag{D.4}$$

where:

$$\nu = \frac{\lambda}{2\left(\mu+\lambda\right)} \tag{D.5}$$

is the strain Poisson's ratio.

In an Euler-Bernoulli beam the microrotations (being identical with the macrorotations) can be obtained as:

$$\begin{aligned}
\vartheta_1 &= \frac{1}{2}\left(u_{3,2} - u_{2,3}\right) = \frac{1}{2}\left(\bar{\theta}_1 + \bar{\theta}_1\right) = \bar{\theta}_1(t, {}^{c}x_1) \\
\vartheta_2 &= \frac{1}{2}\left(u_{1,3} - u_{3,1}\right) = \frac{1}{2}\left(\bar{\theta}_2 - \bar{u}_{3,1} - {}^{c}x_2\,\bar{\theta}_{1,1}\right) = \bar{\theta}_2(t, {}^{c}x_1) - {}^{c}x_2\,\frac{1}{2}\,\bar{\theta}_{1,1}(t, {}^{c}x_1) \\
\vartheta_3 &= \frac{1}{2}\left(u_{2,1} - u_{1,2}\right) = \frac{1}{2}\left(\bar{u}_{2,1} - {}^{c}x_3\,\bar{\theta}_{1,1} + \bar{\theta}_3\right) = \bar{\theta}_3(t, {}^{c}x_1) - {}^{c}x_3\,\frac{1}{2}\,\bar{\theta}_{1,1}(t, {}^{c}x_1)
\end{aligned} \tag{D.6}$$

where the relations of Eq. (D.2) are recalled. Consequently, a 3D Euler-Bernoulli beam has four independent continuous generalized coordinates, *i.e.* three neutral axis displacements $\bar{u}_i$ $(i = 1, 2, 3)$ and one plane section torsional rotation $\bar{\theta}_1$.

Though the microrotation field is given by Eq. (D.6), it is more useful for derivation of the kinetic energy and virtual work expressions to approximate the microrotation field vector as:

$$\underset{\rightarrow}{\vartheta} \approx \underset{\rightarrow}{\bar{\theta}}(t, {}^{c}x_1), \qquad \underset{\sim}{\boldsymbol{\vartheta}} \approx \underset{\sim}{\bar{\boldsymbol{\theta}}}(t, {}^{c}x_1) = \begin{bmatrix} \bar{\theta}_1 & -\bar{u}_{3,1} & \bar{u}_{2,1} \end{bmatrix}^{\mathrm{T}}, \qquad \vartheta_i \approx \bar{\theta}_i(t, {}^{c}x_1) \tag{D.7}$$

This approximation results in the microrotational velocity and acceleration field vectors as:

$$\begin{aligned} \underset{\rightarrow}{\dot{\vartheta}} &\approx \underset{\rightarrow}{\dot{\theta}}(t, {}^{c}x_1), \qquad \underset{\sim}{\dot{\boldsymbol{\vartheta}}} \approx \underset{\sim}{\dot{\boldsymbol{\theta}}}(t, {}^{c}x_1) = \left[\begin{array}{ccc} \dot{\bar{\theta}}_1 & -\dot{\bar{u}}_{3,1} & \dot{\bar{u}}_{2,1} \end{array}\right]^{\mathrm{T}}, \qquad \dot{\vartheta}_i \approx \dot{\bar{\theta}}_i(t, {}^{c}x_1) \\ \underset{\rightarrow}{\ddot{\vartheta}} &\approx \underset{\rightarrow}{\ddot{\theta}}(t, {}^{c}x_1), \qquad \underset{\sim}{\ddot{\boldsymbol{\vartheta}}} \approx \underset{\sim}{\ddot{\boldsymbol{\theta}}}(t, {}^{c}x_1) = \left[\begin{array}{ccc} \ddot{\bar{\theta}}_1 & -\ddot{\bar{u}}_{3,1} & \ddot{\bar{u}}_{2,1} \end{array}\right]^{\mathrm{T}}, \qquad \ddot{\vartheta}_i \approx \ddot{\bar{\theta}}_i(t, {}^{c}x_1) \end{aligned} \tag{D.8}$$

and the virtual microrotation filed vector as:

$$\delta\underset{\rightarrow}{\vartheta} \approx \delta\underset{\rightarrow}{\bar{\theta}}(t, {}^{c}x_1), \quad \delta\underset{\sim}{\boldsymbol{\vartheta}} \approx \delta\underset{\sim}{\bar{\boldsymbol{\theta}}}(t, {}^{c}x_1) = \left[\begin{array}{ccc} \delta\bar{\theta}_1 & -\delta\bar{u}_{3,1} & \delta\bar{u}_{2,1} \end{array}\right]^{\mathrm{T}}, \quad \delta\vartheta_i \approx \delta\bar{\theta}_i(t, {}^{c}x_1) \tag{D.9}$$

D.3 Potential energy expression

Based on the results obtained in the previous section and by utilizing the classical constitutive relations the elements of the force stress tensor will be derived as:

$$\begin{aligned} \sigma_{11} &= E\,\varepsilon_{11} \\ \sigma_{22} &= \sigma_{33} = 0 \\ \sigma_{12} &= \sigma_{21} = 2\,\mu\,\varepsilon_{12} \\ \sigma_{13} &= \sigma_{31} = 2\,\mu\,\varepsilon_{13} \\ \sigma_{23} &= \sigma_{32} = 0 \end{aligned} \tag{D.10}$$

where E and μ are the tensile (Young's) and shear moduli, respectively. Then, the potential energy expression of an Euler-Bernoulli gyrobeam can be written as:

$$\begin{aligned} \mathcal{U} = \frac{1}{2}\,E\,A \int_L \bar{u}_{1,1}\,\bar{u}_{1,1}\,dL + \frac{1}{2}\,E\,I_3 \int_L \bar{u}_{2,11}\,\bar{u}_{2,11}\,dL + \frac{1}{2}\,E\,I_2 \int_L \bar{u}_{3,11}\,\bar{u}_{3,11}\,dL \\ + \frac{1}{2}\,\mu\,I_1 \int_L \bar{\theta}_{1,1}\,\bar{\theta}_{1,1}\,dL \\ = \int_L \mathcal{U}^{\scriptscriptstyle L}\,dL \end{aligned} \tag{D.11}$$

D.4 Kinetic energy expression

Recalling the relations of Eqs. (D.7) and (D.8), the kinetic energy expression for an Euler-Bernoulli gyrobeam will be obtained as:

$$\begin{aligned}\mathcal{T} = \frac{1}{2}\left(\rho^V + \varrho^V\right) A \int_L \left(\dot{\bar{u}}_1\,\dot{\bar{u}}_1 + \dot{\bar{u}}_2\,\dot{\bar{u}}_2 + \dot{\bar{u}}_3\,\dot{\bar{u}}_3\right) dL + \frac{1}{2}\left(\rho^V + \varrho^V\right) I_1 \int_L \dot{\bar{\theta}}_1\,\dot{\bar{\theta}}_1\, dL \\ + \frac{1}{2} A \int_L \jmath_{ij}^V \dot{\bar{\theta}}_j\,\dot{\bar{\theta}}_i\, dL + A \int_L \jmath_{ij}^V \left(\dot{\phi}_j + \dot{\psi}_j\right) \dot{\bar{\theta}}_i\, dL \\ + \frac{1}{2} A \int_L \jmath_{ij}^V \left(\dot{\phi}_j\,\dot{\phi}_i + \dot{\psi}_j\,\dot{\psi}_i + 2\,\dot{\phi}_j\,\dot{\psi}_i\right) dL \\ = \int_L \mathcal{T}^L\, dL\end{aligned} \tag{D.12}$$

where $\underset{\leftrightarrow}{\jmath}^V$ is the tensor of the gyros rotational inertia per unit volume of elastic body and the tensor summation convention is used to summarize the expression.

D.5 Virtual work expression

Assuming that the gyrobeam is subjected to the action of external volume and boundary surface forces and moments $\underset{\rightarrow}{f}^V$, $\underset{\rightarrow}{m}^V$, $\underset{\rightarrow}{f}^S$, and $\underset{\rightarrow}{m}^S$ (where boundary surface forces and moments are applied only on the most left and right beam cross sections), the virtual work expression for an Euler-Bernoulli gyrobeam can be written as:

$$\begin{aligned}\delta\mathcal{W} = \int_L \left(A\,\bar{f}_i^V\,\delta\bar{u}_i + \bar{m}_i^L\,\delta\bar{\theta}_i + A\,\bar{m}_i^V\,\delta\bar{\theta}_i\right) dL \\ + A\,\bar{f}_i^S(P_1)\,\delta\bar{u}_i(P_1) + \bar{m}_i^P(P_1)\,\delta\bar{\theta}_i(P_1) + A\,\bar{m}_i^S(P_1)\,\delta\bar{\theta}_i(P_1) \\ + A\,\bar{f}_i^S(P_2)\,\delta\bar{u}_i(P_2) + \bar{m}_i^P(P_2)\,\delta\bar{\theta}_i(P_2) + A\,\bar{m}_i^S(P_2)\,\delta\bar{\theta}_i(P_2) \\ = \int_L \delta\mathcal{W}^L\, dL + \delta\mathcal{W}^P\end{aligned} \tag{D.13}$$

where Eqs. (D.7) and (D.9) are recalled and:

$$\begin{aligned} A\,\bar{f}_i^V &= \int_A f_i^V\,dA, \qquad A\,\bar{m}_i^V = \int_A m_i^V\,dA \\ A\,\bar{f}_i^S &= \int_A f_i^S\,dA, \qquad A\,\bar{m}_i^S = \int_A m_i^S\,dA \end{aligned} \tag{D.14}$$

as well as:

$$\begin{aligned} \bar{m}_1^L &= \int_A \left({}^c x_2\, f_3^V - {}^c x_3\, f_2^V \right) dA \\ \bar{m}_2^L &= \int_A {}^c x_3\, f_1^V\,dA \\ -\bar{m}_3^L &= \int_A {}^c x_2\, f_1^V\,dA \\ \bar{m}_1^P &= \int_A \left({}^c x_2\, f_3^S - {}^c x_3\, f_2^S \right) dA \\ \bar{m}_2^P &= \int_A {}^c x_3\, f_1^S\,dA \\ -\bar{m}_3^P &= \int_A {}^c x_2\, f_1^S\,dA \end{aligned} \tag{D.15}$$

D.6 Equations of motion

Having the potential and kinetic energy expressions along with the virtual work expression, Hamilton's principle can be used to derive the gyrobeam equations of motion and the corresponding I/BCs.

Noting that for an Euler-Bernoulli gyrobeam the matrix of generalized coordinates is:

$$\underset{\sim}{\boldsymbol{q}} = \begin{bmatrix} \bar{u}_1 & \bar{u}_2 & \bar{u}_3 & \bar{\theta}_1 \end{bmatrix}^{\mathrm{T}} \tag{D.16}$$

the motion equations and I/BCs will take the following matrix forms:

$$\underset{\sim}{\boldsymbol{\mathcal{Q}}}^{L} - \underset{\sim}{\boldsymbol{\mathcal{R}}_{\mathbf{1}}}{}^{L}{}_{,1} = \Big(\frac{\partial \mathcal{T}^{L}}{\partial \underset{\sim}{\dot{\boldsymbol{q}}}}\Big)_{,t} - \Big(\frac{\partial \mathcal{T}^{L}}{\partial \underset{\sim}{\dot{\boldsymbol{q}}}_{,1}}\Big)_{,t\,1} - \Big(\frac{\partial \mathcal{U}^{L}}{\partial \underset{\sim}{\boldsymbol{q}}_{,1}}\Big)_{,1} + \Big(\frac{\partial \mathcal{U}^{L}}{\partial \underset{\sim}{\boldsymbol{q}}_{,11}}\Big)_{,11} \tag{D.17}$$

and:

$$\begin{aligned}
&\text{at } t = t_1, t_2 \ ; \quad \text{and } P_1, P_2 : \quad \delta\underset{\sim}{\boldsymbol{q}} = \underset{\sim}{\mathbf{0}} \quad \text{or} \quad \frac{\partial \mathcal{T}^{L}}{\partial \underset{\sim}{\dot{\boldsymbol{q}}}_{,1}} = \underset{\sim}{\mathbf{0}} \\
&\text{at } t = t_1, t_2 \ ; \quad \text{and over } L : \quad \delta\underset{\sim}{\boldsymbol{q}} = \underset{\sim}{\mathbf{0}} \quad \text{or} \quad \frac{\partial \mathcal{T}^{L}}{\partial \underset{\sim}{\dot{\boldsymbol{q}}}} - \Big(\frac{\partial \mathcal{T}^{L}}{\partial \underset{\sim}{\dot{\boldsymbol{q}}}_{,1}}\Big)_{,1} = \underset{\sim}{\mathbf{0}} \\
&\text{at } P_1 \ ; \quad \text{and during } t : \quad \delta\underset{\sim}{\boldsymbol{q}} = \underset{\sim}{\mathbf{0}} \quad \text{or} \quad \underset{\sim}{\boldsymbol{\mathcal{Q}}}^{P} - \underset{\sim}{\boldsymbol{\mathcal{R}}_{\mathbf{1}}}{}^{L} + \frac{\partial \mathcal{U}^{L}}{\partial \underset{\sim}{\boldsymbol{q}}_{,1}} + \Big(\frac{\partial \mathcal{T}^{L}}{\partial \underset{\sim}{\dot{\boldsymbol{q}}}_{,1}}\Big)_{,t} \\
&\qquad\qquad - \Big(\frac{\partial \mathcal{U}^{L}}{\partial \underset{\sim}{\boldsymbol{q}}_{,11}}\Big)_{,1} = \underset{\sim}{\mathbf{0}} \\
&\text{at } P_2 \ ; \quad \text{and during } t : \quad \delta\underset{\sim}{\boldsymbol{q}} = \underset{\sim}{\mathbf{0}} \quad \text{or} \quad \underset{\sim}{\boldsymbol{\mathcal{Q}}}^{P} + \underset{\sim}{\boldsymbol{\mathcal{R}}_{\mathbf{1}}}{}^{L} - \frac{\partial \mathcal{U}^{L}}{\partial \underset{\sim}{\boldsymbol{q}}_{,1}} - \Big(\frac{\partial \mathcal{T}^{L}}{\partial \underset{\sim}{\dot{\boldsymbol{q}}}_{,1}}\Big)_{,t} \\
&\qquad\qquad + \Big(\frac{\partial \mathcal{U}^{L}}{\partial \underset{\sim}{\boldsymbol{q}}_{,11}}\Big)_{,1} = \underset{\sim}{\mathbf{0}} \\
&\text{at } P_1 \ ; \quad \text{and during } t : \quad \delta\underset{\sim}{\boldsymbol{q}}_{,1} = \underset{\sim}{\mathbf{0}} \quad \text{or} \quad \underset{\sim}{\boldsymbol{\mathcal{R}}_{\mathbf{1}}}{}^{P} + \frac{\partial \mathcal{U}^{L}}{\partial \underset{\sim}{\boldsymbol{q}}_{,11}} = \underset{\sim}{\mathbf{0}} \\
&\text{at } P_2 \ ; \quad \text{and during } t : \quad \delta\underset{\sim}{\boldsymbol{q}}_{,1} = \underset{\sim}{\mathbf{0}} \quad \text{or} \quad \underset{\sim}{\boldsymbol{\mathcal{R}}_{\mathbf{1}}}{}^{P} - \frac{\partial \mathcal{U}^{L}}{\partial \underset{\sim}{\boldsymbol{q}}_{,11}} = \underset{\sim}{\mathbf{0}}
\end{aligned} \tag{D.18}$$

where:

$$\begin{aligned}
\underset{\sim}{\boldsymbol{\mathcal{Q}}}^{L} &= \frac{\delta \mathcal{W}^{L}}{\delta \underset{\sim}{\boldsymbol{q}}}, \qquad & \underset{\sim}{\boldsymbol{\mathcal{Q}}}^{P} &= \frac{\delta \mathcal{W}^{P}}{\delta \underset{\sim}{\boldsymbol{q}}} \\
\underset{\sim}{\boldsymbol{\mathcal{R}}_{\boldsymbol{i}}}{}^{L} &= \frac{\delta \mathcal{W}^{L}}{\delta \underset{\sim}{\boldsymbol{q}}_{,i}}, \qquad & \underset{\sim}{\boldsymbol{\mathcal{R}}_{\boldsymbol{i}}}{}^{P} &= \frac{\delta \mathcal{W}^{P}}{\delta \underset{\sim}{\boldsymbol{q}}_{,i}}
\end{aligned} \tag{D.19}$$

However, it is common to simplify the I/BCs given in Eq. (D.18) by assuming zero (or negligible) $\underset{\sim}{\boldsymbol{\mathcal{R}}_{\mathbf{1}}}{}^{L}$ and $\frac{\partial \mathcal{T}^{L}}{\partial \underset{\sim}{\dot{\boldsymbol{q}}}_{,1}}$ at boundary points P_1 and P_2 which results in the following form

for the I/BCs:

$$
\begin{aligned}
&\text{at } t=t_1,t_2\ ; \quad \text{and over } L: \quad \delta\underset{\sim}{\boldsymbol{q}}=\underset{\sim}{\mathbf{0}} \quad \text{or} \quad \frac{\partial\mathcal{T}^{L}}{\partial\underset{\sim}{\dot{\boldsymbol{q}}}}-\Big(\frac{\partial\mathcal{T}^{L}}{\partial\underset{\sim}{\dot{\boldsymbol{q}}}_{,1}}\Big)_{,1}=\underset{\sim}{\mathbf{0}}\\
&\text{at } P_1\ ; \quad \text{and during } t: \quad \delta\underset{\sim}{\boldsymbol{q}}=\underset{\sim}{\mathbf{0}} \quad \text{or} \quad \underset{\sim}{\boldsymbol{\mathcal{Q}}}^{P}+\frac{\partial\mathcal{U}^{L}}{\partial\underset{\sim}{\boldsymbol{q}}_{,1}}-\Big(\frac{\partial\mathcal{U}^{L}}{\partial\underset{\sim}{\boldsymbol{q}}_{,11}}\Big)_{,1}=\underset{\sim}{\mathbf{0}}\\
&\text{at } P_2\ ; \quad \text{and during } t: \quad \delta\underset{\sim}{\boldsymbol{q}}=\underset{\sim}{\mathbf{0}} \quad \text{or} \quad \underset{\sim}{\boldsymbol{\mathcal{Q}}}^{P}-\frac{\partial\mathcal{U}^{L}}{\partial\underset{\sim}{\boldsymbol{q}}_{,1}}+\Big(\frac{\partial\mathcal{U}^{L}}{\partial\underset{\sim}{\boldsymbol{q}}_{,11}}\Big)_{,1}=\underset{\sim}{\mathbf{0}}\\
&\text{at } P_1\ ; \quad \text{and during } t: \quad \delta\underset{\sim}{\boldsymbol{q}}_{,1}=\underset{\sim}{\mathbf{0}} \quad \text{or} \quad \underset{\sim}{\boldsymbol{\mathcal{R}}_{\mathbf{1}}}^{P}+\frac{\partial\mathcal{U}^{L}}{\partial\underset{\sim}{\boldsymbol{q}}_{,11}}=\underset{\sim}{\mathbf{0}}\\
&\text{at } P_2\ ; \quad \text{and during } t: \quad \delta\underset{\sim}{\boldsymbol{q}}_{,1}=\underset{\sim}{\mathbf{0}} \quad \text{or} \quad \underset{\sim}{\boldsymbol{\mathcal{R}}_{\mathbf{1}}}^{P}-\frac{\partial\mathcal{U}^{L}}{\partial\underset{\sim}{\boldsymbol{q}}_{,11}}=\underset{\sim}{\mathbf{0}}
\end{aligned}
\tag{D.20}
$$

Now recalling the definitions given in Eqs. (D.7) and (D.8), it is useful to define the vector of gyros angular momenta per unit volume $\underset{\rightarrow}{\mathcal{J}}^{V}$ and its time derivative with respect to the inertial frame $\dot{\underset{\rightarrow}{\mathcal{J}}}^{V}$ as:

$$
\begin{aligned}
\underset{\rightarrow}{\mathcal{J}}^{V} &= \underset{\leftrightarrow}{\jmath}^{V}\cdot\Big(\underset{\rightarrow}{\dot{\theta}}+\underset{\rightarrow}{\dot{\phi}}+\underset{\rightarrow}{\dot{\psi}}\Big)\\
\dot{\underset{\rightarrow}{\mathcal{J}}}^{V} &= \frac{d}{dt}\Big(\underset{\rightarrow}{\mathcal{J}}^{V}\Big)=\underset{\leftrightarrow}{\jmath}^{V}\cdot\underset{\rightarrow}{\ddot{\theta}}+\underset{\leftrightarrow}{\dot{\theta}}^{\times}\cdot\underset{\leftrightarrow}{\jmath}^{V}\cdot\underset{\rightarrow}{\dot{\theta}}+\underset{\leftrightarrow}{\dot{\theta}}^{\times}\cdot\underset{\leftrightarrow}{\jmath}^{V}\cdot\Big(\underset{\rightarrow}{\dot{\phi}}+\underset{\rightarrow}{\dot{\psi}}\Big)\\
&\quad+\Big(\underset{\leftrightarrow}{\dot{\phi}}^{\times}\cdot\underset{\leftrightarrow}{\jmath}^{V}-\underset{\leftrightarrow}{\jmath}^{V}\cdot\underset{\leftrightarrow}{\dot{\phi}}^{\times}\Big)\cdot\underset{\rightarrow}{\dot{\theta}}+\underset{\leftrightarrow}{\jmath}^{V}\cdot\underset{\rightarrow}{\ddot{\phi}}+\underset{\leftrightarrow}{\jmath}^{V}\cdot\underset{\rightarrow}{\ddot{\psi}}+\underset{\leftrightarrow}{\dot{\phi}}^{\times}\cdot\underset{\leftrightarrow}{\jmath}^{V}\cdot\Big(\underset{\rightarrow}{\dot{\phi}}+\underset{\rightarrow}{\dot{\psi}}\Big)
\end{aligned}
\tag{D.21}
$$

whose component matrices expressed in the inertial frame (after imposing the required first-order approximation on microrotations) are:

$$
\begin{aligned}
\underline{\boldsymbol{\mathcal{J}}}^{V} &= {}^{b}\underline{\underline{\boldsymbol{\jmath}}}^{V}\Big(\underline{\dot{\boldsymbol{\theta}}}+{}^{b}\underline{\dot{\boldsymbol{\phi}}}+{}^{b}\underline{\dot{\boldsymbol{\psi}}}\Big)\\
\dot{\underline{\boldsymbol{\mathcal{J}}}}^{V} &= {}^{b}\underline{\underline{\boldsymbol{\jmath}}}^{V}\,\underline{\ddot{\boldsymbol{\theta}}}+\underline{\dot{\boldsymbol{\theta}}}^{\times}\,{}^{b}\underline{\underline{\boldsymbol{\jmath}}}^{V}\Big({}^{b}\underline{\dot{\boldsymbol{\phi}}}+{}^{b}\underline{\dot{\boldsymbol{\psi}}}\Big)+\Big({}^{b}\underline{\dot{\boldsymbol{\phi}}}^{\times}\,{}^{b}\underline{\underline{\boldsymbol{\jmath}}}^{V}-{}^{b}\underline{\underline{\boldsymbol{\jmath}}}^{V}\,{}^{b}\underline{\dot{\boldsymbol{\phi}}}^{\times}\Big)\,\underline{\dot{\boldsymbol{\theta}}}\\
&\quad+\Big(\underline{\underline{\mathbb{1}}}+\underline{\bar{\boldsymbol{\theta}}}^{\times}\Big)\Big({}^{b}\underline{\underline{\boldsymbol{\jmath}}}^{V}\,{}^{b}\underline{\ddot{\boldsymbol{\phi}}}+{}^{b}\underline{\underline{\boldsymbol{\jmath}}}^{V}\,{}^{b}\underline{\ddot{\boldsymbol{\psi}}}+{}^{b}\underline{\dot{\boldsymbol{\phi}}}^{\times}\,{}^{b}\underline{\underline{\boldsymbol{\jmath}}}^{V}\Big({}^{b}\underline{\dot{\boldsymbol{\phi}}}+{}^{b}\underline{\dot{\boldsymbol{\psi}}}\Big)\Big)
\end{aligned}
\tag{D.22}
$$

Utilizing the aforementioned definitions and after adding the torsion correction factor k_{t} (to account for required adjustments in the case of beams with non-circular cross-sections), the final equations of motion for an Euler-Bernoulli gyrobeam can be derived as the following four equations:

$$\begin{aligned}
\bar{f}_1^{\,V} &= \left(\rho^V + \varrho^V\right) \ddot{\bar{u}}_1 - E\,\bar{u}_{1,11} \\
\bar{f}_2^{\,V} - \bar{m}_{3\,,1}^{\,L} - A\,\bar{m}_{3\,,1}^{\,V} &= \left(\rho^V + \varrho^V\right) \ddot{\bar{u}}_2 - A\,\dot{\mathcal{J}}_{3\,,1}^{\,V} + E\,I_3\,\bar{u}_{2,1111} \\
\bar{f}_3^{\,V} + \bar{m}_{2\,,1}^{\,L} + A\,\bar{m}_{2\,,1}^{\,V} &= \left(\rho^V + \varrho^V\right) \ddot{\bar{u}}_3 + A\,\dot{\mathcal{J}}_{2\,,1}^{\,V} + E\,I_2\,\bar{u}_{3,1111} \\
\bar{m}_1^{\,L} + A\,\bar{m}_1^{\,V} &= \left(\rho^V + \varrho^V\right) I_1\,\ddot{\bar{\theta}}_1 + A\,\dot{\mathcal{J}}_1^{\,V} - k_{\mathrm{t}}\,\mu\,I_1\,\bar{\theta}_{1,11}
\end{aligned} \tag{D.23}$$

which should be solved along with the following I/BCs:

$$\begin{aligned}
&\text{at } t = t_1, t_2 \ ; \ \text{ and over } L : \\
&\quad \delta\bar{u}_1 = 0 \quad \text{or} \quad \left(\rho^V + \varrho^V\right) A\,\dot{\bar{u}}_1 = 0 \\
&\quad \delta\bar{u}_2 = 0 \quad \text{or} \quad \left(\rho^V + \varrho^V\right) A\,\dot{\bar{u}}_2 - \mathcal{J}_{3\,,1}^{\,V} = 0 \\
&\quad \delta\bar{u}_3 = 0 \quad \text{or} \quad \left(\rho^V + \varrho^V\right) A\,\dot{\bar{u}}_3 + \mathcal{J}_{2\,,1}^{\,V} = 0 \\
&\quad \delta\bar{\theta}_1 = 0 \quad \text{or} \quad \left(\rho^V + \varrho^V\right) I_1\,\dot{\bar{\theta}}_1 + A\,\mathcal{J}_1^{\,V} = 0
\end{aligned} \tag{D.24}$$

$$\begin{aligned}
&\text{at } P_1 \ ; \ \text{ and during } t : \\
&\quad \delta\bar{u}_1 = 0 \quad \text{or} \quad A\,\bar{f}_1^{\,S} + E\,A\,\bar{u}_{1,1} = 0 \\
&\quad \delta\bar{u}_2 = 0 \quad \text{or} \quad A\,\bar{f}_2^{\,S} - E\,I_3\,\bar{u}_{2,111} = 0 \\
&\quad \delta\bar{u}_3 = 0 \quad \text{or} \quad A\,\bar{f}_3^{\,S} - E\,I_2\,\bar{u}_{3,111} = 0 \\
&\quad \delta\bar{\theta}_1 = 0 \quad \text{or} \quad \bar{m}_1^{\,P} + A\,\bar{m}_1^{\,S} + k_{\mathrm{t}}\,\mu\,I_1\,\bar{\theta}_{1,1} = 0 \\
&\quad \delta\bar{u}_{2,1} = 0 \quad \text{or} \quad \bar{m}_3^{\,P} + A\,\bar{m}_3^{\,S} + E\,I_3\,\bar{u}_{2,11} = 0 \\
&\quad \delta\bar{u}_{3,1} = 0 \quad \text{or} \quad -\bar{m}_2^{\,P} - A\,\bar{m}_2^{\,S} + E\,I_2\,\bar{u}_{3,11} = 0
\end{aligned} \tag{D.25}$$

at P_2 ; and during t :

$$\begin{array}{lll}
\delta\bar{u}_1 = 0 & \text{or} & A\,\bar{f}_1^S - E\,A\,\bar{u}_{1,1} = 0 \\
\delta\bar{u}_2 = 0 & \text{or} & A\,\bar{f}_2^S + E\,I_3\,\bar{u}_{2,111} = 0 \\
\delta\bar{u}_3 = 0 & \text{or} & A\,\bar{f}_3^S + E\,I_2\,\bar{u}_{3,111} = 0 \\
\delta\bar{\theta}_1 = 0 & \text{or} & \bar{m}_1^P + A\,\bar{m}_1^S - k_{\mathrm{t}}\,\mu\,I_1\,\bar{\theta}_{1,1} = 0 \\
\delta\bar{u}_{2,1} = 0 & \text{or} & \bar{m}_3^P + A\,\bar{m}_3^S - E\,I_3\,\bar{u}_{2,11} = 0 \\
\delta\bar{u}_{3,1} = 0 & \text{or} & -\bar{m}_2^P - A\,\bar{m}_2^S - E\,I_2\,\bar{u}_{3,11} = 0
\end{array} \tag{D.26}$$

D.7 Nondimensionalization

Employing the dimensionless group parameters defined in Section 4.8 and noting that:

$$\underset{\sim}{\hat{\boldsymbol{q}}} = \left[\begin{array}{cccc} \hat{\bar{u}}_1 & \hat{\bar{u}}_2 & \hat{\bar{u}}_3 & \bar{\theta}_1 \end{array}\right]^{\mathrm{T}} \tag{D.27}$$

and:

$$\begin{aligned}
\underline{\bar{\boldsymbol{\theta}}} &= \left[\begin{array}{ccc} \bar{\theta}_1 & -\bar{u}_{3,1} & \bar{u}_{2,1} \end{array}\right]^{\mathrm{T}} = \left[\begin{array}{ccc} \bar{\theta}_1 & -\hat{\bar{u}}_{3,\hat{1}} & \hat{\bar{u}}_{2,\hat{1}} \end{array}\right]^{\mathrm{T}} \\
\underline{\mathring{\bar{\boldsymbol{\theta}}}} &= \left[\begin{array}{ccc} \mathring{\bar{\theta}}_1 & -\mathring{\hat{\bar{u}}}_{3,\hat{1}} & \mathring{\hat{\bar{u}}}_{2,\hat{1}} \end{array}\right]^{\mathrm{T}} \\
\underline{\mathring{\mathring{\bar{\boldsymbol{\theta}}}}} &= \left[\begin{array}{ccc} \mathring{\mathring{\bar{\theta}}}_1 & -\mathring{\mathring{\hat{\bar{u}}}}_{3,\hat{1}} & \mathring{\mathring{\hat{\bar{u}}}}_{2,\hat{1}} \end{array}\right]^{\mathrm{T}} \\
\delta\underline{\bar{\boldsymbol{\theta}}} &= \left[\begin{array}{ccc} \delta\bar{\theta}_1 & -\delta\hat{\bar{u}}_{3,\hat{1}} & \delta\hat{\bar{u}}_{2,\hat{1}} \end{array}\right]^{\mathrm{T}}
\end{aligned} \tag{D.28}$$

the potential and kinetic energy and virtual work expressions of an Euler-Bernoulli gyrobeam can be nondimensionalized as:

$$\begin{aligned}
\hat{\mathcal{U}} &= \int_{\hat{L}} \hat{\mathcal{U}}^{L}\, d\hat{L} \\
&= \frac{1}{2}\int_{\hat{L}} \hat{\bar{u}}_{1,\hat{1}}\,\hat{\bar{u}}_{1,\hat{1}}\, d\hat{L} + \frac{1}{2}\,\hat{I}_3 \int_{\hat{L}} \hat{\bar{u}}_{2,\hat{1}\hat{1}}\,\hat{\bar{u}}_{2,\hat{1}\hat{1}}\, d\hat{L} + \frac{1}{2}\,\hat{I}_2 \int_{\hat{L}} \hat{\bar{u}}_{3,\hat{1}\hat{1}}\,\hat{\bar{u}}_{3,\hat{1}\hat{1}}\, d\hat{L} \\
&\quad + \frac{1}{2}\,k_{\mathrm{t}}\,\hat{\mu}\,\hat{I}_1 \int_{\hat{L}} \bar{\theta}_{1,\hat{1}}\,\bar{\theta}_{1,\hat{1}}\, d\hat{L}
\end{aligned} \tag{D.29}$$

$$
\begin{aligned}
\hat{\mathcal{T}} &= \int_{\hat{L}} \hat{\mathcal{T}}^{L}\, d\hat{L} \\
&= \frac{1}{2}\left(1+\hat{\varrho}^{V}\right) \int_{\hat{L}} \left(\mathring{\hat{u}}_1\,\mathring{\hat{u}}_1 + \mathring{\hat{u}}_2\,\mathring{\hat{u}}_2 + \mathring{\hat{u}}_3\,\mathring{\hat{u}}_3\right) d\hat{L} + \frac{1}{2}\left(1+\hat{\varrho}^{V}\right)\hat{I}_1 \int_{\hat{L}} \mathring{\bar{\theta}}_1\,\mathring{\bar{\theta}}_1\, d\hat{L} \\
&\quad + \frac{1}{2}\int_{\hat{L}} \hat{\jmath}^{V}_{ij}\,\mathring{\bar{\theta}}_j\,\mathring{\bar{\theta}}_i\, d\hat{L} + \int_{\hat{L}} \hat{\jmath}^{V}_{ij}\left(\mathring{\phi}_j + \mathring{\psi}_j\right)\mathring{\bar{\theta}}_i\, d\hat{L} \\
&\quad + \frac{1}{2}\int_{\hat{L}} \hat{\jmath}^{V}_{ij}\left(\mathring{\phi}_j\,\mathring{\phi}_i + \mathring{\psi}_j\,\mathring{\psi}_i + 2\,\mathring{\phi}_j\,\mathring{\psi}_i\right) d\hat{L}
\end{aligned}
\tag{D.30}
$$

and:

$$
\begin{aligned}
\delta\hat{\mathcal{W}} &= \int_{\hat{L}} \delta\hat{\mathcal{W}}^{L}\, d\hat{L} + \sum_{P} \delta\hat{\mathcal{W}}^{P} \\
&= \int_{\hat{L}} \left(\hat{\bar{f}}^{V}_i\,\delta\hat{u}_i + \hat{\bar{m}}_i^{\,V}\,\delta\bar{\theta}_i + \hat{\bar{m}}_i^{\,L}\,\delta\bar{\theta}_i\right) d\hat{L} + \sum_{P}\left(\hat{\bar{f}}^{S}_i\,\delta\hat{u}_i + \hat{\bar{m}}_i^{\,S}\,\delta\bar{\theta}_i + \hat{\bar{m}}_i^{\,P}\,\delta\bar{\theta}_i\right)
\end{aligned}
\tag{D.31}
$$

Finally, the dimensionless equations of motion of an Euler-Bernoulli gyrobeam will be obtained as:

$$
\begin{aligned}
\hat{\bar{f}}^{V}_1 &= \left(1+\hat{\varrho}^{V}\right)\mathring{\mathring{\hat{u}}}_1 - \hat{u}_{1,\hat{1}\hat{1}} \\
\hat{\bar{f}}^{V}_2 - \hat{\bar{m}}^{L}_{3\,,\hat{1}} - \hat{\bar{m}}^{V}_{3\,,\hat{1}} &= \left(1+\hat{\varrho}^{V}\right)\mathring{\mathring{\hat{u}}}_2 - \mathring{\hat{\mathcal{J}}}^{\,V}_{3\,,\hat{1}} + \hat{I}_3\,\hat{u}_{2,\hat{1}\hat{1}\hat{1}\hat{1}} \\
\hat{\bar{f}}^{V}_3 + \hat{\bar{m}}^{L}_{2\,,\hat{1}} + \hat{\bar{m}}^{V}_{2\,,\hat{1}} &= \left(1+\hat{\varrho}^{V}\right)\mathring{\mathring{\hat{u}}}_3 + \mathring{\hat{\mathcal{J}}}^{\,V}_{2\,,\hat{1}} + \hat{I}_2\,\hat{u}_{3,\hat{1}\hat{1}\hat{1}\hat{1}} \\
\hat{\bar{m}}^{L}_1 + \hat{\bar{m}}^{V}_1 &= \left(1+\hat{\varrho}^{V}\right)\hat{I}_1\,\mathring{\mathring{\bar{\theta}}}_1 + \mathring{\hat{\mathcal{J}}}^{\,V}_1 - k_{\mathrm{t}}\,\hat{\mu}\,\hat{I}_1\,\bar{\theta}_{1,\hat{1}\hat{1}}
\end{aligned}
\tag{D.32}
$$

D.8 Finite element formulation

The dynamic equations of an Euler-Bernoulli gyrobeam, *i.e.* the set of well-posed linear hyperbolic PDEs given in Eq. (D.32), can be transformed into a set of coupled ODEs

through employing the FEM. The Euler-Bernoulli gyrobeam dynamic equations given by Eq. (D.32) are derived from a combination of C^0 and C^1 variational problems. To be more precise, the C^0 longitudinal and torsional deformation problems and C^1 bending deformation problems characterize the dynamics of a 3D Euler-Bernoulli gyrobeam. Consequently, one may use different basis functions with C^0 and C^1 continuities to generate the consistent displacement-based finite element matrices of an Euler-Bernoulli gyrobeam.

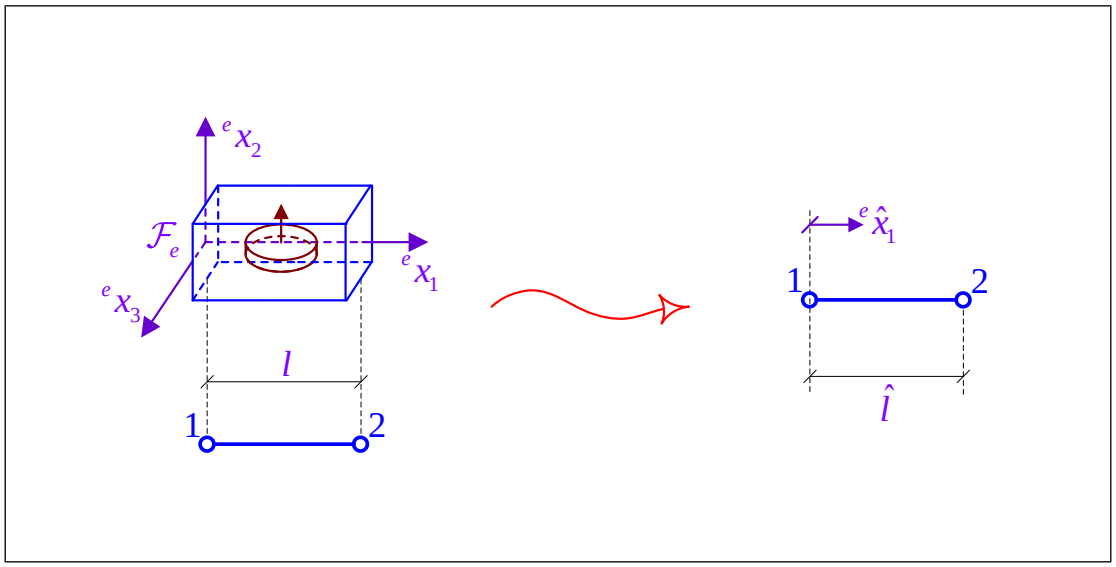

Figure D.1: The dimensional and dimensionless forms of the Euler-Bernoulli gyrobeam two-node element.

A two-node element, as shown in Figure D.1, with C^0 linear basis functions for expansion of longitudinal and torsional deformations:

$$\begin{aligned} \hat{H}^{\langle 1 \rangle}({}^e\hat{x}_1) &= 1 - \frac{{}^e\hat{x}_1}{\hat{l}} \\ \hat{H}^{\langle 2 \rangle}({}^e\hat{x}_1) &= \frac{{}^e\hat{x}_1}{\hat{l}} \end{aligned} \tag{D.33}$$

and C^1 cubic Hermite basis functions [100] for expansion of bending deformations:

$$\begin{aligned}
\hat{H}^{\langle 10\rangle}({}^e\hat{x}_1) &= 1 - 3\,\frac{{}^e\hat{x}_1^2}{\hat{l}^2} + 2\,\frac{{}^e\hat{x}_1^3}{\hat{l}^3} \\
\hat{H}^{\langle 11\rangle}({}^e\hat{x}_1) &= {}^e\hat{x}_1 - 2\,\frac{{}^e\hat{x}_1^2}{\hat{l}} + \frac{{}^e\hat{x}_1^3}{\hat{l}^2} \\
\hat{H}^{\langle 20\rangle}({}^e\hat{x}_1) &= 3\,\frac{{}^e\hat{x}_1^2}{\hat{l}^2} - 2\,\frac{{}^e\hat{x}_1^3}{\hat{l}^3} \\
\hat{H}^{\langle 21\rangle}({}^e\hat{x}_1) &= -\frac{{}^e\hat{x}_1^2}{\hat{l}} + \frac{{}^e\hat{x}_1^3}{\hat{l}^2}
\end{aligned} \tag{D.34}$$

will be used to generate the 3D Euler-Bernoulli gyrobeam FEM matrices. Note that $\hat{l}$ and ${}^e\hat{x}_1$ are the dimensionless forms of the element length l and local frame coordinate ${}^e x_1$ defined as:

$$\begin{aligned}
\hat{l} &= \frac{l}{L} \\
{}^e\hat{x}_1 &= \frac{{}^e x_1}{L}, \qquad 0 \le {}^e\hat{x}_1 \le \hat{l}
\end{aligned} \tag{D.35}$$

The two-node element has six DOFs at each node or 12 DOFs in total which can be summarized into the matrix of nodal generalized coordinates $\underset{\sim}{\hat{\boldsymbol{q}}}^{\langle \mathrm{j}\rangle}$:

$$\begin{aligned}
\underset{\sim}{\hat{\boldsymbol{q}}}^{\langle \mathrm{j}\rangle} = \left[\hat{q}_i^{\langle \mathrm{j}\rangle}\right] &= \begin{bmatrix} \hat{\bar{u}}_1^{\langle \mathrm{j}\rangle} & \hat{\bar{u}}_2^{\langle \mathrm{j}\rangle} & \hat{\bar{u}}_3^{\langle \mathrm{j}\rangle} & \bar{\theta}_1^{\langle \mathrm{j}\rangle} & \bar{\theta}_2^{\langle \mathrm{j}\rangle} & \bar{\theta}_3^{\langle \mathrm{j}\rangle} \end{bmatrix}^{\mathrm{T}} \\
&= \begin{bmatrix} \hat{\bar{u}}_1^{\langle \mathrm{j}\rangle} & \hat{\bar{u}}_2^{\langle \mathrm{j}\rangle} & \hat{\bar{u}}_3^{\langle \mathrm{j}\rangle} & \bar{\theta}_1^{\langle \mathrm{j}\rangle} & -\hat{\bar{u}}_3^{\langle \mathrm{j}\rangle}{}_{,\hat{1}} & \hat{\bar{u}}_2^{\langle \mathrm{j}\rangle}{}_{,\hat{1}} \end{bmatrix}^{\mathrm{T}}
\end{aligned} \tag{D.36}$$

and the matrix of element(al) generalized coordinates $\underset{\sim}{\hat{\boldsymbol{q}}}^{\langle \mathrm{e}\rangle}$:

$$\underset{\sim}{\hat{\boldsymbol{q}}}^{\langle \mathrm{e}\rangle} = \left[\underset{\sim}{\hat{\boldsymbol{q}}}^{\langle \mathrm{j}\rangle}\right] = \begin{bmatrix} \underset{\sim}{\hat{\boldsymbol{q}}}^{\langle 1\rangle\,\mathrm{T}} & \underset{\sim}{\hat{\boldsymbol{q}}}^{\langle 2\rangle\,\mathrm{T}} \end{bmatrix}^{\mathrm{T}} \tag{D.37}$$

where $\hat{q}_i^{\langle \mathrm{j}\rangle}$ denotes the single nodal generalized coordinates.

Using the element basis shape functions in Eqs. (D.33) and (D.34) the within-element generalized coordinates $\hat{q}_i$ can be interpolated in terms of the nodal generalized coordinates

$\hat{q}_i^{\langle \mathrm{j} \rangle}$ as:

$$
\begin{aligned}
\hat{\bar{u}}_1 &= \hat{H}^{\langle 1 \rangle}\, \hat{\bar{u}}_1^{\langle 1 \rangle} + \hat{H}^{\langle 2 \rangle}\, \hat{\bar{u}}_1^{\langle 2 \rangle} \\
\hat{\bar{u}}_2 &= \hat{H}^{\langle 10 \rangle}\, \hat{\bar{u}}_2^{\langle 1 \rangle} + \hat{H}^{\langle 11 \rangle}\, \bar{\theta}_3^{\langle 1 \rangle} + \hat{H}^{\langle 20 \rangle}\, \hat{\bar{u}}_2^{\langle 2 \rangle} + \hat{H}^{\langle 21 \rangle}\, \bar{\theta}_3^{\langle 2 \rangle} \\
\hat{\bar{u}}_3 &= \hat{H}^{\langle 10 \rangle}\, \hat{\bar{u}}_3^{\langle 1 \rangle} - \hat{H}^{\langle 11 \rangle}\, \bar{\theta}_2^{\langle 1 \rangle} + \hat{H}^{\langle 20 \rangle}\, \hat{\bar{u}}_3^{\langle 2 \rangle} - \hat{H}^{\langle 21 \rangle}\, \bar{\theta}_2^{\langle 2 \rangle} \\
\bar{\theta}_1 &= \hat{H}^{\langle 1 \rangle}\, \bar{\theta}_1^{\langle 1 \rangle} + \hat{H}^{\langle 2 \rangle}\, \bar{\theta}_1^{\langle 2 \rangle} \\
\bar{\theta}_2 = -\hat{\bar{u}}_{3,\hat{1}} &= \hat{H}'^{\langle 11 \rangle}\, \bar{\theta}_2^{\langle 1 \rangle} - \hat{H}'^{\langle 10 \rangle}\, \hat{\bar{u}}_3^{\langle 1 \rangle} + \hat{H}'^{\langle 21 \rangle}\, \bar{\theta}_2^{\langle 2 \rangle} - \hat{H}'^{\langle 20 \rangle}\, \hat{\bar{u}}_3^{\langle 2 \rangle} \\
\bar{\theta}_3 = +\hat{\bar{u}}_{2,\hat{1}} &= \hat{H}'^{\langle 11 \rangle}\, \bar{\theta}_3^{\langle 1 \rangle} + \hat{H}'^{\langle 10 \rangle}\, \hat{\bar{u}}_2^{\langle 1 \rangle} + \hat{H}'^{\langle 21 \rangle}\, \bar{\theta}_3^{\langle 2 \rangle} + \hat{H}'^{\langle 20 \rangle}\, \hat{\bar{u}}_2^{\langle 2 \rangle}
\end{aligned}
\tag{D.38}
$$

where:

$$
\frac{d}{d\hat{x}_i} = {}^{e}\frac{d}{d\hat{x}_i} \tag{D.39}
$$

and:

$$
\hat{H}'^{\langle \mathrm{j} \rangle} = \hat{H}'^{\langle \mathrm{j} \rangle}({}^{e}\hat{x}_1) = {}^{e}\frac{d}{d\hat{x}_i}\Big(\hat{H}^{\langle \mathrm{j} \rangle}({}^{e}\hat{x}_1)\Big) = {}^{e}\frac{d\hat{H}^{\langle \mathrm{j} \rangle}}{d\hat{x}_i} \tag{D.40}
$$

By using the expansions of the form given in Eq. (D.38) to substitute into the potential and kinetic energy and virtual work expressions, while taking into account the essential first-order approximation with respect to $\bar{\vartheta}$, one can generate the variational or weak form of the FEM formulation and derive the finite element matrices of the selected Euler-Bernoulli gyrobeam two-node element. Then, the so-obtained element(al) stiffness matrix $\hat{\underset{\sim}{\boldsymbol{\mathcal{K}}}}^{\langle \mathrm{e} \rangle}$, mass matrix $\hat{\underset{\sim}{\boldsymbol{\mathcal{M}}}}^{\langle \mathrm{e} \rangle}$, gyricity matrix $\hat{\underset{\sim}{\boldsymbol{\mathcal{G}}}}^{\langle \mathrm{e} \rangle}$, circulatory matrix $\hat{\underset{\sim}{\boldsymbol{\mathcal{C}}}}^{\langle \mathrm{e} \rangle}$, generalized moment matrix $\hat{\underset{\sim}{\boldsymbol{\mathcal{R}}}}^{\langle \mathrm{e} \rangle}$, and generalized force matrix $\hat{\underset{\sim}{\boldsymbol{\mathcal{Q}}}}^{\langle \mathrm{e} \rangle}$ are assembled to form the system's global matrices $\hat{\underset{\sim}{\boldsymbol{\mathcal{K}}}}^{\langle \mathrm{g} \rangle}$, $\hat{\underset{\sim}{\boldsymbol{\mathcal{M}}}}^{\langle \mathrm{g} \rangle}$, $\hat{\underset{\sim}{\boldsymbol{\mathcal{G}}}}^{\langle \mathrm{g} \rangle}$, $\hat{\underset{\sim}{\boldsymbol{\mathcal{C}}}}^{\langle \mathrm{g} \rangle}$, $\hat{\underset{\sim}{\boldsymbol{\mathcal{R}}}}^{\langle \mathrm{g} \rangle}$, and $\hat{\underset{\sim}{\boldsymbol{\mathcal{Q}}}}^{\langle \mathrm{g} \rangle}$.

The gyrobeam potential and kinetic energy variations and virtual work can be expressed in terms of these global matrices as:

$$
\begin{aligned}
\Delta\hat{\mathcal{U}} &= \delta\hat{\underset{\sim}{\boldsymbol{q}}}^{\langle \mathrm{g} \rangle\,\mathrm{T}}\, \hat{\underset{\sim}{\boldsymbol{\mathcal{K}}}}^{\langle \mathrm{g} \rangle}\, \hat{\underset{\sim}{\boldsymbol{q}}}^{\langle \mathrm{g} \rangle} \\
\Delta\hat{\mathcal{T}} &= -\delta\hat{\underset{\sim}{\boldsymbol{q}}}^{\langle \mathrm{g} \rangle\,\mathrm{T}}\, \hat{\underset{\sim}{\boldsymbol{\mathcal{M}}}}^{\langle \mathrm{g} \rangle}\, \hat{\underset{\sim}{\boldsymbol{q}}}^{\circ\circ\langle \mathrm{g} \rangle} - \delta\hat{\underset{\sim}{\boldsymbol{q}}}^{\langle \mathrm{g} \rangle\,\mathrm{T}}\, \hat{\underset{\sim}{\boldsymbol{\mathcal{G}}}}^{\langle \mathrm{g} \rangle}\, \hat{\underset{\sim}{\boldsymbol{q}}}^{\circ\langle \mathrm{g} \rangle} - \delta\hat{\underset{\sim}{\boldsymbol{q}}}^{\langle \mathrm{g} \rangle\,\mathrm{T}}\, \hat{\underset{\sim}{\boldsymbol{\mathcal{C}}}}^{\langle \mathrm{g} \rangle}\, \hat{\underset{\sim}{\boldsymbol{q}}}^{\langle \mathrm{g} \rangle} - \delta\hat{\underset{\sim}{\boldsymbol{q}}}^{\langle \mathrm{g} \rangle\,\mathrm{T}}\, \hat{\underset{\sim}{\boldsymbol{\mathcal{R}}}}^{\langle \mathrm{g} \rangle} \\
\delta\hat{\mathcal{W}} &= \delta\hat{\underset{\sim}{\boldsymbol{q}}}^{\langle \mathrm{g} \rangle\,\mathrm{T}}\, \hat{\underset{\sim}{\boldsymbol{\mathcal{Q}}}}^{\langle \mathrm{g} \rangle}
\end{aligned}
\tag{D.41}
$$

and (based on Hamilton's principle) the semi-discretized gyrobeam dynamic ODEs can be derived as:

$$
\hat{\underset{\sim}{\boldsymbol{\mathcal{Q}}}}^{\langle \mathrm{g} \rangle} - \hat{\underset{\sim}{\boldsymbol{\mathcal{R}}}}^{\langle \mathrm{g} \rangle} = \hat{\underset{\sim}{\boldsymbol{\mathcal{M}}}}^{\langle \mathrm{g} \rangle}\, \hat{\underset{\sim}{\boldsymbol{q}}}^{\circ\circ\langle \mathrm{g} \rangle} + \hat{\underset{\sim}{\boldsymbol{\mathcal{G}}}}^{\langle \mathrm{g} \rangle}\, \hat{\underset{\sim}{\boldsymbol{q}}}^{\circ\langle \mathrm{g} \rangle} + \hat{\underset{\sim}{\boldsymbol{\mathcal{C}}}}^{\langle \mathrm{g} \rangle}\, \hat{\underset{\sim}{\boldsymbol{q}}}^{\langle \mathrm{g} \rangle} + \hat{\underset{\sim}{\boldsymbol{\mathcal{K}}}}^{\langle \mathrm{g} \rangle}\, \hat{\underset{\sim}{\boldsymbol{q}}}^{\langle \mathrm{g} \rangle} \tag{D.42}
$$

Finally, the imposition of EBCs will result in the final semi-discretized Euler-Bernoulli gyrobeam dynamic ODEs:

$$\hat{\underset{\sim}{\mathcal{Q}}} - \hat{\underset{\sim}{\mathcal{R}}} = \hat{\underset{\sim}{\mathcal{M}}}\, \overset{\circ\circ}{\hat{\underset{\sim}{q}}} + \hat{\underset{\sim}{\mathcal{G}}}\, \overset{\circ}{\hat{\underset{\sim}{q}}} + \hat{\underset{\sim}{\mathcal{C}}}\, \hat{\underset{\sim}{q}} + \hat{\underset{\sim}{\mathcal{K}}}\, \hat{\underset{\sim}{q}} \tag{D.43}$$

which can be integrated with an ODE integration technique provided the ICs are given or can be used for modal vibration analysis even if the ICs are unknown.

D.9 Verification

As mentioned earlier, the 3D Euler-Bernoulli gyrobeam model is very useful for comparison, verification, and examination of the more extended gyrobeam models developed in this text, *i.e.* the 3D Timoshenko-based classical gyrobeam model and the 3D micropolar gyrobeam model. However, a preliminary step before employment of the herein-developed 3D Euler-Bernoulli gyrobeam model is to verify it (*i.e.* its corresponding dynamic equations and FEM discretization).

Due to the lack of information about the Euler-Bernoulli gyrobeam model developed by D'Eleuterio [2, 16] (the FEM formulation is not explained in detail) and the erroneous nature of the dynamic equations derived by Zee [33] (based on his equations gyricity effects may result in longitudinal deflections which cannot be correct), the best way of verifying the 3D Euler-Bernoulli gyrobeam model developed in this text is to use the model for reproduction of the results obtained by D'Eleuterio [2, 16].

However, one should note that, compared to the model developed by D'Eleuterio [2, 16], the Euler-Bernoulli gyrobeam model developed here is a more complete model as it does not impose any constraint or approximation on the gyros' attitude changes and is also capable of modeling the beam's longitudinal and torsional deformations. Therefore, to reproduce the results obtained by D'Eleuterio, the herein-developed unrestricted 3D Euler-Bernoulli gyrobeam model is firstly reduced to a zero-order restricted model, without the longitudinal and torsional deformation modes, to match the zero-order restricted Euler-Bernoulli gyrobeam model developed by D'Eleuterio [2, 16]. Then, this zero-order restricted Euler-Bernoulli gyrobeam model is implemented in MATLAB® [66] as a FEM-based numerical model and is used to obtain the natural frequencies and mode shapes of the simple

Euler-Bernoulli gyrobeams addressed in [16] and [2]. Tables D.1 and D.2 summarize the parameters which are used to implement the FEM-based numerical model in MATLAB®.

The Euler-Bernoulli gyrobeam selected in [16] for the numerical example is a slender cantilevered rod carrying a linearly decreasing (or triangular) distribution of gyricity parallel to the beam's neutral axis. The gyrobeam has a constant mass density, constant bending stiffnesses, and a bending stiffness ratio of 1.5. The modal results obtained for such a gyrobeam using (the zero-order restricted version of) the herein-developed 3D Euler-Bernoulli gyrobeam model are shown in Figures D.2–D.5. While knowing that 10 elements (or 11 nodes) does not guarantee the accuracy of all the natural frequencies and mode shapes depicted in Figures D.2–D.5, a 10-element FEM is used to produce these results. This provides the possibility of an even comparison with D'Eleuterio results in [16], copied in Figures D.13 and D.14 for ease of access, which were also obtained using a 10-element FEM. A comparison of the results obtained in this text with those obtained by D'Eleuterio [16], while neglecting the small differences which might be due to taking different integration approaches for derivation of the finite element matrices and especially the gyricity matrix, verifies the Euler-Bernoulli gyrobeam model and the FEM formulation developed in this appendix. Note that D'Eleuterio's dimensionless symbols $\hat{\omega}_\alpha$ and $\hat{h}_T$ can be represented in terms of the current text dimensionless parameters as:

$$\begin{aligned}
\hat{\omega}_\alpha &\equiv \frac{\hat{\omega}^{(\alpha)}}{\sqrt[4]{\hat{I}_2\,\hat{I}_3}} = \sqrt{\hat{R}_2\,\hat{R}_3}\,\hat{\omega}^{(\alpha)} \\
\hat{h}_T &\equiv \frac{1}{\sqrt[4]{\hat{I}_2\,\hat{I}_3}} \int_{\hat{L}} \left(\overset{\scriptscriptstyle\leftrightarrow}{\hat{\jmath}}^{V} \cdot \overset{\circ}{\underset{\scriptscriptstyle\rightarrow}{\psi}} \right) \cdot \underset{\scriptscriptstyle\rightarrow}{c}_1 \, d\hat{L} = \frac{1}{\sqrt[4]{\hat{I}_2\,\hat{I}_3}} \int_{\hat{L}} {}^{a}\hat{\jmath}^{V}_{33}\,\mathring{\varphi}_3 \, d\hat{L} = \sqrt{\hat{R}_2\,\hat{R}_3} \int_{\hat{L}} {}^{a}\hat{\jmath}^{V}_{33}\,\mathring{\varphi}_3 \, d\hat{L}
\end{aligned} \tag{D.44}$$

Based on the definition of $\hat{h}_T$ in Eq. (D.44), the gyricity distribution corresponding to a given $\hat{h}_T$ is a triangular function as:

$${}^{a}\hat{\jmath}^{V}_{33}\,\mathring{\varphi}_3 = \hat{h}_T \sqrt[4]{\hat{I}_2\,\hat{I}_3}\,2\left(1 - {}^{c}\hat{x}_1\right) = \hat{h}_T \frac{1}{\sqrt{\hat{R}_2\,\hat{R}_3}}\,2\left(1 - {}^{c}\hat{x}_1\right) \tag{D.45}$$

The Euler-Bernoulli gyrobeam considered in [2] is again a slender cantilevered rod with a constant mass density, constant bending stiffnesses, and a bending stiffness ratio of 1.5, carrying a gyricity distribution which is again parallel to the beam's neutral axis. The only

Table D.1: Summary of the main dimensionless parameters used in the numerical Euler-Bernoulli gyrobeam model.

Parameter	**Value(s)**
$\hat{R}_3 = \sqrt{\frac{3}{2}}\,\hat{R}_2 = \sqrt{\frac{5}{2}}\,\hat{R}_1$	50
$\hat{\mu}$	$\frac{3}{8}$
k_{t}	1
(φ_1, φ_2)	$(0, \frac{\pi}{2})$
$(\mathring{\varphi}_1, \mathring{\varphi}_2)$	$(0, 0)$
$\hat{\varrho}^V$	0
$\hat{h}_T^{\frac{1}{2}}$	$[0, 12]$

Table D.2: Summary of the main FEM parameters used in the numerical Euler-Bernoulli gyrobeam model.

Parameter	**Value**
Element Type	C^0 two-node (for tension and torsion)
	C^1 two-node (for bending)
Basis Functions	linear Lagrange polynomials (for tension and torsion)
	cubic Hermitian polynomials (for bending)
Number of Elements	10
Number of Nodes	11 (distributed evenly)
DOFs per Node	6
Longitudinal BCs	fixed-free
Torsional BCs	classical fixed-free
Bending BCs	classical clamped-free
Gyricity Distribution Function	triangular (to regenerate the results of [16])
	sinusoidal (to regenerate the results of [2])

difference is the gyricity distribution which has a sinusoidal shape this time (instead of a triangular distribution). The modal results obtained for this gyrobeam using (the zero-order restricted version of) the herein-developed 3D Euler-Bernoulli gyrobeam model are shown in Figures D.6–D.12. Once more, a comparison of these results with those obtained by D'Eleuterio [2], copied in Figures D.15–D.17, justifies the Euler-Bernoulli gyrobeam model and the FEM formulation developed in this appendix. Note that in [2] D'Eleuterio has replaced his symbol $\hat{\omega}_\alpha$ by $\hat{\Omega}_\alpha$ and this time the (sinusoidal-distributed) gyricity function corresponding to a given $\hat{h}_T$ is:

$$ {}^{a}\hat{\jmath}^{V}_{33}\,\mathring{\varphi}_3 = \hat{h}_T\,\sqrt[4]{\hat{I}_2\,\hat{I}_3}\,\frac{\pi}{2}\,\sin(\pi\,{}^{c}\hat{x}_1) = \hat{h}_T\,\frac{1}{\sqrt{\hat{R}_2\,\hat{R}_3}}\,\frac{\pi}{2}\,\sin(\pi\,{}^{c}\hat{x}_1) \tag{D.46} $$

At the end of this appendix it is useful noting that the complete unrestricted 3D Euler-Bernoulli gyrobeam model developed in this appendix (with no constraint on the attitude changes of gyros and capable of modeling the beam's longitudinal and torsional deformations) is used for comparison and analysis presented in Chapter 5.

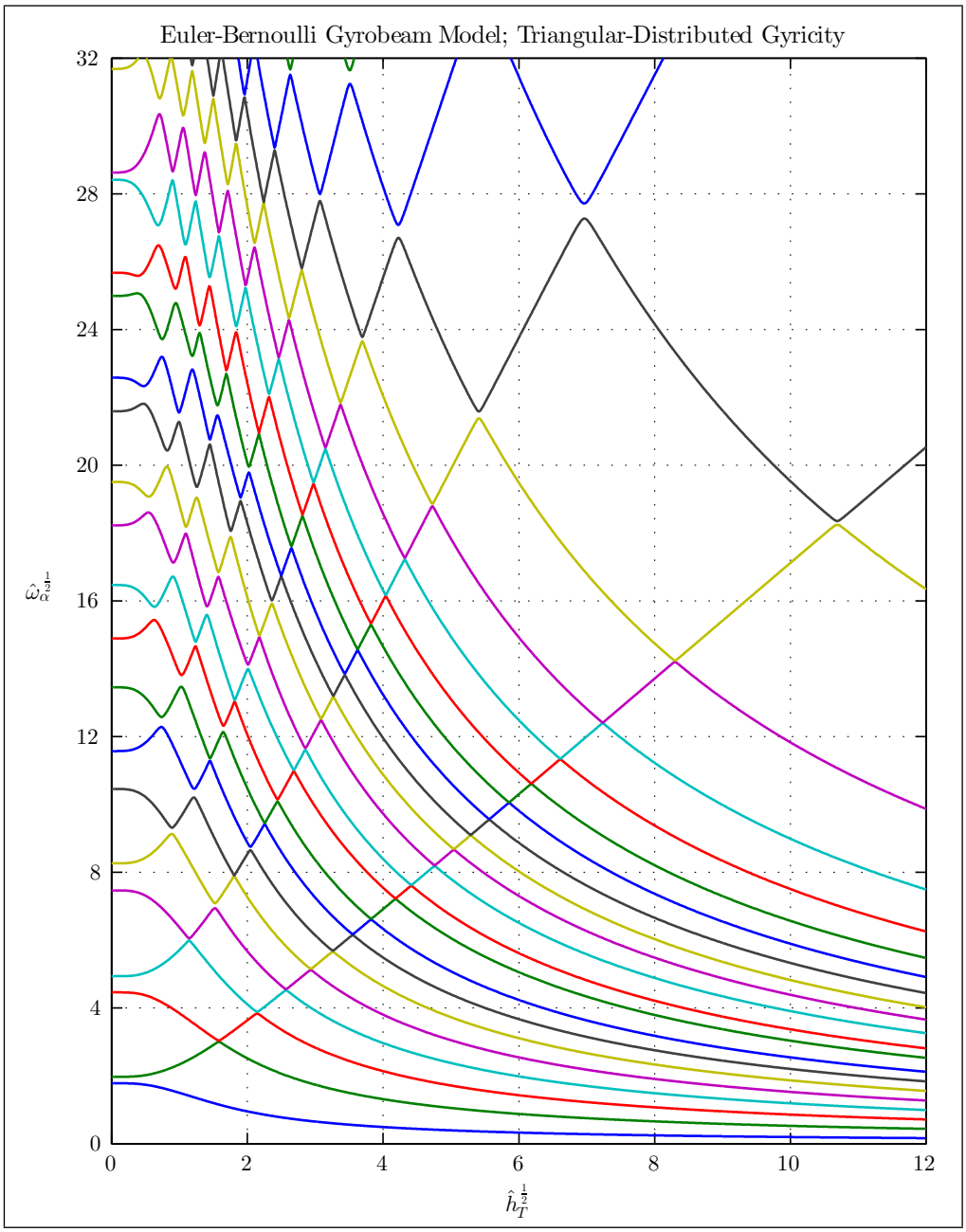

Figure D.2: Natural frequencies of D'Eleuterio's Euler-Bernoulli gyrobeam example in [16] with a triangular-distributed gyricity parallel to the beam's neutral axis.

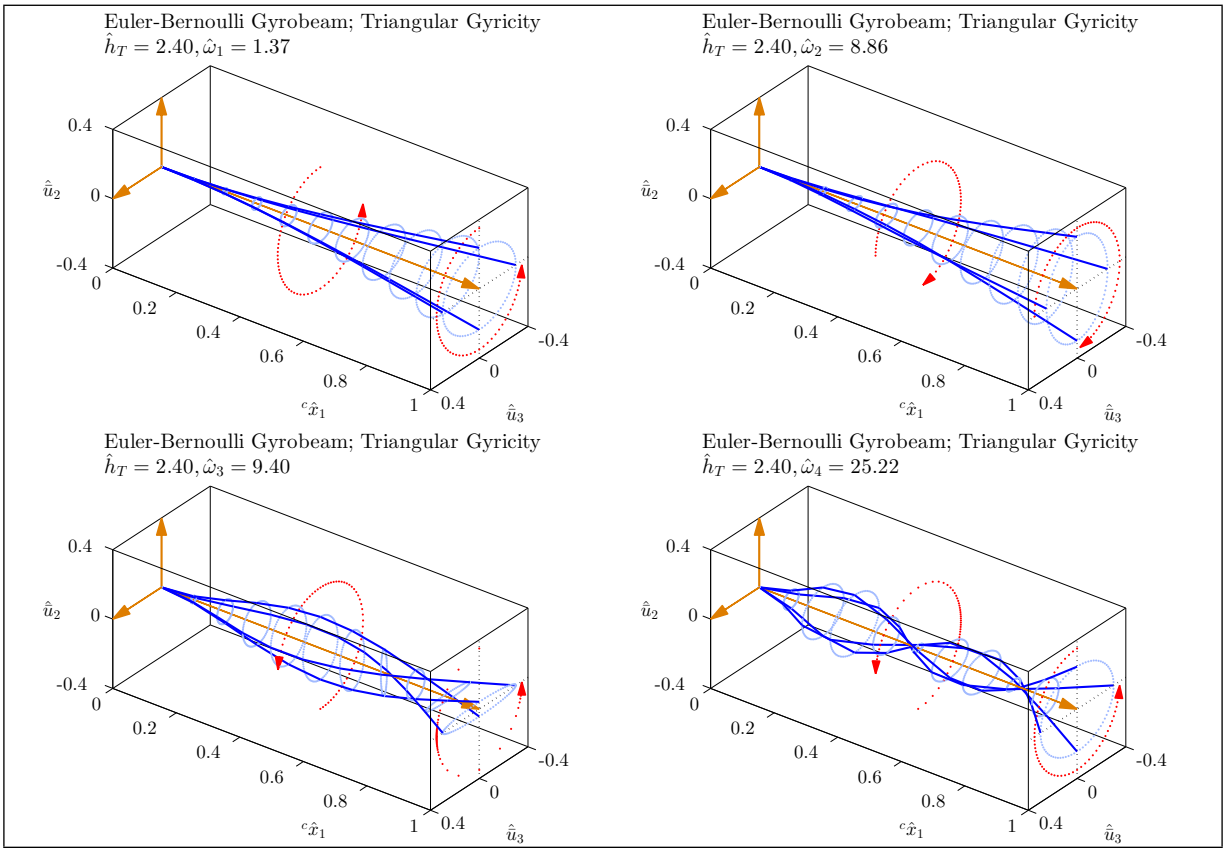

Figure D.3: Mode shapes of D'Eleuterio's Euler-Bernoulli gyrobeam example in [16] with a triangular-distributed gyricity parallel to the beam's neutral axis – Set 1.

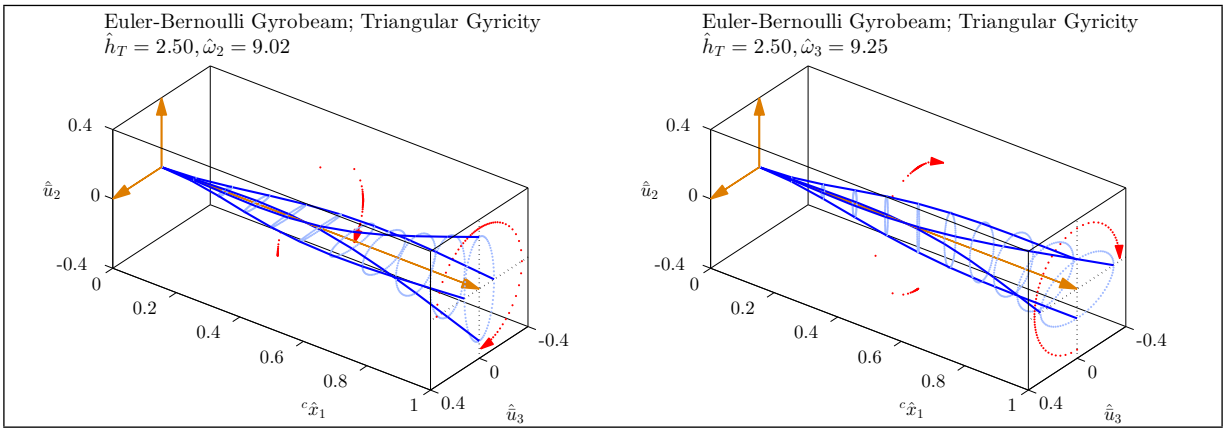

Figure D.4: Mode shapes of D'Eleuterio's Euler-Bernoulli gyrobeam example in [16] with a triangular-distributed gyricity parallel to the beam's neutral axis – Set 2.

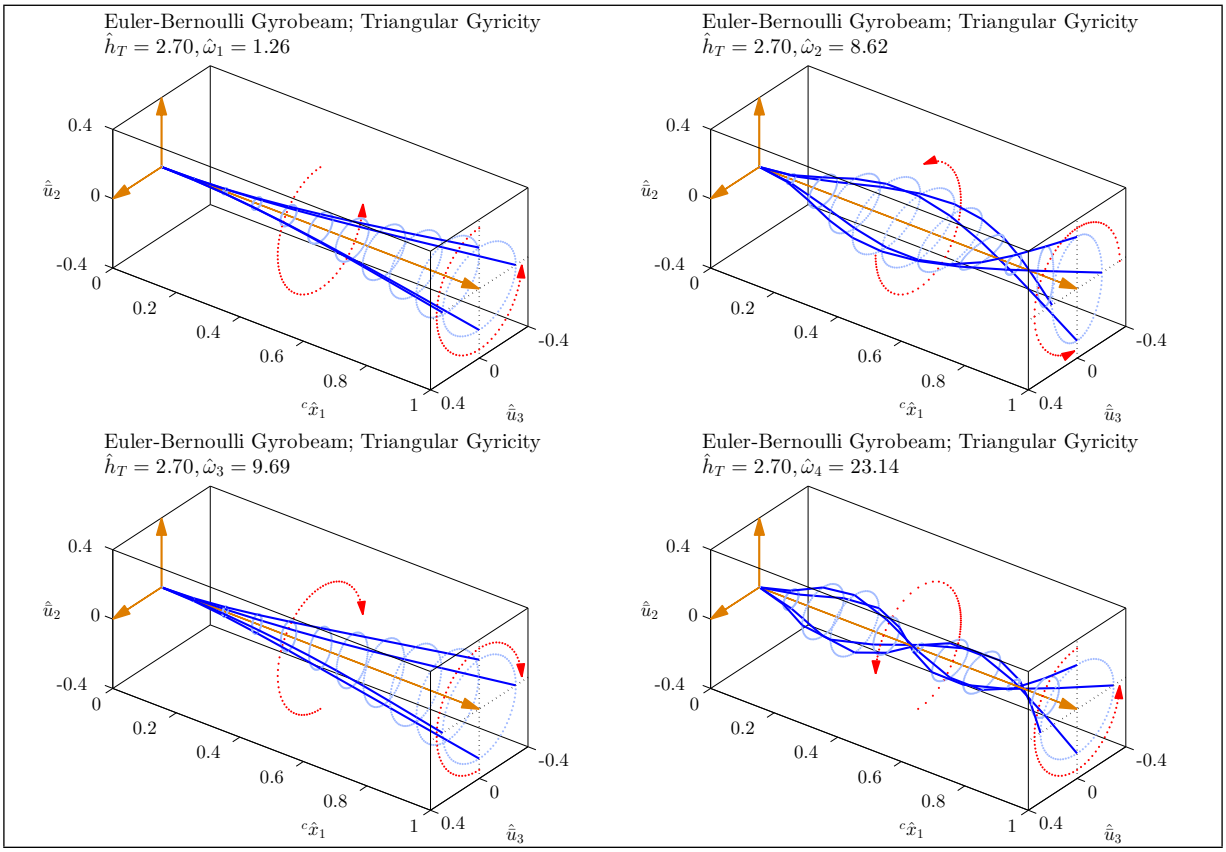

Figure D.5: Mode shapes of D'Eleuterio's Euler-Bernoulli gyrobeam example in [16] with a triangular-distributed gyricity parallel to the beam's neutral axis – Set 3.

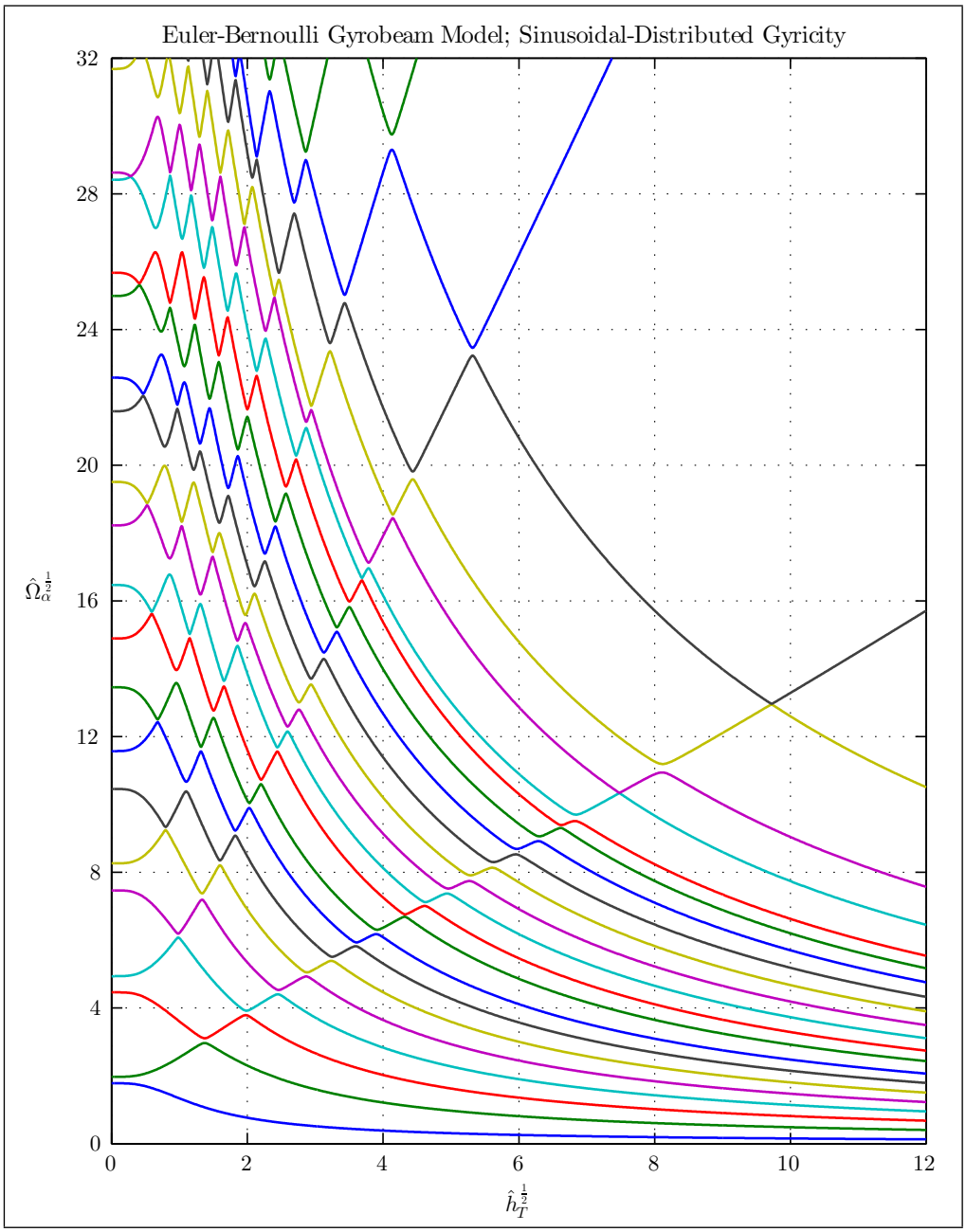

Figure D.6: Natural frequencies of D'Eleuterio's Euler-Bernoulli gyrobeam example in [2] with a sinusoidal-distributed gyricity parallel to the beam's neutral axis.

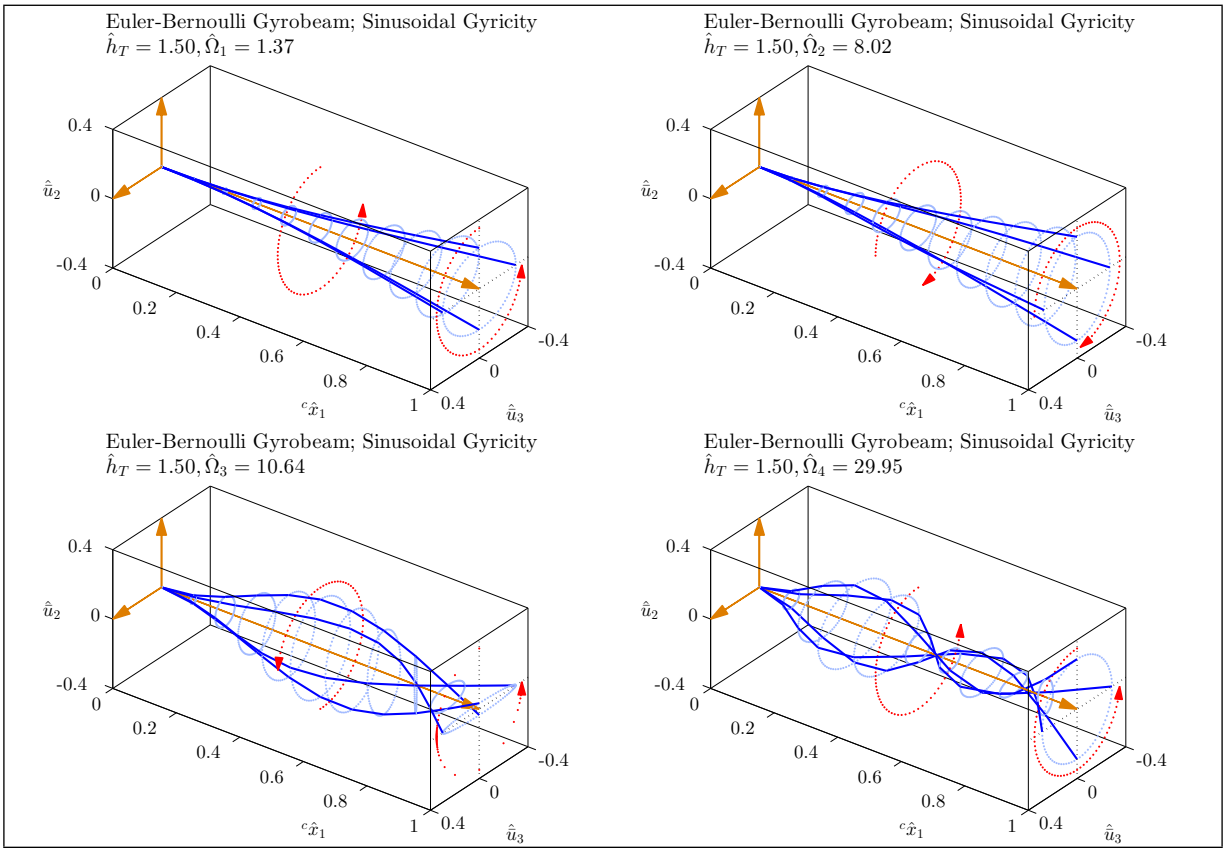

Figure D.7: Mode shapes of D'Eleuterio's Euler-Bernoulli gyrobeam example in [2] with a sinusoidal-distributed gyricity parallel to the beam's neutral axis – Set 1.

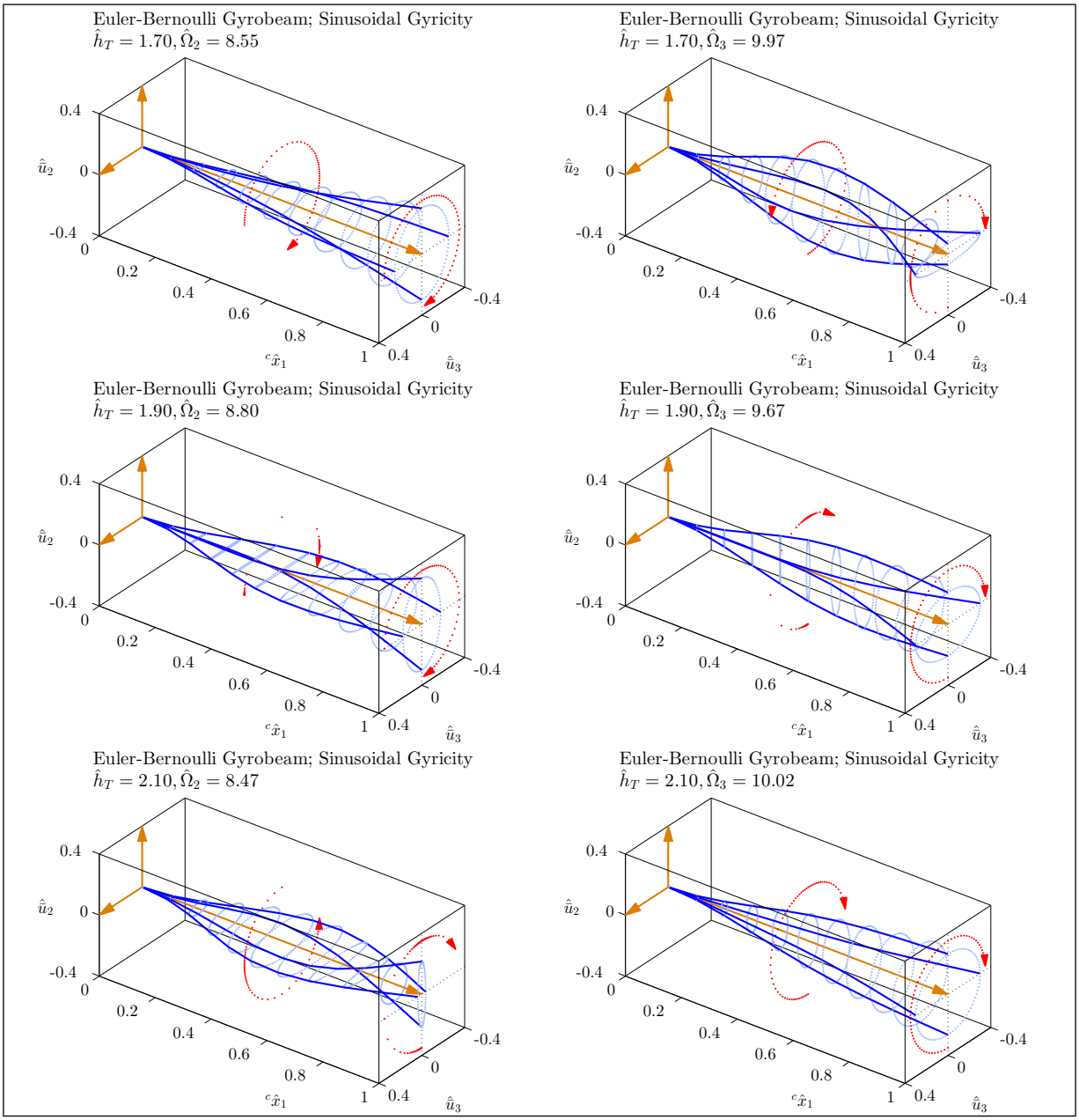

Figure D.8: Mode shapes of D'Eleuterio's Euler-Bernoulli gyrobeam example in [2] with a sinusoidal-distributed gyricity parallel to the beam's neutral axis – Set 2.

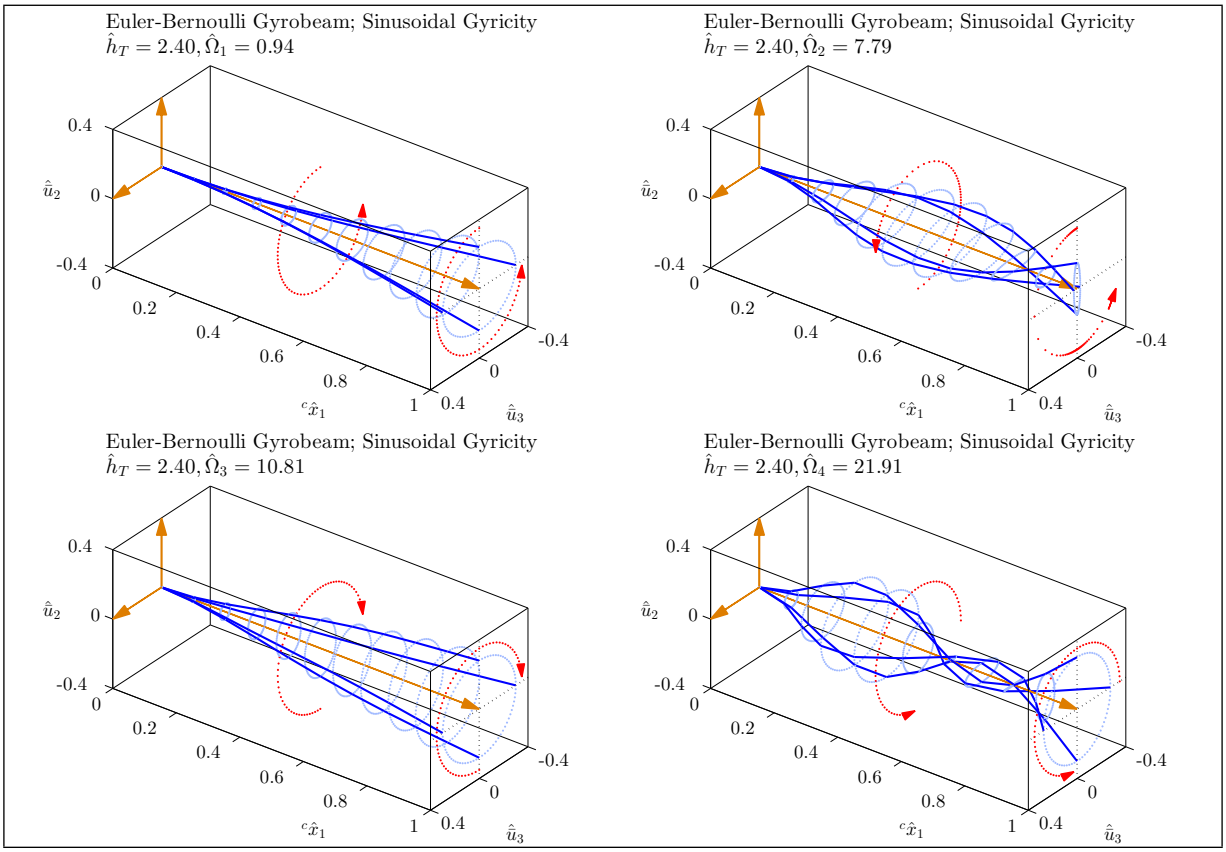

Figure D.9: Mode shapes of D'Eleuterio's Euler-Bernoulli gyrobeam example in [2] with a sinusoidal-distributed gyricity parallel to the beam's neutral axis – Set 3.

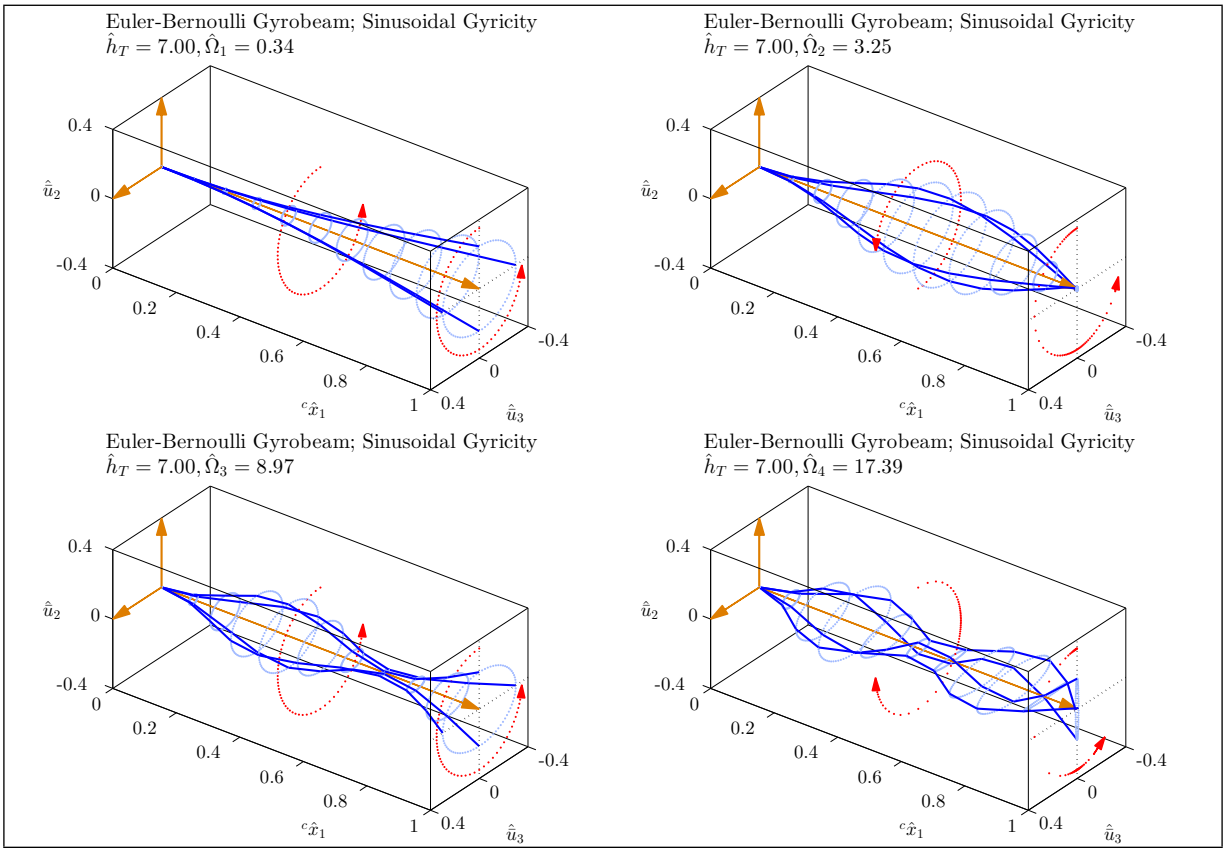

Figure D.10: Mode shapes of D'Eleuterio's Euler-Bernoulli gyrobeam example in [2] with a sinusoidal-distributed gyricity parallel to the beam's neutral axis – Set 4.

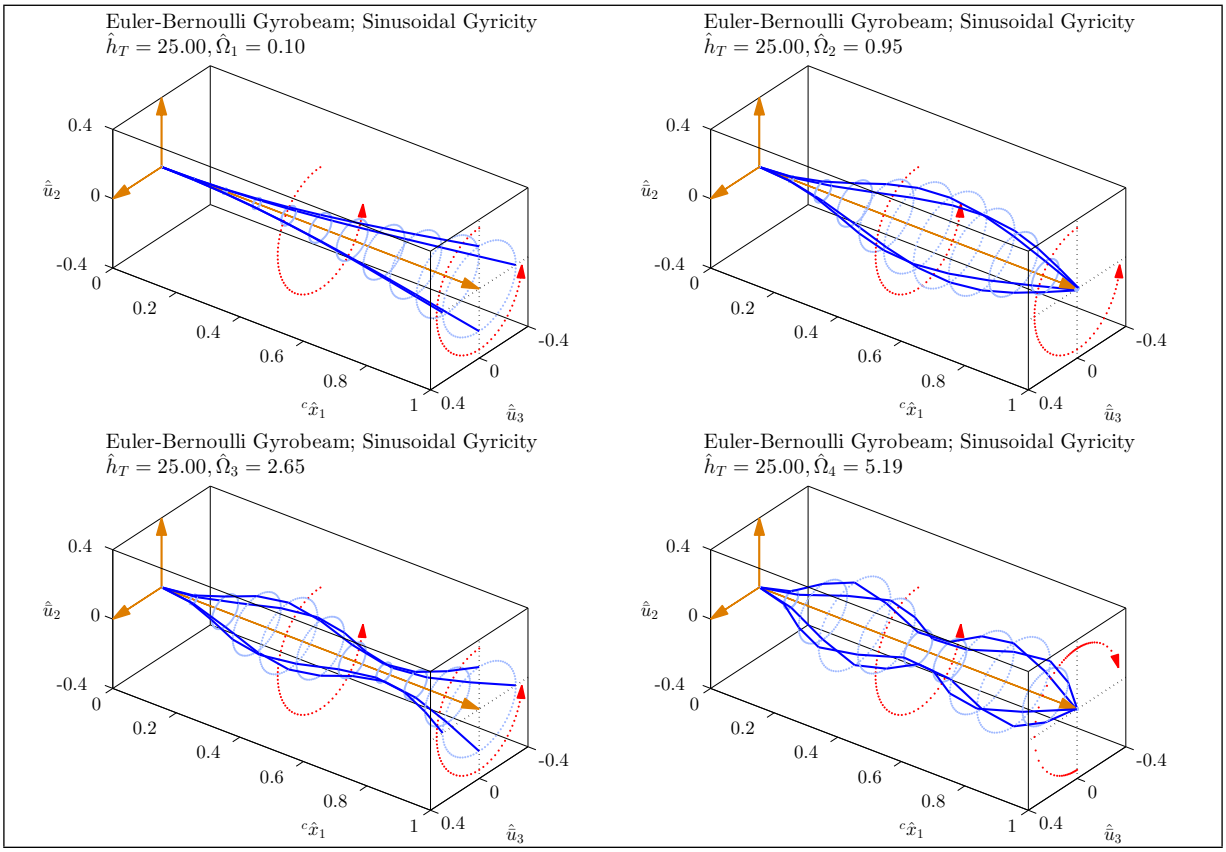

Figure D.11: Mode shapes of D'Eleuterio's Euler-Bernoulli gyrobeam example in [2] with a sinusoidal-distributed gyricity parallel to the beam's neutral axis – Set 5.

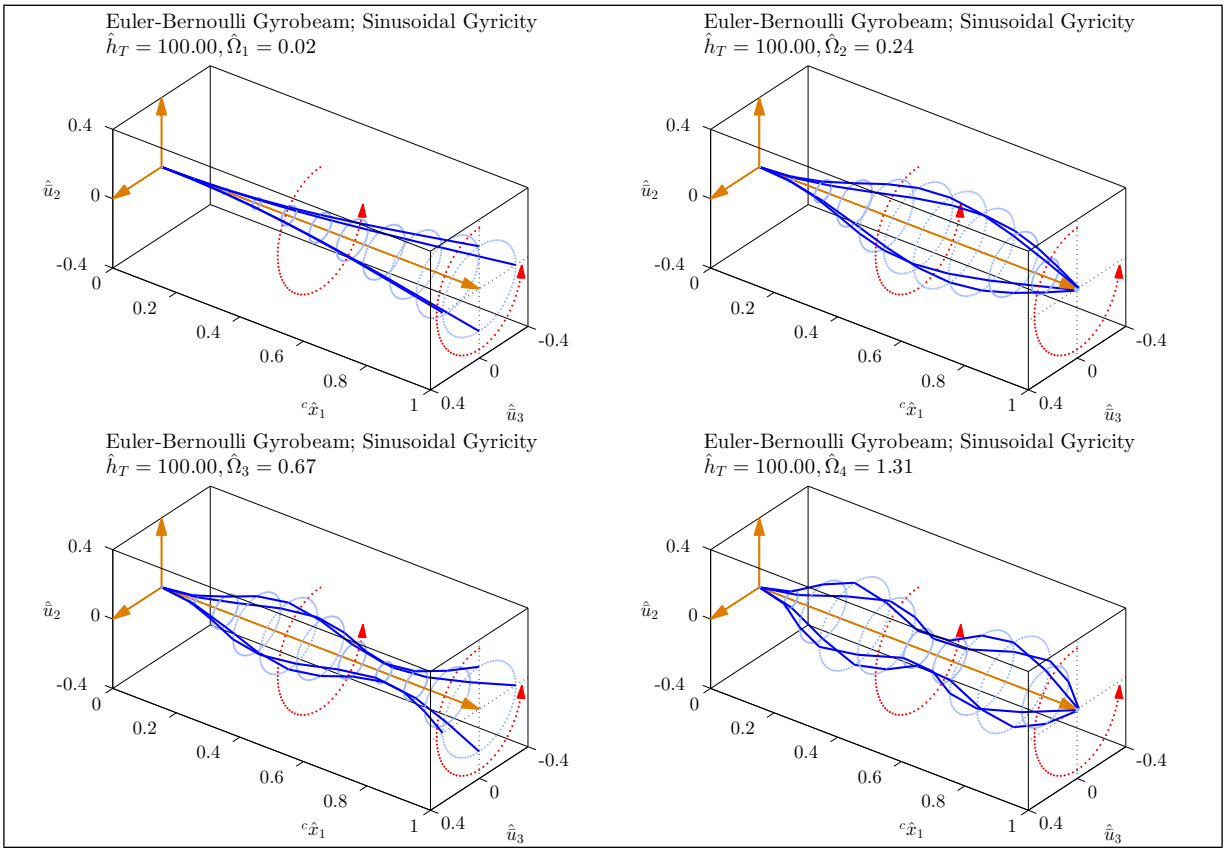

Figure D.12: Mode shapes of D'Eleuterio's Euler-Bernoulli gyrobeam example in [2] with a sinusoidal-distributed gyricity parallel to the beam's neutral axis – Set 6.

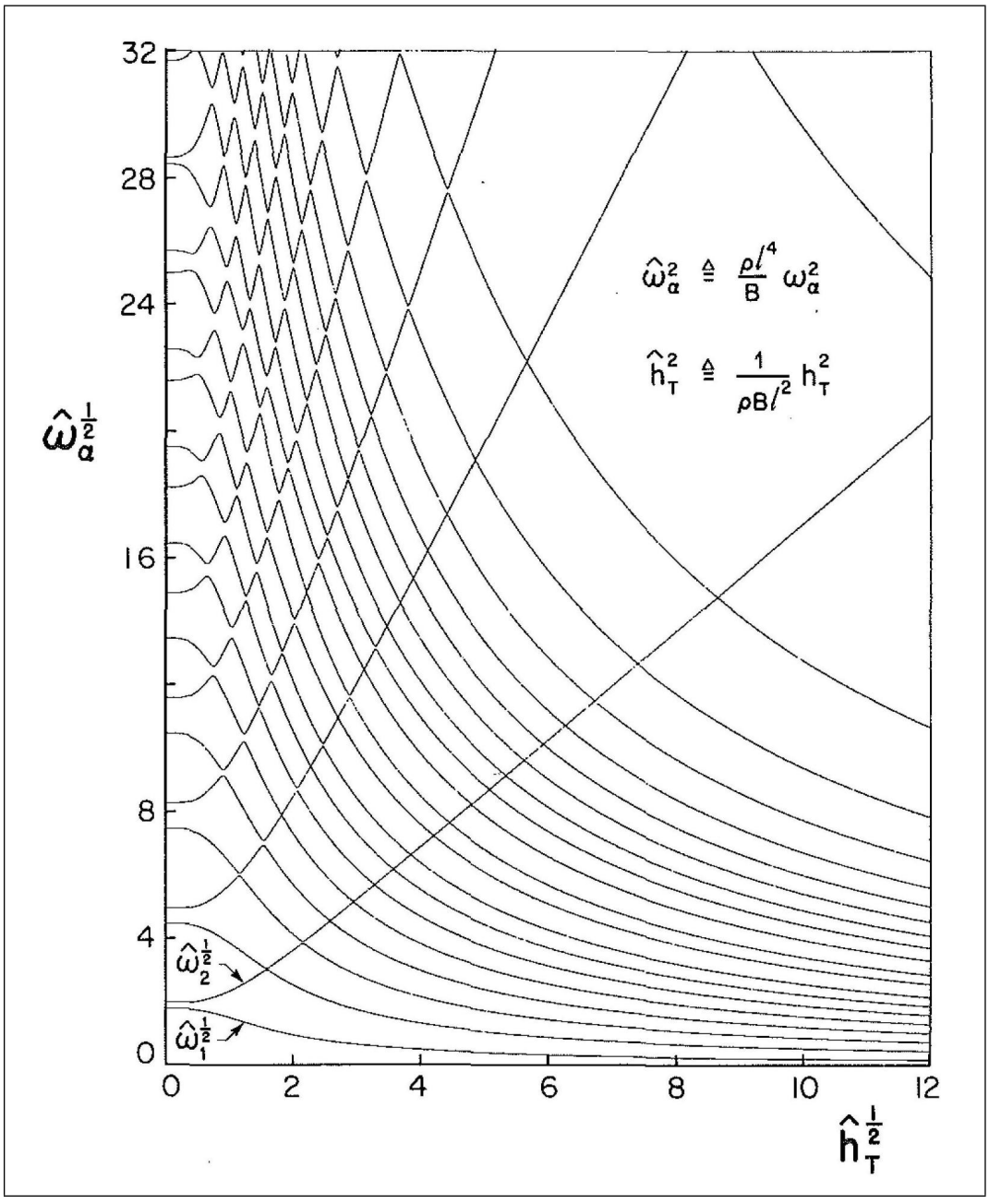

Figure D.13: Figure 5 of [16].

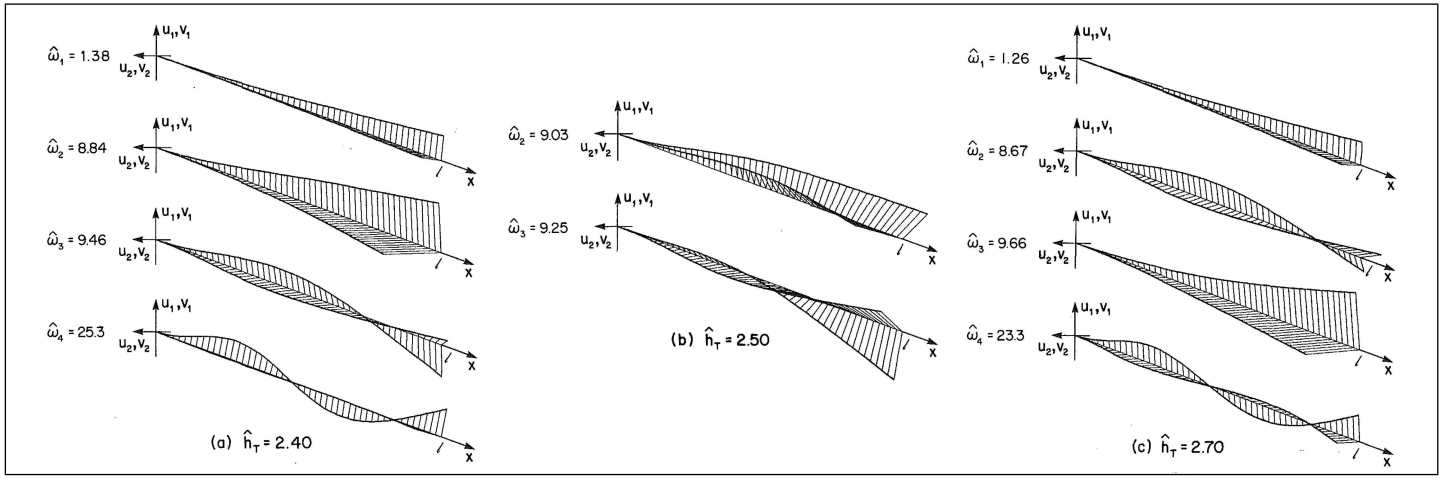

Figure D.14: Figure 6 of [16].

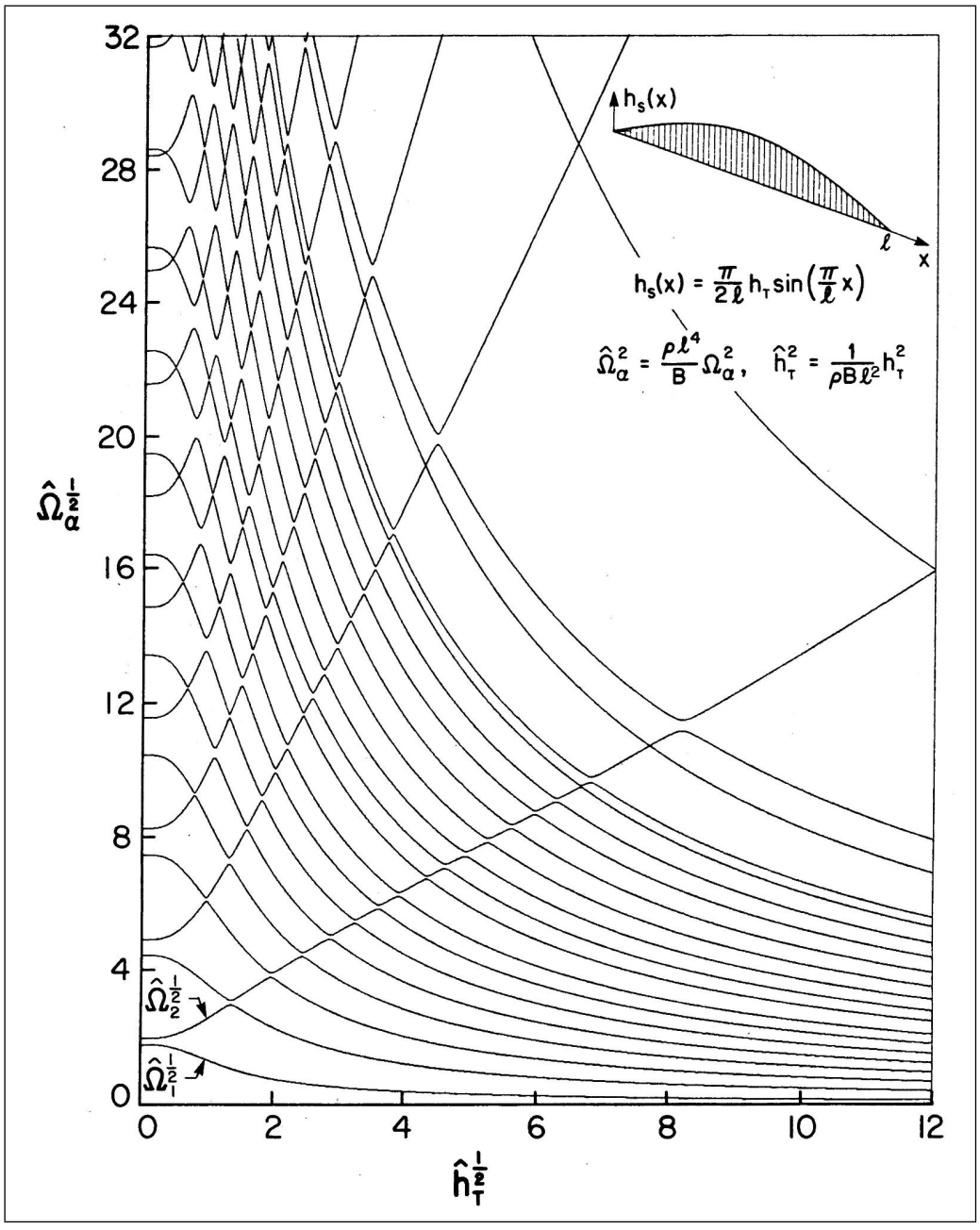

Figure D.15: Figure 5.3 of [2].

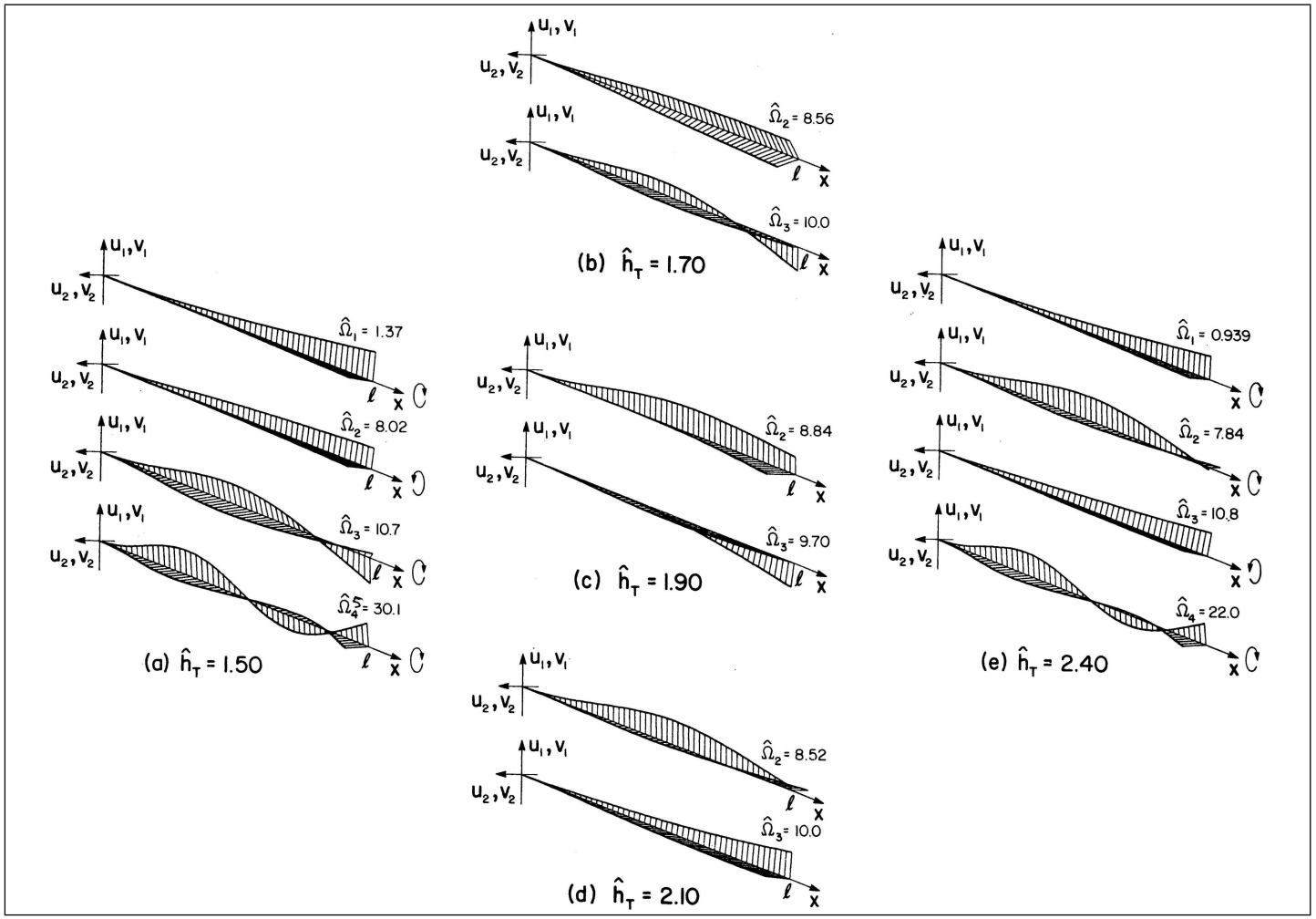

Figure D.16: Figure 5.5 of [2].

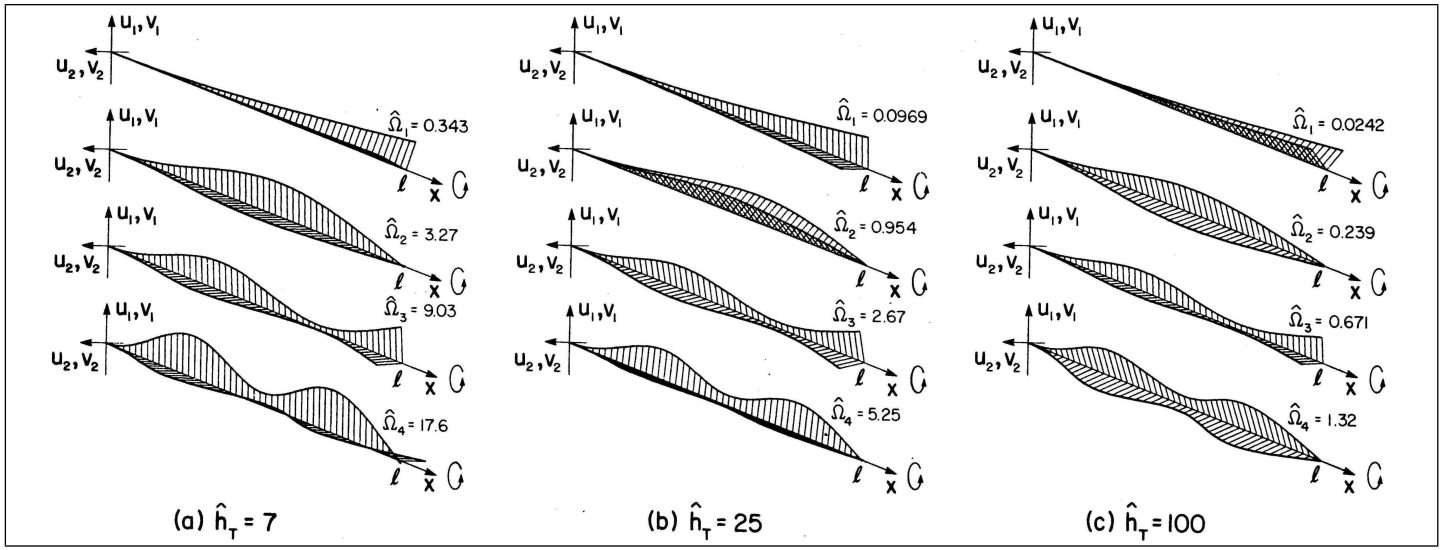

Figure D.17: Figure 5.7 of [2].

Appendix E

Gyroelastic Beams with Non-Uniform Gyricity

E.1 Introduction

This appendix shows how complicated and interesting the natural frequency loci (and their associated curve veering) and the mode shapes of classical (Timoshenko) and micropolar gyroelastic beams with non-uniform gyricity distributions are. Note that this is just a preliminary investigation and the subject deserves more future work. The model and the FEM parameters used to generate the results of this appendix are as those given in Chapters 5 and 6 (see Tables 5.1 and 5.3 and Tables 6.1–6.3). The micropolar gyrobeam is based on the first micropolar model addressed in Table 6.3 for which $\hat{\kappa} = 10^2$ and $\hat{\gamma} = 10^{-10}$.

E.2 Half sinusoidal gyricity distribution

The main numerical results provided in Chapters 5 and 6 for the uniform gyricity distribution are expressly repeated in this section by considering half sinusoidal (instead of uniform) axial and transverse gyricity distributions. Here, for a given total gyricity spin

rate $\mathring{\varphi}_{3\mathrm{T}}$, the distribution of the gyricity spin rate over the beam length $\mathring{\varphi}_3({}^c\hat{x}_1)$ is:

$$\mathring{\varphi}_3({}^c\hat{x}_1) = \mathring{\varphi}_{3\mathrm{T}} \frac{\pi}{2} \sin(\pi\, {}^c\hat{x}_1) \tag{E.1}$$

The natural frequency loci of a classical gyrobeam with a medium thickness ($\hat{R}_3 = 50$) and half sinusoidal axial and trnasverse gyricity distributions are given in Figures E.1 and E.3. Also the first six gyricity-affected mode shapes for the medium axial and transverse gyricity cases (*i.e.* $\mathring{\varphi}_{3\mathrm{T}} = 30$) are plotted in Figures E.2 and E.4. Analogous plots for a medium micropolar gyrobeam, with half sinusoidal axial and trnasverse gyricity distributions, are given in Figures E.5–E.8.

Whereas there are only slight differences between the natural loci plotted in this section and those plotted in Chapters 5 and 6 (compare, for example, Figure E.1 with Figure 5.6), the mode shapes given in this section for the half sinusoidal gyricity distribution differ significantly from those plotted in Chapters 5 and 6 for the uniform gyricity distribution (see, for example, Figure E.2 which can be compared with Figure 5.12).

E.3 Full sinusoidal gyricity distribution

This section will expressly repeat the key results of Chapters 5 and 6 by considering full sinusoidal (instead of uniform) axial and transverse gyricity distributions in which the distribution of gyricity spin rate over the beam length corresponding to a given total gyricity spin rate is:

$$\mathring{\varphi}_3({}^c\hat{x}_1) = \mathring{\varphi}_{3\mathrm{T}} \frac{\pi}{2} \sin(2\,\pi\, {}^c\hat{x}_1) \tag{E.2}$$

The natural frequency loci and the first six gyricity-affected mode shapes of a classical gyrobeam with full sinusoidal axial and transverse gyricity distributions are given in Figures E.9–E.12. Analogous plots for a micropolar gyrobeam are given in Figures E.13–E.16.

For a gyrobeam carrying a full sinusoidal gyricity distribution (in either the axial or the transverse direction) both natural frequency loci and mode shapes are significantly different than those corresponding to a gyrobeam with a uniform gyricity distribution. One may, for example, respectively compare the results shown in Figures E.13 and E.16 with the results given in Figures 6.11 and 6.50.

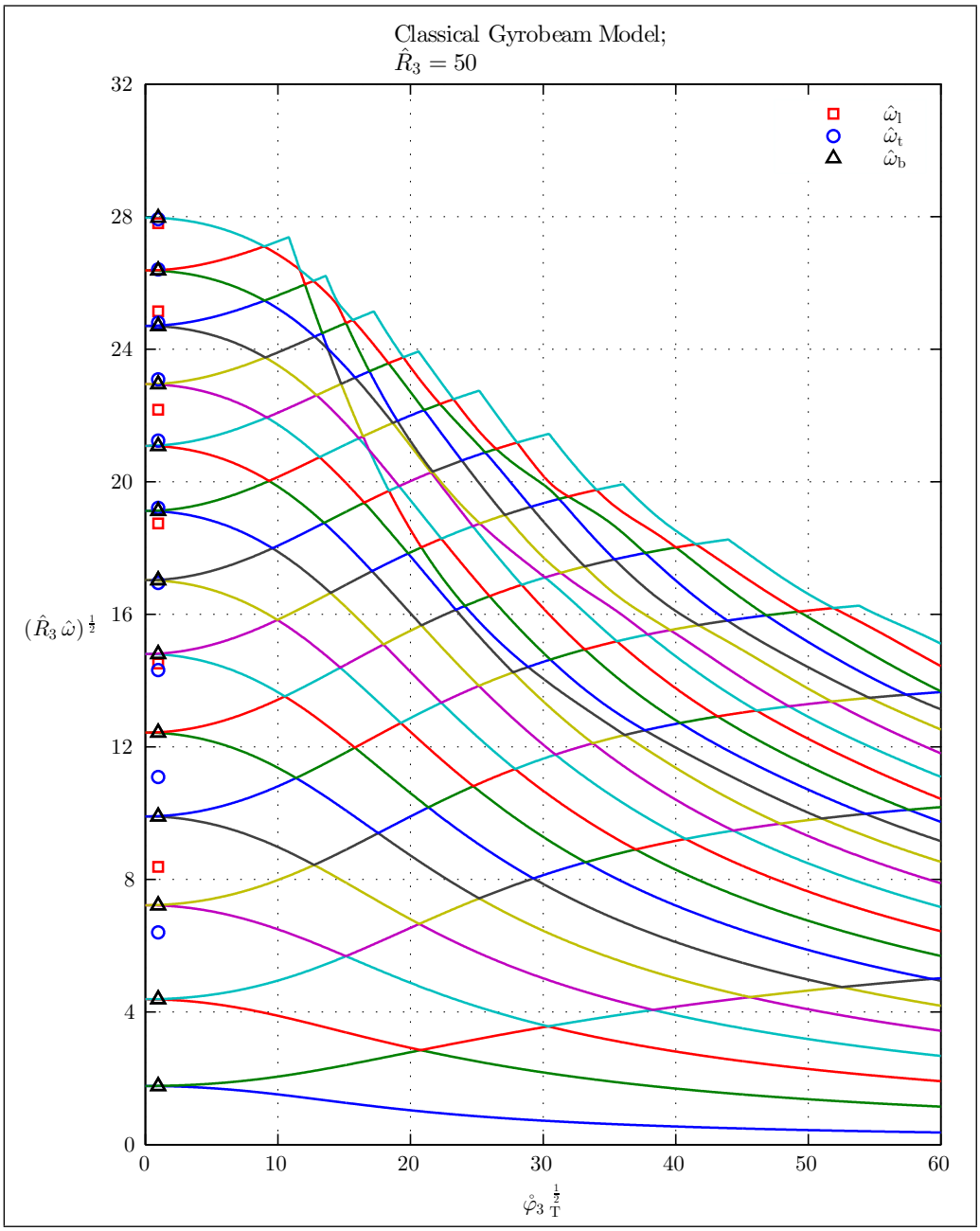

Figure E.1: Natural frequencies of a medium classical gyrobeam with a half sinusoidal axial gyricity.

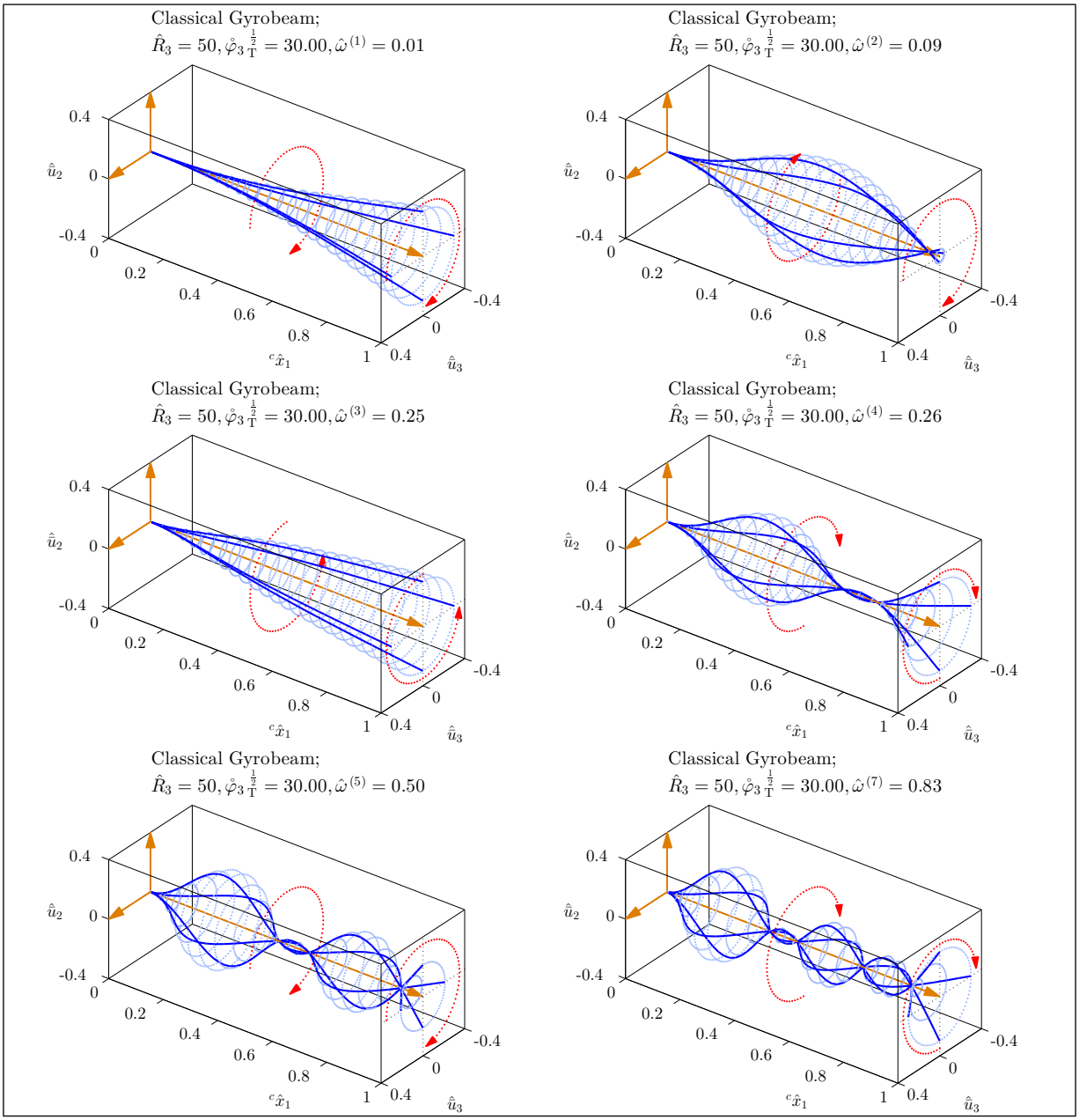

Figure E.2: Mode shapes of a medium classical gyrobeam with a medium half sinusoidal axial gyricity.

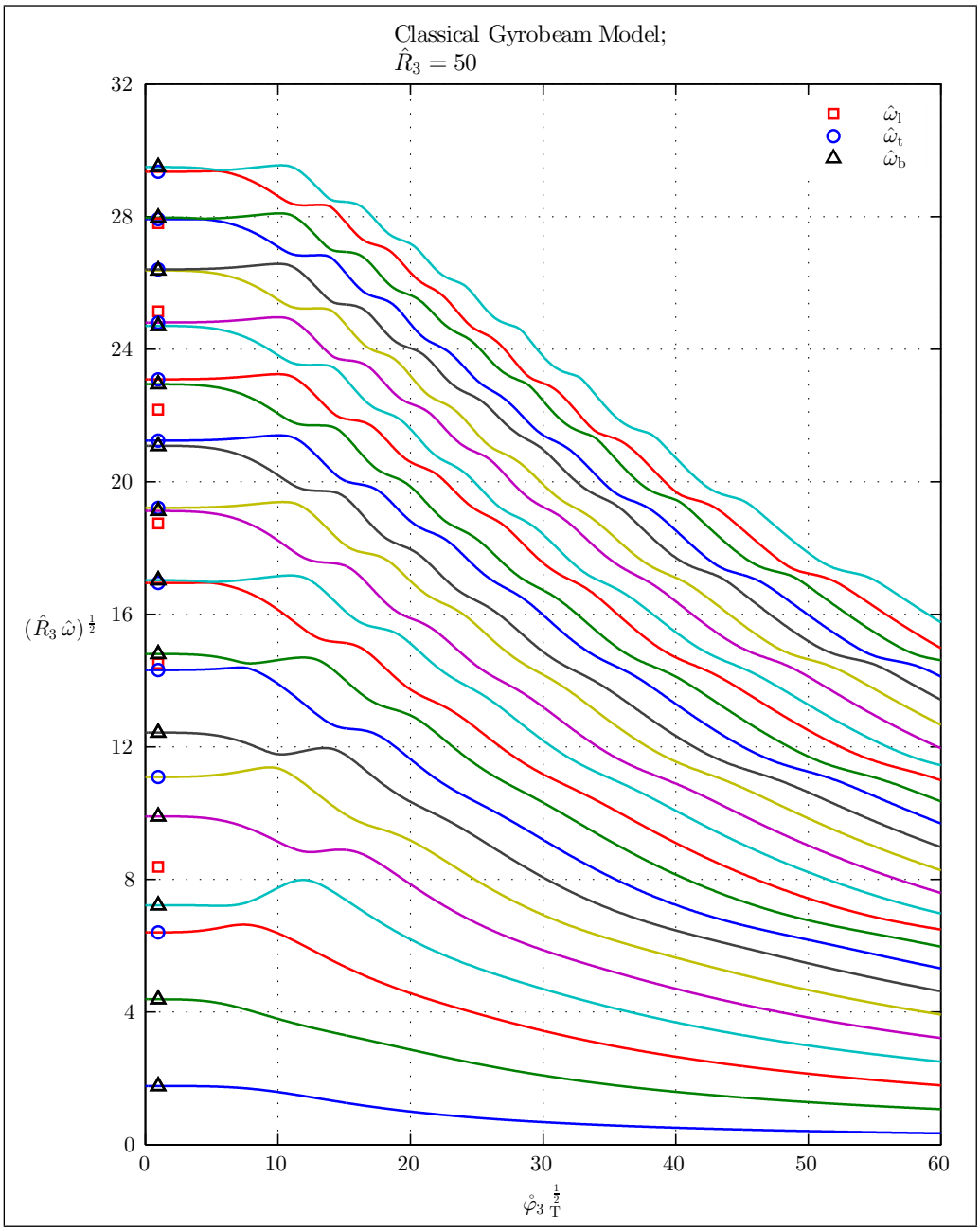

Figure E.3: Natural frequencies of a medium classical gyrobeam with a half sinusoidal transverse gyricity.

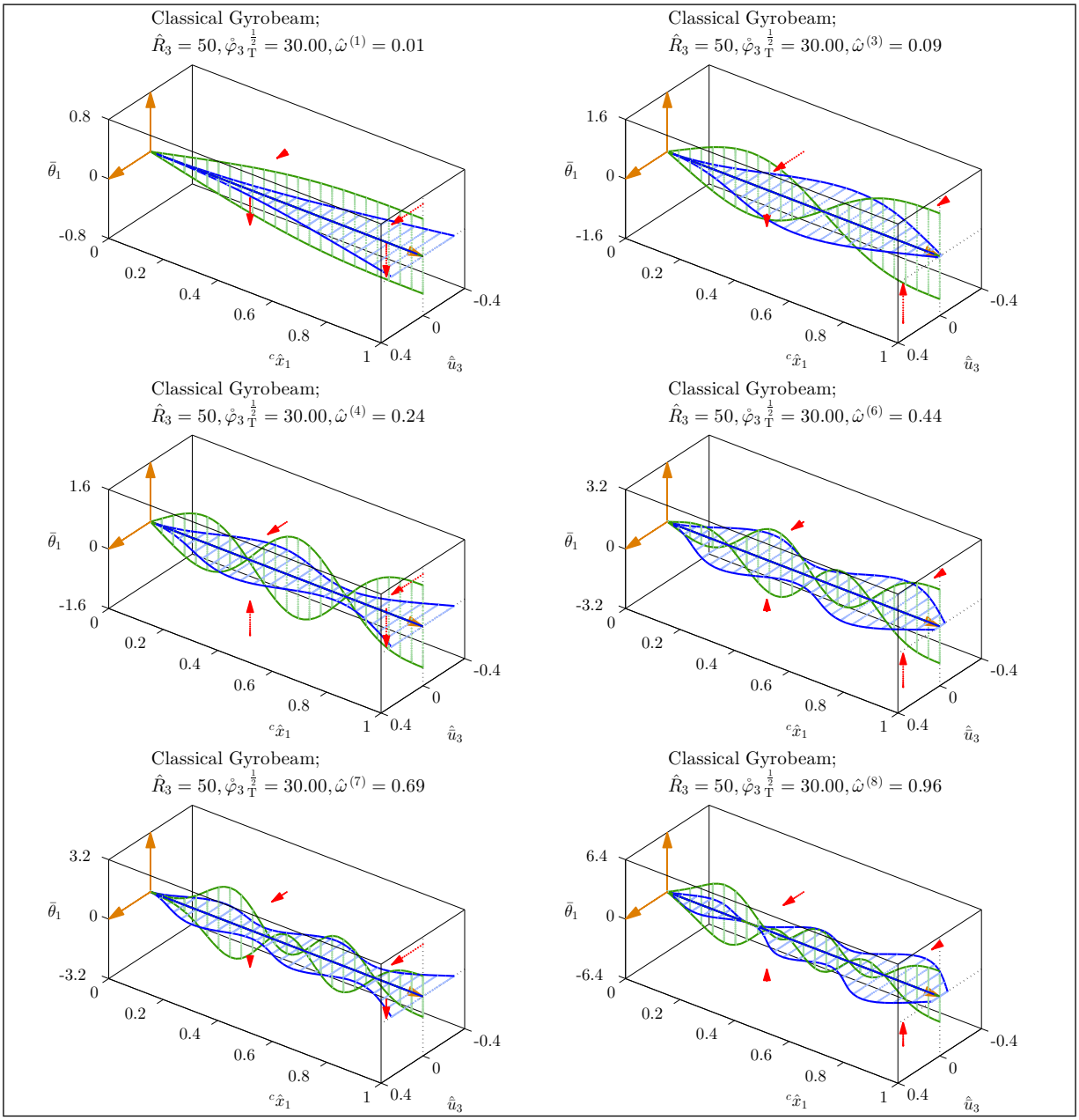

Figure E.4: Mode shapes of a medium classical gyrobeam with a medium half sinusoidal transverse gyricity.

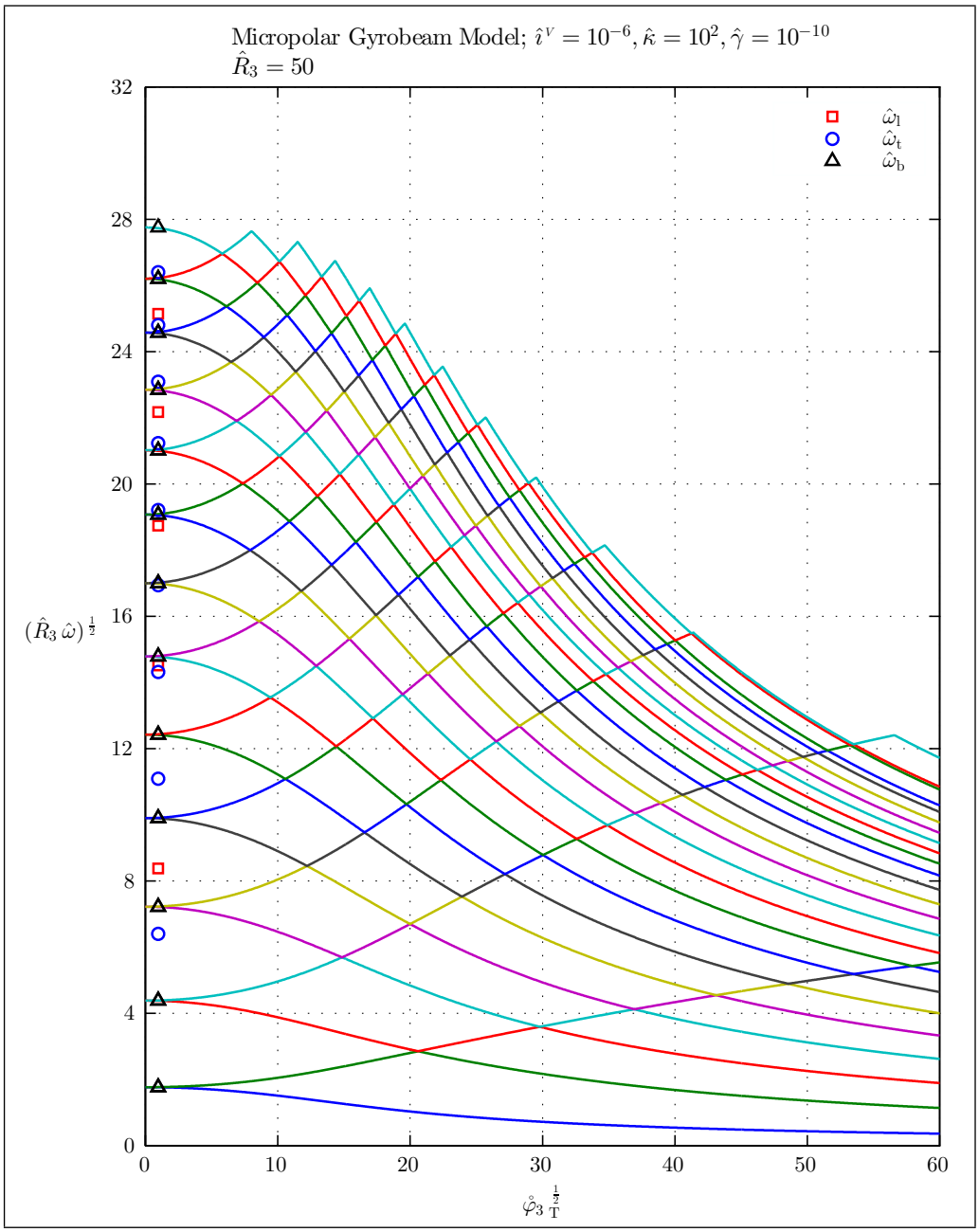

Figure E.5: Natural frequencies of a medium micropolar gyrobeam with a half sinusoidal axial gyricity.

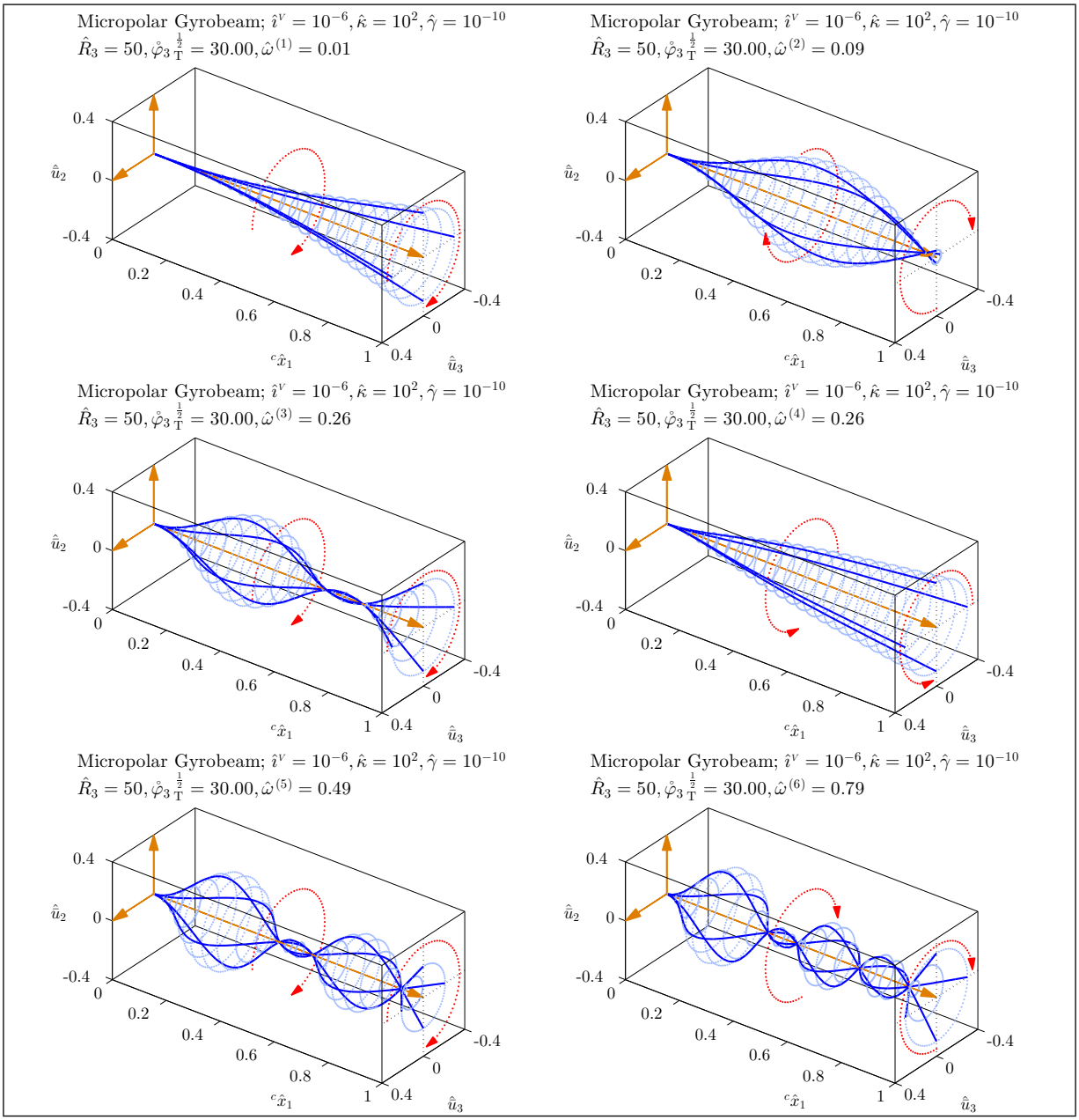

Figure E.6: Mode shapes of a medium micropolar gyrobeam with a medium half sinusoidal axial gyricity.

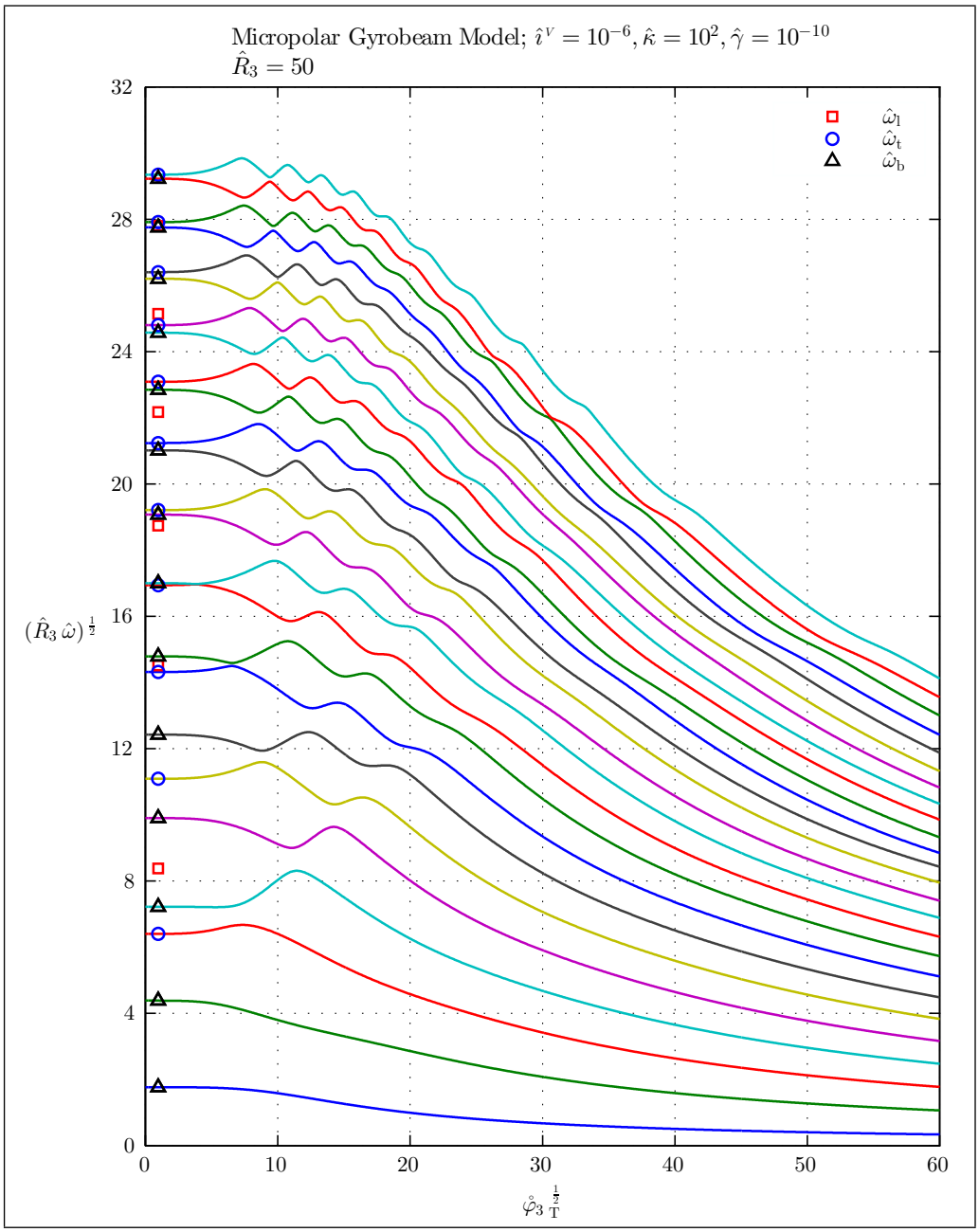

Figure E.7: Natural frequencies of a medium micropolar gyrobeam with a half sinusoidal transverse gyricity.

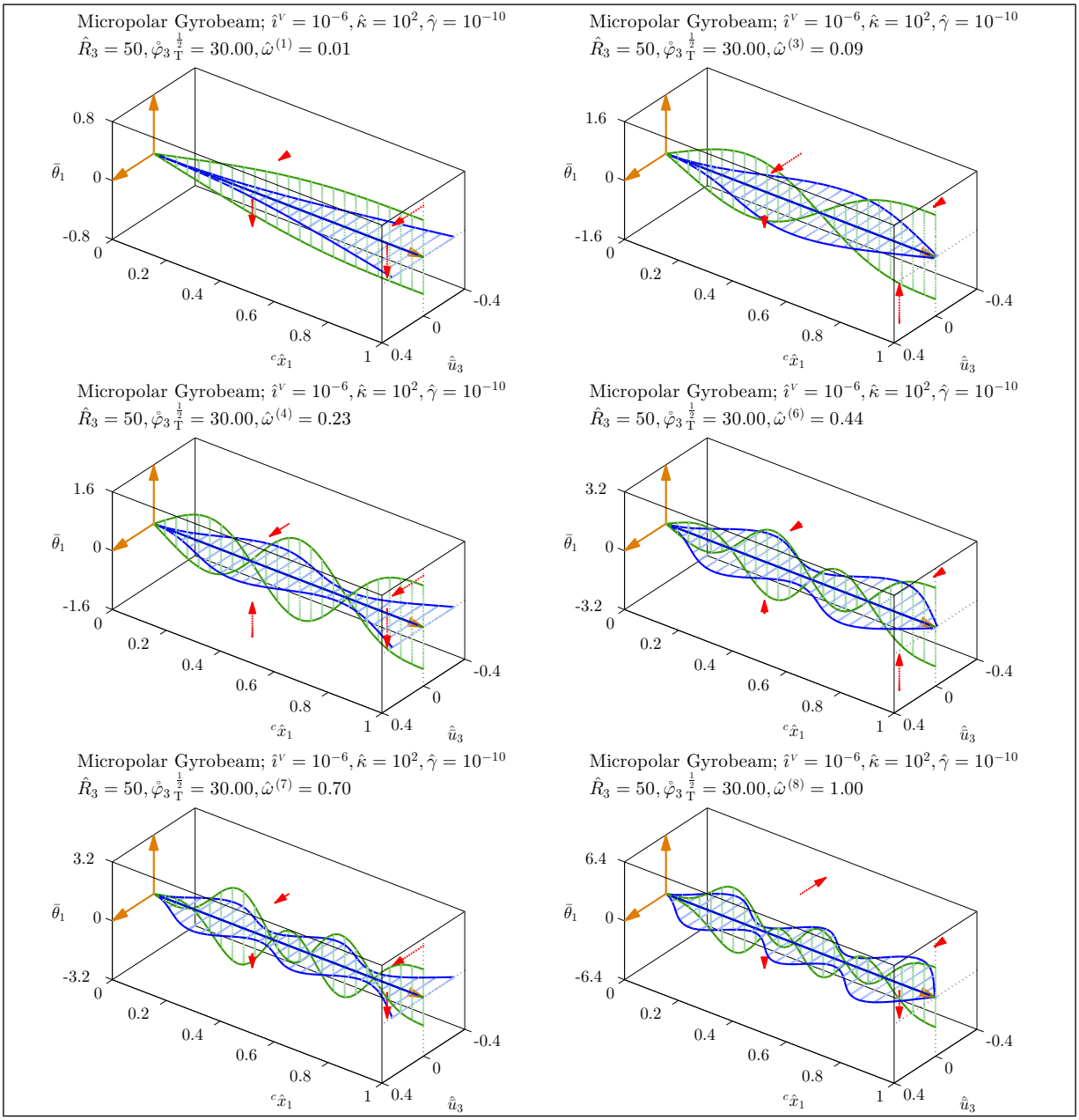

Figure E.8: Mode shapes of a medium micropolar gyrobeam with a medium half sinusoidal transverse gyricity.

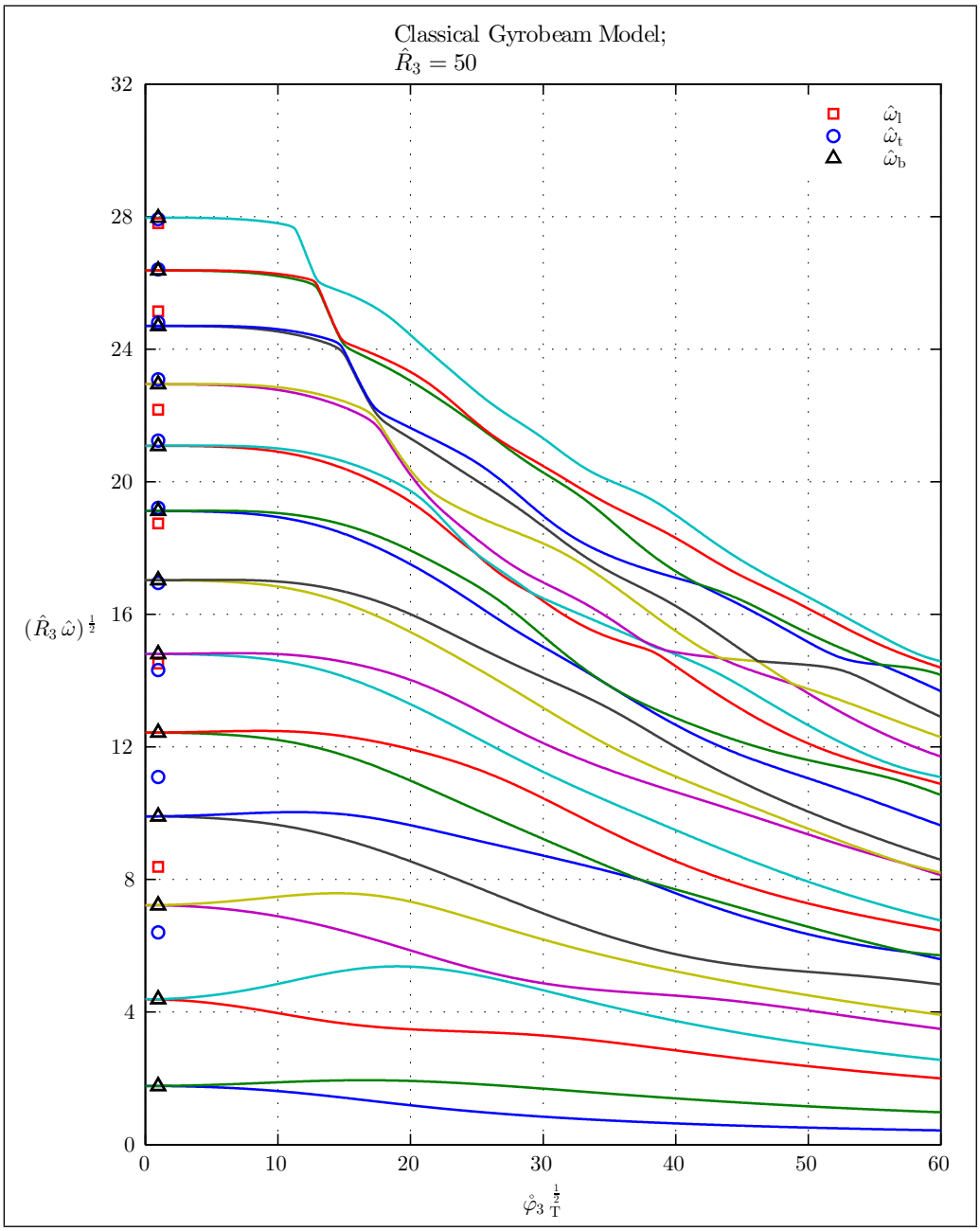

Figure E.9: Natural frequencies of a medium classical gyrobeam with a full sinusoidal axial gyricity.

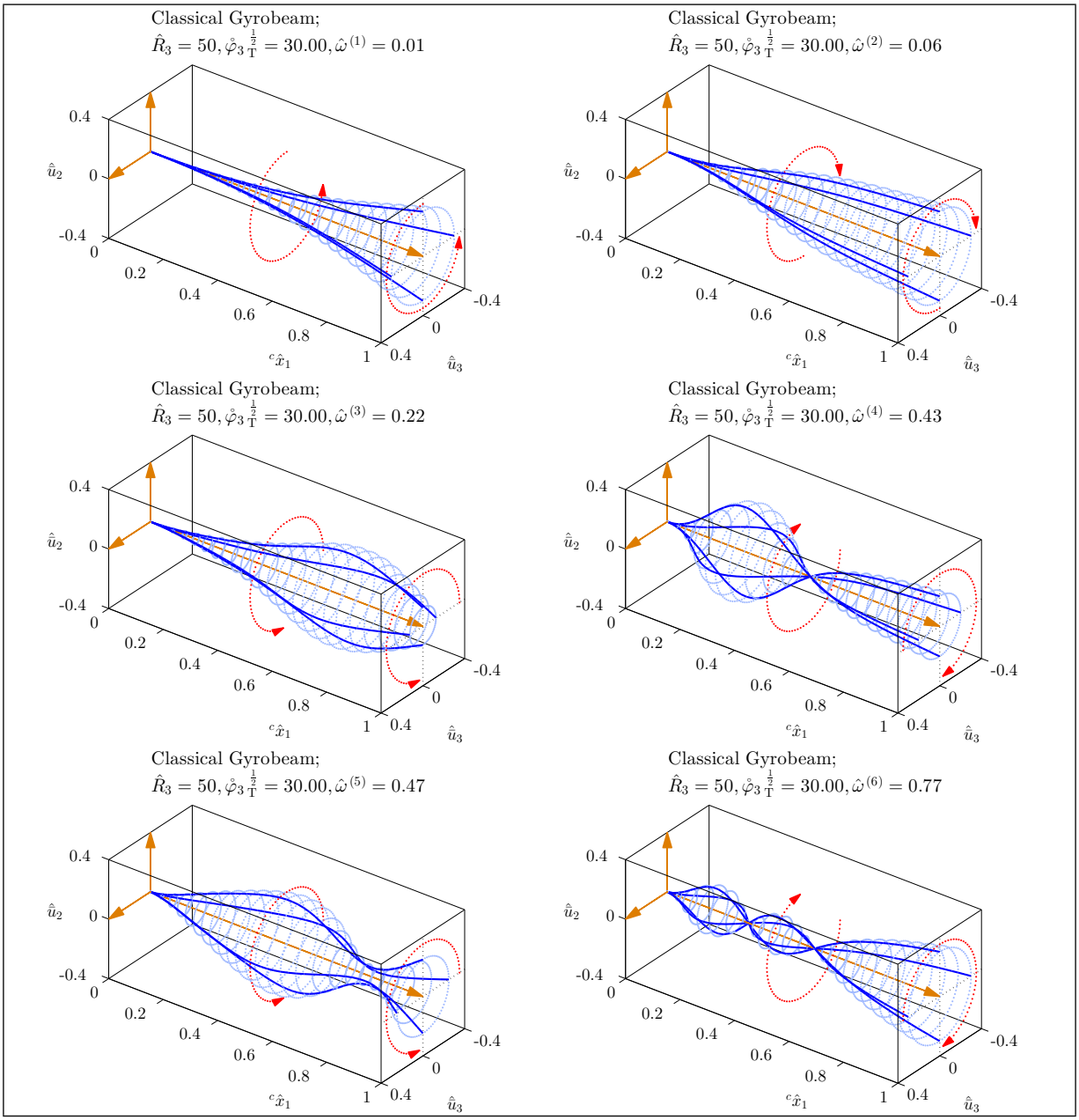

Figure E.10: Mode shapes of a medium classical gyrobeam with a medium full sinusoidal axial gyricity.

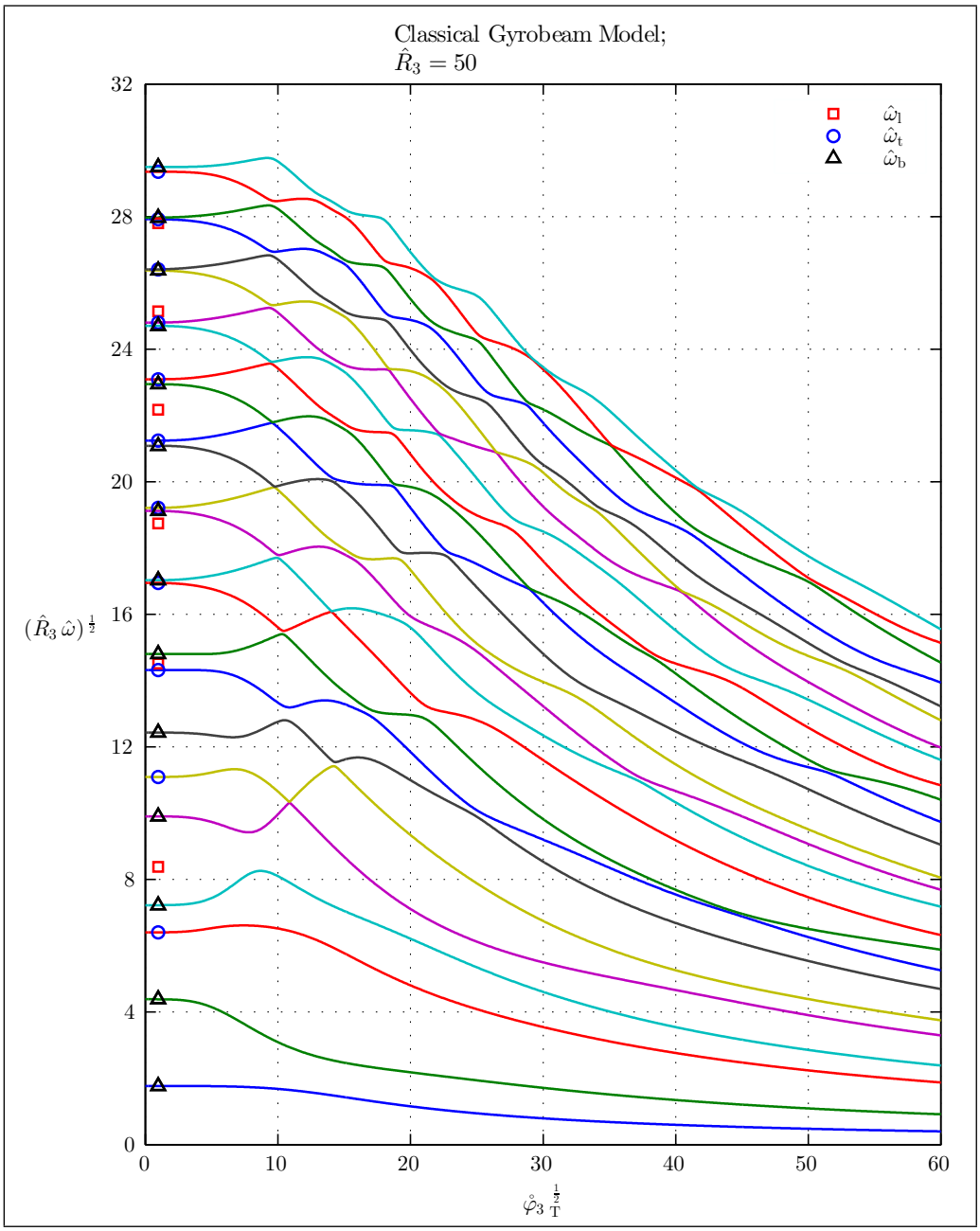

Figure E.11: Natural frequencies of a medium classical gyrobeam with a full sinusoidal transverse gyricity.

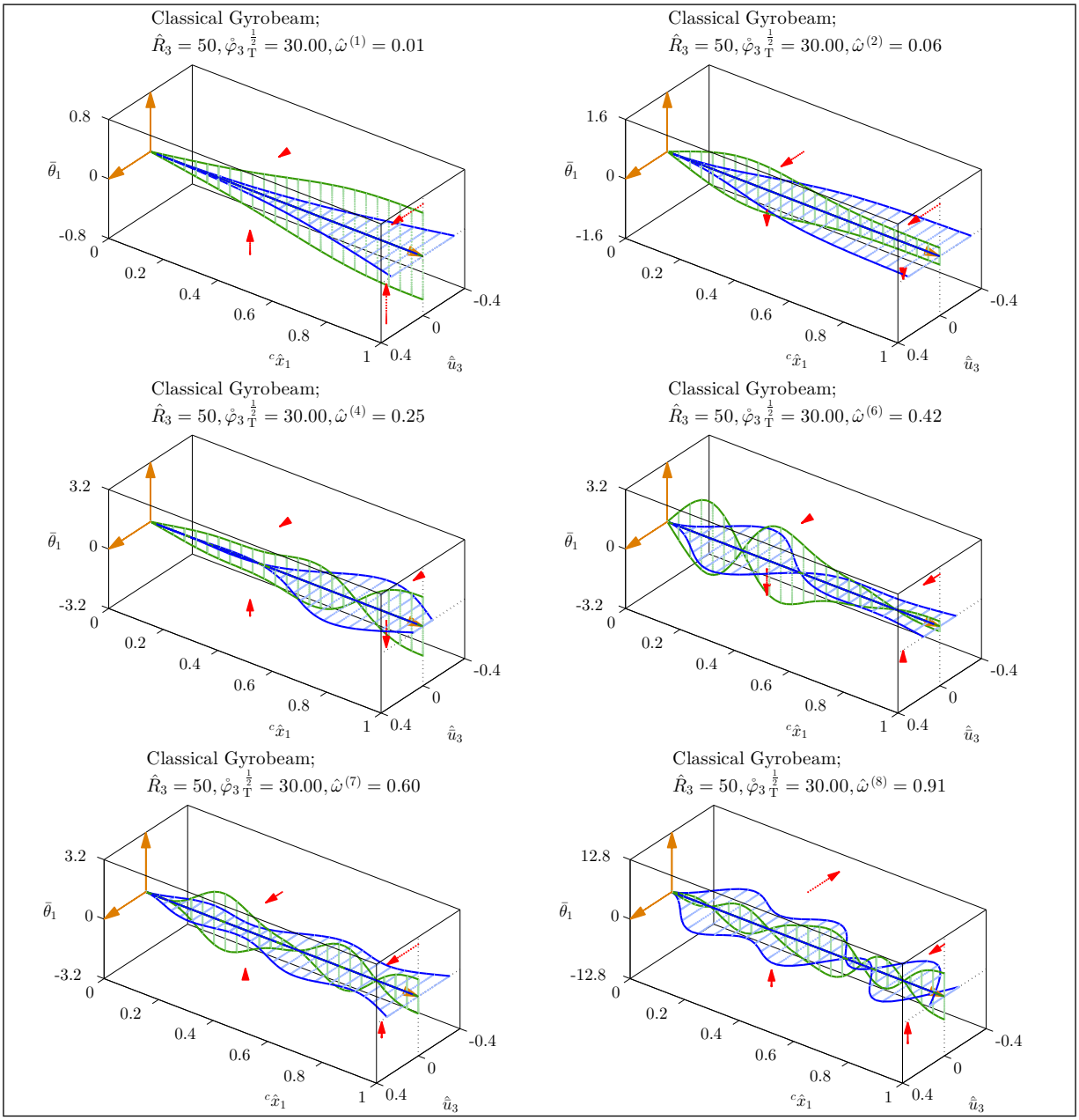

Figure E.12: Mode shapes of a medium classical gyrobeam with a medium full sinusoidal transverse gyricity.

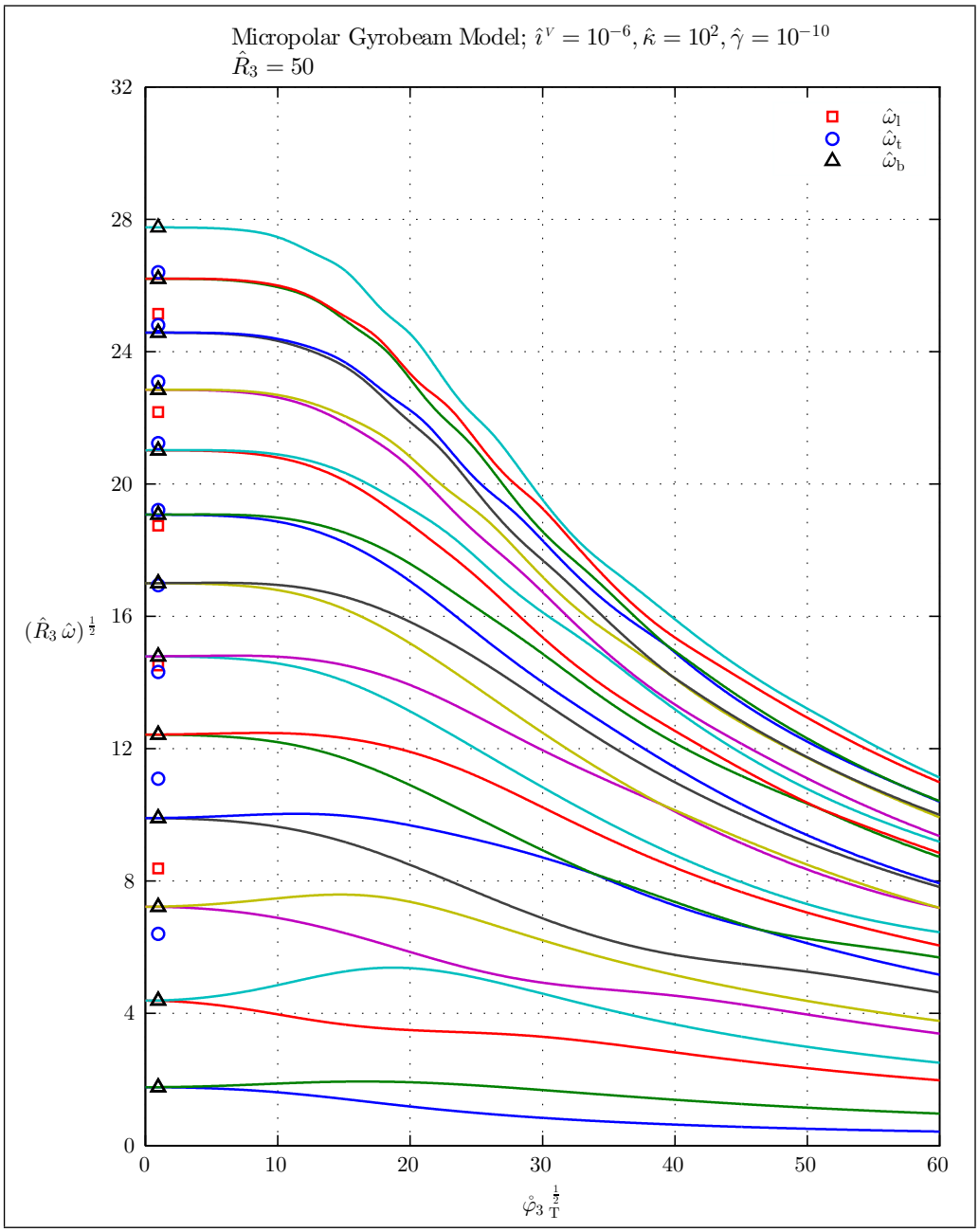

Figure E.13: Natural frequencies of a medium micropolar gyrobeam with a full sinusoidal axial gyricity.

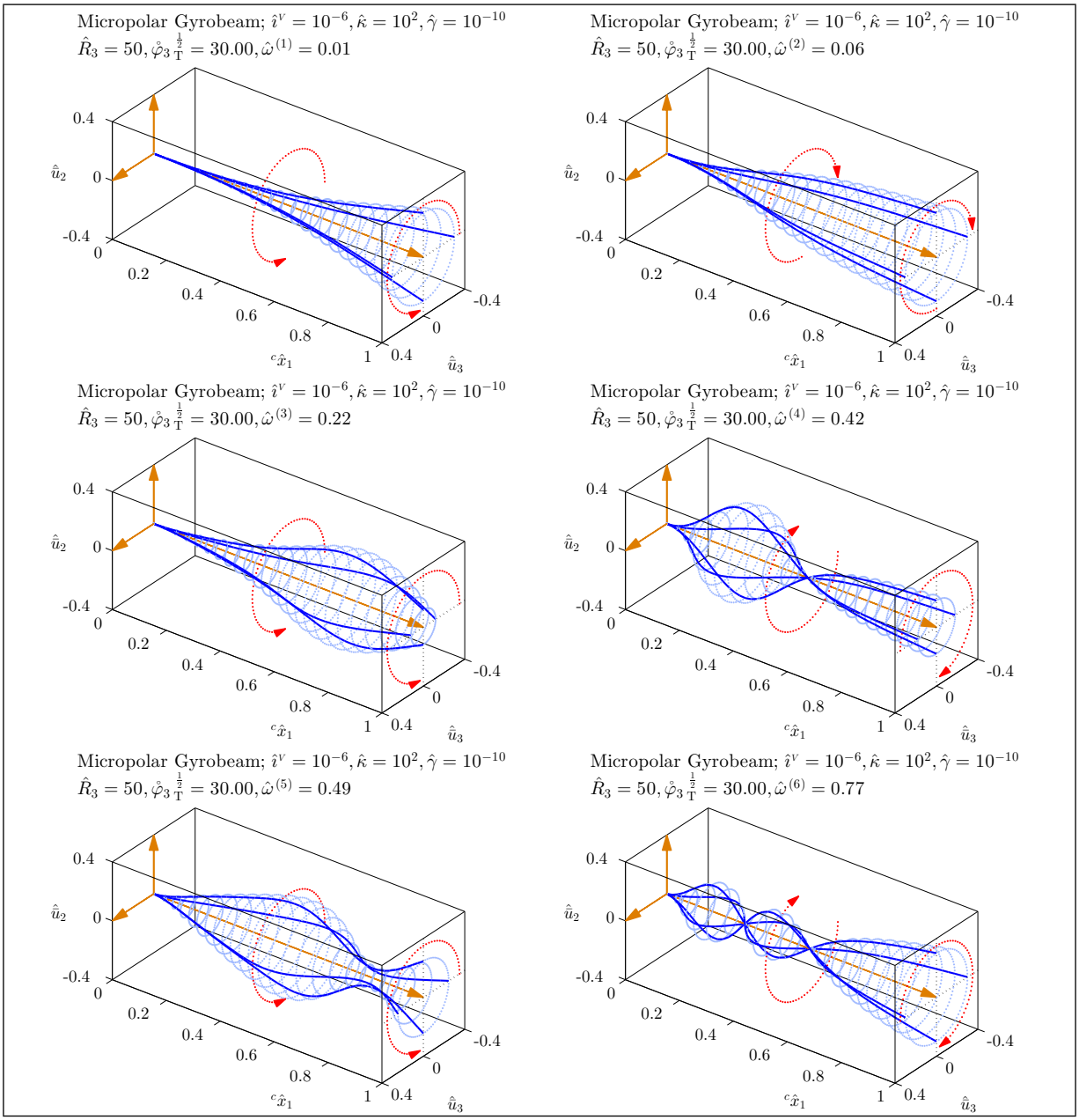

Figure E.14: Mode shapes of a medium micropolar gyrobeam with a medium full sinusoidal axial gyricity.

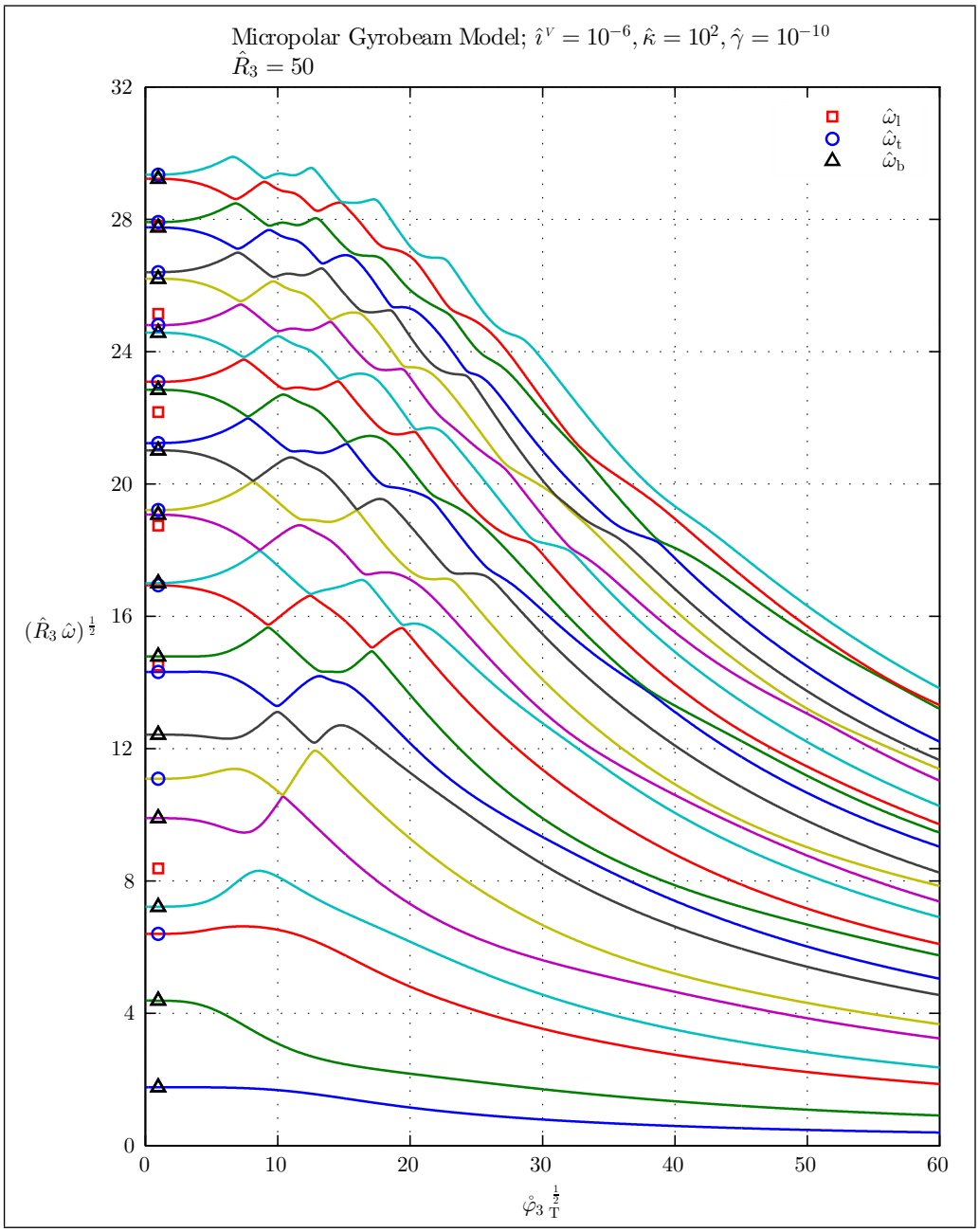

Figure E.15: Natural frequencies of a medium micropolar gyrobeam with a full sinusoidal transverse gyricity.

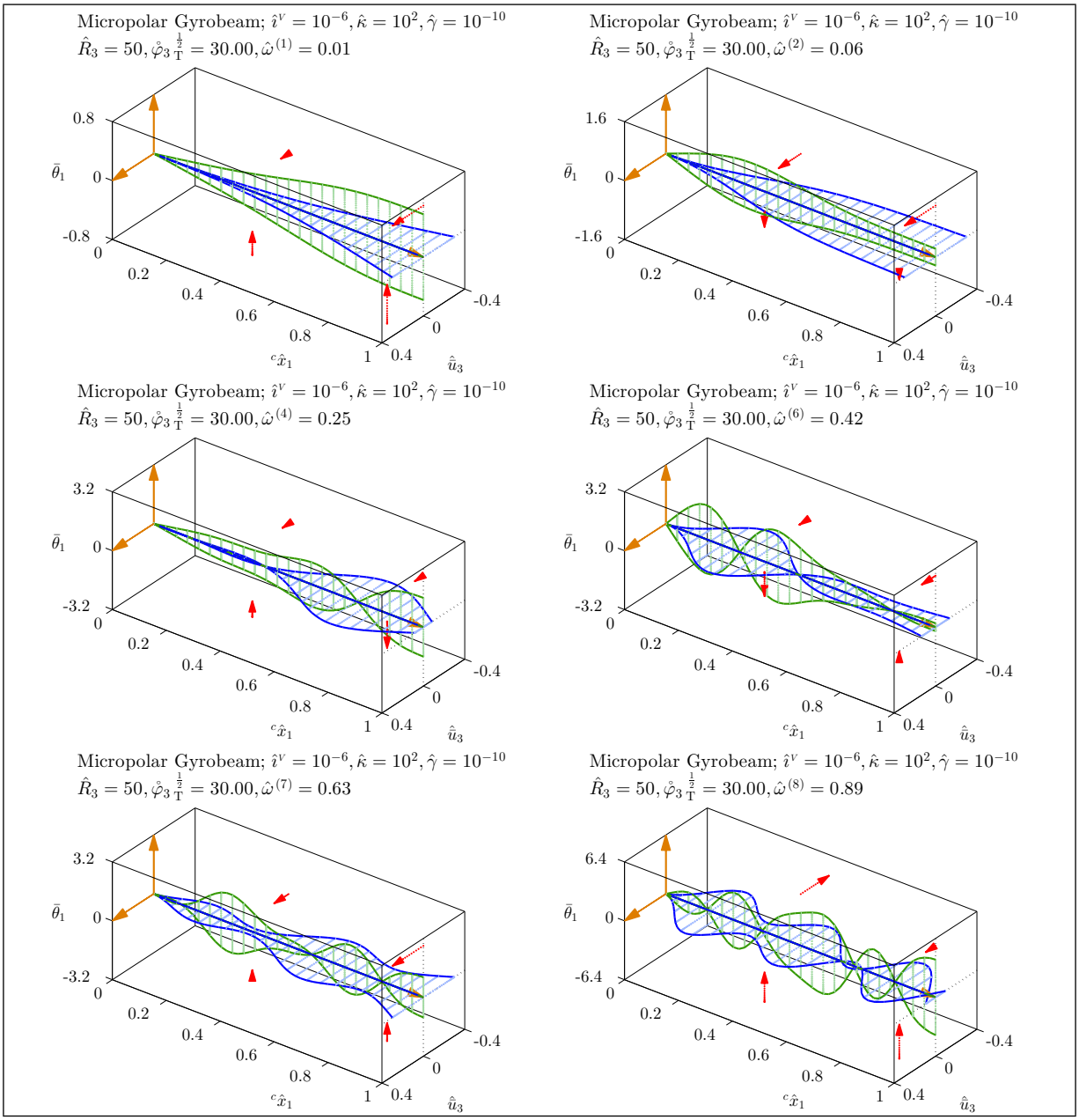

Figure E.16: Mode shapes of a medium micropolar gyrobeam with a medium full sinusoidal transverse gyricity.

Appendix F

Nomenclature

F.1 Notational Conventions

In this text, Cartesian tensor concepts and accompanying index notations are used, where it is meaningful. Generally, small Latin subscripts i, j, k, l, m, and n take the values 1, 2, and 3 (unless mentioned otherwise). For expressions with repeated Latin subscripts, the Einstein summation convention over that subscript, from 1 to 3, is understood. Those readers not familiar with these subjects or those wishing a review are referred to the books on Continuum Mechanics, *e.g.* the book by Hodge [101] or the book by Irgens [41].

A frame, characterized by three orthonormal (*i.e.* mutually perpendicular and of unit length) and dextral (*i.e.* right-handed) vectors and a reference origin, named a is referred to as $\mathcal{F}_a$, and its i^{th} position coordinate (or coordinate axis) and unit basis vector are represented by ${}^{a}x_i$ and $\underset{\rightarrow}{a}_i$, respectively. The inertial reference frame is shown as $\mathcal{F}_o$ and is the default reference frame for all descriptions and operations unless mentioned otherwise. Hence, whenever the reference frame for an operation or a description is not mentioned, that operation or description is done with respect to the inertial reference frame $\mathcal{F}_o$. For two arbitrary frames $\mathcal{F}_a$ and $\mathcal{F}_b$, the transformation or rotation matrix from frame $\mathcal{F}_a$ to frame $\mathcal{F}_b$ is shown as ${}^{ba}\underset{\sim}{\boldsymbol{C}}$.

A vector (first-order tensor) is shown with a right-headed arrow under the name of that

vector, *e.g.* $\underset{\rightarrow}{v}$, and a dyadic (second-order tensor) is denoted by the name of that dyadic with a double-headed arrow underneath, *e.g.* $\underset{\leftrightarrow}{d}$. Consequently, $\underset{\rightarrow}{0}$ and $\underset{\leftrightarrow}{0}$ represent the zero vector and zero dyadic, respectively. The component matrices of vector $\underset{\rightarrow}{v}$ and dyadic $\underset{\leftrightarrow}{d}$, described in frame $\mathcal{F}_a$, are shown as ${}^a\underline{\boldsymbol{v}}$ and ${}^a\underline{\underline{\boldsymbol{d}}}$. The elements of these component matrices are represented by ${}^a v_i$ and ${}^a d_{ij}$, respectively. In general, a leading superscript denotes the name of the frame in which a description or operation is done. This leading superscript is omitted when the inertial frame $\mathcal{F}_o$ serves as the reference frame.

Note that any general (symmetric or asymmetric) dyadic $\underset{\leftrightarrow}{d}$ can be decomposed into its symmetric and antisymmetric (skew-symmetric) parts $\underset{\leftrightarrow}{d}^{\mathrm{s}}$ and $\underset{\leftrightarrow}{d}^{\mathrm{a}}$ where:

$$\begin{aligned} {}^a d_{ij}^{\mathrm{s}} &= \frac{1}{2}\Big({}^a d_{ij} + {}^a d_{ji}\Big) \\ {}^a d_{ij}^{\mathrm{a}} &= \frac{1}{2}\Big({}^a d_{ij} - {}^a d_{ji}\Big) \end{aligned} \tag{F.1}$$

The sine and cosine functions will often be shortened to s and c, respectively, *i.e.* $\mathrm{s}_z = \sin z$ and $\mathrm{c}_z = \cos z$.

Symbols $\mathbb{1}_{ij}$ and ϵ_{ijk} denote the elements of the Kronecker dyadic (second-order Kronecker tensor or Kronecker delta) and the third-order Levi-Civita (permutation or alternating) tensor, both being frame-independent. They are defined as:

$$\mathbb{1}_{ij} = \begin{cases} 1 & i = j \\ 0 & i \neq j \end{cases} \tag{F.2}$$

$$\epsilon_{ijk} = \begin{cases} +1 & (i,j,k) = (1,2,3) \text{ or } (2,3,1) \text{ or } (3,1,2) \\ -1 & (i,j,k) = (3,2,1) \text{ or } (2,1,3) \text{ or } (1,3,2) \\ 0 & \text{otherwise: } i = j \text{ or } j = k \text{ or } k = i \end{cases} \tag{F.3}$$

Note that the identity matrix of size 3 (the 3×3 identity matrix) and the component matrix of the second-order Kronecker delta, *i.e.* $\underline{\underline{\mathbb{1}}}$, are the same. In addition, keep in mind the difference between ϵ_{ijk} which refers to the elements of third-order Levi-Civita tensor, and ε_{ij} which denotes the elements of the second-order strain tensor $\underset{\leftrightarrow}{\varepsilon}$.

For a vector $\underset{\rightarrow}{v}$, symbol $\underset{\leftrightarrow}{v}^{\times}$ denotes the antisymmetric dyadic, associated with the vector

cross product, whose component matrix is defined as:

$$ {}^{a}\underline{\underline{\boldsymbol{v}}}^{\times} = \begin{bmatrix} 0 & -{}^{a}v_3 & {}^{a}v_2 \\ {}^{a}v_3 & 0 & -{}^{a}v_1 \\ -{}^{a}v_2 & {}^{a}v_1 & 0 \end{bmatrix} = \left[{}^{a}v_{ij}^{\times} \right], \qquad {}^{a}v_{ij}^{\times} = -\epsilon_{ijk}\, {}^{a}v_k \tag{F.4} $$

Considering this definition, for arbitrary vectors $\underset{\rightarrow}{v_1}$ and $\underset{\rightarrow}{v_2}$ the following useful identities can be proved:

$$ \begin{aligned} \underline{\underline{\boldsymbol{v_1}}}^{\times}\, \underline{\underline{\boldsymbol{v_2}}}^{\times} &= \underline{\boldsymbol{v_2}}\, \underline{\boldsymbol{v_1}}^{\mathrm{T}} - \left(\underline{\boldsymbol{v_1}}^{\mathrm{T}}\, \underline{\boldsymbol{v_2}} \right) \underline{\underline{\mathbb{1}}} \\ \left(\underline{\underline{\boldsymbol{v_1}}}^{\times}\, \underline{\boldsymbol{v_2}} \right)^{\times} &= \underline{\boldsymbol{v_2}}\, \underline{\boldsymbol{v_1}}^{\mathrm{T}} - \underline{\boldsymbol{v_1}}\, \underline{\boldsymbol{v_2}}^{\mathrm{T}} \\ \left(\underline{\underline{\boldsymbol{v_1}}}^{\times}\, \underline{\boldsymbol{v_2}} \right)^{\times} &= \underline{\underline{\boldsymbol{v_1}}}^{\times}\, \underline{\underline{\boldsymbol{v_2}}}^{\times} - \underline{\underline{\boldsymbol{v_2}}}^{\times}\, \underline{\underline{\boldsymbol{v_1}}}^{\times} \end{aligned} \tag{F.5} $$

which hold true in any reference frame.

Time is denoted by t and the time derivative of a variable z (which can be a scalar, vector, tensor, or any matrix function) with respect to frame $\mathcal{F}_a$ is represented by ${}^{a}\frac{dz}{dt}$, ${}^{a}z_{,t}$, or ${}^{a}\dot{z}$. Analogously, ${}^{a}\frac{d^2z}{dt^2}$, ${}^{a}z_{,tt}$, or ${}^{a}\ddot{z}$ will represent the second time derivative. It is noteworthy that the time derivative of z with respect to $\mathcal{F}_a$ is defined as the time derivative of its description in $\mathcal{F}_a$, denoted by ${}^{a}z$:

$$ {}^{a}\frac{dz}{dt} = \frac{d^a z}{dt} \tag{F.6} $$

Besides, the spatial derivative of variable z with respect to the i$^{\text{th}}$ coordinate of frame $\mathcal{F}_a$ is denoted by $\frac{dz}{d^a x_i}$, ${}^{a}\frac{dz}{dx_i}$, or ${}^{a}z_{,i}$. Consequently, the following relations will be concluded:

$$ {}^{a}\dot{z}_{,i} = {}^{a}z_{,ti} = {}^{a}\frac{d}{dt}\Big({}^{a}\frac{dz}{dx_i} \Big) \tag{F.7} $$

$$ {}^{a}z_{,ij\ldots k} = {}^{a}\frac{d}{dx_k}\Big(\cdots \Big({}^{a}\frac{d}{dx_j}\Big({}^{a}\frac{dz}{dx_i} \Big) \Big) \Big) \tag{F.8} $$

Also, symbol $\underset{\rightarrow}{\nabla}$ will stand for the gradient (del) vector operator whose component matrix in frame $\mathcal{F}_a$ is defined as:

$$ {}^{a}\underline{\boldsymbol{\nabla}} = \begin{bmatrix} {}^{a}\frac{d}{dx_1} & {}^{a}\frac{d}{dx_2} & {}^{a}\frac{d}{dx_3} \end{bmatrix}^{\mathrm{T}}, \qquad {}^{a}\nabla_i = {}^{a}\frac{d}{dx_i} \tag{F.9} $$

The small and capital form of the Greek letter delta are reserved for the calculus of variations where the existence of a capital delta, *i.e.* Δ, before a function or variable means the variation of that function or variable, and the existence of a small delta, *i.e.* δ, before a variable of type displacement or work means a virtual displacement or a virtual work. Analogous to the definition of the frame dependent time derivative, the variation of a variable with respect to a frame is defined as the variation of the variable description in that frame, that is:

$$ {}^a\Delta z = {}^a\Delta\Big(z\Big) = \Delta\Big({}^a z\Big) = \Delta {}^a z \tag{F.10} $$

This is explained in more detail in Appendix B.

For an arbitrary matrix $\underset{\sim}{\boldsymbol{m}}$, its transpose and inverse (if it is square) are shown as $\underset{\sim}{\boldsymbol{m}}^{\mathrm{T}}$ and $\underset{\sim}{\boldsymbol{m}}^{-1}$, respectively, and its elements are represented by m_{ij}. The 1-norm condition number of a matrix $\underset{\sim}{\boldsymbol{m}}$, illustrating how well-conditioned or ill-conditioned the matrix is, is denoted as $K_{\underset{\sim}{\boldsymbol{m}}}$. The partial derivative of a scaler z with respect to a matrix $\underset{\sim}{\boldsymbol{m}}$ is a matrix of the same dimensions as $\underset{\sim}{\boldsymbol{m}}$ defined by:

$$ \frac{\partial z}{\partial \underset{\sim}{\boldsymbol{m}}} = \left[\frac{\partial z}{\partial m_{ij}}\right] \tag{F.11} $$

More generally, the division of a scalar z by a matrix $\underset{\sim}{\boldsymbol{m}}$ is equivalent to the division of the scalar by each element of the matrix, that is:

$$ \frac{z}{\underset{\sim}{\boldsymbol{m}}} = \left[\frac{z}{m_{ij}}\right] \tag{F.12} $$

which is a matrix of the same dimensions as $\underset{\sim}{\boldsymbol{m}}$.

Symbols $\int_t z\, dt$, $\int_L z\, dL$, $\int_S z\, dS$, and $\int_V z\, dV$ represent time, line (or path or curve), surface, and volume integrals of z, respectively, and $\Big[z\Big]_{P_1}^{P_2}$ stands for the point integral of z *i.e.* the value of z at P_2 minus the value of z at P_1. The summation of an arbitrary sequence, *e.g.* $z(i)$, from $i = 1$ to $i = N$ is represented by $\sum_{i=1}^{N} z(i)$. Note that closed line (or path or curve) and closed surface integrals are illustrated as $\oint_L z\, dL$ and $\oint_S z\, dS$.

Assuming z to be an arbitrary field variable, *i.e.* a scalar, vector, tensor, or matrix field defined inside a volume domain V in 3D space $\mathbb{R}^3$ and on its boundary surface S, Gauss' theorem in tensor notation can be written as:

$$\int_V z_{,i}\, dV = \oint_S z\, n_i\, dS \tag{F.13}$$

where n_i is the i$^{\text{th}}$ element of $\underset{\rightarrow}{n}$, the unit vector (outward) normal to the boundary surface S. Now, considering z to be the product of two other field variables z_1 and z_2, *i.e.* $z = z_1\, z_2$, one will get on substitution:

$$\int_V \Big(z_1\, z_2\Big)_{,i}\, dV = \int_V z_{1,i}\, z_2\, dV + \int_V z_1\, z_{2,i}\, dV = \oint_S \Big(z_1\, z_2\Big)\, n_i\, dS \tag{F.14}$$

and hence:

$$\int_V z_1\, z_{2,i}\, dV = \oint_S z_1\, z_2\, n_i\, dS - \int_V z_{1,i}\, z_2\, dV \tag{F.15}$$

The corresponding formula for a surface domain S, in 2D space $\mathbb{R}^2$ and bounded by a boundary line (or path or curve) L, will be:

$$\int_S z_1\, z_{2,i}\, dS = \oint_L z_1\, z_2\, n_i\, dL - \int_S z_{1,i}\, z_2\, dS, \qquad i = 1, 2 \tag{F.16}$$

In 1D space $\mathbb{R}$, Gauss' theorem will reduce to the integration by parts formula, that is:

$$\int_L z_1\, z_{2,i}\, dL = \Big[z_1\, z_2\Big]_{P_1}^{P_2} - \int_L z_{1,i}\, z_2\, dL, \qquad i = 1 \tag{F.17}$$

where P_1 and P_2 are the boundary points of the line domain L. The corresponding formula in a time domain is:

$$\int_t z_1\, \dot{z}_2\, dt = \Big[z_1\, z_2\Big]_{t_1}^{t_2} - \int_t \dot{z}_1\, z_2\, dt \tag{F.18}$$

Symbols ∞ and ¿ represent an infinite and an indeterminate numerical quantity respectively (or infinity and indeterminacy). Following are some indeterminate forms:

$$0 \times \infty, \qquad \infty - \infty, \qquad \frac{0}{0}, \qquad \frac{\infty}{\infty}, \qquad 0^0, \qquad \infty^0, \qquad 1^\infty \tag{F.19}$$

The absolute value and 2-norm of a parameter z are shown as $|z|$ and $\| z \|$, respectively. In dimensional analysis, the dimension of a parameter z is represented by $[z]$ and the symbols M, L, and T denote the mass, length, and time dimensions. A dimensionless or dimension-reduced (group) parameter corresponding (and directly proportional) to dimensional parameter z is referred to as $\hat{z}$.

F.2 Alphabetical list of abbreviations

The following list summarizes the abbreviations used in this text.

1D	**1**-**d**imensional
2D	**2**-**d**imensional
3D	**3**-**d**imensional
BC	**B**oundary **c**ondition
CL	**Cl**assical
DOF	**D**egree **o**f **f**reedom
EB	**E**uler-**B**ernoulli
EBC	**E**ssential **b**oundary **c**ondition
FEM	**F**inite **e**lement **m**ethod
IC	**I**nitial **c**ondition
I/BCs	**I**nitial and **b**oundary **c**onditions
MGM1	**M**icropolar **g**yrobeam **m**odel **1**
MGM2	**M**icropolar **g**yrobeam **m**odel **2**
MGM3	**M**icropolar **g**yrobeam **m**odel **3**
MGM4	**M**icropolar **g**yrobeam **m**odel **4**
MP	**M**icro**p**olar
NBC	**N**atural **b**oundary **c**ondition

ODE **O**rdinary **d**ifferential **e**quation

PDE **P**artial **d**ifferential **e**quation

TM **T**i**m**oshenko

F.3 Alphabetical list of symbols

The following list summarizes the denotations of principal symbols used in this text. Every attempt is made to use the standard symbols for a particular discipline and simultaneously not to use the same symbol to denote more than one thing. Note that the symbols, z as a general variable (can be a scalar, vector, tensor, or matrix), a and b as general frames, and i and j as general sub/super scripts are used to define some other symbols and operations. There are other (non-principal) symbols in the text which are defined in local context as they occur.

F.3.1 Underneath/overhead symbols

$\underset{\rightarrow}{\square}$ Vector

$\underset{\leftrightarrow}{\square}$ Dyadic

$\underset{\_}{\square}$ Vector component matrix

$\underset{=}{\square}$ Dyadic component matrix

$\underset{\sim}{\square}$ Matrix

$\bar{\square}$ Beam-related (neutral-axis-related)

$\hat{\square}$ Dimensionless or dimension-reduced

$\dot{\square}$ First time derivative

$\ddot{\square}$ Second time derivative

$\mathring{\square}$ Nondimensional first time derivative

$\mathring{\mathring{\square}}$ Nondimensional second time derivative

F.3.2 Leading sub/super scripts

${}^{a}\square$ With respect to (in) or belong to frame a

$\square$ With respect to (in) or belong to inertial frame
(leading superscript is omitted)

F.3.3 Post sub/super scripts

$\square_{\mathrm{b}}$ Corresponding to bending deformation mode

$\square_{\mathrm{cn}}$ Conservative

$\square_{i}$ i^{th}

$\square_{i}$ Vector element

$\square_{ij}$ Dyadic element

$\square_{ij}$ Matrix element

$\square_{,i}$ Spatial derivative

$\square_{,\hat{i}}$ Nondimensional spatial derivative

$\square_{\mathrm{l}}$ Corresponding to longitudinal deformation mode

$\square_{\mathrm{nc}}$ Non-conservative

$\square_{\mathrm{t}}$ Corresponding to torsional deformation mode

$\square_{\mathrm{T}}$ Total (obtained by integration or summation)

$\square^{-1}$ Inverse

$\square'$ Spatial derivative with respect to first coordinate of element frame

$\square^{\times}$ Cross product dyadic

$\square^{\mathrm{a}}$ Antisymmetric or skew-symmetric

$\square^{\mathrm{ang}}$ Angular or rotational

$\square^{\langle \mathrm{e} \rangle}$ Corresponding to element

$\square^{\langle \mathrm{g} \rangle}$ Corresponding to global assemblage

$\square^{\langle \mathrm{i} \rangle}$ Corresponding to i^{th} node

$\square^{(i)}$ Corresponding to i^{th} vibration mode

$\square^{\mathrm{lin}}$ Linear or translational

$\square^{\mathrm{s}}$ Symmetric

$\square^{L}$ Linear density (per unit length of elastic body)

$\square^{P}$ Point density (at point of elastic body)

$\square^{S}$ Surface density (per unit surface of elastic body)

$\square^{\mathrm{T}}$ Transpose

$\square^{V}$ Volume density (per unit volume of elastic body)

F.3.4 Bracket delimiters

$\left(\square\right)$ Multiplication parentheses

$(\square)$ Function parentheses

$(\square)$ Pair parentheses

$[\square]$ Range parentheses (square brackets)

$[\square]$ Dimension

$\left[\square\right]$ Point integral

$|\square|$ Absolute value

$\|\square\|$ 2-norm

$(\square)_{\mathrm{cl}}$ Corresponding to classical elastic continuum

$(\square)_{\mathrm{mp}}$ Corresponding to micropolar elastic continuum

F.3.5 Non-letter characters

$\mathbb{1}$ Kronecker delta

∂ Partial derivative

∇ Gradient (del)

$\sum$ Summation

$\int$ Integral

$\oint$ Closed integral

∞ Infinity

¿ Indeterminate

F.3.6 Uppercase English letters

A Beam cross sectional area

B Tensile bulk modulus

C Transformation (rotation) matrix

${}^{ba}\underset{\sim}{\boldsymbol{C}}$	Transformation matrix from frame a to frame b
E	Tensile (Young's) modulus
H	Finite element shape function
$\underset{\sim}{\boldsymbol{H}}_z$	Shape function matrix corresponding to z
I	Beam cross sectional second/polar moment of area
K	1-norm condition number
K_z	1-norm condition number of z
L	General (boundary) line (path or curve)
L	Length of beam
L	Fundamental length dimension
M	Fundamental mass dimension
N	General number
N	Number of generalized coordinates
P	General (boundary) point
P_1	Beam left boundary point
P_2	Beam right boundary point
R	Beam slenderness ratio
$\mathbb{R}$	General space
S	General (boundary) surface
S	Boundary surface of elastic body
T	Fundamental time dimension
V	General volume
V	Volume of elastic body

F.3.7 Lowercase English letters

a	General frame and frame a basis vector
a	Axis frame and axis frame basis vector
b	General frame and frame b basis vector
b	Body frame and body frame basis vector
c	General frame and frame c basis vector
c	Beam frame attached to left end of beam and beam frame basis vector
c	Shortened cosine
c_z	Cosine of z
d	General dyadic
d	Differential and total derivative
d	Damping coefficient
$d_{\mathcal{M}}$	Coefficient of mass matrix (operator) in Rayleigh damping definition
$d_{\mathcal{K}}$	Coefficient of stiffness matrix (operator) in Rayleigh damping definition
e	Element frame attached to the first node of element and element frame basis vector
f	Force
$\bar{f}$	Beam force
g	Gravitational acceleration
h	Gyros spin angular momentum magnitude
i	General sub/super script
$\imath$	Microrotational inertia (microinertia) of elastic body

j General sub/super script

$\jmath$ Rotational inertia of gyro

k Correction factor

k_{s_2} Beam shear correction factor for bending parallel to second coordinate of beam frame

k_{s_3} Beam shear correction factor for bending parallel to third coordinate of beam frame

k_{t} Beam torsion correction factor

l Beam element length

m General matrix

m Moment

$\bar{m}$ Beam moment

n Outward normal unit vector

o Inertial frame and inertial frame basis vector

p Position of elastic body element

q Generalized coordinate

r Characteristic root

s General rotation screw axis (rotation axis unit vector)

s Shortened sine

s_z Sine of z

t Time

u Displacement

$\bar{u}$ Beam displacement

v General vector

w General angular velocity

$\dot{w}$ General angular acceleration

x General coordinate (axis)

y General variable (can be scalar, vector, tensor, or matrix)

z General variable (can be scalar, vector, tensor, or matrix)

F.3.8 Uppercase calligraphic letters

$\mathcal{A}$ Action integral (action functional)

$\mathcal{B}$ Tortile (torsional) bulk modulus

$\mathcal{C}$ Circulatory (operator)

$\mathcal{D}$ Damping (operator)

$\mathcal{E}$ Tortile (torsional) modulus

$\mathcal{F}$ Frame

$\mathcal{F}_a$ Frame a

$\mathcal{G}$ Gyricity or gyroscopic (operator)

$\mathcal{I}$ Elastic body angular momentum

$\dot{\mathcal{I}}$ Time derivative of $\mathcal{I}$ with respect to inertial frame

$\mathcal{J}$ Gyro total angular momentum

$\dot{\mathcal{J}}$ Time derivative of $\mathcal{J}$ with respect to inertial frame

$\mathcal{K}$ Stiffness (operator)

$\mathcal{L}$ Lagrangian function

$\mathcal{M}$ Mass (operator)

$\mathcal{Q}$ Generalized force

$\mathcal{R}$ Generalized moment

$\mathcal{T}$ Kinetic energy

$\mathcal{U}$ Potential energy

$\mathcal{U}_{\mathrm{e}}$ Elastic energy (total strain energy)

$\mathcal{W}$ Work

F.3.9 Uppercase Greek letters

Δ Variation

F.3.10 Lowercase Greek letters

α Micropolar (Cosserat) twist elastic constants

β Micropolar (Cosserat) twist elastic constants

γ Micropolar (Cosserat) twist elastic constants

δ Virtual

ϵ Levi-Civita (alternating or permutation) tensor

ϵ_{M} MATLAB® epsilon (or machine precision)

ε Strain

θ Macrorotation (classical rotation)

$\bar{\theta}$ Beam plane (section) rotation

ϑ General rotation angle

ϑ Microrotation (micropolar rotation)

$\bar{\vartheta}$ Beam microrotation

$\dot{\vartheta}$ Angular microrotational velocity

$\ddot{\vartheta}$	Angular microrotational acceleration
κ	Micropolar (Cosserat) coupling elastic constant (couple modulus)
λ	Lamé second elastic constants
μ	Lamé first elastic constants
μ	Shear modulus
ν	Strain Poisson's ratio
ξ	Twist Poisson's ratio
ρ	Translational inertia of elastic body
ϱ	Translational inertia of gyro
σ	Force stress
τ	Twist (wryness or torsion)
$\dot{\phi}$	Angular velocity of axis frame (gyro axis) with respect to body frame
$\ddot{\phi}$	Time derivative of $\dot{\phi}$ with respect to axis frame
φ_1	First rotation angle of gyro axis
φ_2	Second rotation angle of gyro axis
φ_3	Spin rotation angle of gyro wheel
$\mathring{\varphi}_{3\mathrm{T}}$	Total nondimensional gyricity spin rate
χ	Couple stress
$\dot{\psi}$	Angular velocity of gyro wheel with respect to axis frame
$\ddot{\psi}$	Time derivative of $\dot{\psi}$ with respect to axis frame
ω	Natural frequency

References

[1] GRIN. "Solar Power Satellite". URL: http://grin.hq.nasa.gov/ABSTRACTS/GPN-2003-00108.html, 1976. [Online; accessed 30-March-2010].

[2] G.M.T. D'Eleuterio. Dynamics of gyroelastic vehicles. Technical Report No. 300, Institute for Aerospace Studies (UTIAS), University of Toronto, Toronto, ON, Canada, 1986.

[3] NASA. "Explorer 1". URL: http://nssdc.gsfc.nasa.gov/nmc/masterCatalog.do?sc=1958-001A, 2009. [Online; accessed 12-April-2009].

[4] L. Meirovitch. A modal analysis for the response of linear gyroscopic systems. *Journal of Applied Mechanics, Transactions of the ASME, Series E-*, 42:446–450, 1975.

[5] L. Meirovitch and G. Ryland II. Response of slightly damped gyroscopic systems. *Journal of Sound and Vibration*, 67(1):1–19, 1979.

[6] L. Meirovitch and H. Oz. Modal-space control of distributed gyroscopic systems. *Journal of Guidance and Control*, 3(2):140–150, 1980.

[7] L. Meirovitch and H. Baruh. Optimal control of damped flexible gyroscopic systems. *Journal of Guidance and Control*, 4(2):157–163, 1981.

[8] P.W. Likins. Attitude stability criteria for dual spin spacecraft. *Journal of Spacecraft and Rockets*, 4(12):1638–1643, 1967.

[9] A.H. Gale and P.W. Likins. Influence of flexible appendages on dual-spin spacecraft dynamics and control. *Journal of Spacecraft and Rockets*, 7(9):1049–1056, 1970.

[10] D.B. Cherchas and P.C. Hughes. Attitude stability of a dual-spin satellite with a large flexible solar array. *Journal of Spacecraft and Rockets*, 10(2):126–132, 1973.

[11] P.C. Hughes. Dynamics of flexible space vehicles with active attitude control. *Journal of Celestial Mechanics and Dynamical Astronomy*, 9(1):21–39, 1974.

[12] P.C. Hughes and H.N. Sharpe. Influence of stored angular momentum on the modal characteristics of spacecraft with flexible appendages. *Journal of Applied Mechanics, Transactions of the ASME, Series E-*, 42:785–788, 1975.

[13] J.N. Aubrun and G. Margulies. Gyrodampers for large space structures. Technical Report No. 159171, National Aeronautics and Space Administration (NASA), Hampton, VA, United States, 1979. [NASA Contractor Report].

[14] H.B. Hablani and R.E. Skelton. Generic model of a large flexible space structure for control concept evaluation. In *19th AIAA Aerospace Sciences Meeting*, St. Louis, MO, USA, January 12-15 1981. AIAA Paper 81-0086.

[15] H.B. Hablani. Modal analysis of gyroscopic flexible spacecraft: A continuum approach. *Journal of Guidance, Control and Dynamics*, 5(5):448–457, 1982.

[16] G.M.T. D'Eleuterio and P.C. Hughes. Dynamics of gyroelastic continua. *Journal of Applied Mechanics, Transactions of the ASME*, 51(2):415–422, 1984.

[17] M. Lindroos. "Space Station 1984 — Big T Station". URL: http://www.astronautix.com/craft/span1984.htm, 2010. [Online; accessed 1-March-2010].

[18] L.S. Weisstein. Introduction and survey on continuum models for repetitive lattice structures. In *JPL Proceedings of the Workshop on Applications of Distributed System Theory to the Control of Large Space Structures*, pages 63–70, USA, 1983. See N83-36061 24-18.

[19] P.C. Hughes and G.M.T. D'Eleuterio. Modal parameter analysis of gyroelastic continua. *Journal of Applied Mechanics, Transactions of the ASME*, 53(4):918–924, 1986.

[20] G.M.T. D'Eleuterio and P.C. Hughes. General motion of gyroelastic vehicles in terms of constrained modes. In *Collection of Technical Papers, 26th AIAA/ASME/ASCE/AHS/ASC Structures, Structural Dynamics and Materials Conference*, number 2, pages 384–390, Orlando, FL, USA, April 15-17 1985.

[21] G.M.T. D'Eleuterio and P.C. Hughes. Dynamics of gyroelastic spacecraft. *Journal of Guidance, Control, and Dynamics*, 10(4):401–405, 1987.

[22] G.M.T. D'Eleuterio. On the theory of gyroelasticity. *Journal of Applied Mechanics, Transactions of the ASME*, 55(2):488–489, 1988.

[23] C.J. Damaren. An optimal control formulation for lightly damped gyroelastic continua. M.A.Sc. thesis, Department of Aerospace Science and Engineering, University of Toronto, Toronto, ON, Canada, 1987.

[24] C.J. Damaren and G.M.T. D'Eleuterio. Optimal control of large space structures using distributed gyricity. *Journal of Guidance, Control, and Dynamics*, 12(5):723–731, 1989.

[25] C.J. Damaren and G.M.T. D'Eleuterio. Controllability and observability of gyroelastic vehicles. *Journal of Guidance, Control, and Dynamics*, 14(5):886–894, 1991.

[26] C.J. Damaren. *Optimal control of large space structures using distributed gyricity: A continuum approach*. Ph.D. thesis, Department of Aerospace Science and Engineering, University of Toronto, Toronto, ON, Canada, 1990.

[27] K. Yamanaka, G.R. Heppler, and K. Huseyin. On the dynamics and stability of a beam with a tip rotor. In *Proceedings of the 35th AIAA/ASME/ASCE/AHS/ASC Structures, Structural Dynamics and Materials Conference*, pages 1031–1038, Hilton Head, SC, USA, April 18-20 1994.

[28] K. Yamanaka, G.R. Heppler, and K. Huseyin. The stability of a flexible link with a tip rotor and a compressive tip load. *IEEE Transactions on Robotics and Automation*, 11(6):882–887, 1995.

[29] O. Song, H.D. Kwon, and L. Librescu. Bending vibration of gyroelastic thin-walled beams incorporating adaptive capabilities. In *Proceedings of the 39th AIAA/ ASME/ASCE/AHS/ASC Structures, Structural Dynamics and Materials Conference and Exhibit, and AIAA/ASME Adaptive Structures Forum*, pages 2870–2880, Long Beach, CA, USA, April 20-23 1998.

[30] O. Song, H.D. Kwon, and L. Librescu. Modeling, vibration, and stability of elastically tailored composite thin-walled beams carrying a spinning tip rotor. *Journal of the Acoustical Society of America*, 110(2):877–886, 2001.

[31] O. Song, L. Librescu, and H.D. Kwon. Vibration and stability control of robotic manipulator systems consisting of a thin-walled beam and a spinning tip rotor. *Journal of Robotic Systems*, 19(10):469–82, 2002.

[32] L. Librescu and O. Song. *Thin-walled composite beams: theory and application*. Springer, Dordrecht, Netherlands, 2006.

[33] R.E. Zee and G.R. Heppler. Dynamics of gyroelastic beams. In *Proceedings of the 35th AIAA/ASME/ASCE/AHS/ASC Structures, Structural Dynamics and Materials Conference, AIAA/ASME Adaptive Structures Forum*, volume 2, pages 1048–1057, Hilton Head, SC, USA, April 18-20 1994.

[34] K. Yamanaka, G.R. Heppler, and K. Huseyin. Stability of gyroelastic beams. *AIAA Journal*, 34(6):1270–1278, 1996.

[35] M.A. Peck and A.R. Cavender. Structural tuning through embedded angular momentum. In *Collection of Technical Papers, 44th AIAA/ASME/ASCE/AHS/ASC Structures, Structural Dynamics, and Materials Conference*, volume 2, pages 1462–1469, Norfolk, VA, USA, April 7-10 2003.

[36] M.A. Peck and A.R. Cavender. Practicable gyroelastic technology. In *Proceedings of the 27th Annual AAS Guidance and Control Conference*, volume 118, pages 239–253, Breckenridge, CO, USA, February 4-8 2004.

[37] M. Brocato and G. Capriz. Gyrocontinua. *International Journal of Solids and Structures*, 38(6-7):1089–1103, 2001.

[38] C.L. Dym and I.H. Shames. *Solid mechanics: a variational approach*. McGraw-Hill, New York, NY, United States, 1973.

[39] S.P. Timoshenko and J.N. Goodier. *Theory of elasticity*. McGraw-Hill Book Company, New York, NY, United States, 1951.

[40] I.H. Shames. *Introduction to solid mechanics*. Prentice-Hall College Division, Englewood Cliffs, NJ, United States, 1989.

[41] F. Irgens. *Continuum mechanics*. Springer-Verlag Berlin Heidelberg, Berlin, Germany, 2008.

[42] W. Nowacki. *Theory of asymmetric elasticity (translated by H. Zorski)*. Polish Scientific Publishers (PWN) & Pergamon Press, Warsaw (Warszawa), Poland & Oxford, United Kingdom, 1986.

[43] R.D. Mindlin and H.F. Tiersten. Effects of couple-stresses in linear elasticity. *Archive for Rational Mechanics and Analysis*, 11(1):415–448, 1962.

[44] E. Shmoylova. *Boundary integral equation method in elasticity with microstructure*. Ph.D. thesis, Department of Civil Engineering, University of Waterloo, Waterloo, ON, Canada, 2006.

[45] D.J. Inman. *Vibration: with control, measurement, and stability*. Prentice-Hall, Englewood Cliffs, NJ, United States, 1989.

[46] Wikipedia contributors. "Principle of least action — Wikipedia, The Free Encyclopedia". URL: http://en.wikipedia.org/w/index.php?title=Principle_of_least_action&oldid=285977554, 2009. [Online; accessed 25-April-2009].

[47] M.D. Ardema. *Analytical dynamics: theory and applications*. Kluwer Academic/ Plenum Publishers (Springer), New York, NY, United States, 2005.

[48] S.P. Timoshenko. On the transverse vibrations of bars of uniform cross-section. *Philosophical Magazine Series 6*, 43(253):125–131, 1922.

[49] S. Ramezani, R. Naghdabadi, and S. Sohrabpour. Analysis of micropolar elastic beams. *European Journal of Mechanics-A/Solids*, 28(2):202–208, 2009.

[50] M.A. Jayaram. *Mechanics of materials with programs in C*. Prentice-Hall of India Private Limited, New Delhi, India, 2007.

[51] P.P. Benham. *Elementary mechanics of solids*. Pergamon Press, Oxford, United Kingdom, 1965.

[52] S.M. Han, H. Benaroya, and T. Wei. Dynamics of transversely vibrating beams using four engineering theories. *Journal of Sound and Vibration*, 225(5):935–988, 1999.

[53] D. Iesan. Torsion of micropolar elastic beams. *International Journal of Engineering Science*, 9(11):1047–1060, 1971.

[54] R.D. Gauthier and W.E. Jahsman. A quest for micropolar elastic constants. *Transactions of the ASME, Series E-Journal of Applied Mechanics*, 42(2):369–374, 1975.

[55] H.C. Park and R.S. Lakes. Torsion of a micropolar elastic prism of square cross-section. *International Journal of Solids and Structures*, 23(4):485–503, 1987.

[56] S. Potapenko and E. Shmoylova. Weak solutions of the problem of torsion of micropolar elastic beams. *Zeitschrift für Angewandte Mathematik und Physik (ZAMP)*, 61(3):529–536, 2010.

[57] R.D. Gauthier and W.E. Jahsman. Bending of a curved bar of micropolar elastic material. *Transactions of the ASME, Series E-Journal of Applied Mechanics*, 43(3):502–503, 1976.

[58] G.V.K. Reddy and N.K. Venkatasubramanian. On the flexural rigidity of a micropolar elastic cylinder. *Transactions of the ASME, Journal of Applied Mechanics*, 45(2):429–431, 1978.

[59] G.V.K. Reddy and N.K. Venkatasubramanian. On the flexural rigidity of a micropolar elastic circular cylindrical tube. *International Journal of Engineering Science*, 17(9):1015–1021, 1979.

[60] F.Y. Huang, B.H. Yan, J.L. Yan, and D.U. Yang. Bending analysis of micropolar elastic beam using a 3-d finite element method. *International Journal of Engineering Science*, 38(3):275–286, 2000.

[61] A.C. Eringen. Theory of micropolar plates. *Zeitschrift für Angewandte Mathematik und Physik (ZAMP)*, 18(1):12–30, 1967.

[62] R.W. Fox, A.T. McDonald, and P.J. Pritchard. *Introduction to fluid mechanics*. John Wiley & Sons, New York, NY, United States, 2004.

[63] K.J. Bathe. *Finite element procedures in engineering analysis*. Prentice-Hall, Upper Saddle River, NJ, United States, 1982.

[64] J.E.F. Guimaraes. On trigonometric basis functions for C^1 beam finite elements. M.A.Sc. thesis, Department of System Design Engineering, University of Waterloo, Waterloo, ON, Canada, 1990.

[65] R.D. Cook, D.S. Malkus, M.E. Plesha, and Witt R.J. *Concepts and applications of finite element analysis*. John Wiley & Sons, New York, NY, United States, 2002.

[66] *MATLAB*. 64-bit (win64), version 8.1.604 (R2013a). The MathWorks Inc., Natick, MA, United States, 2013. [Computer software].

[67] A. W. Leissa. On a curve veering aberration. *Zeitschrift für Angewandte Mathematik und Physik (ZAMP)*, 25(1):99–111, 1974.

[68] J.R. Kuttler and V.G. Sigillito. On curve veering. *Journal of Sound and Vibration*, 75(4):585–588, 1981.

[69] N.C. Perkins and C.D. Mote. Comments on curve veering in eigenvalue problems. *Journal of Sound and Vibration*, 106(3):451–463, 1986.

[70] C. Pierre. Mode localization and eigenvalue loci veering phenomena in disordered structures. *Journal of Sound and Vibration*, 126(3):485–502, 1988.

[71] J.F.C. Yang and R.S. Lakes. Experimental study of micropolar and couple stress elasticity in compact bone in bending. *Journal of Biomechanics*, 15(2):91–98, 1982.

[72] R.S. Lakes. *Continuum models for materials with microstructure (Edited by H.B. Mühlhaus)*, chapter Experimental methods for study of Cosserat elastic solids and other generalized elastic continua, pages 1–22. John Wiley & Sons, Chichester, United Kingdom, 1995.

[73] P. Neff. The cosserat couple modulus for continuous solids is zero viz the linearized cauchy-stress tensor is symmetric. *Zeitschrift für Angewandte Mathematik und Mechanik (ZAMM)*, 86(11):892–912, 2006.

[74] P. Neff. Relations of constants for isotropic linear cosserat elasticity. Technical Report No. AG6, Fachberiech Mathematik, Technische Universität Darmstadt, Darmstadt, Germany, 2008.

[75] R.D. Gauthier. *Mechanics of micropolar media (Edited by O. Brulin and R.K.T. Hsieh)*, chapter Experimental investigations on micropolar media, pages 395–463. World Scientific Publishing Co., Singapore, 1982.

[76] R. Mora and A.M. Waas. Measurement of the cosserat constant of circular-cell polycarbonate honeycomb. *Philosophical Magazine A*, 80(7):1699–1713, 2000.

[77] J. Chung and A.M. Waas. The micropolar elasticity constants of circular cell honeycombs. *Proceedings of the Royal Society A: Mathematical, Physical and Engineering Science*, 465(2101):25–39, 2009.

[78] R.S. Lakes. Experimental microelasticity of two porous solids. *International Journal of Solids and Structures*, 22(1):55–63, 1986.

[79] R.S. Lakes. "Cosserat Elasticity; micropolar elasticity". URL: http://silver.neep.wisc.edu/~lakes/Coss.html, 2003. [Online; accessed 20-February-2009].

[80] R.S. Lakes. Size effects and micromechanics of a porous solid. *Journal of Materials Science*, 18(9):2572–2580, 1983.

[81] R.S. Lakes. Experimental micro mechanics methods for conventional and negative poissons ratio cellular solids as cosserat continua. *Journal of Engineering Materials and Technology*, 113:148–155, 1991.

[82] W.B. Anderson and R.S. Lakes. Size effects due to cosserat elasticity and surface damage in closed-cell polymethacrylimide foam. *Journal of Materials Science*, 29(24):6413–6419, 1994.

[83] P. Neff. "Cosserat Theory". URL: http://www.mathematik.tu-darmstadt.de/fbereiche/analysis/pde/staff/neff/patrizio/Cosserat.html, 2009. [Online; accessed 11-June-2012].

[84] S.C. Cowin. Stress functions for cosserat elasticity. *International Journal of Solids and Structures*, 6(4):389–398, 1970.

[85] A.C. Eringen. Linear theory of micropolar elasticity. *Journal of Mathematics and Mechanics*, 15(6):909–923, 1966.

[86] S.C. Cowin. An incorrect inequality in micropolar elasticity theory. *Zeitschrift für Angewandte Mathematik und Physik (ZAMP)*, 21(3):494–497, 1970.

[87] R.S. Lakes. A pathological situation in micropolar elasticity. *Journal of Applied Mechanics*, 52:234–235, 1985.

[88] V. Chiroiu and L. Munteanu. Estimation of micropolar elastic moduli by inversion of vibrational data. *Complexity International Journal*, 9:16–25, 2002.

[89] O. Brulin. *Mechanics of micropolar media (Edited by O. Brulin and R.K.T. Hsieh)*, chapter Linear micropolar media, pages 87–145. World Scientific Publishing Co., Singapore, 1982.

[90] J. Jeong, H. Ramézani, I. Münch, and P. Neff. A numerical study for linear isotropic cosserat elasticity with conformally invariant curvature. *Zeitschrift für Angewandte Mathematik und Mechanik (ZAMM)*, 89(7):552–569, 2009.

[91] J. Jeong and P. Neff. Existence, uniqueness and stability in linear cosserat elasticity for weakest curvature conditions. *Mathematics and Mechanics of Solids*, 15(1):78–95, 2010.

[92] R.S. Lakes, S. Nakamura, J.C. Behiri, and W. Bonfield. Fracture mechanics of bone with short cracks. *Journal of Biomechanics*, 23(10):967–975, 1990.

[93] H.A. Erbay. An asymptotic theory of thin micropolar plates. *International Journal of Engineering Science*, 38(13):1497–1516, 2000.

[94] R.S. Lakes. Dynamical study of couple stress effects in human compact bone. *Journal of Biomechanical Engineering*, 104:6–11, 1982.

[95] P.C. Hughes. *Spacecraft attitude dynamics*. John Wiley & Sons, New York, NY, United States, 1986.

[96] L.W. Tsai. *Robot analysis: the mechanics of serial and parallel manipulators*. John Wiley & Sons, New York, NY, United States, 1999.

[97] J.J. Craig. *Introduction to robotics: mechanics and control*. Addison-Wesley Longman Publishing Co., Boston, MA, United States, 1989.

[98] O.A. Bauchau. *Flexible multibody dynamics*. Springer Science+Business Media, Houten, Netherlands, 2011.

[99] J.F. Shi and C.J. Damaren. Control law for active structural damping using a control moment gyro. *Journal of Guidance, Control and Dynamics*, 28(3):550–552, 2005.

[100] Y.W. Kwon and H. Bang. *The finite element method using MATLAB*. CRC Press, Boca Raton, FL, United States, 2000.

[101] P.G. Hodge. *Continuum mechanics*. McGraw-Hill, New York, NY, United States, 1970.